Experimental Characterization and Quantification of Cement-Bentonite Interaction using Core Infiltration Techniques Coupled with X-ray Tomography

Inauguraldissertation

der Philosophisch-naturwissenschaftlichen Fakultät

der Universität Bern

vorgelegt von

Florian D. Dolder

von Kilchberg ZH

Leiter der Arbeit:

PD Dr. U. Mäder & Dr. A. Jenni

Institut für Geologie

10. September 2015

Experimental Characterization and Quantification of Cement-Bentonite Interaction using Core Infiltration Techniques Coupled with X-ray Tomography

Inauguraldissertation

der Philosophisch-naturwissenschaftlichen Fakultät

der Universität Bern

vorgelegt von

Florian D. Dolder

von Kilchberg ZH

Leiter der Arbeit:

PD Dr. U. Mäder & Dr. A. Jenni

Institut für Geologie

Von der Philosophischen-naturwissenschaftlichen Fakultät angenommen.

Bern, den 10. September 2015 *Der Dekan*

Prof. Dr. Gilberto Colangelo

Urheberrechtlicher Hinweis

„Und sie laufen! Naß und nässer
wirds im Saal und auf den Stufen.
Welch entsetzliches Gewässer!
Herr und Meister! hör mich rufen! -
Ach, da kommt der Meister!
Herr, die Not ist groß!
Die ich rief, die Geister
werd ich nun nicht los.“

Der Zauberlehrling von Johann Wolfgang von Goethe

Abstract

Deep geological storage of radioactive waste foresees cementitious materials as reinforcement of tunnels and as backfill. Bentonite is proposed to enclose spent fuel canisters and as drift seals. Sand/bentonite (s/b) is foreseen as backfill material of access galleries or as drift seals. The emplacement of cementitious material next to clay material generates an enormous chemical gradient in pore-water composition that drives diffusive solute transport. Laboratory studies and reactive transport modeling predicted significant mineral alteration at and near interfaces, mainly resulting in a decrease of porosity in bentonite.

The goal of this thesis was to characterize and quantify the cement/bentonite interactions both spatially and temporally in laboratory experiments. A newly developed mobile X-ray transparent core infiltration device was used to perform X-ray computed tomography (CT) scans without interruption of running experiments. CT scans allowed tracking the evolution of the reaction plume and changes in core volume/diameter/density during the experiments.

In total 4 core infiltration experiments were carried out for this study with the compacted and saturated cores consisting of MX-80 bentonite and sand/MX-80 bentonite mixture (s/b; 65/35%). Two different high-pH cementitious pore-fluids were infiltrated: a young (early) ordinary Portland cement pore-fluid (APW_{OPC}; K^+–Na^+–OH^-; pH 13.4; ionic strength 0.28 mol/kg) and a young 'low-pH' ESDRED shotcrete pore-fluid (APW_{ESDRED}; Ca^{2+}–Na^+–K^+–formate; pH 11.4; ionic strength 0.11 mol/kg). The experiments lasted between 1 and 2 years.

In both bentonite experiments, the hydraulic conductivity was strongly reduced after switching to high-pH fluids, changing eventually from an advective to a diffusion-dominated transport regime. The reduction was mainly induced by mineral precipitation and possibly partly also by high ionic strength pore-fluids. Both bentonite cores showed a volume reduction and a resulting transient flow in which pore-water was squeezed out during high-pH infiltration. The outflow chemistry was characterized by a high ionic strength, while chloride in the initial pore water got replaced as main anionic charge carrier by sulfate, originating from gypsum dissolution. The chemistry of the high-pH fluids got strongly buffered by the bentonite, consuming hydroxide and in case of APW_{ESDRED} also formate. Hydroxide got consumed by mineral reactions (saponite and possibly talc and brucite precipitation), while formate being affected by bacterial degradation. Post-mortem analysis showed reaction zones near the inlet of the bentonite core, characterized by calcium and magnesium enrichment, consisting predominately of calcite and saponite, respectively. Silica got enriched in the outflow, indicating dissolution of silicate-minerals, identified as preferentially cristobalite.

In s/b, infiltration of APW_{OPC} reduced the hydraulic conductivity strongly, while APW_{ESDRED} infiltration had no effect. The reduction was mainly induced by mineral precipitation and probably partly also by high ionic strength pore-fluids. Not clear is why the observed mineral precipitates in the APW_{ESDRED} experiment had no effect on the fluid flow. Both s/b cores showed a volume expansion along with decreasing ionic strengths of the outflow, due to mineral reactions or in case of APW_{ESDRED} infiltration also mediated by microbiological activity, consuming hydroxide and formate, respectively. The chemistry of the high-pH fluids got strongly buffered by the s/b. In the case of APW_{ESDRED} infiltration, formate reached the outflow only for a short time, followed by enrichment in acetate, indicating most likely biological activity. This was in agreement to post-mortem analysis of the core, observing black spots on the inflow surface, while the sample had a rotten-egg smell indicative of some sulfate reduction. Post-mortem analysis showed further in both cores a Ca-enrichment in the first 10 mm of the core due to calcite precipitation. Mg-enrichment was only observed in the APW_{OPC} experiment, originating from newly formed saponite. Silica got enriched in the outflow of both experiments, indicating dissolution of silicate-minerals, identified in the OPC experiment as cristobalite.

The experiments attested an effective buffering capacity for bentonite and s/b; a progressing coupled hydraulic-chemical sealing process and also the preservation of the physical integrity of the interface region in this setup with a total pressure boundary condition on the core sample. No complete pore-clogging was observed but the hydraulic conductivity got rather strongly reduced in 3 experiments, explained by clogging of the intergranular porosity (macroporosity). Such a drop in hydraulic conductivity may impact the saturation time of the buffer in a nuclear waste repository, although the processes and geometry will be more complex in repository situation.

Danksagung

Einen riesen Dank gehört meinen beiden Betreuern Urs und Ändu für das interessante und spannende Projekt, sowie die schöne Zeit, die wir zusammen an Universität und Kongressen hatten. Ein besonderes Vergnügen war es mir, in unserem Daniel Düsentrieb Labor (Bunker) zu walten, zu basteln und zu musizieren, was ich sicherlich in Zukunft vermissen werde.

Einen grossen Dank an allen MitarbeiterInnen des Geologischen Institutes für die tolle Zeit, die wir zusammen in Bern hatten. Einen grossen Dank an all die geleisteten Arbeiten, die mich auf meinem Weg zu dem Doktorat weitergebracht haben.

Danke Chrigi, Sam und Nicolas, für die tolle Zeit die wir zusammen hier in Bern hatten. Auch einen grossen Dank an meine Bürokollegen (216), für die interessante Zeit die wir zusammen hatten. Ohne Euch alle hätte das Doktorat nie so viel Spass gemacht! Ich möchte mich ganz herzlichst beim Laborpersonal bedanken, die für mich unzählige Analysen durchgeführt haben. Einen besonderen Dank gilt Chrigi, die mich bei XRD Messungen tatkräftig unterstützt hat. Auch essentiell für meine Arbeit waren die vielen geochemischen Analysen, die von Priska, Stefan und Gisela durchgeführt wurden. Danke für die tatkräftige Hilfe, die Unterstützung und die Geduld und Nachsicht, wenn ich wieder mal als Geist im Labor mein Unwesen getrieben habe. Nicht zu vergessen sind die beiden entsprechenden Laborverantwortlichen Urs Eggenberger und Nick Waber, die mir immer bei Unklarheiten und Problem zur Seite standen, wobei ich mich an dieser Stelle für den ganzen Kaffee bedanken möchte, den ich Dank Urs Kaffeemaschine im Tonlabor geniessen durfte.

Ein herzlicher Dank gilt auch dem ganzen technischen Personal aus Werkstatt und Dünnschliffpräparation. Danke Nadine, Adrian, Dänu, Stephan, Thomas A. und Thomas, S. für all die geleistete Arbeit und das sich Rumschlagen mit Bentonite. Auch nicht zu vergessen ist Nicole vom Forensischen Institut, mit der ich viele Stunden im CT verbracht habe und die neben ihren ‚Patienten' immer noch Zeit für meine Experimente hatte. Einen speziellen Dank geht auch an Sarah, Barbara und Sigrid vom Sekretariat und Uli und Werner vom Informatikdienst. Weiter einen grossen Dank an unsere Gesteins-Wasser Interaktionsgruppe und all die netten und guten Seelen des geologischen Institutes, die mit mir diese tolle Zeit verbrachte haben. Weiter möchte ich mich bei Barbara Lothenbach und Beat Münch von der EMPA für die Zusammenarbeit und Hilfe im Bereich Zementchemie respektive Bildverarbeitung bedanken.

Einen ganz herzlichen Dank gehört auch dem Geldgeber, der Nationale Genossenschaft für die Lagerung radioaktiver Abfälle (NAGRA), die mir dieses Projekt finanziell ermöglicht hat. Im speziellen möchte ich mich bei Oli und Veerle bedanken, für all die geleisteten Arbeiten und im Speziellen für die vielen Inputs.

Den grössten Dank aber gehört meinen Eltern, die mir all das ermöglicht haben, ohne dass ich nicht diese schöne Arbeit hätte schreiben können. Auch einen ganz grossen Dank an meinen Bruder und seine Frau Kathrin, sowie an die beiden Knirpse Lars und Jan, die mich immer unterstützt und zum Lachen gebracht haben. Auch einen ganz grossen Dank an meine Freundin Maartje, die mich in schwierigen Zeiten immer unterstützt und ertragen hat.

Table of Contents

Abstract vii

Danksagung ix

Table of Contents xi

1 Introduction 1

- 1.1. Nuclear waste disposal 1
- 1.2. Bentonite 2
- 1.3. Cement, concrete, shotcrete 4
- 1.4. Cement–clay interaction 4
- 1.5. Natural analogues, laboratory experiments and modeling 5
- 1.6. Aims 7
- 1.7. Structure of the thesis 7

2 Core Infiltration Experiment 11

- 2.1. Introduction 11
- 2.2. Core production (pre-treatment device) 11
- 2.3. Core infiltration device 13
- 2.4. Artificial pore-waters (APW) 21

3 X-ray Computed Tomography (CT) 25

- 3.1. Introduction 25
- 3.2. Medical CT scanners 26
- 3.3. CT scans 27
  - 3.3.1. Software 27
  - 3.3.2. Reference material sample 27
  - 3.3.3. CT scans of the experiments 28

4 Experimental characterization of cement-bentonite interaction using core infiltration techniques and 4D computed tomography 31

- 4.1. Introduction 33
- 4.2. Materials and methods 35
  - 4.2.1. Bentonite starting material and pre-treatment 35
  - 4.2.2. Core Infiltration Experiment 35
  - 4.2.3. The high-pH fluid (APW$_{OPC}$) 37
  - 4.2.4. Analytical methods 37
- 4.3. Results 38
  - 4.3.1. Core Infiltration Experiment 38
  - 4.3.2. Computed Tomography 39
- 4.4. Discussion 41
  - 4.4.1. Core Infiltration Experiment 41
  - 4.4.2. Computed Tomography 42
- 4.5. Conclusions 44

5 Alteration of MX-80 bentonite backfill material by high-pH cementitious fluids under lithostatic conditions – An experimental approach using core infiltration techniques 49
5.1. Introduction 51
5.2. Methods and material 51
5.2.1. Core infiltration experiment 51
5.2.2. Analytical methods 52
5.2.3. Aqueous geochemical modeling 53
5.2.4. Starting material 53
5.2.5. Saturation fluid 54
5.3. Results 55
5.3.1. Hydraulic evolution of the experiment 55
5.3.2. Chemical evolution of the outflow 56
5.3.3. Physical evolution: Computed tomography (CT) 57
5.3.4. Post-mortem analysis: physical parameters 60
5.3.5. XRD analysis 61
5.3.6. Microscopy and SEM/EDX analysis 63
5.3.7. Raman spectroscopy 69
5.4. Discussion 69
5.4.1. Equilibration phase 69
5.4.2. High-pH infiltration phase 70
5.5. Conclusion 75
6 Alteration of MX-80 bentonite by ‘low-pH’ shotcrete (ESDRED) fluids – An experimental approach using core infiltration techniques 79
6.1. Introduction 80
6.2. Methods and material 81
6.2.1. Core infiltration experiment 81
6.2.2. Analytical methods 81
6.2.3. Aqueous geochemical modeling 82
6.2.4. Starting material and saturation and equilibration fluids ($APW_{Äspö}$ & APW_{OPA}) 82
6.2.5. The ’low-pH’ artificial pore-water (APW_{ESDRED}) 83
6.3. Results 84
6.3.1. Physical and hydraulic evolution of the experiment 84
6.3.2. Chemical evolution of the outflow 85
6.3.3. Computed tomography (CT) 87
6.3.4. Post-mortem analysis: physical parameters 89
6.3.5. XRD analysis 89
6.3.6. Microscopy and SEM/EDX analysis 90
6.3.7. Raman spectroscopy 94

6.4. Discussion 95

6.4.1. The equilibration phase 95

6.4.2. The APW_{ESDRED} infiltration phase 96

6.5. Conclusion 100

7 Alteration of sand/bentonite backfill material by high-pH cementitious fluids – An experimental approach using core infiltration techniques 105

7.1. Introduction 106

7.2. Methods and Materials 107

7.2.1. Core infiltration experiment 107

7.2.2. Analytical methods 107

7.2.3. Starting material 108

7.2.4. Saturation and infiltration fluids 108

7.3. Results 109

7.3.1. Aqueous extracts 109

7.3.2. Hydraulic evolution of the experiment 110

7.3.3. Chemical evolution of the outflow 111

7.3.4. Computed tomography (CT) 114

7.3.5. Post-mortem analysis: physical parameters 116

7.3.6. XRD analysis 117

7.3.7. Microscopy and SEM/EDX analysis 119

7.3.8. Raman Spectroscopy 124

7.4. Discussion 124

7.4.1. Equilibration phase 125

7.4.2. High-pH infiltration phase 127

7.5. Conclusions 131

8 Alteration of sand/bentonite backfill material by 'low-pH' shotcrete (ESDRED) fluid – An experimental approach using core infiltration techniques 135

8.1. Introduction 136

8.2. Methods and material 136

8.1.1. Core infiltration experiment 136

8.1.2. Analytical methods 137

8.1.3. Starting material and pre-treatment 137

8.1.4. The infiltration fluids ($APW_{Äspö}$, APW_{OPA} and APW_{ESDRED}) 138

8.2. Results 139

8.2.1. Physical and hydraulic evolution of the experiment 139

8.2.2. Chemical evolution of the outflow 141

8.2.3. Computed tomography (CT) 143

8.2.4. Post-mortem analysis: physical parameters 145

8.2.5. XRD analysis 146

8.2.6. Microscopy and SEM/EDX analysis 147

8.2.7. Raman spectroscopy 152

8.3. Discussion 152

8.3.1. Equilibration phase 152

8.3.2. High-pH (APW_{ESDRED}) infiltration 153

8.4. Conclusion 156

9 Scoping calculation: reproducing experimental data of the ordinary Portland cement fluid/bentonite experiment using the reactive transport code CrunchFlow 159

9.1. Introduction 160

9.2. Code properties 161

9.3. Thermodynamic and kinetic data 161

9.4. Initial conditions 164

9.5. Results and Discussion 165

9.6. Conclusions 168

10 Conclusions 172

11 Appendices 178

11.1. X-ray Computed Tomography (CT) – density calculations 179

11.2. Tables 182

11.3. CrunchFlow script 209

12 Curriculum Vitae 211

1 Introduction

Early in the last century, the discovery of radioactivity by Mrs. and Mr. Curie was the beginning of a new age, the era of nuclear technology. The ability to control and make use of natural and artificially induced radioactivity was a big step forward for our society. Radioactive materials are used for various purposes in industry, research, and medicine: radiation therapy, measurements (e.g. moisture content, density, and thickness), luminous paints, radioactive chemicals, and nuclear power production.

The discovery and finally the use of nuclear technologies opened also Pandora's box, passing a point of no return. Radioactive waste puts at risk man and environment due to ionizing radiation. During the last 120 years various approaches were used to dispose radioactive wastes such as abandoned mines or dumping into the sea. In the last 40 years things changed and society became aware of the implication of a careless handling of radioactive waste, and that a more sustainable solution to the problem was required.

In 1957, the International Atomic Energy Agency (IAEA) was established as autonomous organization of the United Nations (UN), for the peaceful use of nuclear technology and nuclear power as well as for the safe storage of nuclear waste (IAEA, 2003, 2004). The IAEA provides international safeguard against misuse of nuclear technology/material and promotes security standards (IAEA, 2015).

1.1. Nuclear waste disposal

Based on an international disposal consensus (IAEA, 2003) disposal of radioactive waste in geological repositories is the best option. Host rock and an engineered barrier system (EBS) attenuate radionuclide release to the biosphere (e.g. Nagra, 2002). Various rock formations were investigated and analyzed for their properties and suitability to store nuclear waste. Three types of lithologies are currently of main interest for such a purpose: salt and clay formations, and igneous rocks (granitic or gneissic rocks). In Switzerland, a clay formation called Opalinus Clay (OPA) is proposed to host an underground repository for spent fuel and high-level nuclear waste (SF/HLW) (Nagra, 2002). OPA is a Jurassic clay formation, consisting mainly of clay minerals with amounts of quartz, feldspar, and calcite (Nagra, 2002).

In the reference case the EBS consists for SF/HLW of steel canisters, bentonite buffer and in case of HLW of a glass matrix (Nagra, 2002) (see Figure 1-1). For L/ILW the EBS consists of a cementitious matrix and a cementitious or steel emplacement container or buffer. Bentonite seals and concrete plugs are closing the emplacement tunnels for SF/HLW and L/ILW, respectively (see Figure 1-1; Nagra (2002)). Sand/bentonite (s/b) will be used as backfill material for access, operation and construction tunnels (Nagra, 2002). In the current work, the word 'buffer' is used for material enclosing the nuclear waste in the emplacement tunnels while the word 'backfill' is related to backfill material of access and operation tunnels. The technical requirements for the buffer and backfill are: a low hydraulic conductivity/permeability; a self-sealing ability; and durability of properties (Nagra, 2002). The low hydraulic conductivity of the saturated buffer should prevent advective flow, retard radionuclide transport and the self-sealing ability should close possible cracks in the buffer (Nagra, 2002).

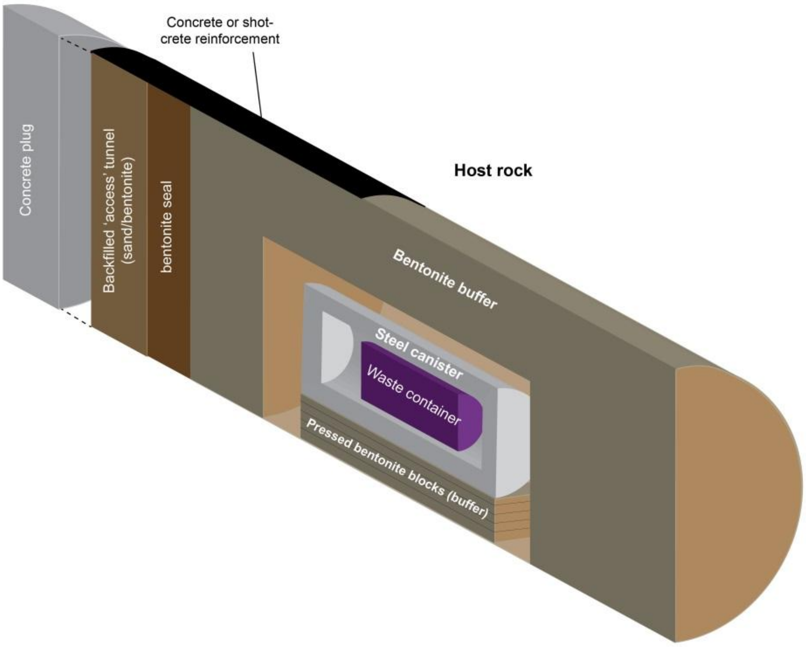

Figure 1-1: Schematic of a possible Nagra storage concept for SF/HLW after Nagra (2002).

1.2. Bentonite

Bentonite is a clay-based rock, formed either by diagenetic or hydrothermal alteration of volcanic glass or by dissolution of detrital smectites (Christidis and Huff, 2009). The most common bentonite deposits like the North American Wyoming bentonite (MX-80) are formed by alteration of pyroclastic rocks (Christidis and Huff, 2009). The rock is named after the Benton shale formation in Wyoming, USA. Bentonite consists predominantly of smectite group clay minerals like montmorillonite and of minor amounts of illite, quartz, mica, cristobalite, feldspar, pyrite, calcite, and gypsum (Figure 2–3).

Montmorillonite is a smectite group clay and a hydrous aluminum phyllosilicate mineral (sheet silicate). It is a 2:1 layer clay with 2 tetrahedral sheets and one sandwiched octahedral sheet (Güven, 2009). In the case of montmorillonite, a dioctahedral smectite, the tetrahedral layers consist mainly of silica and minor alumina, the octahedral layer of alumina, magnesium, iron, and titanium. The interlayer, situated between two T-O-T layers, can be filled with various amounts of sodium, calcium, magnesium, potassium as well as water (Figure 1-2) (Karnland et al., 2006; Newman and Brown, 1987). The characteristics of montmorillonite are the sheet-like structure, large surface area, significant negative layer charge, and associated counter-balancing exchangeable surface cations (Güven, 2009). The negative surface charge origins from charge defects in the clay lattice whereby ions of lower charge are incorporated (Glaus et al., 2010).

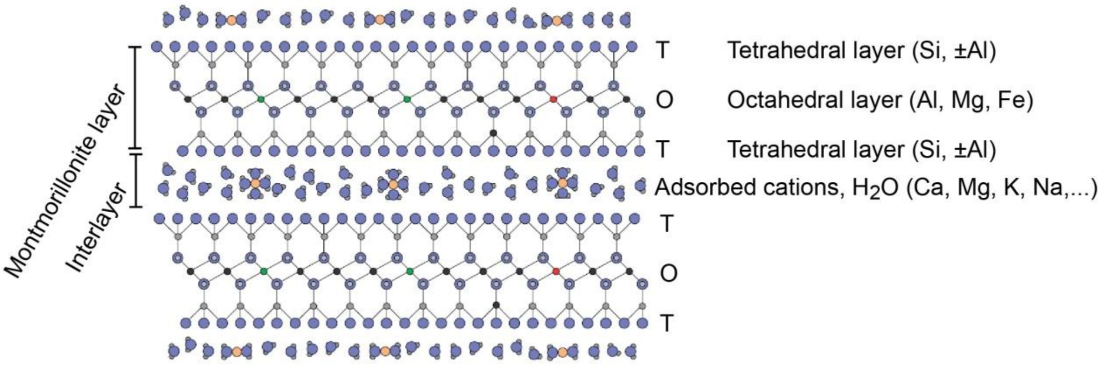

Figure 1-2: Sketch of the montmorillonite lattice structure modified after Karnland et al. (2006).

Bentonites have important physical and chemical properties, including high capacity for ion exchange, colloidal properties, and hydration and swelling behavior (Christidis and Huff, 2009).

Porosity (void fraction) is the space available for water. In compacted and saturated bentonite, the physical porosity (total porosity) can be divided into internal (interlayer or microporosity; including diffuse layer) and external porosity (intergranular, free-water, bulk water, flow-active, mobile, macroporosity) (Pusch et al. 1990; Pearson, 1999; Bradbury and Baeyens, 2003). Simplified, 3 water types can be distinguished in bentonite: interlayer water, diffuse layer (DL) water, and bulk free water (Bradbury and Baeyens, 2003). Interlayer water refers to water between the T-O-T layers of the montmorillonite in the internal (interlayer) porosity and it is characterized by strong anion exclusion, while cations charge balance the charge deficit of the clay layers. The water in the vicinity of the charged surfaces, occurring in a transition zone between interlayer water and bulk water, is called diffuse layer (DL), diffuse double-layer (DDL) or electrostatic double-layer (EDL) water. It contains cations and anions with an excess of cations present due to the negative surface charge. The DL is counted as interlayer (internal, bound) water in a simplified two-porosity concept used in this work. The bulk water is charge-balanced and in case of a high bentonite density, the only water fraction readily accessible for anions. The bulk water corresponds to the pore-water of the bentonite, occurring in the intergranular (external) porosity. The porosity determined by drying at 105°C in the oven, corresponds to near the total porosity of bentonite. The apparent transport porosity for water is determined by δ^2H or tritiated tracer tests. The anion-accessible porosity or flow-active porosity corresponds to the intergranular (external) porosity, accessible for anions, which is smaller compared to the bulk water. Advection takes place only in the macroporosity (intergranular porosity, anion-accessible porosity), while diffusion occurs in the total porosity. In case of clogging of the macroporosity (intergranular porosity), the diffusive transport in the microporosity (interlayer porosity) will be the dominant transport mechanism.

Several swelling process can be distinguished in bentonite: crystalline swelling occurs between montmorillonite layers in the interlayer (internal) porosity, diffuse double-layer swelling in the DL of the intergranular porosity, co-volume swelling, and Brownian swelling (Herbert et al., 2008; Laird, 2006). The swelling process is induced by osmosis between the interlayer water and DL water and bulk water (Figure 1-3), transporting water and/or ions to reach equal chemical potentials (Bradbury and Baeyens, 2003; Glaus et al., 2010; Karnland et al., 2006; Tournassat and Appelo, 2011). Low ionic strength solutions induce strong montmorillonite swelling by transporting pore-water into the interlayer and the DL.

At high temperature (beyond 100°C) smectite becomes unstable and transforms to more stable silicate phases like illite/smectite mixed layers (I/S), illite, chlorite, micas and zeolites (Birgersson et al., 2014; Wersin et al., 2007).

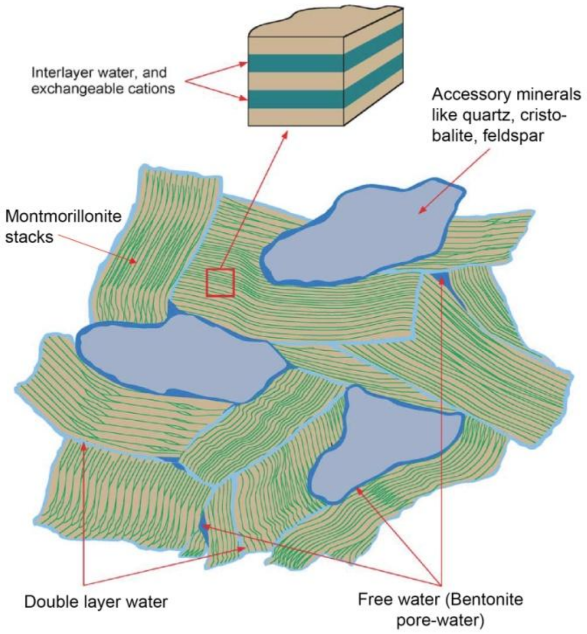

Figure 1-3: Sketch of compacted bentonite and its water pools, modified after Bradbury and Baeyens (2003).

1.3. Cement, concrete, shotcrete

Hydraulic cement like ordinary Portland cement (OPA) is a binder material consisting of ground clinker, a mixture of silicate and oxide minerals (alite (Ca_3SiO_5); belite (Ca_2SiO_4); tricalcium aluminate ($Ca_3Al_2O_6$); tetracalcium aluminoferrite ($Ca_2(Al, Fe)_2O_5$)), and some additives like gypsum powder. OPC hardens by hydration, consuming water and forming hydroxide minerals like portlandite, ettringite and C–(A)–S–H phases (calcium-(aluminum-)silicate hydrates). During the hydration phase of cement (initially the pH is ~13.5), which lasts for several months to years, the pore-fluids are dominated by alkaline and hydroxide ions (also called young cement pore-fluids). Once sodium and potassium hydroxides are leached, portlandite dissolution is controlling the pH at ~12.6. After consumption of portlandite, the pH is controlled by C–S–H dissolution at pH 10–12.6 (mature cement pore-fluids) (Adenot and Buil, 1992; Atkins et al., 1992; Faucon et al., 1998; Glasser and Atkins, 1994; Lovera et al., 1997).

'Low-pH' or low-alkali cements/shotcretes should optimally exhibit an initial pore-water close to pH 11 (Lothenbach et al., 2013). This is achieved by substituting parts of the OPC cement by reactive fly ash, silica fume or granulated blast furnace slag (García Calvo et al., 2010; Lothenbach et al., 2013; Lothenbach et al., 2011). The reduction in OPC reduces the amount of alkali ions as well as portlandite, the major source of hydroxide. The high silica content of this blend consumes portlandite by the pozzolanic reaction and forming C–S–H (portlandite + silica-acid = C–S–H). In contact with formation-water this blend shows much lower alkali and hydroxide concentration in the pore-water; pH is controlled by the C–S–H dissolution reaction. The use of SiO_2-rich blends modifies significantly the cement properties, its rheology in particular. For this purpose special chemicals have to be added, namely superplasticizer and accelerators (in the case of shotcrete applications). The notation of the word 'low-pH' with apostrophes should point out, that the pH of these low-pH solutions is in fact still a high-pH. But in contrast to OPC pore-fluids, it is rather a low-pH.

- *Concrete* is a composite material composed of cement (binder), aggregate (sand, gravel), water and possibly some additives (chemicals).
- *Shotcrete* is a special kind of concrete, which can be sprayed onto walls. It has initially a lower viscosity due to additives (superplasticizer).

In the current project two different cementitious pore-fluids are used for the core infiltration experiments: an ordinary Portland cement (OPC) pore-fluid and a 'low-pH' shotcrete type blended cement pore-fluid called ESDRED (Engineering Studies and Demonstrations of Repository Designs), named after the European Union Project that funded its development (Alonso et al., 2009; Bäckblom, 2007).

1.4. Cement–clay interaction

The long-term behavior of clay buffers in geological underground repositories is of great importance for nuclear waste storage and a subject of ongoing research. The main requirement for the EBS is longevity, which is influenced by external and internal processes, altering the chemical-physical-mechanical properties. The close coupling between chemical, physical and mechanical processes in bentonite (e.g., pore-water chemistry–swelling pressure) is of great importance in understanding and predicting its behavior. The EBS will be saturated by pore-water from the surrounding host rock over a period of several decades. By saturating the bentonite buffer, the smectite will swell, sealing the system and inhibiting advective transport (Figure 1-1).

The use of cement/shotcrete in the current Swiss concept for nuclear waste storage is foreseen as reinforcement of galleries, as backfill material for L/ILW, and as tunnel seals (Nagra, 2002). Inflowing water from the host-rock may pass cementitious materials like shotcrete liners or concrete plugs, leaching cement minerals. This generates in an early stage of a repository a hyperalkaline fluid, in equilibrium with the cementitious mineral assemblage, consisting during the hydration phase predominantly of portlandite, ettringite, and C–S–H. These fluids will be strongly enriched in alkaline elements (potassium, sodium) and hydroxide (high-pH), inducing a high-pH reaction plume in the clay buffer. In the reaction zone mineral and porosity alteration may occur, changing the physical-chemical-mechanical properties of the buffer material as well as of the cement (Figure 1-4).

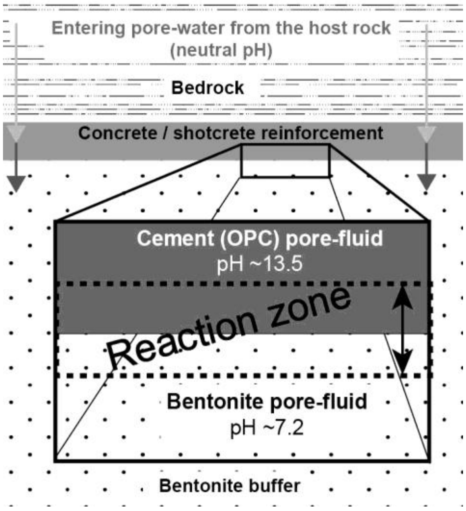

Figure 1-4: Cement–bentonite interaction: hyperalkaline reaction plume in the bentonite buffer.

1.5. Natural analogues, laboratory experiments and modeling

The long-term influence (>1000s of years) of hyperalkaline fluids (pH 12.5 – 12.8) penetrating clay-bearing limestone along fracture systems was studied at the natural analogue site near Maqarin, Jordan (Khoury et al., 1992; Pitty et al., 2011; Smellie, 1998). It was shown that such fluids can modify the existing mineral assemblage by dissolution of clay minerals and precipitation of ettringite, calcite and C–S–H phases (Ca-silicate-hydrates), among other phases (Smellie, 1998). This alteration may proceed until the pore-space in the adjacent rock matrix becomes completely clogged, or flow in the fracture becomes blocked or inactive. The sealing ability of a clayey EBS in a deep geological repository is a fundamental function and has to be guaranteed for thousands of years. Over the past decades various studies were done on clay stability under alkaline perturbation. In a recent summary, Gaucher and Blanc (2006) distinguished five main reaction processes for smectite-type clays, a major component in bentonite:

I. Modification of the adsorbed cations on clay minerals. A clay originally enriched in sodium becomes more potassium and calcium enriched over time (Bauer and Berger, 1998; Bouchet et al., 2004; Karnland et al., 2007; Mosser-Ruck and Cathelineau, 2004; Ramirez et al., 2002a).
II. Dissolution of clay (smectite, illite) minerals is localized at the interface where the high pH front is buffered (Bauer and Berger, 1998; Bauer and Velde, 1999; Bouchet et al., 2004; De La Villa et al., 2001; Eberl et al., 1993; Fernández et al., 2006; Fernández et al., 2009a; Fernández et al., 2013; Huertas et al., 2004; Nakayama et al., 2004; Ramirez et al., 2002a; Sánchez et al., 2006).
III. Dissolution of accessory minerals like quartz, cristobalite, feldspar, plagioclase, gypsum and calcite are important with respect to pH buffering and ionic strength of the pore water. The dissolution of silicate minerals leads to the formation of zeolites (phillipsite and analcime), C–(A)–S–H phases (Ca–Al–silicate–hydrates), saponite or hydrotalcite (Bauer and Berger, 1998; Bouchet et al., 2004; Claret et al., 2002; Cuevas et al., 2006; De La Villa et al., 2001; Fernández et al., 2006; Fernández et al., 2009a; Fernández et al., 2010a; Fernández et al., 2013; Huertas et al., 2004; Karnland, 1997; Karnland et al., 2007; Nakayama et al., 2004; Ramirez et al., 2002a; Sánchez et al., 2006; Savage et al., 2007).
IV. The role of pCO_2 in the system is important with respect to the chemical evolution of the system, due to its buffering capacity.
V. The heterogeneous distribution of newly formed minerals in the bentonite affects the evolution of the pH gradient.

Of direct interest are the results of experiments at high-pH conditions using FEBEX bentonite (Spain) and MX-80 bentonite (USA).

Eberl et al. (1993) showed a collapse of expandable smectite layers (montmorillonite) in MX-80 bentonite by formation of illite and I/S (up to 25 %) under influence of K–Na–OH solution at 35°C. Karnland (1997) performed experiments on compacted MX-80 bentonite using hydrothermal percolation and diffusion cells at 40°C. He could show that alkali-chloride based fluids did not alter the bentonite significantly. Alkali-hydroxide based fluids show weak alteration of the bentonite by cristobalite dissolution and precipitation of C–S–H (or calcite), chlorite (?), but no zeolites. Further, a decrease in swelling pressure was observed, inducing a higher hydraulic conductivity. Bauer and Berger (1998) performed experiments on smectite using batch reactors at 35° and 80°C. The K–OH based solution altered mineralogy by dissolution of tetrahedral and octahedral sheets in smectite; increasing the illite content up to 40%. Further precipitation of mica, zeolites, K-feldspar and quartz were observed. In case of Ca was available, precipitation of C–S–H and hydrogarnet was observed. De La Villa et al. (2001) observed the formation of phillipsite, analcime, rodesite and smectite by dissolution of volcanic glass (obsidian) in Na–K–Ca–OH solutions (pH >11.6 at 35–60°C) using FEBEX bentonite and pure montmorillonite (<2 µm). Ramirez et al. (2002a) examined the stability of FEBEX bentonite in a Na–K–Ca–OH solution (pH <12.6 at 30–90°C). The dissolution of silica minerals started at pH >12.6, and it could be accelerated by increasing temperature. In a hyperalkaline sodic solution (pH 13.5) a formation of phillipsite was observed. By increasing the temperature to 90°C, the precipitation of zeolites, C–S–H phases and Mg-smectite appeared. Furthermore, the dissolution of the primary mineral assemblage was observed whereas illitisation was found to be of minor importance. An ion-exchange of magnesium and sodium by calcium and potassium was also reported, forming a new Mg-silicate phase. The Mg-enrichment was reported to take place in the <0.5 µm fraction, which is related to smectite; most likely forming trioctahedral Mg-smectite as well as beidellite. Pusch et al. (2003) reported for batch experiments using Friedland Ton, increased temperatures and KOH–NaOH–$Ca(OH)_2$ fluids the interstratifications of I/S when the solution was K^+-rich. Uptake of magnesium in the montmorillonite lattice yielded the smectite species saponite. Further they reported the drop in hydraulic conductivity while smectite gets dissolved at the interface releasing silica, aluminum and magnesium. Huertas et al. (2004) performed flow-through experiments on FEBEX bentonite at 25°, 50°, and 70°C. The smectite dissolution rate was reported to be strongly depended on the temperature and pH of the infiltration solution. Precipitation of secondary phases like zeolites or gels may contribute to maintain a low hydraulic conductivity in the most reactive regions. Bouchet et al. (2004) demonstrated alteration of MX-80 bentonite in a Na–K–OH fluid (pH 14, 60–100°C) with strong dissolution of quartz and cristobalite along with precipitation of zeolites and beidellite. In these experiments the precipitation of phillipsite was favored by a highly concentrated potassium solution, whereas analcime was favored by high sodium concentration. Strong dissolution of primary minerals and formation of C–S–H, calcite and gypsum was observed in an alkaline solution enriched in calcium. Nakayama et al. (2004) performed alteration and diffusion experiments on Na-type bentonite (Kunigel V1) as well as on sand/bentonite (30/70%) mixtures using Na–K–Si–Al–Ca–OH fluids at 10–170°C. They reported for sand/bentonite dissolution of smectite and precipitation of analcime, increasing the porosity by 10–20%. Cuevas et al. (2006) performed batch experiments with FEBEX bentonite under hyperalkaline conditions (NaOH 0.5 to 0.1 M) in the presence of portlandite at temperatures between 25 and 200°C. Formation of phillipsite, analcime, saponite, Mg-clays, brucite and C–(A)–S–H and dissolution of smectite was observed at 125–200°C. At lower temperatures (25–75°C) and lower pHs, formation of amorphous C–S–H gels and transformation of montmorillonite were observed. Fernández et al. (2006) showed that hyperalkaline sodic solutions (pH 13.3) altered FEBEX bentonite by formation of C–S–H phases and brucite at temperatures between 25 and 60°C, and in addition Mg-saponite and analcime at 120°C. The same experiment performed with a solution enriched in calcium (pH 12.6) showed less reactivity and led to precipitation of C–S–H phases at the interface. Sánchez et al. (2006) performed batch experiments using FEBEX bentonite at 25–200°C. NaOH solution in presence of portlandite led to montmorillonite dissolution and precipitation of zeolites (analcime at 125–175°C, phillipsite at 75°C), saponite (Mg-smectite) and C–S–H phases (C–S–H gels at 25-125°C, tobermorite at 125–200°C, gyrolite at 200°C). Karnland et al. (2007) showed that the swelling pressure of MX-80 bentonite was significantly reduced under influence of a sodic solution (pH ~13.5). This reduction was related to dissolution of silica minerals (incl. montmorillonite) and an increase of the CEC of clay minerals (cation exchange capacity) by 20-25%. The dissolution of montmorillonite proceeded via an intermediate step of beidellitization. Fernández et al. (2009a) showed in flow-through experiments with a K–Na–Ca–OH–SO_4 solution (pH 13.5) the dissolution of montmorillonite and precipitation of brucite, hydrotalcite in FEBEX bentonite at 60°C. Using a solution enriched in calcium only (pH 12.5) showed a low reactivity. Fernández et al. (2010a) showed for a K–Na-dominated solution the dissolution of montmorillonite in FEBEX bentonite, while Mg sheet silicates and zeolites (chabazite, merlinoite and some phillipsite) were formed at 60°C. At 90°C, merlinoite was the dominant neo-formed zeolite. The reactivity of a Ca-rich solution (pH 12.5) was slow, independent of temperature and showed minor montmorillonite dissolution and precipitations of C–S–H gels coating clay aggregates. Fernández et al. (2013) observed for an Mg-saturated compacted FEBEX bentonite at 90°C using a diffusion cell. Ca–OH dominated solution had a negligible effect on the alteration of the mineralogy. Na–K–OH based fluids showed precipitation of interlayer-brucite in the smectite complex while smectite dissolved. One may conclude that at low temperature and relatively low pH (<12.5) alkaline solutions do not react significantly with bentonite at laboratory time scales, whereas elevated temperature and higher pH accelerates the mineral dissolution and precipitation reaction rates. A summary of all experiments performed using different EBS materials is given by Gaucher and Blanc (2006) and more recently by Dauzeres et al. (2010).

Various modeling studies were performed on the same topic and showed the evolution of the Clay–Cement interface over a large time-scale. Savage et al. (2002) used PRECIP (Noy, 1998) to model a saline groundwater saturated bentonite, which reacts with cementitious pore-waters of different ages (pH 11.3, 12.5, 13.2) at a temperature of 25°C and 70°C. The following reactions were observed in the bentonite: calcium silicate hydrate (C–S–H) and zeolite formation close to the interface. Most alterations were observed at high-pH conditions with porosity increase due to dissolution of primary mineral phases and C–S–H precipitation at the interface, decreasing the total porosity and hence the fluid flow. Gaucher et al. (2004) used PhreeqC to model alteration of a MX-80 bentonite buffer, saturated with a Callovian-Oxfordian (COX) pore-water, with OPC pore-fluid. Three main stages were defined over a period of 100’000 years: (1) adsorbed cation population of montmorillonite changes from sodium to potassium and calcium dominated, (2) illitisation of montmorillonite and precipitation of zeolites, (3) replacement of zeolites by cement mineral (like C–S–H). Watson et al. (2009) used Raiden-3 (Ueda et al., 2007) model the alteration of a FEBEX bentonite by a Ca dominated (pH 11.3) and a K-Na-OH dominated (pH 12.3) cementitious pore-fluid. The latter altered the mineralogy by 2 mm in 1 year, clogging the porosity by precipitation of hydrotalcite, gibbsite, and brucite. They reported further that montmorillonite stability depends strongly on the used montmorillonite dissolution model. Berner et al. (2013) used the multi-component reactive transport code OpenGeoSys-GEM to model the effect of low-pH concrete (ESDRED) on Clay-based materials like MX-80 bentonite. After ~30’000 years an alteration zone of ~10 cm extended into the bentonite buffer, forming some calcite, hydro-magnetite and possibly some hydrotalcite, while small amount of smectite got dissolved. The mineral precipitation reduced the porosity directly at the interface, while the pH increased to >9. Fernández et al. (2010b) used the multi-component reactive flow and transport code CrunchFlow (Steefel, 2006). The model simulates a diffusion experiment in bentonite at 60 and 90°C using a Na–K–OH (pH 13.5) and a $Ca(OH)_2$ based cementitious solution (pH 11.5). Dissolution in the bentonite material, mainly montmorillonite was observed only with the Na–K–OH solution. Further the precipitation of Mg-silicates (talc-like), hydrotalcite and brucite along with cation exchange process was observed at 60°C, while at 90°C the alteration affected a larger area. The $Ca(OH)_2$ based fluid showed mainly precipitation of brucite and calcite. Porosity decrease was observed near the interface for both infiltration fluids.

1.6. Aims

This thesis aims at characterizing the influence of high-pH solutions on the stability of bentonite and s/b using the core infiltration technique combined with X-ray CT. The study analyzes the physical, mechanical and chemical behavior of the two buffer/backfill materials over a period of up to 2 years using young artificial pore-fluids of OPC (APW_{OPC}) and ESDRED shotcrete (APW_{ESDRED}).

The main goal is to verify if and how pore clogging occurs in clay-based materials, as predicted by various modeling studies.

1.7. Structure of the thesis

Chapter 1:	Introduction into the topic with short descriptions of nuclear waste storage, bentonite, cement, and cement–bentonite interaction.
Chapter 2:	Introduction into the core infiltration device with history, concept, method, and application.
Chapter 3:	Introduction into the X-ray CT scanning technique.
Chapters 4 & 5:	Bentonite – APW_{OPC} experiment (incl. method)
Chapter 6:	Bentonite – APW_{ESDRED} experiment
Chapter 7:	Sand/Bentonite – APW_{OPC} experiment

Chapter 8:	Sand/Bentonite – APW_{ESDRED} experiment
Chapter 9:	CrunchFlow modeling of the Bentonite – APW_{OPC} experiment
Chapter 10:	Conclusions
Appendices:	Data tables of all experiments and additional information

The chapters are written as stand-alone papers, some published or submitted. As a result, there is some repetition of text in the introductions, literature citations, discussions, and acknowledgments.

References

Adenot, F., Buil, M., 1992. Modelling of the corrosion of the cement paste by deionized water. Cement and Concrete Research 22, 489-496.

Alonso, J., Bárcena, I., Alonso, M.C., Pettersson, S., Bodén, A., 2009. ESDRED Temporary sealing technology. Final Technical Report, Nuclear Energy. European Commission, Brussels, Belgium.

Atkins, M., Glasser, F., Kindness, A., Bennett, D., Dawes, A., Read, D., 1992. A thermodynamic model for blended cements. DoE/HMIP/RR/92/005, Department of the Environment.

Bäckblom, G., 2007. ESDRED: Deliverable D4 of Module 5, WP2. Supporting documents of second training workshop, final technical report. Proc. of the Third Low pH Workshop, Paris June 13–14, 2007. European Commission, Brussels, Belgium.

Bauer, A., Berger, G., 1998. Kaolinite and smectite dissolution rate in high molar KOH solutions at 35°C and 80°C. Applied Geochemistry 13, 905-916.

Bauer, A., Velde, B., 1999. Smectite transformation in high molar KOH solutions. Clay Minerals 34, 259-273.

Berner, U., Kulik, D.A., Kosakowski, G., 2013. Geochemical impact of a low-pH cement liner on the near field of a repository for spent fuel and high-level radioactive waste. Physics and Chemistry of the Earth, Parts A/B/C 64, 46-56.

Birgersson, M., Karnland, O., Korkeakoski, P., Leupin, O.X., Mäder, U., Sellin, P., Wersin, P., 2014. Montmorillonite stability under nearfield conditions. Nagra Technical Report NTB 14-12, Nagra, Wettingen, Switzerland.

Bouchet, A., Casagnabère, A., Parneix, J.C., 2004. Batch experiments: results on MX80, in: Michau, N. (Ed.), Ecoclay II: Effect of Cement on Clay Barrier Performance Phase II. Final report. (ANDRA) European contract FIKW-CT-2000-0028, pp. 79-86.

Bradbury, M.H., Baeyens, B., 2003. Porewater chemistry in compacted re-saturated MX-80 bentonite. Journal of Contaminant Hydrology 61, 329-338.

Christidis, G.E., Huff, W.D., 2009. Geological Aspects and Genesis of Bentonites. Elements 5, 93-98.

Claret, F., Bauer, A., Schäfer, T., Griffault, L., Lanson, B., 2002. Experimental investigation of the interaction of clays with high-pH solutions: A case study from the Callovo-Oxfordian formation, Meuse-Haute Marne underground laboratory (France). Clays and Clay Minerals 50, 633-646.

Cuevas, J., Vigil de la Villa, R., Ramírez, S., Sánchez, L., Fernández, R., Leguey, S., 2006. The alkaline reaction of FEBEX bentonite: a contribution to the study of the performance of bentonite/concrete engineered barrier systems. Journal of Iberian Geology 32 (2), 151-174.

Dauzeres, A., Le Bescop, P., Sardini, P., Cau Dit Coumes, C., 2010. Physico-chemical investigation of clayey/cement-based materials interaction in the context of geological waste disposal: Experimental approach and results. Cement and Concrete Research 40, 1327-1340.

De La Villa, R.V., Cuevas, J., Ramirez, S., Leguey, S., 2001. Zeolite formation during the alkaline reaction of bentonite. European Journal of Mineralogy 13, 635-644.

Eberl, D.D., Velde, B., McCormick, T., 1993. Synthesis of illite-smectite from smectite at earth surface temperatures and high pH. Clay Minerals 28, 49-60.

Faucon, P., Adenot, F., Jacquinot, J.F., Petit, J.C., Cabrillac, R., Jorda, M., 1998. Long-term behaviour of cement pastes used for nuclear waste disposal: review of physico-chemical mechanisms of water degradation. Cement and Concrete Research 28, 847-857.

Fernández, R., Cuevas, J., Sanchez, L., de la Villa, R.V., Leguey, S., 2006. Reactivity of the cement-bentonite interface with alkaline solutions using transport cells. Applied Geochemistry 21, 977-992.

Fernández, R., Mäder, U., Rodríguez, M., de la Villa, R.V., Cuevas, J., 2009. Alteration of compacted bentonite by diffusion of highly alkaline solutions. European Journal of Mineralogy 21, 725-735.

Fernández, R., Rodríguez, M., de la Villa, R.V., Cuevas, J., 2010a. Geochemical constraints on the stability of zeolites and C-S-H in the high pH reaction of bentonite. Geochimica et Cosmochimica Acta 74, 890-906.

Fernández, R., Cuevas, J., Mäder, U.K., 2010b. Modeling experimental results of diffusion of alkaline solutions through a compacted bentonite barrier. Cement and Concrete Research 40, 1255-1264.

Fernández, R., Vigil de la Villa, R., Ruiz, A.I., García, R., Cuevas, J., 2013. Precipitation of chlorite-like structures during OPC porewater diffusion through compacted bentonite at 90°C. Applied Clay Science 83–84, 357-367.

García Calvo, J.L., Hidalgo, A., Alonso, C., Fernández Luco, L., 2010. Development of low-pH cementitious materials for HLRW repositories: Resistance against ground waters aggression. Cement and Concrete Research 40, 1290-1297.

Gaucher, E.C., Blanc, P., Matray, J.-M., Michau, N., 2004. Modeling diffusion of an alkaline plume in a clay barrier. Applied Geochemistry 19, 1505-1515.

Gaucher, E.C., Blanc, P., 2006. Cement/clay interactions - A review: Experiments, natural analogues, and modeling. Waste Management 26, 776-788.

Gaus, I., Garitte, B., Senger, R., Gens, A., Vasconcelos, R., Garcia-Sineriz, J.-L., Trick, T., Wieczorek, K., Czaikowski, O., Schuster, K., Mayor, J.C., Velasco, M., Kuhlmann, U., Villar, M.V., 2014. The HE-E Experiment: Lay-out, Interpretation and THM Modelling. Nagra Working Report, Nagra, Wettingen, Switzerland.

Glasser, F.P., Atkins, M., 1994. Cements in Radioactive Waste Disposal. MRS Bulletin 19, 33-38.

Güven, N., 2009. Bentonites - Clays for Molecular Engineering. Elements 5, 89-92.

Huertas, F.J., Rozalen, M.L., Garcia-Palma, S., 2004. Dissolution kinetics of bentonite under alkaline conditions, in: Michau, N. (Ed.), Ecoclay II: Effect of Cement on Clay Barrier Performance Phase II. Final report. (ANDRA) European contract FIKW-CT-2000-0028, pp. 132-142.

IAEA, 2003. The long term storage of radioactive waste: safety and sustainability, A Position Paper of International Experts. International Atomic Energy Agency (IAEA), Vienna, Austria.

IAEA, 2004. Geological Disposal of Radioactive Waste, Draft Safety Requirements, DS154. International Atomic Energy Agency (IAEA), Vienna, Austria.

IAEA, 2015. International Atomic Energy Agency (IAEA). www.iaea.org, Vienna, Austria.

Karnland, O., 1997. Cement/bentonite interaction: results from 16 month laboratory tests. SKB Technical Report 97-32, Stockholm, Sweden.

Karnland, O., Olsson, S., Nielsson, U., 2006. Mineralogy and sealing properties of various bentonites and smectite-rich clay materials. SKB Technical Report 06-30, Stockholm, Sweden.

Karnland, O., Olsson, S., Nilsson, U., Sellin, P., 2007. Experimentally determined swelling pressures and geochemical interactions of compacted Wyoming bentonite with highly alkaline solutions. Physics and Chemistry of the Earth, Parts A/B/C 32, 275-286.

Karnland, O., 2010. Chemical and mineralogical characterization of the bentonite buffer for the acceptance control procedure in a KBS-3 repository. SKB Technical Report 10-60, Stockholm, Sweden.

Khoury, H.N., Salameh, E., Clark, I.D., Fritz, P., Bajjali, W., Milodowski, A.E., Cave, M.R., Alexander, W.R., 1992. A natural analogue of high pH cement pore waters from the Maqarin area of northern Jordan. I: introduction to the site. Journal of Geochemical Exploration 46, 117-132.

Lothenbach, B., Scrivener, K., Hooton, R.D., 2011. Supplementary cementitious materials. Cement and Concrete Research 41, 1244-1256.

Lothenbach, B., Rentsch, D., Wieland, E., 2013. Hydration of a silica fume blended low-alkali shotcrete cement. Physics and Chemistry of the Earth, Parts A/B/C.

Lovera, P., Le Bescop, P., Adenot, F., Li, G., Tanaka, Y., Owaki, E., 1997. Physico-chemical transformations of sulphated compounds during the leaching of highly sulphated cemented wastes. Cement and Concrete Research 27, 1523-1532.

Mosser-Ruck, R., Cathelineau, M., 2004. Experimental transformation of Na,Ca-smectite under basic conditions at 150 °C. Applied Clay Science 26, 259-273.

Nagra, 2002. Demonstration of disposal feasibility for spent fuel, vitrified high-level waste and long-lived intermediate-level waste (Entsorgungsnachweis). Nagra Technical Report NTB 02-05, Nagra, Wettingen, Switzerland.

Nakayama, S., Sakamoto, Y., Yamaguchi, T., Akai, M., Tanaka, T., Sato, T., Iida, Y., 2004. Dissolution of montmorillonite in compacted bentonite by highly alkaline aqueous solutions and diffusivity of hydroxide ions. Applied Clay Science 27, 53-65.

Newman, A.C.D., Brown, G., 1987. The chemical constitution of clays. Mineralogical Society Monography No.6, Longman Harlow, New York.

Noy, D.J., 1998. User Guide to PRECIP, a Program for Coupled Flow and Reactive Solute Transport. Brit. Geol. Surv. Tech. Rep. WE/98/13. British Geological Survey, Keyworth, UK.

Pitty, A., Alexander, R., Eds., 2011. Maqarin Phase IV report. A joint-funded international project report between NDA, RWMD, Andra, CEA, SKB, Nagra and JNC.

Pusch, R., Zwahr, H., Gerber, R., Schomburg, J., 2003. Interaction of cement and smectitic clay—theory and practice. Applied Clay Science 23, 203-210.

Ramirez, S., Cuevas, J., de la Villa, R.V., Leguey, S., 2002. Hydrothermal alteration of La Serrata bentonite (Almeria, Spain) by alkaline solutions. Applied Clay Science 21, 257– 269.

Rothfuchs, T., Czaikowski, O., Hartwig, L., Hellwald, K., Komischke, M., Miehe, R., Zhang, C.-L., 2012. Self-bealing barriers of sand/bentonite-mixtures in a clay repository. GRS Technical report 302, Braunschweig, Germany.

Sánchez, L., Cuevas, J., Ramírez, S., Riuiz De León, D., Fernández, R., Vigil Dela Villa, R., Leguey, S., 2006. Reaction kinetics of FEBEX bentonite in hyperalkaline conditions resembling the cement–bentonite interface. Applied Clay Science 33, 125-141.

Savage, D., Noy, D., Mihara, M., 2002. Modelling the interaction of bentonite with hyperalkaline fluids. Applied Geochemistry 17, 207-223.

Savage, D., Walker, C., Arthur, R., Rochelle, C., Oda, C., Takase, H., 2007. Alteration of bentonite by hyperalkaline fluids: A review of the role of secondary minerals. Physics and Chemistry of the Earth, Parts A/B/C 32, 287-297.

Smellie, J.A.T., 1998. Maqarin natural analogue study: Phase III. SKB Technical Report 98-04, Stockholm, Sweden.

Steefel, C.I., 2006. CrunchFlow. Software for Modeling Multicomponent Reactive Flow and Transport, User's manual. E. S. Division Ed. Lawrence Berkeley National Laboratory: Berkeley, CA.

Ueda, H., Takase, H., Savage, D., Benbow, S., Noda, M., 2007. Evaluation of the kinetics of cement–bentonite interaction in a HLW repository using the reactive solute transport simulator, 15th International Conference on Nuclear Engineering, Nagoya, Japan.

Watson, C., Hane, K., Savage, D., Benbow, S., Cuevas, J., Fernández, R., 2009. Reaction and diffusion of cementitious water in bentonite: Results of "blind" modelling. Applied Clay Science 45, 54-69.

Wersin, P., Johnson, L.H., McKinley, I.G., 2007. Performance of the bentonite barrier at temperatures beyond 100°C: A critical review. Physics and Chemistry of the Earth, Parts A/B/C 32, 780-788.

2

Core Infiltration Experiment

2.1. Introduction

Different experimental methods are used to study the influence of hyperalkaline solutions on clay materials. Batch experiments (Bauer and Velde, 1999; Bouchet et al., 2004; Cuevas et al., 2006; De La Villa et al., 2001; Nakayama et al., 2004; Pusch et al., 2003; Ramirez et al., 2002a; Sánchez et al., 2006) and flow-through experiments (Cuevas et al., 2006; Fernández et al., 2006; Fernández et al., 2010a; Huertas et al., 2004; Karnland, 1997; Karnland et al., 2007; Nakayama et al., 2004; Watson et al., 2009) are the most common ones.

The current experiment uses a core infiltration device. The infiltration experiment are carried out under a confining fluid pressure, which is a total pressure constraint for swelling materials rather than a constant-volume condition as used in common soil-testing equipment. The core infiltration method was improved since a pioneering study with a long-term experiment that investigated the effects of hyperalkaline solutions on Opalinus Clay (Adler, 2001; Adler et al., 2001). The first applications focused on chemical rock–water interaction, and tracer transport and retardation (Adler, 2001; Adler et al., 2001; Mäder et al., 2004). The application was extended to pore-water extraction by advective displacement in clay rocks (Mäder et al., 2004; Mazurek et al., 2013) and reactive transport experiments in granitic rocks (Mäder and Ekberg, 2006). The next step in development was the demonstration that the infiltration technique could not just be used for high-strength rock cores but also for plastic clay materials such as compacted bentonite (Fernández et al., 2011b; Mäder et al., 2012). The latest development is the coupling of core infiltration experiments and X-ray computed tomography (CT), shown in Dolder et al. (2014).

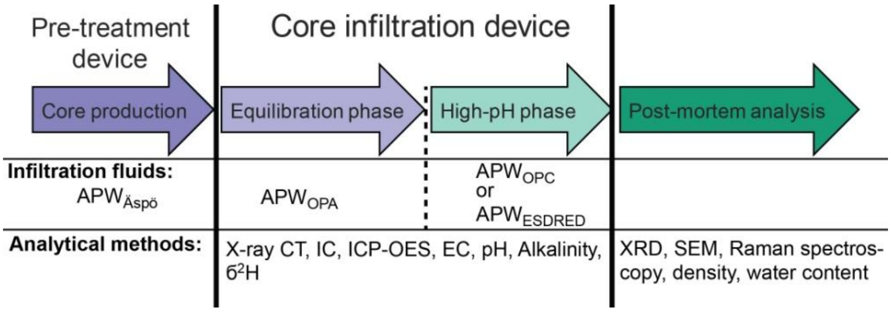

Figure 2-1: Sketch of the experimental procedure showing the three main stages of a core infiltration experiment, including the saturation and infiltration fluids and the applied analytical methods.

2.2. Core production (pre-treatment device)

Core infiltration experiments are performed either on drilled rock core samples or on self-produced cores using a pre-treatment device (Figure 2-2). The pre-treatment device produces core samples by compaction and saturation of dry rock powder at uniaxial pressure condition (Figure 2-1).

Two separate pre-treatment devices were available to produce two cores at the time (Figure 2-2). One of the devices consisted of 4 pistons (1), the other one of 5 stamps (2). Both devices had a separate fluid infiltration system, consisting of a pressurized infiltration tank, valves and an outflow collecting system (3 & 4). Both devices could produce two cores at the time, while an additional 5th stamp on one of the setups was only used for core stacking. The two setups were interconnected with a hydraulic system, sharing one mechanical pump (5). The pressure of each device could be adjusted separately and was controlled by manometers, each. The hydraulic system was secured by over-pressure valves at 100 MPa. A sensor could be placed between stamp and hydraulic piston, measuring the applied force. The gained force and temperature data were logged and visualized on a computer. The sample saturation and compaction was performed in titanium molds (Figure 2-2), consisting of a cylindrical titanium container (6), baseplate (7), hydraulic piston (8), and a fluid infiltration system. The solution was infiltrated through the baseplate into the core and collected through a drilled hole in the titanium piston in a syringe. Titanium filters were placed on both sides of the core, collecting or dispersing the fluid.

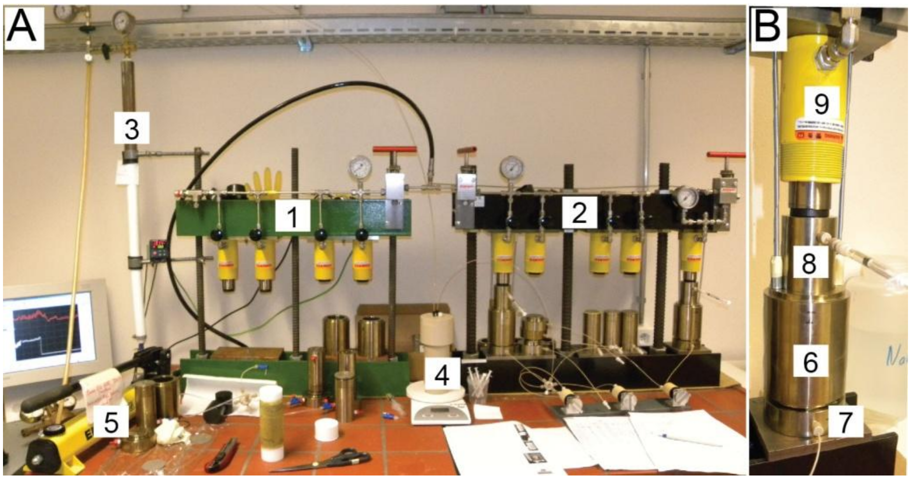

Figure 2-2: Pre-treatment device: (A) both setups; (B) one single titanium mold in use.

Raw materials. In the current study, two different raw materials were used (Figure 2-4): dry MX-80 bentonite powder and dry sand/MX-80 bentonite (s/b) powder. Untreated MX-80 Wyoming bentonite powder was used, manufactured by Volclay LTD, Merseyside, UK (Karnland, 2010). The mineralogy of MX-80 bentonite is composed of sodium montmorillonite (~81.4 wt%), tridymite (~3.8 wt%), plagioclase (~3.5 wt%), muscovite (~3.4 wt%), quartz (~3.0 wt%), gypsum (~0.9 wt%), cristobalite (~0.9 wt%), illite (~0.8 wt%), pyrite (~0.6 wt%), and calcite (~0.2 wt%) (Karnland, 2010). The exchanger of montmorillonite is dominated by Na^+ with 75 eq%, followed by Ca^{2+}, Mg^{2+} and K^+ with 17, 6 and 2 eq%, respectively (Karnland, 2010). The measured particles size distribution is enriched in fines (1–10 µm) and ranges to a maximum size of 50 µm. The 65/35% s/b was provided by MPC, Limay/France and it was the identical material used in the context of the PEBS project (long-term performance of engineered barrier systems) in the HE-E (heater test) experiment in the Mont Terri Rock Laboratory in Switzerland (Gaus et al., 2014). The mineralogy is composed of ~66 wt% quartz , ~31 wt% montmorillonite, ~2 wt% plagioclase, ~1 wt% muscovite, ~0.4 wt% gypsum, ~0.3 wt% cristobalite, and ~0.01 wt% calcite (all calculated values). The sand grains have a grain spectrum of 0.5–1.8 mm, which is similar to that of bentonite powder (Gaus et al., 2014; Rothfuchs et al., 2012).

Bentonite core fabrication (Figure 2-3)**.** One single core consisted of 4 stacked disks of ~1.25 cm length (Figure 2-3B). The fabrication of one core took ~2 months, while the core stacking was performed at half-time. At the beginning, 4 sets of molds were prepared. The titanium containments were mounted on baseplates, equipped with titanium filters. 39.4 g of MX-80 bentonite powder were poured into each containment (Figure 2-3A). The containments were closed by hydraulic pistons, with a second titanium filter placed in-between. Containments were separated from baseplates and hydraulic pistons by O-rings, sealing the system watertight. The oil pressure of the hydraulic system was set to 6 MPa, corresponding to a force of 8.7 kN. The powder was saturated using the $\mathrm{APW}_{\text{Äspö}}$ infiltration fluid (see *section 2.4*), infiltrated with a pressure of 0.45 MPa. After 1 month, the four saturated small disks were stacked to one single core, further infiltrated, and compacted (Figure 2-3C). The end product was a saturated bentonite rock core of ~187 g weight, ~50 mm length and 50 mm diameter (Figure 2-3D). The saturated density was ~1.9 kg/m^3 and the water content ~33 wt%. The core stacking procedure was implemented to reduce the saturation time as well as to avoid formation of pre-textures like density gradation.

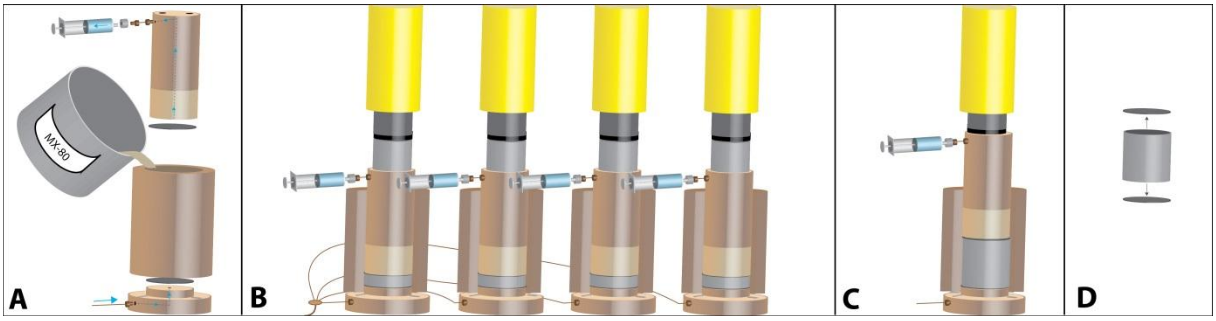

Figure 2-3: Sample fabrication procedure in detail.

S/b core fabrication. The production procedure of s/b cores differed from the one of bentonite, as the low cohesion of the saturated and compacted s/b material made a proper core stacking difficult. Therefore, the stacking step was omitted and the entire core was produced in one single step. The fabrication procedure took ~1 month in total. 180 g of s/b powder were filled in a single titanium containment (Figures 2-4B & D). The s/b powder was poured into the containment using a small spoon in order to minimize the risk of inducing pre-textures. As the hydraulic conductivity of s/b is higher compared to bentonite, a lower infiltration fluid pressure of ~0.1 MPa was used, while the infiltration fluid was $APW_{Äspö}$. The s/b core had a final weight of ~179 g, a length of ~45 mm and a diameter of ~50 mm. This corresponded to a water content of ~16 wt%, a total saturated density of ~2.03 kg/m^3, and a bentonite dry density of 1.06 kg/m^3.

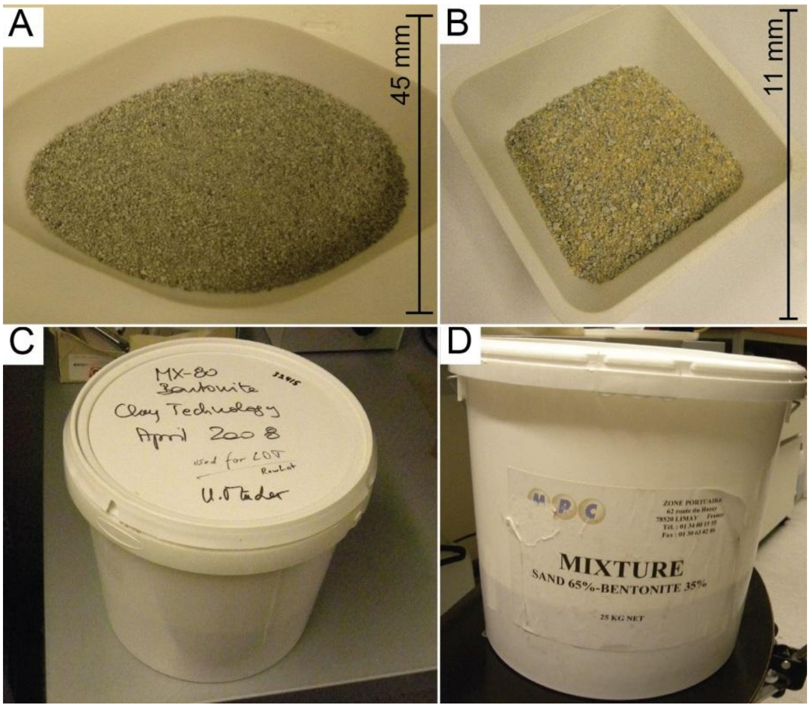

Figure 2-4: Raw bentonite and s/b material: (A & C) bentonite powder; (B & D) s/b powder.

2.3. Core infiltration device

The current approach used a core infiltration method whereby experiments on cores were carried out under a confining fluid pressure (P_{conf}) that mimics lithostatic/hydrostatic pressure conditions. This external pressure is a total pressure constraint for swelling materials like bentonite. Approximate in-situ pressure conditions are transferred to the laboratory. Unwanted effects due to stress relief are minimized; any by-pass of flow along interfaces is avoided. The feasibility of the method is depending on a well-connected porosity in a relatively homogeneous clay material that results in an approximate one dimensional advective–dispersive flow when a strong hydraulic gradient across the length of the core sample is applied. The hydraulic gradient consists of the difference of the infiltration fluid pressure (P_{inf}) and the exfiltration fluid pressure at the outflow (P_{exf}). The induced fluid fluxes are relatively low (0.03-0.1 ml/day) and the dispersion is large and dominated by diffusion (Mäder et al., 2004).

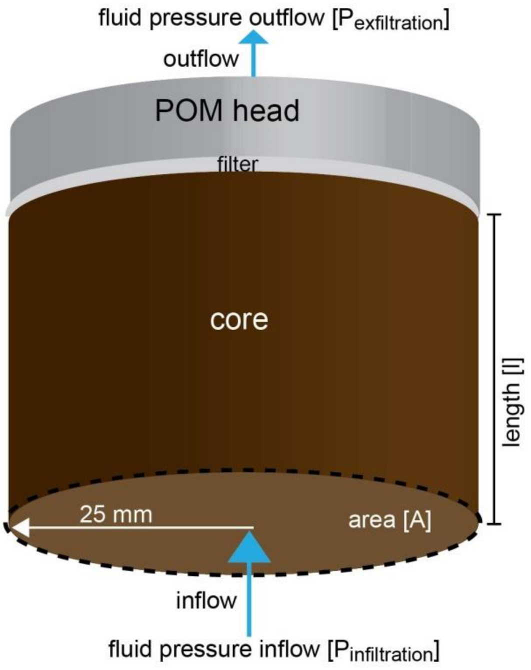

Figure 2-5: Conceptual model of the core infiltration experiment.

The X-ray transparent core infiltration device. The innovation of this new setup was the mobile, detachable X-ray transparent core infiltration device. The X-ray transparency was achieved by the use of carbon fiber for the pressure cylinder and polymer plastics for the other components (Figure 2-7A). The experiment could be detached and run independently from the main experimental rig for some days using two small pressurized fluid tanks for maintaining the confining and infiltration fluid pressure. The CT measurements were performed with the mobile part of the apparatus mounted on a special frame for a medical CT that guarantees an identical positioning for each scan. A detailed description of the CT measurement procedure is given in *chapter 3*.

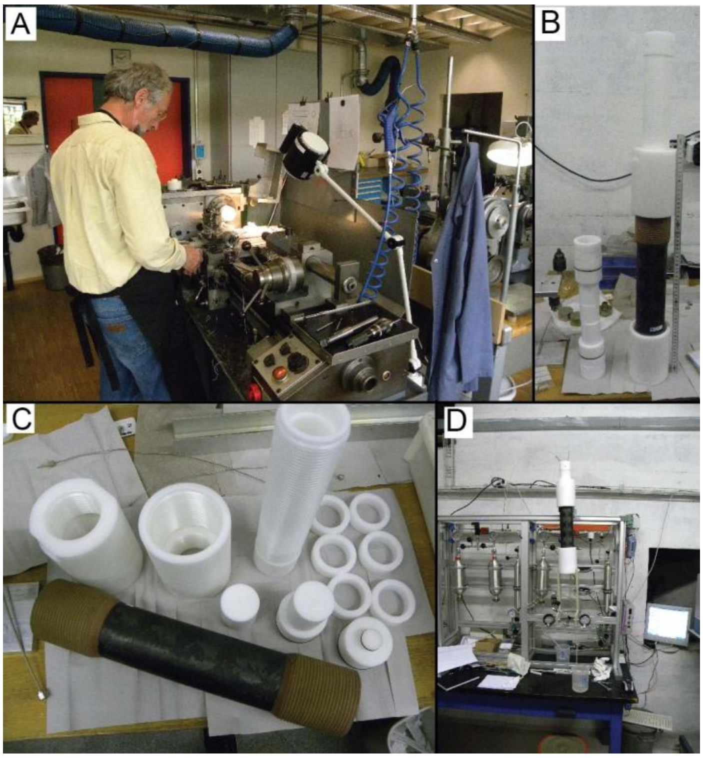

Figure 2-6: Production of the detachable X-ray transparent core infiltration device: (A) Adrian Liechti produces the POM pieces by turning; (B & C) one setup; (D) core infiltration setup mounted on the aluminum rig.

Three core infiltration devices were constructed for this project, located in the hydrothermal laboratory at University of Bern (Figures 2-5 & 2-6B). All core infiltration devices were mounted on an aluminum rig, positioned on a table. One of the rigs was constructed to be detachable from the two others for external measurements. The main component of the current core infiltration device was a carbon fiber cylinder, which was connected to a confining fluid water tank, pressurized by argon gas (Figures 2-6 & 2-12). The carbon fiber cylinder was tested to a confining fluid pressure (P_{conf}) of 8.1 MPa, showing a maximum deformation in the upper part by 0.25 mm. The infiltration fluid was discharged from a PFA-coated (perfluoroalkoxy) stainless steel tank, pressurized by helium gas. A dual tank system and a stream switching valve allowed for a change of fluids at constant pressure. PEEK (polyetheretherketone) capillary tubing and chromatography-type fittings were used for connections. Outflow was directed to a syringe with a small-volume electrical conductivity cell (EC) mounted in between and connected to a Jumo industrial meter (ecoTRANS Lf 03). The electrical conductivity gave in-line information about the ionic strength of the outflow fluid. The pH of one of the core infiltration devices could be logged in-line using a small-volume pH electrode, connected to a Jumo industrial meter (ecoTRANS pH 03). For the measurement, the outflow was redirected into the pre-calibrated pH-cell. Pressures, temperature, pH and electrical conductivity were monitored using a data acquisition system (DAQ) from Measurement Computing (USB-2416) connected to a computer (Figure 2-7B). The system was equipped with an emergency power supply, which kept all electrical parts of the system running, in case of a power failure, for several hours.

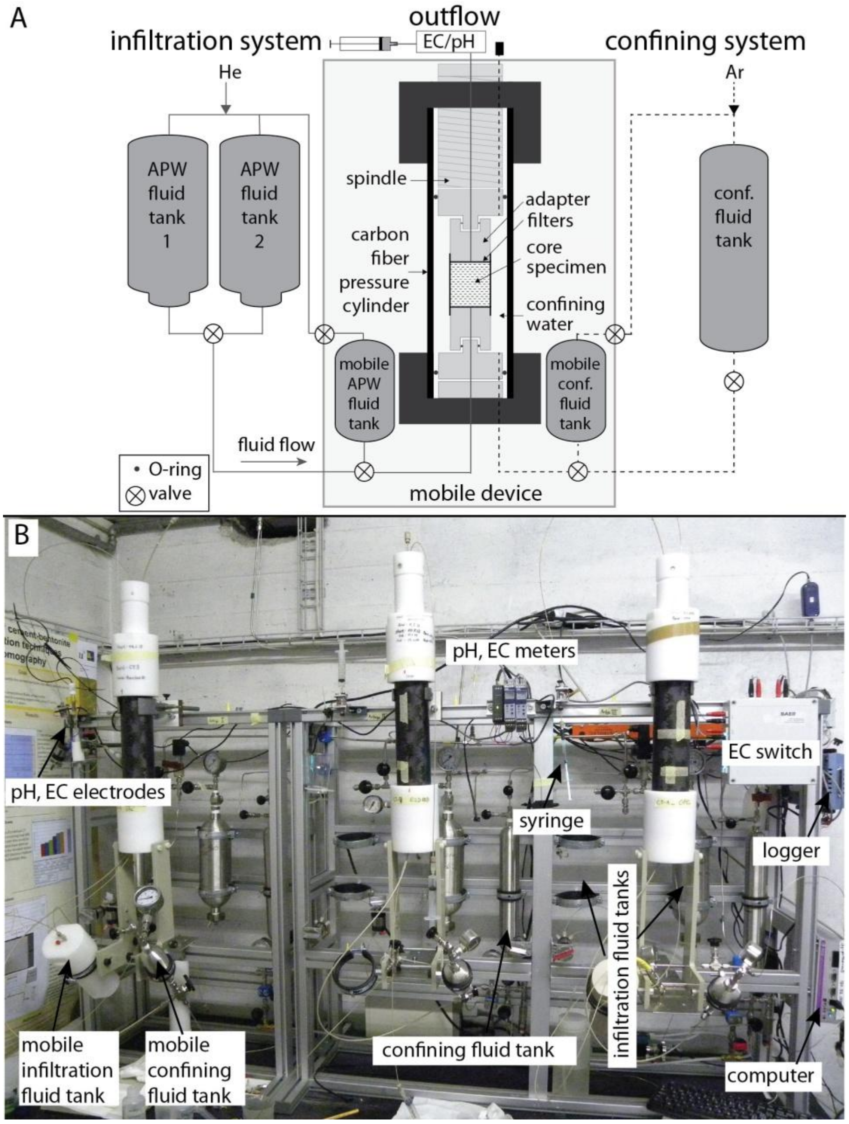

Figure 2-7: Core infiltration device (A) schematic consisting of an infiltration system and a confining system. The central part is the X-ray transparent mobile core infiltration device. EC: electrical conductivity cell; APW: artificial pore-water; (B) image of the three core infiltration stations in the laboratory.

Core packing and mounting. Bentonite and s/b cores were subjected to a hydraulic confining pressure in a carbon fiber pressure cylinder (Figures 2-6 & 2-12). The sample cores (Figure 2-8A) were isolated from the confining medium (water) by multiple layers of Teflon tape (Figure 2-8B & C) and latex sleeves (Figure 2-8D). Adapters maid of POM (polyoxymethylene) were placed at the top and bottom of the bentonite core, separated by 0.5 mm thick PVC filters (Figure 2-5). The Teflon tape was wrapped around core, filters and approx. 5 mm of the POM adapters (Figure 2-8B). Then, 2 latex sleeves covered the tape and are sealed with silicon glue, while electro tape sealed the fissure (Figure 2-8D). The filters guaranteed a homogeneous distribution of the infiltration fluid at the core bottom, and collection of the outflowing fluid at the core top over the entire cross-section. The cores with adapters were positioned in the middle of the pressure cylinder with inserts at either end that couple to the adapters with O-ring seals (Figure 2-8E). Screw-on POM caps at either end held the axial force. A POM spindle was adjusted to samples of different lengths, and an axial confining force may be applied initially.

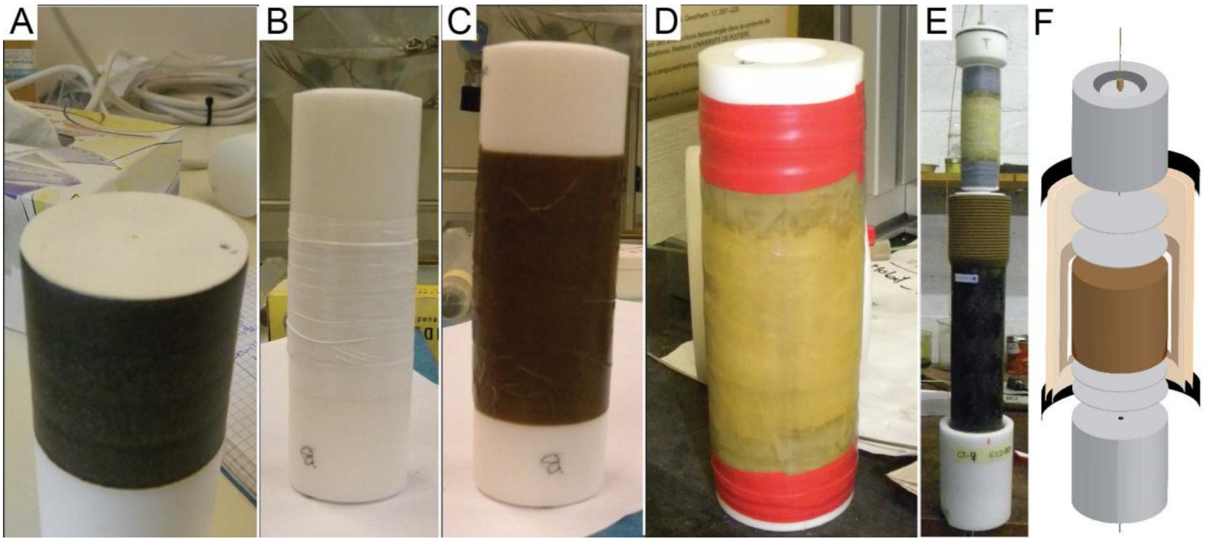

Figure 2-8: Core packing and insertion into the core infiltration device: (A) bentonite core including PVC-filters; (B) POM adapters and Teflon tape; (C) Teflon tape; (D) Latex sleeves and sealing tape; (E) packed core; (F) sketch of the multi-layer packing.

Starting the experiment. Before the experiment was started, the confining system had to be filled with water (half tap water and half distilled water) using the water-pump and the corresponding valves (Figure 2-13; c_4, c_2). Further, a copper wire was placed into the tank to inhibit microbial activity. The infiltration fluid tank was removed for filling, as otherwise the metal connections could not be tightened enough. The infiltration and confining fluid tanks were pressurized using the following valves: i_1, i_2, i_3 for the infiltration system and c_1 for the confining system. The mobile tanks were pressurized using valves i_7, c_7 and c_8. The infiltration tank was flushed with pressurized He gas several times, while the pressure was released after each time to make sure that no atmospheric gas was present. The core infiltration experiment was started by step-wise increasing the confining fluid pressure over a period of 2–3 days, while leaving the inflow and outflow capillary tubes open. The open capillary tubes allowed for detecting leakages in the core packing, while outflowing solution would led to abrupt stop of the experiment. Gas was squeezed out of the dead volumes of the experiment (filters, capillaries) at this stage, indicating further core compaction. The infiltration capillary could be attached to the experiment, while the infiltration fluid pressure was step-wise increased after 1–2 days. The aimed confining fluid pressure was ~4 MPa for bentonite and ~1.7 MPa for s/b. The corresponding infiltration fluid pressures were ~2 MPa for bentonite and ~0.1 MPa for s/b.

Equilibration phase. In a first period, the core adapted to the new confining pressure in the core infiltration device, and an artificial Opalinus Clay pore-water (APW_{OPA}) was infiltrated (Figure 2-1). This period was called equilibration phase and last for 0.5–1 year. The running experiment had to be controlled regularly, including maintenance work like changing syringes. The periodic disconnection of the mobile infiltration device for CT scans induced drops in the confining and infiltration fluid pressures, which made it necessary to readjust the pressures from time to time. A problem often observed was a small leaking of outflow solution directly at the EC cell connections and at the syringe due to the repeat disconnection for CT measurements. It would have been better not to disconnect the outflow system from the core (experiment) but rather disconnect the EC cell from the electricity, in order to leave the continuous outflow undisturbed.

High-pH phase. Two different high-pH solutions were used in the current project (APW_{OPC}, APW_{ESDRED}). The period was called high-pH phase and last for 1–2 years (Figure 2-1). The change to high-pH infiltration solution was done by switching the fluid infiltration temporally to the mobile infiltration device (Figure 2-13; i_6), while the main infiltration tanks were exchanged or the valve between the two infiltration tanks was turned (Figure 2-13; i_4). In both cases, the capillary tube between the infiltration tank and the valve, used to switch from mobile to the main infiltration system or vice versa, had to be disconnected and drained. Afterwards, the drained capillary had to be filled with the high-pH fluid. After connecting the capillary tube to the valve, it could be switched back to the main infiltration system (Figure 2-13; i_6). This procedure was necessary to be able to estimate time the high-pH fluids needed to reach the core. At current measured hydraulic conductivities, the time the high-pH fluid needed to reach the inflow filter after switching fluids was between 2–6 days in case of bentonite and 3–5 h in case of s/b. Important was also to exchange syringes in this moment.

CT sessions. For CT measurements the experiment had to be disconnected from the main infiltration and confining fluid systems. This was done by changing to the mobile infiltration and confining systems by switching the two corresponding valves (Figure 2-13; c_6 and i_6). Previously, the pressures had to be readjusted, as the mobile infiltration tank was not entirely He tight on the long-term. After turning the valves, the capillary tubes of the infiltration system and the steel tubes of the confining systems could be disconnected from the mobile device (Figure 2-13; c_5 and i_4). The final step was to disconnect the capillary tube of the outflow from the EC cell, and connect the syringe directly to the outflow tube. The in- and outflow of the EC cell were closed with an adapter. The mobile core infiltration device could now carefully be removed from the rack. After the CT measurement, the same procedure was reverted.

Termination and dismantling. The core infiltration experiment was terminated by stopping the fluid infiltration (closing valve i_6) and step-wise reducing the confining fluid pressure to atmospheric conditions over a period of 2 days (Figure 2-9A). After removing all capillary and steel tubes, the mobile infiltration device could be detached and dismantled (Figure 2-9B). The core was ejected using a spindle to push the core out, from bottom to top (Figure 2-9C).

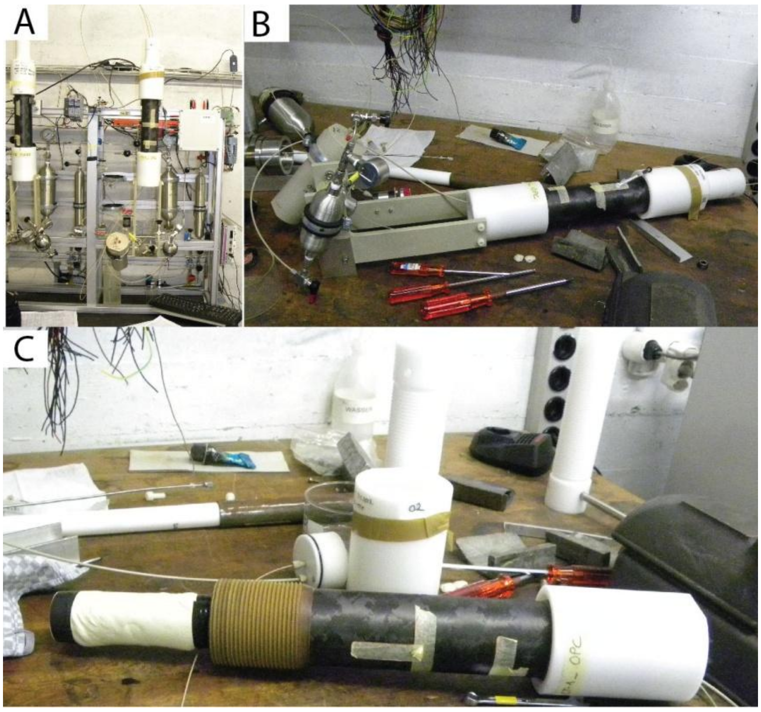

Figure 2-9: Dismantling procedure: (A) Running experiment; (B) removal of the mobile device; (C) dismantling of the packed core.

Core processing for post-mortem analyses. The further sample procession was performed in the chemical laboratory (Figure 2-10A). The core was carefully unpacked (Figure 2-10B) and length, diameter and weight were measured. The sample was thereafter cut into pieces using a band-saw with a saw band for wood (Figure 2-10C). The standard cutting pattern is shown in Figure 2-11. In the center two longitudinal samples of 2x5x1 cm (XRD and SEM samples) were cut and freeze-dried (Figure 2-10E). The further processing is described below. From the inflow surface in contact with the filter of the sample, a triangular shaped piece was cut, freeze-dried and stabilized in resin to analyze the inlet surface morphology (unpolished SEM surface sample). The second longitudinal sample was dedicated to XRD (X-ray diffraction) analysis. The rest of the core was cut into two longitudinal profiles for water content and density (ρ) measurements. Two profiles were located at the outer surface of the cylinder (abbr. rim) and two profiles in 1 cm off-axis (abbr. cen) (Figure 2-10D). The filters were immersed in isopropyl alcohol after removing and dried in a nitrogen filled desiccator to prevent carbonation.

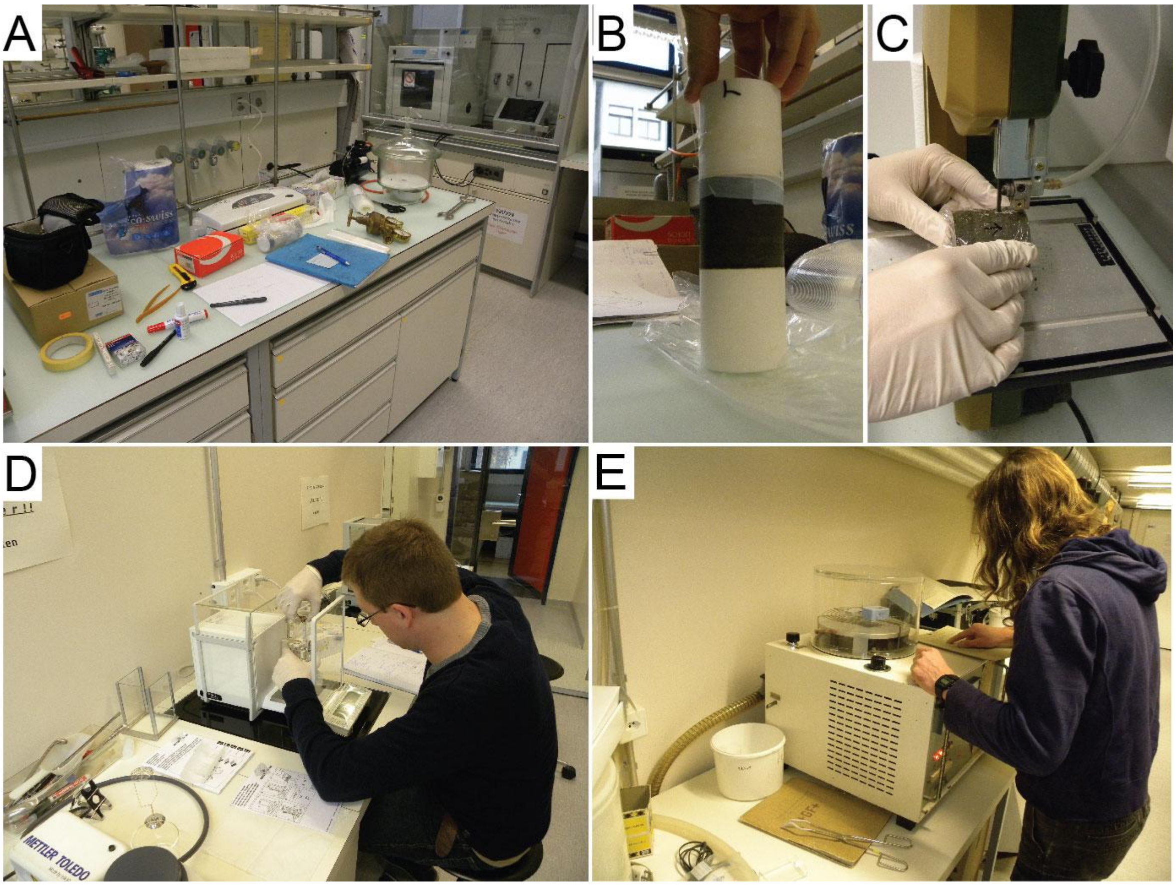

Figure 2-10: Core dismantling and sample preparation in the laboratory: (A) workspace in the lab; (B) sample unwrapping; (C) sawing of the core; (D) weighting the samples; (E) freeze-drying of the sample (Andreas Jenni).

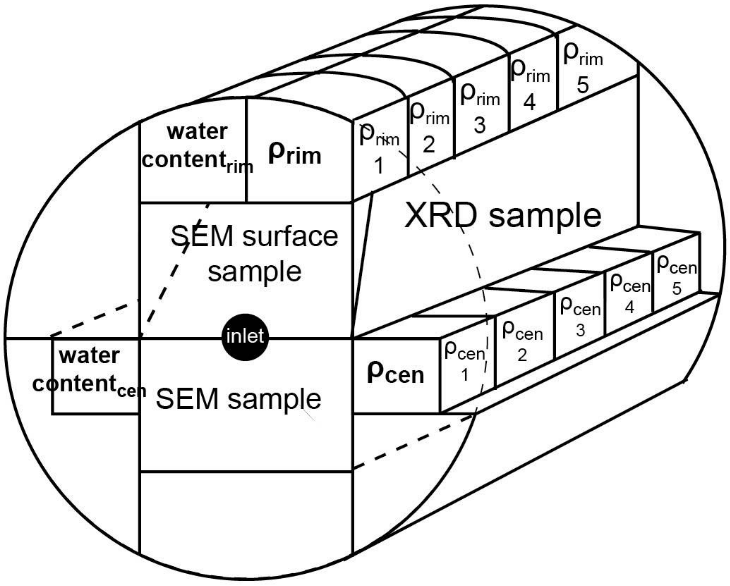

Figure 2-11: Standard cutting pattern of the core.

Samples for XRD, SEM and Raman spectroscopy analysis were freeze-dried using liquid nitrogen and a vacuum-drier (Figure 2-9E). The samples were exposed to liquid nitrogen (-196°C) for ~5 min in a sealed plastic bag. They were unpacked and put for 2 days in the freeze-drying machine. The vacuum was <1 Pa and the samples were exposed in the machine to room temperature. Thereafter, one sample for SEM (Scanning electron microscope) as well as Raman spectroscopy analysis was vacuum impregnated with resin and polished with petroleum and oil-based diamond suspensions with grain sizes down to 1 µm (Figure 2-12A). The sample shown in Figure 2-12D represents a profile parallel to the flow direction from the inflow filter to outflow (longitudinal), including a reaction zone at the inlet.

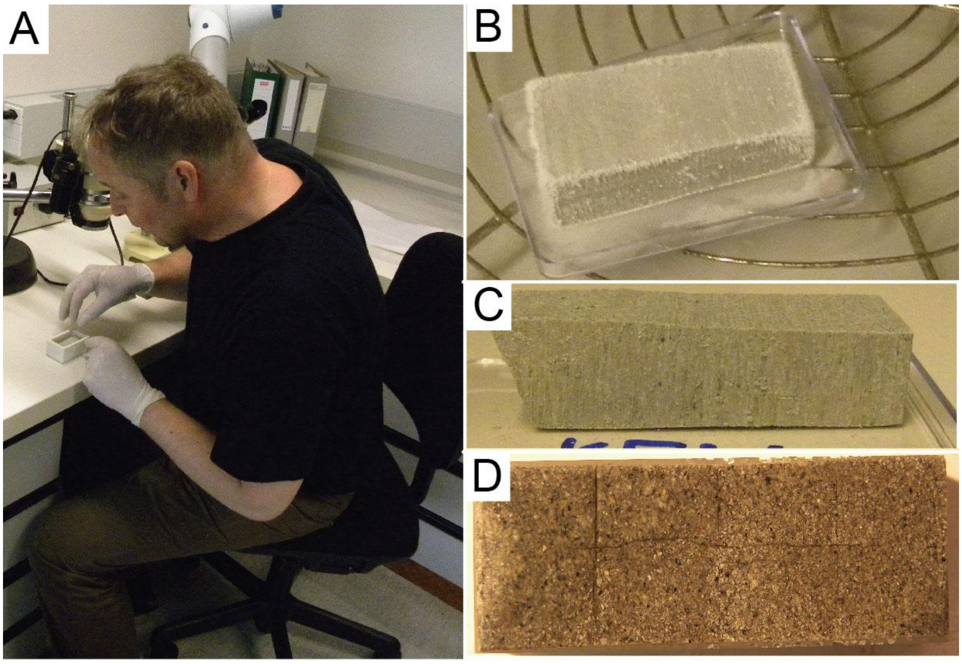

Figure 2-12: (A) Resin impregnation of the dried sample performed by Stephan Brechbühl; (B) frozen bentonite sample; (C) dried sample before impregnation; (D) impregnated and polished bentonite sample.

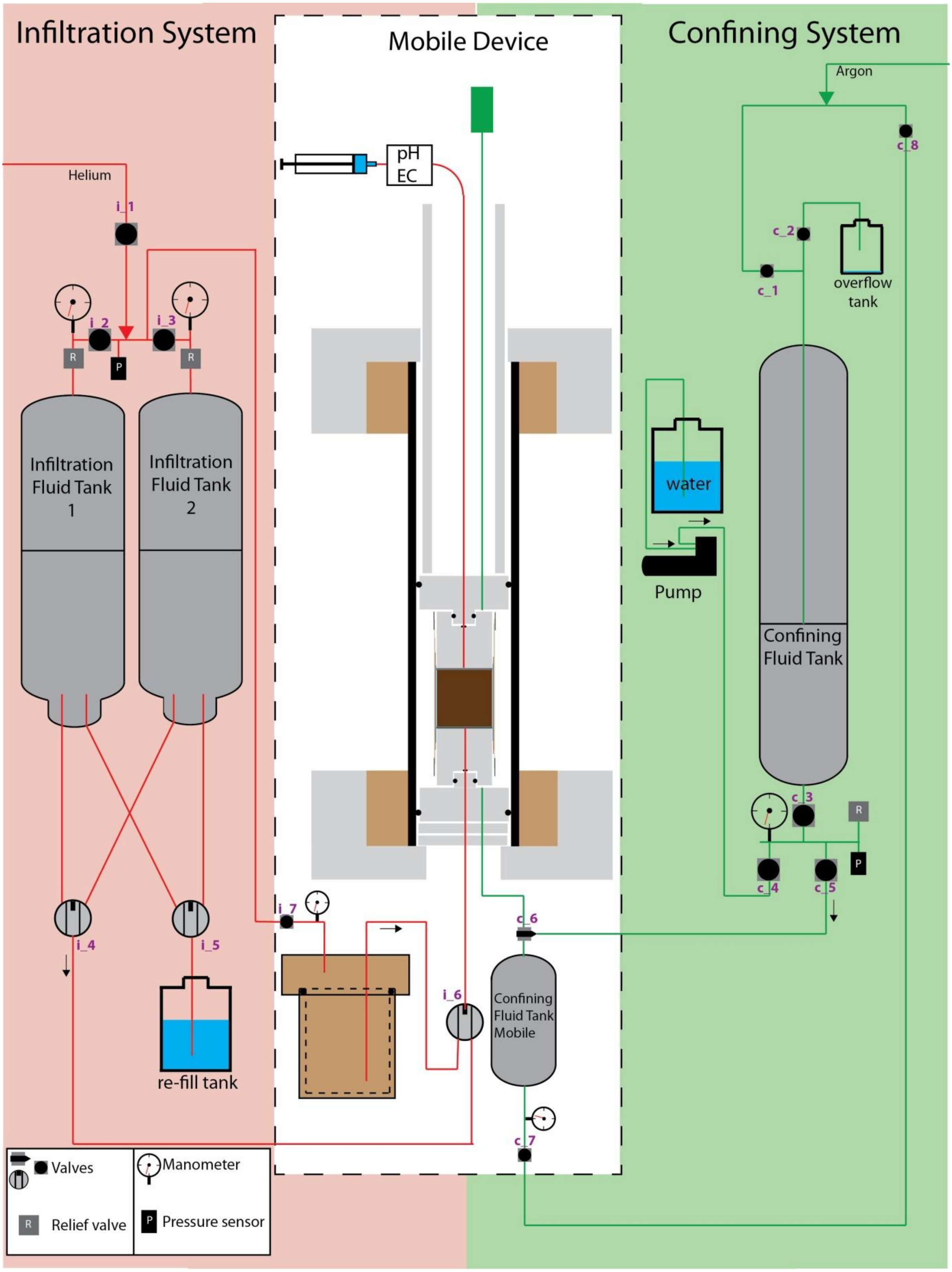

Figure 2-13: Detailed sketch of the core infiltration device.

2.4. Artificial pore-waters (APW)

$APW_{Äspö}$ (*chapter 4*)

The core saturation fluid was an APW, simulating a moderately saline groundwater at Äspö underground rock laboratory, Sweden ($APW_{Äspö}$) (Table 2-1). The recipe is shown in Table 2-2.

APW_{OPA} (*chapter 4*)

An artificial Opalinus Clay pore-water (APW_{OPA}) was infiltrated during the equilibration phase (Table 2-1). This APW_{OPA} was similar to the $APW_{Äspö}$ with higher chloride and lower sulfate concentration, and a higher Na^+/Ca^{2+} ratio. The recipe is shown in Table 2-2.

APW_{OPC} (*chapters 4, 5 & 7*)

The APW_{OPC} was an artificial, high-pH ordinary Portland cement pore-water after ~625 days of hydration, based on modeled data of experimental measurements (Lothenbach and Winnefeld (2006)) (Table 2-1). The recipe is shown in Table 2-2.

APW_{ESDRED} (*chapters 6 & 8*)

APW_{ESDRED} was an artificial 'low-pH' shotcrete pore-water after ~365 days of hydration, based on experimental data of Lothenbach et al. (2013) (Table 2-1). The recipe is shown in Table 2-2.

Table 2-1: Chemistry of all used APWs. -: means below detection limit.

	$APW_{Äspö}$[1]	**APW_{OPA}**[2]	**APW_{OPC}**[3]	**APW_{ESDRED}**[4]
pH	7.2	7.2	13.5	11.7
Ionic strength [mol/kg]	0.26	0.23	0.28	0.11
		--[mM]--		
Na^+	92.23	164.4	122.70	25.00
K^+	0.26	2.6	222.38	14.00
Ca^{2+}	56.14	12.51	2.70	27.00
Mg^{2+}	1.65	9.63	-	-
Sr^{2+}	0.46	0.210	-	-
Cl^-	204.39	160	-	-
SO_4^{2-}	1.76	24.7	3.10	2.20
Br^-	0.15	-	-	-
HCO_3^-	0.1	2.5	0.7	-
Formate	-	-	-	83.20

[1] Karnland et al. (2009), [2] Mäder (2009), [3] *chapters 4, 5 & 7*, [4] *chapters 6 & 8.*

Table 2-2: Recipes for all APWs'.

Ingredients	**Producer and no.**	**APW$_{Äspö}$**	**APW$_{OPA}$**	**APW$_{OPC}$**	**APW$_{ESDRED}$**
solids				g/kg	
$Al_2(SO_4)_3$ 16×H_2O	Fluka: 06421			0.0096	0.000
KCl	Merck: 1.04936	19.6	0.19		
KCHOO	Sigma-Aldrich: 294454-25G				0.354
KOH	Merck: 1.05033			12.5	0.303
Na_2SO_4	Merck: 1.06649	249.9	3.41	0.43	
K_2SO_4	Merck: 1.05153				0.383
NaCl	Merck: 1.06404	5164.2	6.74		
Na_2CO_3	Merck: 6398	10.3			
NaCHOO	Merck: 1.06443.0500				1.699
$NaHCO_3$	Fluka: 71329		0.05		
NaBr	Fluka: 71329	15.4			
NaOH	Merck: 1.06498			4.5	
$MgCl_2$ 6×H_2O	Merck: 1.05833	334.8	1.86		
$CaCl_2$ 2×H_2O	Merck: 1.02382	8253.0	1.75		
$Ca(OH)_2$	Merck: 1.02047			0.147	
$CaCO_3$	Merck: 1.02066			0.072	
$Ca(CHOO)_2$	Sigma-Aldrich: 21134-250G-F				3.513
$SrCl_2$ 6×H_2O	Fluka: 85892	121.411			
solution					ml/kg
$Na_2O_7Si_3$	Sigma-Aldrich: 338443-1			0.0094	0.007

References

Adler, M., Mäder, U., Waber, H.N., 2001. Core infiltration experiment investigating high-pH alteration of low-permeability argillaceous rock at 30°C, in: Cidu, R. (Ed.), Proceedings WRI-10 (10th International Symposium on Water-Rock Interaction). Balkema, Villasimius, Italy, pp. 1299-1302.

Adler, M., 2001. Interaction of claystone and hyperalkaline solutions at 30°C: A combined experimental and modeling study. . University of Bern, Switzerland.

Bauer, A., Velde, B., 1999. Smectite transformation in high molar KOH solutions. Clay Minerals 34, 259-273.

Bouchet, A., Casagnabère, A., Parneix, J.C., 2004. Batch experiments: results on MX80, in: Michau, N. (Ed.), Ecoclay II: Effect of Cement on Clay Barrier Performance Phase II. Final report. (ANDRA) European contract FIKW-CT-2000-0028, pp. 79-86.

Cuevas, J., Vigil de la Villa, R., Ramírez, S., Sánchez, L., Fernández, R., Leguey, S., 2006. The alkaline reaction of FEBEX bentonite: a contribution to the study of the performance of bentonite/concrete engineered barrier systems. Journal of Iberian Geology 32 (2), 151-174.

De La Villa, R.V., Cuevas, J., Ramirez, S., Leguey, S., 2001. Zeolite formation during the alkaline reaction of bentonite. European Journal of Mineralogy 13, 635-644.

Dolder, F., Mäder, U., Jenni, A., Schwendener, N., 2014. Experimental characterization of cement–bentonite interaction using core infiltration techniques and 4D computed tomography. Physics and Chemistry of the Earth, Parts A/B/C 70–71, 104-113.

Fernández, R., Cuevas, J., Sanchez, L., de la Villa, R.V., Leguey, S., 2006. Reactivity of the cement-bentonite interface with alkaline solutions using transport cells. Applied Geochemistry 21, 977-992.

Fernández, R., Rodríguez, M., de la Villa, R.V., Cuevas, J., 2010. Geochemical constraints on the stability of zeolites and C-S-H in the high pH reaction of bentonite. Geochimica et Cosmochimica Acta 74, 890-906.

Fernández, R., Mäder, U., Jenni, A., 2011. Multi-component advective-diffusive transport experiment in MX-80 compacted bentonite: Method and results of 1st phase of experiment. Internal Nagra Working Report, Wettingen, Switzerland.

Gaus, I., Garitte, B., Senger, R., Gens, A., Vasconcelos, R., Garcia-Sineriz, J.-L., Trick, T., Wieczorek, K., Czaikowski, O., Schuster, K., Mayor, J.C., Velasco, M., Kuhlmann, U., Villar, M.V., 2014. The HE-E

Experiment: Lay-out, Interpretation and THM Modelling. Nagra Working Report, Nagra, Wettingen, Switzerland.

Huertas, F.J., Rozalen, M.L., Garcia-Palma, S., 2004. Dissolution kinetics of bentonite under alkaline conditions, in: Michau, N. (Ed.), Ecoclay II: Effect of Cement on Clay Barrier Performance Phase II. Final report. (ANDRA) European contract FIKW-CT-2000-0028, pp. 132-142.

Karnland, O., 1997. Cement/bentonite interaction: results from 16 month laboratory tests. SKB Technical Report 97-32, Stockholm, Sweden.

Karnland, O., Olsson, S., Nilsson, U., Sellin, P., 2007. Experimentally determined swelling pressures and geochemical interactions of compacted Wyoming bentonite with highly alkaline solutions. Physics and Chemistry of the Earth, Parts A/B/C 32, 275-286.

Karnland, O., Olsson, S., Dueck, A., Birgersson, M., Nilsson, U., Hernan-Håkansson, T., Pedersen, K., Nilsson, S., Eriksen, T., Rosborg, B., 2009. Long term test of buffer material at the Äspö Hard Rock Laboratory, LOT project. Final report on the A2 test parcel. SKB Technical Report 09-29, Stockholm, Sweden.

Karnland, O., 2010. Chemical and mineralogical characterization of the bentonite buffer for the acceptance control procedure in a KBS-3 repository. SKB Technical Report 10-60, Stockholm, Sweden.

Lothenbach, B., Winnefeld, F., 2006. Thermodynamic modelling of the hydration of Portland cement. Cement and Concrete Research 36, 209-226.

Lothenbach, B., Rentsch, D., Wieland, E., 2013. Hydration of a silica fume blended low-alkali shotcrete cement. Physics and Chemistry of the Earth, Parts A/B/C.

Mäder, U., Waber, H.N., Gautschi, A., 2004. New method for porewater extraction from claystone and determination of transport properties with results for Opalinus Clay (Switzerland), in: Wanty, R.B., Seal, R.R. (Eds.), Proceedings WRI-10 (11th International Symposium on Water-Rock Interaction). Balkema, Saratoga Springs, New York, USA, pp. 445-448.

Mäder, U., Ekberg, C., 2006. GTS HPF Project: Geochemical evolution of porewater in the granitic shear zone AU-126 during 3 years of interaction with a hyperalkaline fluid, and its interpretation. Unpublished report. Internal Nagra Arbeitsbericht, Wettingen, Switzerland.

Mäder, U., Jenni, A., Fernández, R., de Soto, I., 2012. Reactive transport in compacted bentonite: porosity concepts, experiments and applications. Mineralogical Magazine 76(6), 2052.

Mazurek, M., Waber, H.N., Mäder, U., de Haller, A., Koroleva, M., 2013. Geochemical synthesis for the Effingen Member in boreholes at Oftringen, Gösgen and Küttigen. Nagra Technical Report NTB 12-07 Nagra, Wettingen, Switzerland.

Nakayama, S., Sakamoto, Y., Yamaguchi, T., Akai, M., Tanaka, T., Sato, T., Iida, Y., 2004. Dissolution of montmorillonite in compacted bentonite by highly alkaline aqueous solutions and diffusivity of hydroxide ions. Applied Clay Science 27, 53-65.

Pusch, R., Zwahr, H., Gerber, R., Schomburg, J., 2003. Interaction of cement and smectitic clay—theory and practice. Applied Clay Science 23, 203-210.

Ramirez, S., Cuevas, J., de la Villa, R.V., Leguey, S., 2002. Hydrothermal alteration of La Serrata bentonite (Almeria, Spain) by alkaline solutions. Applied Clay Science 21, 257– 269.

Rothfuchs, T., Czaikowski, O., Hartwig, L., Hellwald, K., Komischke, M., Miehe, R., Zhang, C.-L., 2012. Self-bealing barriers of sand/bentonite-mixtures in a clay repository. GRS Technical report 302, Braunschweig, Germany.

Sánchez, L., Cuevas, J., Ramírez, S., Riuiz De León, D., Fernández, R., Vigil Dela Villa, R., Leguey, S., 2006. Reaction kinetics of FEBEX bentonite in hyperalkaline conditions resembling the cement–bentonite interface. Applied Clay Science 33, 125-141.

Watson, C., Hane, K., Savage, D., Benbow, S., Cuevas, J., Fernández, R., 2009. Reaction and diffusion of cementitious water in bentonite: Results of "blind" modelling. Applied Clay Science 45, 54-69.

3

X-ray Computed Tomography (CT)

3.1. Introduction

X-ray computed tomography (CT) is a non-destructive technology, developed in medical science to examine human bodies for bone fractures or tumors. The CT scanner produces slices (tomographic/radiographic images in 2D) of the object that can be digitally processed and rendered to a 3D image. The use of X-ray computed tomography in geosciences is becoming more common paired with technical improvements (Ketcham and Carlson, 2001; Mees et al., 2003). Micro-CT measurements in clay rocks are able to resolve mineral and pore distributions (Keller et al., 2013; Robinet et al., 2012; Van Geet et al., 2005). The use of medical CT for real-time flow monitoring experiments in a single fracture was shown by Hirono et al. (2003). The tracking of mineral reactions was achieved in recent studies using synchrotron micro-CT on sedimentary rocks (Berg et al., 2013; Fusseis et al., 2012).

The X-ray source is an X-ray vacuum tube that rotates around a center with an X-ray detector rotating on the opposite side of the orbit. The X-ray source of the medical CT scanner used for this thesis produced polychromatic X-rays, which means that the energy spectra does not show a sharp peak at the selected X-ray energy but rather a broad hump. The investigated object is moved slowly through the X-ray ring while the machine is continuously scanning. X-rays are penetrating the object and getting attenuated by interaction with matter. Dense materials (atoms are close together) as well as large atoms affect X-rays stronger. X-ray attenuations of an object are measured in small sections, building up a cross-section of the object. The attenuation values (coefficients) are displayed as grayscale coded pixels (2D), which can be processed along the length of the slices to voxels (3D). The attenuation coefficient is primarily a function of the X-ray energy and the material property. The CT data are expressed in X-ray attenuation values using the generic Hounsfield unit (HU); a scale dedicated to medical use. This scale defines air at -1024 HU (least attenuation), water at ~0 HU and ends at +3071 HU (most attenuation). It is a linear transformation of the X-ray attenuation coefficient. Medical CT scanners are calibrated every time prior to the measurements on air. The sensitivity analysis was performed using reference samples consisting of polymer plastics with known densities, mounted in an identical water-filled pressure cylinder as used for the experiment (*see section 3.3.2*).

CT data recorded on a medical X-ray CT scanner are processed and optimized using various internal, manufacturer-specific filters. Unfortunately, these algorithms are not published and apart from improving the image quality for the normal medical user their effect on the raw data is unknown. A further aspect of medical CT scanners is their lower resolution compared to industrial CT scanners or synchrotron-based tomographic methods. The currently used resolution was too low to resolve single pores or clay mineral grains in bentonite, but rather bulk values were determined. Attenuation coefficients of minerals and materials can be calculated from measured HU values, assuming a monoenergetic X-ray beam. As the currently used CT scanners produced a polychromatic X-ray beam, the calculations shown in the *Appendix (11.1)* are just an approximation rather than exact values. The linear attenuation coefficient as well as the mass-attenuation coefficient can be calculated as follows (Hubbell and Seltzer, 1996):

$$\mu_x = \left(\frac{\mu}{\rho}\right)_{\text{mineral}} = \sum_i w_i \left(\frac{\mu}{\rho}\right)_i$$

where μ_x is the linear attenuation coefficient of the mineral, $\frac{\mu}{\rho}$ the mass attenuation coefficient, w_i is the fraction by weight of the current atomic constituent, and *i* the atomic constituent. The transformation of the linear attenuation coefficient to the HU is performed as follows (Mees et al., 2003):

$$HU = 1000 \times \frac{\mu_x - \mu_{water}}{\mu_{water}}$$

where μ_{water} is the linear attenuation of water of 0.15949 1/cm (Hubbell and Seltzer, 1996). Calculations of theoretical attenuation coefficients of specific materials/minerals, as shown in the *Appendix 11.1*, were performed by using the online database for mass attenuation values for materials and/or single elements, published by the NIST (National Institute of Standards and Technology) (Hubbell and Seltzer, 1996).

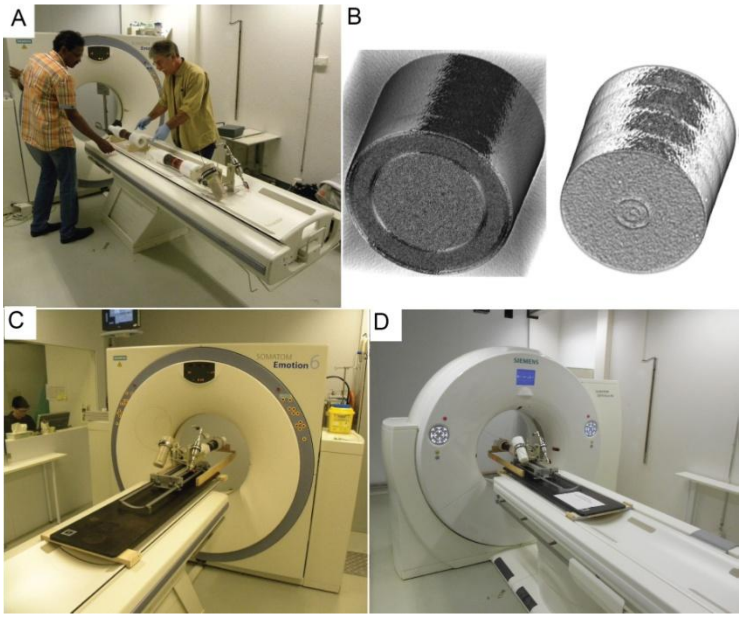

Figure 3-1: X-ray CT measurements: (A) first CT measurement; (B) 3D rendered experiment (left side: bentonite core surrounded by confining water; right side: bentonite core); (C) Siemens Somatom Emotion 6 (first/old scanner); (D) Siemens Somatom Definition AS 40 (second/new scanner).

3.2. Medical CT scanners

The CT measurements were performed on two medical CT scanners, both operated by the Institute of Forensic Medicine at the University of Bern (Figure 3-1 and Table 3-1). The machine specific parameters like X-ray energy and X-ray tube current were chosen to optimize the contrast of the images (Table 3-1).

Table 3-1: Technical parameters of CT scanners.

Machine		**Siemens Somatom Emotion 6**	**Siemens Somatom Definition AS 40**
X-ray energy	keV	130	140
X-ray tube current	mAs	111	132
MTF2 in-plane (x-y)	mm	0.32	0.208
MTF2 z-axis	mm	0.45	0.238
Voxel size	mm	0.109x0.109x0.5	0.107x0.107x0.5
Slice thickness	mm	0.5	0.5

3.3. CT scans

CT scans were performed on decoupled, mobile infiltration devices. A special frame was mounted on the CT table, which allowed identical alignment of the mobile infiltration devices (Figure 3-1C, black plate). Prior to the experiments, a reference material sample was scanned each time in order to check the stability and reproducibility of the measurements (see *section 3.2.2*). In total 28 CT scanning sessions were performed over a period of 3 years (see list in *Appendix 11.2*). A CT dataset of a single experiment consisted of 108–113 gray scale images with a total size of ~56 MB, while a single slice accounts for ~517 KB. The files were saved as IMA-files (disk image files) and named using the experiment abbreviation and a continuous numbering (see *Appendix*). The measurements on the Siemens Somatom Definition AS scanner (second scanner) had to be corrected for a data offset, induced by the higher X-ray energy. The data correction was performed by matching the same bentonite or s/b peaks in the histogram of an experiment scanned both machines at different times.

3.3.1. Software

The data was processed using the following software: Mango, 3DSlicer CT and Fiji. Mango (Multi-Image Analysis GUI) is an open-source software, used to get trans-section and cross-section lines (cuts) through the experiment as well as bulk HU-histograms (Lancaster and Martinez, 2007). 3DSlicer is a free, open-source CT visualization program, used for 3D rendering. Fiji is an open source image processing package based on the software ImageJ (Schindelin et al., 2012). The software was used for core volume, diameter and histogram calculations. The volume of the core was calculated by segmentation of the 3D image using a region of interest (ROI) and multiplying the resultant number of voxels by their dimensions. The core diameter was calculated by segmentation of each single slice, resulting in the core area, which can be transformed further into the core diameter. The uncertainty of the results was ~1–2% as the packing could not be accurately distinguished from the bentonite or s/b cores and beam hardening artifacts occurred on the interface bentonite–packing–confining water. 3D modeling of the reaction plume was performed by Beat Münch from the EMPA using MATLAB and Fiji.

3.3.2. Reference material sample

The initial idea of the reference material sample was to determine absolute densities in the experiments using X-ray attenuations (HU values) of the well-known reference materials. As this approach was not so successful (see *Appendix 11.1*), the reference material sample was only used for the sensitivity analysis. The reference material sample consisted of polymer plastics, mounted in an identical water-filled pressure cylinder (Figure 3-2). The sample consisted of the following materials: acryl/PMMA (poly(methyl methacrylate); ρ = 1.18 g/cm^3), PEEK (polyether ether ketone; ρ = 1.32 g/cm^3), POM-C (polyoxymethylene; ρ = 1.41 g/cm^3), PVDF (polyvinylidene fluoride; ρ = 1.76 g/cm^3), PTFE (25%) (polytetrafluoroethylene; ρ = 2.09 g/cm^3), and PTFE (ρ = 2.17 g/cm^3) (all density data from Amsler & Fey AG).

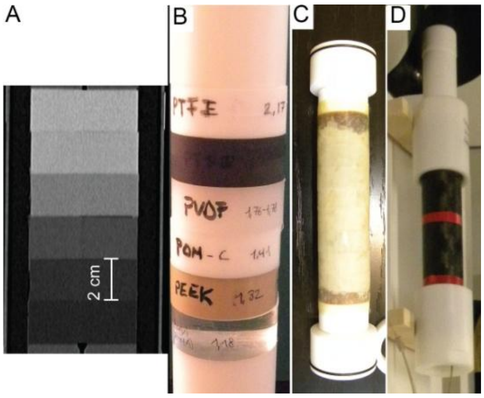

Figure 3-2: Reference material sample: (A) longitudinal section; (B) image of the reference material samples; (C) packing of the sample; (D) reference material sample setup.

The attenuations of the reference materials are shown in Figure 3-3. The error (standard deviation) increased with an increasing attenuation or density. As medical CT scanners are adapted to human bodies (range: -100–500 HU), measurements in the high HU range had a larger error. The reference material showed on the

Siemens Definition AS (second scanner) higher HU values for densities <1.32 g/cm^3 and lower HU values for densities >1.41 g/cm^3, relative to the Siemens Somatom 6 (first scanner) (Figure 3-3). The difference is explained by the different X-ray energies with higher energies being stronger attenuated.

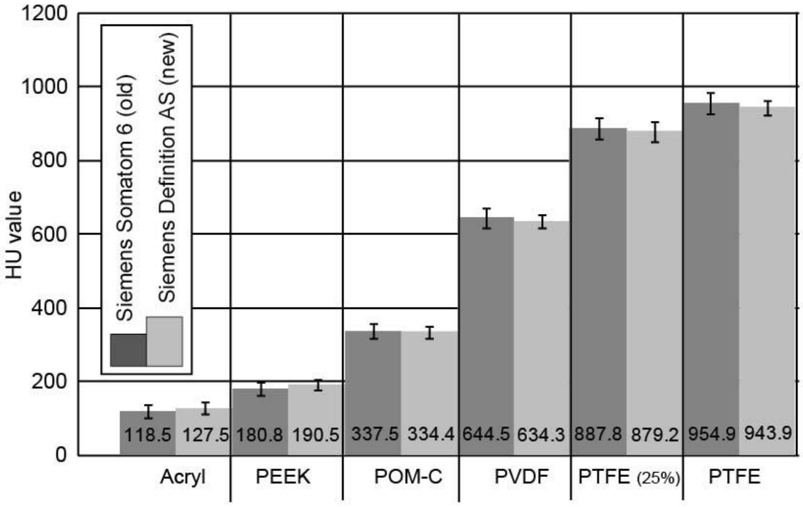

Figure 3-3: Attenuation values of the reference materials measured on the Siemens Somatom 6 and the Siemens Definition AS scanners, including errors (standard deviation).

3.3.3. CT scans of the experiments

The Siemens Definition AS (second) scanner measured lower attenuations in bentonite and s/b due to the higher X-ray energy (Figures 3-4 & 3-6). S/b showed higher attenuations compared to pure bentonite, due to the large amount of quartz grains that have a higher grain density relative to the water saturated smectite (Figures 3-4 & 3-6).

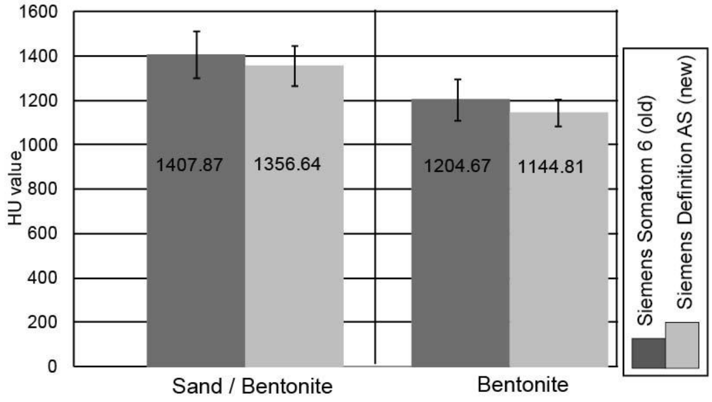

Figure 3-4: Bentonite and s/b measured on the Siemens Somatom 6 and Siemens Definition AS scanners, plotted against the attenuation.

An X-ray attenuation gradient was observed in bentonite along the core axis with higher values in direction of the outlet. It is explained by the bulk density increase induced by the pore-pressure gradient (Figure 3-6A, see *chapter 4*). This is in agreement to post-mortem analysis, showing a density gradient from inlet to outlet with lower values at the inlet. S/b showed no attenuation gradient, which could be explained by the sand grain based framework as well as by the quartz grains, which possibly cover such a signal by their high attenuation. Post-mortem analysis showed in one s/b core no density gradient (s/b-CT 4), while another core exhibited lower densities at the inlet (s/b-CT 3).

The X-ray attenuations across the cross-section of bentonite and s/b showed higher values at the core rim (Figure 3-5). Post-mortem analysis of bentonite cores showed slightly lower densities at the core rim, which is in contradiction to the CT data. For s/b, the higher attenuations at the core rim were in agreement to post-mortem analysis. It indicates that the X-ray attenuations are not only a function of the bulk core density but rather influenced by other factors like chemical composition or beam hardening (artefact).

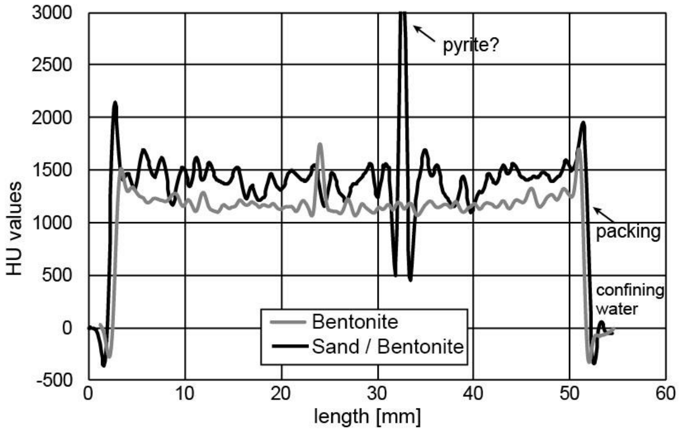

Figure 3-5: Section line of one pixel width across the cross-section of a bentonite and s/b core sample.

The HU-histograms of the experiments showed distinct peaks of core infiltration equipment (POM adapters, pressure vessel (carbon-fibers), PVC filters, confining water, and bentonite or s/b (Figure 3-6B). The intensities of the peaks in the HU-histograms cannot be compared, as the sample was not always identically aligned.

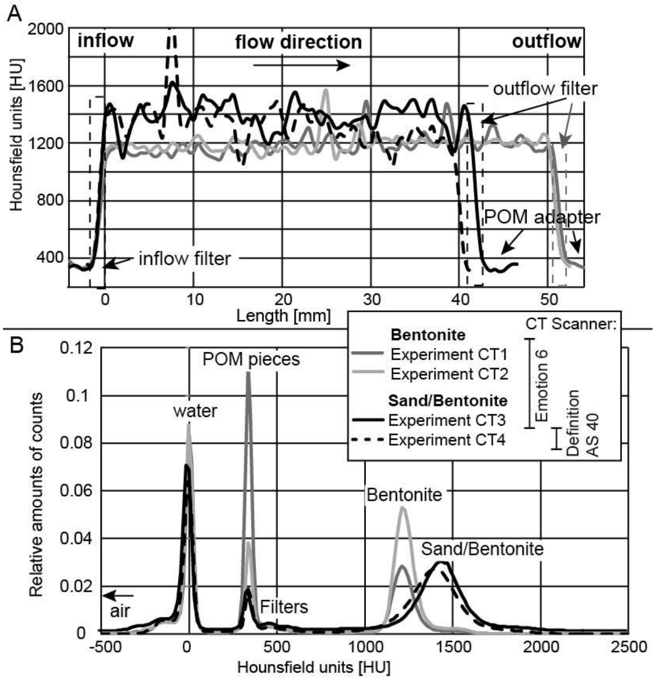

Figure 3-6: Comparison of the experiments: (A) longitudinal section (one pixel width) through the center of the experiments; (B) histograms of the experiments.

Tomographic images were used to monitor attenuation/density changes in the cores over time. The feasibility to detect a reaction plume by CT was confirmed. A clearly distinguishable plume of high attenuation was observed in the filter and the adjacent bentonite core, reflecting mineral precipitation. As the resolution of medical CT scanners was below the clay mineral grain size, the measured attenuation values reflect mineral assemblages. Images of unaltered bentonite exhibited a uniform grayish shade with heterogeneously distributed bright spots (Figure 3-7). The s/b had a brighter shade relative to bentonite with larger and more intense bright spots. The brighter gray in the s/b matrix reflected the occurrence of quartz as well as the lower water content, which led to a higher X-ray attenuation. The bright spots were high density minerals like pyrite. The black margins around bright spots were hardening artifacts.

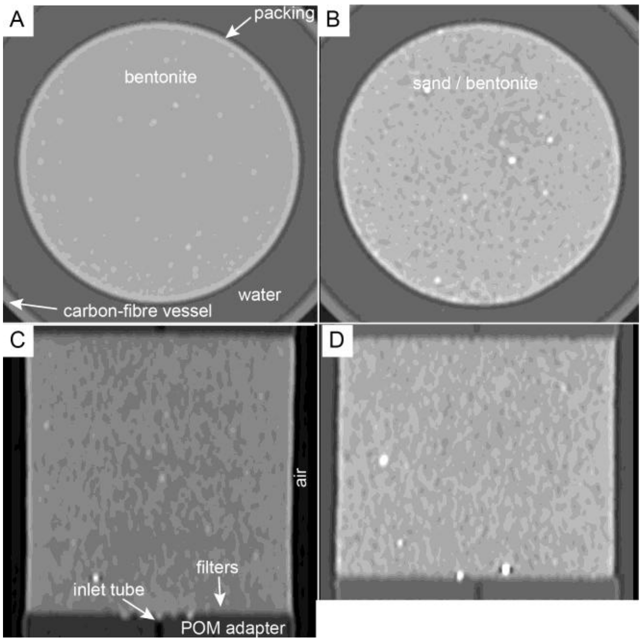

Figure 3-7: Cross-sectional and longitudinal CT images of the bentonite (A & C) and s/b experiments (C & D).

References

Berg, S., Ott, H., Klapp, S.A., Schwing, A., Neiteler, R., Brussee, N., Makurat, A., Leu, L., Enzmann, F., Schwarz, J.-O., Kersten, M., Irvine, S., Stampanoni, M., 2013. Real-time 3D imaging of Haines jumps in porous media flow. Proceedings of the National Academy of Sciences 110, 3755-3759.

Fusseis, F., Schrank, C., Liu, J., Karrech, A., Llana-Funez, S., Xiao, X., Regenauer-Lieb, K., 2012. Pore formation during dehydration of polycrystalline gypsum observed and quantified in a time-series synchrotron radiation based X-ray micro-tomography experiment. Solid Earth 3, 71-86.

Hirono, T., Takahashi, M., Nakashima, S., 2003. Direct imaging of fluid flow in fault-related rocks by X-ray CT. Geological Society, London, Special Publications 215, 107-115.

Hubbell, J.H., Seltzer, S.M., 1996. Tables of X-ray mass attenuation coefficients and mass energy-absorption coefficients 1 keV to 20 MeV for elements Z=1 to 92 and 48 additional substances of dosimetric interest [electronic resource]. U.S. Department of Commerce, Technology Administration, National Institute of Standards and Technology, Gaithersburg, MD.

Keller, L.M., Schuetz, P., Erni, R., Rossell, M.D., Lucas, F., Gasser, P., Holzer, L., 2013. Characterization of multi-scale microstructural features in Opalinus Clay. Microporous and Mesoporous Materials 170, 83-94.

Ketcham, R.A., Carlson, W.D., 2001. Acquisition, optimization and interpretation of X-ray computed tomographic imagery: applications to the geosciences. Computers & Geosciences 27, 381-400.

Lancaster, J.L., Martinez, M.J., 2007. Mango - Multi-image analysis GUI. Research Imaging Institute, UT Health Science Center at San Antonio, TX, USA, URL: http://ric.uthscsa.edu/mango/index.html.

Mees, F., Swennen, R., Van Geet, M., Jacobs, P., 2003. Applications of X-ray computed tomography in the geosciences. The Geological Society Special Publication, 215, London.

Robinet, J.-C., Sardini, P., Coelho, D., Parneix, J.-C., Prêt, D., Sammartino, S., Boller, E., Altmann, S., 2012. Effects of mineral distribution at mesoscopic scale on solute diffusion in a clay-rich rock: Example of the Callovo-Oxfordian mudstone (Bure, France). Water Resources Research 48.

Schindelin, J., Arganda-Carreras, I., Frise, E., Kaynig, V., Longair, M., Pietzsch, T., Preibisch, S., Rueden, C., Saalfeld, S., Schmid, B., Tinevez, J.-Y., White, D.J., Hartenstein, V., Eliceiri, K., Tomancak, P., Cardona, A., 2012. Fiji: an open-source platform for biological-image analysis. Nat Meth 9, 676--682.

Van Geet, M., Volckaert, G., Roels, S., 2005. The use of microfocus X-ray computed tomography in characterising the hydration of a clay pellet/powder mixture. Applied Clay Science 29, 73-87.

4

Experimental characterization of cement-bentonite interaction using core infiltration techniques and 4D computed tomography

Published in Physics and Chemistry of the Earth, Volume 70, p. 104-113 (2014); F. Dolder, U. Mäder, A. Jenni, N. Schwendener

Abstract. Deep geological storage of radioactive waste foresees cementitious materials as reinforcement of tunnels and as backfill. Bentonite is proposed to enclose spent fuel drums, and as drift seals. The emplacement of cementitious material next to clay material generates an enormous chemical gradient in pore water composition that drives diffusive solute transport. Laboratory studies and reactive transport modeling predict significant mineral alteration at and near interfaces, mainly resulting in a decrease of porosity in bentonite. The goal of this project is to characterize and quantify the cement/bentonite skin effects spatially and temporally in laboratory experiments. A newly developed mobile X-ray transparent core infiltration device was used, which allows performing X-ray computed tomography (CT) periodically without interrupting a running experiment. A pre-saturated cylindrical MX-80 bentonite sample (1920 kg/m^3 average wet density) is subjected to a confining pressure as a constant total pressure boundary condition. The infiltration of a hyperalkaline (pH 13.4), artificial OPC (ordinary Portland cement) pore water into the bentonite plug alters the mineral assemblage over time as an advancing reaction front. The related changes in X-ray attenuation values are related to changes in phase densities, porosity and local bulk density and are tracked over time periodically by non-destructive CT scans.

Mineral precipitation is observed in the inflow filter. Mineral alteration in the first millimeters of the bentonite sample is clearly detected and the reaction front is presently progressing with an average linear velocity that is 8 times slower than that for anions. The reaction zone is characterized by a higher X-ray attenuation compared to the signal of the pre-existing mineralogy. Chemical analysis of the outflow fluid showed initially elevated anion and cation concentrations compared to the infiltration fluid due to anion exclusion effects related to compaction of the bentonite core that was adjusting to the experimental conditions. Subsequently, the OPC fluid is fully buffered, and a gradually decreasing ionic strength is observed as a result of progressive consumption of hydroxide at the mineral reaction front.

Keywords: Core infiltration experiment, ordinary Portland cement, Bentonite, nuclear waste storage, porosity reduction, high-pH alteration, computed tomography

4.1. Introduction

The long-term behavior of clay barriers in geological underground repositories is of importance for nuclear waste storage and is a topic of ongoing investigation. Longevity of the engineered barrier system (EBS) is a requirement but its performance is influenced over time by different external boundary conditions and internal chemico-physical processes. Bentonite is proposed as EBS enclosing spent fuel drums and as drift seals. Because of close coupling between chemical processes and mechanical processes (e.g., pore-water chemistry and swelling pressure), perturbations can be caused by inflowing fresh-water or by hyperalkaline fluids (pH >12.5). The use of cement in the current Swiss concept for nuclear waste storage is foreseen as reinforcement of access galleries, deposition galleries for long-lived intermediate-level waste, backfill material for intermediate-level-waste, and for tunnel seals (Nagra, 2002). Pore waters emanating from cement, mortar or concrete induce a high pH reaction front that may degrade clay materials in the EBS or result in porosity/permeability changes.

The long-term influence (>1000s of years) of hyperalkaline fluids (pH 12.5-12.8) penetrating clay-bearing limestone along fracture systems was studied at the natural analogue site near Maqarin, Jordan (Khoury et al., 1992; Pitty et al., 2011; Smellie, 1998). It was shown that such fluids can modify the existing mineral assemblage by dissolution of clay minerals and precipitation of ettringite, calcite and CSH phases (Ca-silicate-hydrates), among other phases (Smellie, 1998). This alteration may proceed until the pore-space in the adjacent rock matrix becomes completely clogged, or flow in the fracture becomes blocked or inactive. The sealing ability of a clayey EBS in a deep geological repository is a fundamental function and has to be guaranteed for thousands of years. Over the past decades various studies were done on clay stability under alkaline perturbation. In a recent summary, Gaucher and Blanc (2006) distinguished five main reaction processes for smectite-type clays, a major component in bentonite:

I. Modification of the adsorbed cations on clay minerals. A clay originally enriched in sodium becomes more potassium and calcium enriched over time (Bauer and Berger, 1998; Bouchet et al., 2004; Karnland et al., 2007; Mosser-Ruck and Cathelineau, 2004; Ramirez et al., 2002a).
II. Dissolution of clay (smectite, illite) minerals is localized at the interface where the high pH front is buffered (Bauer and Berger, 1998; Bouchet et al., 2004; De La Villa et al., 2001; Fernández et al., 2006; Fernández et al., 2009a; Nakayama et al., 2004; Ramirez et al., 2002a; Sánchez et al., 2006).
III. Dissolution of accessory minerals like quartz, cristobalite, feldspar, plagioclase, gypsum and calcite are important with respect of pH buffering and ionic strength of the pore water. The dissolution of silicate minerals leads to the formation of zeolites (phillipsite and analcime), C(A)SH phases (Ca-Al-silicate-hydrates), saponite or hydrotalcite (Bouchet et al., 2004; Cuevas et al., 2006; De La Villa et al., 2001; Fernández et al., 2006; Fernández et al., 2009a; Fernández et al., 2010a; Karnland et al., 2007; Nakayama et al., 2004; Ramirez et al., 2002a; Savage et al., 2007).
IV. The role of pCO_2 in the system is important with respect to the chemical evolution of the system, due to its buffering capacity.
V. The heterogeneous distribution of newly formed minerals in the bentonite affects the evolution of the pH gradient.

Of direct interest are the results of experiments at high-pH conditions using FEBEX bentonite (Spain) and MX-80 bentonite (USA). Eberl et al. (1993) showed a collapse of expandable smectite layers (montmorillonite) in MX-80 bentonite by formation of illite and illite/smectite mixed-layers (up to 25 %) under influence of K-Na-OH solution at 35°C. De La Villa et al. (2001) observed the formation of phillipsite and analcime in Na-K-Ca-OH solutions (pH >11.6 at 35–60°C) using FEBEX bentonite and pure montmorillonite (<2 µm). Ramirez et al. (2002a) examined the stability of FEBEX bentonite in a Na-K-Ca-OH solution (pH <12.6 at 30–90°C). The dissolution of silica minerals started at pH >12.6, and it could be accelerated by increasing temperature. In a hyperalkaline sodic solution (pH 13.5) a formation of phillipsite was observed. By increasing the temperature to 90°C, the precipitation of zeolites, CSH phases and Mg-smectite appeared. Furthermore, the dissolution of the primary mineral assemblage was observed whereas illitisation was found to be of minor importance. An ion-exchange of magnesium and sodium by calcium and potassium was also reported. Bouchet et al. (2004) demonstrated alteration of MX-80 bentonite in a Na-K-OH fluid (pH 14, 60–100°C) with strong dissolution of quartz and cristobalite along with precipitation of zeolites and beidellite. In these experiments the precipitation of phillipsite was favored by a highly concentrated potassium solution, whereas analcime was favored by high sodium concentration. Strong dissolution of primary minerals and formation of CSH, calcite and gypsum was observed in an alkaline solution enriched in calcium. Cuevas et al. (2006) showed the formation of phillipsite, analcime, saponite, Mg-clays, brucite and C(A)SH in FEBEX bentonite under influence of a hyperalkaline solution enriched in sodium and calcium at 25-120°C. It was shown that montmorillonite can buffer an alkali-rich hyperalkaline plume by forming mineral reaction fronts. Ca-hydroxide saturated fluids (pH ~12.5) had insignificant effects on the bentonite mineralogy at low temperatures. At 120°C the precipitation of CSH, analcime and Mg-clays was observed at the cement/bentonite interface. Calcium diffusion from the cement into the bentonite led to a progressive calcium exchange in montmorillonite. Magnesium was displaced and diffused towards the cement interface and precipitated as Mg-clay coating. Fernández et al. (2006) showed that hyperalkaline sodic solutions (pH 13.3) altered FEBEX bentonite by formation of CSH phases and brucite at temperatures between 25 and 60°C, and in addition Mg saponite and analcime at 120°C. The same experiment performed with a solution enriched in calcium (pH 12.6) showed less reactivity and led to precipitation of CSH phases at the interface. Karnland et al. (2007) showed that the swelling pressure of MX-80 bentonite was significantly reduced under influence of a sodic solution (pH ~13.5). This reduction was related to dissolution of silica minerals (incl. montmorillonite) and an increase of the CEC of clay minerals (cation exchange capacity) by 20–25%. The dissolution of montmorillonite proceeded via an intermediate step of beidellitization. Fernández et al. (2009a) showed in flow-through experiments with a K-Na-Ca-OH-SO_4 solution (pH 13.5) the dissolution of montmorillonite and precipitation of brucite, hydrotalcite in FEBEX bentonite at 60°C. Using a solution enriched in calcium only (pH 12.5) showed a low reactivity. Fernández et al. (2010a) showed for a K-Na-dominated solution the dissolution of montmorillonite in FEBEX bentonite, while Mg sheet silicates and zeolites (chabazite, merlinoite and some phillipsite) were formed at 60°C. At 90°C, merlinoite was the dominant neo-formed zeolite. The reactivity of a Ca-rich solution (pH 12.5) was slow, independent of temperature and showed minor montmorillonite dissolution and precipitations of CSH gels coating clay aggregates. One may conclude that at low temperature and relatively low pH (<~12.5) alkaline solutions do not react significantly with bentonite at laboratory time scales, whereas elevated temperature and higher pH accelerates the mineral dissolution and precipitation reaction rates. A summary of all experiments performed using different EBS materials is given by Gaucher and Blanc (2006) and more recently by Dauzeres et al. (2010).

Different experimental methods were applied to study the influence of hyperalkaline solutions on clay materials. Batch experiments (Bouchet et al., 2004; Cuevas et al., 2006; De La Villa et al., 2001; Ramirez et al., 2002a) and flow-through experiments (Cuevas et al., 2006; Fernández et al., 2006; Fernández et al., 2010a; Karnland et al., 2007; Nakayama et al., 2004; Watson et al., 2009) were the most common ones. Our approach uses a core infiltration method whereby experiments on rock cores are carried out under a confining pressure that may represent lithostatic pressure conditions. This external pressure is a total pressure constraint for swelling materials rather than a constant-volume condition as used in common soil-testing equipment. Approximate in-situ pressure conditions are transferred to the laboratory. Unwanted effects due to stress relief are minimized; any by-pass of flow along interfaces is avoided. The method was improved since a pioneering study with a long-term experiment that investigated the effects of hyperalkaline solutions on Opalinus Clay (Adler, 2001). The first applications focused on chemical rock-water interaction, and tracer transport and retardation (Adler, 2001; Adler et al., 2001; Mäder et al., 2004). The application was extended to pore water extraction by advective displacement in clay rocks (Mäder et al., 2004; Mazurek et al., 2013) and reactive transport experiments in granitic rocks (Mäder et al., 2006). The next step in development was the demonstration that the infiltration technique could not just be used for high-strength rock cores but also for plastic clay materials such as compacted bentonite (Fernández et al., 2011a; Mäder et al., 2012). The latest development is the coupling of core infiltration experiments and X-ray computed tomography (CT), the subject of this study.

The use of X-ray computed tomography in geosciences is becoming more common paired with technical improvements (Ketcham and Carlson, 2001; Mees et al., 2003). Micro-CT measurements in clay rocks are able to resolve mineral and pore distributions (Keller et al., 2013; Robinet et al., 2012). The use of medical CT for real-time flow monitoring experiments in a fault was shown by Hirono et al. (2003). The tracking of mineral reactions was achieved in recent studies using synchrotron micro-CT on sedimentary rocks (Berg et al., 2013; Fusseis et al., 2012).

This work reports an on-going core infiltration experiment using a pre-conditioned and compacted MX-80 bentonite sample and a hyperalkaline infiltration solution (pH 13.4) that mimics an ordinary Portland cement fluid after full hydration. The combination of CT measurements and core infiltration technique allows tracking the hyperalkaline reaction front in the experiment at desired time intervals while the experiment is kept running. It is a unique combination and a new tool to detect mineral reactions in a long-term experiment prior to post-mortem analysis.

4.2. Materials and methods

4.2.1. Bentonite starting material and pre-treatment

Untreated MX-80 Wyoming bentonite powder was used, manufactured by Volclay LTD, Merseyside, UK (Karnland, 2010). The mineralogy of MX-80 bentonite is composed of sodium montmorillonite (~81.4 wt%), tridymite (~3.8 wt%), plagioclase (~3.5 wt%), muscovite (~3.4 wt%), quartz (~3.0 wt%), gypsum (~0.9 wt%), cristobalite (~0.9 wt%), illite (~0.8 wt%), pyrite (~0.6 wt%), and calcite (~0.2 wt%) (Karnland, 2010). Karnland (2010) reports an ion-exchange capacity of 0.76 eq/kg for bulk bentonite, which is composed of sodium (~75%), calcium (~17%), magnesium (~6%) and minor amounts of potassium (~2%). The measured particles size distribution is enriched in fines (1–10 µm) and ranges to a maximum size of 50 µm.

157.66 g of air dry MX-80 bentonite powder with a residual water-content of 11.98 wt% was compacted to 1450 kg/m^3 dry density and saturated with a dedicated pre-treatment device. It consists of cylindrical titanium containers with baseplate and hydraulic piston, and a fluid saturation system with an inlet at the base, and an outlet at the top. A cylindrical core was fabricated by stacking 4 short segments produced in parallel to save time required for saturation. The final bentonite core was 50 mm in length and 50 mm in diameter (Figure 4-2c) with a weight of 186.69 g, a wet density of 1920 kg/m^3 and a water content of 32.6 wt% (rel. to dry mass) which equals 45.9 g of water. The saturation fluid was an artificial pore water (APW), simulating a moderately saline groundwater at the Äspö underground rock laboratory, Sweden ($APW_{Äspö}$) (Table 4-1). Karnland et al. (2009) showed that the distribution of cations on the exchanger did not change significantly in MX-80 bentonite saturated/equilibrated with Äspö groundwater at low temperature.

4.2.2. Core Infiltration Experiment

The concept of our core infiltration experiment is to produce a reaction front in a bentonite cylinder by injecting a hyperalkaline fluid, similar to what Adler et al. (2001) did with Opalinus Clay. The feasibility of the method is depending on a well-connected porosity in a relatively homogeneous clay material that results in an approximate one dimensional advective-dispersive flow when a strong hydraulic gradient across the length of the core sample is applied. The induced fluid fluxes are relatively low (0.03–0.1 ml/day) and the dispersion is large and dominated by diffusion (Mäder et al., 2004). Figure 4-1 is a schematic of the core infiltration system that can be examined by X-ray tomography. A bentonite core is subjected to a hydraulic confining pressure in a carbon fiber pressure cylinder. The sample core is isolated from the confining medium by multiple layers of Teflon tape and latex sleeves (Figure 4-2b). Adapters maid of POM (polyoxymethylene) are placed at the top and bottom of the bentonite core, separated by 0.5 mm thick Teflon filters. The filters guarantee a homogeneous distribution of the infiltration fluid and collection of the outflowing fluid over the entire cross-section. The bentonite core with adapters is positioned in the middle of the pressure cylinder with inserts at either end that couple to the adapters with O-ring seals. Screw-on POM caps at either end hold the axial force. A POM spindle is adjusted to samples of different lengths, and an axial confining force may be applied initially. The carbon fiber cylinder is connected to a water tank, set under argon gas pressure to generate a desired confining pressure. The infiltration fluid is discharged from a PFA-coated (perfluoroalkoxy) stainless steel tank set under a helium gas pressure. A dual tank system and a stream switching valve allow a change of fluids at constant pressure. PEEK (polyetheretherketone) capillary tubing and chromatography-type fittings are used for connections. Outflow is directed to a syringe with a small-volume electrical conductivity cell (EC) mounted in between. Pressures, temperature and electrical conductivity are monitored using a data acquisition system (DAQ) from Measurement Computing (USB-2416) connected to a computer.

The innovation of this new setup is the mobile, detachable X-ray transparent core infiltration device (Figures 4.1 & 4.2a). The X-ray transparency is achieved by the use of carbon fiber for the pressure cylinder and polymer plastics for the other components. The experiment can be detached and run independently from the main experimental rig for some days using two small pressurized fluid tanks for maintaining the confining pressure and infiltration pressure (Figure 4-3a). The CT measurements are performed with the mobile part of the apparatus mounted on a special frame for a medical CT that guarantees an identical positioning for each scan.

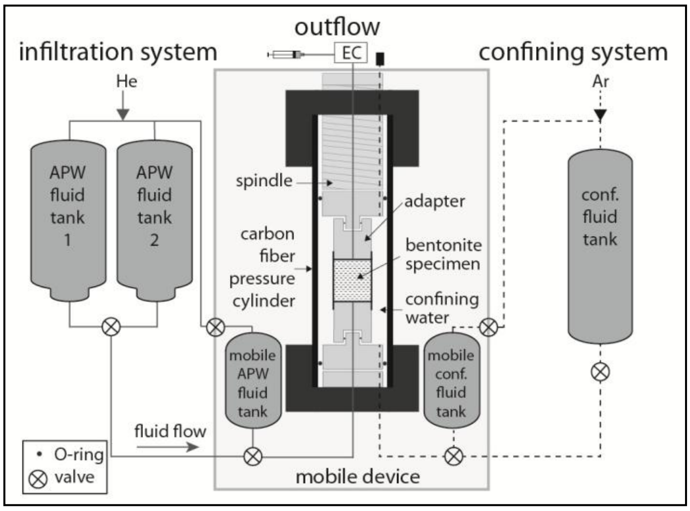

Figure 4-1: Schematic of the core infiltration device consisting of an infiltration system and a confining system. The central part is the X-ray transparent mobile core infiltration device. EC: electrical conductivity cell; APW: artificial pore water.

Our core infiltration experiment was started by applying about half of the final confining pressure while leaving capillary connections to infiltration and outflow open. This was to ascertain that the sample core was perfectly sealed against the confining medium. The final confining pressure was set to 4.1 MPa, while the infiltration fluid pressure was set to 2.1 MPa. During the first 136 days the experiment had time to equilibrate to the new pressure distribution and the new chemical condition of the APW. An artificial Opalinus Clay pore water (APW_{OPA}) was used for infiltration during this phase (Table 4-1). This APW_{OPA} is similar to the $APW_{Äspö}$ but with higher chloride and lower sulfate concentration, and a higher Na/Ca ratio.

Table 4-1: Artificial pore water solutions (APW) used for saturation and infiltration of the bentonite core. $APW_{Äspö}$ and APW_{OPA} are based on reported recipes, whereas the APW_{OPC} is based on published model data.

	$APW_{Äspö}$		**APW_{OPA}**		**APW_{OPC}**
	recipe[1]	fluid	recipe[2]	fluid	fluid[3]
pH	7	7.2	7.8	7.6	13.36
EC [mS/cm] measured at 25°C	19	17.7	-	16.6	56
EC [mS/cm] calc. at 25°C	-	20.5	-	19.7	71.4
Ionic strength [mol/kg]	0.26	0.26	0.23	0.23	0.28
	--[mM]--				
Na^+	92.23	88.2	163.8	165.9	115.4
K^+	0.26	< 1.3	2.55	2.7	180.7
Ca^{2+}	56.14	54.3	11.91	11.9	1.3
Si^{4+}	-	-	-	-	0.06
Al^{3+}	-	-	-	-	0.03
Mg^{2+}	1.65	< 2.1	9.17	9.1	< 0.04
Sr^{2+}	0.46	< 0.6	-	< 0.1	< 0.04
Cl^-	204.39	203.6	160	157.6	0.1
SO_4^{2-}	1.76	1.8	24	22.1	2.9
Br^-	0.15	0.1	-	< 0.02	< 0.02

[1] Mazurek et al. (2013), [2] Mäder (2011), [3] Lothenbach and Winnefeld (2006).

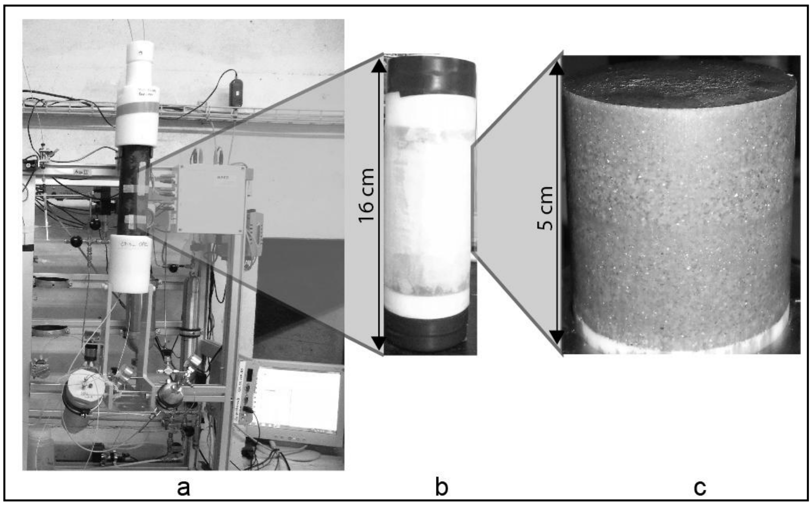

Figure 4-2: (a) Core infiltration device; (b) bentonite core sample including POM adapters covered with latex sleeve; (c) MX-80 bentonite specimen after compaction and saturation.

The hydraulic conductivity can be calculated using Darcy's law for each time interval during which a sample with a known volume was collected:

$$K = -\frac{Q}{A}\frac{l}{\Delta h}$$

where:

K (m/s) is the hydraulic conductivity

Q (m^3/s) is the volumetric flow rate

A (m^2) is the cross-sectional area of the sample core

l (m) is the length of the sample core

Δh (m_{H2O}) is the difference in hydraulic head between in- and outflow.

4.2.3. The high-pH fluid (APW_{OPC})

The infiltration fluid for reactive transport is a hyperalkaline solution representing an ordinary Portland cement pore fluid (APW_{OPC}) (Table 4-1). Its composition is based on Lothenbach and Winnefeld (2006) and it represents a thermodynamically modeled cement pore fluid observed experimentally after a hydration period of 625 days, e.g. corresponding to a more or less complete hydration under closed-system conditions. The aqueous speciation was calculated with PhreeqC (Parkhurst and Appelo, 1999) using a thermodynamic database that includes relevant cement hydration phases (Jacques, 2009; Lothenbach and Winnefeld, 2006). The high pH of 13.36 is characteristic for an alkali-activated portlandite-ettringite dominant composition. The APW_{OPC} was prepared from the following chemicals: $Al_2(SO_4)_3 \cdot 16\times H_2O$, $CaCO_3$, $Ca(OH)_2$, KOH, NaOH, $Na_2O_7Si_3$ (water glass) and Na_2SO_4. Surplus $Ca(OH)_2$ and $CaCO_3$ was added to form a buffer for any unwanted ingress of atmospheric CO_2 by precipitation of calcite (Mäder et al., 2006).

4.2.4. Analytical methods

X-ray computed tomography (CT) is an X-ray imaging technique whereby a helical scan is processed into closely spaced 2D cross-sectional views and further to a 3D image. The CT scans were made on a medical CT scanner (Siemens Somatom 6). It is a six-row multislice scanner operated by the Institute of Forensic Medicine at the University of Bern (Figure 4.3a). The scanning parameters were chosen to optimize contrast between different minerals and to have an adequate penetration depth of the X-rays. The X-ray energy setting was 130 keV with an X-ray tube current of 120 mA. The field of scan was 55 mm in diameter and 122 mm in length. The tomograms have a matrix size of 512 x 512 pixels and a calculated voxel dimension of 0.109 x 0.109 x 0.5 mm.

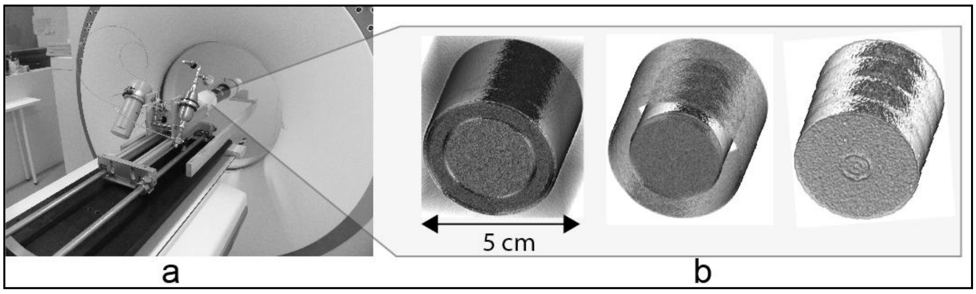

Figure 4-3: (a) Medical CT scanner including experimental frame and mobile part of core infiltration apparatus; (b) CT scans of the pressure cylinder as thresholded 3D rendered images: entire experiment left, air and the confining water removed (middle), peeled off bentonite specimen (right).

The CT scanner is calibrated on air. The sensitivity analysis was performed using reference samples consisting of polymer plastics with known densities that were mounted in an identical water-filled pressure cylinder as used for the experiment. The CT data are expressed in attenuation values using Hounsfield units (HU). This scale defines air at -1000 HU and water at 0 HU, and it is a linear transformation of the X-ray attenuation coefficient. The attenuation coefficient is primarily a function of the X-ray energy and the material properties like density and mean atomic number. This means that for a given X-ray energy an increase in attenuation is related to an increase in density and mean atomic number. The CT data is processed and displayed using the open-source software Mango (Multi-Image Analysis GUI) (Lancaster and Martinez, 2007) (Figure 4.3b).

Ion chromatography (IC, Metrohm 850 Professional) was used to measure major and minor anion and cation concentrations in the collected outflow and samples of the different types of APW. Separation columns A-Supp7-250 and C4-150 were used for anions and cations, respectively. The error of the measurements is ± 5% relative. The pH was measured with an Orion PerpHecT ROSS combination micro electrode and a 780 pH meter from Metrohm. The electrical conductivity measurements were performed with a small-volume flow-through cell normally used in Metrohm ion chromatographs that was connected to a Jumo industrial meter (ecoTRANS Lf 03) and recorded with a data acquisition system. This unit was not accurately calibrated and may behave nonlinearly towards high ionic strengths (see comparison with calculated conductivities, Table 4-1), but it served to record relative changes. The stainless steel electrodes may passivate with time leading to a gradual decrease in measured conductivities, but this effect is normally small.

4.3. Results

4.3.1. Core Infiltration Experiment

Room temperature in the laboratory varies between 24°C in summer and 18°C in winter time (Figure 4-4a). The confining fluid pressure was increased stepwise to 4.1 MPa (Figure 4-4a). Sealing problems with the pressure cylinder forced us to briefly stop and resume the pressure increase of the experiment after 13 days. The target infiltration fluid pressure of 2.1 MPa was applied on day 14. The confining fluid pressure was held at approximately 4.1 MPa. The infiltration fluid pressure shows small variations in particular during the first 136 days due to removal and transportation of the mobile part of the apparatus for CT measurements. The first outflow arrived in the syringe after 19 days.

The hydraulic conductivity decreased from 2.2×10^{-13} m/s to 1.1×10^{-13} m/s during the equilibration period with saline APW_{OPA} (Figure 4-4b). After changing to APW_{OPC}, a sudden reduction to 3.2×10^{-14} m/s was observed, followed by a recovery to 4.7×10^{-14} m/s. The lowest values were due to a technical problem with the fluid sampling and a small leak at the inlet of the electrical conductivity cell. Hydraulic conductivity remained approximately constant during infiltration with APW_{OPC}, with a slightly decreasing trend. It should be noted that also a change in water content of the bentonite core will contribute to the very small APW fluxes, and thus apparent low or high hydraulic conductivities may result. This is especially the case when physical or chemical conditions are changed (e.g., start-up phase, change in APW condition).

The electrical conductivity measurements started after 127 days at 26.5 mS/cm (Figure 4-4*b*). After changing to APW_{OPC}, a slight but sudden increase was followed by a gradual decrease to 22.7 mS/cm. Figure 4-4*b* shows the correlation between the moderate increase in the electrical conductivity and the drop in hydraulic conductivity, suggesting some transient phenomenon induced by the change in fluid composition. The electrical conductivity of the APW_{OPC} is significantly larger than that of the saline fluids despite a similar ionic strength. This is due to the much larger molar conductivity associated with OH^- compared to other ions. The calculated ionic strength of the outflow solutions decreased from 0.44 to 0.34 mol/kg over a period of 282 days during the infiltration with APW_{OPC}. The outflow solution showed an overall decreasing trend for all major ion concentrations with the exception of sulfate (Figure 4-4*c*). Sulfate increased from 53 mM up to 80 mM within 282 days. Sodium concentrations decreased from 400 mM to 274 mM and chloride decreased from 337 mM to 142 mM. Potassium remained constant at 3 mM and calcium decreased from 18 mM to 11 mM. Magnesium decreased from 9 mM to 6 mM. Bromide decreased from 0.3 mM to 0.1 mM. The pH of the outflowing fluid was near 5.1 for the first 118 days, but increased afterwards to ~7.5.

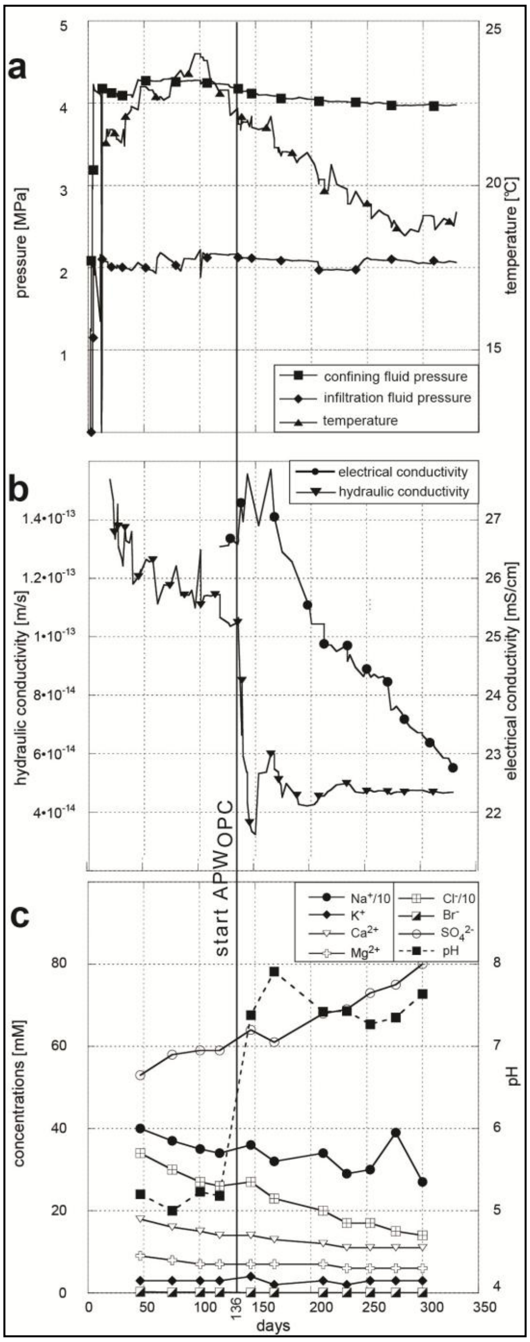

Figure 4-4: Measured parameters and analytical results of the core infiltration experiment: (a) pressures of infiltration and confining fluid, and temperature; (b) hydraulic and electrical conductivity of the outflow fluid; (c) chemical composition and pH of the outflow fluid.

4.3.2. Computed Tomography

Twelve CT scans were performed over a period of 254 days. The sensitivity analysis shows an average standard deviation for the synthetic calibration samples of ±23 HU. Any difference that is greater than ±23 HU can thus be explained by a change in density or/and atomic number. The histogram of the experimental setup shows clearly identifiable peaks for the different materials: 0 HU (water), 320 HU (POM adapters), 450 HU (PVC (polyvinyl chloride) filter, APW saturated), and 1200 HU (compacted bentonite) (Figure 4-5). The variation in attenuation in the sample core is small suggesting a homogenous material distribution. A few small grains are characterized by values up to 3071 HU. Figure 4-6 shows a profile of attenuation along the length and width of the experiment and the bentonite sample. Attenuation values in the water and the POM adapter are uniform, near 0 HU and 320 HU, respectively.

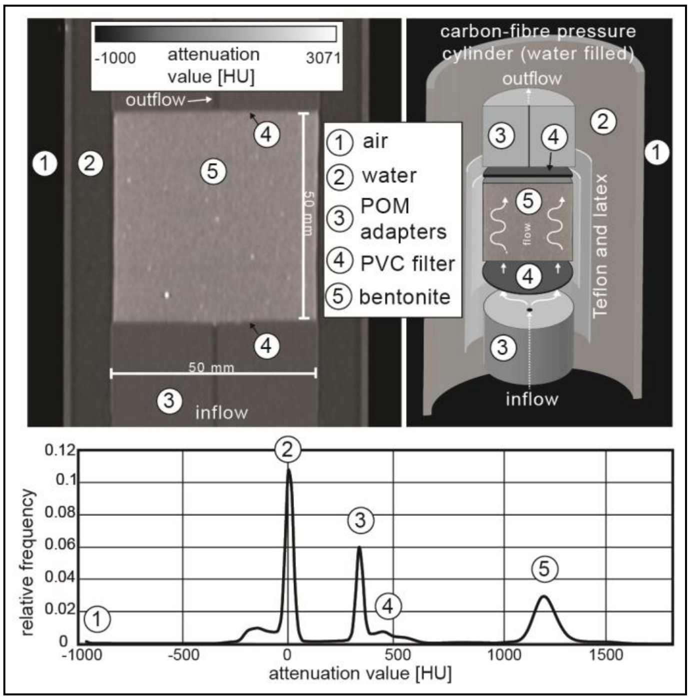

Figure 4-5: Tomographic image of the experiment and schematic (top); histogram of attenuation values of the experimental setup.

Artifacts of beam hardening can be seen along the interface of bentonite/Teflon+latex/water (Figure 4-5). The attenuation value along a section across the length of the bentonite core assembly starts at 340 HU in the POM adapter, increases at the transition to the inlet filter and reaches a first local maximum at 1140 HU in bentonite (Figure 4-5). The attenuation value increases constantly to 1250 HU across the length of the bentonite. The value decreases again to 340 HU in the filter at the outlet. The attenuation value across the width of the bentonite assembly starts at -15 HU in the confining water, jumps to 1500 HU at the Teflon/latex sleeve, and reaches 1230 HU at the sleeve-bentonite interface. The signal in the bentonite reaches a constant value of 1200 HU at 9 mm depth.

Figure 4-7 shows tomographic cross-sectional images through the experimental setup, spaced 1 mm apart covering the interface region at the fluid inlet, including POM adapter, filter, and bentonite. The sections are oriented perpendicular to the axis of the bentonite cylinder (direction of flow), and this transect is shown for 3 different times after the start of infiltration with hyperalkaline fluid. Line profiles across the center of the sections are shown below, and an explanatory figure for geometry and location. The tomographic images and the corresponding diagrams across the POM adapter reveal constant attenuation values over time near 320 HU. The attenuation value in the inlet filter is 480–500 HU at the beginning of the experiment with a bright central spot at 740 HU at the fluid inlet. A reaction front develops in the filter as a set of concentric rings with different attenuation values, reaching 1160 HU in the center after 136 days. This reaction front appears in the bentonite at the transition to the filter initially as rings but develops into a diffuse zone of elevated attenuation in the bentonite sample. This zone penetrates 1.75 mm deep into the bentonite in a hemispherical shape. The bentonite appears unchanged at 2 mm depth with attenuation values of 1150 HU. The average linear propagation velocity for the reaction zone can be calculated by dividing its width measured in axial direction by the elapsed time since switching to APW_{OPC}. After 136 days of APW_{OPC} infiltration the average linear velocity of the reaction front is ~0.013 mm/day, which may not represent a stationary state.

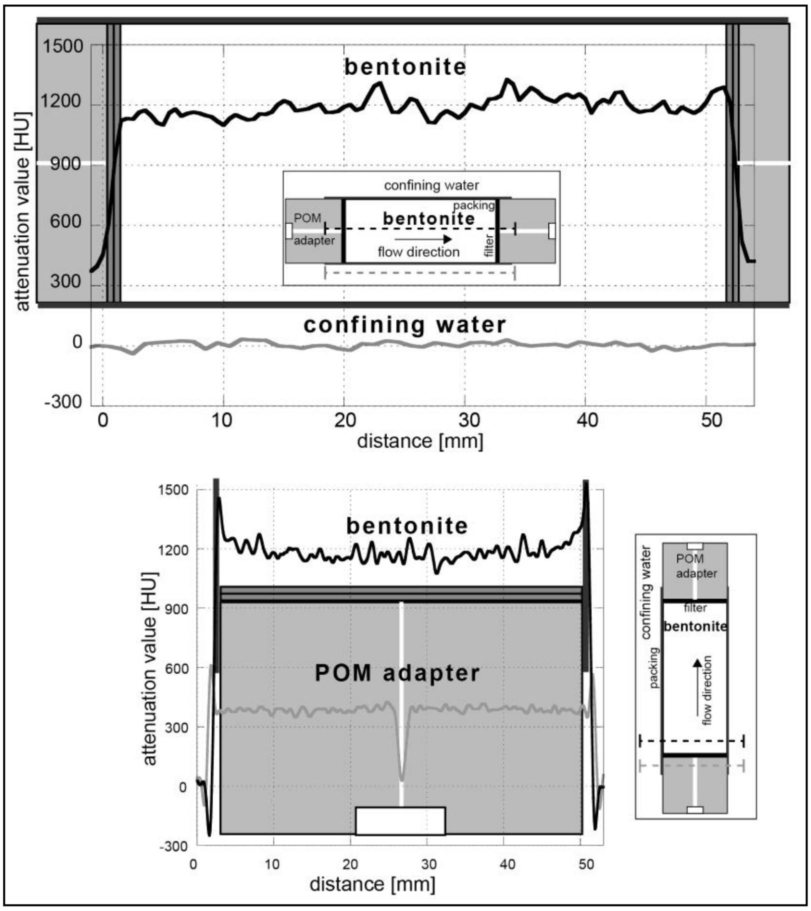

Figure 4-6: Profiles of attenuation value across the bentonite assembly before infiltration of APW$_{OPC}$. The inserts show the locations of the profiles. The profiles across water and POM adapter serve as reference.

4.4. Discussion

4.4.1. Core Infiltration Experiment

Porosity in the bentonite is assumed to consist conceptually of macroporosity (pore-water not affected by charged clay surfaces) and microporosity (interlayer porosity, and region near clay outer surfaces that are affected by surface charge) that is subject to electrostatic interactions. There is a redistribution of chemical constituents relative to bulk pore water composition into an anion-poor micro porosity charge-balanced mainly by negative permanent charges on clay, and a charge-balanced electrolyte relatively enriched in anions. When a hydraulic gradient is applied, advection is affecting the macro porosity, and this results in a relatively fast transport of anions and charge-compensating cations compared to a water tracer such as deuterium (Appelo and Wersin, 2007; Bradbury and Baeyens, 2003; Tournassat and Appelo, 2011). Any change in the injected fluid composition will lead to a re-distribution of these two porosities and their solute content (Mäder et al., 2012), in addition to mechanical processes coupled via swelling pressure that will affect the total water content of a sample by compaction or expansion.

The first gradual decrease in confining fluid pressure up to day 40 (Figure 4-4a) can be explained by a density increase (reduction in porosity/water content) in bentonite due to a change in fluid composition (saturation fluid followed by APW$_{OPA}$) and/or due to sample compaction as a result of the applied confining pressure that may have been larger than that used during sample pre-treatment. A change of infiltration fluids can cause a reduction of swelling pressure due to cation exchange (e.g. di-valent for mono-valent) and/or a change in ionic strength (Karnland et al., 2007). The observed decrease in hydraulic conductivity during the first 100 days of APW$_{OPA}$ infiltration correlates with a slight decrease in confining fluid pressure and this is interpreted to be a result of a density increase in the bentonite core as detailed above. The hydraulic conductivity leveled off at 1.13×10^{-13} m/s, which is in the same range as was measured during sample pre-treatment. It is also similar to data obtained by Karnland et al. (2009) on MX-80 bentonite samples recovered from a long-term field experiment at comparable densities.

The hydraulic conductivity dropped sharply by a factor of two after exchanging APW_{OPA} for $APW_{OPC.}$ The reason for this is unclear. The somewhat higher ionic strength of APW_{OPC} is expected to induce a reduction of the diffuse layer (shorter Debye length) and an increase in macroporosity, and hence an increase in hydraulic conductivity. Also, a reduction in swelling pressure is likewise induced that would result in compaction at our constant-pressure constraint. While this latter effect will eventually lead to a reduced flux, there would be a compaction-driven additional flux during an early transient period. Mineral precipitation is considered unlikely to cause such a sharp decrease in hydraulic conductivity because the mineralogical/density changes were observed to progress very slowly. The hydraulic conductivity stabilized after this transient phase, and presently shows only a minor decrease with time suggesting the absence of extensive pore clogging related to mineral alteration at the inlet of the experiment. The trend in decreasing electrical conductivity after 165 days is corresponding to a decrease in ionic strength in the outflow solution.

The first pH measurements near pH 5 are distinctly low compared to all later values. Such a low pH is also not in agreement with proposed pH values in compacted MX-80 bentonite based on thermodynamic considerations and mineral equilibria (Bradbury and Baeyens, 2003). Fernández et al. (2011b) observed the same effect at the beginning of their experiment. The reason for this apparent artefact is not understood.

The evolution of ion concentrations in the outflow is complex and it is controlled by a number of processes: ionic-strength effects due to changes in the injected fluid composition and coupled transient compaction/de-compaction (releasing or taking up pore water), internal control by minor soluble accessory phases (gypsum, calcite), cation exchange processes, and also silicate mineral dissolution/precipitation after injection of the hyperalkaline fluid. Here, we attempt to provide a qualitative explanation; a detailed reactive transport modeling approach will be presented in a follow-up paper. During the 136-day equilibration phase with saline pore water (APW_{OPA}), more chloride-rich fluid is expelled compared to either of the APW's used for pre-treatment or injection, but it is gradually approaching the input concentration (Figure 4-4). Chloride is the major anionic charge carrier, and this trend is explained by a compaction of the bentonite core whereby initially more saline pore water is expelled from intergranular pore space where chloride is enriched due to anion exclusion effects. After injection of the hyperalkaline fluid, chloride is no longer supplied and it is washed out gradually thereafter. This elution behavior will form a constraint on the proportion of intergranular porosity involved in advection, relative to the proportion of stagnant interlayer porosity where diffusive transport is dominant. Sulfate is enriched in the outflow 30 times compared to $APW_{Äspö}$ and a bit more than 2 times compared to the injected APW_{OPA}. The elution trend is most likely related to the dissolution of gypsum in bentonite. Gypsum is known to be part of the MX-80 bentonite mineralogy (Fernández et al., 2011b; Karnland, 2010). In fact, control by gypsum solubility is also suggested by the concomitant decrease in Ca concentration as sulfate is increasing. The elution trends of the cations during the early phase are constrained by the sum of the anionic charges, and by ion-exchange processes that shift cation ratios. The Na/Ca ratio in the APW_{OPA} is larger compared to the pre-treatment fluid $APW_{Äspö}$ (Table 4-1), and one would expect that the inflowing Na is displacing some Ca from the clay exchanger. This may indeed be the case, but a solubility control by gypsum would mask this trend and suppress Ca in the pore solution accordingly. The aqueous speciation of the outflow solutions was calculated using PhreeqC and the PhreeqC database (Parkhurst and Appelo, 1999), including the ionic strength (Table 4-1) and mineral saturation indices. It was assumed that all samples were saturated with respect to calcite, and this constrained the carbonate alkalinity at given pH and Ca^{2+} concentration. The saturation index for gypsum was between -0.1 and -0.04 for all samples. This is in good agreement with the hypothesis of solubility control by gypsum during the entire experiment. This process was quantitatively modeled in a multi-component transport experiment in MX-80 bentonite by Fernández et al. (2011a).

The anion-accessible porosity is difficult to assess at this stage. The chloride concentration is still somewhat above 50% of the concentration when APW_{OPC} was injected containing no chloride. This suggests that the residence time of chloride in the porosity fraction subject to advection is more than 166 days. Literature data on anion accessible porosity in MX-80 bentonite is summarized in Tournassat and Appelo (2011) and suggests that this porosity may be near 10% at our conditions (dry density ~1400 kg/m^3, ionic strength ~0.25 mol/kg), with a scatter in data and models covering at least a range of 5-15%. The volumetric flow rate stabilized at 0.027 ml/day during the high-pH phase, corresponding to a Darcy flux of 1.75×10^{-10} m/s. Assuming 10% accessible porosity this would lead to an average linear velocity for anions of 2×10^{-9} m/s (0.17 mm/day) or a residence time of 286 days.

4.4.2. Computed Tomography

A clear trend to higher attenuation values at the outlet is observed along the length axis, and this can be explained by a density increase in bentonite due to a pressure gradient in the sample (Figure 4-6, upper diagram). The bentonite is subjected to a confining pressure of 4.1 MPa at the inlet and to an infiltration pressure of 2.1 MPa. This reduces the pressure difference at the inlet compared to that at the outlet where the fluid pressure is 0 MPa. Linear gradients in density will form as a result of this linear gradient in differential pressure. These variations in bulk wet density relate directly to variations in water content. This interpretation is in agreement with density measurements on compacted bentonite during previous core infiltration experiments where profiles in density and water content were measured after termination. The attenuation line across the bentonite cross-section shows a decrease from higher values at the rim to lower ones in the center and this can be explained by a higher density at the rim compared to the center (Figure 4-6, lower diagram). This is either linked to the confining pressure that induces some preferential compaction at the rim, or it is inherited from the sample pre-treatment.

The tomographic images and the attenuation diagrams document changes in the bentonite that evolve with time. These changes reflect differences in densities and these relate to changes in mineralogy and water content. Because the resolution of the CT is much lower than the grain size, the measured attenuations reflect mineral assemblages including porosity rather than single phases. The peaks with high attenuation imply the presence of higher-density minerals like feldspar, mica, quartz or pyrite and/or regions with low porosity.

The time sequence of tomographic images shows the impact of the hyperalkaline APW_{OPC} on the bentonite sample and on the inlet filter *(*Figure 4-7). After 16 days of APW_{OPC} infiltration, a dot-shaped increase in attenuation in the inlet filter formed and a circular region of increased attenuation reached 1mm in depth. After 136 days of APW_{OPC} infiltration the reaction zone in the filter increased and formed concentric circular structures related to mineral precipitation. It was evident that the alteration reactions were restricted to the center part of the sample core and filter. The reaction front advanced into the bentonite as a zone of increased attenuation with the highest values at the filter interface. The circular front reached 1.75 mm in depth and had a radius of 6 mm. The elevated attenuation in the filter is interpreted as mineral precipitates in the pore space. The reaction front in the bentonite is indicated by an increase in attenuation compared to the unreacted bentonite. This can be either interpreted as an increase in average mineral densities by dissolution and precipitation of new minerals or as a change in montmorillonite compaction by loss of water due to the increased ionic strength of APW_{OPC} compared to APW_{OPA}, or both. The identity of the secondary mineral phases cannot be deduced – mineral densities of the possible hydrates that may form are similar, and the changes in densities cannot be spatially resolved at the scale of a pure mineral precipitate. It is clear, however, that a reduction in porosity must be involved due to the fact that all secondary phases are hydrates with a lower specific density (attenuation) compared to the primary bentonite minerals, including montmorillonite (Balonis and Glasser, 2009).

The reaction front advances with an average linear velocity of 0.013 mm/day, which is somewhat smaller than the average linear fluid velocity of 0.015 mm/day assuming total water content. The more relevant average linear velocity for anions of 0.17 mm/day (see above) would imply a retardation factor of ~8 for the reaction front, with an uncertainty of at least a factor of two.

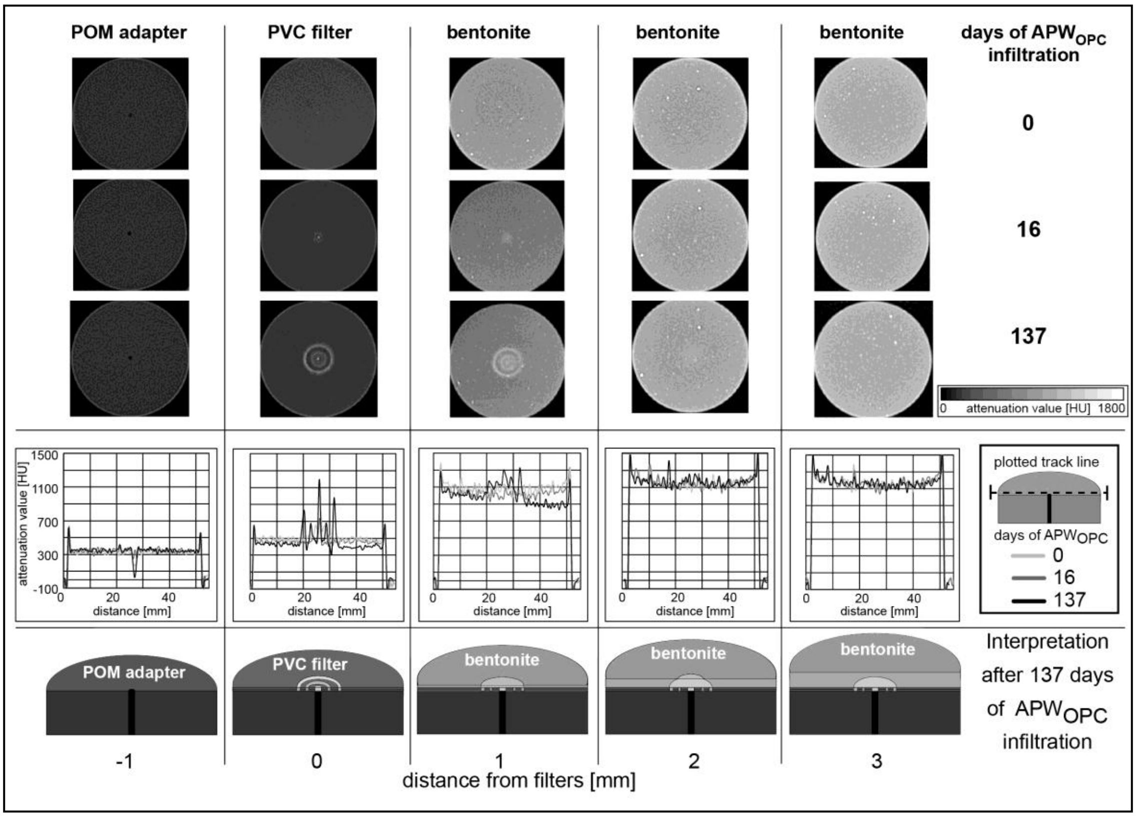

Figure 4-7: Tomographic cross-section perpendicular to the cylinder axis of the bentonite sample with the associated cross-sectional track lines shown below. The evolution in sections across the interface POM adapter-filter-bentonite is shown at 0, 16, and 137 days after starting infiltration with APW_{OPC}. The figures at the bottom are showing an interpretation of the data after 137 days of APW_{OPC} infiltration.

4.5. Conclusions

The feasibility of 4D computed tomography was demonstrated as a tool to record mineral alteration and bulk density changes in MX-80 bentonite during a long-term experiment with a hyperalkaline solution that is still ongoing. The core infiltration technique allows to set up a small advective flux and record the chemical evolution of the outflow and this provides constraints on the clay-internal processes. Namely, solubility control by gypsum paired with anion exclusion effects and the reduction in ionic strength by uptake of hydroxide anions in silicate reactions is evident. The transport of anions other than hydroxide is significantly larger compared to bulk water due to electrostatic interaction in form of anion exclusion. The advective component is small such that diffusion is significant at the scale of the observed alteration zone.

The CT sections across the inlet-region of the high-pH fluid document a gradually enlarging region of higher attenuation due to mineral alteration and porosity reduction that reached nearly 2 mm after 137 days. Also documented is a linear profile in bulk density/water content across the length of the core as a result of the boundary conditions: a constant confining pressure, a constant fluid inlet pressure, and fluid outlet at ambient condition. Hydraulic conductivities responded to chemical changes in the inlet fluid, but stabilized during the high-pH phase at 4.7×10^{-14} m/s. This suggests that potential pore clogging processes which are inferred from the CT measurements are not yet affecting the hydraulics properties significantly.

The experiment is still running and will be dismantled at the beginning of 2014, after more than 1.5 years of infiltration with hyperalkaline fluid, followed by a post-mortem mineralogical analysis. Detailed modeling of the experiment with a generalized kinetic reactive transport computer code is expected to more precisely constrain the physic-chemical processes.

Acknowledgments

Financial support from Nagra is gratefully acknowledged. The Department of Forensic Medicine at the University of Bern is acknowledged for granting access and providing technical support for operating their CT scanner. The machine shop at our institute was instrumental in constructing the experimental apparatus, and our analytical laboratory performed the IC analyses. We thank Barbara Lothenbach (EMPA) for providing the modeled fluid composition for OPC, and Florian Fusseis (University of Edinburgh) helped in discussing CT data.

References

Adler, M., Mäder, U., Waber, H.N., 2001. Core infiltration experiment investigating high-pH alteration of low-permeability argillaceous rock at 30 ºC, in: Cidu, R. (Ed.), Proceedings WRI-10 (10th International Symposium on Water-Rock Interaction). Balkema, Villasimius, Italy, pp. 1299-1302.

Adler, M., 2001. Interaction of claystone and hyperalkaline solutions at 30 °C: A combined experimental and modeling study. PhD Thesis, University of Bern, Switzerland.

Appelo, C.A.J., Wersin, P., 2007. Multicomponent diffusion modeling in clay systems with application to the diffusion of tritium, iodide, and sodium in Opalinus Clay. Environmental Science & Technology 41, 5002-5007.

Balonis, M., Glasser, F.P., 2009. The density of cement phases. Cement and Concrete Research 39, 733-739.

Bauer, A., Berger, G., 1998. Kaolinite and smectite dissolution rate in high molar KOH solutions at 35°C and 80°C. Applied Geochemistry 13, 905-916.

Berg, S., Ott, H., Klapp, S.A., Schwing, A., Neiteler, R., Brussee, N., Makurat, A., Leu, L., Enzmann, F., Schwarz, J.-O., Kersten, M., Irvine, S., Stampanoni, M., 2013. Real-time 3D imaging of Haines jumps in porous media flow. Proceedings of the National Academy of Sciences 110, 3755-3759.

Bouchet, A., Casagnabère, A., Parneix, J.C., 2004. Batch experiments: results on MX80, in: Michau, N. (Ed.), Ecoclay II: Effect of Cement on Clay Barrier Performance Phase II. Final report. (ANDRA) European contract FIKW-CT-2000-0028, pp. 79-86.

Bradbury, M.H., Baeyens, B., 2003. Porewater chemistry in compacted re-saturated MX-80 bentonite. Journal of Contaminant Hydrology 61, 329-338.

Cuevas, J., Vigil de la Villa, R., Ramírez, S., Sánchez, L., Fernández, R., Leguey, S., 2006. The alkaline reaction of FEBEX bentonite: a contribution to the study of the performance of bentonite/concrete engineered barrier systems. Journal of Iberian Geology 32 (2), 151-174.

Dauzeres, A., Le Bescop, P., Sardini, P., Cau Dit Coumes, C., 2010. Physico-chemical investigation of clayey/cement-based materials interaction in the context of geological waste disposal: Experimental approach and results. Cement and Concrete Research 40, 1327-1340.

De La Villa, R.V., Cuevas, J., Ramirez, S., Leguey, S., 2001. Zeolite formation during the alkaline reaction of bentonite. European Journal of Mineralogy 13, 635-644.

Eberl, D.D., Velde, B., McCormick, T., 1993. Synthesis of illite-smectite from smectite at earth surface temperatures and high pH. Clay Minerals 28, 49-60.

Fernández, R., Cuevas, J., Sanchez, L., de la Villa, R.V., Leguey, S., 2006. Reactivity of the cement-bentonite interface with alkaline solutions using transport cells. Applied Geochemistry 21, 977-992.

Fernández, R., Mäder, U., Rodríguez, M., de la Villa, R.V., Cuevas, J., 2009. Alteration of compacted bentonite by diffusion of highly alkaline solutions. European Journal of Mineralogy 21, 725-735.

Fernández, R., Rodríguez, M., de la Villa, R.V., Cuevas, J., 2010. Geochemical constraints on the stability of zeolites and C-S-H in the high pH reaction of bentonite. Geochimica et Cosmochimica Acta 74, 890-906.

Fernández, R., Mäder, U., Steefel, C., 2011a. Modelling of a bentonite column experiment with CrunchFlow including new clay-specific transport features. Mineralogical Magazine 75(3), 839.

Fernández, R., Mäder, U., Jenni, A., 2011b. Multi-component advective-diffusive transport experiment in MX-80 compacted bentonite: Method and results of 1st phase of experiment. Unpublished report. Internal Nagra Working Report, Wettingen, Switzerland.

Fusseis, F., Schrank, C., Liu, J., Karrech, A., Llana-Funez, S., Xiao, X., Regenauer-Lieb, K., 2012. Pore formation during dehydration of polycrystalline gypsum observed and quantified in a time-series synchrotron radiation based X-ray micro-tomography experiment. Solid Earth 3, 71-86.

Gaucher, E.C., Blanc, P., 2006. Cement/clay interactions - A review: Experiments, natural analogues, and modeling. Waste Management 26, 776-788.

Hirono, T., Takahashi, M., Nakashima, S., 2003. Direct imaging of fluid flow in fault-related rocks by X-ray CT. Geological Society, London, Special Publications 215, 107-115.

Jacques, D., 2009. Benchmarking of the cement model and detrimental chemical reactions including temperature dependent parameters. Project near surface disposal of catergory A waste at Dessel. NIRAS-MP5-03 DATA-LT(NF) Version 1 NIROND-TR 2008-30 E.

Karnland, O., Olsson, S., Nilsson, U., Sellin, P., 2007. Experimentally determined swelling pressures and geochemical interactions of compacted Wyoming bentonite with highly alkaline solutions. Physics and Chemistry of the Earth, Parts A/B/C 32, 275-286.

Karnland, O., Olsson, S., Dueck, A., Birgersson, M., Nilsson, U., Hernan-Håkansson, T., Pedersen, K., Nilsson, S., Eriksen, T., Rosborg, B., 2009. Long term test of buffer material at the Äspö Hard Rock Laboratory, LOT project. Final report on the A2 test parcel. SKB Technical Report 09-29, Stockholm, Sweden.

Karnland, O., 2010. Chemical and mineralogical characterization of the bentonite buffer for the acceptance control procedure in a KBS-3 repository. SKB Technical Report 10-60, Stockholm, Sweden.

Keller, L.M., Schuetz, P., Erni, R., Rossell, M.D., Lucas, F., Gasser, P., Holzer, L., 2013. Characterization of multi-scale microstructural features in Opalinus Clay. Microporous and Mesoporous Materials 170, 83-94.

Ketcham, R.A., Carlson, W.D., 2001. Acquisition, optimization and interpretation of X-ray computed tomographic imagery: applications to the geosciences. Computers & Geosciences 27, 381-400.

Khoury, H.N., Salameh, E., Clark, I.D., Fritz, P., Bajjali, W., Milodowski, A.E., Cave, M.R., Alexander, W.R., 1992. A natural analogue of high pH cement pore waters from the Maqarin area of northern Jordan. I: introduction to the site. Journal of Geochemical Exploration 46, 117-132.

Lancaster, J.L., Martinez, M.J., 2007. Mango - Multi-image analysis GUI. Research Imaging Institute, UT Health Science Center at San Antonio, TX, USA, URL: http://ric.uthscsa.edu/mango/index.html.

Lothenbach, B., Winnefeld, F., 2006. Thermodynamic modelling of the hydration of Portland cement. Cement and Concrete Research 36, 209-226.

Mäder, U., Waber, H.N., Gautschi, A., 2004. New method for porewater extraction from claystone and determination of transport properties with results for Opalinus Clay (Switzerland), in: Wanty, R.B., Seal, R.R. (Eds.), Proceedings WRI-10 (11th International Symposium on Water-Rock Interaction). Balkema, Saratoga Springs, New York, USA, pp. 445-448.

Mäder, U., Fierz, T., Frieg, B., Eikenberg, J., Rüthi, M., Albinsson, Y., Möri, A., Ekberg, S., Stille, P., 2006. Interaction of hyperalkaline fluid with fractured rock: Field and laboratory experiments of the HPF project (Grimsel Test Site, Switzerland). Journal of Geochemical Exploration 90, 68-94.

Mäder, U., Jenni, A., Fernández, R., de Soto, I., 2012. Reactive transport in compacted bentonite: porosity concepts, experiments and applications. Mineralogical Magazine 76(6), 2052.

Mazurek, M., Waber, H.N., Mäder, U., de Haller, A., Koroleva, M., 2013. Geochemical synthesis for the Effingen Member in boreholes at Oftringen, Gösgen and Küttigen. Nagra Technical Report NTB 12-07 Nagra, Wettingen, Switzerland.

Mees, F., Swennen, R., Van Geet, M., Jacobs, P., 2003. Applications of X-ray computed tomography in the geosciences. The Geological Society Special Publication, 215, London.

Mosser-Ruck, R., Cathelineau, M., 2004. Experimental transformation of Na,Ca-smectite under basic conditions at 150 °C. Applied Clay Science 26, 259-273.

Nagra, 2002. Demonstration of disposal feasibility for spent fuel, vitrified high-level waste and long-lived intermediate-level waste (Entsorgungsnachweis). Nagra Technical Report NTB 02-05, Nagra, Wettingen, Switzerland.

Nakayama, S., Sakamoto, Y., Yamaguchi, T., Akai, M., Tanaka, T., Sato, T., Iida, Y., 2004. Dissolution of montmorillonite in compacted bentonite by highly alkaline aqueous solutions and diffusivity of hydroxide ions. Applied Clay Science 27, 53-65.

Parkhurst, D.L., Appelo, C.A.J., 1999. User's guide to PHREEQC (version 2) – a computer program for speciation, batch reaction, one-dimensional transport, and inverse geochemical calculations. US Geological Survey Water-Resources Investigations Report 99-4259.

Pitty, A., Alexander, R., Eds., 2011. Maqarin Phase IV report. A joint-funded international project report between NDA, RWMD, Andra, CEA, SKB, Nagra and JNC.

Ramirez, S., Cuevas, J., de la Villa, R.V., Leguey, S., 2002. Hydrothermal alteration of La Serrata bentonite (Almeria, Spain) by alkaline solutions. Applied Clay Science 21, 257– 269.

Robinet, J.-C., Sardini, P., Coelho, D., Parneix, J.-C., Prêt, D., Sammartino, S., Boller, E., Altmann, S., 2012. Effects of mineral distribution at mesoscopic scale on solute diffusion in a clay-rich rock: Example of the Callovo-Oxfordian mudstone (Bure, France). Water Resources Research 48.

Sánchez, L., Cuevas, J., Ramírez, S., Riuiz De León, D., Fernández, R., Vigil Dela Villa, R., Leguey, S., 2006. Reaction kinetics of FEBEX bentonite in hyperalkaline conditions resembling the cement–bentonite interface. Applied Clay Science 33, 125-141.

Savage, D., Walker, C., Arthur, R., Rochelle, C., Oda, C., Takase, H., 2007. Alteration of bentonite by hyperalkaline fluids: A review of the role of secondary minerals. Physics and Chemistry of the Earth, Parts A/B/C 32, 287-297.

Smellie, J.A.T., 1998. Maqarin natural analogue study: Phase III. SKB Technical Report 98-04, Stockholm, Sweden.

Tournassat, C., Appelo, C.A.J., 2011. Modelling approaches for anion-exclusion in compacted Na-bentonite. Geochimica et Cosmochimica Acta 75, 3698-3710.

Watson, C., Hane, K., Savage, D., Benbow, S., Cuevas, J., Fernández, R., 2009. Reaction and diffusion of cementitious water in bentonite: Results of "blind" modelling. Applied Clay Science 45, 54-69.

5 Alteration of MX-80 bentonite backfill material by high-pH cementitious fluids under lithostatic conditions – An experimental approach using core infiltration techniques

Submitted to Geological Society, London, Special Publications (2015); F. Dolder, U. Mäder, A. Jenni, B. Münch
(*Extended version of paper published in this thesis*)

Abstract. We characterize and quantify processes at a cement/bentonite interface spatially and temporally during a long-term core infiltration experiment.

A young ordinary Portland cement pore-fluid (K^+–Na^+–OH^-; pH 13.4) was infiltrated into a MX-80 bentonite core with an initial saturated density of 1.92 g/cm^3 that shifted to 1.89–1.93 g/cm^3 after 761 days. A hydrostatic external pressure of 4.1 MPa and an infiltration pressure of 2.1 MPa were applied in a triaxial-type apparatus. A decrease in hydraulic conductivity from $\sim 1.1 \times 10^{-13}$ m/s to $\sim 4.2 \times 10^{-15}$ m/s was observed passing from advective-dominated flow to a diffusion-dominated regime. The outflow showed replacement of chloride by sulphate during the high-pH infiltration period controlled by dissolution of gypsum, uptake of K^+ by ion-exchange, and a complex mineral reaction front very near the inlet. X-ray CT scans performed repeatedly during the experiment tracked a progressing hemispherical reaction plume in the first mm's of the bentonite revealing a zone of bulk density increase. This zone was related to two distinct but overlapping zones of Mg and Ca-enrichment related to precipitation of saponite and calcite among more complex details. The experiment attested an effective buffering capacity for bentonite, a progressing coupled hydraulic-chemical sealing process and also the preservation of the physical integrity of the interface region in this setup with a total pressure boundary condition on the core sample.

Keywords: Core infiltration experiment, Ordinary Portland cement, Bentonite, High-pH alteration, Nuclear waste storage, Saponite, X-ray tomography

5.1. Introduction

Long-term storage of high level nuclear waste (HLW) and spent fuel (SF) is one of the great challenges of our society. The Swiss concept for a geological repository foresees a multiple barrier system (EBS) to protect the biosphere from SF/HLW (Nagra, 2002). The role of the EBS is to attenuate diffusion of nuclides. Cement-based materials as tunnel reinforcement and tunnel plugs/seals may affect the EBS (Nagra, 2002). Pore-water emanating from concrete or mortar induces a high-pH reaction plume that may influence the chemical and physical properties of the EBS by dissolution/precipitation of minerals followed by changes in permeability, swelling pressure and radionuclide retention.

Bentonite is considered a possible material for the EBS and consists predominantly of the clay mineral montmorillonite (smectite) (Karnland, 2010). Properties like swelling in contact with water and adsorption of cations are induced by a negative charge of the clay surface giving rise to a cation exchange capacity (CEC) and swelling capacity.

Pore-fluids of fresh OPC (ordinary Portland cement) are strongly enriched in K^+ and Na^+ with initial pH of 13–14. Pore-water during early hydration is mainly controlled by portlandite, C–S–H, ettringite and monosulphate saturation (Lothenbach and Winnefeld, 2006).

In case of cement-rock interaction, the period of highest pH at the cement/clay interface is estimated to be relatively short due to buffering reactions. Various experimental and modeling studies predicted relatively rapid and significant cement and rock alterations near the interfaces (De Windt et al., 2004; Gaucher and Blanc, 2006; Kosakowski et al., 2014; Savage et al., 2002; Watson et al., 2009).

Two main experimental approaches were used in laboratories to perform interaction experiments: batch reactors with high water/solid (w/s) ratio, and flow-through devices using a compacted sample (low w/s ratio). Higher w/s ratio led to faster and more prolific reactions and more available space for mineral precipitation. A lower w/s ratio meant slower but also in general less extensive reactions. Of direct interest are the results of experiments at alkaline, high-pH conditions using MX-80 bentonite (WY, USA) or FEBEX bentonite (Almería, Spain). Two main types of infiltration fluids were used for experiments; alkaline (K–Na–OH) based fluids, simulating young cement pore-waters (pH 13–14), and Ca–OH fluids, simulating more mature pore-fluids (pH < 12.5) buffered by portlandite. It could be shown that the Ca-dominated pore-fluids are much less reactive even at elevated temperatures (Fernández et al., 2009a; Fernández et al., 2010a; Karnland, 1997; Karnland et al., 2007; Ramirez et al., 2002b). Hyperalkaline pore-fluids were shown to be highly reactive, associated with changing physical and chemical parameters. Experiments have shown that the temperature is of great importance for the EBS durability near the cement interface. At high temperature the reactivity is strongly increased mainly by pH-dependent faster kinetics. Therefore results of high temperature experiments can be used for interpolation to low temperature interpolation because the kinetics are often too slow to observe any reaction at feasible time scales. At temperatures >60°C strong mineral alterations with mineral precipitation/dissolution and reduction of swelling pressures were observed. Precipitation of zeolites was reported at temperature >75°C with analcime occurring in sodium dominated and phillipsite in potassium dominated solutions. C–(A)–S–H and hydrotalcite were observed as well. Clays, mainly smectite and illite, were reported to get transformed, inter-layered with new mineral phases as well as precipitated/dissolved. Dissolution of silica minerals like quartz, cristobalite, smectite, and feldspar as well as calcite, gypsum and brucite were observed. Finally, changes in swelling pressures were reported. At ambient temperature (20–35°C) most of the studies reported minor changes: formation of smectite (random mixed-layered I/S), brucite, C–S–H gels, zeolites (phillipsite), and reduction in swelling pressure (Bauer and Berger, 1998; Bauer and Velde, 1999; De La Villa et al., 2001; Eberl et al., 1993; Fernández et al., 2006; Fernández et al., 2010a; Karnland, 1997; Karnland et al., 2007; Ramirez et al., 2002a; Sánchez et al., 2006).

This work summarizes a core infiltration experiment using compacted MX-80 bentonite sample and an alkaline cement solution (pH 13.4) that mimics an ordinary Portland cement pore-fluid after full hydration. CT measurements allowed tracking the reaction plume and density/volume changes over time, while XRD, SEM, Raman, and optical microscopy were used for post-mortem characterization.

5.2. Methods and material

5.2.1. Core infiltration experiment

Our experimental approach used a core infiltration method, which is characterized by a low w/s ratio. Constant confining pressure is applied to the rock samples that may represent lithostatic/hydrostatic pressure conditions. This external pressure is a total pressure constraint for swelling materials rather than a constant-volume condition used in standard percolation or diffusion equipment. The method was first described in

Adler (2001) and Adler et al. (2001) and focused on chemical rock-water interaction combined with tracer transport and retardation in Opalinus Clay. The application was continuously extended to pore-water extraction by advective displacement in clay rocks (Mäder et al., 2004; Mazurek et al., 2013), and reactive transport in bentonite (Fernández et al., 2011b; Mäder et al., 2012). Most recently, the analytical capability was extended with an X-ray transparent setup to monitor a reaction plume during a running experiment (*chapter 4*).

A confining fluid pressure is applied to a sealed cylindrical clay rock sample and an infiltration fluid is injected on one side, inducing an advective flow by a pressure gradient between in- and outflow. Two filter pairs on each side of the core guarantee a uniform distribution of the infiltration fluid and collection of the outflowing fluid. A detailed description of the method is given in *chapters 2 & 4*. The current study was performed in an X-ray transparent core infiltration device, consisting of a base-station and a detachable pressure vessel, containing the rock sample, both equipped with pressure tanks for autonomous operation (Dolder et al. (2014), *chapter 4*).

During the first 136 days (equilibration phase), the bentonite core had time to equilibrate to the new pressure conditions using artificial Opalinus Clay pore-water (APW_{OPA}). During the following 625 days artificial Ordinary Portland cement pore-water (APW_{OPC}) was infiltrated. The experiment was stopped by closing the infiltration and reducing the confining fluid pressure stepwise to atmospheric conditions. After dismantling the experiment, the rock sample was unpacked, measured (length, diameter, mass) and sectioned. Two longitudinal samples of 2x5x1 cm (Figure 5-1; XRD and SEM samples) were cut along the centre. Both samples were exposed to liquid nitrogen (-196°C) in a sealed plastic bag and dried for 2 days in a freeze-dryer at <1 Pa and ambient temperature. Samples for SEM (scanning electron microscope) and Raman spectroscopy analysis were vacuum impregnated with resin and polished using oil-based diamond suspensions and petroleum. The second longitudinal sample was dedicated to XRD (X-ray diffraction) analysis and cut into 15 samples of 2–7 mm thickness perpendicular to the sample axis. The rest of the core was cut into two longitudinal profiles for water content and density (ρ) measurements, 5 samples each. Two profiles were located along the outer surface of the cylinder (subscript: rim) and two profiles at 1 cm off-axis (subscript: cen) (see Figure 5-1). The filters were immersed in isopropyl alcohol and dried in a nitrogen filled desiccator to prevent carbonation.

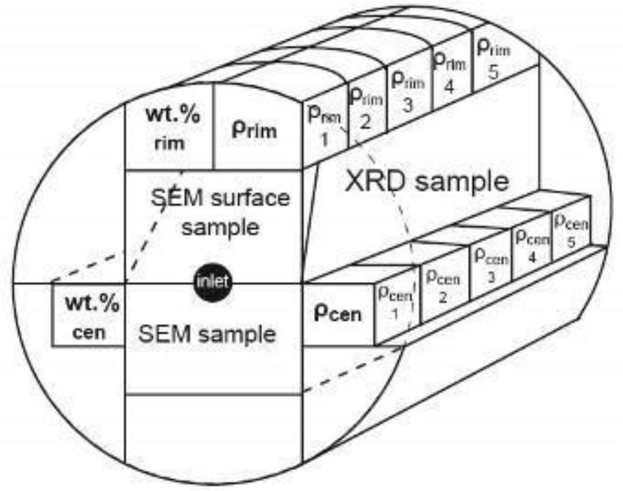

Figure 5-1: Post-mortem bentonite core cutting pattern (bent-CT1).

5.2.2. Analytical methods

Ion chromatography (IC, Metrohm 850 Professional) was used to measure cation and anion concentrations in the collected outflow and in the different types of APW (separation columns C4-150 and A-Supp7-250). The analytical error of these measurements varied between ±5 and ±20%. The pH was measured with an Orion PerpHecT Ross combination micro-electrode. The alkalinity was measured on a 785 DMP titrino from Metrohm. Ion coupled plasma atomic emission spectroscopy (ICP-OES) measurements were performed on a Varian 720-ES. This method was used to measure minor and some trace elements like aluminium, barium, silica, and strontium.

The electrical conductivity measurements were performed in-line with a small-volume flow-through cell (from Metrohm) that was connected to a Jumo industrial meter (ecoTRANS Lf 03) and recorded with a data acquisition system. This device was not accurately calibrated due to its small volume, but it served for recording relative changes.

Density and water content of the bentonite core were determined post-mortem. The bulk density was measured on saturated samples directly after opening the experiment using a Mettler Toledo density accessory kit (immersion in paraffin oil) mounted on a Mettler Toledo balance (AT261 Delta Range). The grain density of the original MX-80 was measured using a He-gas pycnometer (Micromeritics AccuPyc II 1340). Water content was determined by weighing a sample wet and after 2 weeks of oven drying at 105°C.

The mineralogy was determined by XRD on an X'Pert PRO PANalytical diffractometer with a Cu-Kα radiation and an X'Celerator detector using a current intensity and voltage of 40 mA and 40 kV. The XRD runs were performed from 4–60° or to 70° 2θ with step times of 1.1 s and step size of 0.017°. The scans were either performed on disoriented powder samples (grain size ~10 µm) or, in case of insufficient material, deposited on a silica wafer (samples taken directly at the interface to the inlet filter). All samples were preconditioned at 33 %rh (relative humidity) using a saturated $MgCl_2$ solution. All XRD traces were normalized on the 3.34 Å quartz peak. Additional samples were measured saturated with ethylene-glycol (EG).

SEM measurements were performed on uncoated sample surfaces with a Zeiss EVO-50 XVP microscope equipped with an EDAX Sapphire light element detector. The machine was used in the low vacuum mode with a beam acceleration of 20 kV and a working distance of ~9 mm. Energy dispersive spectroscopy (EDX) was used for elemental analyses of points and areas as well as element maps. EDX point measurements were acquired for 1 min and semi-quantitatively analyzed without standardization using the EDAX Genesis software. All detected elements except for C and O were normalized to 100 wt%; carbon and oxygen could not be used as it is the main constituent of resin. Analytical errors are below 2 wt% in low-vacuum mode. EDX element maps with a resolution of 512x400 pixels were acquired using a dwell time of 200 µs and frames were averaged for 1–2 h. Back-scattered electron (BSE) images were taken with a resolution of 1024x800 pixels.

The Raman spectroscopy measurements were performed on the polished SEM sample surfaces, where points of interest localized by SEM could be revisited. The Raman microscope consist of a Jobin Yvon LabRAM-HR800 (800 mm focal-length spectrograph) combined with an Olympus BX41 microscope. A He–Ne laser with an excitation wavelength of 632.817 nm (red) was focused on the sample surface in a spot of approx. 2 µm in diameter using a 100x objective, and the Raman signal was collected in backscattered mode. The spectra were recorded with Labspec V4.14 software.

The X-ray computed tomography (CT) measurements were performed on medical CT scanners (Siemens Somatom Emotion 6 and Siemens Somatom Definition AS), operated both by the Institute of Forensic Medicine at the University of Bern. In total 17 CT scans were performed during the experiment, 16 on the first machine and 1 on the second after replacement of the original instrument. The parameters used were chosen to optimize the contrast of the images. The generated X-ray energy was 130 keV (polychromatic X-ray beam) with an X-ray tube current of 120 mA for the first machine and 140 keV and 140 mA for the second. The voxel dimension of the recorded images was 0.109x0.109x0.5 mm for the first scanner and 0.107x0.107x0.5 mm for the second. The change of the CT machines made a direct comparison of the different datasets difficult. For this reason the last dataset measured on the new machine was corrected by a best fit of the bulk absorbance not affected by chemical changes in order to compare the last dataset with previous once. The CT scanners were calibrated on air and its images are shown in Hounsfield units (HU), a generic unit used in medicine. It is defined by air (-1000 HU) and distilled water at 0 HU. The data were processed and analyzed using the open-source software Mango (Multi-Image Analysis GUI, Lancaster and Martinez (2007)) and Fiji, an open-source image processing software package based on ImageJ (Schindelin et al., 2012). 3D image analyses were performed using Fiji and Matlab.

5.2.3. Aqueous geochemical modeling

Aqueous speciation calculations and saturation states at 25°C were performed using PhreeqC (V2.18) (Parkhurst and Appelo, 1999, 2013). The PhreeqC.dat database was used for neutral-pH fluids, extended by montmorillonite, cristobalite (Thermoddem database, Blanc et al., 2007) and tridymite (llnl.dat database, Wolery (1992)). Modeling of the high-pH cementitious fluid required a database containing cement minerals. For this purpose the CEMDATA07 (version 07.02) for PhreeqC was used (Jacques, 2009; Lothenbach et al., 2008), and the references therein).

5.2.4. Starting material

Untreated MX-80 bentonite powder was used, manufactured by Volclay LTD, Merseyside, UK. It consists of Na-montmorillonite (81–85 wt%), feldspars (~5 wt%), quartz (~3 wt%), muscovite (~3 wt%), gypsum (~1 wt%), cristobalite (~1 wt%), calcite (~0.2 wt%) (Karnland, 2010). The exchanger of montmorillonite is dominated by

Na^+ with 75 eq%, followed by Ca^{2+}, Mg^{2+} and K^+ with 17, 6 and 2 eq%, respectively (Karnland, 2010). The MX-80 bentonite sample was compacted and saturated in a pre-treatment device using 157.66 g of air-dry rock powder with a residual water-content of 11.98 wt%, corresponding to 45.9 g of pore-water after saturation (w/s ratio 0.33) (Dolder et al., 2014). This amount corresponds to one pore-volume (PV) used to convert transport time to number of PV passing through the core. The saturated MX-80 bentonite core was 49.5 mm in length, 50 mm in diameter and had a mass of 186.69 g, corresponding to a saturated density (ρ_{sat}) of 1920 kg/m^3 (ρ_{dry} 1448 kg/m^3) and a water-content porosity of 44.73%.

5.2.5. Saturation fluid

APW$_{Äspö}$ and APW$_{OPA}$ were used for saturation and during the equilibration phase of the experiment (Table 5-1). APW$_{Äspö}$ was based on moderately saline fracture water from the Äspö underground rock laboratory (Dolder et al., 2014; Karnland et al., 2009). The aqueous modeling showed under-saturation with respect to gypsum, near saturation with calcite and a partial CO_2 pressure (pCO_2) similar to atmospheric conditions (Table 5-5). APW$_{OPA}$ was based on a recipe of Mäder (2009) for pore-water from the Opalinus Clay Formation and is described also in *chapter 4*. The fluid was saturated with calcite and gypsum and the pCO_2 was atmospheric (Table 5-5). Both recipes are shown in Table 5-3.

Table 5-1: Measured APW$_{Äspö}$ and APW$_{OPA}$ properties (errors are ~5 %) and calculated saturation indices.

	APW$_{Äspö}$[a]	**APW$_{OPA}$**[a]
pH	7.2	7.6
Ionic strength (mol/kg)	0.26	0.23
	(mM)	
Na^+	88	165.9
K^+	0.3	2.7
Ca^{2+}	54	11.9
Si^{4+}	<0.007	<0.007
Al^{3+}	4.10E-04	5.70E-04
Mg^{2+}	1.65	9.1
Cl^-	203	157.6
SO_4^{2-}	1.8	22.1
HCO_3^-	0.24	0.66

[a] Dolder et al. (2014)

APW$_{OPC}$ represented a cement pore-fluid of a fully hydrated OPC with a pH of 13.36 (Table 5-2). The composition was based on Lothenbach and Winnefeld (2006) and it represented a thermodynamically modeled ordinary Portland cement fluid in agreement with measurements on reference samples after a hydration for 625 days under closed-system conditions. The corresponding modeling was carried out using the Gibbs free energy minimization program GEMS (Lothenbach and Winnefeld, 2006). The APW$_{OPC}$'s saturation with respect to selected phases is shown in Table 5-5. The main differences between the modeled solution of Lothenbach and Winnefeld (2006) and APW$_{OPC}$ are the lower K^+ and higher OH^- and HCO_3^- concentrations. The check of the APW$_{OPC}$ after 625 days of infiltration revealed only minor changes. The recipe is shown in Table 5-3.

Table 5-2: Composition of the APW_{OPC} and comparison to literature.

	Data of Lothenbach and Winnefeld (2006)		**Infiltrated fluid, measured (APW_{OPC})**	
	Measured data	Modelled data	Start	End (after 625 days)
Hydration time	360	625		
pH	13.3	13.36	13.36	13.34
Ionic strength [mol/kg]	-	-	0.28	0.27
Percent charge error	-	-	-0.02	0.19
	mM			
Na^+	90	118.7	115.4	114
K^+	208	222	180.7	173.3
Ca^{2+}	1.9	0.9	1.3	0.5
Si^{4+}	0.05	0.06	0.17	unkn.
Al^{3+}	0.01	0.03	0.03	unkn.
Mg^{2+}	-	-	< 0.41	< 0.1
Cl^-	-	-	0.08	<1.6
SO_4^{2-}	3.4	2.9	2.9	2.9
C	13 (DOC)	0.22	1.5 (DIC)	unkn.

Table 5-3: Recipes of the three APWs, including formulae, LOT number, molar mass and amounts of the chemicals (+ means surplus).

Ingredients	**Producer and no.**	**M (mfw)**	**$APW_{Äspö}$**	**APW_{OPA}**	**APW_{OPC}**
Solids			g/kg	g/kg	g/kg
$Al_2(SO_4)_3$ 16×H_2O	Fluka: 06421	630.4			0.0096
KCl	Merck: 1.04936	74.6	19.6	0.1902	
KOH	Merck: 1.05033	56.1			12.5
Na_2SO_4	Merck: 1.06649	142.0	249.9	3.4089	0.43
NaCl	Merck: 1.06404	58.4	5164.2	6.7356	
Na_2CO_3	Merck: 6398	106.0	10.3		
$NaHCO_3$	Fluka: 71329	84.0		0.0456	
NaBr	Fluka: 71329	102.9	15.4		
NaOH	Merck: 1.06498	40.0			4.5
$MgCl_2$ 6×H_2O	Merck: 1.05833	203.3	334.8	1.8635	
$CaCl_2$ 2×H_2O	Merck: 1.02382	147.0	8253.0	1.751	
$Ca(OH)_2$	Merck: 1.02047	74.1			0.047 + 0.1
$CaCO_3$	Merck: 1.02066	100.1			0.022 + 0.05
$SrCl_2$ 6×H_2O	Fluka: 85892	266.62	121.411		
Solution					ml/kg
$Na_2O_7Si_3$	Sigma-Aldrich: 338443-1				0.0094

5.3. Results

5.3.1. Hydraulic evolution of the experiment

The experiment duration was 761 days. In total 0.44 PV were flushed through the core; 0.18 PV of APW_{OPA} and 0.26 PV of APW_{OPC}. The experiment was carried out in a laboratory with minor temperature variation (18–24°C, Figure 5-2a). The confining fluid pressure was increased stepwise to 4.1 MPa (Figure 5-2a). In the first 12 days, 0.26 l of gas were collected in syringes at the outflow, indicating a sealing problem in the exfiltration system. The exceptional gas outflow was related to trapped atmospheric gas in the confining fluid system, leaking continuously into the fluid outflow of the experiment. The experiment had to be stopped and re-started after 13 days, including re-packing of the core. Switching to APW_{OPC} induced a decrease to 3.9 MPa, caused by core volume shrinkage in combination with pressure loss during decoupling for CT scans. The infiltration fluid pressure was set to 2.1 MPa (Figure 5-2a). After re-starting the experiment the pressure was again re-adjusted and stayed constant during the experiment with some minor deviations. After 642 days the infiltration pressure was increased to 2.8 MPa in order to increase the fluid flow.

The hydraulic conductivity shown in Figure 5-2b was based on averages of 4 single water-level measurements on syringes at the fluid outflow, with time spans of 2–4 weeks. The hydraulic conductivity was calculated based on Darcy's law (Dolder et al., 2014). The hydraulic conductivity decreased during the equilibration period to 1.1×10^{-13} m/s due to adaption of the core to the new pressure, compacting the core and initially releasing water. APW_{OPC} infiltration induced a drop to 4.7×10^{-14} m/s and a more gradual decrease to 2.0×10^{-14} m/s after 460 days (Figure 5-2b). After 643 days the conductivity reached 4.2×10^{-15} m/s. The sharp decrease after switching to APW_{OPC} happened over a period of ~30 days; frequent removal of the experiment for CT scanning perturbated the outflow (Dolder et al., 2014) giving rise to some of the fluctuations.

The electrical conductivity measurement started after 127 days at 26.5 mS/cm, decreased to a minimum of 21.4 mS/cm after 450 days and increased finally to 23 mS/cm (Figure 5-2b).

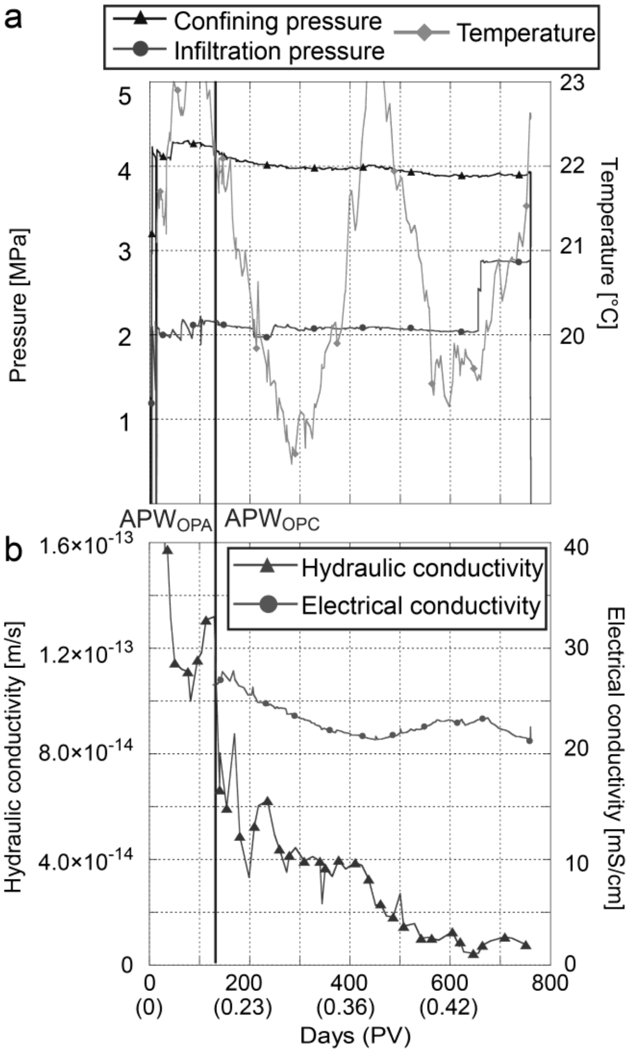

Figure 5-2: Evolution of the physical parameters: (a) pressure and temperature, (b) hydraulic- and electrical conductivity.

5.3.2. Chemical evolution of the outflow

20 outflow aliquots were collected in syringes, 5 syringes were sample during the equilibration phase and 15 during the high-pH infiltration phase. The average solution-loss in the syringes before and after cold storage was between 1–2 mg, corresponding to 0.01–0.05 vol%. Samples were analysed for the inorganic aqueous constituents and pH (Figure 5-3). The alkalinity was measured on combined samples of two aliquots each, due to small fluid volumes. The pH of the first four syringes was ~5.2 and increased after 134 days (0.18 PV) to 7.4.

During APW$_{OPC}$ infiltration a gradual increase to pH ~8.2 after 756 days (0.43 PV) was observed. The values below pH 6 were most likely artefacts due to the ingress of compressed air mentioned above.

The outflow gradually approached the APW$_{OPA}$ composition during the equilibration phase; reduction in all ion concentrations was observed with the exception of sulphate (Figure 5-3). High-pH infiltration reduced ion concentrations further, with the exception of potassium, sulphate, silica, alumina and bicarbonate. All ion concentrations were approaching APW$_{OPC}$ composition with the exception of silica, sulphur, and bicarbonate (Figure 5-3). After switching fluids, chloride got replaced as main anion charge carrier by sulphate after 0.4 PV$_{OPC}$ corresponding to the end of the transient-flow phase. Measured ammonium, barium, fluoride, and nitrate were mostly below or near the detection limit.

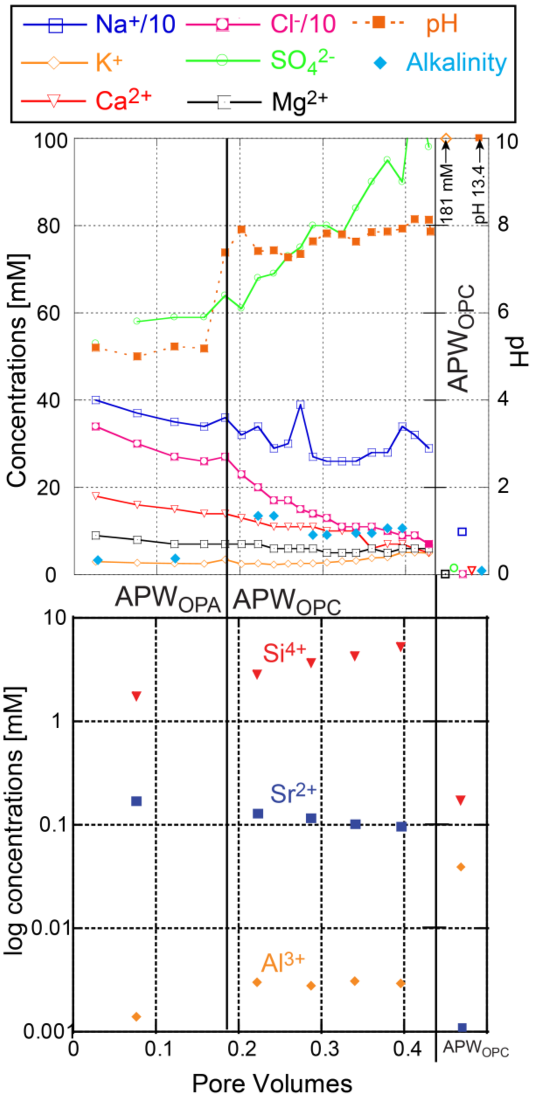

Figure 5-3: Ion concentrations, alkalinity, and pH of the outflow plotted against PV.

5.3.3. Physical evolution: Computed tomography (CT)

The calculations of core volume were based on the HU histograms of each dataset. A region of interest (ROI) was experimentally defined; the voxels were counted and multiplied by the voxel dimension. For the first CT scanner the ROI was 1000–2700 HU and for the second scanner 960–2800 HU. The bulk density of the core is linearly dependent to the HU. The pre-experiment (pre-exp.) bentonite volume was 97.2 cm^3 and decreased after insertion into the infiltration device and applying pressure by 1 vol% (Figure 5-4). A further volume decrease started at day 137 of high-pH infiltration and ended after 588 days, corresponding to -1.5 vol% relative to time 0. It corresponds to a shrinkage rate of ~0.0017 cm^3/day and a pore-water volume of 1.2 ml.

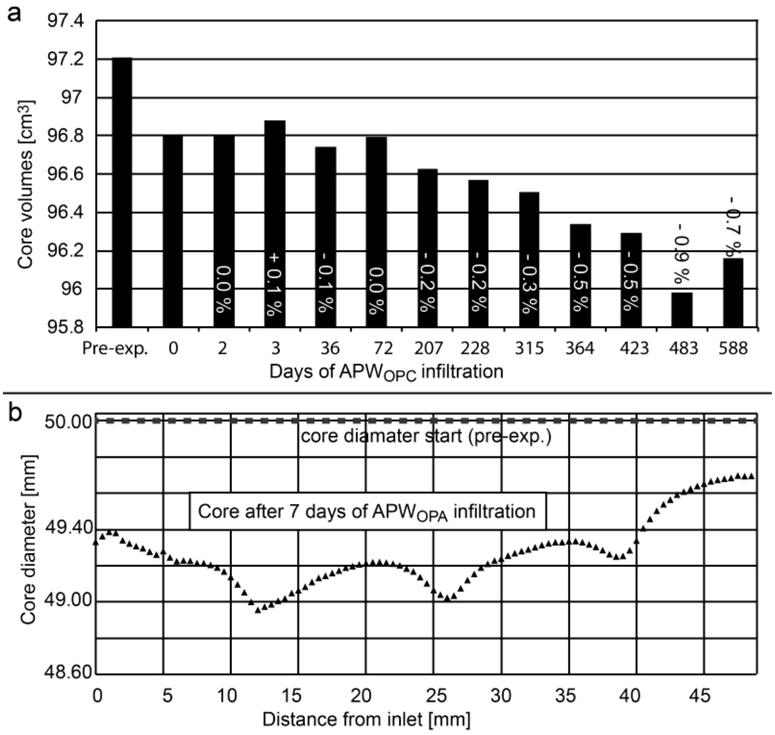

Figure 5-4: Core evolution based on CT measurements: (a) core volumes; (b) core diameters.

The core diameter calculations were performed the same way as the volume calculations. In doing this for all CT-slices of a dataset, the evolution of the core sectional area and the core diameter over time could be evaluated along the core axis (Figure 5-4b). The core diameter was after 107 days of APW$_{OPA}$ infiltration reduced relative to the pre-experimental value by ~0.7 mm (inlet), ~1 mm (12 mm from the inlet), and ~0.3 mm (outlet), respectively (Figure 5-4b). It is in agreement with the postulated density increase along the core axis in Dolder et al. (2014) (*chapter 4*). The core diameter still exhibited four distinct domains of ~12 mm length each, which were remnants of the sample compaction and saturation process (assembled from 4 saturated discs).

The diameter differences as well as the histogram evolution of the core during high-pH infiltration relative to a measurement after 102 day of APW$_{OPA}$ infiltration is shown in Figure 5-5b. The main volume/diameter reduction happened between 72 and 207 days of APW$_{OPC}$ infiltration and onwards, the maximum core diameter shrinkage occurred between 5 and 16 mm depth. The maximum stage was reached after 588 days with a core diameter reduction of 0.7 vol%. The diameter shrinkage reached the end of the core sample between 315 and 364 days of APW$_{OPC}$ infiltration. The last measured diameters of the core were ~49.2 mm for the inlet, 48.8 mm for the middle part and 49.7 mm for the outlet, which is in agreement with post-mortem measurements. The comparison of the bentonite transection image and the core diameter evolution in Figure 5-5b showed that the zone of maximum diameter decrease matches the zone of whitish discoloration of the sample material. HU-histograms of single CT slices at 0.5, 1.0, 8.5, and 12.5 mm from the inlet are plotted over time in Figure 5-5c. The CT slice at 0.5 mm from the inlet showed a drastic reduction in intensity and HU over time, which can be related to a bulk density decrease. In the subsequent histograms further away from the inlet the opposite trend was observed. This means that the rest of the core showed an increasing HU intensity and bulk density over time, which is in agreement with the diameter reduction mentioned before.

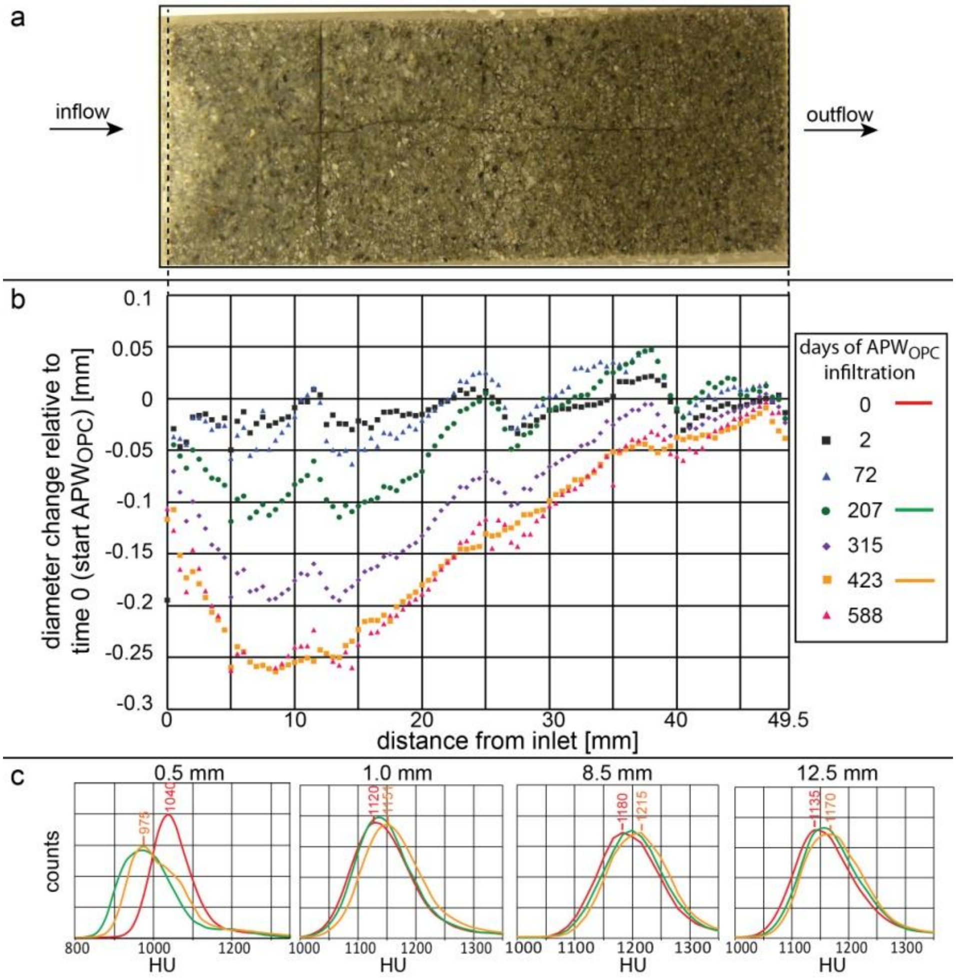

Figure 5-5: Bentonite core size evolution: (a) trans-section photograph of the bentonite after the experiment (optical image); (b) diameter of the core relative to time 0 (end of equilibration phase, day 102); (c) variations of the HU histograms over time.

Tomographic cross-sections of the bentonite core at time 0 (equilibration phase) showed a homogeneous material of greyish colour with whitish dots of denser minerals like pyrite (Figure 5-6). The colour code of tomographic images is the following: bright shades are low X-ray attenuations (HU) and dark shades represent higher densities. Interestingly, a concentric pattern of circular rings grew out of the filter into the first millimetre of bentonite. The first ring structure appeared after 137 days of APW_{OPC} infiltration and reached a depth of 1.75 mm. The circular precipitations in the filter remained constant after they reached maximum extension and intensity after 137 days. The reaction front in the filter had a diameter of ∼12.5 mm and comprised 3 distinct circular shaped zones of increased X-ray attenuation/density. The circular shaped reaction plume grew cylindrically into the bentonite sample. The maximum extension of the diffuse plume was reached after 588 days of APW_{OPC} infiltration with a maximum penetration depth of 5–8 mm.

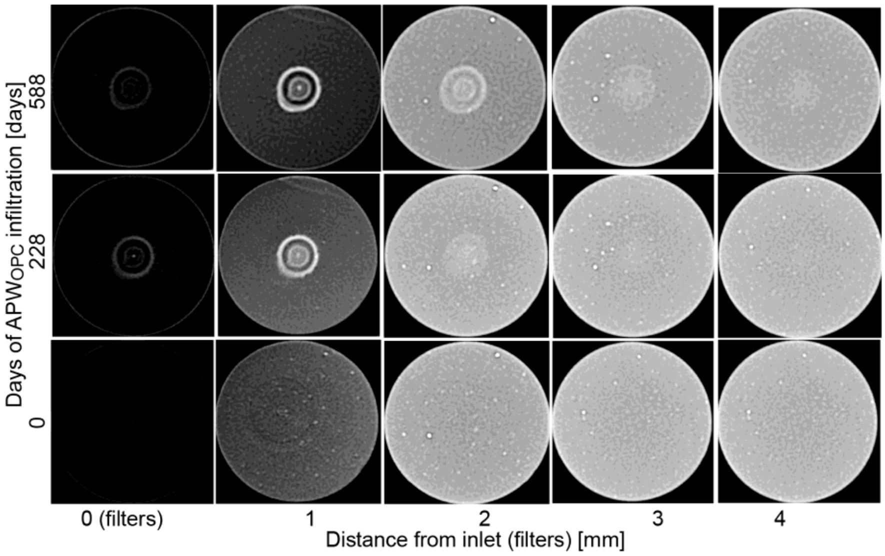

Figure 5-6: Evolution of CT slices in the inflow region of the experiment over time.

The 3D evolution of the reaction plume was monitored by CT. Image processing applied to each dataset showed in detail the evolution over time (Figure 5-7). It included its segmentation, quantitative assessment, and rendering. Segmentation was achieved by thresholding after image normalization as a pre-processing step. The plume was indicated by an increase of X-ray attenuation, which is related to a higher bulk density. Newly formed calcite and/or saponite as well as a higher bulk density of the bentonite may have induced this increase. Normalization was required in order to hide the transition of the filter to the bentonite zone and thereby enabling simple thresholding of the reaction plume without inducing a discontinuous junction. The resulting binary mask of the reaction plume was both quantified with respect to its geometric expanse as well as triangulated and Gouraud-shaded for generating 3D views.

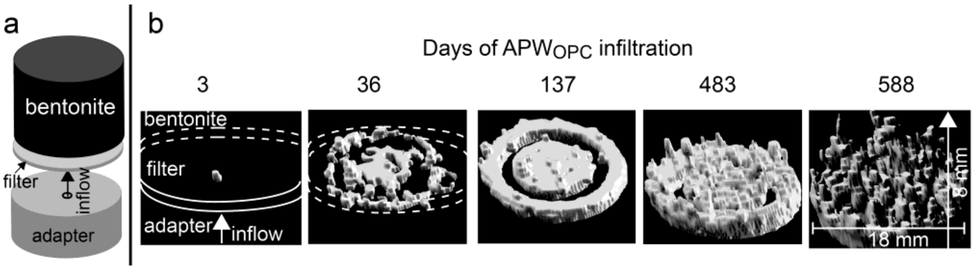

Figure 5-7: Evolution of the reaction plume based on CT images and analysed by image processing: (A) sketch of the analysed section; (B) zone of reaction consisting of an increased X-ray attenuation (time in days after infiltration of APW$_{OPC}$).

5.3.4. Post-mortem analysis: physical parameters

The bentonite core weighed at the end in wet condition 187.74 g (including a small piece of the broken inlet filter), which is a gain of 1.05 g. The sample length was 51.26 mm, grown by 1.8 mm. The sample diameter was 49.4 mm near the inlet, 49.4 mm in the middle part and 50.0 mm near the outlet. The water content showed in both profiles a decreasing trend from inlet to outlet with slightly higher values in the centre (Figure 5-8). The saturated density showed in both profiles reduced densities at the inlet and values between 1920–1930 kg/m^3 in the rest of the core with higher values in centre. The porosity was 46% at the inlet and ~44% in the rest of the sample. The degree of saturation varied between 0.98 and 1.00 for both profiles, reflecting saturation within measurement uncertainties.

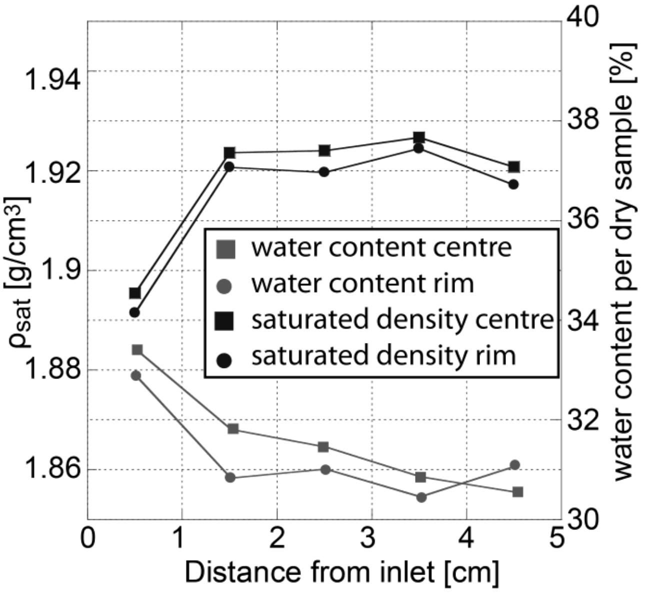

Figure 5-8: Saturated density and water content profiles of the bentonite sample at the end of the experiment.

5.3.5. XRD analysis

The XRD spectrum of MX-80 bentonite showed the following major minerals: smectite (montmorillonite), quartz (3.3 and 4.2 Å), cristobalite (4.0 Å), alkali feldspar (3.21 and 3.22 Å), plagioclase feldspar (3.18 Å), muscovite and/or illite (~10 Å), gypsum (7.6 Å), and calcite (3.03 Å) (Figure 5-9). Variations in the (001) smectite reflection, result from different hydration states and cation occupancy. The differentiation of di- and trioctahedral sub–groups of smectites was done on the (060) reflection (Brindley and Brown, 1980). Peaks at ~1.49 Å are related to dioctahedral and peaks at ~1.52 Å to trioctahedral smectites. The °Δ2Θ((003)-(002)) of EG saturated samples may be used to identify illite/smectite (I/S) interlayers (Moore and Reynolds (1989). The (002) peak of smectite at 4.5 Å was used for intensity comparison along the bentonite core.

The (001)-spacing of the raw MX-80 bentonite was 12.3 Å, which is a characteristic value for a Na-saturated MX-80 bentonite (Ferrage et al., 2005). The MX-80 bentonite sample had a (060) reflection at 1.49 Å, which is characteristic for a dioctahedral smectite. The EG saturated sample had a (001) peak at 16.9 Å, (002) peak at 8.5 Å and (003) peak at 5.7 Å, corresponding to a °Δ2Θ((003)-(002)) of 5.29°, which is after Moore and Reynolds (1989) a pure montmorillonite with no I/S.

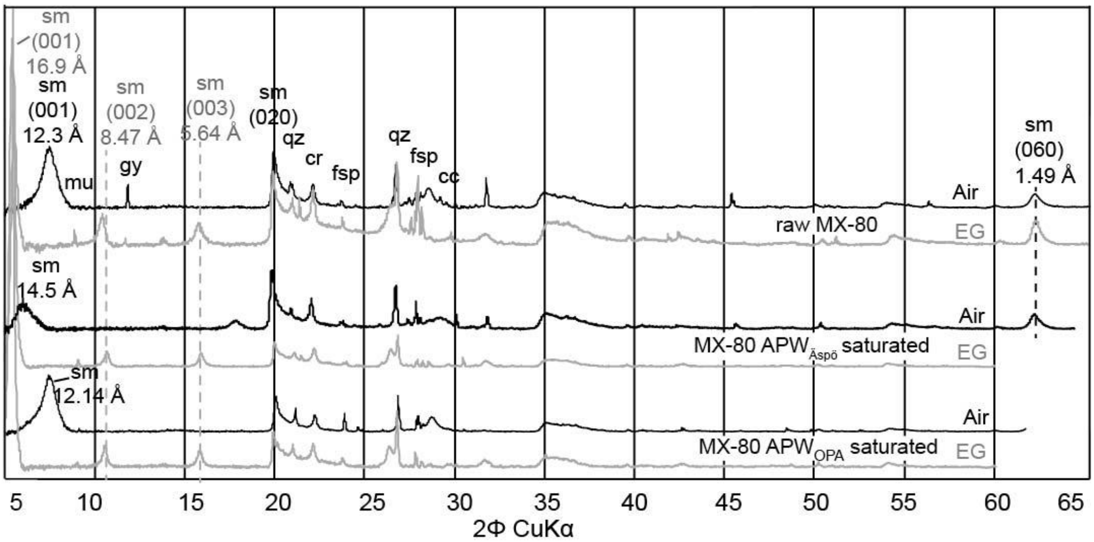

Figure 5-9: XRD spectra of the original MX-80 material, MX-80 saturated with APW$_{Äspö}$ and APW$_{OPA}$: sm: smectite; mu: muscovite; gy: gypsum; qz: quartz; cr: cristobalite; fsp: feldspar; cc: calcite. All curves are normalized to the 3.3 Å qz peak.

XRD spectra of the filters showed a broad hump of amorphous material at 22.25 2Θ from the PVC-filter material (Figure 5-10). An inlet filter sample from the center consisted of scratched of minerals and showed therefore no PVC signal (Figure 5-10). The inlet filter showed strong enrichment in calcite on both sides. On the clay side of the inlet filter the main bentonite minerals were identified (smectite, muscovite, quartz and feldspar). Talc, gypsum, and brucite could be identified as well. The outlet filters showed precipitation of halite with a reflection at 2.8 Å.

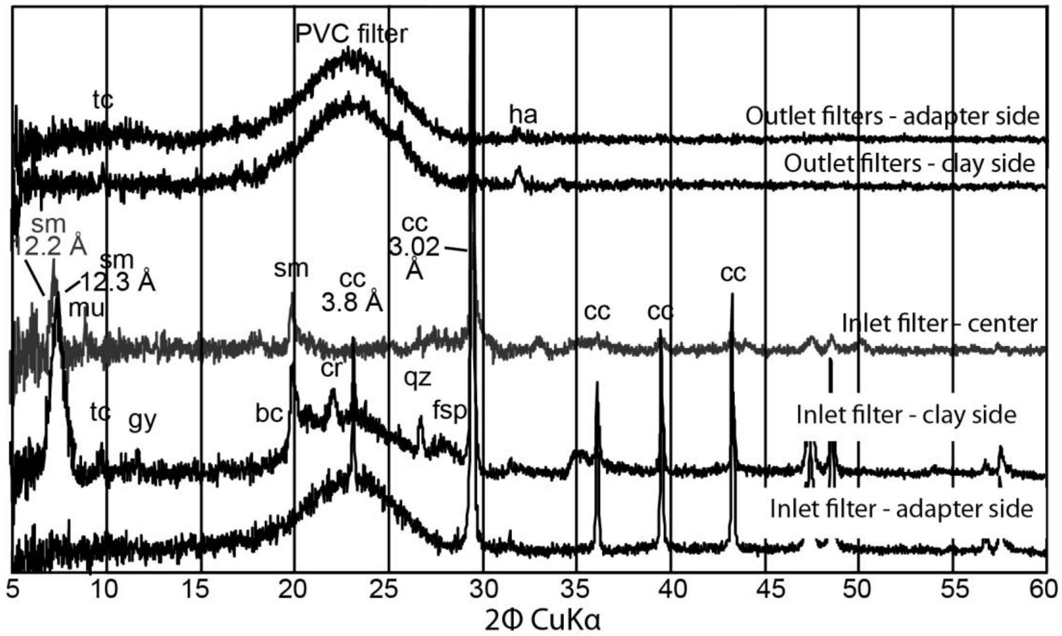

Figure 5-10: XRD spectra of the in- and outlet filters: sm: smectite; mu: muscovite; qz: quartz; cr: cristobalite; fsp: feldspar; cc: calcite; tc: talc; ha: halite; gy: gypsum; bc: brucite.

XRD measurements of the core sample showed for the (001) reflection of smectite in the centre, as well as 5 mm off-centre directly at the interface a value of 12.1 Å (Figure 5-11). The rest of the bentonite had this peak at 11.8 Å with a tendency of peak broadening. Repetitive sample preparation and scanning showed that the occurrence of peak broadening and the change in intensities of the (001) smectite peak varied and was most likely an artefact of sample preparation; e.g. incomplete random orientation or rehydration during measurement. The sample directly at the inlet was depleted by 2% in smectite (peak height), whereas the samples up to 5.5 mm were enriched by max. 3% relative to the unreacted bentonite parts. The (060) peak of smectite was in all measurements at 1.5 Å and hence it could be identified as dioctahedral clay like montmorillonite. Samples at the interface and up to 4 mm depth showed peaks at 1.519 and 1.516 Å which are related to trioctahedral smectite like saponite. The d-spacing of the smectite was in all samples smaller compared to the starting material and clay pore-water saturated MX-80 bentonite, indicating an exchange of calcium and some sodium by potassium. This is in agreement with Ferrage et al. (2005) who measured and calculated for a K^+-saturated MX-80 bentonite at ~35 %rh a c–cell distance of 11.36 Å, and 12.44 Å for a Na^+-saturated MX-80 bentonite. EG saturated spectra showed for all samples (001) peaks at 16.9 Å, (002) peaks at 8.5 Å and (003) peaks at 5.6 Å, which corresponds to a °Δ2Θ((003)-(002)) of 5.29 Å, and thus no significant illite interstratification.

All samples showed a clear peak of mica like muscovite or illite, quartz, and feldspar. Samples between 11.5 and 44.5 mm depth showed small amounts of gypsum. Cristobalite peak intensities were reduced towards the inlet. Directly at the interface, a maximal intensity reduction by 32% was observed, extending up to 8.5 mm depth. The most prominent variation occurred in the calcite peak, which showed strong enrichment in the first 3 mm. The calcite peak height was 6.6× higher directly at the interface compared to the average sample, and at 3 mm distance an increase by 1.7× was observed.

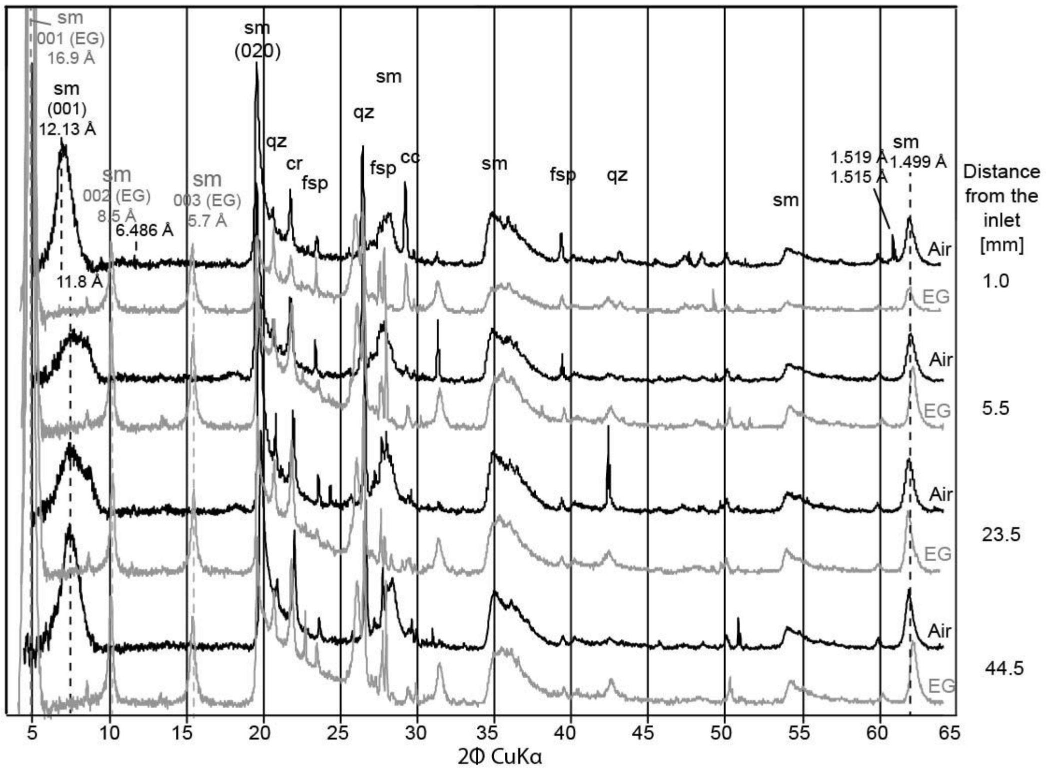

Figure 5-11: XRD spectra of the bentonite core indicated as distances from the inlet. Sm: smectite; qz: quartz; cr: cristobalite; fsp: feldspar; cc: calcite; EG: ethylene glycol saturated. All curves are normalized on the 3.3 Å qz peak.

5.3.6. Microscopy and SEM/EDX analysis

Capillary tubes. Optical images and SEM analyzes were performed on the in-and outlet PEEK capillary tubes (1/16” OD). The inlet tube showed rusty precipitations which consisted mainly of calcium, iron, sodium and potassium (Figure 5-12c). As no anions were measured, it suggests that these are most likely hydroxides or carbonates based. The outlet tube had no precipitates.

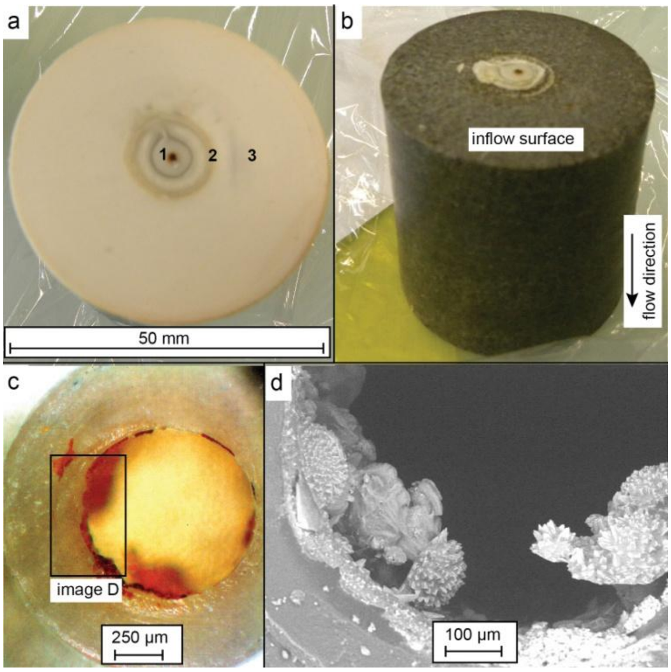

Figure 5-12: (a) Inlet filter after dismantling; (b) bentonite inflow surface with the stuck PVC filters; (c) photographs of the inlet PEEK capillary; (d) BSE image of the precipitates.

Filters. The inlet filter showed discoloured concentric rings of 13.8 mm, 6.5 mm and 1.4 mm diameter on the adapter side (Figure 5-12a). The innermost rings consisted of a rusty coloured centre surrounded by a greyish ring (both zone 1), and the outer circle had a greyish to brownish colour (zone 2). The rest of the filter looked unaltered (zone 3). Zone 2 consisted of the filter of a ring of stuck bentonite material on the clay side of the filter and of an undetermined mineral phase on the adapter side. Zone 3 showed small patches of bentonite material on the clay side (Figure 5-13a).

The growth of minerals was seen under the microscope in the fabric-like fiber structure of the two inlet filters. BSE images of zone 1 and 2 indicated a filled porosity, separated by a small zone of open pores (Figure 5-13). EDX measurements of zone 1 showed the following composition: CaO 34 wt%, SiO_2 50 wt%, and Cl_2O 6 wt% (carbon detected but not quantified, Figure 5-13). The SiO_2/ Cl_2O ratio was ~3× higher compared to pristine filter material, indicating SiO_2 enrichment. The calcium might be related to precipitation of calcite. Zone 2 showed for each side a different trend. On the clay side a clear bentonite signal together with calcite and PVC filter material, dominated by silica, alumina, chlorine and calcium was observed. On the adapter side of the inlet filters the signal was dominated by calcium, silica and chlorine, suggesting the presence of more calcite. Zone 3 showed still the original open porosity of 0.9 µm size without fillings. The chemistry matched the pristine filter material (SiO_2 70 wt% and Cl_2O 30 wt%).

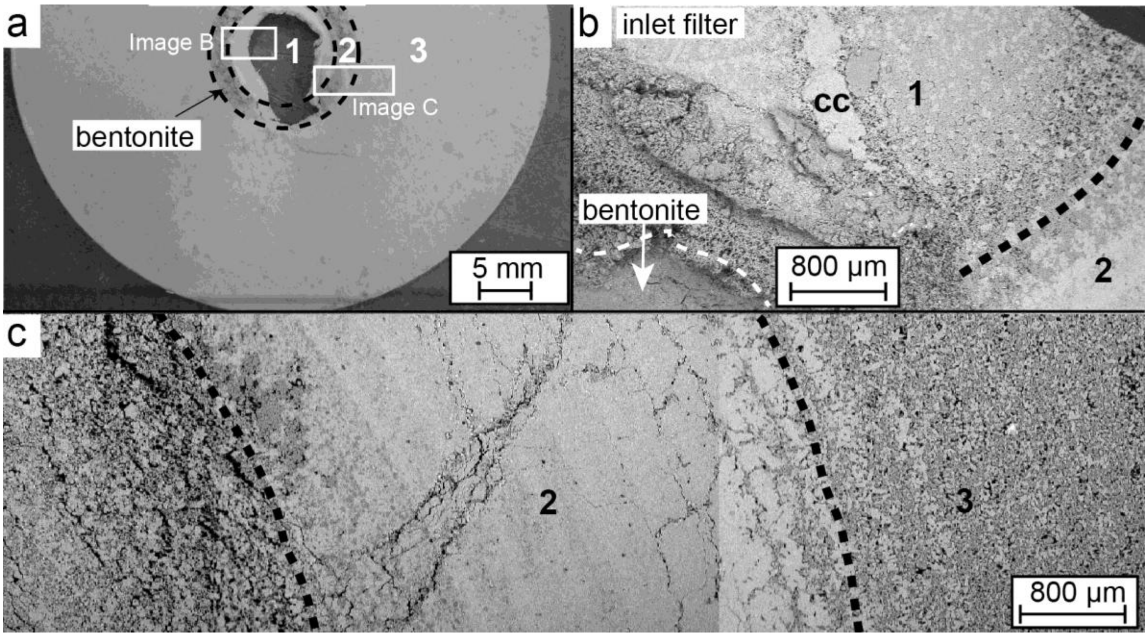

Figure 5-13: Inlet filters after the experiment: (a) photograph of the bentonite side of the inlet filters; (b & c) BSE images of the adapter side of the inlet filters. Cc: calcite.

Bentonite core. From the inflow surface, a whitish reaction plume penetrated 8 mm into the bentonite in form of a hemisphere (Figures 5a and 11d). BSE images of the inflow region revealed a high density of mostly resin filled cracks, which are artefacts of sample preparation (Figure 5-14a). The first 0.5 mm of the bentonite had a darker shade due to an uneven, dipping sample surface, exhibiting lower signal intensity. The bentonite displayed a clay dominated mineralogy with randomly embedded accessory mineral grains of higher mean atomic number (Figure 5-14a). The minerals were identified by means of SEM-EDX spot analysis. Pre-existing calcite and muscovite grains had diameters up to 500 µm. Alkali and plagioclase feldspar grains were sharp-edged and <50 µm. SiO_2-group minerals like quartz, cristobalite and tridymite could be observed but not distinguished. Pyrite occurred in grains <5 µm.

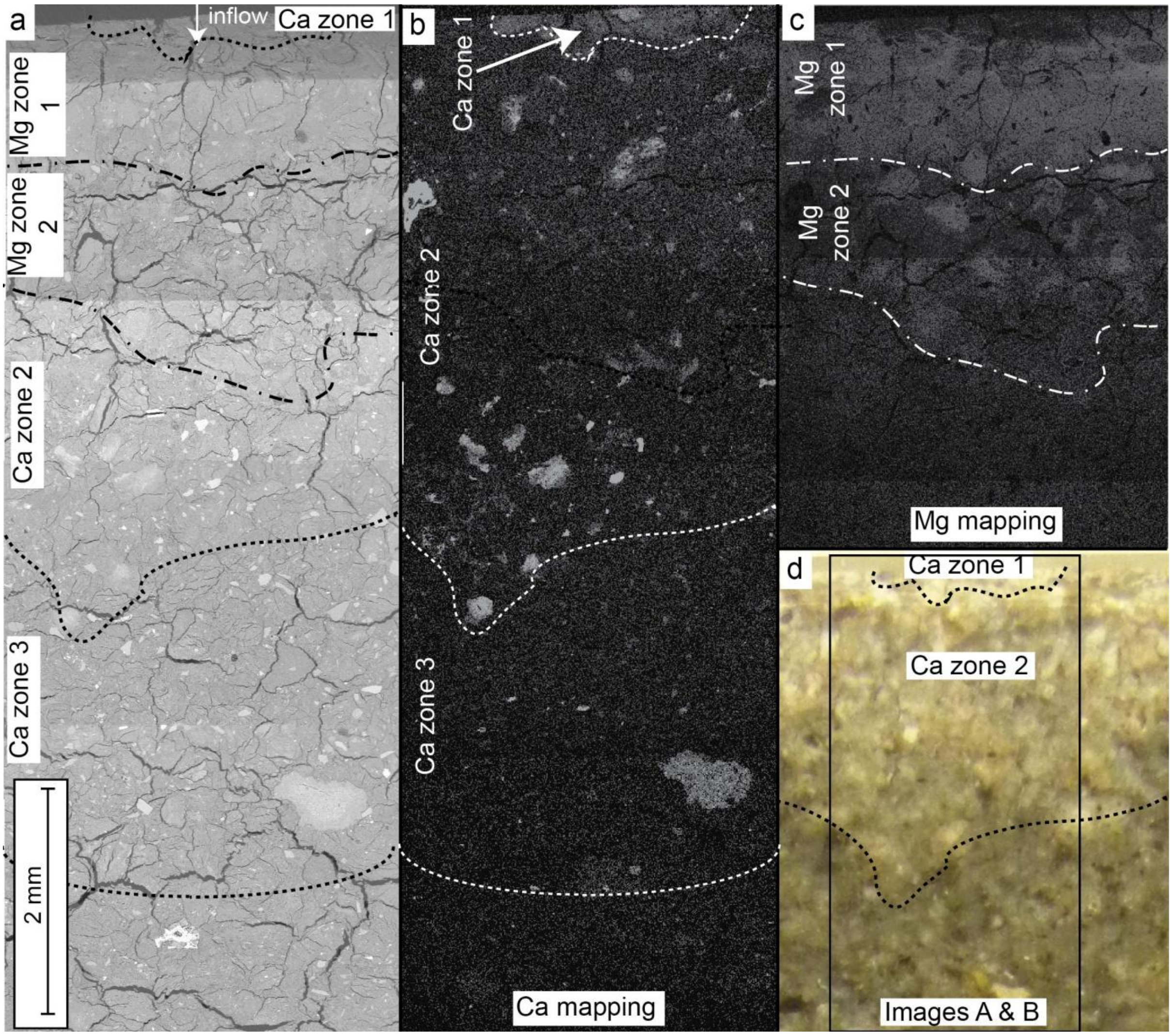

Figure 5-14: Detailed section of the first 8 mm of the bentonite sample: (a) BSE image; (b) Ca element map; (c) Mg element map and (d) reflected light micrograph of the part close to the inlet. Boarders of distinct zones are indicated.

The average oxide composition of the pristine clay matrix and of the bulk sample is shown in Table 5-4. The Al_2O_3/SiO_2 ratio was in agreement with measured montmorillonite from MX-80 in Karnland (1997). This means that the tetrahedral sheet was almost entirely filled with Si^{4+} and contained just traces of Al^{3+}. The octahedral sheet was dominated by Al^{3+} with minor amounts of Mg^{2+} and Fe^{3+} and the adsorbed cations were dominated by Na^+ with minor amounts of Ca^{2+} and just traces of K^+ and Mg^{2+}.

Table 5-4: SEM-EDX measurements of the bentonite and the Ca and Mg-enriched zones.

	Bentonite (pristine)	**Clay Matrix (pristine)**	**Ca zone 1**	**Ca zone 2**	**Ca zone 3**	**Mg zone 1**	**Mg zone 2**
Type of measurement	bulk	point	bulk	bulk	bulk	point	point
				[wt%]			
SiO_2	69.6±0.7	71.1±0.9	62.6±0.7	63.9±3.4	69.2±0.6	61.9±0.7	67.8±1.4
Al_2O_3	20.0±0.4	19.9±0.8	17.6±1.7	18.5±0.9	19.8±0.5	17.7±0.6	17.7±2.5
Fe_2O_3	4.2±0.3	3.8±0.3	2.5±1.1	4.3±0.3	4.4±0.2	3.3±0.2	3.4±0.5
MgO	2.2±0.1	2.3±0.2	12.4±2.0	9.0±5.2	2.3±0.2	14.5±1.6	8.0±2.5
CaO	1.6±0.4	1.1±0.2	2.8±0.6	2.1±0.5	1.8±0.6	1.1±0.1	1.5±0.8
Na_2O	1.7±0.1	1.4±0.1	1.6±0.1	1.5±0.3	1.7±0.1	0.9±0.2	1.1±0.2
K_2O	0.6±0.1	0.5±0.2	0.4±0.5	0.7±0.1	0.9±0.1	0.5±0.1	0.6±0.1
Al_2O_3/SiO_2	0.29±0.01	0.28±0.02	0.28±0.03	0.29±0.01	0.29±0.01	0.29±0.01	0.26±0.04
MgO/SiO_2	0.032±0.001	0.033±0.003	0.20±0.03	0.15±0.09	0.033±0.003	0.24±0.03	0.12±0.04

In the inflow region, zones enriched in Ca and Mg-enrichments were detected (Figures 14b & 16). The Ca-enrichment could be separated in three distinct zones with various amounts of newly precipitated calcite (previously shown by XRD): Ca zone 1–3. Ca zone 1 was a small domain of 2.2 mm diameter and 0.4 mm depth in the centre of the interface. No distinct mineral phases were visible and bulk SEM-EDX measurement revealed only a small Ca-enrichment (Table 5-4). Most likely this zone was directly related to the massive calcite precipitation in the inlet filter. Ca zone 2 was shaped like a half circle with a radius of ~4.4 mm. It consisted of a weak Ca-enrichment in the clay matrix (see Table 5-4), containing small (<5 µm), Ca-rich mineral grains of variable size (Figures 15c and d). In some locations they seemed to grow along preferred flow paths around pre-existing clay stacks, overgrowing the matrix. The larger size fraction was between 25 and 400 µm and consisted of Ca minerals replacing pre-existing mineral grains. The bulk SEM-EDX signal was clearly clay-dominated, including an increased Mg amount of the Mg-enriched zone. The Ca enrichment mainly occurred in small, newly grown minerals, which were therefore not clearly detectable in the bulk EDX transection measurements shown in Figure 5-16. In some cases, replacement of gypsum by calcite could be observed. Ca zone 3 was marked as a zone of continuously fading out of Ca and ended at ~8 mm depth (see Table 5-4). The zone volumes calculated were: 0.5 mm^3 (zone 1), 277 mm^3 (zone 2), and 795 mm^3 (zone 3).

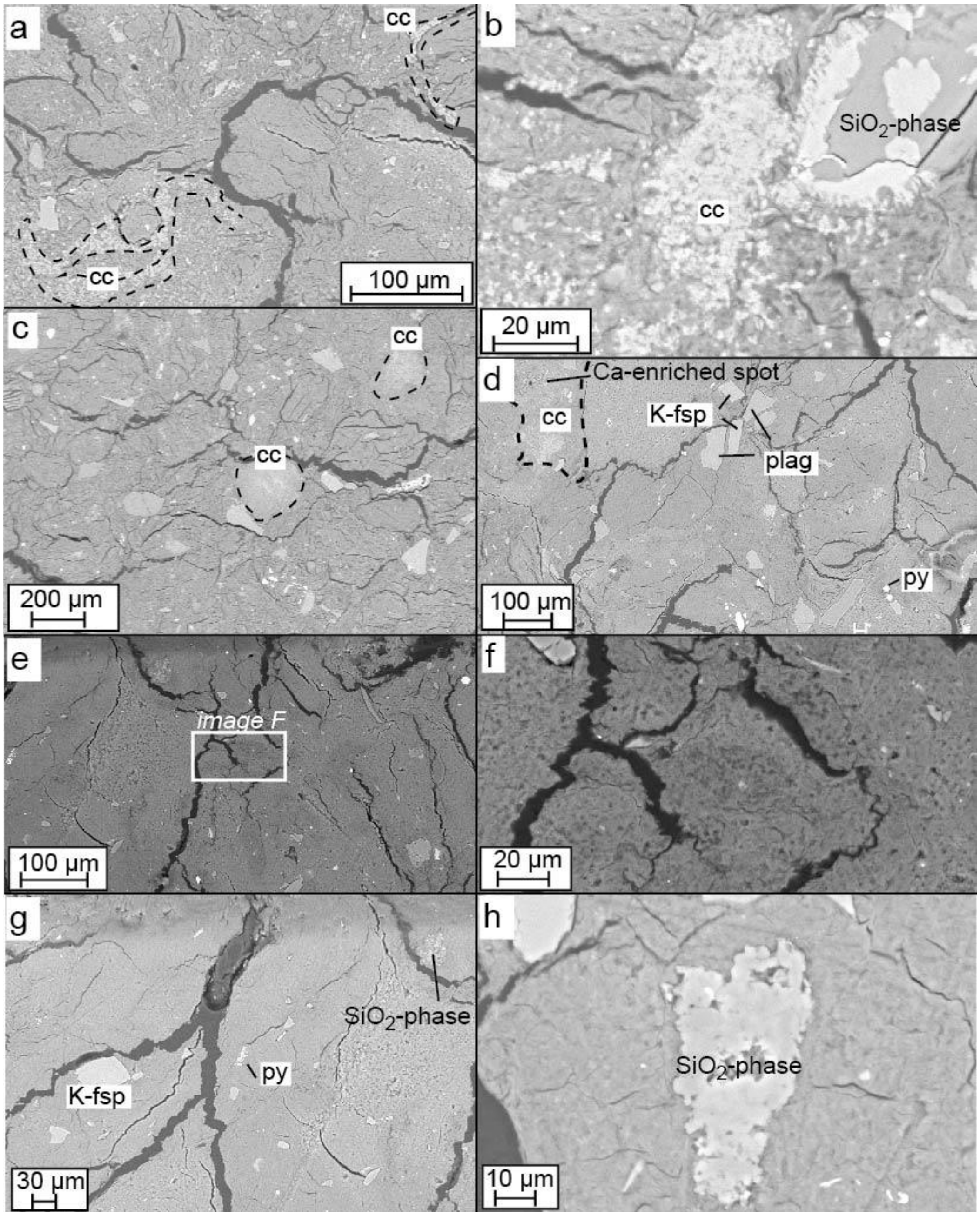

Figure 5-15: BSE images of the first 5 mm of the bentonite core: (a) calcite precipitation in Ca zone 2 at 7 mm depth; (b) calcite growth along dissolution of SiO_2-phase at 3.5 mm depth in Ca zone 2; (c) calcite growth in Ca zone 2 at 6 mm depth; (d – f) Mg zone 1 between 0.4 – 0.8 mm depth; (g – h) Mg zone 1 with SiO_2-phase dissolution. Cc: calcite; qz: quartz, py: pyrite; K-fsp: alkali feldspar; plag: plagioclase.

The Mg-enrichment occurred in the first millimetres of the bentonite and could be divided into two zones: Mg zone 1 and 2 (Figures 14c, 15, 17). The Mg zone 1 extended from 0.4 to 1.9 mm from the inflow interface and coincided with Ca zone 1. It was a zone of massive and homogeneous Mg-enrichment in the clay matrix (Table 5-4). The measured Mg concentration was enriched seven fold; the Al_2O_3/SiO_2 ratio was identical to the one of unreacted clay (Figures 15e & f, 17). The comparison of spot analysis in the clay matrix with the bulk bentonite measurements showed clearly higher Mg amounts in the single spot analysis. This identified the clay as location of magnesium enrichment, either fixed in smectite crystals or in newly grown very fine grained Mg-phases. The Mg zone 2 extended from 1.9 to 3.1 mm from the inflow interface. It was characterized by heterogeneously distributed Mg-enriched patches of clay that fade out gradually away from the inlet, indicating a heterogeneous shape of the progressing reaction front (Table 5-4). The zone volume calculated was 0.062 cm^3.

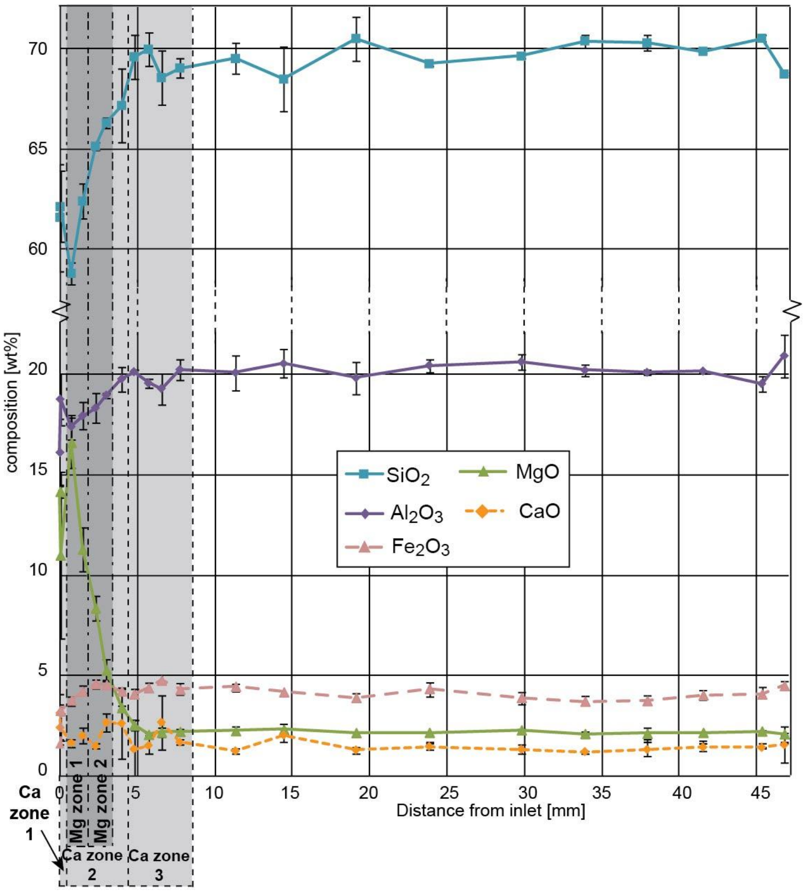

Figure 5-16: SEM-EDX oxide compositions of scanned areas of 1x0.8 mm along a central trans-section. The error bars were the standard deviations of 3 measurements at different locations within the same zone.

Dissolution of certain SiO_2-rich grains, which were <20 µm in size was observed near the inlet (Figure 5-15b, g and h). In some cases, SiO_2-phases were replaced by Ca or S-minerals; most likely calcite or gypsum (Figure 5-15b). XRD measurements indicated that the dissolved SiO_2-phase was cristobalite.

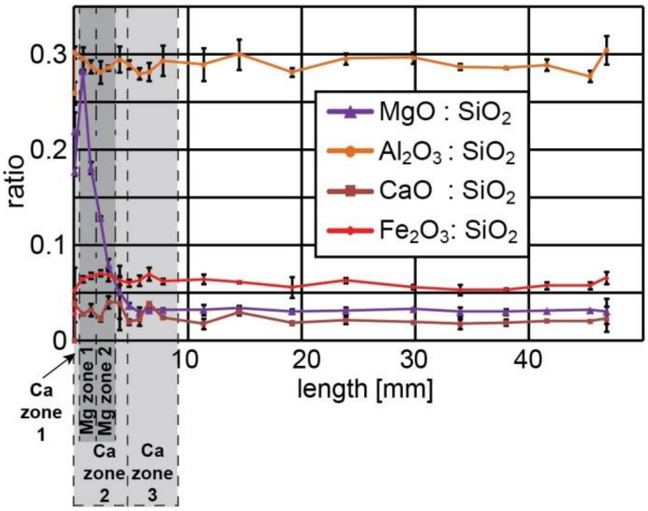

Figure 5-17: SEM-EDX oxide wt% ratios of average areas of 1x0.8 mm along a transection.

5.3.7. Raman spectroscopy

Raman spectroscopy was used to identify mineral phases along the bentonite section (Figure 5-5a). Clays tend to be highly fluorescent in the laser light due to associated iron(III) hydroxide minerals and/or organic matter, saturating the detector over the entire wavelength region (Alia et al., 1999; Blacksberg et al., 2010; Košařová et al., 2013). Measurements in the clay matrix near the inlet (Mg-enriched part), 8 mm from the interface, and at the outlet showed all identical patterns with peaks at 254 cm^{-1}, 371 cm^{-1}, 707 cm^{-1}, 819 cm^{-1}, and 1111 cm^{-1} (Figure 5-18a). No trend was observed between Mg-enriched parts and unaltered bentonite, indicating no significant changes in structure. The Raman shift patterns of the newly precipitated Ca-phase at the interface showed bands at 281 and 1086 cm^{-1}, identified as calcite bands (Figure 5-18b).

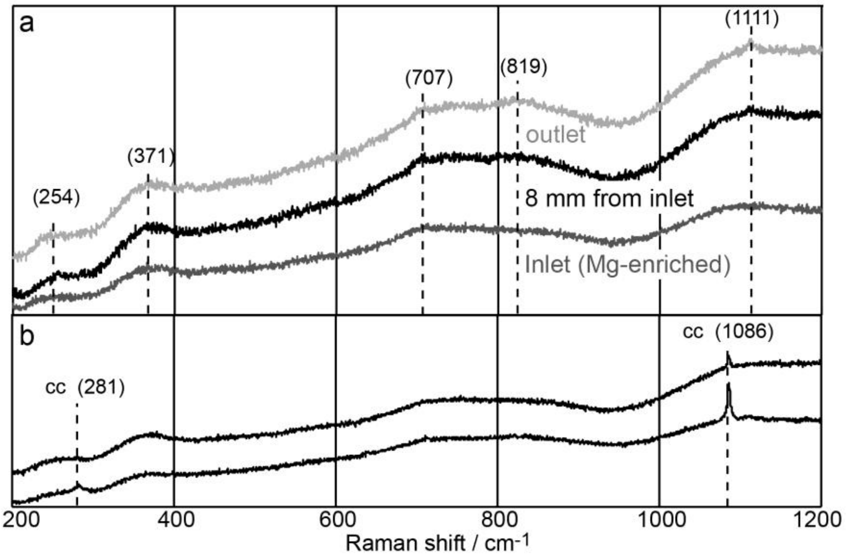

Figure 5-18: Raman shift patterns: (a) bentonite matrix; (b) newly grown calcite near the bentonite interface. Cc: calcite.

5.4. Discussion

The evolution of the core volume and hydraulic conductivity as well as ion concentrations and pH in the outflow is complex and reflects coupling between physical and chemical processes. The main controlling processes are: ionic strength effects and coupled transient compaction/de-compaction (shrinkage or expansion of the core due to changes in montmorillonite interlayer distance/water content), internal pore water control by minor soluble accessory phases (sulphate and/or carbonate minerals), cation exchange processes, carbonate precipitation, and also silicate mineral dissolution/precipitation of reactive “cement phases” after injection of the APW_{OPC}.

5.4.1. Equilibration phase

Evolution of physical properties. The bentonite core volume decreased after applying a confining fluid pressure at the beginning of the experiment. This indicated a further compaction of the bentonite core relative to the pre-confined sample. With the compaction of the core, pore-water was released from the porosity, leading to an apparent initially increased hydraulic conductivity, which was calculated based on the net outflow volume only. The hydraulic conductivity decreased continuously and approached apparent steady-state condition of $\sim 1.1\times10^{-13}$ m/s, which is in agreement with Karnland et al. (2006), who measured for a similar density and ionic strength values between 3.0×10^{-13} m/s and 6.0×10^{-14} m/s. CT data showed no mineral reactions during the equilibration phase. The Péclet number was at the end of the equilibration phase ~13, which corresponds to an advective-dominated flow. The bentonite core length of 4.95 cm was used as characteristic length, an anion accessible porosity of 13%, based on chloride through-diffusion and chloride break-through curve data, and an effective diffusion coefficient for chloride of 1.6×10^{-11} m^2/s (Fernández et al., 2011b; Fernández et al., 2011a; Van Loon et al., 2007).

Chemical evolution of outflow. At the beginning, a high ionic strength fluid was expelled (I≈0.48 mol/kg). This can be explained either by the saturation and compaction procedure of the bentonite during sample preparation or by an initial compaction of the core. The first option assumes that the saturation of the bentonite led to strong ion enrichment in the porosity due to dissolution of salts and sulphate minerals. The second option assumes that the initial compaction of the bentonite core in the applied triaxial set-up was due to a lower compaction used for sample preparation, and therefore initially more saline pore-water was expelled from the intergranular pore-space where chloride is enriched due to anion exclusion effects. As reported in Dolder et al. (2014), the first pH measurements near pH 5 were distinctly low compared to all later values. Such a low pH is not in agreement with proposed values in compacted MX-80 bentonite based on thermodynamic considerations and mineral equilibria (Bradbury and Baeyens, 2009). The effect was most likely an artefact triggered by an incident at the beginning of the experiment whereby compressed air leaked into the outflow system.

The ion concentrations during the equilibration phase with APW_{OPA} infiltration were in agreement with squeezing experiments performed by Muurinen and Lehikoinen (1999). At similar densities and lower w/s, their data showed the same ion enrichment relative to the inflow/external water, controlled mainly by dissolution of carbonates and sulphates and ion exchange processes. The calculated ionic strengths ranged from 0.4–0.48 mol/kg (Table 5-5) and were slightly higher compared to the pore-water measurements performed on MX-80 by Muurinen et al. (2004) at similar dry density and variable chloride concentrations. This may indicate that our pore-water was not yet in equilibrium with the bentonite. Calculations of SI (Table 5-5) showed saturation of the outflow with respect to gypsum and amorphous silica. The erroneous low pH led to an apparent under-saturation with respect to calcite in the first aliquots, followed by saturation at neutral pH.

Table 5-5: Calculated SI of the outflow solution. Cc: calcite; gy: gypsum; K-fsp: kali feldspar; mont: montmorillonite; cristo: cristobalite; pCO_2: partial pressure of CO_2.

APW / Time	**PV (PV APW_{OPC})**	**Ionic Strength**	**Charge balance error**	**Saturation indices (SI)**							
[days]		[mol/kg]		cc	gy	K-fsp	mont	qz	cristo	SiO_2 amorph	$pCO_{2\,(g)}$
$APW_{Äspö}$		0.26		-0.3	-0.83						-3.24
APW_{OPA}		0.23		-0.1	-0.34						-3.21
APW_{OPC}		0.28		1	-2.6	-10		-4.4	-5.2	-5.7	-12
31	0.03 (0)	0.48	1.62	-2.8	-0.04	0.28	3	1.26	0.47	0.01	-1.08
134	0.18 (0)	0.43	0.84	0.25	-0.06	3.81	7.29	1.25	0.46	0.01	-2.25
191	0.22 (0.04)	0.39	5.02	0.8	-0.1	4.64	8.64	1.46	0.67	0.22	-1.69
290	0.29 (0.11)	0.34	-0.05	0.79	-0.05	4.9	8.76	1.56	0.76	0.31	-2.07
497	0.4 (0.21)	0.36	16.84	0.94	-0.23	5.66	9.24	1.71	0.92	0.46	-2.29
690	0.43 (0.25)	0.34	7.21	1	-0.31	5.62	9.03	1.7	0.91	0.46	-2.48

5.4.2. High-pH infiltration phase

Evolution of fluid composition. APW_{OPC} infiltration led to a further reduction in ionic strength in the outflow, which was in agreement with the electrical conductivity measurements (Table 5-5). Chloride as major anionic charge carrier dropped continuously and got replaced after 0.2 PV_{OPC} mainly by sulphate (Figure 5-3). If chloride is considered as non-reactive tracer mostly present in intergranular porosity (microporosity), the chloride decrease represents a breakout curve, whereby the time required to flush out chloride to half of its initial concentration would represent approximately one volume of flow-active porosity. This time was ~310 days or equivalent to 0.196 PV relative to the initial full water content. The mass-balance showed a difference of 2.9 mmol between cumulative inflow and outflow, indicating that chloride was still present in the bentonite core at the end of the experiment (Table 5-6). Hydroxide, the main anion of the cement fluid (~271 mM), reached the outflow sparsely. Even after 577 days of APW_{OPC} injection the hydroxide concentration never exceeded 0.002 mM, indicating a complete consumption. Directly related to the OH^- concentration is the pH, which increased during 0.12 PV to pH ~7.8.

The increase of the ionic strength after 275 days of APW_{OPC} infiltration was mainly the result of a sulphate increase despite the lower concentration in APW_{OPC} compared to APW_{OPA}. Dissolution of gypsum was the most likely mechanism, and this process may proceed at gypsum saturation and will bring more sulphates into solution as long as there is a sink for calcium by mineral precipitation (e.g. calcite). The extra cations to balance the increase in sulphate were generated by mineral dissolution (OH^- consumption), and this overall process was therefore limited to the reactive zone located very near the infiltration region.

The mass-balance showed a loss of sodium from the core, released from the exchanger (Table 5-6). Potassium and calcium were retained in the bentonite by ion exchange for K$^+$, and for Ca^{2+} possibly also by calcite precipitation. Si^{4+} and Al^{3+} got enriched in the outflow during high-pH infiltration.

Table 5-6: Ion mass-balance of in- and outflow.

Ions	Total elements in infiltration fluids			Total elements in outflow	Difference between in- and outflow
	APW$_{Äspö}$	APW$_{OPA}$	APW$_{OPC}$		
			[mmol]		
Na$^+$	2.56	1.4	1.35	6.93	-1.61
K$^+$	-	0.02	2.12	0.06	2.08
Ca^{2+}	1.58	0.1	0.02	0.25	1.44
Mg^{2+}	0.05	0.08	-	0.15	-0.02
Al^{3+}	-	-	3.50E-04	4.60E-05	4.60E-05
Si^{4+}	-	-	7.00E-04	0.06	-0.06
SO$_4^{2-}$	0.05	0.19	0.03	1.47	-1.2
Cl$^-$	5.91	1.33	-	4.34	2.9
HCO$_3^-$	0.007	0.006	0.003	0.16	-0.15

Evolution of hydraulic conductivity. The hydraulic conductivity dropped twice during high-pH infiltration phase: the first time directly after switching fluids and the second time after ~450 days (0.2 PV$_{OPC}$). The first phase of reduced hydraulic conductivity was interpreted as a transient phase (Dolder et al., 2014), while the second one seemed to approach steady-state conditions. The Péclet number during the transient flow-phase indicated advection dominated flow. It decreased thereafter to ~3.6 and reached after ~650 days (0.24 PV$_{OPC}$) a value between 0.9 and 1.4, becoming more diffusion-dominated. Two main mechanisms for the reduction were proposed by Dolder et al. (2014) *(chapter 4)*: (1) mineral precipitation and (2) reduction in swelling pressure and resultant compaction due to the higher ionic strength of the APW$_{OPC}$. The sharp change in hydraulic conductivity after switching fluids postulated in Dolder et al. (2014) has to be revised because the repeat removal of the experiment for CT scanning induced artefacts in the measurements of the outflow. Mechanism (1) relates the drop in hydraulic conductivity to mineral precipitation in the filter as well as in the bentonite. Mineral precipitation in the filter was recognized in the CT scans after 8 days of APW$_{OPC}$ infiltration and had a diameter of ~12 mm in the last scan. Post-mortem analysis of the experiment identified these precipitates in the filter as calcite with minor amounts of gypsum, talc and possibly some brucite. In the bentonite precipitation of calcite and possibly an Mg-smectite was observed; identical to the features detected in CT. Mechanism (2) is based on the idea that an increase in ionic strength of the infiltration solution reduces the interlayer porosity (microporosity) and the diffuse layer (DL), which induces core compaction and hence a reduction of the intergranular porosity (macroporosity) in the pressure-constrained experimental setup. As fluid flow occurs in bentonite mainly in the intergranular porosity, reduction in the intergranular porosity reduces the hydraulic conductivity. APW$_{OPC}$ had a slightly higher ionic strength compared to APW$_{OPA}$ (Table 5-5). Not known is how the high-pH, K$^+$–Na$^+$–Ca^{2+}–OH$^-$ fluid evolved in the bentonite in detail. The possibilities range from locally increasing ionic strength due to gypsum dissolution to lowering it by consumption of hydroxide ions.

Aqueous speciation modeling using PhreeqC was performed to identify possible processes. Directly at the interface we expect the original high-pH of the APW$_{OPC}$ at or near gypsum saturation. This leads to a hypothetical pore-fluid with an ionic strength of ~0.4 mol/kg which is clearly higher compared to 0.28 mol/kg of APW$_{OPC}$. This fluid would be over-saturated with respect to talc, calcite, and cement phases like C–S–H and ettringite. A bit further away from the interface, the pH of the APW$_{OPC}$ is expected to be buffered to ~7.8 (Figure 5-3). At gypsum saturation, this would lead to a hypothetical fluid of ~0.38 mol/kg ionic strength, induced mainly by the high sulphate concentration. This fluid would be over-saturated with respect of Si-Al-phases but under-saturated with respect to calcite and cement phases.

The calculations indicate that the hypothetical local pore-fluids had a higher ionic strength compared to the APW$_{OPC}$ as well as to the APW$_{OPA}$. Karnland et al. (2006) observed in experiments, using fixed-volume cells, in MX-80 bentonite the following relationships for NaCl-based fluids: the higher the ionic strength of a pore-water, the higher the hydraulic conductivity, the lower the swelling pressure, and the lower the material density. Karnland et al. (2007) showed further for NaCl and NaOH-based solutions that both have at higher ionic strengths lower swelling pressures. In case of replacing a Cl^--based solution with an OH^--based solution at constant ionic strength; the swelling pressure did drop drastically. They suggest that the dissolution of cristobalite and smectite mainly induced this effect. Karnland et al. (2006) reported further that a small increase in the ionic strength of NaCl-based solutions induces in bentonite only a small drop in hydraulic conductivity, whereas at current dry density and ionic strengths, no changes were observed.

For our experimental approach at constant-total pressure the expected behaviour is different and may be summarized as follows: an increased ionic strength reduces the interlayer and DL (microporosity) volume allowing for compaction if the volume is not fixed (Dolder et al., 2014). A reduction of the core volume was confirmed by CT measurements, and started 72 days after switching fluids (Figure 5-4). A compaction could be observed in the CT data as well as in the post-mortem density measurements (Figures 5-5 & 5-8).

In summary, the drop in hydraulic conductivity after switching infiltration fluid was most likely dominated by extensive mineral precipitation (calcite, Mg-saponite) in the filter region and in the first mm of bentonite, while the transient phase was linked to core compaction induced by gypsum dissolution as well as by an increase in ionic strength of the pore-water, while releasing water from the porosity.

Volume reduction and gypsum dissolution. The main period of core volume reduction happened in the transient phase described in detail above (Figure 5-4). The propagation of the core diameter reduction reached the end of the core simultaneously with the drop in hydraulic conductivity, inferring that the core shrinkage and compaction was related to this pore-water chemistry change (ionic strength). The core shrinkage stopped at the moment the hydraulic conductivity reached the lowest level. This was the time at which the flow-pattern changed from advective-dominated to diffusion-dominated. The absolute amount of shrinkage measured by CT was ~0.8 cm^3, which amounted to ca. 10% of the 9.3 ml of pore-water sampled during the transient-flow phase. The water ejection could explain a small fraction of the higher flow during this phase. It is argued that the core shrinkage was a combined effect of the above described increase in ionic strength and the continuous dissolution of gypsum.

XRD measurements of the bentonite core showed much smaller quantities of gypsum in comparison to the pristine material, suggesting that significant quantities were most likely already dissolved. In order to estimate the quantities, a mass-balance calculation for sulphate was performed (Table 5-6). MX-80 bentonite contains ~0.9±0.3 wt% gypsum (Karnland, 2010), which corresponds in our core to 1.27 g, respectively 7.36 mmol (gypsum, sulphate). In total 0.27 mmol of sulphate were infiltrated and 1.47 mmol were measured in the outflow, which is an excess of 1.2 mmol (Table 5-6). If we now compare the maximal amount of sulphate originating from gypsum (only sulphate mineral) dissolution with the measured sulphate in the outflow, subtracting the inflows, we get the minimal amount of dissolved gypsum of ~19 wt%, neglecting the sulphate ions in solution. Saturation indices of gypsum are shown in Table 5-5 and indicate that the outflow was initially at saturation and got over time under-saturated, due to an unknown mechanism.

Dissolution of silica and silicate minerals. The silica concentration in the outflow doubled directly after switching to APW_{OPC} and tripled until the end of the experiment, showing higher concentrations compared to the infiltration fluid (Figure 5-3). The alumina concentration doubled after changing fluids but was still lower compared to APW_{OPC}. The equilibrium modeling showed that the silica concentration in the outflow was in equilibrium with amorphous SiO_2 during APW_{OPA} infiltration (Table 5-5). The change to APW_{OPC} led to an over-saturation with respect to amorphous silica. The fact that much more silica was in solution relative to alumina indicates that a pure SiO_2-phase like quartz, cristobalite or tridymite was involved. All these phases were distinctly oversaturated in the last aliquot samples (Table 5-5). Preferential dissolution of cristobalite is in agreement with our XRD data as well as with previous studies (Bouchet et al., 2004; Fernández et al., 2013; Karnland, 1997, 2004, 2010; Karnland et al., 2007). The dissolution of quartz, as reported in previous studies (Fernández et al., 2006; Karnland et al., 2007), could not be confirmed.

Reaction zones. Two overlapping reaction zones could be distinguished in the bentonite by SEM–EDX and CT measurements. One was characterized by strong Mg-enrichment in the clay matrix, the other by Ca-enrichment in the form of calcite precipitation (Figure 5-14).

The magnesium enriched zone contained ~0.21 mmol Mg, which is 0.15 mmol more compared to the amount in same volume of pristine bentonite. The mass-balance of the entire core showed a small net loss of 0.02

mmol Mg (Table 5-5), presumably displaced from the exchanger. Mg-enrichment could only take place if an additional source was available. Two hypotheses are discussed: (1) infiltration of magnesium by APW$_{OPA}$ or (2) dissolution of a magnesium phase. (1) In total 0.08 mmol magnesium were infiltrated during the equilibration phase (Table 5-5), explaining half of that of the enrichment. (2) The only major Mg-bearing mineral phase in MX-80 bentonite is montmorillonite. Dissolution of ~0.1 cm^3 raw montmorillonite could explain the additional magnesium in the Mg-enriched region using magnesium amounts of 0.074 mmol for Mg zone 1 and 0.14 mmol for Mg zone 2. A reduced core density and smaller core diameters in the inflow region support the dissolution theory. It seems that at high-pH conditions the observed Mg-phase was the only stable magnesium bearing mineral phase. No magnesium depletion zone was observed in the bentonite which excludes diffusion of magnesium during APW$_{OPC}$ infiltration, which might have happened by precipitation of an Mg-phase. The magnesium enrichment happened in the clay matrix but with no distinct new mineral phases was observed at the given resolution.

A triangular SiO_2–Al_2O_3+Fe_2O_3–MgO plot (Figures 5-19) is used for further interpretation. Montmorillonite plots in a field with an average composition of 71 wt% SiO_2, 26 wt% Al_2O_3+Fe_2O_3 and 3 wt% MgO, in agreement with Fernández et al. (2006) and Karnland (2010). The Mg-exchanged MX-80 smectite does not shift strongly in MgO direction and the composition is far from the measured Mg-enriched one. The Mg-enriched zone plots in a region of 61 wt% SiO_2, 20 wt% Al_2O_3+Fe_2O_3 and 19 wt% MgO. The measurements indicate a transition state between unreacted bentonite or original montmorillonite and a newly formed mineral phase like saponite, M–S–H, hydrotalcite, talc or brucite (see dotted lines in Figures 5-19). Because we assume that the Mg-enriched phase is related to the trioctahedral clay peak in the XRD spectra, presumably saponite. The main chemical difference to montmorillonite is the strong magnesium enrichment in the octahedral layer. Raman spectroscopy measurements indicated no major changes in the clay structure. Especially M-S-H is amorphous and XRD revealed weak broad humps (Brew and Glasser, 2005). Brucite and talc were detected by XRD in small amounts in the inlet filter, but could not be seen in the bentonite. Several others observed similar reactions in alkaline, high-pH experiments: Karnland (1997) observed at ambient temperature in MX-80 bentonite increased Mg content in the clay; Ramirez et al. (2002a) observed in FEBEX bentonite the formation of a trioctahedral Mg-silicate-phase and the dissolution of smectite at pH >12.6 and temperatures ≥35°C; Cuevas et al. (2006) showed in FEBEX bentonite at 35–90°C the formation of a new trioctahedral smectite, which was determined as saponite-stevensite phase and the dissolution of montmorillonite; Fernández et al. (2006) observed brucite precipitation in FEBEX bentonite while montmorillonite dissolves at pH >13 and ambient temperatures; Fernández et al. (2009a) observed in FEBEX bentonite at 60°C the formation of brucite interlayer in the smectite (di-trioctahedral chlorite-like phase without a continuous and ordered intercalation of brucite); Fernández et al. (2010a) observed in FEBEX bentonite at 60°C formation of a trioctahedral sheet silicate, which they described as talc; Fernández et al. (2013) observed in FEBEX bentonite at 90°C formation of a Mg-layer silicate-phase (di-trioctahedral chlorites).

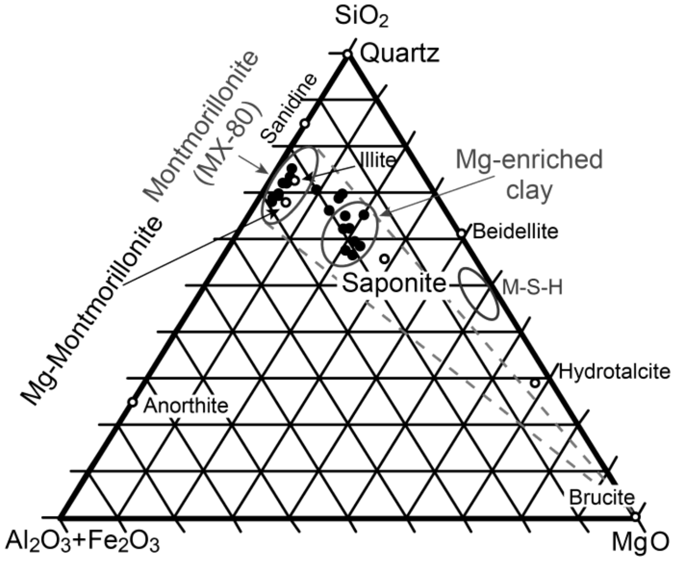

Figures 5-19: Triangular SiO_2–Al_2O_3+Fe_2O_3–MgO plot including SEM-EDX point analysis of the Mg-enriched zone. Filled circles correspond to EDX measurements and open circle as well as ellipses to mineral composition from literature.

The Ca-enrichment propagated 7.7 mm into the bentonite core characterized by intense calcite precipitation, verified by XRD and Raman spectroscopy measurements. SEM-EDX elemental spot analyses indicate strong Ca-enrichment in this new phase but due to the small grain size other possible phases like C-S-H and C-(A)-S-H cannot be excluded. A triangular SiO_2–(Al_2O_3+Fe_2O_3)–CaO plot is shown in Figure 5-20 with analysis of the newly grown Ca-phase. The data plot along a line, ending in the CaO/pure calcite edge. It can be concluded that the measurements are either pure calcite or clay intermixed with calcite. Some measurements may have a small C-(A)-S-H component, but neither XRD nor Raman spectroscopy measurements support this hypothesis.

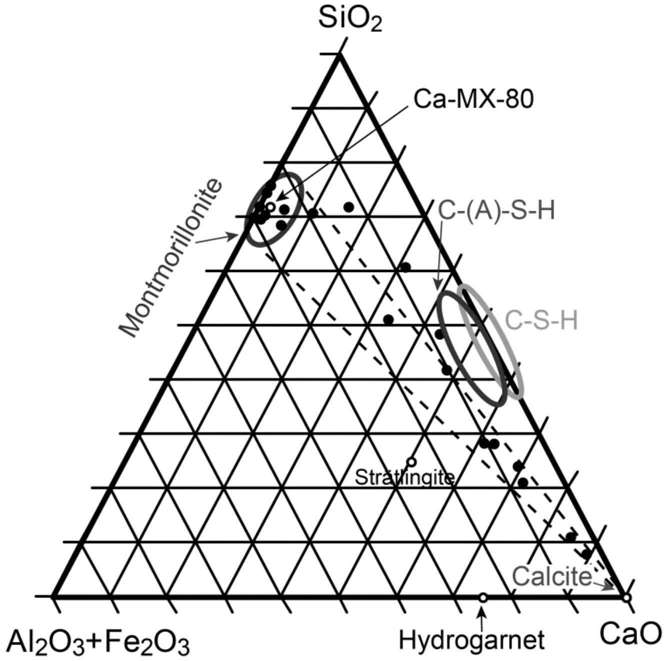

Figure 5-20: Triangular SiO_2–Al_2O_3+Fe_2O_3–CaO plot including SEM-EDX point analysis of the newly formed Ca-phase as well as of Ca-enriched regions. Filled circles correspond to EDX measurements and open circle as well as ellipses to mineral composition from literature.

The Ca mass-balance showed a net gain in the core (Table 5-6). The calcium source for the calcite precipitation was the dissolution of gypsum, a displacement form the clay exchanger by Na^+ and K^+, and minor inflowing APW_{OPC}.

The bicarbonate mass-balance showed a net loss of 0.15 mmol from the core, indicating dissolution of carbonates (Table 5-5). The amount of infiltrated bicarbonate from the APWs was 0.016 mmol, with 0.003 mmol originating from the APW_{OPC}. This could induce the precipitation of 0.6 mm^3 of calcite, while the fraction originating from APW_{OPC} contributed only 0.09 mm^3. A calcite content of 0.5–1.5 wt% in the reaction zone, based on XRD data corresponds to ~4 mm^3 of pure calcite. This indicates that an additional carbonate source is required, which may originate from dissolution of carbonate compounds, reported by Karnland (2010) and associated back-diffusion. PhreeqC equilibrium calculations showed that an increase in pH of a clay pore-water saturated bentonite, led to calcite oversaturation.

Precipitation of Ca-mineral phases like calcite in high-pH environments are described in various studies: Sánchez et al. (2006) observed increased calcite concentrations (<5%) in low and high temperature batch experiments using FEBEX bentonite; Jenni et al. (2014) observed a Ca-enriched layer at a clay (OPA)–OPC interface along with elevated calcite concentration therein. No C-S-H precipitation was observed in our experiment in contrast to previous studies at ambient temperatures (Bouchet et al., 2004; Fernández et al., 2006; Fernández et al., 2010a; Karnland, 1997; Mosser-Ruck and Cathelineau, 2004; Ramirez et al., 2002a; Ramirez et al., 2002b).

Judging from its shape and its evolution it is most likely that the imaged reaction plume in CT represented parts of the calcite precipitation zone (mainly Ca zone 1+2) and the Mg-mineral precipitation zone (Figure 5-7). The first change was observed after 3 days of APW_{OPC} infiltration with a small plug of most likely calcite in the filter. After 36 and 137 days the zone kept growing mainly in the filter and it evolved into two ring structures. The ring structures were most likely induced by the grooved POM-adapter surface supporting the filter. It originated from the production of the piece in the workshop by turning. After 483 days there was clear evidence that the reaction plume proceeded into the bentonite, emanating from the pre-set structures into the filter. After 588 days a reaction plume of 8 mm thickness, a diameter of 18 mm, and a volume of 393 mm^3, was observed. The heterogeneous nature of the plume was mainly due to preferential flow paths. The position of the reaction plume seen in CT scan close to the end of the experiment was in agreement with the post-mortem measured extension of the Ca and calcite-enrichment zone. Analyses of the growth of the reaction plume yielded an average growth rate between 1.0 mm^3/day in the first 137 days and thereafter to ~0.6 mm^3/day. A comparison between volumetric flow and reaction progress showed a retardation of 34 during the first 137 days and 20 by the end. This leads to the conclusion that the system could first buffer the high-pH fluid and after ~228 days the main phase of calcite and saponite precipitation started, while cristobalite dissolved.

5.5. Conclusion

The change to the high-pH pore-fluid after 136 days led to a decrease in hydraulic conductivity from $\sim 1.1\times10^{-13}$ m/s to $\sim 4.2\times10^{-15}$ m/s. The former advective-dominated flow changed into a diffusive-dominated flow pattern with Péclet numbers below 1. The decrease resulted from a combination of extensive mineral precipitation in filter and bentonite core as well as partly from an increase in ionic strength of the pore-water mainly by extensive gypsum dissolution. The high-pH infiltration could led to core shrinkage of ~0.9 vol%, detected by CT measurements, induced by gypsum dissolution and increasing ionic strength. It is inferred that at hydrostatic conditions, high ionic strength pore-fluids may reduce the interlayer porosity and the corresponding DL, which induce core compaction and hence a reduction of the intergranular porosity, resulting in a lower hydraulic conductivity.

The outflow showed a decrease in all ion concentrations with the exception of sulphate, silica, aluminium and potassium, while pH just slightly increased from ~7.5 to ~8. After switching fluids, chloride got replaced as main anionic charge carrier by sulphate after 0.4 PV_{OPC}.

CT scans tracked a progressing hemispherical reaction plume from the filter into the first mm of the bentonite sample, revealing a distinct zone of bulk density increase. This plume was characterized in the bentonite by two distinct but overlapping zones of Mg and Ca-enrichment. The region enriched in calcium related to intense calcite precipitation in the clay matrix. The Mg-enriched zone was most likely related to saponite but the occurrence of other Mg-phases could not be excluded. In the same region dissolution of cristobalite was observed which was the main source for elevated silica in the outflow.

The experiment attests an effective buffering capacity for bentonite and a progressing coupled hydraulic-chemical sealing process. Also, the physical integrity of the interface region was preserved in this setup with a total pressure boundary condition on the core sample. This is in contrast to some experiments carried out at constant-volume condition, where shrinkage in bentonite led to the formation of preferential pathways and breakthrough of the high-pH plume (e.g. Fernández et al. (2009a)). Constant confining pressure constraints may be more realistic for a repository environment due to the ability of the surrounding and unaltered bentonite to compensate volumetric changes at the interface.

Acknowledgments

Financial support from Nagra is gratefully acknowledged. The Department of Forensic Medicine at the University of Bern is acknowledged for granting access and providing technical support for operating their CT scanner. The machine shop at our institute was instrumental in constructing the experimental apparatus, and our analytical laboratory performed the IC and ICP-OES analyses. We thank Barbara Lothenbach (EMPA) for providing the modelled fluid composition for OPC.

References

Adler, M. 2001. *Interaction of claystone and hyperalkaline solutions at 30°C: A combined experimental and modeling study.* Ph.D. Thesis, University of Bern, Switzerland.

Adler, M., Mäder, U. & Waber, H.N. 2001. Core infiltration experiment investigating high-pH alteration of low-permeability argillaceous rock at 30°C. *In*: Cidu, R. (ed.) *Proceedings WRI-10 (10th International Symposium on Water-Rock Interaction)*. Balkema, Villasimius, Italy, 1299-1302.

Alia, J.M., Edwards, H.G., Garcia-Navarro, F.J., Parras-Armenteros, J. & Sanchez-Jimenez, C.J. 1999. Application of FT-Raman spectroscopy to quality control in brick clays firing process. *Talanta*, **50**, 291-298.

Bauer, A. & Berger, G. 1998. Kaolinite and smectite dissolution rate in high molar KOH solutions at 35°C and 80°C. *Applied Geochemistry*, **13**, 905-916, doi: http://dx.doi.org/10.1016/S0883-2927(98)00018-3.

Bauer, A. & Velde, B. 1999. Smectite transformation in high molar KOH solutions. *Clay Minerals*, **34**, 259-273.

Blacksberg, J., Rossman, G.R. & Gleckler, A. 2010. Time-resolved Raman spectroscopy for in situ planetary mineralogy. *Applied Optics*, **49**, 4951-4962, doi: 10.1364/ao.49.004951.

Bouchet, A., Casagnabère, A. & Parneix, J.C. 2004. *Batch experiments: results on MX80.* (ANDRA) European contract FIKW-CT-2000-0028.

Bradbury, M.H. & Baeyens, B. 2009. Experimental and modelling studies on the pH buffering of MX-80 bentonite porewater. *Applied Geochemistry*, **24**, 419-425, doi: http://dx.doi.org/10.1016/j.apgeochem.2008.12.023.

Brew, D.R.M. & Glasser, F.P. 2005. Synthesis and characterisation of magnesium silicate hydrate gels. *Cement and Concrete Research*, **35**, 85-98, doi: http://dx.doi.org/10.1016/j.cemconres.2004.06.022.

Brindley, G.W. & Brown, G. 1980. Crystal Structures of Clay Minerals and Their X-ray Identification. Mineralogical Society.

Cuevas, J., Vigil de la Villa, R., Ramírez, S., Sánchez, L., Fernández, R. & Leguey, S. 2006. The alkaline reaction of FEBEX bentonite: a contribution to the study of the performance of bentonite/concrete engineered barrier systems. *Journal of Iberian Geology*, **32 (2)**, 151-174.

De La Villa, R.V., Cuevas, J., Ramirez, S. & Leguey, S. 2001. Zeolite formation during the alkaline reaction of bentonite. *European Journal of Mineralogy*, **13**, 635-644.

De Windt, L., Pellegrini, D. & van der Lee, J. 2004. Coupled modeling of cement/claystone interactions and radionuclide migration. *Journal of Contaminant Hydrology*, **68**, 165-182, doi: http://dx.doi.org/10.1016/S0169-7722(03)00148-7.

Dolder, F., Mäder, U., Jenni, A. & Schwendener, N. 2014. Experimental characterization of cement–bentonite interaction using core infiltration techniques and 4D computed tomography. *Physics and Chemistry of the Earth, Parts A/B/C*, **70–71**, 104-113, doi: http://dx.doi.org/10.1016/j.pce.2013.11.002.

Eberl, D.D., Velde, B. & McCormick, T. 1993. Synthesis of illite-smectite from smectite at earth surface temperatures and high pH. *Clay Minerals*, **28**, 49-60.

Fernández, R., Cuevas, J., Sanchez, L., de la Villa, R.V. & Leguey, S. 2006. Reactivity of the cement-bentonite interface with alkaline solutions using transport cells. *Applied Geochemistry*, **21**, 977-992.

Fernández, R., Mäder, U. & Jenni, A. 2011a. *Multi-component advective-diffusive transport experiment in MX-80 compacted bentonite: Method and results of 1st phase of experiment.* Internal Nagra Working Report.

Fernández, R., Mäder, U., Rodríguez, M., de la Villa, R.V. & Cuevas, J. 2009. Alteration of compacted bentonite by diffusion of highly alkaline solutions. *European Journal of Mineralogy*, **21**, 725-735, doi: 10.1127/0935-1221/2009/0021-1947

Fernández, R., Mäder, U. & Steefel, C. 2011b. Modelling of a bentonite column experiment with CrunchFlow including new clay-specific transport features. *Mineralogical Magazine*, **75(3)**, 839.

Fernández, R., Rodríguez, M., de la Villa, R.V. & Cuevas, J. 2010. Geochemical constraints on the stability of zeolites and C-S-H in the high pH reaction of bentonite. *Geochimica et Cosmochimica Acta*, **74**, 890-906.

Fernández, R., Vigil de la Villa, R., Ruiz, A.I., García, R. & Cuevas, J. 2013. Precipitation of chlorite-like structures during OPC porewater diffusion through compacted bentonite at 90°C. *Applied Clay Science*, **83–84**, 357-367, doi: http://dx.doi.org/10.1016/j.clay.2013.07.021.

Ferrage, E., Lanson, B., Sakharov, B.A. & Drits, V.A. 2005. Investigation of smectite hydration properties by modeling experimental X-ray diffraction patterns. Part I. Montmorillonite hydration properties. Mineralogical Society of America, Washington, DC, USA.

Gaucher, E.C. & Blanc, P. 2006. Cement/clay interactions - A review: Experiments, natural analogues, and modeling. *Waste Management*, **26**, 776-788, doi: http://dx.doi.org/10.1016/j.wasman.2006.01.027.

Jacques, D. 2009. Benchmarking of the cement model and detrimental chemical reactions including temperature dependent parameters. Project near surface disposal of catergory A waste at Dessel. *NIRAS-MP5-03 DATA-LT(NF) Version 1 NIROND-TR 2008-30 E*.

Jenni, A., Mäder, U., Lerouge, C., Gaboreau, S. & Schwyn, B. 2014. In situ interaction between different concretes and Opalinus Clay. *Physics and Chemistry of the Earth, Parts A/B/C*, **70–71**, 71-83, doi: http://dx.doi.org/10.1016/j.pce.2013.11.004.

Karnland, O. 1997. *Cement/bentonite interaction: results from 16 month laboratory tests.* SKB Technical Report 97-32.

Karnland, O. 2004. *Laboratory experiments concerning compacted bentonite contacted to high-pH solutions.* (ANDRA) European contract FIKW-CT-2000-0028.

Karnland, O. 2010. *Chemical and mineralogical characterization of the bentonite buffer for the acceptance control procedure in a KBS-3 repository.* SKB Technical Report 10-60.

Karnland, O., Olsson, S., Dueck, A., Birgersson, M., Nilsson, U., Hernan-Håkansson, T., Pedersen, K., Nilsson, S., Eriksen, T. & Rosborg, B. 2009. *Long term test of buffer material at the Äspö Hard Rock Laboratory, LOT project. Final report on the A2 test parcel.* SKB Technical Report 09-29.

Karnland, O., Olsson, S. & Nielsson, U. 2006. *Mineralogy and sealing properties of various bentonites and smectite-rich clay materials.* SKB Technical Report 06-30.

Karnland, O., Olsson, S., Nilsson, U. & Sellin, P. 2007. Experimentally determined swelling pressures and geochemical interactions of compacted Wyoming bentonite with highly alkaline solutions. *Physics and Chemistry of the Earth, Parts A/B/C*, **32**, 275-286.

Kosakowski, G., Berner, U., Wieland, E., Glaus, M. & Degueldre, C. 2014. Geochemical evolution of the L/ILW near-field. *Nagra Technical Report NTB 97-04, Nagra, Wettingen, Switzerland*.

Košařová, V., Hradil, D., Němec, I., Bezdička, P. & Kanický, V. 2013. Microanalysis of clay-based pigments in painted artworks by the means of Raman spectroscopy. *Journal of Raman Spectroscopy*, **44**, 1570-1577, doi: 10.1002/jrs.4381.

Lancaster, J.L. & Martinez, M.J. 2007. Mango - Multi-image analysis GUI.

Lothenbach, B., Matschei, T., Möschner, G. & Glasser, F.P. 2008. Thermodynamic modelling of the effect of temperature on the hydration and porosity of Portland cement. *Cement and Concrete Research*, **38**, 1-18, doi: http://dx.doi.org/10.1016/j.cemconres.2007.08.017.

Lothenbach, B. & Winnefeld, F. 2006. Thermodynamic modelling of the hydration of Portland cement. *Cement and Concrete Research*, **36**, 209-226.

Mäder, U. 2009. *Reference pore water for the Opalinus Clay and "Brown Dogger" for the provisional safety-analysis in the framework of sectoral plan - interim results (SGT-ZE).* Nagra Working Report.

Mäder, U., Jenni, A., Fernández, R. & de Soto, I. 2012. Reactive transport in compacted bentonite: porosity concepts, experiments and applications. *Mineralogical Magazine*, **76(6)**, 2052.

Mäder, U., Waber, H.N. & Gautschi, A. 2004. New method for porewater extraction from claystone and determination of transport properties with results for Opalinus Clay (Switzerland). *In*: Wanty, R.B. & Seal, R.R. (eds.) *Proceedings WRI-10 (11th International Symposium on Water-Rock Interaction)*. Balkema, Saratoga Springs, New York, USA, 445-448.

Mazurek, M., Waber, H.N., Mäder, U., de Haller, A. & Koroleva, M. 2013. *Geochemical synthesis for the Effingen Member in boreholes at Oftringen, Gösgen and Küttigen.* Nagra Technical Report NTB 12-07

Moore, D.M. & Reynolds, R.C. 1989. X-ray diffraction and the identification and analysis of clay minerals. Oxford University Press, New York.

Mosser-Ruck, R. & Cathelineau, M. 2004. Experimental transformation of Na,Ca-smectite under basic conditions at 150 °C. *Applied Clay Science*, **26**, 259-273, doi: http://dx.doi.org/10.1016/j.clay.2003.12.011.

Muurinen, A., Karnland, O. & Lehikoinen, J. 2004. Ion concentration caused by an external solution into the porewater of compacted bentonite. *Physics and Chemistry of the Earth, Parts A/B/C*, **29**, 119-127, doi: http://dx.doi.org/10.1016/j.pce.2003.11.004.

Muurinen, A. & Lehikoinen, J. 1999. Porewater chemistry in compacted bentonite. *Engineering Geology*, **54**, 207-214.

Nagra. 2002. *Demonstration of disposal feasibility for spent fuel, vitrified high-level waste and long-lived intermediate-level waste (Entsorgungsnachweis).* Nagra Technical Report NTB 02-05.

Parkhurst, D.L. & Appelo, C.A.J. 1999. User's guide to PHREEQC (version 2) – a computer program for speciation, batch reaction, one-dimensional transport, and inverse geochemical calculations. *US Geological Survey Water-Resources Investigations Report 99-4259*.

Parkhurst, D.L. & Appelo, C.A.J. 2013. Description of Input and Examples for PHREEQC Version 3--A Computer Program for Speciation, Batch Reaction, One-Dimensional Transport, and Inverse Geochemical Calculations. U.S. Geological Survey.

Ramirez, S., Cuevas, J., de la Villa, R.V. & Leguey, S. 2002a. Hydrothermal alteration of La Serrata bentonite (Almeria, Spain) by alkaline solutions. *Applied Clay Science*, **21**, 257– 269.

Ramirez, S., Cuevas, J., Petit, S., Righi, D. & Meunier, A. 2002b. Smectite reactivity in alkaline solutions. *Geologica Carpathica*, **53**, 87-92.

Sánchez, L., Cuevas, J., Ramírez, S., Riuiz De León, D., Fernández, R., Vigil Dela Villa, R. & Leguey, S. 2006. Reaction kinetics of FEBEX bentonite in hyperalkaline conditions resembling the cement–bentonite interface. *Applied Clay Science*, **33**, 125-141, doi: http://dx.doi.org/10.1016/j.clay.2006.04.008.

Savage, D., Noy, D. & Mihara, M. 2002. Modelling the interaction of bentonite with hyperalkaline fluids. *Applied Geochemistry*, **17**, 207-223.

Schindelin, J., Arganda-Carreras, I., Frise, E., Kaynig, V., Longair, M., Pietzsch, T., Preibisch, S., Rueden, C., Saalfeld, S., Schmid, B., Tinevez, J.-Y., White, D.J., Hartenstein, V., Eliceiri, K., Tomancak, P. & Cardona, A. 2012. Fiji: an open-source platform for biological-image analysis. *Nat Meth*, **9**, 676--682.

Van Loon, L.R., Glaus, M.A. & Müler, W. 2007. Anion exclusion effects in compacted bentonites: Towards a better understanding of anion diffusion. *Applied Geochemistry*, **22**, 2536-2552.

Watson, C., Hane, K., Savage, D., Benbow, S., Cuevas, J. & Fernández, R. 2009. Reaction and diffusion of cementitious water in bentonite: Results of "blind" modelling. *Applied Clay Science*, **45**, 54-69.

Wolery, T.J. 1992. *EQ3/6, a software package for geochemical modeling of aqueous systems: Package overview and installation guide (Version 7.0)*.

6

Alteration of MX-80 bentonite by ‘low-pH’ shotcrete (ESDRED) fluids – An experimental approach using core infiltration techniques

6.1. Introduction

The long-term behavior of clay barriers in deep geological repositories is of major importance for nuclear waste storage and is a topic of ongoing research. Bentonite is considered as possible material for the engineered barrier system (EBS), consisting predominately of the smectite-group clay mineral montmorillonite (Karnland, 2010). Montmorillonite exhibits unique mineral properties like swelling in contact with water and adsorption of cations on the negatively charged clay surface. Cement-based materials like concrete or shotcrete are used as tunnel reinforcement, tunnel plugs/seals or buffer of low- and intermediate-level waste (Nagra, 2002). Pore-water emanating from cementitious materials induces a high-pH reaction plume that may affect the EBS. Various studies showed that such high-pH fluids perturbate the bentonite buffer strongly by changing physical and chemical properties (Bauer and Velde, 1999; Cuevas et al., 2006; Cuevas et al., 2002; Dauzeres et al., 2010; De La Villa et al., 2001; Dolder et al., 2015; Dolder et al., 2014; Eberl et al., 1993; Fernández et al., 2006; Fernández et al., 2009a; Fernández et al., 2010a; Fernández et al., 2014; Fernández et al., 2013; Gaucher and Blanc, 2006; Karnland et al., 2007; Nakayama et al., 2004; Ramirez et al., 2002a; Ramirez et al., 2002b; Sánchez et al., 2006).

Ordinary Portland cement (OPC) is the most common type of cement, consisting initially of clinker phases (containing mainly CaO, SiO_2, Al_2O_3, Fe_2O_3) and gypsum. OPC (CEM I Portland cement (PC)) sets when mixed with water (hydration), forming mainly portlandite and ettringite and minor amounts of monocarbonate, hydrotalcite, and C–S–H phases (Lothenbach and Winnefeld, 2006). Calcite forms by carbonization in case CO_2 is available. The characteristic of the hydration reaction is the enrichment in alkalis in the pore-water combined with an increase in pH (≥13.5) (Lothenbach and Winnefeld, 2006; Matschei et al., 2007). An alternative to OPC is the use of 'low-pH' cements/shotcretes, consisting of PC, water and silica fume (SF), blast furnace slag or fly ashes (García Calvo et al., 2010; Lothenbach et al., 2013; Lothenbach et al., 2011). In the following study, a low-alkali shotcrete mixture called ESDRED was used, consisting of 60 wt% CEM I PC blended with 40 wt% SF and an aluminum salt as set accelerator. The mixture was originally developed for the EU-project Engineered Studies and Demonstration of Repository Designs (ESDRED) (Bäckblom, 2007; García Calvo et al., 2010; Lothenbach et al., 2013). This low-alkali shotcrete exhibits a pH drop from ~13 to ~11.7 during the hydration phase. During hydration, clinker phases and silica fume dissolve, while ettringite, C-S-H phases (low Ca/Si), calcite, and hydrotalcite are precipitated. In contrast to OPC, portlandite is only formed as an intermediate phase during the first weeks/months and dissolves subsequently by the pH drop (pH <12.5). SF accelerates the hydration reaction by providing additional silica and surfaces for nucleation (Lothenbach et al., 2013). The lower pH origins from the dilution of PC by SF and C–(A)-S–H phases with a low Ca/Si ratio, which can take up more alkalis (Lothenbach et al., 2013). Adding superplasticizer and set accelerator to the cement material gives the mixture a higher viscosity and it sets faster. The set accelerator used for the ESDRED admixture is alkali-free in order to reduce the hydroxide impact, and rather based on aluminum-sulfate and aluminum-formate (Lothenbach et al., 2013; Wieland et al., 2014). The set accelerator increases further the amount of ettringite, while reducing portlandite (Lothenbach et al., 2013; Maltese et al., 2007). The pore-water chemistry of an ESDRED shotcrete differs after complete hydration from an OPC pore-fluid mainly by lower Na^+, K^+, OH^-, SO_4^{2-} concentrations, while Ca^{2+}, Si^{4+}, C_{org} are increased. Formate (C_{org}) originates from the set accelerator and it is in the ESDRED pore-water the main anionic charge carrier, as the hydroxide activity is low. Blending of PC with SiO_2 and using set accelerator and superplasticizer leads to a much more complex pore-water chemistry (Lothenbach et al., 2011; Savage and Benbow, 2007).

Various studies analyzed the effect of mature OPC solutions (pH ~12.5), consisting mainly of Ca^{2+} and OH^-, on clay material (Fernández et al., 2010a; Fernández et al., 2013; Karnland et al., 2007; Mosser-Ruck and Cathelineau, 2004; Ramirez et al., 2002a). As such pore-waters exhibit a similar chemical composition (in particular pH) like 'low-pH' shotcrete fluids, experimental results can applied for interpretation of the behavior of 'low-pH' fluids on clay. The reactivity of such fluids in clay was reported to be low at ambient as well as at increased temperatures. Only precipitation of C–S–H phases and cation exchange processes were observed, while the primary mineralogy and the swelling pressure were not affected. Lothenbach et al. (2013) showed in hydration experiments using ESDRED cement a pore-water chemistry dominated on the cationic charge by Ca^{2+}, Na^+ and K^+ whereas the anionic charge is mainly C_{org} (formate). Savage and Benbow (2007) modeled the influence of 'low-pH' cement on bentonite, pointing to the following constraints: the effect of a lower pH on secondary mineral formation poorly known, change in the aqueous speciation of silica at lower pH may have an impact on the montmorillonite stability, reduction in porosity is likely to happen at the interface but how this may influence transport processes is unclear. Berner et al. (2013) modeled the influence of ESDRED pore-fluids on clay formations and bentonite. The modeling showed for bentonite a reduction in porosity directly at the interface along with precipitation of various amounts of calcite, hydro-magnetite and hydrotalcite.

This work summarizes a core infiltration experiment using a pre-compacted and pre-saturated MX-80 bentonite sample and a 'low-pH' artificial cement solution (pH 11.8) that mimics an ESDRED shotcrete pore-fluid after full hydration. CT measurements allowed tracking volume/density changes over time, while XRD, SEM, Raman spectroscopy, and optical microscopy were used for post-mortem characterization.

6.2. Methods and material

6.2.1. Core infiltration experiment

The current experimental approach used a core infiltration method. Constant confining pressure was applied to a rock sample, while a fluid was injected on one side, generating a pressure gradient and hence an advective-dispersive fluid flow. A detailed description of the concept, setup, and procedures are described in *chapters 2 and 4*.

During the first 271 days, called equilibration phase, the bentonite sample got adapted to the new pressure conditions while infiltrating an artificial Opalinus Clay pore-water (APW$_{OPA}$). During the following 272 days, called high-pH phase, artificial ESDRED shotcrete pore-water (APW$_{ESDRED}$) was injected.

For the post-mortem analysis, the core and filters were measured (length, diameter, mass) and cut into pieces (Figure 6-1). Two longitudinal samples of 2×5×1.5 cm were cut along to the center (see Figure 6-1; SEM and XRD samples) and freeze-dried. The SEM (scanning electron microscope) sample was vacuum impregnated with resin and polished using ethanol. The XRD (X-ray diffraction) sample was cut into 11 samples of 2–12 mm thickness perpendicular to the sample axis. The rest of the bentonite core was cut into two longitudinal profiles for water content and density (ρ) measurements, 5 samples each. Two profiles were located along the outer surface of the core (subscript: rim) and two profiles at 1 cm off-axis (subscript: cen) (see Figure 6-1). The filters were immersed in isopropyl alcohol and dried in a nitrogen filled desiccator.

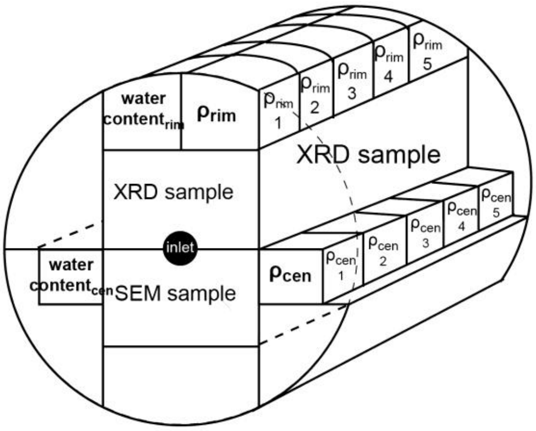

Figure 6-1: Post-mortem cutting pattern of the bentonite core (bent-CT2).

6.2.2. Analytical methods

The outflow was chemically analyzed using the following methods: ion chromatography (IC) for ion concentrations (error: ±5–20%), titration for alkalinity, ion coupled plasma atomic emission spectroscopy (ICP-OES) for minor ions and trace elements (Al^{3+}, Si^{4+}, and Sr^{2+}), pH, and electrical conductivity (EC).

Physical parameters like water content, saturated density, and grain density were analyzed post-mortem in the laboratory. The mineralogy was determined by XRD on grinded (grain size ∼10 µm) and preconditioned (33 %rh) powder samples. Samples were measured untreated and ethylene glycol (EG) saturated. All XRD traces were normalized on quartz. Raman spectroscopy was used to identify mineral phases. SEM was used to analyze the structural, textural and chemical composition of the core using back-scattered electron images (BSE) and energy dispersive spectroscopy (EDX). Elemental maps were recorded by EDX, with bright shades representing high concentrations.

X-ray computed tomography (CT) measurements were performed on a medical CT scanner (Siemens Somatom Emotion 6) operated by the Institute of Forensic Medicine at the University of Bern. In total 8 CT scans were performed during the experiment. The used parameters were chosen to optimize the contrast of the images. The generated X-ray energy was 130 keV (polychromatic X-ray beam) with an X-ray tube current of 120 mA and the voxel dimension of the recorded images was 0.109x0.109x0.5 mm. The CT scanner was calibrated prior to each measurement on air. Tomographic images are shown in Hounsfield units (HU), a generic unit used in medicine. It is defined by air and distilled water at -1000 and 0 HU, respectively. The data were processed and analyzed using the open-source software Mango (Multi-Image Analysis GUI (Lancaster and Martinez, 2007) and Fiji, an open-source image processing software package based on ImageJ. More information on the methods is given in *chapters 3, 4 and 5.*

6.2.3. Aqueous geochemical modeling

Aqueous speciation calculations and saturation states at 25°C were performed using PhreeqC (V2.18) (Parkhurst and Appelo, 1999, 2013). The PhreeqC.dat database was used for neutral-pH fluids, extended by montmorillonite, cristobalite (both Thermoddem database, Blanc et al., 2007) and tridymite (llnl.dat database, Wolery (1992)). Modeling of high-pH shotcrete fluids required a database containing cement minerals. For this purpose the CEMDATA07 (version 07.02) for PhreeqC was used (Babushkin et al., 1985; Hummel et al., 2002; Jacques, 2009; Lothenbach et al., 2008; Lothenbach and Winnefeld, 2006; Matschei et al., 2007; Möschner et al., 2008; Thoenen and Kulik, 2003).

6.2.4. Starting material and saturation and equilibration fluids (APW$_{\text{Äspö}}$ & APW$_{\text{OPA}}$)

Untreated MX-80 bentonite powder was used, manufactured by Volclay LTD, Merseyside, UK. It consists of montmorillonite (81–85 wt%), feldspars (~5 wt%), quartz (~3 wt%), muscovite (~3 wt%), gypsum (~1 wt%), cristobalite (~1 wt%), calcite (~0.2 wt%) (Karnland, 2010). The exchanger of montmorillonite is dominated by Na^+ with 75 eq%, followed by Ca^{2+}, Mg^{2+} and K^+ with 17, 6 and 2 eq%, respectively (Karnland, 2010). The MX-80 bentonite sample was compacted and saturated in a pre-treatment (*chapter 2*) device using 157.66 g of dry rock powder with a residual water-content of 11.98 wt% (Dolder et al., 2014). For saturation APW$_{\text{Äspö}}$ was used, a moderately saline fracture water from the Äspö underground rock laboratory, Sweden (Tables 6-1 and 6-3). The final bentonite core was 51.2 mm long, had a diameter of 50 mm, a volume of 1005 mm^3, and a saturated weight of 187.75 g (dry weight 140.79 g). This corresponds to a dry density of ~1408 kg/m^3 and a saturated density of 1868 kg/m^3 with a water content of 33.4 wt% (rel. to dry mass), which is equal to 46.96 g of water (1 PV). PVs were used to convert transport time to the amount of water passing through the core.

APW$_{\text{OPA}}$, which was based on an artificial pore-water from Opalinus Clay Formation, was injected during the equilibration phase (Tables 6-1 & 6-3). The re-measured APW$_{\text{OPA}}$ of the mobile infiltration tank showed after 271 days a slightly increased ionic strength (see Table 6-5). Saturation indices (SI) of both fluids are shown in Table 6-5.

Table 6-1: Chemical compositions of APW$_{\text{Äspö}}$ and APW$_{\text{OPA}}$ (error of major ion concentrations: 5%, up to 20% for low concentrations); unkn.: not measured.

	APW$_{\text{Äspö}}$[1]	**APW$_{\text{OPA}}$**[2]	
	start	Start	end
pH	7.2	7.6	7.6
	--[mM]--		
Na^+	88.2	165.88	239.18
K^+	< 1.3	2.7	3.63
Ca^{2+}	54.3	11.92	17.07
Mg^{2+}	< 2.1	9.08	13
Sr^{2+}	< 0.6	< 0.1	< 0.1
Cl^-	203.6	157.6	171
SO_4^{2-}	1.8	22.14	24.63
Br^-	0.1	< 0.02	0.03
HCO_3^-	0.24	0.66	unkn.

[1] Karnland et al. (2009), [2] Mäder (2009).

6.2.5. The 'low-pH' artificial pore-water (APW_{ESDRED})

APW_{ESDRED} represented a young low-alkali pore-fluid with a pH of 11.8. The composition was based on experimental data of Lothenbach et al. (2013), representing an ESDRED pore-fluid after 365 days of hydration (Table 6-2). The reported pore-water chemistry was equilibrated with the predominant mineralogy reported by Lothenbach et al. (2013) using PhreeqC (Parkhurst and Appelo, 1999, 2013): ettringite (Jacques, 2009; Lothenbach et al., 2008; Matschei et al., 2007), C–S–H 1.33 (Si^{4+}:Ca^{2+} 1.33) (Traber and Mäder, 2006) and calcite. Lothenbach et al. (2013) reported that the dissolved organic carbon (DOC) consisted mainly of formate ($CHOO^-$), the main negative charge carrier of the solution. The chemical composition and the recipe of the APW_{ESDRED} are shown in Tables 6-2 and 6-3. SI of the APW_{ESDRED} are shown in Table 6-5. The main difference of APW_{ESDRED} and the reported experimental data of Lothenbach et al. (2013) were the lower silica and alumina concentrations, mainly induced by a solubility limit of ettringite and C–S–H 1.33. The long-term stability of APW_{ESDRED} showed reduction in hydroxide and formate concentrations after 271 days.

Table 6-2: Composition of the APW_{ESDRED} and comparison to literature; unkn.: not measured.

	Experimental data of Lothenbach et al. (2013)	**Aqueous speciation**	**APW_{ESDRED}**	
			Start	End (after 271 days)
pH	11.3	11.3	11.8	11.4
		--[mM]--		
Na^+	25	25	24.78	24.17
K^+	14	14	12.77	12.23
Ca^{2+}	27	27	27.2	26
Si^{4+}	0.4	0.046	0.074	unkn.
Al^{3+}	0.012	0.0003	0.002	unkn.
SO_4^{2-}	2.2	2.2	2.12	2.1
DIC	unkn.	0.0067	0.31	unkn.
Formate	(85)	81.56	76.02	66.13
DOC	164	unkn.	86.17	unkn.

Table 6-3: Recipes of the three APWs, including composition, number and molar weight of the chemicals.

Ingredients	**Producer and no.**	**M (mfw)**	**$APW_{Äspö}$**	**APW_{OPA}**	**APW_{ESDRED}**
Solids			g/l	g/l	g/l
$Al_2(SO_4)_3\ 16{\times}H_2O$	Fluka: 06421	630.4			0.000
KCl	Merck: 1.04936	74.6	19.57	0.190	
K_2SO_4	Merck: 1.05153	174.3			0.383
KOH	Merck: 1.05033	56.1			0.303
KCHOO	Sigma-Aldrich: 294454-25G	84.1			0.354
Na_2SO_4	Merck: 1.06649	142.0	249.87	3.409	
NaCl	Merck: 1.06404	58.4	5164.24	6.736	
Na_2CO_3	Merck: 6398	106.0	10.27		
NaCHOO	Merck: 1.06443.0500	68.0			1.699
$NaHCO_3$	Fluka: 71329	84.0		0.046	
NaBr	Fluka: 71329	102.9	15.35		
NaOH	Merck: 1.06498	40.0			
$MgCl_2\ 6{\times}H_2O$	Merck: 1.05833	203.3	334.83	1.864	
$CaCl_2\ 2{\times}H_2O$	Merck: 1.02382	147.0	8253.03	1.751	
$Ca(OH)_2$	Merck: 1.02047	74.1			
$CaCO_3$	Merck: 1.02066	100.1			
$Ca(CHOO)_2$	Sigma-Aldrich: 21134-250G-F	130.1			3.513
$SrCl_2\ 6{\times}H_2O$	Fluka: 85892	266.62	121.41		
Solution					ml/l
$Na_2O_7Si_3$	Sigma-Aldrich: 338443-1				0.007

6.3. Results

6.3.1. Physical and hydraulic evolution of the experiment

The experiment duration was 543 days. In total 15 ml fluid were flushed through the core; 12.2 ml (0.26 PV) of APW_{OPA} and 2.8 ml (0.32 PV) APW_{ESDRED}. The temperature in the laboratory showed a seasonal oscillation between 18.5 and 23.2°C (Figure 6-2A). The confining fluid pressure was at the beginning step-wise increased to 4.1 MPa (Figure 6-2A). The confining pressure was reduced to 3.6 MPa after 109 days, in order to increase the fluid flow. During the APW_{ESDRED} infiltration, the pressure continuously decreased to 3.4 MPa, caused by pressure loss during decoupling for CT scans. The infiltration fluid pressure was set to 2.2 MPa (Figure 6-2A). The pressure was increased to 2.5 MPa after 427 days, in order to increase the fluid flow.

The hydraulic conductivity, shown in Figure 6-2B, was based on averages of 4 single water-level measurements on syringes at the fluid outflow, with time spans of 1–4 weeks. The hydraulic conductivity was calculated based on Darcy's law (see *chapter 2*). The hydraulic conductivity decreased from 1.4×10^{-13} m/s to ~1.0×10^{-13} m/s during the first 100 days, due to adaption of the core to the new pressure conditions, compacting the core and initially releasing water. Lowering the confining fluid pressure reduced the hydraulic conductivity to ~6.0×10^{-14} m/s over a transient phase directly after reducing pressure. The strong variations during the equilibration phase originated from sealing problems at the fluid outflow. During the high-pH infiltration phase, the hydraulic conductivity decreased to ~3.6×10^{-14} m/s and ~3.0×10^{-15} m/s after 290 and 397 days, respectively. The increase of the infiltration fluid pressure had no effect on the fluid flow. The permeability is linked to the hydraulic conductivity by the multiplication of the quotient of dynamic viscosity of the fluid (8.91×10^{-4} Pa×s) divided by the fluid density (1019 kg/m^3) times the gravity (9.8 m/s^2). The permeability was initially ~1.2×10^{-20} m^2 and dropped to $4.8.0\times10^{-21}$ m^2 during the equilibration phase. During the high-pH infiltration phase, the permeability dropped further to 2.5×10^{-22} m^2.

The EC measurements of the outflow were started after 108 days and showed at the beginning a value of ~30 mS/cm. The EC dropped initially to 26.7 mS/cm and was 37.6 mS/cm at the end (Figure 6-2B). The peaks at 145 and 470 days were related to technical perturbations (sealing problems) in the outflow system, induced by decoupling for CT scans.

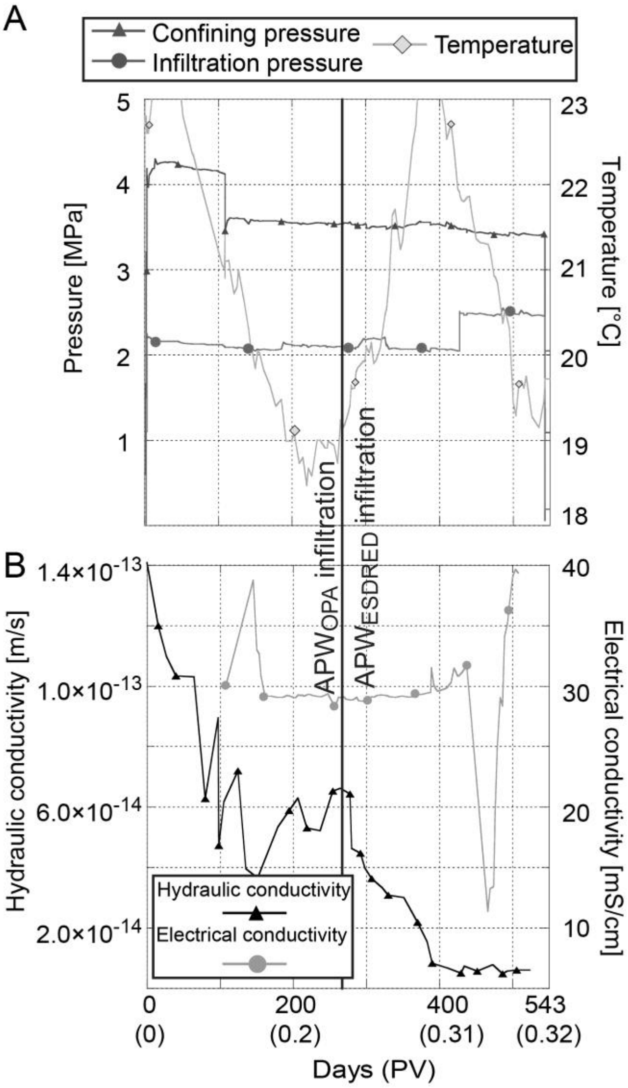

Figure 6-2: Evolution of the physical parameters: (a) pressure and temperature, (b) hydraulic- and electrical conductivity.

6.3.2. Chemical evolution of the outflow

14 outflow aliquots were collected in syringes of 1–5 ml volume and stored in a fridge. 10 syringes were sampled during the equilibration phase and 4 during the high-pH infiltration phase. The average solution-loss in the syringes before and after storage was between 0.01–0.05 vol%. Samples were analyzed for the aqueous constituents by IC, ICP-OES, titration and pH (Figure 6-3).

The pH varied between 7.6 and 8.0 and showed no change after switching to APW_{ESDRED}. The chemical composition of the outflow gradually approached the APW_{OPA} composition during the equilibration phase; all ion concentrations decreased or remained constant with the exception of sulfate, alkalinity (bicarbonate) and aluminum (Figure 6-3). At the end of the equilibration phase, the outflow showed the following trend with respect to APW_{OPA}: Na^+, Si^{4+} and SO_4^{2-} were enriched, Mg^{2+} and alkalinity (HCO_3^-) were depleted, while the rest of the elements were equal. High-pH infiltration only affected chloride and calcium, both showing decreasing trends, while silica and sulfate, showing increasing trends. At the end of the experiment, the outflow showed increased ion concentrations with respect to APW_{ESDRED}, with the exception of hydroxide (pH), potassium, calcium, and formate. The last measurement showed a strong disequilibrium in charges, which indicates that the measured cation concentrations were most likely too high and rather an artefact of sample preparation or measurement. Therefore this last aliquot was not used for further calculations or interpretations. Propionate was the only organic compound detected in the outflow, showing a decreasing trend. No formate, the main anionic charge carrier of APW_{ESDRED}, was detected in the outflow. Measured ammonium, nitrate and, fluoride were all below detection limit.

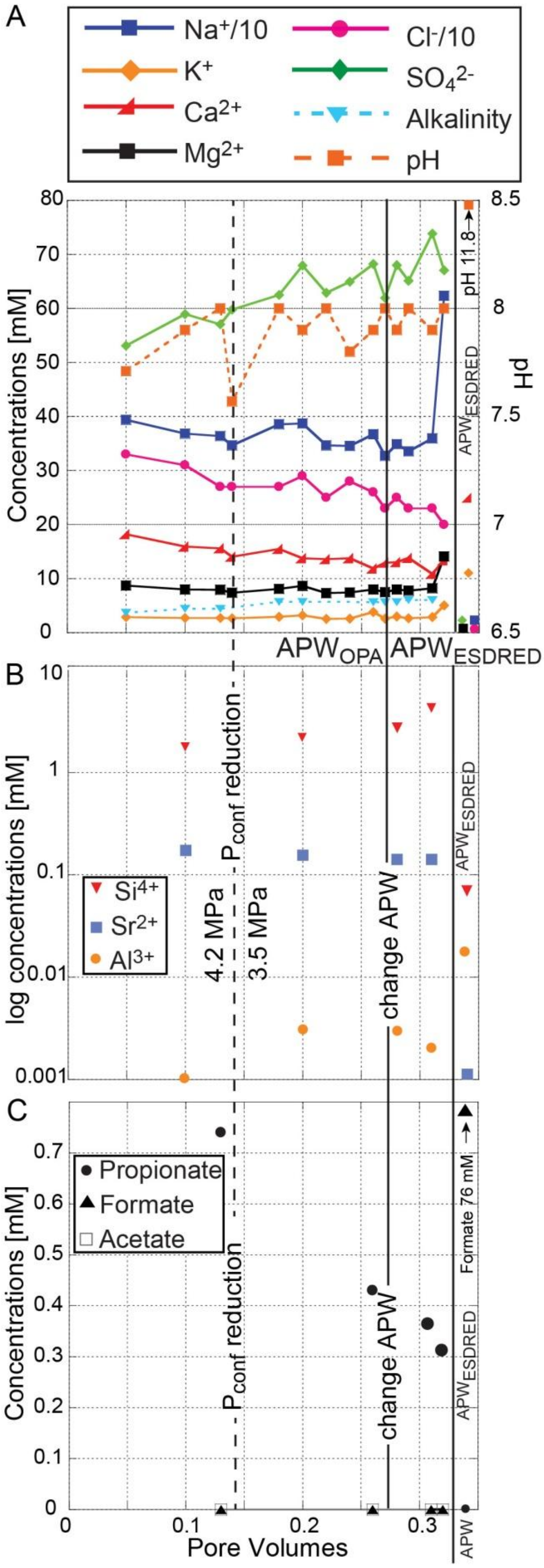

Figure 6-3: Aqueous chemistry of the outflow solutions: (A) ion chromatography, alkalinity and pH; (B) ICP-OES; (C) organic acids measured by IC.

6.3.3. Computed tomography (CT)

The calculations of core volume were based on the HU histograms of each dataset (*chapter 3*). CT data of the experiment were segmented, while a region of interest (ROI: 815–3055 HU) was defined for bentonite (*chapter 3).* For the core volume calculation, all voxels in the ROI were counted and multiplied by the voxel dimension. The bulk density of the bentonite core is linearly depended to the HU/attenuation. The uncertainty of the results was ~1%, as the sealing layer could not be distinguished from the sample and beam hardening artifacts occurred at the interface bentonite–seal–confining water.

The pre-experiment core volume was 100.51 cm^3 and decreased after insertion into the infiltration device and applying pressure by ~4 vol% (Figure 6-4A). Reducing the confining pressure induced a core expansion by 0.6 vol%. During the high-pH infiltration, the core volume decreased, which corresponds to shrinkage of 0.4 vol%. The main phase of volume reduction happened in a period between 57 and 117 days of $\text{APW}_{\text{ESDRED}}$ infiltration. The core diameter calculations were performed the same way as the volume calculations. In doing this for all CT-slices of a dataset, the evolution of the core sectional area and the core diameter could be evaluated along the core axis over time (Figure 6-4B). The core diameter increased from inlet towards the outlet, showing 4 distinct domains, which were remnants of the sample production procedure (Figure 6-4B). The confining pressure release increased the core diameter by 0.1–0.2 mm, with higher values in the middle of the core (Figure 6-4C).

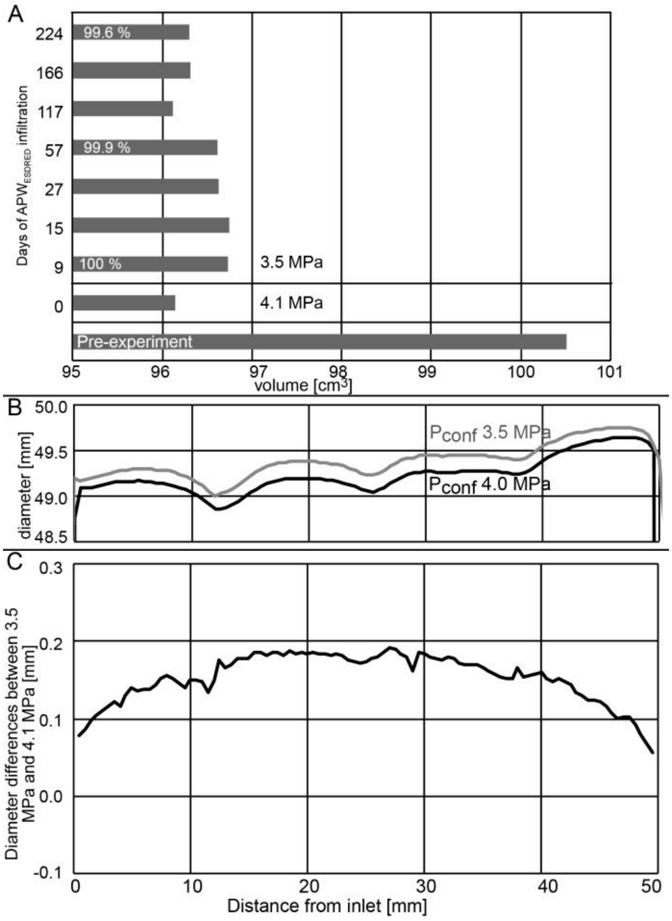

Figure 6-4: (A) Core volume evolution with percentage change relative to the first measurement at 3.5 MPa confining pressure; (B) core diameters; (C) core diameter difference between the two curves shown in B.

The $\text{APW}_{\text{ESDRED}}$ infiltration reduced the core diameter by up to 0.2 mm, reaching maximum extension in a zone between 8 and 15 mm from the inlet after ~117 days (Figure 6-5B). HU histograms showed compaction of the bentonite core after 223 days of $\text{APW}_{\text{ESDRED}}$ infiltration (Figure 6-5C), which was in agreement to the post-mortem analysis.

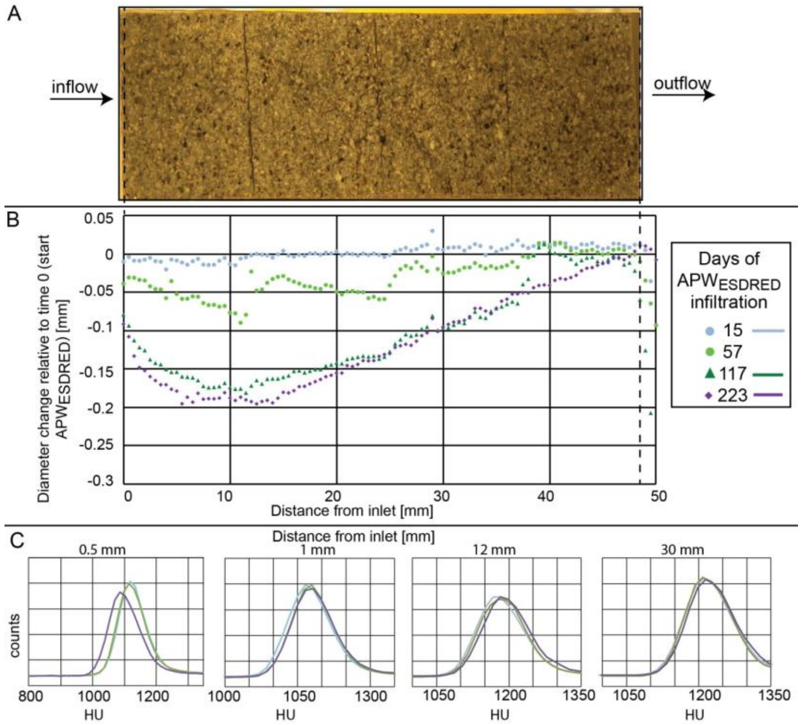

Figure 6-5: CT image analysis: (A) optical image of the bentonite core; (B) diameter evolution of the core relative to day 9 (3.5 MPa); (C) HU histograms at different locations in the core at various times.

Tomographic cross-sections of the bentonite core showed initially, during the equilibration phase (time 0), a homogeneous material of grayish shade with whitish dots of denser minerals like pyrite (Figure 6-6). The color code of tomographic images is the following: bright shades are low X-ray attenuations or densities and dark shades represent high attenuations/densities. The inlet filter revealed no changes while in the first 0.5 mm of the bentonite a small zone of increased density appeared in the center of the core after 117 days of APW_{ESDRED} infiltration (see circle in Figure 6-6).

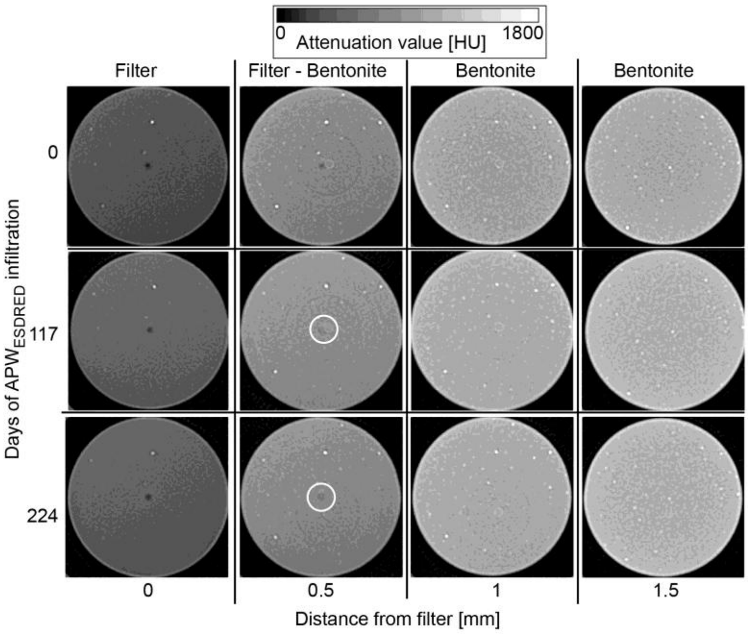

Figure 6-6: CT images of the interface inlet filter – bentonite at day 0, 117 and 224 of APW_{ESDRED} infiltration. The circles highlight the small reaction zone.

6.3.4. Post-mortem analysis: physical parameters

The weight of the inlet and outlet filters increased during the experiment by 24 mg and 1 mg, respectively. The dismantled bentonite core weighed in wet condition 186.13 g, which is a gain of ~1.47 g. The sample length was 50.8 mm, grown by 0.6 mm. The saturated density showed in both profiles a higher density in the middle part of the core (Figure 6-7). The water content was in both profiles reduced in the middle of the core, with higher water amounts in the core center (Figure 6-7). The calculated degree of saturation was 99.7–100% for the inner and 96.7–97.8% for the outer profile. The calculated porosities were between 44–46% for both profiles using a grain density of 2.75 g/cm^3. The dry bentonite density varied between 1.07 g/cm^3 and 1.14 g/cm^3.

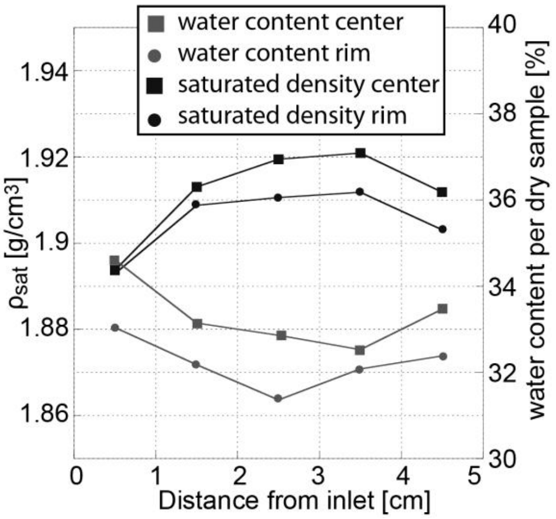

Figure 6-7: Saturated density and water content profiles of the bentonite sample at the end of the experiment.

6.3.5. XRD analysis

The mineralogy of raw MX-80 bentonite consisted of smectite (montmorillonite), quartz, cristobalite, alkali and plagioclase feldspar, calcite and gypsum (Figure 6-9).

Inlet and outlet filters were scanned separately. All spectra showed a broad hump at 4.01 Å of the amorphous filter material (PVC) (Figure 6-8). The inlet filter showed peaks of gypsum and calcite and the outlet filter of halite.

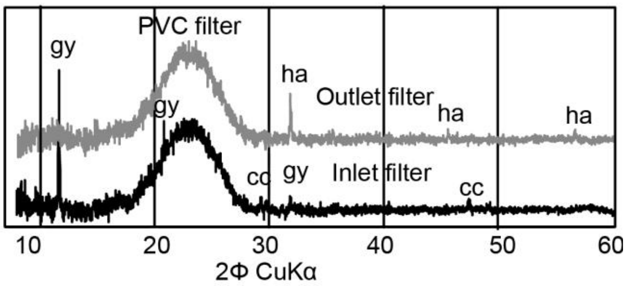

Figure 6-8: XRD spectra of the inlet and outlet filters. Cc: calcite; gy: gypsum; ha: halite.

11 preconditioned powder samples were measured by XRD along a central transection of the core (Figure 6-9). The (001) reflection of smectite was at 12.2 Å at the interface and at 12.3 Å in the rest of the core. The (001) peak shape varied in intensity and width as not all powder sample exhibited a complete random oriented sample surface. The (060) peak of smectite was in all samples at 1.49 Å, which is characteristic for a dioctahedral smectite like montmorillonite. The EG saturated samples showed (001), (002) and (003) smectite peaks at 17, 8.5 and 5.7 Å, respectively. The °Δ2Θ((003)-(002)) was 5.25°, indicating no illite interlayers in the smectite (Moore and Reynolds, 1989). The intensity of the smectite (020) peak was used to detect changes in the clay content. No changes were observed or the variations were in the uncertainty of the measurement

(±5%). Quartz showed main peaks at 3.3 and 4.2 Å with strong intensity variations. Cristobalite had a main peak at 4.0 Å, which showed no intensity variations. The feldspar peaks were at 3.18, 3.21 and 3.22 Å; the first two peaks origin from orthoclase (alkali feldspar) and the latter from anorthite (plagioclase). Variations in intensities were explained by the coarse grain size of feldspar, which gives strong intensity variation for the (010) and (001) peaks (Olsson and Karnland, 2011). All samples had a reflection at 9.9 Å, indicating the occurrence of mica or muscovite however illite could not be excluded. Calcite showed a main reflection at 3.0 Å with strong, random variations. Few samples showed a gypsum peak at 7.6 Å.

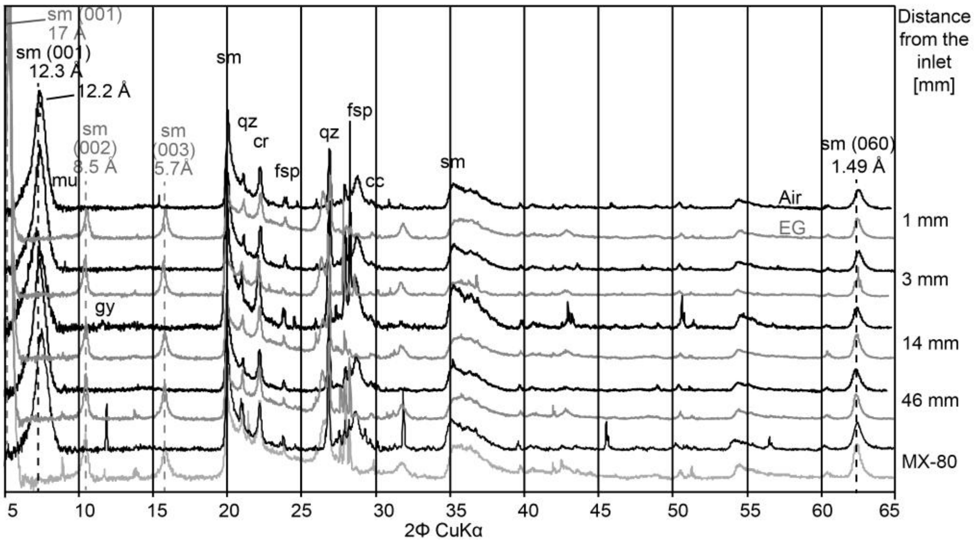

Figure 6-9: XRD spectra of the bentonite core at different distances from the inlet. Sm: smectite; qz: quartz; cr: cristobalite; fsp: feldspar; cc: calcite; mu: muscovite; gy: gypsum; EG: ethylene glycol.

6.3.6. Microscopy and SEM/EDX analysis

Filters. Two filter pairs were used on each side of the core in order to achieve a better fluid distribution/collection (Figure 6-10). The inlet tube was too long and pierced the outer inlet filter and imprinted the inner one at the beginning of the experiment. The effect of this geometry on the fluid distribution was not clear but measured hydraulic conductivities indicated only minor disturbance (Figure 6-2). BSE images of the inner inlet filter revealed few mineral precipitates in the imprinted region along with an open porosity in the rest of the filter (Figures 6-10A & B). EDX analyses of the precipitates showed a chemistry dominated by CaO (>63 wt%), Cl_2O and SiO_2, which indicated the presence of a Ca-phase, identified as calcite by XRD analysis. The chlorine and silica originated both from the PVC filter material and thereby identified as not to be a pure PVC material. Both outflow filters had an imprint of the outflow tube in its center while the rest of the filter showed an open porosity with few halite crystals on the core facing surface (Figure 6-10C and D).

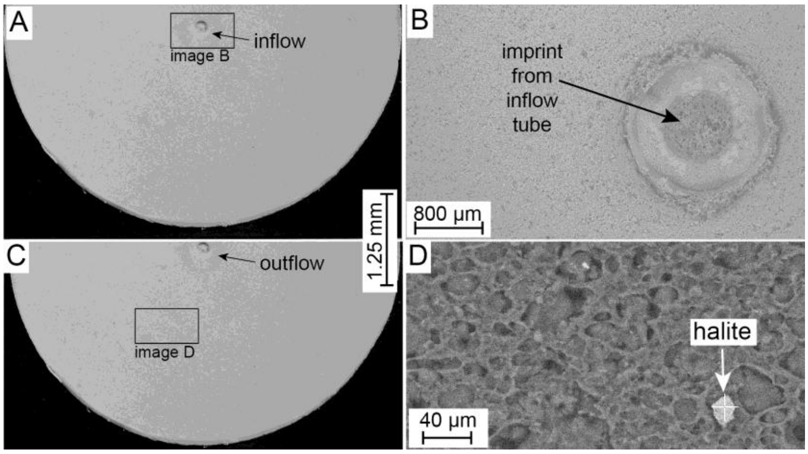

Figure 6-10: Optical and BSE micrographs of the inlet filter (A & B) and outlet filter (C & D).

Bentonite core. The bentonite inflow surface exhibited a whitish precipitate of <1 mm size in the center of the core after dismantling (Figure 6-11B).

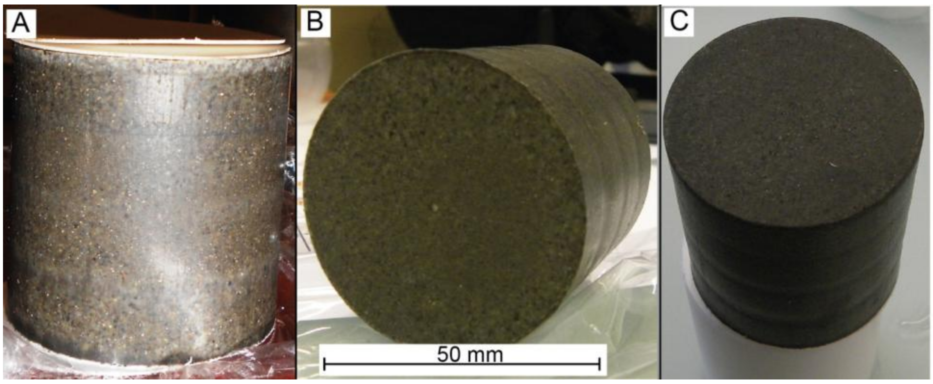

Figure 6-11: Bentonite sample before (A) and after the experiment (B & C): (B) inflow surface of the bentonite with the whitish precipitate in the center; (C) outflow surface of core.

BSE micrographs of the longitudinal transect sample revealed in the center of the inflow surface a resin filled notch of 1.52 mm diameter and 0.14 mm depth from the capillary imprinting in the filters (Figure 6-13). Mineral reactions were restricted to the adjacent inflow zone, penetrating 0.27 mm into the bentonite core. The newly formed mineral phase exhibited a higher density (atomic number) compared to the clay matrix (Figure 6-13). Precipitation occurred in channel like structures, most likely preferential flow path (Figure 6-12).

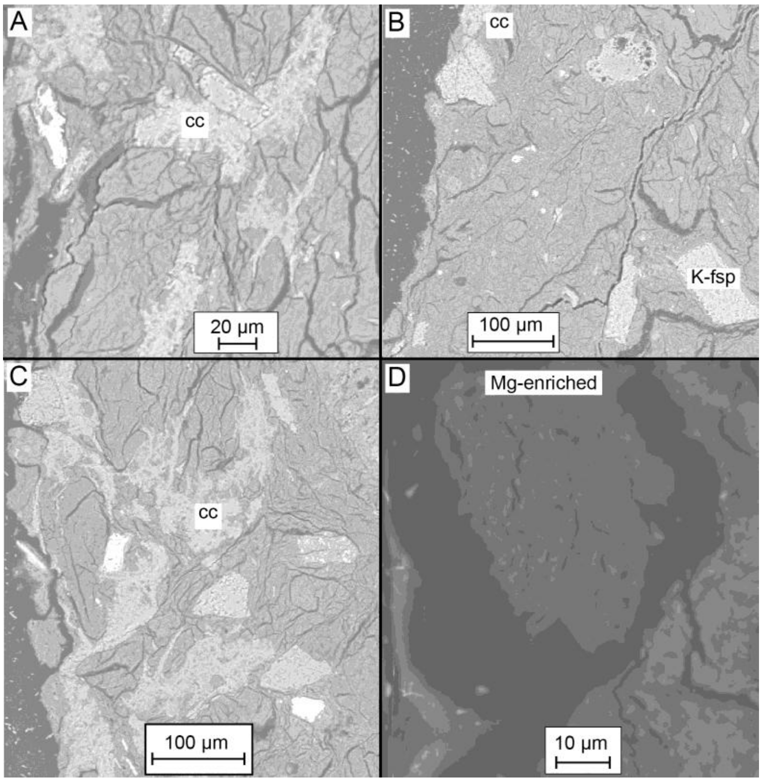

Figure 6-12: BSE images of the inflow zone: (A – C) new mineral phase in the clay matrix (calcite); (D) altered clay directly at the interface. Cc: calcite; K-fsp: alkali feldspar.

The average oxide composition of pristine clay is shown in Table 6-4. In the inflow region, zones enriched in Ca and Mg were detected (Figure 6-13). The Ca-enrichment occurred by the previously described newly precipitated mineral phase, which showed in EDX measurements composition of up to 65 wt% CaO (Table 6-4). These minerals were identified by XRD and Raman spectroscopy as calcite. Small enrichment in phosphorous and sulfate was observed around the newly formed calcite (Figure 6-14). The Ca-enriched zone covered an area of 1.52×0.14 mm size, respectively an area of 0.2 mm^2. Carbonate was not measured as the resin was carbon-based.

Table 6-4: SEM-EDX measurements of the bentonite and the Ca and Mg-enriched zones.

	Bentonite (pristine)	Clay Matrix (pristine)	Ca zone	Mg zone
Type of measurement	bulk	point	point	point
		[wt%]		
SiO_2	69.5±0.7	72±4	24±8	69±2
Al_2O_3	20.3±0.5	22±3	8±2	22±2
Fe_2O_3	3.9±0.2	1.5±1.8	0.2±0.5	0.6±1.5
MgO	2.2±0.1	2.6±0.4	2±1	5±2
CaO	1.8±0.3	0.1±0.5	65±12	1±1
Na_2O	1.6±0.1	2±0.5	1±1	1.8±0.2
K_2O	0.6±0.1	-	0.2±0.4	-
Al_2O_3/SiO_2	0.29	0.31	0.33	0.32
MgO/SiO_2	0.03	0.04	0.08	0.08

The Mg-enrichment happened directly at the interface inlet filter–bentonite, in a zone of 0.8×0.1 mm size (0.08 mm^2). The enrichment was restricted to the clay matrix and showed a clay characteristic chemical composition with MgO-enrichment by ±3 wt%, while the Al_2O_3:SiO_2 ratio was identical to pristine clay (Table 6-4). As aluminum and silica are the main building blocks of montmorillonite, a change in this ratio would imply to have a different Si-mineral phase present. The MgO:SiO_2 ratio of 0.08 indicated magnesium enrichment relative to pristine clay (Table 6-4 and Figure 6-16).

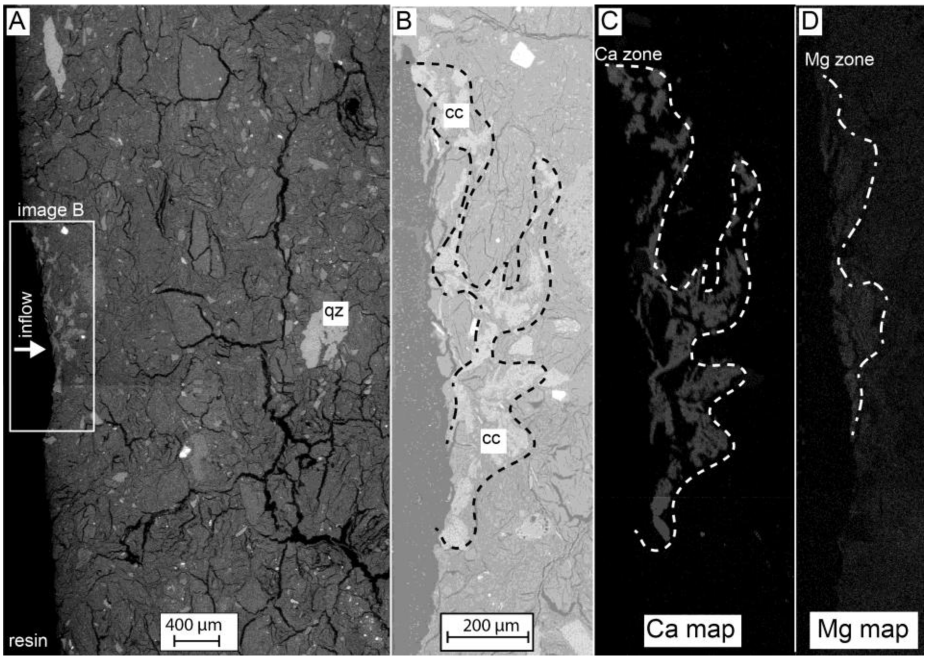

Figure 6-13: BSE images and element maps of the reaction zones in the bentonite: (A) overview of the inlet region; (B) detailed image of the reaction zone including the zone boundaries; (C) Ca map; (D) Mg map. Cc: calcite; qz: quartz.

The sodium containing minerals were mainly plagioclase feldspar, while potassium containing minerals were alkali feldspar, muscovite or illite (Figure 6-14). The iron map revealed fine grained pyrite crystals.

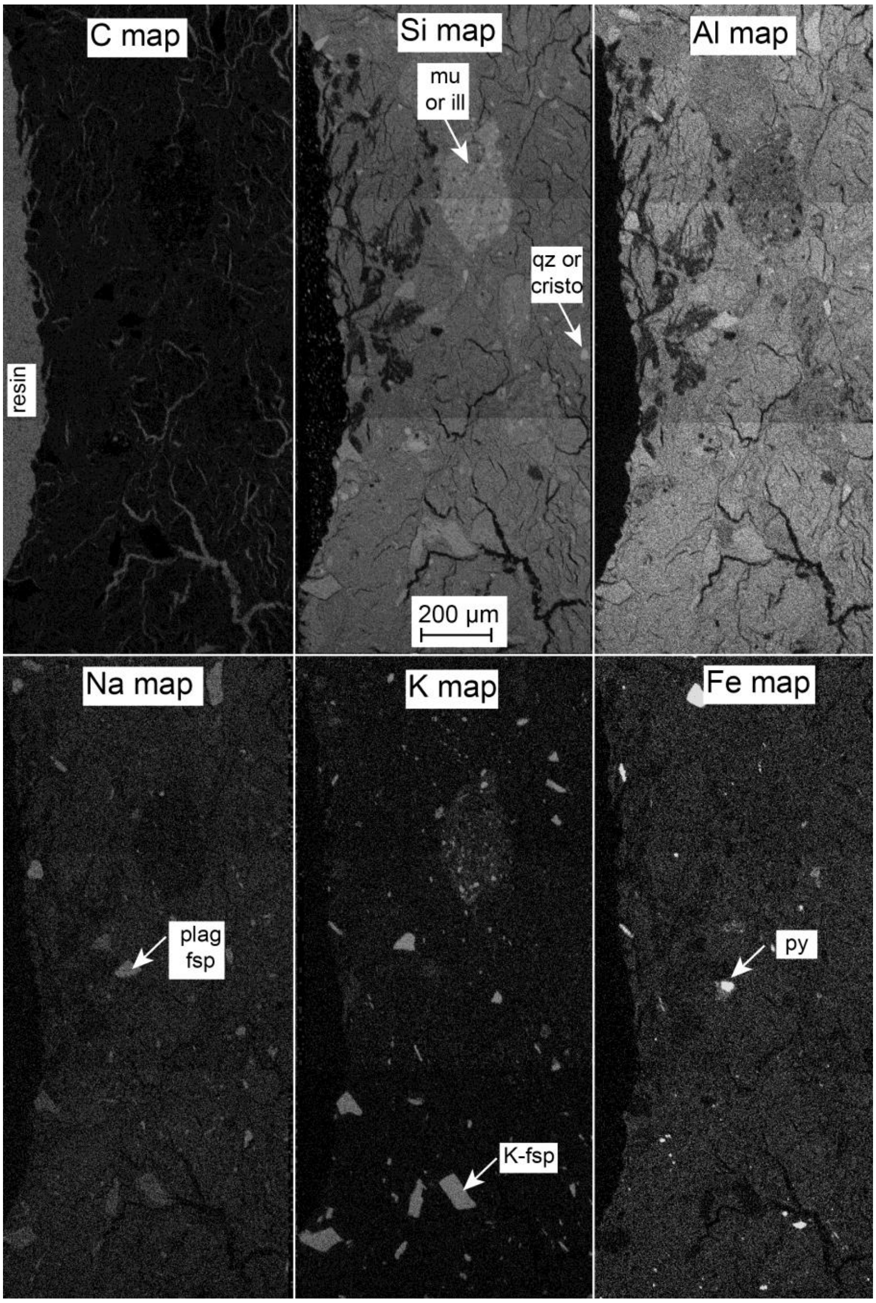

Figure 6-14: Element maps of the inflow and reaction zone. Mu: muscovite; ill: illite; qz: quartz, py: pyrite; plag: plagioclase feldspar, K-fsp: alkali feldspar; cristo: cristobalite.

An element oxide transection of multiple areas of 0.1x0.07 mm size showed SiO_2 depletion with values of 53 wt% in the first 0.07 mm of the bentonite (Figure 6-15). Al_2O_3 and Fe_2O_3 showed both in the same region depletion, while MgO was enriched up to 6.3 wt%, relative to the unreacted bentonite (2.2±0.1 wt%). CaO was enriched near the interface to 18.4 wt%, relative to pristine bentonite (1.8±0.3 wt%).

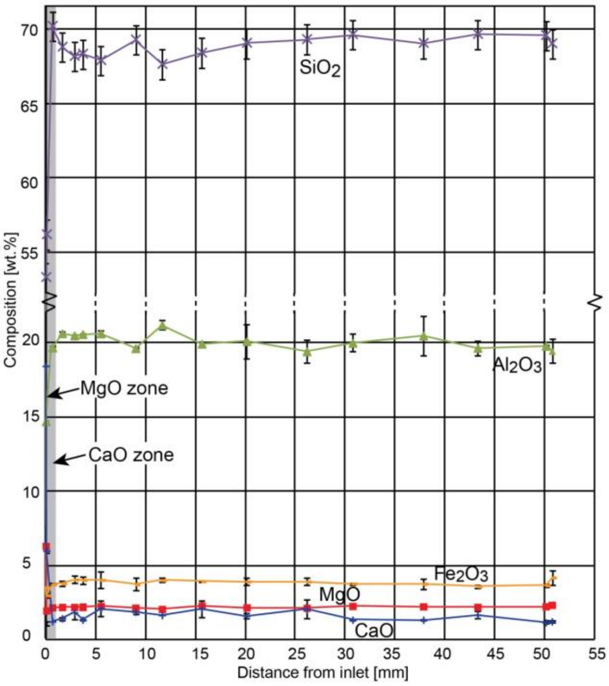

Figure 6-15: Main elemental oxides of constant-size areas along a transection from inlet to outlet.

The Al_2O_3:SiO_2 showed minor variations while the MgO:SiO_2 ratio was enriched near the interface (Figure 6-16).

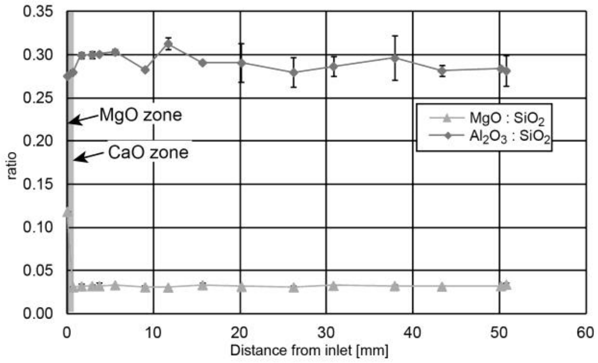

Figure 6-16: Oxide ratio of single point measurements along a profile in the bentonite.

6.3.7. Raman spectroscopy

Raman spectroscopy was used to identify mineral phases on the bentonite transection. Clays tend to be highly fluorescent due to iron(III) and/or associated organic matter (Alia et al., 1999; Blacksberg et al., 2010) in the laser light, which covers the weaker characteristic Raman spectrum. Raman shift patterns of the newly precipitated Ca-phase showed bands at 281 and 1086 cm^{-1}, characteristic for calcite.

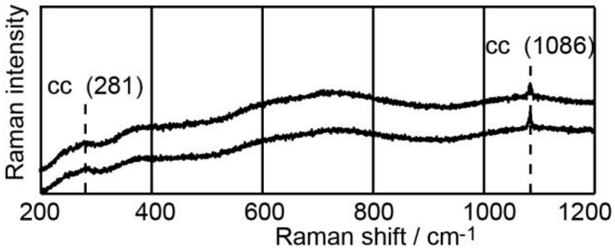

Figure 6-17: Raman shift pattern of the newly formed Ca-phase. Cc: calcite.

6.4. Discussion

The evolution of the core volume and hydraulic conductivity as well as ion concentrations and pH in the outflow is complex and reflects coupling between physical and chemical processes. The main controlling processes are: ionic strength effects and coupled transient compaction/de-compaction (shrinkage or expansion of the core due to changes in montmorillonite interlayer distance/water content), internal pore-water control by minor soluble accessory phases (sulfate and/or carbonate minerals), cation exchange processes, and also silicate mineral dissolution/precipitation of reactive “cement phases” after injection of the APW_{ESDRED}.

6.4.1. The equilibration phase

Evolution of physical parameters. The bentonite core volume decreased initially, after applying a confining fluid pressure. This indicated a further compaction of the bentonite core relative to the pre-confined sample, explained by the change from uniaxial to hydrostatic pressure conditions. The confining pressure reduction induced a core volume expansion (water uptake), which corresponds in a core infiltration device (constant total pressure approach) to a lower swelling pressure (Figure 6-4). Along with a volume expansion, the density of the core got reduced.

With the initial core volume reduction, pore-water was released from the porosity, leading to an apparent initially increased hydraulic conductivity, which was calculated based on the net outflow volume only. The measured values were similar to the previous bentonite experiment (*chapter 5*) and in agreement with Karnland et al. (2006), who measured for a similar density and ionic strength values between 3.0×10^{-13} m/s and 6×10^{-14} m/s. The confining pressure reduction reduced the hydraulic conductivity. The lower confining respectively swelling pressure enabled the clay minerals to expand (swell), taking up more pore-water in the interlayer porosity and the diffuse layer (DL). This process induced transient water storage in the core while the outflow was reduced. Considering the measured volume difference of 0.6 cm^3, the time required to refill this volume would be ~16 days, based on an average measured rate of discharge (Q) of 0.037 ml/day. Using only the ΔQ between the transient and the equilibration phase of 0.017 ml/day, the expansion of the core would take ~40 days, which is slightly faster compared to the measured ~60 days. Initially, the flow showed strong variations during the transient flow phase, induced by perturbations from the decoupling for CT measurements. The measured hydraulic conductivities at the end of the equilibration phase represent steady conditions rather than a transient state. Karnland et al. (2006) observed in constant-volume cells using MX-80 bentonite, higher hydraulic conductivities at lower densities. The observed behavior indicates that the hydraulic conductivity of a bentonite core is not only a function of the current confining pressure and swelling pressure but rather influenced by the previous compaction history. Strong compaction changes the core properties irreversibly.

The Péclet number was 8.8 at a confining pressure of 4.2 MPa and 4.9 at a pressure of 3.5 MPa, which corresponds in both cases to an advective dominated flow regime. The bentonite core length of 5.1 cm was used as characteristic length, an anion accessible porosity of 13%, based on chloride through-diffusion and chloride break-through curve data, and an effective diffusion coefficient for chloride of 1.6×10^{-11} m^2/s (Van Loon et al., 2007). CT data showed no mineral reactions during the equilibration phase.

Chemical evolution of the outflow. The initially expelled pore-fluid showed a high ionic strength ($I\approx0.47$ mol/kg), which was doubled compared to $APW_{Äspö}$ or APW_{OPA} (Table 6-5). The first syringe represented a period of 34 days, which means that the salinity of the initial outflow could have been even higher. This can be explained either by the saturation and compaction procedure of the bentonite during sample production or by an initial compaction of the core. The first option assumes that the saturation of the bentonite led to a strong ion enrichment in the porosity due to dissolution of soluble salts and sulfate minerals. The second possibility assumes that the hydrostatic pressure conditions of the core infiltration device further compacted the bentonite core sample, and therefore initially more saline pore-water was expelled from the intergranular pore-space, where anions are enriched due to anion exclusion effects. The same effect was observed in the previous experiment using a comparable bentonite sample (*chapter 5* and Alt-Epping et al. (2014)). The ion concentrations during the equilibration phase are in agreement with squeezing experiments performed by Muurinen and Lehikoinen (1999). At similar densities and lower w/s, their data showed the same ion enrichment relative to the inflow/external water, controlled mainly by dissolution of sulfates and carbonates and ion exchange processes. The calculated ionic strengths range from 0.39–0.47 mol/kg (Table 6-5) and are slightly higher compared to the pore-water measurements performed on MX-80 bentonite by Muurinen et al.

(2004) at similar density and variable chloride concentrations. This may indicates that our pore-water was not yet in equilibrium with the bentonite. SI showed saturation of the outflow with respect to gypsum, while calcite and silicate-phases were clearly over-saturated (Table 6-5). Gypsum saturation indicated that the pore-fluid was in equilibrium with gypsum. The outflow was slightly over-saturated with respect to calcite, which was initially possibly only an artefact of a too high pH (see discussion in *chapter 7*). During the transient flow phase, increased ion concentrations were measured in the outflow, which must be related to the lower flow rate and possibly to variations in the internal porosity proportions, ejecting excess ions.

6.4.2. The APW_{ESDRED} infiltration phase

Evolution of the fluid composition. APW_{ESDRED} infiltration induced a slight increase in ionic strength in the outflow, which was in agreement with the EC measurements (Table 6-5 and Figure 6-2). Chloride was the main anionic charge carrier for the entire time. The mass-balance showed a difference of 3.5 mmol between cumulative inflow and outflow, indicating that chloride was still present in the bentonite core at the end of the experiment (Table 6-6), in agreement with the small fraction of pore volume infiltrated during the APW_{ESDRED} phase. From aqueous leaching data of raw MX-80 bentonite, an initial chloride pool of 0.38 mmol could be calculated, based on the initial pore-water volume (Fernández et al., 2008). Including the initial chloride in the calculation, shifts the difference to 3.88 mmol, indicating that the current core is far from equilibrium conditions. Formate, the main anionic charge carrier of the shotcrete fluid (~66.1 mM), did not reach the outflow before the experiment was stopped. No conclusion can be made on the behavior of formate in the core, as no accumulation or biological activity was observed. Carbon is difficult to determine because it cannot be distinguished in the EDX map from the resin. Propionate was measured during the equilibration and the high-pH phase and showed a strong decreasing trend. This indicates that it is not connected to the formate but rather present in or derived from the pristine bentonite material. Hydroxide, the second most common anion in the APW_{ESDRED} (~6 mM), reached the outflow sparsely. Even after 272 days of APW_{ESDRED} injection, the hydroxide concentration never exceeded 0.001 mM, indicating complete consumption by the core. Directly related to the hydroxide concentration is the pH, which increased to pH 8. Hydroxide is assumed to be consumed by mineral dissolution and precipitation as brucite and saponite as a possible candidate. See discussion later in this section.

The increase in ionic strength during the high-pH phase was mainly the result of a sulfate increase despite the lower concentration in APW_{ESDRED} compared to APW_{OPA}. Dissolution of gypsum was the most likely mechanism, and this process may proceed at gypsum saturation and will bring more sulfate into the solution as long as there is a sink for calcium by mineral precipitation (e.g. calcite). The extra cations to balance this increase were generated by mineral dissolution (hydroxide consumption), and this overall process was therefore most likely limited to the reaction zone near the inlet. The mass-balance showed excess of sulfate in the outflow, indicating ongoing gypsum dissolution (Table 6-6). The mass-balance showed a loss of sodium from the core, released from the clay exchanger (Table 6-6). Calcium was retained in the core by ion exchange and possibly by calcite precipitation. The silica concentration showed a small enrichment in the outflow, while the aluminum concentration was unaffected by the high-pH infiltration.

Table 6-5: Calculated saturation indices (SI) of the outflow solution. Cc: calcite; gy: gypsum; K-fsp: alkali feldspar; mont: montmorillonite; cristo: cristobalite; $pCO_{2(g)}$: partial pressure of CO_2.

Time (time APW_{ESDRED}) / APW [days]	**PV**	**Ionic strength** [mol/kg]	**Charge balance error**	**SI**						
				cc	gy	mont	qz	cristo	SiO_2 amorph	$pCO_{2\,(g)}$
$APW_{Äspö}$		0.26		-0.3	-0.83					-3.24
APW_{OPA}		0.23		-0.1	-0.34					-3.21
APW_{ESDRED}		0.11		1.67	-0.8	-16	-3.2	-4	-4.4	-10
17 (0)	0.05	0.47	0.85	0.74	-0.04	6.59	1.26	0.47	0.02	-2.56
75 (0)	0.13	0.43	3.32	0.94	-0.05	6.76	1.26	0.46	0.01	-2.66
168 (0)	0.20	0.46	0.38	0.97	-0.07	7.96	1.35	0.56	0.11	-2.55
273 (0)	0.30	0.39	1.92	1.06	-0.08	8.11	1.42	0.63	0.18	-2.65
318 (34)	0.29	0.40	2.81	1.1	-0.05	8.12	1.42	0.63	0.18	-2.62
353 (106)	0.31	0.42	1.81	0.88	-0.12	8.76	1.63	0.84	0.39	-2.52
459 (272)	0.32	0.54?	36.41	1.06	-0.16	8.94	1.65	0.85	0.4	-2.66

Table 6-6: Ion mass-balance of in- and outflow. Bicarbonate is based on the alkalinity.

Ions	**Inflow**			**Outflow**	**Δ**
	$APW_{Äspö}$	**APW_{OPA}**	**APW_{ESDRED}**		
			[mmol]		
Na^+	2.56	2.03	0.07	5.80	-1.14
K^+	0.01	0.03	0.04	0.12	-0.04
Ca^{2+}	1.57	0.15	0.08	0.23	1.56
Si^{4+}	-	-	-	0.034	-0.034
Al^{3+}	-	-	5.6E-06	2.8E-05	-2.2E-05
Mg^{2+}	0.05	0.11	0.00	0.13	0.03
Sr^{2+}	0.01	0.00	0.00	0.00	0.01
Cl^-	5.9	1.9	0.0	4.3	3.5
SO_4^{2-}	0.05	0.27	0.01	0.95	-0.62
HCO_3^-	7.0E-03	8.1E-03	1.7E-04	0.08	-0.06
Formate	-	-	0.21	0.00	0.21

Evolution of hydraulic conductivity *and of the core volume.* The APW_{ESDRED} infiltration induced core shrinkage. The diameter decreased in both experiments most pronounced in a zone ~10 mm from the inlet (*chapter 5*). Possible mechanisms for this shrinkage are mineral dissolution (e.g. gypsum) and/or changes in the ionic strength of the pore-fluid, induced by the APW_{ESDRED}. The observed volume reduction in the current experiment is contradictory to the reported swelling behavior of MX-80 bentonite in Karnland et al. (2006) and to the previous experiment described in *chapter 5*. Karnland et al. (2006) showed that low ionic strength fluids induce strong swelling in smectite by increasing the interlayer porosity. At constant hydrostatic conditions, this is assumed to induce core expansion. The observed core volume reduction would rather indicate a high ionic strength pore-fluid present in this region of the bentonite core.

APW_{ESDRED} infiltration reduced the hydraulic conductivity over a period of 110 days (~0.04 PV_{ESDRED}). The measured hydraulic conductivity was ~50× smaller compared to the values of Fernández et al. (2006) measured in a transport-cell using a dry density of 1400 kg/m^3 and a $Ca(OH)_2$ based fluid (pH ~9.1). The increase of the infiltration pressure after 156 days of APW_{ESDRED} infiltration had no effect on the fluid flow. The final Péclet number was ~0.2 using an anion velocity of 6.7×10^{-11} m/s and an anion porosity of 0.13 (Van Loon et al., 2007), which can be interpreted as a diffusion dominated flow. Two mechanisms for the reduction are possible: (1) mineral precipitation and (2) variations in swelling pressure and resultant volume changes due to an increase in the ionic strength of the pore-water.

The first option (1) relates the drop in hydraulic conductivity to mineral precipitation in the filter as well as in the adjacent bentonite. The first mineral precipitations on the filter–bentonite interface were observed after 117 days of APW_{ESDRED} infiltration by CT scans. Post-mortem analysis of the experiment identified these newly formed minerals as calcite and possibly Mg-smectite. The second option (2) is based on the idea that high ionic strength fluids reduce the interlayer porosity and the DL, leading to core compaction and hence decreasing the intergranular porosity used for advective fluid flow in a pressure-constraint setup, as observed in *chapter 5*. In case of APW_{ESDRED} infiltration, the ionic strength of the high-pH fluid was much lower compared to the saturation and equilibration fluids (Table 6-1), which would rather induce core expansion along with higher hydraulic conductivities in a constant-pressure approach. This discrepancy between assumed and observed behavior in bentonite shows that the evolution of APW_{ESDRED} in the core is not entirely understood. The evolution of APW_{ESDRED} in the bentonite can possibly range from locally increased ionic strength due to gypsum dissolution to lower ionic strength due to consumption of formate or hydroxide anions. Aqueous speciation modeling using PhreeqC was performed to identify possible processes. Directly at the interface we expect the original high-pH of the APW_{ESDRED} at or near gypsum saturation which would lead to a hypothetical pore-fluid with an ionic strength of ~0.10 mol/kg, over-saturated with respect to calcite and ettringite. This is almost identical to the initial APW_{ESDRED}. A bit further away from the interface, the pH of the APW_{ESDRED} is assumed to be buffered to pH ~8.0 (Figure 6-3). At gypsum saturation, this would lead to a hypothetical fluid of ~0.11 mol/kg ionic strength, which is at saturation with respect of calcite but under-saturated with respect to quartz. The calculations indicate that the hypothetical local pore-fluids are always similar in ionic strength to the high-pH fluid, which may not be entirely true and indicates that possibly more processes are involved, not considered in these calculations. Interestingly, the observed reduced hydraulic conductivity of low ionic strength fluids in bentonite is in agreement to Karnland et al. (2006), who observed at a similar density in a constant-volume cell the same behavior.

Most likely, mineral precipitation (calcite) in the first millimeter of the core as well as in the inlet filter reduced mainly the hydraulic conductivity, while the influence and existence of a higher ionic strength pore-fluid, originating from evolved APW_{ESDRED} is unclear.

Dissolution of silica and silicate minerals. The silica and aluminum concentrations in the outflow were during the equilibration phase increased, compared to $APW_{Äspö}$ and APW_{OPA}, indicating dissolution of Si-Al-mineral phases. This is in agreement with increased SI of silicate-phases (Table 6-5). The silica concentration in the outflow got almost doubled after 104 days of APW_{ESDRED} infiltration, showing higher concentrations compared to the infiltration solution (Figure 6-3). Equilibrium modeling showed that the silica concentration in the outflow was in equilibrium with the SI of amorphous SiO_2 during the equilibration phase and over-saturated during the high-pH phase (Table 6-5). The fact that only silica got enriched in the outflow, while aluminum showed even lower concentrations compared to the infiltration solution, indicates that a pure SiO_2-phase like quartz, cristobalite or tridymite was dissolved. All these mineral phases were distinctly over-saturated in the end of the experiment (Table 6-5). XRD data showed no intensity decrease for a pure-SiO_2 phase and the variations were within the error of the measurements.

Reaction zones. Two distinct reaction zones could be distinguished in the bentonite by SEM-EDX measurements. One was characterized by Mg-enrichment in the clay matrix and the other by Ca-enrichment in form of newly formed calcite (Figure 6-13).

The Ca-enrichment zone propagated 0.27 mm into the bentonite core and was characterized by extensive calcite precipitation, verified by XRD and Raman spectroscopy measurements. EDX elemental analysis indicated strong Ca-enrichment in this newly formed phase but due to the small grain size other possible phases like C–(A)–S–H could not be excluded. A triangular SiO_2–Al_2O_3+Fe_2O_3–CaO plot is shown in Figure 6-18 with measurements of the newly grown calcium-rich phase. The data plot along a line, ending in the CaO/pure calcite edge. It can be concluded that the measurements were most likely pure calcite or clay intermixed with calcite but the existence of C–(A)–S–H cannot be excluded. Neither XRD nor Raman spectroscopy measurements supported a hypothesis of having only calcite present. In total 7.6×10^{-4} mmol of calcite (Ca^{2+}, HCO_3^-) were precipitated in the reaction zone, assuming that the reaction zone contained 33 vol% calcite. The Ca^{2+} mass-balance showed a net gain in the core (Table 6-6). The calcium source for the calcite formation was the dissolution of gypsum, a displacement from the clay exchanger by sodium and potassium, and the inflowing APW_{ESDRED}. The bicarbonate mass-balance showed a net loss of 0.06 mmol from the core, indicating dissolution of carbonates (Table 6-6). The amount of infiltrated bicarbonate was 0.015 mmol, with 1.7×10^{-4}

mmol originating from APW_{ESDRED}. This could have induced precipitation of 0.55 mm^3 of calcite, while the fraction originating from APW_{ESDRED} contributed only 0.006 mm^3. Due to the small amount of newly formed calcite, no calcium or bicarbonate source can be excluded or favored. PhreeqC equilibrium calculation showed that an increase in pH of a bentonite, saturated with clay pore-water, leads to calcite over-saturation and hence calcite precipitation. Precipitation of carbonate-mineral phases like calcite in 'low-pH' shotcrete (ESDRED) was observed by Jenni et al. (2014) in an in-situ experiment at Mont Terri underground laboratory. They reported intense calcite precipitation in the ESDRED shotcrete, but not in the adjacent Opalinus Clay. No C–S–H precipitation was observed in our experiment in contrast to previous studies using $Ca(OH)_2$-based infiltration fluids at pH 11–12 (Fernández et al., 2006; Fernández et al., 2010a).

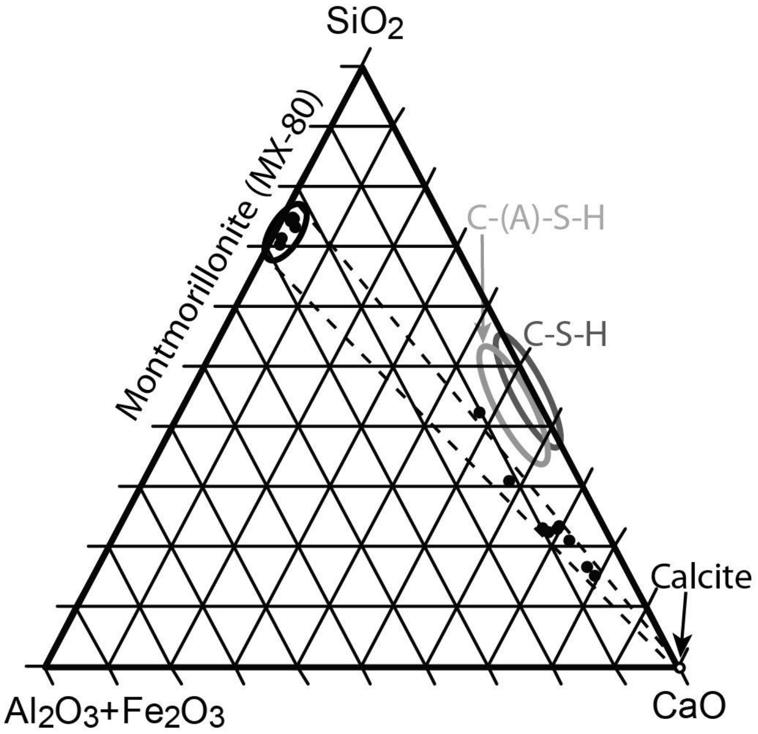

Figure 6-18: Triangular SiO_2–Al_2O_3+Fe_2O_3–CaO plot including SEM-EDX point analysis of the newly formed Ca-phase as well as of Ca-enriched regions. Filled circles correspond to EDX measurements and open circle as well as ellipses to mineral composition from literature. MX-80 montmorillonite (Karnland, 2010), C–S–H (Lothenbach et al., 2008) and C–(A)–S–H (Lothenbach et al., 2008; Lothenbach and Winnefeld, 2006).

The Mg-enrichment happened in the first µm of the bentonite core at the fluid inlet. The enrichment was observed in the clay matrix at sub-micron scale by EDX analysis. The Mg-enriched zone contained ~0.06 µmol Mg^{2+}, which is 2.4× more compared to amount in same volume of pristine smectite. The mass-balance of magnesium showed a net gain in the core, possibly displaced to the clay exchanger (Table 6-6). Mg-enrichment could only take place if an additional magnesium source was available. The possibilities are either that the additional magnesium originated from the APWs (1) or from dissolution of smectite (2). (1) APW_{OPA} as well as $APW_{Äspö}$ could provide enough magnesium to enrich the Mg-enriched zone. (2) Dissolution of 3×10^{-4} μm^3 of montmorillonite could provide enough magnesium to get the measured Mg-enrichment. The dissolution of this small amount would be too small to be observed by XRD. In a triangular SiO_2–Al_2O_3+Fe_2O_3–MgO plot, single point measurements plot adjacent to the pure montmorillonite field, slightly shifted in direction of the MgO edge (Figure 6-19). This can be interpreted as montmorillonite intermixed with saponite or brucite, while M–S–H or talc cannot be excluded. Several others observed in experiments similar Mg-enrichments using alkaline, Ca-based fluids (11–12): Fernández et al. (2006) observed Mg-enrichment at temperatures between 25 and 125°C. They interpreted the Mg-enrichments as brucite (low temperature) or saponite-type clay (high temperature); Jenni et al. (2014) observed at the interface ESDRED shotcrete–OPA the migration of magnesium from OPA into the shotcrete, forming Mg-hydroxide minerals.

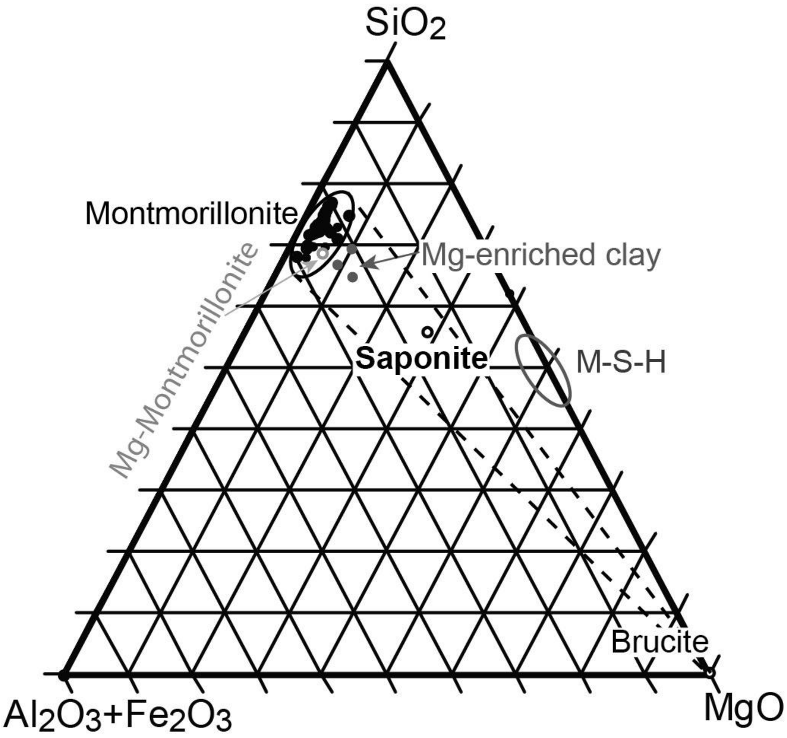

Figure 6-19: Triangular SiO_2–Al_2O_3+Fe_2O_3–MgO plot including SEM-EDX point analysis of the Mg-enriched clay. Filled circles correspond to EDX measurements and open circle as well as ellipses to mineral composition from literature. MX-80 montmorillonite (Karnland, 2010), Mg-saturated montmorillonite (Karnland et al., 2006), illite (Gaines et al., 1997), beidellite (Gaines et al., 1997), saponite (Duda, 1990), hydrotalcite (Anthony et al., 1995), and magnesium silicate hydrate gel (M–S–H) (Brew and Glasser, 2005).

6.5. Conclusion

The change to the 'low-pH' (pH 11.6) shotcrete pore-fluid (ESDRED) induced a hydraulic conductivity reduction in the bentonite. The former advective-dominated flow changed gradually into a diffusion-dominated flow pattern with Péclet numbers ≤1. The reduction resulted mainly from mineral precipitation (e.g. calcite) in the bentonite core (intergranular porosity) and possibly in the filter. The existence and effect of high ionic strength pore-fluids on the fluid flow, evolved from the low ionic strength APW_{ESDRED}, is not clear. The high-pH infiltration led to core shrinkage, detected by CT measurements, induced by gypsum dissolution and/or possibly by a high ionic strength pore-fluid. Volume reduction and ionic strength of the outflow rather indicate a high ionic strength pore-fluid in the bentonite, which is in contradiction to the infiltrated APW_{ESDRED}.

The outflow showed initially a decrease or constant behavior in all ion concentrations with the exception of sulfate, bicarbonate (alkalinity) and aluminum. Switching to the high-pH fluid induced a further decrease in all ion concentrations, with the exception of silica, sulfate, and potassium, which increased, while the pH got slightly increased from ~7.7 to ~8.

The inlet filter showed precipitation of gypsum and minor amounts of calcite. Bentonite exhibited distinct zones of Ca and Mg-enrichment near the solution inlet. The Ca-enriched zone consisted of newly formed calcite, precipitated in preferential flow path structures in the clay matrix. Calcite precipitation was induced by the high-pH plume, saturating the pore-fluid with respect to calcite. A small zone of weak Mg-enrichment was detected directly at the inlet surface, in the center of the core. MgO amounts of up to 7 wt% were detected in this zone, while the alumina to silica ratio was not affected and may indicate precipitation of saponite or brucite. Elevated silica concentrations were detected in the outflow, indicating dissolution of a silicate mineral.

The experiment attests an effective buffering capacity for bentonite and a progressing coupled hydraulic-chemical-mineralogical sealing process.

Acknowledgments

Financial support from Nagra is gratefully acknowledged. The Department of Forensic Medicine at the University of Bern is acknowledged for granting access and providing technical support for operating their CT scanner. The machine shop at our institute was instrumental in constructing the experimental apparatus, and our analytical laboratory performed the IC and ICP-OES analyses. We thank Barbara Lothenbach (EMPA) for providing the modeled fluid composition for ESDRED shotcrete as well as for intense discussions on this shotcrete type.

References

Alia, J.M., Edwards, H.G., Garcia-Navarro, F.J., Parras-Armenteros, J., Sanchez-Jimenez, C.J., 1999. Application of FT-Raman spectroscopy to quality control in brick clays firing process. Talanta 50, 291-298.

Alt-Epping, P., Tournassat, C., Rasouli, P., Steefel, C.I., Mayer, K.U., Jenni, A., Mäder, U., Sengor, S.S., Fernández, R., 2014. Benchmark reactive transport simulations of a column experiment in compacted bentonite with multispecies diffusion and explicit treatment of electrostatic effects. Comput Geosci, 1-16.

Anthony, J.W., Bideaux, R.A., Bladh, K.W., Nichols, M.C., 1995. Handbook of mineralogy. Mineral Data Publishing.

Babushkin, V.I., Matveyev, G.M., Mchedlov-Petrossyan, O.P., 1985. Thermodynamics of Silicates. Springer-Verlag, Berlin.

Bäckblom, G., 2007. ESDRED: Deliverable D4 of Module 5, WP2. Supporting documents of second training workshop, final technical report. Proc. of the Third Low pH Workshop, Paris June 13–14, 2007. European Commission, Brussels, Belgium.

Bauer, A., Velde, B., 1999. Smectite transformation in high molar KOH solutions. Clay Minerals 34, 259-273.

Berner, U., Kulik, D.A., Kosakowski, G., 2013. Geochemical impact of a low-pH cement liner on the near field of a repository for spent fuel and high-level radioactive waste. Physics and Chemistry of the Earth, Parts A/B/C 64, 46-56.

Blacksberg, J., Rossman, G.R., Gleckler, A., 2010. Time-resolved Raman spectroscopy for in situ planetary mineralogy. Applied Optics 49, 4951-4962.

Brew, D.R.M., Glasser, F.P., 2005. Synthesis and characterisation of magnesium silicate hydrate gels. Cement and Concrete Research 35, 85-98.

Cuevas, J., Villar, M.V., Martín, M., Cobeña, J.C., Leguey, S., 2002. Thermo-hydraulic gradients on bentonite: distribution of soluble salts, microstructure and modification of the hydraulic and mechanical behaviour. Applied Clay Science 22, 25-38.

Cuevas, J., Vigil de la Villa, R., Ramírez, S., Sánchez, L., Fernández, R., Leguey, S., 2006. The alkaline reaction of FEBEX bentonite: a contribution to the study of the performance of bentonite/concrete engineered barrier systems. Journal of Iberian Geology 32 (2), 151-174.

Dauzeres, A., Le Bescop, P., Sardini, P., Cau Dit Coumes, C., 2010. Physico-chemical investigation of clayey/cement-based materials interaction in the context of geological waste disposal: Experimental approach and results. Cement and Concrete Research 40, 1327-1340.

De La Villa, R.V., Cuevas, J., Ramirez, S., Leguey, S., 2001. Zeolite formation during the alkaline reaction of bentonite. European Journal of Mineralogy 13, 635-644.

Dolder, F., Mäder, U., Jenni, A., Schwendener, N., 2014. Experimental characterization of cement–bentonite interaction using core infiltration techniques and 4D computed tomography. Physics and Chemistry of the Earth, Parts A/B/C 70–71, 104-113.

Duda, R., and Rejl, L., 1990. Minerals of the world. Arch Cape Press, New York.

Eberl, D.D., Velde, B., McCormick, T., 1993. Synthesis of illite-smectite from smectite at earth surface temperatures and high pH. Clay Minerals 28, 49-60.

Fernández, R., Cuevas, J., Sanchez, L., de la Villa, R.V., Leguey, S., 2006. Reactivity of the cement-bentonite interface with alkaline solutions using transport cells. Applied Geochemistry 21, 977-992.

Fernández, R., Mäder, U., Koroleva, M., 2008. Appendix 8: Geochemical analysis of samples of MX-80 compacted bentonite from Block 13 / Parcel A2 of the LOT Experiment, Äspö Hardrock Laboratory, Sweden., Long term test of buffer material at the Äspö Hard Rock Laboratory, LOT project. Final report on the A2 test parcel. SKB Technical Report 09-29, Stockholm, Sweden.

Fernández, R., Mäder, U., Rodríguez, M., de la Villa, R.V., Cuevas, J., 2009. Alteration of compacted bentonite by diffusion of highly alkaline solutions. European Journal of Mineralogy 21, 725-735.

Fernández, R., Rodríguez, M., de la Villa, R.V., Cuevas, J., 2010. Geochemical constraints on the stability of zeolites and C-S-H in the high pH reaction of bentonite. Geochimica et Cosmochimica Acta 74, 890-906.

Fernández, R., Vigil de la Villa, R., Ruiz, A.I., García, R., Cuevas, J., 2013. Precipitation of chlorite-like structures during OPC porewater diffusion through compacted bentonite at 90°C. Applied Clay Science 83–84, 357-367.

Fernández, R., Ruiz, A.I., Cuevas, J., 2014. The role of smectite composition on the hyperalkaline alteration of bentonite. Applied Clay Science 95, 83-94.

Gaines, R.V., Skinner, H.C.W., Foord, E.E., Rosenzweig, A., 1997. Dana's New Mineralogy, Eighth Edition ed. John Wiley & Sons, New York.

García Calvo, J.L., Hidalgo, A., Alonso, C., Fernández Luco, L., 2010. Development of low-pH cementitious materials for HLRW repositories: Resistance against ground waters aggression. Cement and Concrete Research 40, 1290-1297.

Gaucher, E.C., Blanc, P., 2006. Cement/clay interactions - A review: Experiments, natural analogues, and modeling. Waste Management 26, 776-788.

Hummel, W., Berner, U., Curti, E., Pearson, F.J., Thoenen, T., 2002. Nagra/PSI Chemical Thermodynamic Data Base 01/01. Universal Publishers/uPUBLISH.com, USA, also published as Nagra Technical Report NTB 02-16, Wettingen, Switzerland.

Jacques, D., 2009. Benchmarking of the cement model and detrimental chemical reactions including temperature dependent parameters. Project near surface disposal of catergory A waste at Dessel. NIRAS-MP5-03 DATA-LT(NF) Version 1 NIROND-TR 2008-30 E.

Jenni, A., Mäder, U., Lerouge, C., Gaboreau, S., Schwyn, B., 2014. In situ interaction between different concretes and Opalinus Clay. Physics and Chemistry of the Earth, Parts A/B/C 70–71, 71-83.

Karnland, O., Olsson, S., Nielsson, U., 2006. Mineralogy and sealing properties of various bentonites and smectite-rich clay materials. SKB Technical Report 06-30, Stockholm, Sweden.

Karnland, O., Olsson, S., Nilsson, U., Sellin, P., 2007. Experimentally determined swelling pressures and geochemical interactions of compacted Wyoming bentonite with highly alkaline solutions. Physics and Chemistry of the Earth, Parts A/B/C 32, 275-286.

Karnland, O., Olsson, S., Dueck, A., Birgersson, M., Nilsson, U., Hernan-Håkansson, T., Pedersen, K., Nilsson, S., Eriksen, T., Rosborg, B., 2009. Long term test of buffer material at the Äspö Hard Rock Laboratory, LOT project. Final report on the A2 test parcel. SKB Technical Report 09-29, Stockholm, Sweden.

Karnland, O., 2010. Chemical and mineralogical characterization of the bentonite buffer for the acceptance control procedure in a KBS-3 repository. SKB Technical Report 10-60, Stockholm, Sweden.

Lancaster, J.L., Martinez, M.J., 2007. Mango - Multi-image analysis GUI. Research Imaging Institute, UT Health Science Center at San Antonio, TX, USA, URL: http://ric.uthscsa.edu/mango/index.html.

Lothenbach, B., Winnefeld, F., 2006. Thermodynamic modelling of the hydration of Portland cement. Cement and Concrete Research 36, 209-226.

Lothenbach, B., Matschei, T., Möschner, G., Glasser, F.P., 2008. Thermodynamic modelling of the effect of temperature on the hydration and porosity of Portland cement. Cement and Concrete Research 38, 1-18.

Lothenbach, B., Scrivener, K., Hooton, R.D., 2011. Supplementary cementitious materials. Cement and Concrete Research 41, 1244-1256.

Lothenbach, B., Rentsch, D., Wieland, E., 2013. Hydration of a silica fume blended low-alkali shotcrete cement. Physics and Chemistry of the Earth, Parts A/B/C.

Mäder, U., 2009. Reference pore water for the Opalinus Clay and "Brown Dogger" for the provisional safety-analysis in the framework of sectoral plan - interim results (SGT-ZE). Nagra Working Report, Nagra, Wettingen, Switzerland.

Maltese, C., Pistolesi, C., Bravo, A., Cella, F., Cerulli, T., Salvioni, D., 2007. A case history: Effect of moisture on the setting behaviour of a Portland cement reacting with an alkali-free accelerator. Cement and Concrete Research 37, 856-865.

Matschei, T., Lothenbach, B., Glasser, F.P., 2007. Thermodynamic properties of Portland cement hydrates in the system CaO-Al2O3-SiO2-CaSO4-CaCO3-H2O. Cement and Concrete Research 37, 1379-1410.

Moore, D.M., Reynolds, R.C., 1989. X-ray diffraction and the identification and analysis of clay minerals. Oxford University Press, New York.

Möschner, G., Lothenbach, B., Tose, J., Ulrich, A., Figi, R., Kretschmar, R., 2008. Solubility of Fe-ettringite (Ca6[Fe(OH)6]2(SO4)3 26H2O). Geochimica et Cosmochimica Acta 72, 1-18.

Mosser-Ruck, R., Cathelineau, M., 2004. Experimental transformation of Na,Ca-smectite under basic conditions at 150 °C. Applied Clay Science 26, 259-273.

Muurinen, A., Lehikoinen, J., 1999. Porewater chemistry in compacted bentonite. Engineering Geology 54, 207-214.

Muurinen, A., Karnland, O., Lehikoinen, J., 2004. Ion concentration caused by an external solution into the porewater of compacted bentonite. Physics and Chemistry of the Earth, Parts A/B/C 29, 119-127.

Nagra, 2002. Demonstration of disposal feasibility for spent fuel, vitrified high-level waste and long-lived intermediate-level waste (Entsorgungsnachweis). Nagra Technical Report NTB 02-05, Nagra, Wettingen, Switzerland.

Nakayama, S., Sakamoto, Y., Yamaguchi, T., Akai, M., Tanaka, T., Sato, T., Iida, Y., 2004. Dissolution of montmorillonite in compacted bentonite by highly alkaline aqueous solutions and diffusivity of hydroxide ions. Applied Clay Science 27, 53-65.

Olsson, S., Karnland, O., 2011. Mineralogical and chemical characteristics of the bentonite in the A2 test parcel of the LOT field experiments at Äspö HRL, Sweden. Physics and Chemistry of the Earth, Parts A/B/C 36, 1545-1553.

Parkhurst, D.L., Appelo, C.A.J., 1999. User’s guide to PHREEQC (version 2) – a computer program for speciation, batch reaction, one-dimensional transport, and inverse geochemical calculations. US Geological Survey Water-Resources Investigations Report 99-4259.

Parkhurst, D.L., Appelo, C.A.J., 2013. Description of Input and Examples for PHREEQC Version 3--A Computer Program for Speciation, Batch Reaction, One-Dimensional Transport, and Inverse Geochemical Calculations. U.S. Geological Survey.

Ramirez, S., Cuevas, J., de la Villa, R.V., Leguey, S., 2002a. Hydrothermal alteration of La Serrata bentonite (Almeria, Spain) by alkaline solutions. Applied Clay Science 21, 257– 269.

Ramirez, S., Cuevas, J., Petit, S., Righi, D., Meunier, A., 2002b. Smectite reactivity in alkaline solutions. Geologica Carpathica 53, 87-92.

Sánchez, L., Cuevas, J., Ramírez, S., Riuiz De León, D., Fernández, R., Vigil Dela Villa, R., Leguey, S., 2006. Reaction kinetics of FEBEX bentonite in hyperalkaline conditions resembling the cement–bentonite interface. Applied Clay Science 33, 125-141.

Savage, D., Benbow, S., 2007. Low pH Cements. SKI Report 2007:32, Swedish Nuclear Power Inspectorate, Stockholm, Sweden.

Thoenen, T., Kulik, D., 2003. Nagra/PSI chemical thermodynamic database 01/01 for the GEM-Selektor (V.2-PSI) geochemical modeling code. PSI, Villigen; available at http://les.web.psi.ch/Software/GEMSPSI/doc/pdf/TM-44-03-04-web.pdf.

Traber, D., Mäder, U., 2006. Reactive transport modelling of the diffusive interaction between Opalinus Clay and concrete. Unpublished report. Internal Nagra Working Report, Wettingen, Switzerland.

Van Loon, L.R., Glaus, M.A., Müler, W., 2007. Anion exclusion effects in compacted bentonites: Towards a better understanding of anion diffusion. Applied Geochemistry 22, 2536-2552.

Wieland, E., Lothenbach, B., Glaus, M.A., Thoenen, T., Schwyn, B., 2014. Influence of superplasticizers on the long-term properties of cement pastes and possible impact on radionuclide uptake in a cement-based repository for radioactive waste. Applied Geochemistry 49, 126-142.

Wolery, T.J., 1992. EQ3/6, a software package for geochemical modeling of aqueous systems: Package overview and installation guide (Version 7.0), Other Information: PBD: 14 Sep 1992, p. Medium: ED; Size: 70 p.

7

Alteration of sand/bentonite backfill material by high-pH cementitious fluids – An experimental approach using core infiltration techniques

7.1. Introduction

The long-term behavior of clay barriers in deep geological repositories is of major importance for nuclear waste storage and is a topic of ongoing research. The packed nuclear waste will be stored in emplacement tunnels and galleries, protected by a multiple engineered barriers system (EBS) (Nagra, 2002). The EBS consist in the emplacement tunnels for high-level nuclear waste (HLW) of bentonite, while in access galleries and drift seals a mixture of sand and bentonite (s/b) will be used (Nagra, 2002). The use of s/b as buffer or sealing material around nuclear waste instead of pure bentonite is discussed in some countries as well.

Bentonite and s/b have been proposed as EBS component by its physical and chemical properties like low permeability, high swelling capacity and high ion adsorption capacity. Extensive swelling and high gas entry/break-through pressure of bentonite can damage the EBS and the host rock. Hydrogen gas produced by anaerobic corrosion of steel canisters or by radiolysis of water can build up gas pressures in the near-field of the HLW. In case the gas pressure exceeds the lithostatic pressure of the surrounding rock formation or the EBS, fracturing will be induced, which may form path-ways for material transport (Rothfuchs et al., 2012; Rothfuchs et al., 2007). An alternative would be the use of s/b, exhibiting a lower swelling capacity and a lower gas entry/break-through pressure, even in saturated state. The real extent of these processes is currently not well known. Hydrogen production and gas accumulation is most likely limited by a low gas production rate, discharged from the steel canister by a two phase-flow (Rothfuchs et al., 2007). Rothfuchs et al. (2012) analyzed s/b in several experiments in laboratory and in-situ in the Opalinus Clay at Mont-Terri rock laboratory in St-Ursanne, Switzerland. Rothfuchs et al. (2012) studied the following s/b mixture ratios in detail: 65/35%, 50/50% and 30/70%. They showed that the 65/35 and 50/50 mixtures fulfilled the requirements of low water permeability and low swelling and gas break-through pressures. Kawaragi et al. (2009) showed in permeability and X-ray CT measurements that in a 90/10% s/b, the permeability and the microstructure are independent of the sedimentary texture of the samples.

S/b is produced by mixing of quartz sand and bentonite, while bentonite is an alteration product, consisting predominantly of the smectite-group clay mineral (montmorillonite) (Dolder et al., 2014; Karnland, 2010). MX-80 bentonite is the technical name for a bentonite from Wyoming, U.S., originating from an altered volcanic ash deposit. The swelling pressure of compacted s/b is mainly a function of the bentonite dry density (ρ_{dry_bent}) and the bentonite (clay) content (B) (Agus and Schanz, 2008; Arifin, 2008). The bentonite dry density can be calculated as following, assuming that water and void space only belongs to the bentonite (Agus and Schanz, 2008):

$$\rho_{dry\_bent} = \frac{B \times \rho_{mix} \times G_{ss}}{G_{ss} \times (1 + WT_{mix}) - \rho_{mix} \times (1 - B)}$$

where B is the amount of bentonite in s/b, ρ_{mix} the saturated density of s/b, G_{ss} the specific gravity of sand (2650 kg/m^3), WT_{mix} the water content. This implies that a higher bentonite content leads at a given s/b density to a higher bentonite dry density and hence to a higher swelling pressure (Agus and Schanz, 2008). Mechanical compaction of a s/b depends on the bentonite content, the mechanical compaction coefficient and the porosity (Revil et al., 2002). The mechanical compaction coefficient described the compressibility of the s/b, while a decreasing value indicates stronger compaction. S/b with a clay (bentonite) content <0.4 and a total porosity between 0.25–0.3 is characterized by a sand grain framework, partially filled with clay, named clayey sand (Revil et al., 2002). In case of a clay content >0.5, the framework is clay dominated, named sandy shale. A critical point is reached in the case when all the porosity of sand is occupied by clay, which corresponds to the ideal packing. This point is in s/b around a bentonite content of 0.4 and a porosity of 0.25. Analysis of compacted s/b showed a bimodal pore distribution, of inter-aggregate (intergranular) and intra-aggregate (interlayer) pores (Saba et al., 2014). They observed further that sand grains are inter-connected with large interjacent pores and that these grains are not homogeneously distributed over the entire sample. The nomenclature of s/b would be consolidated sand-supported or sandy-clay rock.

Cement, concrete and shotcrete are used in underground construction as wall and roof supporting materials. In underground repository cement based materials will be further used for closing the tunnel system and as buffer around low- and intermediate-level nuclear waste (Nagra, 2002). Various studies showed that alkaline, high-pH fluids attack bentonite, changing the physical and chemical properties (Bauer and Velde, 1999; Cuevas et al., 2006; Cuevas et al., 2002; Dauzeres et al., 2010; De La Villa et al., 2001; Dolder et al., 2014; Eberl et al., 1993; Fernández et al., 2006; Fernández et al., 2009a; Fernández et al., 2010a; Fernández et al., 2014; Fernández et al., 2013; Gaucher and Blanc, 2006; Karnland et al., 2007; Nakayama et al., 2004; Ramirez et al., 2002a; Ramirez et al., 2002b; Sánchez et al., 2006). The effect of high-pH alteration on s/b is up to now not of main interest. Nakayama et al. (2004) used a 30/70% s/b mixture to perform through-diffusion and alteration experiments to determine the hydroxide diffusion coefficent and the montmorillonite dissolution rate. The effective diffusivity of hydroxide was between 10^{-10} and 10^{-11} m^2/s for temerpatures of 10–50°C and it was similar to measurements using chloride, iodide and water.

This work summarizes a core infiltration experiment using a compacted and saturated 65/35% s/b core sample and an alkaline cement solution (pH 13.5) that mimics an ordinary Portland cement pore-fluid after full hydration. CT measurements allowed tracking density/volume changes over time, while SEM, XRD, Raman spectroscopy and optical microscopy were used for post-mortem characterization.

7.2. Methods and Materials

7.2.1. Core infiltration experiment

The experimental approach used a core infiltration method to study the effect of high-pH fluid infiltration on an s/b core sample, exposed to confining pressure, which may represent lithostatic pressure conditions. A detailed description of the method is given in *chapters 2 & 4*. A s/b core of 44.6 mm length and furnished with 2 PVC-filters (polyvinyl chloride) on either side was confined and a hydraulic gradient applied to drive a small advective-dispersive flux.

During the first 352 days (equilibration phase), the s/b core had time to equilibrate to the new pressure conditions using artificial clay pore-water (APW_{OPA}). The following 227 days artificial Ordinary Portland cement pore-water (APW_{OPC}) was infiltrated (high-pH phase). After stopping, dismantling and unpacking the experiment, the s/b core was measured (length, diameter, mass) and sectioned. Two longitudinal samples of 2×4.3×1 cm (Figure 7-1; XRD and SEM samples) were cut along the center and freeze-dried. The sample for SEM (scanning electron microscope) analysis was vacuum impregnated with resin and polished with ethanol. The XRD sample was cut into 10 subsamples of 1–6 mm thickness perpendicular to the sample axis. From the XRD sample, a small triangular surface sample was cut to study the inflow surface (Figure 7-1). The rest of the core was cut into two longitudinal profiles for water content and density (ρ) measurements, 5 samples each. Two profiles were located at the outer surface of the core (subscript: rim) and two profiles at 1 cm off-axis (subscript: cen) (see Figure 7-1). The filters were immersed in isopropyl alcohol and dried in a N_2 filled desiccator.

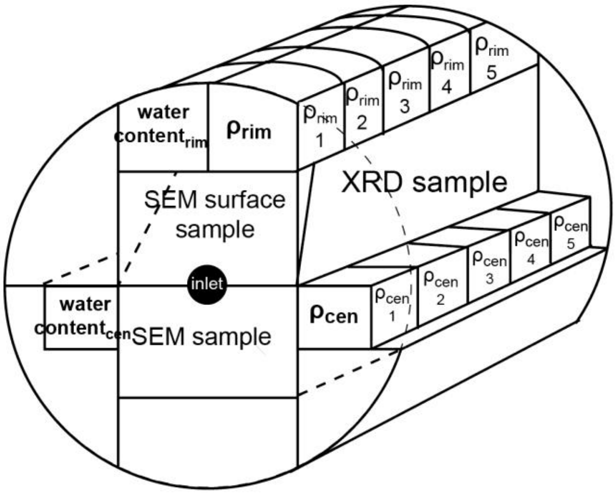

Figure 7-1: Post-mortem s/b core cutting pattern of the s/b (s/b-CT 3).

7.2.2. Analytical methods

The collected outflow was analyzed for the following parameters: main ion concentrations by ion chromatography (IC), alkalinity by titration, minor and some trace elements by ion coupled plasma atomic emission spectroscopy (ICP-OES), organic and inorganic carbon content by TOC/TN (multi N/C 2100s with a NDIR detector from Analytik Jena), pH, and electrical conductivity. The pH was analyzed in-line and later in the laboratory as bulk samples (syringes), after several weeks of cold storage. Both measurements used an Orion

PerpHecT Ross combination micro-electrode, connected to a Jumo industrial meter (ecoTRANS pH03) in case of the in-line measurement or to a Metrohm meter (780 pH meter) in case of the laboratory measurement. δ^2H isotope ratios were measured using a Picarro cavity ring-down spectrometer (L2130-i).

Density and water content were determined post-mortem using a Mettler Toledo density accessory kit (immersion in paraffin oil) mounted on a Mettler Toledo balance (AT261 Delta Range). The grain density was determined using an AccuPYC II 1340 gas pycnometer (micromeritics). The mineralogy was determined by X-ray diffraction (XRD) on disoriented, preconditioned (33 %rh) powder samples. All XRD spectra were normalized on the 3.34 Å peak of quartz. Additional samples were measured saturated with ethylene-glycol (EG). Scanning electron measurements (SEM) were performed on uncoated sample surfaces, while energy dispersive spectroscopy (EDX) was used for elemental analyses of points and areas (1.8x1.3 mm) as well as element maps. In elemental maps brighter shades indicate higher relative concentrations. Raman spectroscopy was used for mineral identification.

The X-ray computed tomography (CT) were performed on medical CT scanners (Siemens Somatom Emotion 6 and Siemens Somatom Definition AS), operated both by the Institute of Forensic Medicine at the University of Bern. In total 11 scans were performed during the experiment, 7 on the first machine and 4 on the second after replacement of the original machine. The generated X-ray energy was 130 keV (polychromatic X-ray beam) with an X-ray tube current of 120 mA for the first scanner and 140 keV and 140 mA for the second. The voxel dimension of the recorded dataset was 0.109×0.109×0.5 mm for the first CT scanner and 0.107×0.107×0.5 mm for the second. The change of the CT scanners made a direct comparison of the different datasets difficult. The data were processed and analyzed using the open-source software Mango (Multi-Image Analysis GUI, Lancaster and Martinez (2007)) and Fiji, an open-source image processing software package based on ImageJ (Schindelin et al., 2012). A detailed description of all analytical methods is given in *chapters 4 & 5*, including specifications and parameters.

7.2.3. Starting material

Granular sand/bentonite mixture of 65% quartz sand and 35% MX-80 bentonite was used (65/35 s/b), provided by MPC, Limay/France. The identical material was used in the context of the PEBS project (long-term performance of engineered barrier systems) in the HE-E (heater test) experiment in Mont Terri Rock Laboratory in St-Ursanne Switzerland (Gaus et al., 2014). The s/b consists of MX-80 bentonite (GELCLAY WH2) mixed with quartz sand (TH1000). The sand grains have a grain spectrum of 0.5–1.8 mm, which is similar to the spectrum of the bentonite powder (Gaus et al., 2014; Rothfuchs et al., 2012). MX-80 bentonite consists of Na-montmorillonite (81–85 wt%), feldspars (~5 wt%), quartz (~3 wt%), muscovite (~3 wt%), gypsum (~1 wt%), cristobalite (~1 wt%), and calcite (~0.2 wt%) (Karnland, 2010). S/b has the following theoretical composition: quartz (~66 wt%), Na-montmorillonite (~31 wt%), feldspars (~2 wt%), muscovite (~1 wt%), gypsum (~0.4 wt%), and calcite (~0.01 wt%). The s/b sample was compacted and saturated in a pre-treatment device (*chapter 2*) using 157.6 g of dry powder with a residual water content of 3.6 wt%, corresponding to 26.8 g of pore-water after saturation (w/s ratio 0.18) (Dolder et al., 2014). This amount corresponds to one pore-volume (PV) used to convert transport time to number of PV flowing through the core. The pre-treatment procedure described in Dolder et al. (2014) was adapted to the s/b by performing the compaction and saturation procedure in one single step, due to the low cohesion of the material. The saturated s/b core was 50 mm in diameter, 44.6 mm in length and had a mass of 179 g, corresponding to a saturated density of 2045.7 kg/m^3 (1739.4 kg/m^3) and a water-content per dry mass of 17.6 wt%. The core had a porosity of 32% and a degree of saturation of 81%. The measured grain density of s/b was 2650 kg/m^3, which is slightly lower compared to 2700 kg/m^3, measured by Gaus et al. (2014). The bentonite dry density of s/b mixture is 1105 kg/cm^3, based on the formula of Agus and Schanz (2008). This corresponds to a swelling pressure of 0.3–0.5 MPa if fully hydrated, which is approximately half of that to be expected of pure MX-80 bentonite (Agus and Schanz, 2008; Karnland, 2010).

7.2.4. Saturation and infiltration fluids

The s/b core was saturated using an artificial groundwater from Äspö underground laboratory in Sweden ($APW_{Äspö}$; Tables 7-1 & 7-2) (Dolder et al., 2014; Karnland et al., 2009). The s/b was equilibrated using APW_{OPA}, an artificial pore-water from the Opalinus Clay Formation (Tables 7-1 & 7-2) (Dolder et al., 2014; Mäder, 2009). The APW_{OPC} was an artificial high-pH ordinary Portland cement pore-water, based on modeled data of Lothenbach and Winnefeld (2006) (Tables 7-1 & 7-2). A detailed description of the APW_{OPC} is given in *chapters 4 and 5*. The re-measurement of APW_{OPA} and APW_{OPC} after the experiment confirmed the long-term stability of two solutions. The measured chloride in APW$_{OPC}$ was most likely an artefact of sample preparation. Saturation indices (SI) and ionic strengths of all APWs are shown in Table 7-4.

Table 7-1 Artificial pore-fluids used in the current infiltration experiment (error of major ion concentrations: 5%, up to 20% for low concentrations; error δ^2H: <4‰); unkn.: not measured; -: below detection limit.

	APW$_{Äspö}$[1]	**APW$_{OPA}$[2]**		**APW$_{OPC}$[3]**	
	fluid	**start**	**end**	**start**	**end**
pH	7.2	7.6	7.6	13.40	13.35
δ^2H [‰]	-81.5	-81.6	-	273.70	-
		--[mM]--			
Na^+	88.2	165.88	166.88	122.63	119.62
K^+	<1.3	2.7	3.7	186.71	182.62
Ca^{2+}	54.3	11.92	12.92	0.58	0.46
Mg^{2+}	<2.1	9.08	13	<0.4	<0.4
Sr^{2+}	<0.6	0.001	<0.1	-	unkn.
Si^{4+}	-	-	-	0.07	unkn.
Al^{3+}	-	-	-	0.002	unkn.
Cl^-	203.6	157.6	158.53	0.41	5.00
SO_4^{2-}	1.8	22.14	23	3.47	3.05
HCO_3^-	0.24	0.66	unkn.	1.5 (DIC)	unkn.

[1]Karnland et al. (2009), [2] Mäder (2009), [3] Dolder et al. (2014) (*chapters 4 & 5*)

Table 7-2: Recipes of the three APWs, including composition, number and molar weight of the chemicals (+ means surplus, see chapter 4).

Ingredients	**Producer and no.**	**M (mfw)**	**APW$_{Äspö}$**	**APW$_{OPA}$**	**APW$_{OPC}$**
Solids			g/kg	g/kg	g/kg
$Al_2(SO_4)_3$ 16×H_2O	Fluka: 06421	630.4			0.0096
KCl	Merck: 1.04936	74.6	19.6	0.1902	
KOH	Merck: 1.05033	56.1			12.5
Na_2SO_4	Merck: 1.06649	142.0	249.9	3.4089	0.43
NaCl	Merck: 1.06404	58.4	5164.2	6.7356	
Na_2CO_3	Merck: 6398	106.0	10.3		
$NaHCO_3$	Fluka: 71329	84.0		0.0456	
NaBr	Fluka: 71329	102.9	15.4		
NaOH	Merck: 1.06498	40.0			4.5
$MgCl_2$ 6×H_2O	Merck: 1.05833	203.3	334.8	1.8635	
$CaCl_2$ 2×H_2O	Merck: 1.02382	147.0	8253.0	1.751	
$Ca(OH)_2$	Merck: 1.02047	74.1			0.047 + 0.1
$CaCO_3$	Merck: 1.02066	100.1			0.022 + 0.05
$SrCl_2$ 6×H_2O	Fluka: 85892	266.62	121.41		
Solution					ml/kg
$Na_2O_7Si_3$	Sigma-Aldrich: 338443-1				0.0094

7.3. Results

7.3.1. Aqueous extracts

The main components of the initial pore-water chemistry were measured with an aqueous extract. 6.02 g of raw s/b material was immersed in 60 ml of miliQ-water and shaken for 2 days. The aqueous extract showed the following chemistry (S:L = 0.1:1): Na^+ 4.4±0.2 mM, K^+ 0.08±0.02 mM, Cl^- 0.13±0.01 mM, SO_4^{2-} 0.84±0.04 mM and acetate 0.1±0.02 mM.

7.3.2. Hydraulic evolution of the experiment

The experiment duration was 579 days. In total 6.8 PV were flushed trough the core; 5.8 PV of APW_{OPA} and 1.0 PV of APW_{OPC} (PV_{OPC}). The experiment was carried out at ambient temperature (18.5–23.5°C; Figure 7-2A). The confining fluid pressure was initially increased step-wise to 4.2 MPa (Figure 7-2A). After 13 and 17 days, the pressure was reduced to 2.2 MPa and 1.7 MPa, respectively. The infiltration fluid pressure was set to 1.1 MPa and reduced to 0.1 MPa after 1 hour, due to a too high fluid flow (Figure 7-2A). The pressure was increased to 0.16, 0.21 and 0.27 MPa after 300, 390 and 560 days, respectively. The idea to increase the infiltration pressure was to increase/stimulate the fluid flow.

The hydraulic conductivity was based on averages of 4 single water-level measurements on syringes at the fluid outflow, with a time span of 2–4 days. The hydraulic conductivity showed initially strong variations during the equilibration phase induced by the reduction of the confining pressure and small pressure variations in the infiltration fluid pressure (Figure 7-2A). The hydraulic conductivity was $\sim5.0\times10^{-12}$ m/s and $\sim1.1\times10^{-11}$ m/s at confining fluid pressures of 3.5 and 2.1 MPa, respectively (Figure 7-2B). The average hydraulic conductivity at the end of the equilibration phase was $\sim1.0\times10^{-11}$ m/s. APW_{OPC} infiltration induced a continuous drop to $\sim4.7\times10^{-13}$ m/s, reaching steady conditions after 99 days of high-pH infiltration. Increasing the infiltration fluid pressure had almost no effect on the rate of discharge. The average permeability was $\sim8.9\times10^{-19}$ m^2 during the equilibration phase and $\sim4.2\times10^{-20}$ m^2 during the high-pH infiltration phase using a water density of 1019 kg/m^3. At the beginning of the experiment 5.9 ml of gas were collected in syringes, originating from the dead-volumes. The electrical conductivity was initially $\sim$17 mS/cm, which was similar to $APW_{\text{Äspö}}$ and APW_{OPA} and increased thereafter continuously throughout the equilibration phase (Figure 7-2B). Switching to APW_{OPC} induced a dramatic drop to $\sim$2 mS/cm during $\sim$0.77 PV_{OPC}, indicating strong reduction in ionic strength (Table 7-4).

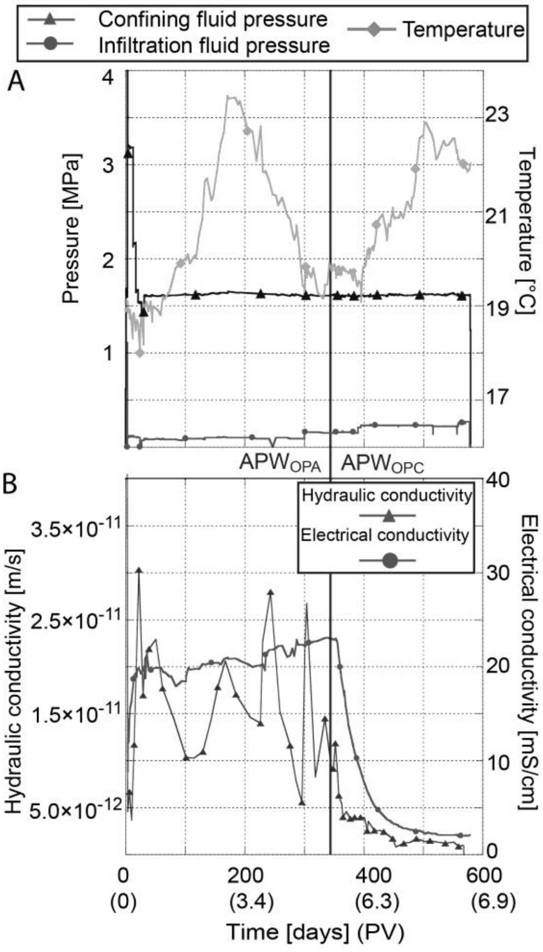

Figure 7-2: Evolution of the physical properties over time: (A) infiltration and confining fluid pressure as well as temperature; (B) electrical and hydraulic conductivity.

7.3.3. Chemical evolution of the outflow

The outflow solution was collected in 35 syringes of 1–10 ml volume. 22 aliquots were sampled during the equilibration phase and 13 during the high-pH infiltration phase. The syringes showed a weight loss of 0.01–0.05 vol% after cold storage for several weeks. Samples were analyzed for the inorganic aqueous constituents and pH (Figures 7–3 and 7–4). The alkalinity was measured in 9 aliquots and the carbon content in one aliquot during the equilibration phase.

The pH of the bulk solution was initially 5.6 and increased during the equilibration phase to ~7.6. The initial pH seemed to be lowered by atmospheric gas (carbon dioxide), present in the core packing at the beginning of the experiment. APW_{OPC} infiltration increased the pH to ~8.6 in 0.9 PV_{OPC}. The outflow gradually approached the APW_{OPA} composition during the equilibration phase, showing the following trends: magnesium and silica increased, calcium and aluminum decreased and sodium and potassium stayed constant. Sulfate and the alkalinity (bicarbonate) showed a complementary trend with an increased sulfate concentration in the first 1.4 PV, followed by a decrease, while the alkalinity increased thereafter (1.7 PV). At the end of the equilibration phase the outflow showed the following trend relative to the infiltration fluid (APW_{OPA}): K^+, Cl^-, SO_4^{2-}, OH^- (pH), and Si^{4+} were equal to APW_{OPA}, Na^+, Sr^{2+}, acetate and alkalinity were enriched, while Ca^{2+} and Mg^{2+} were depleted. During the equilibration phase (67 days, 1.4 PV), 56±3 mM C_{org} and <0.2 mM C_{inorg} were measured in the outflow, based on replicated measurements. One third of the high C_{org} concentration could be explained by acetate, while the speciation of the rest is unknown. The effect of the long storage time (1.5 years) on the C_{org} content is of main importance as a similar measurement in the second s/b experiment showed much lower concentrations; may indicate microbial activity (*chapter 8*).

High-pH infiltration reduced ion concentration strongly, with the exception of pH (OH^-), alkalinity (HCO_3^-), and Si^{4+}. Chloride as main negative charge carrier got replaced by alkalinity (bicarbonate or/and organic compounds) after 0.7 PV_{OPC}. The outflow concentration was only enriched in silica relative to APW_{OPC}, while potassium, sodium, hydroxide (pH), alkalinity, and aluminum were depleted. Between 0.3 and 0.8 PV_{OPC}, acetate was measured in the outflow as the only detectable organic acid. Ammonium, bromide, fluoride and nitrate were mostly below or near the detection limit.

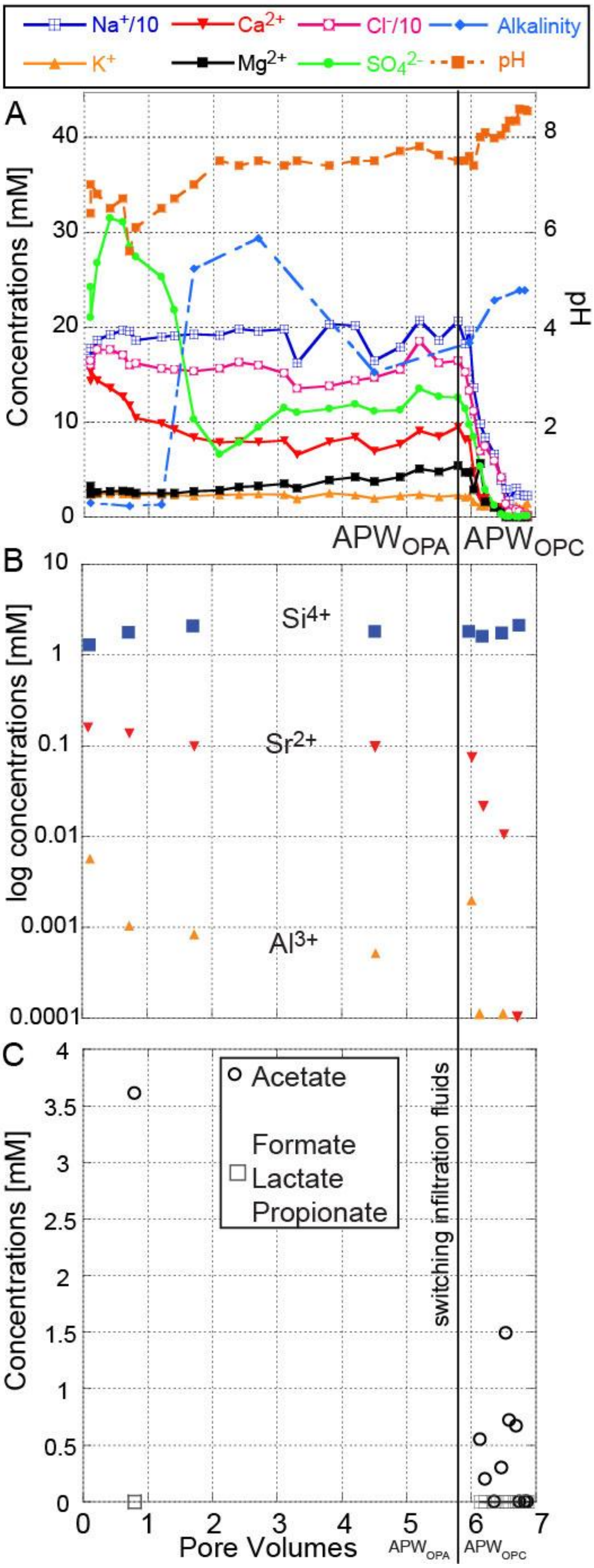

Figure 7-3: Aqueous chemistry of the outflow: (A) ion chromatography measurements of the main ions; (B) ICP-OES measurement of trace elements; (C) organic acids measured by IC.

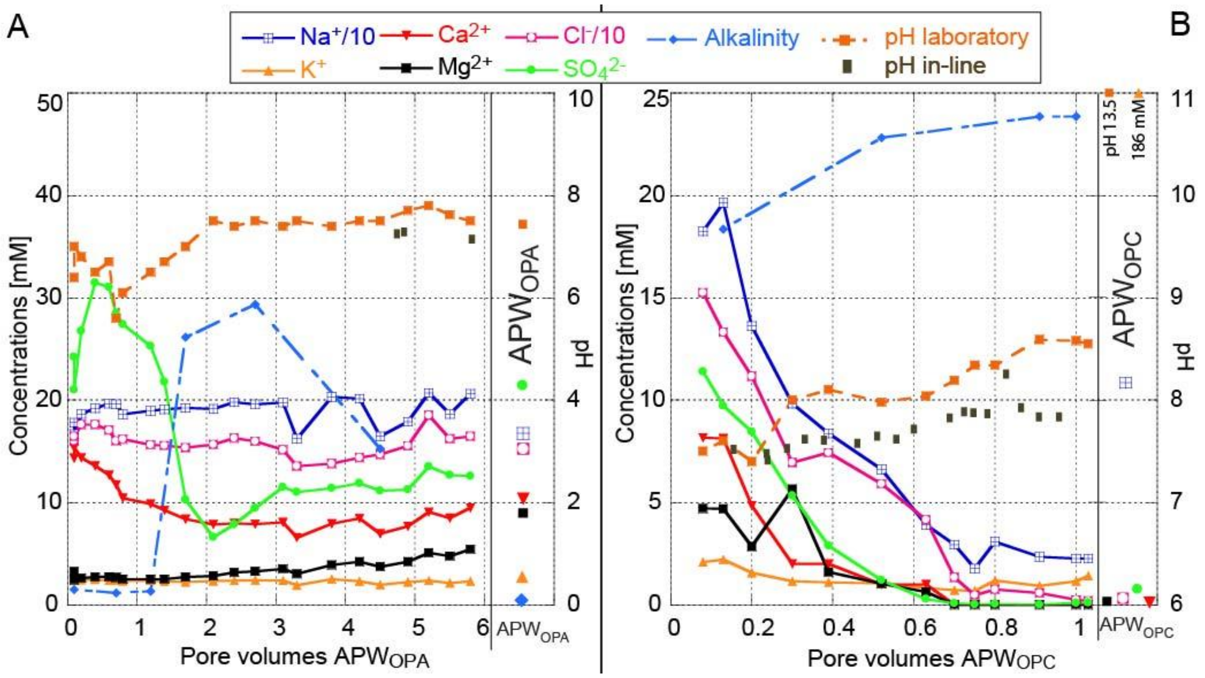

Figure 7-4: Detailed diagram of the ion concentrations during APW_{OPA} (A) and APW_{OPC} (B) infiltration.

The pH was determined with two different pH measurement setups; one electrode was installed in-line at the fluid outflow and calibrated using a two point standardization, while the second electrode was located in the laboratory and the measurements were performed on bulk solution samples after several weeks of cold storage using a three point standardization. The two datasets showed a significant off-set with lower pH values in the in-line measurements (Δ of ~0.5 pH; Figure 7-5). The error induced by using different calibrations is assumed to be small at near neutral pH, while temperature compensation could have influenced the pH value only in the range of ±0.03. This indicates that the measured pHs were in both cases true values rather than technical artifacts, and the in-line measurements are believed to be more relevant (atmospheric CO_2 exchange in case of lab samples).

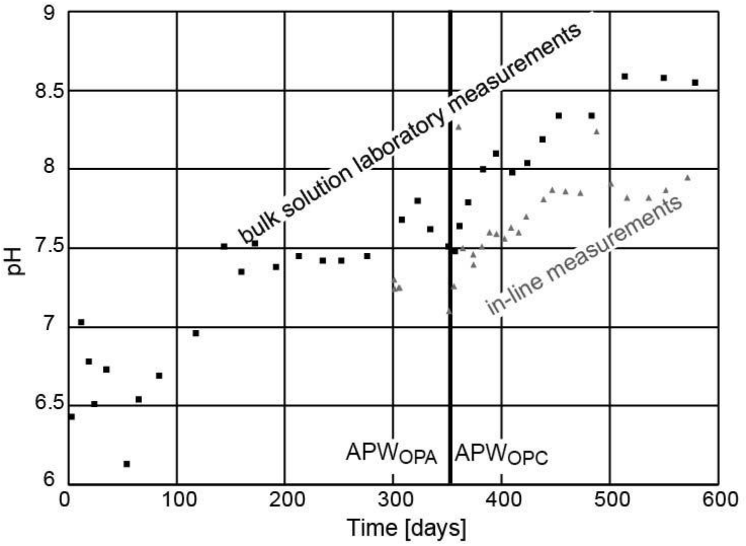

Figure 7-5: pH evolution of the outflow measured in-line and later in the laboratory.

The chloride breakthrough occurred after ~0.75 PV. The δ^2H did not reach the APW_{OPC} level at current time scale (Figure 7-6). The δ^2H curve showed an initial plateau of ~0.1 PV, while the half-height of the breakthrough curve was reached after 0.67 PV.

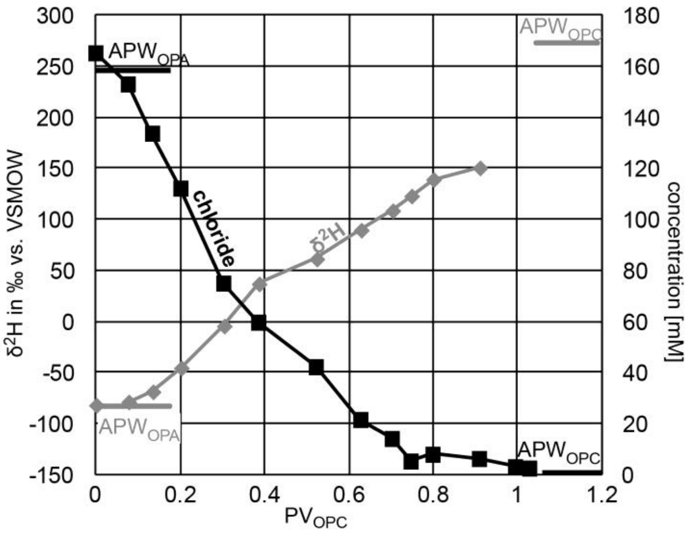

Figure 7-6: δ^2H and chloride breakthrough curve during high-pH infiltration.

7.3.4. Computed tomography (CT)

The calculations of core volumes were based on the HU histograms of each dataset (see *chapter 3*). The scanned experimental setup was segmented and a region of interest (ROI) was defined for the s/b material; the voxels were counted and multiplied by the voxel dimensions (*chapter 3*). For the first CT scanner the ROI was 640–3055 HU and 703–3055 HU for the second machine. The different measurement parameters of the two CT scanners required different ROI. The ROI used for the second CT scanner was obtained by fitting the core diameter data of the second scanner to the one of the first machine using the scans after 39 and 59 days of APW$_{OPC}$ infiltration (Figure 7-8). The change of CT scanners induced a significant error in all datasets, making interpretation of absolute volumes and diameters difficult. The bulk core density is linearly dependent on the HU. The color code of tomographic images is the following: bright shades are low X-ray attenuations (HU) and dark shades represent higher densities (Dolder et al., 2014). The absolute core volumes and diameters shown in Figures 7-7 and 7-8 have to be considered with caution, as the calculations in s/b are a difficult to perform due to the heterogeneity of the s/b material.

The pre-experimental core had a volume of 87.5 cm^3, based on measured length and diameter. After applying a confining fluid pressure of 3.2 MPa, the core volume decreased by ~6.1 vol% (Figure 7-7), while the diameter decrease was larger in direction of the outlet (Figure 7-8C). The reduction of the confining pressure to 1.7 MPa induced a volume expansion by 0.4 vol% and a core diameter increase (Figure 7-8C), while the s/b peak in the HU histogram shifted from 1423 HU to 1439 HU, indicating compaction. The APW$_{OPC}$ infiltration induced a core expansion by ~0.9 vol% (Figure 7-7).

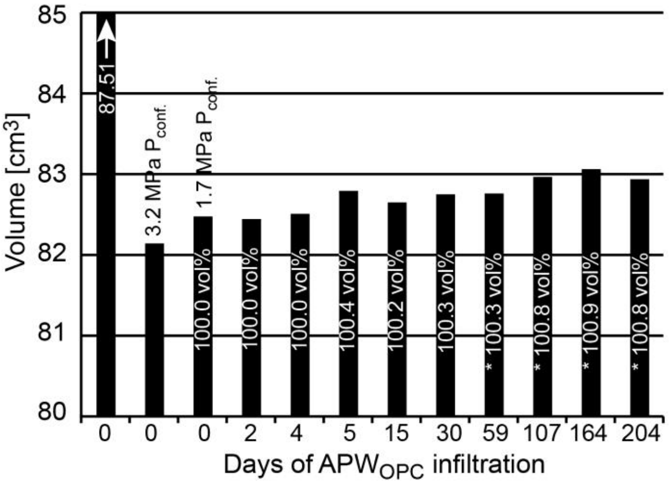

*Figure 7-7: S/b core volume calculation based on CT scan. *second (new) CT scanner.*

The core diameter calculations were performed the same way as the volume calculations. In doing this for all CT-slices of a dataset, the evolution of the core sectional area and the core diameter over time could be evaluated along the core axis (Figure 7-8C). The s/b core diameter was larger near the fluid inlet and reduced in direction of the outlet (Figure 7-8C). During the APW_{OPC} infiltration the core diameter showed small variations between -0.04 and +0.1 mm (Figure 7-8B). The core diameter showed after 204 days of APW_{OPC} infiltration the largest diameter increase directly at the fluid inlet, while between 2.5–12 mm from the inlet a reduction was observed. Almost no diameter change was observed in the middle parts, while in direction of the outlet the diameter increased. Near the fluid inlet in the first 10 mm, a small core compaction was observed.

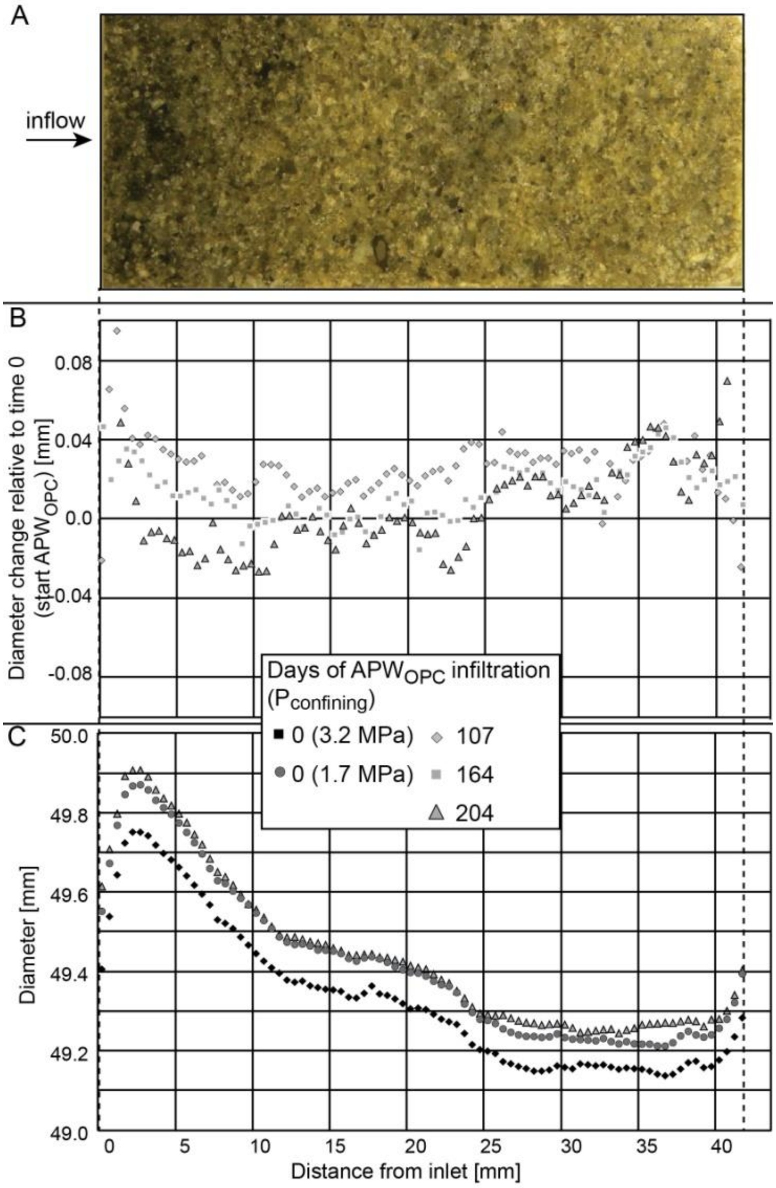

Figure 7-8: Core diameter calculated based on CT image calculations: (A) optical image of the s/b core; (B) diameter evolution of the core relative to day 0 (1.7 MPa); (C) s/b core diameter.

Tomographic cross-sections of the s/b core at time 0 (equilibration phase) showed a material with bright grains of quartz, in a bentonite matrix, exhibiting lower attenuation and hence darker shades. A zone of decreased X-ray attenuation, surrounded by a zone of increased X-ray attenuation occurred after 3 days of APW_{OPC} infiltration in the inlet filter and got more pronounced over time (Figure 7-9). Two circular shaped zones of increased density were visible in the filter after 204 days of APW_{OPC} infiltration, may penetrating into the first mm of the core. Mineral reactions are difficult to identify in s/b as the high X-ray attenuation of quartz grains together with the strong heterogeneity of the material hides possible new formed mineral phases.

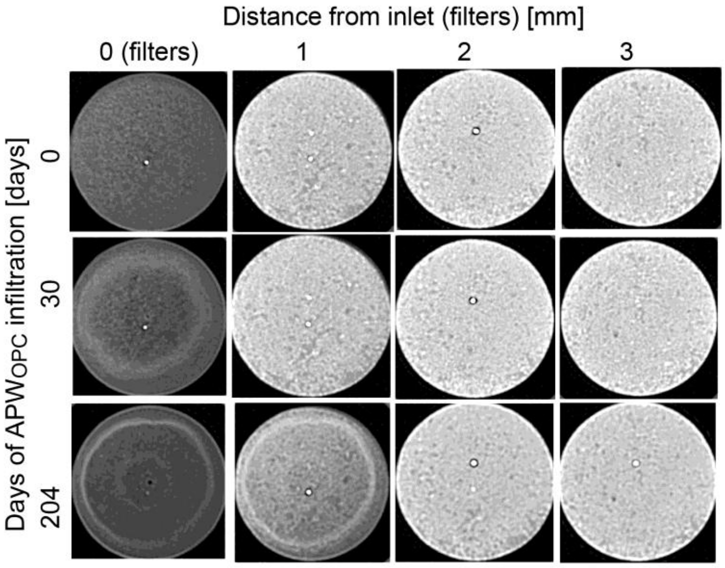

Figure 7-9: Tomographic images of the interface inlet filter–s/b core at day 0, 30 and 204 of APW$_{OPC}$ infiltration.

7.3.5. Post-mortem analysis: physical parameters

The s/b core weighted 177.86 g at the end in wet condition (including a small piece of broken inlet filter material), which is a loss of 1.2 g. The sample length was 43.26 mm, shrunk by 1.31 mm. The sample diameter was 50.1 mm near the inlet, 49.8 mm in the middle part, and 49.7 mm near the outlet. The saturated density (ρ_{sat}) showed in both profiles an increasing trend from inlet to outlet with slightly higher values at the rim, which is in agreement with CT measurements (Figure 7-10). The water content showed in both profiles a decreasing trend towards the middle part of the sample with higher values in the center (Figure 7-10). The degrees of saturation varied between 0.86 and 0.96 for both profiles. The porosity of the sample was between 32.6% and 33.1% for both profiles using a grain density of 2650 kg/m^3.

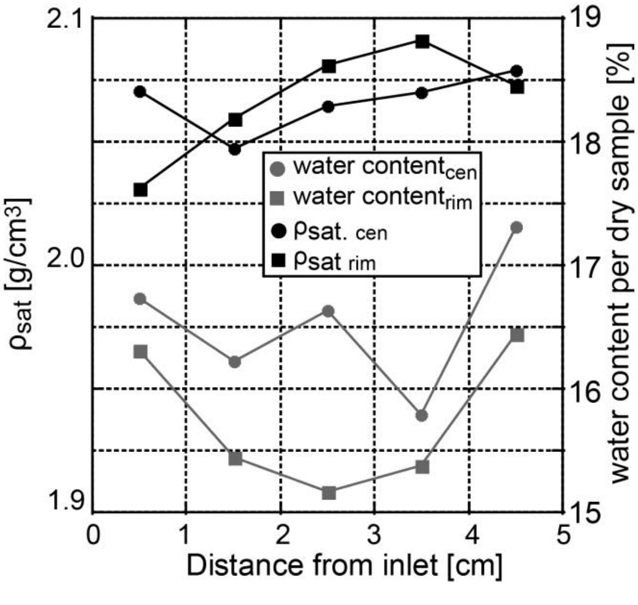

Figure 7-10: Saturated density (ρ_{sat}) and water content profiles in the s/b core.

7.3.6. XRD analysis

The XRD spectrum of s/b showed the following major minerals: quartz (2.12, 2.45, 3.34, and 4.25 Å), montmorillonite (11–12 Å (001), 8.48 Å (002), and 5.63 Å (003)), cristobalite (4.0 Å), alkali and plagioclase feldspar (3.1–3.2 Å), muscovite and/or illite (9.98 Å), gypsum (7.58 Å), and calcite (3.0 Å) (Figures 7-11 and 7-13). Variations in the (001) montmorillonite reflection resulted from different hydration states and cation occupancy. The differentiation of di- and trioctahedral sub-groups of smectite was done on the (060) reflection (Brindley and Brown, 1980). Peaks at ∼1.49 Å were related to dioctahedral and peaks at ∼1.52 Å to trioctahedral smectites. The °Δ2Θ((003)-(002)) of EG saturated samples may be used to identify illite/smectite (I/S) interlayers (Moore and Reynolds, 1989). Quartz exhibited in s/b much stronger intensities compared to all other minerals, masking reflections and made a proper identification of the (001) smectite peak locations as of all other peaks difficult.

The (001)-spacing of the raw s/b was 11.39 Å, which is a characteristic value for a smectite saturated with monovalent cations (Ferrage et al., 2005) (Figure 7-11). The s/b sample had a (060) reflection at 1.499 Å, which is characterized for a dioctahedral smectite (e.g. montmorillonite). The EG saturated sample had a (001) peak at 16.9 Å, (002) peak at 8.48 Å and a (003) peak at 5.63 Å, corresponding to a °Δ2Θ((003)-(002)) of 5.34°, which is after Moore and Reynolds, 1989 a pure montmorillonite with no I/S. APW$_{\text{Äspö}}$ and APW$_{OPA}$ saturated s/b showed a similar pattern to raw s/b with stronger gypsum peaks, which are interpreted as an artefact of sample drying (Figure 7-11).

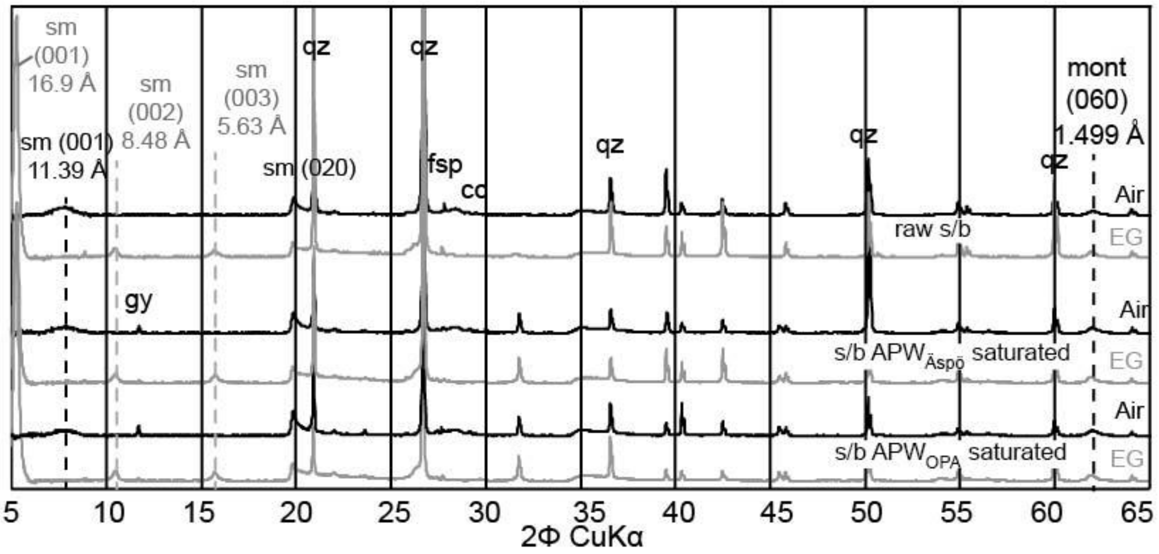

Figure 7-11: XRD spectra of s/b. Black curves are measured at 33 %rh, gray curves are EG saturated. Qz: quartz; sm: smectite; cr: cristobalite; fsp: feldspar; gy: gypsum; cc: calcite.

All filters showed a broad hump of amorphous material at 4.0 Å from the PVC-filter material (Figure 7-12). The inlet filter showed on the core facing side the main s/b minerals, while calcite and gypsum were identified on both sides. Talc and possibly brucite were only detected on the POM-adapter facing side. Not all peaks could be assigned to specific mineral phases, with zeolites, M–S–H (magnesium silicate hydrate), or LDH (layered double hydroxides) as possible phases. The outlet filters showed only the occurrence of the main s/b minerals.

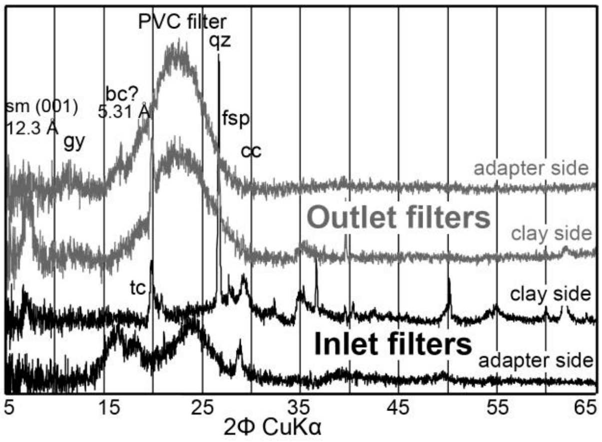

Figure 7-12: XRD spectra of the two inlet filters and the two outlet filters. Sm: smectite; qz: quartz, fsp: feldspar; cc: calcite; tc: talc; bc: brucite.

XRD measurements of the core showed quartz reflections, with strong intensity variations, originating most likely from sample preparation (Figure 7-13). The (001) smectite peak was 11.96 Å in the first 5 mm from the inlet and decreased to 11.44 Å thereafter. Both (001) smectite peaks are related to monovalent cations on the interlayer (Ferrage et al., 2005). The (060) smectite peak was in all measurements at 1.496 Å, which is characteristic for dioctahedral smectite. A sample from the inflow surface showed a peak at 1.52 Å, indicating the occurrence of trioctahedral smectite. The EG saturated samples showed an °Δ2Θ((003) - (002)) of 5.45°, and thus no significant illite interstratification (Moore and Reynolds, 1989). The intensity of the (020) smectite peak showed enrichment by ~9% near the inlet, most likely a result of sample preparation (error 8%). The 4.04 Å peak of cristobalite was reduced up to 7.5 mm by a maximum of 77% (at the interface), which indicates dissolution of cristobalite (error 27%). Alkali feldspar and plagioclase showed strong variation in intensities, which are explained by the coarse feldspar grain size (Olsson and Karnland, 2011). In the first 5 mm of the s/b core the 3.02 Å peak of calcite was increased by 47% (error 33%), indicating calcite precipitation.

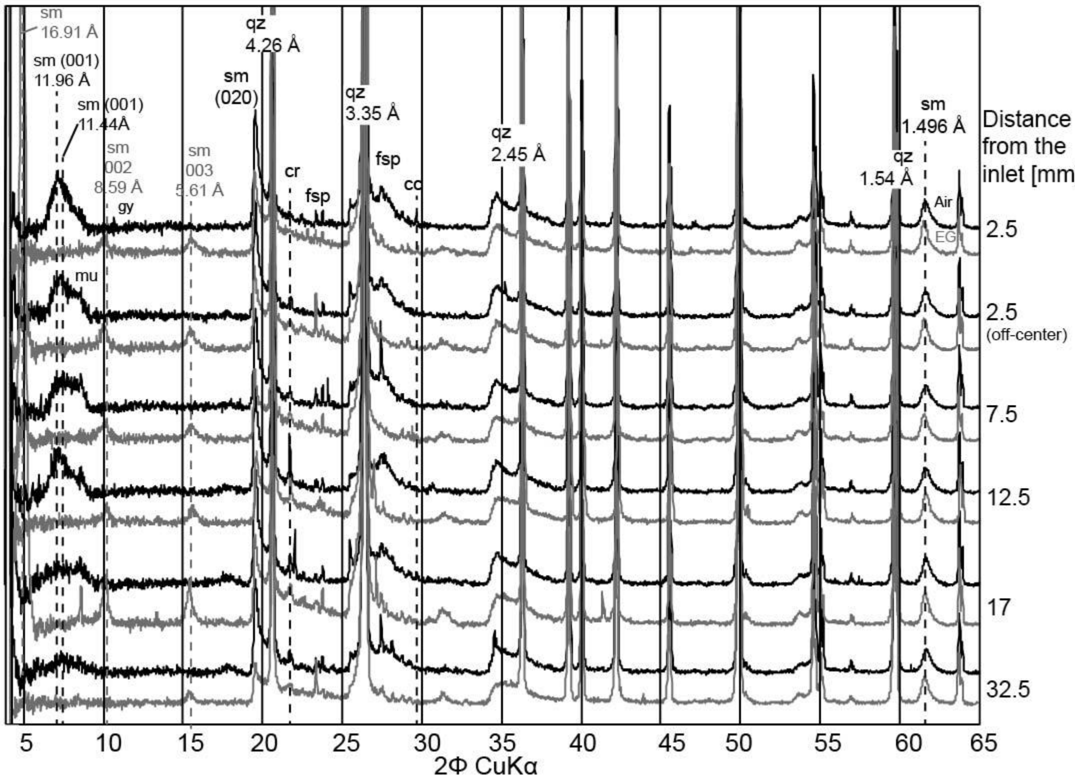

Figure 7-13: XRD spectra of the s/b core. Black curves were measured at 33 %rh and gray curves were EG saturated. Qz: quartz; sm: smectite; cr: cristobalite; fsp: feldspar; cc: calcite; mu: muscovite; gy: gypsum.

7.3.7. Microscopy and SEM/EDX analysis

Capillary tubes. The inlet capillary tube showed in back-scattered electron (BSE) images precipitates, consisting mainly of SiO_2, Al_2O_3 and Fe_2O_3, indicating the presence of most likely clay minerals and an unknown iron phase (Figure 7-14). The outlet capillary tube showed no precipitates (Figure 7-14).

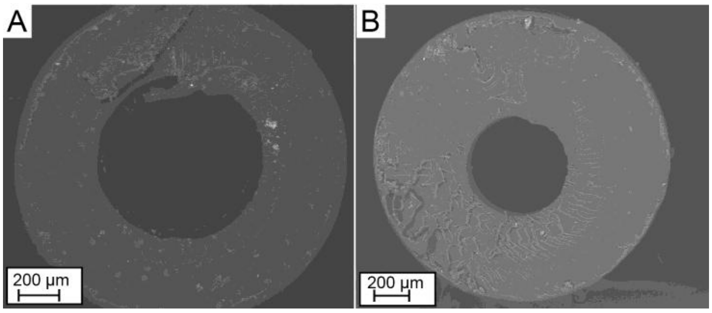

Figure 7-14: BSE micrographs of inlet capillary tube (A) and outlet capillary tube (B).

Filters. The inlet filter showed brown and black discolored spots on the surface facing the core and a whitish covering on both surfaces (Figures 7-15A & 7-16). The two inlet filters were grown together and pieces were stuck to the s/b core, indicating extensive mineral precipitation. Trying to separate the filters from the core surface tore them apart (Figure 7-16C).

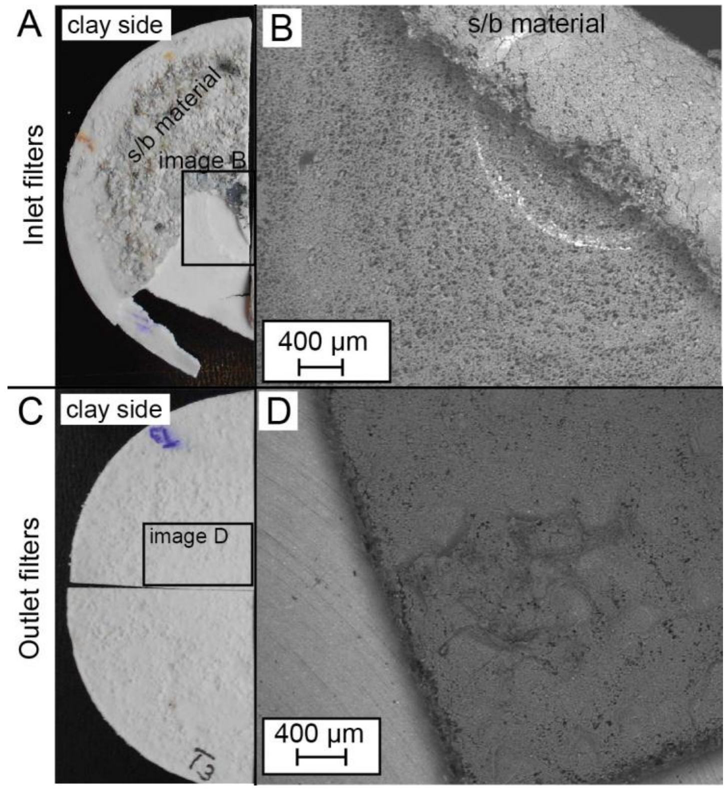

Figure 7-15: In- (A & B) and outlet (C & D) filters after dismantling: (A) photograph of the grown together inlet filters; (B) BSE micrograph; (C) photograph of both outlet filters; (D) BSE micrograph. Filter diameter 50 mm.

BSE micrographs of the stacked inlet filters revealed open porosity in the outer filter (adapter side) and a partially filled porosity in the inner (clay side) (Figure 7-15B). EDX point analyses of the material showed a chemistry dominated by Si, Al, and Ca, indicating occurrence of clay minerals and a Ca-phase, most likely calcite. The outlet filters were covered with a whitish coating after drying, which showed characteristic clay composition (Figure 7-15C).

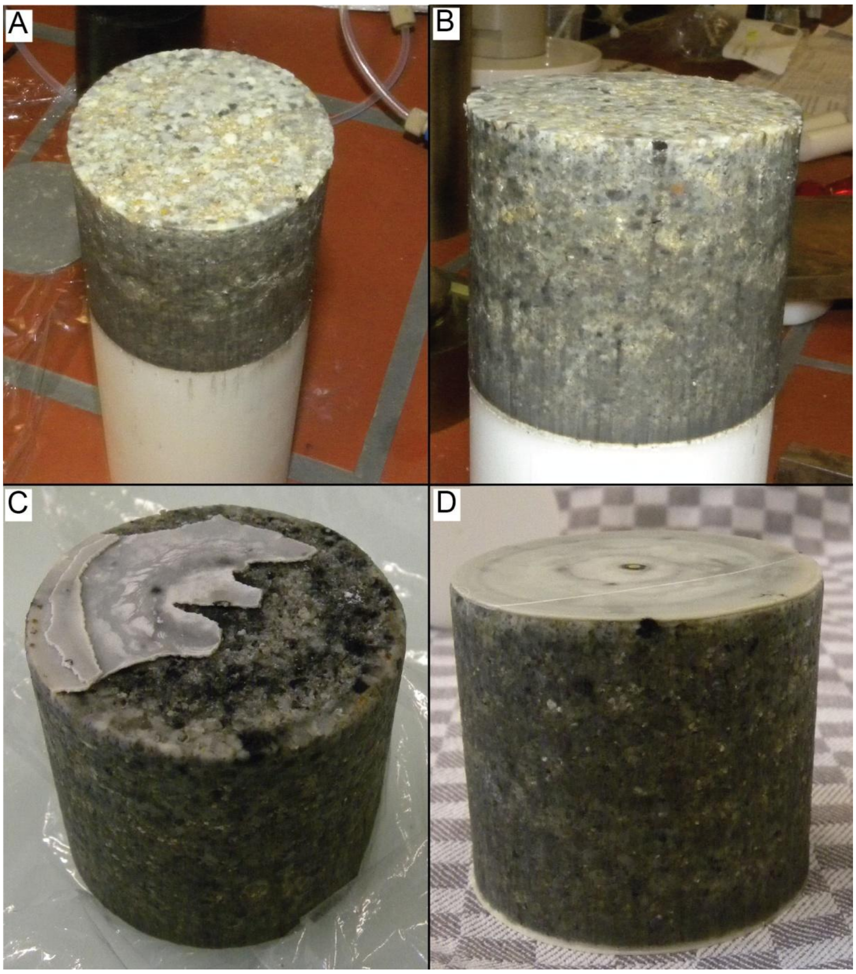

Figure 7-16: The s/b core sample before (A & B) and after the experiment (C & D). In all images the inlet surface is on top. Core diameter 50 mm.

S/b core. The inflow surface was extensively covered with black coatings after the experiment, whereas only the surface near the core rim seemed unaffected (Figures 7-9A & 7-16). The black coating seemed to be related to mineral alteration/dissolution, characterized by a rough, weathered surface (Figure 7-16C). The surface discolorations were identical to the one on the inlet filter. Optical images of the SEM sample revealed in the first 9 mm from the inflow a dark colored clay matrix (Figure 7-8). BSE images showed a sample dominated by 1 mm size, rounded quartz grains, in a matrix of bentonite (Figure 7-17B). Quartz grains were somewhat heterogeneously distribution in the core, building up a compact framework (Figure 7-20). The first 8 mm of the sample were characterized by numerous cracks, which are most likely related to the dark colored clay matrix. This zone was possibly strongly weakened by alteration and in combination with freeze-drying got intensively cracked (Figures 7-17 & 7-20).

The average compositions of the pristine bulk s/b and bentonite matrix are shown in Table 7-3. The bulk EDX measurements were dominated by SiO_2 from quartz, masking potential mineral reactions (Figure 7-20). The average oxide composition of the pristine s/b matrix and the Al_2O_3/SiO_2 ratio shown in Table 7-3 are in agreement with measured montmorillonite from MX-80 bentonite in Karnland (1997) and clay matrix measurements in pure bentonite (*chapter 5*).

Table 7-3: EDX measurements of s/b and the Ca, Mg and Fe-S-enriched zones.

	s/b (pristine)	s/b matrix (pristine)	Ca zone	Mg zone	Fe-Ca-S-phase	Fe-S-phase (pyrite)
Type of measurement	**bulk/area**	**spot**	**spot**	**spot**	**spot**	**spot**
	[wt%]					
SiO_2	86±2	70±2.5	30±5	65.0±0.6	16±4	16
Al_2O_3	9±1.2	19±1.7	3±2	15.0±0.3	5±1	6
Fe_2O_3	2.0±0.3	3.7±0.4	1.2±0.3	2.8±0.4	68±6	26
MgO	1.3±0.6	3±2.0	1.3±0.4	13.9±0.2	5±1	0.9
CaO	0.6±0.2	1.0±0.2	63±6.8	0.8±0.1	3±2	-
Na_2O	0.7±0.1	1.6±0.4	1.6±0.1	1.7±0.1	-	0.8
K_2O	0.6±0.2	1.1±0.4	0.4±0.5	0.9±0.1	-	-
SO_3	0.4±0.1	0.7±0.4	-	-	3±2	50
Al_2O_3/SiO_2	0.1	0.27	0.11	0.23	0.28	0.4
MgO/SiO_2	0.02	0.04	0.05	0.21	0.3	0.05
Ca:S [At%]	2.1	1.9	-	2.5	1.7	-
Fe:S [At%]	5.1	5.6	-	6.3	45	0.58

In the inflow region, zones enriched in Ca, Mg and Fe-S were detected (Figures 7-17 & 7-20).

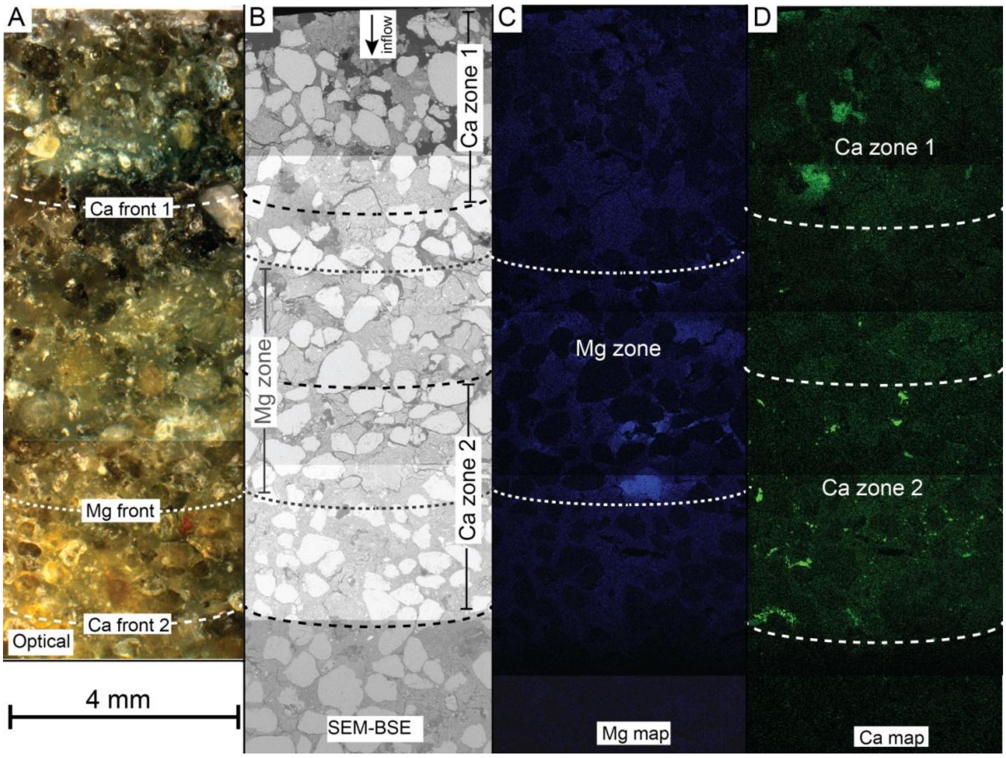

Figure 7-17: Various views of the s/b inflow region: (A) optical image; (B) BSE micrograph; (C) Mg map; (D) Ca map.

The Mg map (Figure 7-17C) and the elemental oxide transections (Figure 7-21) showed Mg-enrichment between 4.5 and 8.5 mm from the inlet. The enrichment occurred in distinct zones in the clay matrix as well as around quartz grains with a maximum enrichment at the front. A possibility could be that the Mg-enriched zones represent preferential flow paths in the s/b (Figure 7-19). Mg-enriched zones were darker in BSE images relative to the rest of the clay matrix, indicating a lower electron density. Furthermore fewer shrinkage cracks were observed in these regions (Figure 7-19B).The Mg-enriched zone showed in EDX point analyses MgO contents of ~13.9 wt% with an increased MgO:SiO_2 ratio, while the Al_2O_3:SiO_2 ratio was identical to the pristine clay matrix (Table 7-3). This is slightly higher compared to the measured Mg-enrichments in the identical experiment using pure MX-80 bentonite (*chapter 5*).

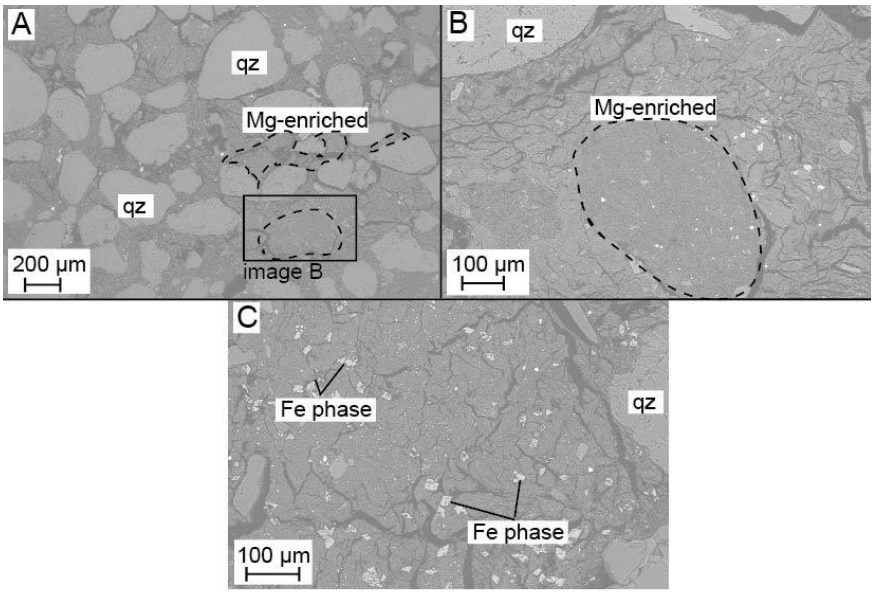

Figure 7-18: (A+B) Mg-enriched region in the clay matrix of the s/b; (C) Fe-S-enriched region. Qz: quartz.

Ca-enrichment was detected in the first ~11 mm of the core in two distinct zones: Ca zone 1 was shaped like a half circle with a radius of 3.3 mm (Figures 7-20 & 7-21). It consisted of enriched patches in the clay matrix with no distinct mineral phases at the given resolution (Figure 7-19A), Ca zone 2 extended from 6.7 to 11 mm into the bentonite and was characterized of distinct, Ca-rich mineral grains (Figures 7-19B–D). Two populations of newly formed crystals were observed: larger grains of ~60 µm size, growing in gaps between quartz grains (Figures 7-19B & C) and smaller grains of <30 µm size, growing in the clay matrix (Figures 7-19C & D). The Ca zone 2 coincided with the Mg zone, while showing a clear front. Chemical point analyses of these precipitates showed a chemistry dominated by calcium while the Al_2O_3:SiO_2 ratio clearly indicated pristine s/b composition (Table 7-3). An explanation for the strong SiO_2 signal in these measurements was most likely its occurrence in the neighborhood of large quartz grains. The grains are related to calcite, verified by XRD and Raman spectroscopy.

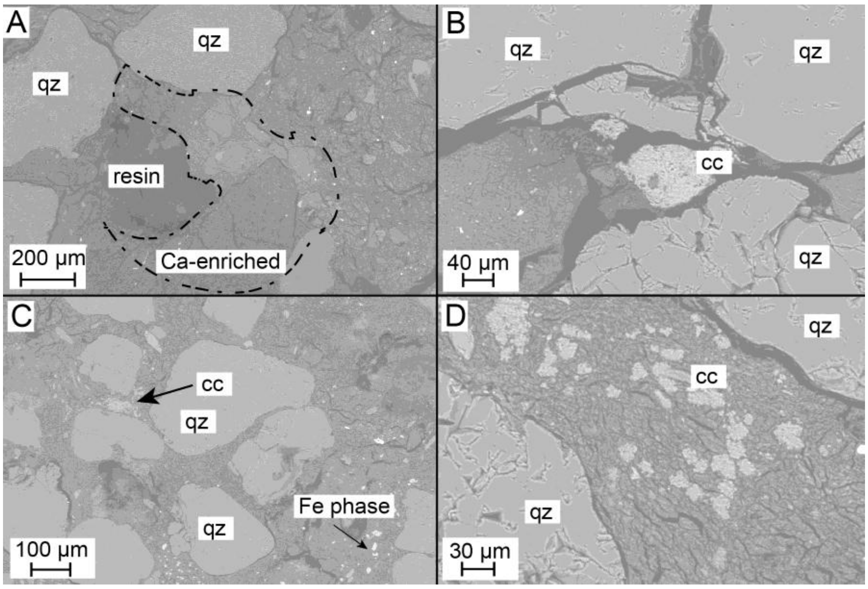

Figure 7-19: BSE images of the newly formed Ca-rich phase, indicated as distance from the inlet : (A) 3.3 mm; (B) 7 mm ; (C) 10 mm; (D) 11 mm. Qz: quartz; cc: calcite.

Iron and sulfur were enriched in two zones; both coincided with the two Ca-enriched zones at ~3.3 and ~11.0 mm from inlet (Figures 7-20 & 7-21). The enrichment occurred in mineral grains of <5 µm size and in the clay matrix, not visible at current resolution (Figure 7-18C). The Fe-S minerals had a chemical composition dominated by iron with strong variations in sulfur, while the Al_2O_3:SiO_2 ratio indicated pristine bentonite (Table 7-3). Some of the grains could be identified as pyrite by the Fe:S ratios, while other grains showed Ca:S ratios characteristic for gypsum, verified by XRD measurements (Table 7-3). Nevertheless, the high iron content in some of the measurement could not be related to a specific iron-phase. Possible mineral, which could explain the high iron content and which are difficult to detect in EDX would be Fe-hydroxides or Fe-carbonates.

Sodium and potassium maps showed the occurrence of feldspar grains in the clay matrix with more alkali-feldspar (K-fsp) relative to plagioclase (Na-fsp) (Figure 7-20). The background signal in the clay matrix of these two elements showed the dominance of sodium on the clay exchanger over the entire core length (Figure 7-21).

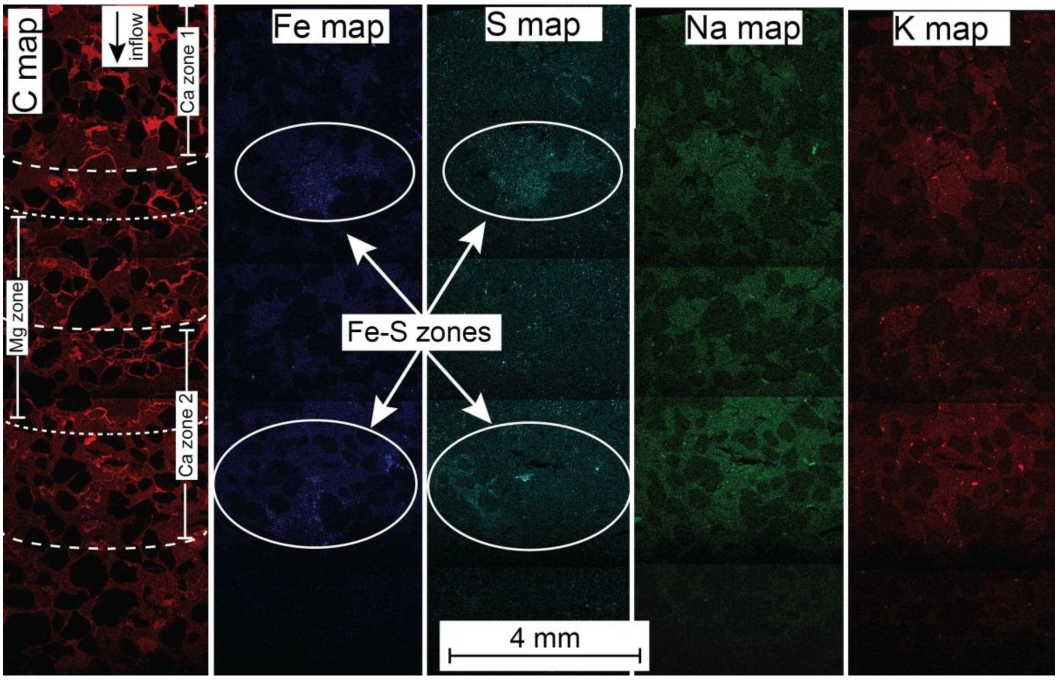

Figure 7-20: Element maps of the inflow region for C, Fe, S, Na, and K.

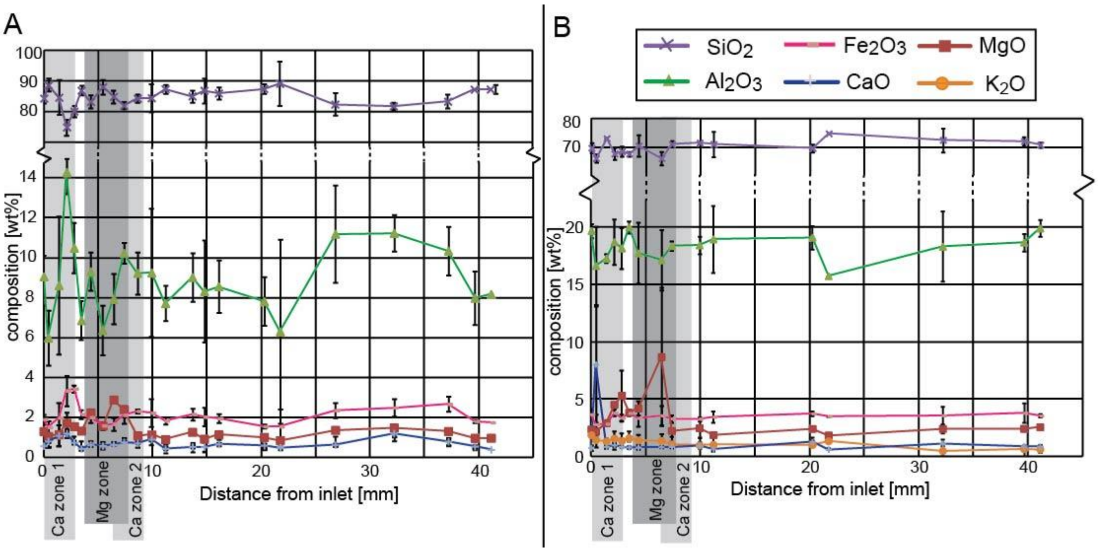

Figure 7-21: SEM-EDX oxide compositions along a central transection: (A) bulk area measurements of 1.8x1.4 mm size; (B) point measurements in the clay matrix.

7.3.8. Raman Spectroscopy

Raman spectroscopy was used to identify mineral phases along the s/b section (Figure 7-22). Clays tend to be highly fluorescent in the laser light due to associated iron(III) hydroxide minerals and/or organic matter, saturating the detector (Alia et al., 1999; Blacksberg et al., 2010). The Raman shift pattern of the newly precipitated Ca-phase showed peaks at 280 and 1083 cm^{-1}, identified as calcite bands (Figure 7-22).

Measurements in the clay matrix showed peaks at 248 cm^{-1}, 364 cm^{-1} and 1111 cm^{-1}, with no variations along the s/b section. The 711 cm^{-1} band was attributed to vibration in the SiO_4 group and the borad hump near 364 cm^{-1} had been assigned to M–OH vibrations and to Si–O–Si(Al) bending modes (Bishop and Murad, 2004). The band at 248 cm^{-1} was most likely due to SiO_4 and influenced by the dioctahedral and trio-ctahedral structure. The band near 800 cm^{-1} came from the OH bending and the 1111 cm^{-1} was most likely due to carbonate minerals in the clay (Bishop and Murad, 2004; Blacksberg et al., 2010). A large grain was identifeid as quartz, showing a main peak at 462 cm^{-1}.

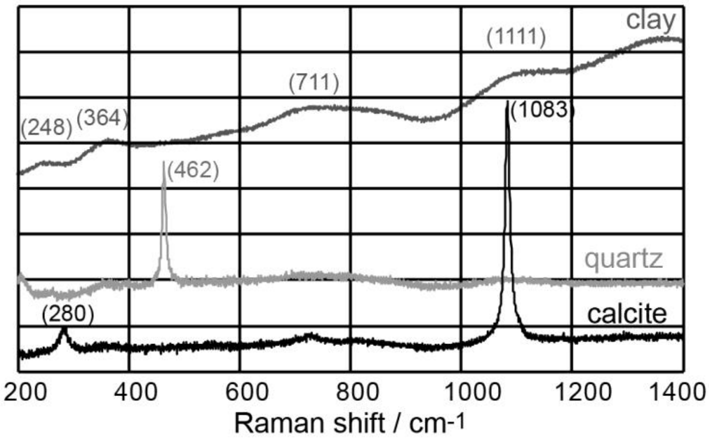

Figure 7-22: Raman shift patterns of the clay matrix (bentonite), quartz and newly grown calcite.

7.4. Discussion

The evolution of the ion concentrations and the pH in the outflow as well as the hydraulic conductivity is complex and reflects a coupling between physical and chemical processes. The main controlling processes are: ionic strength effects, internal pore-water control by minor soluble phases (sulfate and carbonate minerals), cation exchange processes, carbonate precipitation, and silicate mineral dissolution/precipitation of reactive 'cement phases' after injection of APW_{OPC}.

In-line vs. laboratory pH measurements. The in-line pH measurement represented the original pore-fluid, measured directly at the fluid outflow. The lower pH is explained by a higher CO_2 partial pressure (pCO_2), acidifying the solution (Figure 7-23). Performing aqueous speciation calculations using the two different pH datasets together with the measured chemical composition of the outflow, one observes that the in-line measurement always yields higher pCO_2 contents (Figure 7-22) that are distinctly above the partial pressure in the atmosphere. During storage of the syringes, part of the CO_2 got lost, increasing the pH, while the pCO_2 was approaching atmospheric conditions. In case of high-pH infiltration, the $SI_{calcite}$ was reduced by 0.4–0.7 (Figure 7-24).

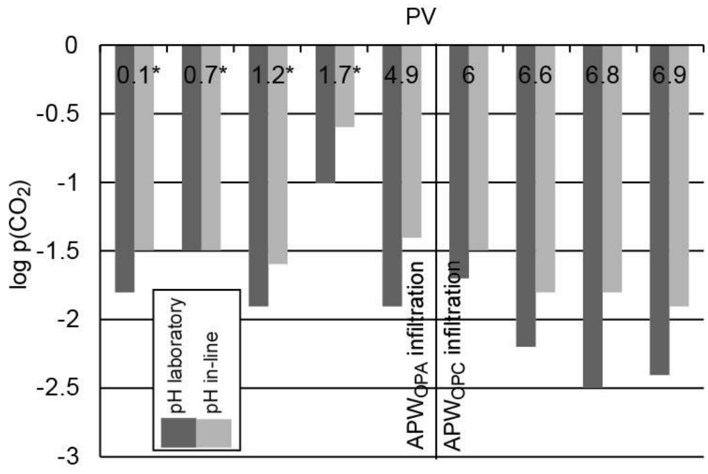

*Figure 7-23: Log pCO_2 based on the two different pH measurement devices. * in-line pH measurements were calculated using the measured shift of 0.5 pH, as the in-line measurement was first started after 4.7 PV.*

7.4.1. Equilibration phase

Evolution of physical properties. Initially, the s/b core volume decreased after applying a confining pressure, which corresponds to a further compaction of the core under hydrostatic pressure conditions relative to the pre-confined sample. Confining pressure conditions consolidated the quartz grain packing further, leading most likely to a near grain-supported framework, with porosity completely filled with bentonite. The s/b core had a void ratio of ~0.5, which corresponds to a dense grain packing, characteristic for clayed sands (Revil et al., 2002).

The hydraulic conductivity showed strong variations due to pressure fluctuations in the infiltration fluid system induced by the decoupling of the mobile device for CT measurements. It was observed that already small variations in the infiltration fluid pressure had a strong effect on the rate of discharge, indicating that the swelling pressure of the clay was low and in the range of the infiltration fluid pressure. The measured hydraulic conductivity (~1×10^{-11} m/s) was higher compared to Cho et al. (2000), who measured ~2×10^{-12} m/s at a similar dry density using a 30/70% sand/Kyungju bentonite. Rothfuchs et al. (2007) measured for a 65/35% sand/MX-80 bentonite mixture with a dry density of 1.9 kg/cm^3 a permeability of 3.3×10^{-17} –9×10^{-18} m^2, which is slightly higher compared to the current results. Gaus et al. (2014) measured in a field experiment for a 65/35% sand/granular MX-80 bentonite with a dry density of 1.38 kg/m^3, a permeability of 1.0×10^{-19} m^2. This is one order of magnitude lower compared to the current results. The hydraulic conductivity of s/b was ~2 orders of magnitude higher compared to pure bentonite (see *chapters 5 & 6*) and 3–4 orders of magnitude lower compared to sandstone or 1–2 orders lower compared to limestone (Bear, 1973). Water-flow only occurred in the bentonite filled clay matrix of the s/b. This leads to the conclusion that the hydraulic conductivity of s/b is a function of the bentonite density, in case the entire porosity is filled with clay. To verify this hypothesis, the calculated bentonite dry density, based on the formula of Agus and Schanz (2008), was compared to measured data for pure MX-80 bentonite of Karnland et al. (2006). At current bentonite dry density this corresponds to a theoretical hydraulic conductivity of ~3×10^{-13} m/s, based on a 0.3 M NaCl solution. This is ~1 order of magnitude lower compared to the measured values in s/b, indicating that the hydraulic conductivity of s/b is not only a function of the bentonite density but rather influenced by other factors like texture, heterogeneities or open porosity (water filled). Further it may indicate that the used formula of Agus and Schanz (2008) is not entirely true and the calculated bentonite density is different from the real density.

The swelling pressure of the current s/b is after Agus and Schanz (2008) between 0.1–0.2 MPa, based on the bentonite dry density. This is in agreement with measurements performed on pure MX-80 bentonite by Karnland et al. (2006). Rothfuchs et al. (2012) measured for a higher s/b density (ρ_{dry} 1876 kg/m^3), a swelling pressure of 0.28 MPa, which is slightly higher compared to the current result. The low swelling pressure of s/b, which was in the range of the used infiltration fluid pressure (0.11 MPa), explains the strong fluctuations in the hydraulic conductivity.

Chemical evolution of the outflow. Initially, the ionic strength of the outflow increased during the first 0.5 PV, due to increasing chloride and sulfate concentrations (Table 7-4). This is explained by the initial compaction of the core, flushing out excess anions. Thereafter, the ionic strength decreased to 0.2 mol/kg in 4.5 PV. This is slightly lower compared to APW_{OPA} and indicates ongoing mineral precipitation reactions in the core (Table 7-4). The main difference between outflow and APW_{OPA} was the lower sulfate, calcium and magnesium concentration in the outflow, indicating sulfate mineral precipitation or in case of cations, ion exchange processes.

The $\text{SI}_{\text{gypsum}}$ started at -0.2 and decreased continuously, while the outflow showed sulfate enrichment between 0–1.4 PV and depletion thereafter (Table 7-4 and Figure 7-4). The initial increased sulfate concentration was either related to the initial squeezing of the core or to gypsum dissolution, both in agreement to $\text{SI}_{\text{gypsum}}$. The later depletion of sulfate relative to APW_{OPA} clearly showed sulfate-mineral (e.g. gypsum) precipitation, while the $\text{SI}_{\text{gypsum}}$ indicated under-saturation (Table 7-4). This may indicate that gypsum was precipitated near the inlet and remained under-saturated in direction of the outflow. The EDX sulfur map showed enrichment in the inflow region, which is possibly related to the newly formed gypsum (Figure 7-20). It also indicates that the pore-fluid was possibly not in equilibrium with the mineralogy due to a flow rate which was much higher compared to the precipitation/dissolution kinetics.

The pH started to increase after 1 PV and reached steady conditions after 2 PV, triggered most likely dissolution of bicarbonate and/or organic compounds (contributing both to alkalinity), which showed a big jump from near 0 to almost 30 mM. The alkalinity seemed further to replace lost anionic charges from the sulfate. PhreeqC modeling showed that the observed pH and alkalinity increase between 1 and 2 PV induced a change in the $\text{SI}_{\text{calcite}}$ from under-saturation to over-saturation, assuming in the model, that the measured alkalinity equals the carbonate alkalinity (Table 7-4). This would theoretically imply that calcite got initially dissolved and precipitated thereafter. The mass-balance calculation for bicarbonate shows disequilibrium between in- and outfluxes during the equilibration phase, indicating loss of bicarbonate in the core, which can be interpreted as calcite dissolution (Table 7-5). This is in agreement to the initial $\text{SI}_{\text{calcite}}$, while the over-saturation is contradictory to be measured outflow concentrations. This may indicates that organic carbon compounds were present in the outflow and/or the pore-fluid was not in equilibrium with the mineralogy due to a high fluid flow rate, but rather shows the $\text{SI}_{\text{calcite}}$ of APW_{OPA}. The charge balance calculation did not show a significant imbalance during the equilibration phase; the assumption of defining the alkalinity only as bicarbonate (monovalent anion) seemed to be rather true. The use of the slightly different pH led to different SI, mainly for calcite, which is strongly pH depended. Performing the $\text{SI}_{\text{calcite}}$ calculations using the lower pH values of the in-line measurement, all $\text{SI}_{\text{calcite}}$ shift to lower values, while the overall trend remains (Figure 7-24).

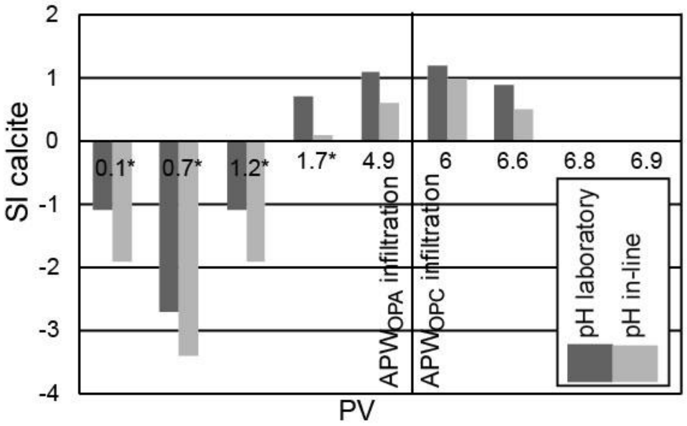

Figure 7-24: $\text{SI}_{\text{calcite}}$ calculated based using the two different pH values; measured in-line and in the laboratory. in-line pHs were calculated assuming a pH difference of 0.5 as the in-line measurement did not start before 4.9 PV.*

The lower initial pH was induced by the saturation fluid, exhibiting a slightly lower pH compared to the equilibration fluid (Table 7-1). The outflow chemistry reached steady conditions for most of the ions after 3 PV (Figure 7-4). The cations showed replacement of sodium from the clay exchanger by calcium and magnesium (Figure 7-3), which is in agreement with the mass-balance calculations (Table 7-5).

7.4.2. High-pH infiltration phase

Evolution of the fluid composition. APW_{OPC} infiltration strongly reduced the ionic strength of the outflow, reaching steady conditions after 0.7 PV_{OPC} (Table 7-4). The ionic strength of the outflow got 10× reduced with respect to the APW_{OPC}, indicating extensive mineral reactions in the core and pH buffering. The observation is in agreement with in-line electrical conductivity measurements (Table 7-4).

Chloride as major anionic charge carrier dropped continuously and got replaced by the alkalinity (bicarbonate and/or organic compounds) after ~0.6 PV_{OPC} (Figure 7-3). The mass-balance showed a difference of 3.5 mmol between cumulative inflow and outflow, indicating that chloride was still present in the s/b core at the end of the experiment (Table 7-5). The aqueous extract showed a total of 7.34 mmol Cl^-/kg of total pore-water in the raw s/b material. The initial inventory was therefore 0.2 mmol Cl^-, based on the total pore-water content, augmenting the difference to 3.7 mmol, which corresponds to the chloride inventory of s/b. The outflow concentration during the core saturation phase, used in the mass-balance calculation, is based on the assumption, that this outflow concentration was equal to the first aliquot measured during the core infiltration experiment. The error caused by this assumption is unknown but may be of importance for all mass-balance calculations. If chloride is considered as non-reactive tracer mostly present in intergranular porosity, the chloride decrease represents a breakout curve, whereby the time required to flush out chloride to half of that of its initial concentration represents approximately one volume of flow-active porosity (anion accessible porosity). This time was ~31.4 days or equivalent to 0.3 PV relative to the initial full water content. The δ^2H breakthrough curve is used to gain information on the apparent transport porosity. The δ^2H first appeared in the outflow after 0.1 PV, while the half-height was reached after ~0.67 PV relative to the initial full water content (Figure 7-6). This indicates that the apparent transport porosity for water was ~67% of the total water-loss porosity, while the flow-active porosity of chloride (intergranular porosity) was 30%. In case of a pure diffusion experiment, the half-height of the δ^2H should be at 1 PV. The ratio of the effective transport porosity for $Cl^-/^2H$ was about 0.5. Hydroxide, the main anionic charge carrier of the APW_{OPC} (~339 mmol), reached the outflow only sparsely. Even after 1 PV_{OPC} injection, the concentration never exceeded 0.004 mM, indicating strong consumption (Table 7-5). Directly related to the hydroxide concentration is the pH, which was ~8.6 (laboratory) and ~8 (in-line) at the end of the experiment. The hydroxide is assumed to be consumed by precipitation of hydroxide minerals, like brucite or saponite. A detailed description is given later in this section. The alkalinity consisted during the high-pH infiltration most likely of bicarbonate and organic compounds. The alkalinity increase during high-pH infiltration was most likely induced by dissolution of calcite and organic compounds. The $SI_{calcite}$ showed over-saturation, calculated based on the assumption that the alkalinity consists only of inorganic carbon, which is rather not entirely correct. The over-saturation can be explained by the high flow rate, while the precipitation kinetics was slower. It indicates that calcite got dissolved and precipitated in the core at the same time. Calcite precipitation will be discussed later. Sulfate reached concentrations <1 mmol after 0.7 PV_{OPC}, simultaneously with calcium and magnesium; these concentrations were identical to APW_{OPC}. The mass-balance showed a loss of sodium from the core, released from the exchanger (Table 7-5). Potassium and calcium were retained in the bentonite by ion exchange in case of potassium and for calcium possibly also by calcite precipitation. Silica got enriched in the outflow, while aluminum concentrations were most of the time below detection limit. Charge imbalance occurred in the outflow aliquots after 0.75 PV_{OPC} onwards (Table 7-4). The imbalance was an effect of the low ion concentrations in the outflow, while the difference was most likely induced by the unknown speciation of the alkalinity, which was assumed to consist mainly of monovalent bicarbonate.

Table 7-4: Equilibrium calculations of the outflow based on the in-line measured pH. Cc: calcite, gy: gypsum, mont: montmorillonite, qz: quartz, cristo: cristobalite.

Time/ APW	**PV (PV_{OPC})**	**Ionic strength**	**Charge balance error**	**SI**						
[days]		[mol/kg]	[%]	cc	gy	mont	qz	$SiO_{2\,amorph}$	cristo	$pCO_{2\,(g)}$
$APW_{Äspö}$		0.25	-2.7	-0.3	-0.8	-	-	-	-	-3.3
APW_{OPA}		0.23	2.1	-0.1	-0.3	-	-	-	-	-3.2
APW_{OPC}		0.29	-3.5	0.6	-2.9	-5.8	-4.7	-6	-5.5	-12.2
1.5	0.1 (0)	0.23	1.6	-1.9	-0.2	7.2	1.1	-0.15	0.3	-1.5
33	0.7 (0)	0.24	1.6	-3.4	-0.3	1.8	1.2	-0.01	0.3	-1.5
254	4.5 (0)	0.20	1.2	0.7	-0.8	6.3	1.2	-0.02	0.4	-1.5
359	6 (0.1)	0.21	14.2	1.0	-0.8	-	1.2	-0.01	0.4	-1.5
403	6.4 (0.5)	0.80	12.7	1.4	-1.4	-	1.2	-0.03	0.4	-1.6
445	6.6 (0.8)	0.02	-21.0	0.5	-4.1	-	1.3	0.03	0.5	-1.8
499	6.8 (0.9)	0.03	-9.0	-	-	-	1.3	0.03	0.5	-1.8
567	6.9 (1.0)	0.03	-3.6	-	-	-	1.3	0.03	0.5	-1.9

Table 7-5: Ion mass-balance of in- and outflow.

Elements	**Inflow**			**Outflow (equilibrium phase)**	**Outflow (tot)**	**Δ**
	$APW_{Äspö}$	**APW_{OPA}**	**APW_{OPC}**			
				[mmol]		
Na^+	2.5	26.00	3.38	29.83	33.13	**-1.3**
K^+	0.01	0.42	5.16	0.36	0.41	**5.2**
Ca^{2+}	1.55	1.87	0.02	1.40	1.56	**1.9**
Si^{4+}	-	-	1.7E-03	0.55	0.59	**-0.59**
Al^{3+}	-	-	8.3E-04	1.4E-04	2.0E-04	**6.3E-04**
Mg^{2+}	0.05	1.42	-	0.55	0.60	**0.87**
Cl^-	5.81	24.70	0.07	24.56	27.06	**3.5**
SO_4^{2-}	0.05	3.46	0.10	2.29	2.54	**1.1**
HCO_3^-	6.9E-03	0.10	8.3E-03	2.56	3.2	**-3.2**
OH-	4.6E-06	6.2E-05	9.4	8.4E-05	7.7E-05	**9.3**

Evolution of hydraulic conductivity and core volume. APW_{OPC} infiltration induced a volume expansion in s/b, while the hydraulic conductivity got reduced to $\sim 1.3 \times 10^{-12}$ m/s within 0.7 PV_{OPC}. Volume expansion is assumed to be induced by a low ionic strength fluid, increasing the interlayer porosity and the diffuse layer (DL), resulting in an increased swelling pressure. At constant hydrostatic conditions, this leads to a volume expansion, indicating that the s/b framework is no more grain but rather matrix-supported.

Three main mechanisms for the hydraulic conductivity reduction are proposed for a constant-pressure approach: (1) mineral precipitation, (2) reduction in interlayer porosity and DL and resultant compaction due to higher ionic strength of the inflowing APW_{OPC} and (3) increase in interlayer porosity and DL and resultant decrease of the intergranular porosity due to lower ionic strength pore-water seen in the effluent. Mechanism (1) relates the drop in hydraulic conductivity to mineral precipitation in filters as well as in the s/b. Tomographic images of the filter revealed mineral precipitation after 3 days of APW_{OPC} infiltration. Post-mortem analysis of the identified these minerals as calcite, gypsum and possibly some talc and brucite. In the s/b core massive precipitation of calcite and possibly saponite were observed in the intergranular porosity, in which advection takes place. Mechanism (2) is based on the idea that an increased ionic strength infiltration fluid reduced the fluid flow in the confining pressure-constrained setup, with APW_{OPC} exhibiting a higher ionic strength compared to APW_{OPA} (Table 7-4, *chapter 5*). High ionic strength pore-water reduces the interlayer porosity and the DL in the current pressure-constraint setup, which may induced a reduction in the hydraulic conductivity and a core volume reduction, observed directly at the fluid inlet. This would be in agreement to Karnland et al. (2006), who measured in fixed-volume cells higher hydraulic conductivities in MX-80 bentonite using high ionic strength fluids. Mechanism (3) is based on the observation that the outflow solution exhibited a much lower ionic strength compared to the infiltration solution. The low ionic strength pore-fluid could induce an osmotic effect with water being transported into the interlayer and the DL and hence reducing the intergranular porosity, used for advective flow. Further it would cause clay mineral swelling, which corresponds in a constant-pressure setup to a volume increase; in agreement to experimental observations. And it is in agreement with Karnland et al. (2006), who observed for MX-80 bentonite high swelling pressures in low ionic strength NaCl solutions. Karnland et al. (2006) reported further that small changes in the ionic strength ($\Delta \approx \pm 0.3$ mol/kg) of NaCl-based solutions induces in MX-80 bentonite (ρ_{dry} 0.7–1.2 g/cm^3) only small changes in hydraulic conductivity; whereas at current conditions, almost no changes could be observed.

A prediction, which of the three options is more realistic and causes the reduction in the fluid flow is difficult. Options (2) and (3) hinge on the unknown detailed evolution of the high-pH fluid in the s/b core except that the initially infiltrated fluid showed a much higher ionic strength compared to what is measured at the fluid outflow. Post-mortem analysis indicated that the mineral reactions occurred only in the first 11 mm from the inlet, which is assumed to be the zone where the pore-fluids evolved strongly by losing its high ionic strength. This is in agreement to core diameter data measured by CT, showing reduced diameter between 1.1 and 12 mm from the inlet, which were most likely induced by high ionic strength fluids.

Comparing all experiments performed on bentonite and s/b (*chapters 4, 5, 6, 8*), it suggests, that most likely extensive mineral precipitation (calcite, saponite) in the intergranular porosity of the s/b (1) caused the reduction of the hydraulic conductivity. The effect of high ionic strength fluids (2) on the fluid flow is unclear and may have only a minor effect. Core expansion was related to the low ionic strength pore-fluid, which is the result of strong alteration of APW_{OPC} and which was present over most of the length of the core.

Gypsum dissolution/precipitation. The sulfate behavior in the s/b core is complex. The initial accumulation of sulfate in the outflow and the SI_{gypsum} showing near saturation conditions with respect to gypsum. If we calculate the sulfate mass-balance for the initial 1.4 PV, a loss of 0.2 mM sulfate was observed, which corresponds to 34 mg of gypsum or 9 wt% of the total gypsum amount. During the rest of the equilibration and high-pH infiltration phases the SI decreased continuously, indicating most likely ongoing gypsum dissolution but not rapidly enough to be fully buffered. The mass-balance calculation indicated a gain of 1.1 mmol of sulfate in the core, which corresponds to $\sim$189 mg of gypsum respectively $\sim$82 mm^3. This may have happened in the sulfate enrichment zones observed in the inflow region of the s/b core.

Dissolution of silica and silicate minerals. The silica concentration in the outflow increased during the equilibration phase, while during the high-pH infiltration phase only in the last aliquot increased concentrations were measured, although both infiltration fluids had much lower silica concentrations. The mass-balance showed for the s/b core a loss of silica while aluminum got slightly enriched (Table 7-5). The equilibrium modeling showed that the silica concentration in the outflow was under-saturated with respect to amorphous SiO_2 during the equilibration phase (Table 7-4). Switching to APW_{OPC} induced an over-saturation with respect to amorphous silica after 0.8 PV_{OPC}. The fact that no increasing trend was observed in the aluminum concentration implies that the dissolved mineral phase must be a pure SiO_2-phase like quartz, cristobalite or tridymite. The last aliquot showed over-saturation with all these phases, while the dissolution of cristobalite was observed in the inflow region by XRD as well as in previous studies (Bouchet et al., 2004; Fernández et al., 2013; Karnland, 1997, 2004; Karnland et al., 2007).

Reaction zones. Three overlapping reactions zones were observed in the s/b by SEM-EDX measurements, characterized by: Ca, Fe-S, and Mg-enrichment.

Ca-enrichment was observed in two zones in the first 11 mm of the s/b; one was located directly at the inflow and the other between 6.7 and 11 mm from the inflow. Both zones were characterized by intense calcite precipitation, verified by XRD and Raman spectroscopy measurements. In the first zone Ca-enrichment took place in the bentonite matrix while the second zone showed precipitation of small calcite crystals in the vicinity of quartz grains. From this observation, it can be interpreted that the main fluid flow happened at the clay–quartz grain transition rather than in the clay matrix. It is assumed that the calcite precipitation happened in the intergranular porosity of the s/b. Precipitation of Ca-mineral phases like calcite in high-pH environments in bentonite were reported by various authors: Karnland et al. (2007) observed Ca-enrichment in a percolation experiment through MX-80 bentonite at ambient temperature by precipitation of C–S–H; Sánchez et al. (2006) observed increased calcite concentrations (<5%) in low and high temperature batch experiments using FEBEX bentonite; Dauzeres et al. (2010) observed calcite precipitation at a clay rock–cement interface but just on the cement side; Jenni et al. (2014) observed a Ca-enriched layer at an OPA–OPC interface along with elevated calcite concentration therein. Further, no C-S-H phase precipitation is observed as reported in previous studies even at ambient temperatures (Bouchet et al., 2004; Fernández et al., 2006; Fernández et al., 2010a; Karnland, 1997; Mosser-Ruck and Cathelineau, 2004; Ramirez et al., 2002a; Ramirez et al., 2002b).

Fe-S-enrichment occurred in two zones at ~3.3 mm and ~11.0 mm from inlet. Both zones were directly related to the front of the Ca-enrichment regions. The minerals could be identified as gypsum and an unknown iron phase, while only little pyrite was observed. If this enrichment was related to the equilibrium phase, as mentioned before, is not clear. Sulfate originates mainly from the APW_{OPA} or from gypsum dissolution, while the origin of iron is not clear. Iron was neither added to the APWs nor measured in the core outflow and only few iron mineral phases are present in raw s/b.

Mg-enrichment occurred in the clay matrix between 4.5 and 8.5 mm from inlet, overlapping in parts with the calcium and iron-sulfur enrichment zones. At current SEM resolution no newly grown mineral phase could be linked to this enrichment. EDX point analyzes of this region showed maximum amounts of 14 wt% MgO. Magnesium infiltration occurred mainly within APW_{OPA}, while APW_{OPC} contained no magnesium (Table 7-5). Magnesium got enriched in the s/b core on the clay exchanger during the equilibration phase, releasing sodium and calcium (Figure 7-4). A triangular SiO_2–Al_2O_3+Fe_2O_3–MgO plot is used for further interpretations (Figure 7-25). EDX analyses of the Mg-enriched zone plot both close to the unaltered smectite and bulk s/b field. The Mg-enriched zone plots on a line that connects unreacted smectite with saponite and brucite. The appearance of a trioctahedral smectite peak indicates the occurrence of saponite. This is in agreement to *chapter 6*, where in pure bentonite saponite was observed. Brucite could only be detected in the filter but not in the s/b core. Further the presences of hydrotalcite or M–S–H phases cannot be excluded, as they are difficult to detect in bulk XRD measurements. Magnesium released from the clay exchanger in exchange for sodium and potassium or from dissolution of smectite may form hydroxide or hydrated silicate minerals like brucite, talc or saponite. PhreeqC modeling shows that in case magnesium is available, an APW_{OPC} fluid would be strongly over-saturated with respect to these mineral phases. Such conditions are assumed to occur near the inlet, where the pore-fluid still exhibits a high pH, induced by APW_{OPC} infiltration. Several authors observed similar reactions in alkaline, high-pH experiments using bentonite: Karnland (1997) observed at ambient temperature in MX-80 bentonite increased Mg content in the clay; Ramirez et al. (2002a) observed in FEBEX bentonite the formation of a trioctahedral Mg-silicate-phase and weak montmorillonite dissolution; Nakayama et al. (2004) observed montmorillonite dissolution in a s/b (Kunigel, V1 bentonite); Cuevas et al. (2006) showed in FEBEX bentonite at 35–90°C the formation of a new trioctahedral smectite, which was determined as saponite-stevensite phase along with montmorillonite dissolution; Sánchez et al. (2006) observed in FEBEX bentonite at high temperatures (mainly >125°C) the formation of a saponite clay as well as dissolution of montmorillonite; Fernández et al. (2006) observed brucite precipitation in FEBEX bentonite along montmorillonite dissolution at ambient temperatures; Fernández et al. (2009a) observed in FEBEX bentonite at 60°C the dissolution of montmorillonite and the formation of brucite interlayer in the smectite (di-trioctahedral chlorite-like phase without a continuous and ordered intercalation of brucite); Fernández et al. (2010a) observed in FEBEX bentonite at 60°C as well dissolution of smectite and formation of a trioctahedral sheet silicate, which they described as talc; Fernández et al. (2013) observed in FEBEX bentonite at 90°C dissolution of montmorillonite at the interface as well as formation of a Mg-layer silicate-phase (di-trioctahedral chlorites). But finally it can be conclude that the crystallographic determination of saponite by XRD is difficult. Small sample volumes, intermixing with other clay phases as well as the strong quartz signal make a clear identification difficult.

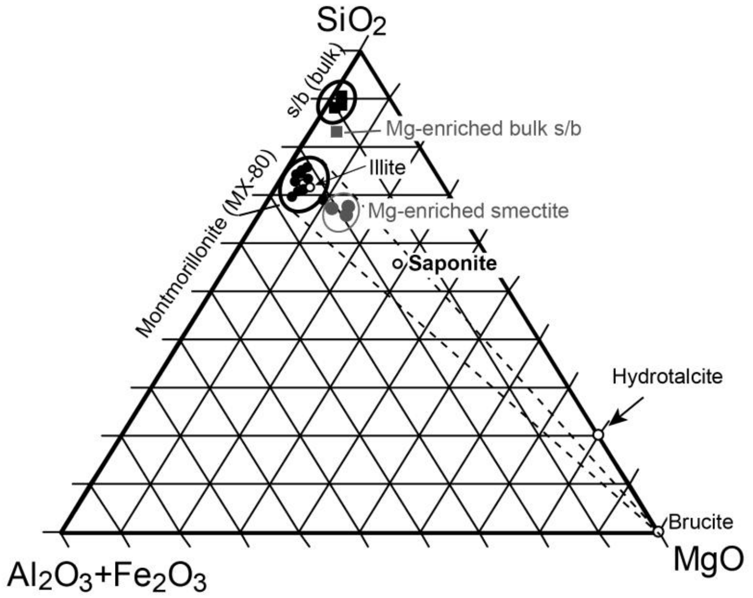

Figure 7-25: Triangular SiO_2–Al_2O_3+Fe_2O_3–MgO plot including SEM-EDX point (circle) and bulk (square) analysis of the Mg-enriched zone. MX-80 montmorillonite (Karnland, 2010), Mg-saturated montmorillonite (Karnland et al., 2006), illite (Gaines et al., 1997), beidellite (Gaines et al., 1997), saponite (Duda, 1990), hydrotalcite (Anthony et al., 1995), and magnesium silicate hydrate gel (M–S–H) (Brew and Glasser, 2005).

7.5. Conclusions

During the first 352 days of the experiment, an artificial clay pore-water was infiltrated, adapting the core to the pressure conditions of the core infiltration device. The change from uniaxial to hydrostatic (lithostatic) pressure conditions reduced the volume of the s/b core by 6 vol%. Infiltration of a high-pH fluid (APW_{OPC}) induced a core volume increase, triggered by the low ionic strength pore-water, which is the result of strong mineral alteration, occurring in the first 11 mm of the core. This expansion indicates that the s/b framework changed from mostly grain-supported to matrix-supported. The hydraulic conductivity reduction was most likely induced by mineral precipitation (calcite, saponite) in the intergranular porosity of s/b (and possibly filter) and probably partly also by osmotic effects, induced by the high ionic strength APW_{OPC}. High ionic strength fluids may reduce the interlayer and the DL, inducing core compaction at constant hydrostatic conditions, which is in agreement to compaction observed near the fluid inlet. Further it possibly reduces the intergranular porosity, in which advective fluid flow takes place and hence reduces the hydraulic conductivity.

After infiltrating 5.8 PV of artificial clay pore-water, the outflow chemistry resembled the infiltration solution with the exception of calcium, magnesium and sulfate, which were lowered, and sodium and alkalinity (mainly bicarbonate), which were increased. This indicated ongoing cation exchange reactions with sodium getting released and calcium and magnesium adsorbed, while gypsum got precipitated. SI showed under-saturation with respect to gypsum, while calcite changed from over- to under-saturation. This indicates a complex behavior of the pore-fluid and dissolution/precipitation fronts in the s/b core, whereupon it has to be assumed that the pore-fluid was not in equilibrium with the mineralogy due to a flow rate which was much higher compared to the precipitation/dissolution kinetics. The high-pH infiltration reduced the ionic strength of the outflow drastically. Potassium, sodium and hydroxide, the main ions of the cementitious solution, were strongly buffered by the s/b and the pH increased only to ~8.5. Silica and the alkalinity were both enriched in the outflow relative to the inflow, indicating dissolution of silica (cristobalite) and carbonate (calcite, organic compounds) mineral phases. Chloride got replaced as main anionic charge carrier by the alkalinity (bicarbonate) and hydroxide during the high-pH phase. The anion-accessible (based on Cl^-) porosity and therefore also the flow-active porosity (intergranular porosity) of s/b was ~30% of the initial water content, while the apparent transport porosity for water was 67%, based on δ^2H measurements.

The inlet filter showed precipitation of calcite and in minor amounts of brucite and talc, measured by XRD. The bentonite exhibited overlapping zones of Mg, Ca, and Fe-S enrichment near the solution inlet. The Ca-enriched regions consisted of newly precipitated calcite in the clay matrix. The precipitation was induced by the high-pH plume, saturating the pore-fluid with respect to calcite. The Mg-enriched regions were heterogeneously distributed in the clay matrix of the s/b, penetrating up to 9 mm into the sample. XRD data confirmed the existence of trioctahedral smectite in the reaction zone, which could be identified as saponite. The Fe-S-enriched regions are overlapping with the Ca-enriched regions and consist of small amounts of gypsums with an unknown iron phase.

The experiment attests an effective pH buffering capacity for s/b and a progressing coupled hydraulic-chemical sealing process.

Acknowledgments

Financial support from Nagra is gratefully acknowledged. The Department of Forensic Medicine at the University of Bern is acknowledged for granting access and providing technical support for operating their CT scanner. The machine shop at our institute was instrumental in constructing the experimental apparatus, and our analytical laboratory performed the IC and ICP-OES analyses. We acknowledge Klaus Wieczorek from GRS to offers us the s/b material.

References

Agus, S.S., Schanz, T., 2008. A method for predicting swelling pressure of compacted bentonites. Acta Geotechnica 3, 125-137.

Alia, J.M., Edwards, H.G., Garcia-Navarro, F.J., Parras-Armenteros, J., Sanchez-Jimenez, C.J., 1999. Application of FT-Raman spectroscopy to quality control in brick clays firing process. Talanta 50, 291-298.

Anthony, J.W., Bideaux, R.A., Bladh, K.W., Nichols, M.C., 1995. Handbook of mineralogy. Mineral Data Publishing.

Arifin, Y.F., 2008. Thermo-hydro-mechanical behaviour of compacted bentonite-sand mixtures: an experimental study, Faculty of Civil Engineering. Bauhaus-University Weimar, Weimar, Germany.

Bauer, A., Velde, B., 1999. Smectite transformation in high molar KOH solutions. Clay Minerals 34, 259-273.

Bear, J., 1973. Dynamics of Fluids in Porous Media. Elsevier, New York , USA.

Bishop, J.L., Murad, E., 2004. Characterization of minerals and biogeochemical markers on Mars: A Raman and IR spectroscopic study of montmorillonite. Journal of Raman Spectroscopy 35, 480-486.

Blacksberg, J., Rossman, G.R., Gleckler, A., 2010. Time-resolved Raman spectroscopy for in situ planetary mineralogy. Applied Optics 49, 4951-4962.

Bouchet, A., Casagnabère, A., Parneix, J.C., 2004. Batch experiments: results on MX80, in: Michau, N. (Ed.), Ecoclay II: Effect of Cement on Clay Barrier Performance Phase II. Final report. (ANDRA) European contract FIKW-CT-2000-0028, pp. 79-86.

Brew, D.R.M., Glasser, F.P., 2005. Synthesis and characterisation of magnesium silicate hydrate gels. Cement and Concrete Research 35, 85-98.

Brindley, G.W., Brown, G., 1980. Crystal Structures of Clay Minerals and Their X-ray Identification. Mineralogical Society.

Cho, W.-J., Lee, J.-O., Kang, C.-H., 2000. Hydraulic Conductivity of Sand-Bentonite Mixture for a Pentitial Backfill Material for a High-level Radioactive Waste Repository. Journal of the Korean Nuclear Society 32, 495-503.

Cuevas, J., Villar, M.V., Martı́n, M., Cobeña, J.C., Leguey, S., 2002. Thermo-hydraulic gradients on bentonite: distribution of soluble salts, microstructure and modification of the hydraulic and mechanical behaviour. Applied Clay Science 22, 25-38.

Cuevas, J., Vigil de la Villa, R., Ramírez, S., Sánchez, L., Fernández, R., Leguey, S., 2006. The alkaline reaction of FEBEX bentonite: a contribution to the study of the performance of bentonite/concrete engineered barrier systems. Journal of Iberian Geology 32 (2), 151-174.

Dauzeres, A., Le Bescop, P., Sardini, P., Cau Dit Coumes, C., 2010. Physico-chemical investigation of clayey/cement-based materials interaction in the context of geological waste disposal: Experimental approach and results. Cement and Concrete Research 40, 1327-1340.

De La Villa, R.V., Cuevas, J., Ramirez, S., Leguey, S., 2001. Zeolite formation during the alkaline reaction of bentonite. European Journal of Mineralogy 13, 635-644.

Dolder, F., Mäder, U., Jenni, A., Schwendener, N., 2014. Experimental characterization of cement–bentonite interaction using core infiltration techniques and 4D computed tomography. Physics and Chemistry of the Earth, Parts A/B/C 70–71, 104-113.

Duda, R., and Rejl, L., 1990. Minerals of the world. Arch Cape Press, New York.

Eberl, D.D., Velde, B., McCormick, T., 1993. Synthesis of illite-smectite from smectite at earth surface temperatures and high pH. Clay Minerals 28, 49-60.

Fernández, R., Cuevas, J., Sanchez, L., de la Villa, R.V., Leguey, S., 2006. Reactivity of the cement-bentonite interface with alkaline solutions using transport cells. Applied Geochemistry 21, 977-992.

Fernández, R., Mäder, U., Rodríguez, M., de la Villa, R.V., Cuevas, J., 2009. Alteration of compacted bentonite by diffusion of highly alkaline solutions. European Journal of Mineralogy 21, 725-735.

Fernández, R., Rodríguez, M., de la Villa, R.V., Cuevas, J., 2010. Geochemical constraints on the stability of zeolites and C-S-H in the high pH reaction of bentonite. Geochimica et Cosmochimica Acta 74, 890-906.

Fernández, R., Vigil de la Villa, R., Ruiz, A.I., García, R., Cuevas, J., 2013. Precipitation of chlorite-like structures during OPC porewater diffusion through compacted bentonite at 90°C. Applied Clay Science 83–84, 357-367.

Fernández, R., Ruiz, A.I., Cuevas, J., 2014. The role of smectite composition on the hyperalkaline alteration of bentonite. Applied Clay Science 95, 83-94.

Ferrage, E., Lanson, B., Sakharov, B.A., Drits, V.A., 2005. Investigation of smectite hydration properties by modeling experimental X-ray diffraction patterns. Part I. Montmorillonite hydration properties. Mineralogical Society of America, Washington, DC, USA.

Gaines, R.V., Skinner, H.C.W., Foord, E.E., Rosenzweig, A., 1997. Dana's New Mineralogy, Eighth Edition ed. John Wiley & Sons, New York.

Gaucher, E.C., Blanc, P., 2006. Cement/clay interactions - A review: Experiments, natural analogues, and modeling. Waste Management 26, 776-788.

Gaus, I., Garitte, B., Senger, R., Gens, A., Vasconcelos, R., Garcia-Sineriz, J.-L., Trick, T., Wieczorek, K., Czaikowski, O., Schuster, K., Mayor, J.C., Velasco, M., Kuhlmann, U., Villar, M.V., 2014. The HE-E Experiment: Lay-out, Interpretation and THM Modelling. Nagra Working Report, Nagra, Wettingen, Switzerland.

Jenni, A., Mäder, U., Lerouge, C., Gaboreau, S., Schwyn, B., 2014. In situ interaction between different concretes and Opalinus Clay. Physics and Chemistry of the Earth, Parts A/B/C 70–71, 71-83.

Karnland, O., 1997. Cement/bentonite interaction: results from 16 month laboratory tests. SKB Technical Report 97-32, Stockholm, Sweden.

Karnland, O., 2004. Laboratory experiments concerning compacted bentonite contacted to high-pH solutions, in: Michau, N. (Ed.), Ecoclay II: Effect of Cement on Clay Barrier Performance Phase II. Final report. (ANDRA) European contract FIKW-CT-2000-0028.

Karnland, O., Olsson, S., Nielsson, U., 2006. Mineralogy and sealing properties of various bentonites and smectite-rich clay materials. SKB Technical Report 06-30, Stockholm, Sweden.

Karnland, O., Olsson, S., Nilsson, U., Sellin, P., 2007. Experimentally determined swelling pressures and geochemical interactions of compacted Wyoming bentonite with highly alkaline solutions. Physics and Chemistry of the Earth, Parts A/B/C 32, 275-286.

Karnland, O., Olsson, S., Dueck, A., Birgersson, M., Nilsson, U., Hernan-Håkansson, T., Pedersen, K., Nilsson, S., Eriksen, T., Rosborg, B., 2009. Long term test of buffer material at the Äspö Hard Rock Laboratory, LOT project. Final report on the A2 test parcel. SKB Technical Report 09-29, Stockholm, Sweden.

Karnland, O., 2010. Chemical and mineralogical characterization of the bentonite buffer for the acceptance control procedure in a KBS-3 repository. SKB Technical Report 10-60, Stockholm, Sweden.

Kawaragi, C., Yoneda, T., Sato, T., Kaneko, K., 2009. Microstructure of saturated bentonites characterized by X-ray CT observations. Engineering Geology 106, 51-57.

Lancaster, J.L., Martinez, M.J., 2007. Mango - Multi-image analysis GUI. Research Imaging Institute, UT Health Science Center at San Antonio, TX, USA, URL: http://ric.uthscsa.edu/mango/index.html.

Lothenbach, B., Winnefeld, F., 2006. Thermodynamic modelling of the hydration of Portland cement. Cement and Concrete Research 36, 209-226.

Mäder, U., 2009. Reference pore water for the Opalinus Clay and "Brown Dogger" for the provisional safety-analysis in the framework of sectoral plan - interim results (SGT-ZE). Nagra Working Report, Nagra, Wettingen, Switzerland.

Moore, D.M., Reynolds, R.C., 1989. X-ray diffraction and the identification and analysis of clay minerals. Oxford University Press, New York.

Mosser-Ruck, R., Cathelineau, M., 2004. Experimental transformation of Na,Ca-smectite under basic conditions at 150 °C. Applied Clay Science 26, 259-273.

Nagra, 2002. Demonstration of disposal feasibility for spent fuel, vitrified high-level waste and long-lived intermediate-level waste (Entsorgungsnachweis). Nagra Technical Report NTB 02-05, Nagra, Wettingen, Switzerland.

Nakayama, S., Sakamoto, Y., Yamaguchi, T., Akai, M., Tanaka, T., Sato, T., Iida, Y., 2004. Dissolution of montmorillonite in compacted bentonite by highly alkaline aqueous solutions and diffusivity of hydroxide ions. Applied Clay Science 27, 53-65.

Olsson, S., Karnland, O., 2011. Mineralogical and chemical characteristics of the bentonite in the A2 test parcel of the LOT field experiments at Äspö HRL, Sweden. Physics and Chemistry of the Earth, Parts A/B/C 36, 1545-1553.

Ramirez, S., Cuevas, J., de la Villa, R.V., Leguey, S., 2002a. Hydrothermal alteration of La Serrata bentonite (Almeria, Spain) by alkaline solutions. Applied Clay Science 21, 257– 269.

Ramirez, S., Cuevas, J., Petit, S., Righi, D., Meunier, A., 2002b. Smectite reactivity in alkaline solutions. Geologica Carpathica 53, 87-92.

Revil, A., Grauls, D., Brévart, O., 2002. Mechanical compaction of sand/clay mixtures. American Geophysical Union, Washington, DC, USA.

Rothfuchs, T., Jockwer, N., Zhang, C.-L., 2007. Self-sealing barriers of clay/mineral mixtures – The SB project at the Mont Terri Rock Laboratory. Physics and Chemistry of the Earth, Parts A/B/C 32, 108-115.

Rothfuchs, T., Czaikowski, O., Hartwig, L., Hellwald, K., Komischke, M., Miehe, R., Zhang, C.-L., 2012. Self-bealing barriers of sand/bentonite-mixtures in a clay repository. GRS Technical report 302, Braunschweig, Germany.

Saba, S., Delage, P., Lenoir, N., Cui, Y.J., Tang, A.M., Barnichon, J.-D., 2014. Further insight into the microstructure of compacted bentonite–sand mixture. Engineering Geology 168, 141-148.

Sánchez, L., Cuevas, J., Ramírez, S., Riuiz De León, D., Fernández, R., Vigil Dela Villa, R., Leguey, S., 2006. Reaction kinetics of FEBEX bentonite in hyperalkaline conditions resembling the cement–bentonite interface. Applied Clay Science 33, 125-141.

Schindelin, J., Arganda-Carreras, I., Frise, E., Kaynig, V., Longair, M., Pietzsch, T., Preibisch, S., Rueden, C., Saalfeld, S., Schmid, B., Tinevez, J.-Y., White, D.J., Hartenstein, V., Eliceiri, K., Tomancak, P., Cardona, A., 2012. Fiji: an open-source platform for biological-image analysis. Nat Meth 9, 676--682.

8

Alteration of sand/bentonite backfill material by ‘low-pH’ shotcrete (ESDRED) fluid – An experimental approach using core infiltration techniques

8.1. Introduction

In a deep geological repository high-level nuclear waste will be stored in emplacement tunnels, protected by a multiple engineered barriers system (EBS) (Nagra, 2002). The main part of the EBS consists in the emplacement tunnels for high-level nuclear waste (HLW) of bentonite, while in access galleries and drift seals a mixture of sand and bentonite (s/b) will be used (Nagra, 2002). Bentonite and s/b have been proposed as EBS component by its physical and chemical properties like low permeability, high swilling capacity and high ion adsorption capacity.

Cement-based materials as tunnel reinforcement, tunnel plugs/seals of as buffer material of low- and intermediate-level nuclear waste may affect the performance of the EBS (Nagra, 2002). Pore-water emanating from OPC (ordinary Portland cement) cement, mortar or concrete induces a high-pH reaction plume (pH >13) that may affect the chemical and physical properties of the clay-based EBS. A possible alternative to OPC is the use of 'low-pH' (pH ≤11) and low-alkalinity cement/shotcretes, consisting of Portland cement (PC), water and silica fume (SF), blast furnace slag or fly ash (García Calvo et al., 2010; Lothenbach et al., 2013; Lothenbach et al., 2011). In the following study, a low-alkali shotcrete mixture called ESDRED will be used, consisting of 60 wt% CEM I PC blended with 40 wt% SF and aluminum-sulfate and aluminum-formate as set accelerator. The mixture was originally developed for the EU-project Engineered Studies and Demonstration of Repository Designs (ESDRED) (Bäckblom, 2007; García Calvo et al., 2010; Lothenbach et al., 2013).

Various studies analyzed the effect of 'low-pH', mature cementitious solutions (pH ~12.5) on clay material, consisting mainly of Ca^{2+} and OH^- (Fernández et al., 2010a; Fernández et al., 2013; Karnland et al., 2007; Mosser-Ruck and Cathelineau, 2004; Ramirez et al., 2002a). The reactivity of such fluids in clay was reported to be low at ambient as well as increased temperatures. Only precipitation of C–S–H phases and cation exchange processes were observed, while the primary mineralogy and the swelling pressure were not affected. Lothenbach et al. (2013) showed in hydration experiments using ESDRED cement a pore-water chemistry dominated on the cationic charge by Ca^{2+}, Na^+ and K^+ whereas the anionic charge was on formate (C_{org}) and OH^-. Savage and Benbow (2007) modeled the influence of 'low-pH' cement on bentonite, pointing to the following constraints: the effect of a lower pH on secondary mineral formation is unknown, change in the aqueous speciation of silica at lower pH may have an impact on the montmorillonite stability, reduction in porosity is likely to happen at the interface but how this may influence transport processes is unclear. Berner et al. (2013) modeled the influence of ESDRED pore-fluids on clay formations and bentonite. The modeling showed for bentonite a reduction in porosity directly at the interface along with precipitation of various amounts of calcite, hydro-magnetite and hydrotalcite.

This work summarizes a core infiltration experiment using a compacted and saturated 65/35% sand/MX-80 bentonite core sample and a 'low-pH' cement solution (pH 11.7) that mimics an ESDRED shotcrete pore-fluid after full hydration. CT measurements allowed tracking density/volume changes over time, while SEM, XRD, Raman spectroscopy and optical microscopy were used for post-mortem characterization.

8.2. Methods and material

8.1.1. Core infiltration experiment

Our experimental approach used a core infiltration method to study the effect of high-pH fluid infiltration (infiltration pressure) on a s/b core sample, exposed to lithostatic/hydrostatic pressure conditions (confining pressure). A detailed description of the method is given in *chapters 2 & 4*. A s/b core of 44.5 mm length and furnished with 2 filters on either side was confined and a hydraulic gradient applied to drive a small dispersive-advective flux from inflow to outflow.

During the first 56 days (equilibration phase), the s/b core had time to equilibrate to the new pressure conditions using artificial clay pore-water (APW_{OPA}). The following 242 days artificial 'low-pH' shotcrete pore-water (APW_{ESDRED}) was infiltrated (high-pH phase). After stopping, dismantling and unpacking the experiment, the s/b core was measured (length, diameter, mass) and sectioned. Two longitudinal samples of 2×4.3×1 cm (Figure 8-1; XRD and SEM samples) were cut along the center and freeze-dried. The sample for SEM (scanning electron microscope) analysis was vacuum impregnated with resin and polished with ethanol. The XRD sample was cut into 12 subsamples of 1–6 mm thickness perpendicular to the sample axis. The rest of the core was cut into two longitudinal profiles for water content and density (ρ) measurements, 5 samples each. Two profiles were located at the outer surface of the core (subscript: rim) and two profiles at 1 cm off-axis (subscript: cen) (see Figure 8-1). The filters were immersed in isopropyl alcohol and dried in a N_2 filled desiccator.

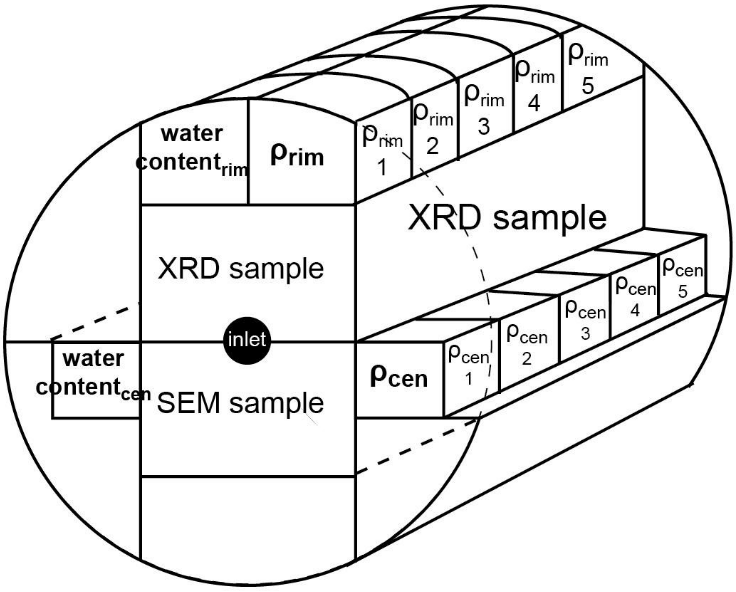

Figure 8-1: Post-mortem s/b core cutting pattern of the s/b (s/b-CT 4).

8.1.2. Analytical methods

The collected outflow was analyzed for the following parameters: ion concentrations by ion chromatography (IC), alkalinity by titration, minor and trace elements by ion coupled plasma atomic emission spectroscopy (ICP-OES), organic and inorganic carbon content by TOC/TN (multi N/C 2100s with a NDIR detector from Analytik Jena), pH, and electrical conductivity. δ^2H isotope ratios were measured using a Picarro cavity ring-down spectrometer (L2130-i).

Density and water content were determined post-mortem in the laboratory. The mineralogy was determined by X-ray diffraction (XRD) on disoriented, preconditioned (33 %rh) powder samples. All XRD spectra were normalized on the 3.34 Å peak of quartz. Additional samples were measured saturated with ethylene-glycol (EG). Scanning electron measurements (SEM) were performed on uncoated sample surfaces, while energy dispersive spectroscopy (EDX) was used for elemental analyses of points and areas (1.7×1.3 mm) as well as element maps. Raman spectroscopy was used for mineral identification.

The X-ray computed tomography (CT) were performed on medical CT scanners (Siemens Somatom Emotion 6 and Siemens Somatom Definition AS), operated both by the Institute of Forensic Medicine at the University of Bern. In total 5 scans were performed during the experiment, 1 on the first machine and 4 on the second after replacement of the original machine. The generated X-ray energy was 130 keV (polychromatic X-ray beam) with an X-ray tube current of 120 mA for the first scanner and 140 keV and 140 mA for the second. The voxel dimension of the recorded dataset was 0.109×0.109×0.5 mm for the first CT scanner and 0.107×0.107×0.5 mm for the second. The change of the CT scanners made a direct comparison of the different datasets difficult. The data were processed and analyzed using the open-source software Mango (Multi-Image Analysis GUI, Lancaster and Martinez (2007)) and Fiji, an open-source image processing software package based on ImageJ (Schindelin et al., 2012). A detailed description of all analytical methods is given in *chapters 4 & 5*, including specifications and parameters.

8.1.3. Starting material and pre-treatment

Granular s/b of 65% sand and 35% MX-80 bentonite was used (65/35 s/b), provided by MPC, Limay, France. The identical material was used in the context of the PEBS project (long-term performance of engineered barrier systems) in the HE-E (heater test) experiment in Mont Terri Rock Laboratory in St-Ursanne, Switzerland (Gaus et al., 2014). The s/b consists of MX-80 bentonite (GELCLAY WH2) mixed with quartz sand (TH1000). The sand grains have a grain spectrum of 0.5–1.8 mm, which is similar to that of the bentonite powder (Gaus et al., 2014; Rothfuchs et al., 2012). MX-80 bentonite consists of Na-montmorillonite (81–85 wt%), feldspars (~5 wt%), quartz (~3 wt%), muscovite (~3 wt%), gypsum (~1 wt%), cristobalite (~1 wt%) and calcite (~0.2 wt%) (Karnland, 2010). S/b has the following calculated composition: quartz (~66 wt%), Na-montmorillonite (~31 wt%), feldspars (~2 wt%), muscovite (~1 wt%), gypsum (~0.4 wt%), and calcite (~0.01 wt%). The s/b sample was compacted and saturated in a pre-treatment device (*chapter 2*) using 157.6 g of dry powder with a residual water content of 3.6 wt%, corresponding to 27.8 g of pore-water after saturation (w/s ratio 0.18) (Dolder et al., 2014). This amount corresponds to one pore-volume (PV) used to convert transport time to number of PV flowing through the core. The pre-treatment procedure, described in *chapters 2 and 4*, was adapted to the s/b by performing the compaction and saturation procedure in one step, due to the low cohesion of the material. The saturated s/b core was 50 mm in diameter, 44.5 mm in length and had a wet mass of 179.8 g, corresponding to a saturated density of 2081 kg/m^3 (1759 kg/m^3) and a water-content per dry mass of 18.3 wt%. The core had a porosity of 34% and showed a degree of saturation of 89%. The measured grain density of s/b was 2650 kg/m^3, which is slightly lower compared to 2700 kg/m^3, measured by Gaus et al. (2014). The bentonite in the s/b mixture had a dry density of 1082 kg/m^3, which is in agreement to Agus and Schanz (2008). This corresponds to a swelling pressure of 0.3–0.5 MPa, which is approximately half of that to be expected of pure MX-80 bentonite (Agus and Schanz, 2008; Karnland, 2010).

8.1.4. The infiltration fluids (APW$_{\text{Äspö}}$, APW$_{\text{OPA}}$ and APW$_{\text{ESDRED}}$)

The s/b core was saturated using an artificial groundwater from Äspö underground laboratory in Sweden (APW$_{\text{Äspö}}$; Tables 8-1 and 8-2) (Dolder et al., 2014; Karnland et al., 2009). The s/b was equilibrated using APW$_{\text{OPA}}$, a pore-water from the Opalinus Clay Formation (Tables 8-1 and 8-2) (Dolder et al., 2014; Mäder, 2009). APW$_{\text{ESDRED}}$ was an artificial 'low-pH' shotcrete pore-water, consisting mainly of sodium, calcium and formate (Table 8-1). A detailed description is given in *chapter 6*. The measured chloride in the APW$_{\text{ESDRED}}$ was most likely an artefact of sample preparation, as it was no more detected at the end of the experiment (Table 8-1). Saturation indices (SI) and ionic strengths of all fluids are shown in Table 8-4.

Table 8-1: Artificial pore-fluids used in the current infiltration experiment (error of major ion concentrations: 5%, up to 20% for low concentrations; error δ^2H: <4‰); unkn.: not measured; -: below detection limit.

	APW$_{\text{Äspö}}$[1]	**APW$_{\text{OPA}}$**[2]		**APW$_{\text{ESDRED}}$**	
	fluid	start	end	start	end
pH	7.2	7.6	7.6	11.70	11.60
δ^2H [‰]	-81.5	-81.6		267	
		--[mM]--			
Na$^+$	88.2	170.2	157.90	24.08	16.57
K$^+$	< 1.3	2.7	2.76	12.60	8.70
Ca^{2+}	54.3	12.36	11.38	26.00	17.60
Mg^{2+}	< 2.1	9.36	8.52	<0.4	<0.4
Si^{4+}	-	<0.007	-	0.074	unkn.
Al^{3+}	-	0	-	0.001	unkn.
Cl$^-$	203.6	157.4	151.90	9.80	<0.05
SO$_4^{2-}$	1.8	22.7	22	4.24	1.46
HCO$_3^-$	0.24	0.66	unkn.	0.31 (DIC)	unkn.
Formate	-	-	-	66.13	79.60
DOC	-	-	-	86.2	unkn.

[1]Karnland et al. (2009), [2] Mäder (2009)

Table 8-2: Recipes of all artificial pore-waters.

Ingredients **Solids**	**Producer and no.**	**M (mfw)**	**APW$_{\text{Äspö}}$** g/l	**APW$_{\text{OPA}}$** g/l	**APW$_{\text{ESDRED}}$** g/l
$Al_2(SO_4)_3$ 16×H_2O	Fluka: 06421	630.4			0.000
KCl	Merck: 1.04936	74.6	19.57	0.190	
K_2SO_4	Merck: 1.05153	174.3			0.383
KOH	Merck: 1.05033	56.1			0.303
KCHOO	Sigma-Aldrich: 294454-25G	84.1			0.354
Na_2SO_4	Merck: 1.06649	142.0	249.87	3.409	
NaCl	Merck: 1.06404	58.4	5164.24	6.736	
Na_2CO_3	Merck: 6398	106.0	10.27		
NaCHOO	Merck: 1.06443.0500	68.0			1.699
$NaHCO_3$	Fluka: 71329	84.0		0.046	
NaBr	Fluka: 71329	102.9	15.35		
NaOH	Merck: 1.06498	40.0			
$MgCl_2$ 6×H_2O	Merck: 1.05833	203.3	334.83	1.864	
$CaCl_2$ 2×H_2O	Merck: 1.02382	147.0	8253.03	1.751	
$Ca(OH)_2$	Merck: 1.02047	74.1			
$CaCO_3$	Merck: 1.02066	100.1			
$Ca(CHOO)_2$	Sigma-Aldrich: 21134-250G-F	130.1			3.513
$SrCl_2$ 6×H_2O	Fluka: 85892	266.62	121.41		
Solution					ml/l
$Na_2O_7Si_3$	Sigma-Aldrich: 338443-1				0.007

8.2. Results

8.2.1. Physical and hydraulic evolution of the experiment

The experiment duration was 298 days. In total 2.8 PV were flushed through the core; 0.7 PV APW$_{\text{OPA}}$ and 2.1 PV APW$_{\text{ESDRED}}$. The temperature varied between 19.5°C in winter and 23°C in summer times (Figure 8-2A). The confining fluid pressure was step-wise increased to 1.75 MPa and decreased continuously thereafter to 1.7 MPa (Figure 8-2A). The infiltration fluid pressure was set to 0.11 MPa and increased to 0.19 MPa after 41 days. During the high-pH infiltration period, the infiltration fluid pressure dropped to 0.17 MPa.

The hydraulic conductivity shown in Figure 8-2B was based on averages of 4 single water-level measurements on syringes at the fluid outflow, with time spans of 2–4 weeks. The calculation of the hydraulic conductivity was based on Darcy's law (*chapter 4*). The hydraulic conductivity decreased during the equilibration phase to 3.7×10^{-12} m/s (Figure 8-2B). Switching to APW$_{\text{ESDRED}}$ increased initially the hydraulic conductivity to 8.0×10^{-12} m/s, followed by a decrease to $\sim4.0\times10^{-12}$ m/s. The increased hydraulic conductivity directly after switching fluids was either a result of gas in the outflow (Figure 8-3) or a slightly higher infiltration fluid pressure in the mobile fluid infiltration tank, used during CT scanning. The final increase in hydraulic conductivity was related to the pressure release at the end of the experiment. The permeability of s/b was 3.3×10^{-19} m^2 at the end of the equilibration phase and 3.6×10^{-19} m^2 during the high-pH infiltration phase, based on a measured fluid density of 1019 kg/m^3.

The electrical conductivity decreased dramatically during the high-pH infiltration from 22.3 mS/cm to 4.3 mS/cm (Figure 8-2B).

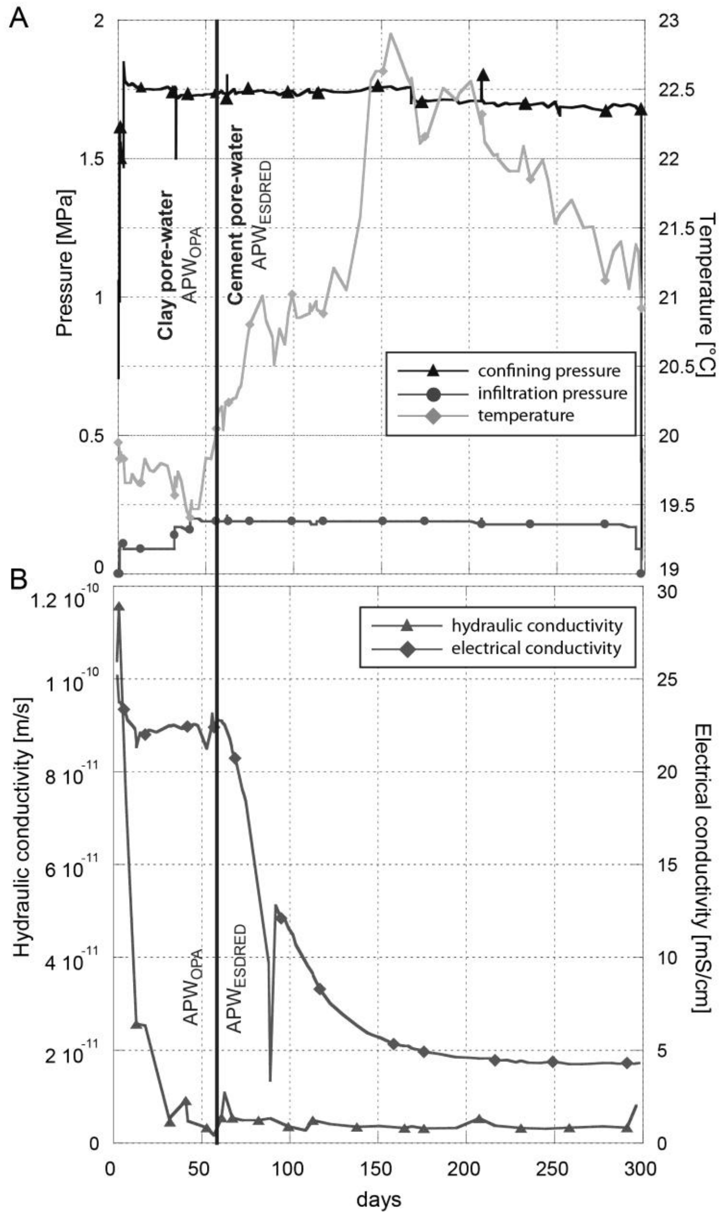

Figure 8-2: Physical parameters of the core infiltration experiment: (A) pressure of infiltration and confining fluid as well as temperature; (B) hydraulic and electrical conductivity.

Two main phases (phase A and B) of gas release were observed in the outflow (Figure 8-3). Phase A lasted for the first 3 days of the experiment and in total ~8.1 ml of gas were accumulated in the outflow. Phase B occurred between 67 and ~95 days (0.2–0.5 PV_{ESDRED}) of infiltration and 15.5 ml of gas were accumulated.

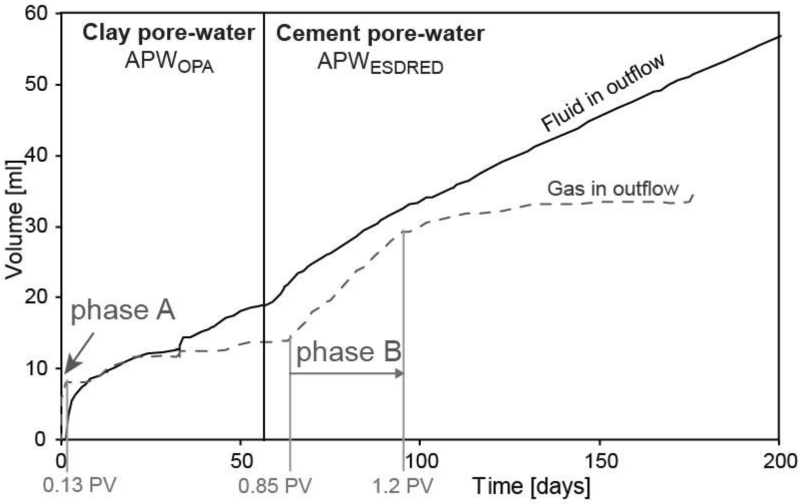

Figure 8-3: Cumulative gas and water outflow evolution.

8.2.2. Chemical evolution of the outflow

22 outflow aliquots were collected in syringes of 2.5–10 ml volume; 5 syringes during the equilibration phase and 17 during the high-pH phase. The average solution-loss in the syringes before and after cold storage was between 1–2 mg, corresponding to 0.01–0.05 vol%. Samples were analyzed for the aqueous constituents and pH (Figures 8-4 and 8-5). The alkalinity was measured in 8 aliquots, trace elements in 5 aliquots and the carbon content in one aliquot during the equilibration phase. The pH of the bulk solution was initially 6.5 and increased during the equilibration phase to 7.5. The initial pH seemed to be lowered by atmospheric gas (CO_2), present in the core packing at the beginning of the experiment.

The outflow approached the APW$_{OPA}$ composition during the equilibration phase; reduction in all ion concentrations was observed with the exception of sulfate and hydroxide (pH). At the end of the equilibration phase, the outflow showed the following trend relative to APW$_{OPA}$: K^+, SO_4^{2-}, OH^- (pH), and alkalinity were equal to APW$_{OPA}$, Mg^{2+} was enriched, while Ca^{2+}, Na^+ and Cl^- were depleted. During the equilibration phase, 4.1±0.2 mM C_{org} and <1.9 mM C_{inorg} were measured in the outflow, indicating that possibly half of that of the alkalinity was organic origin.

High-pH infiltration strongly reduced ion concentrations, with the exception of OH^- (pH), alkalinity and Si^{4+}. Chloride, as main negative charge carrier got replaced intermittently by formate followed by acetate after 1.2 PV$_{ESDRED}$. The alkalinity increased after 0.2 PV$_{ESDRED}$, formate after 0.4 PV$_{ESDRED}$ and acetate after 0.6 PV$_{ESDRED}$. The outflow concentration showed relative to APW$_{ESDRED}$ enrichment in silica, acetate and alkalinity, while potassium, calcium, sulfate, hydroxide (pH), formate and aluminum were depleted. Formate, the main negative charge carrier of APW$_{ESDRED}$, was measured in the outflow only between 0.4 and 0.7 PV$_{ESDRED}$. Ammonium, bromide, fluoride and nitrate were mostly below or near the detection limit.

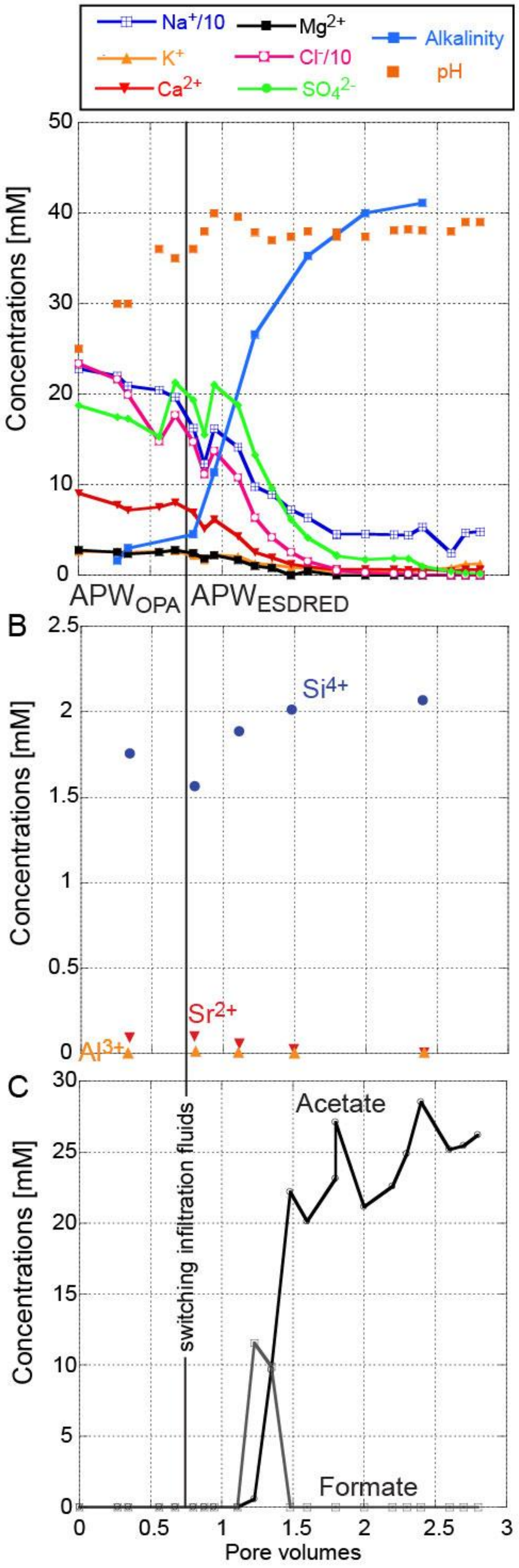

Figure 8-4: Chemical evolution of the outflow chemistry: (A) main ions, alkalinity and pH; (B) trace elements; (C) organic acids.

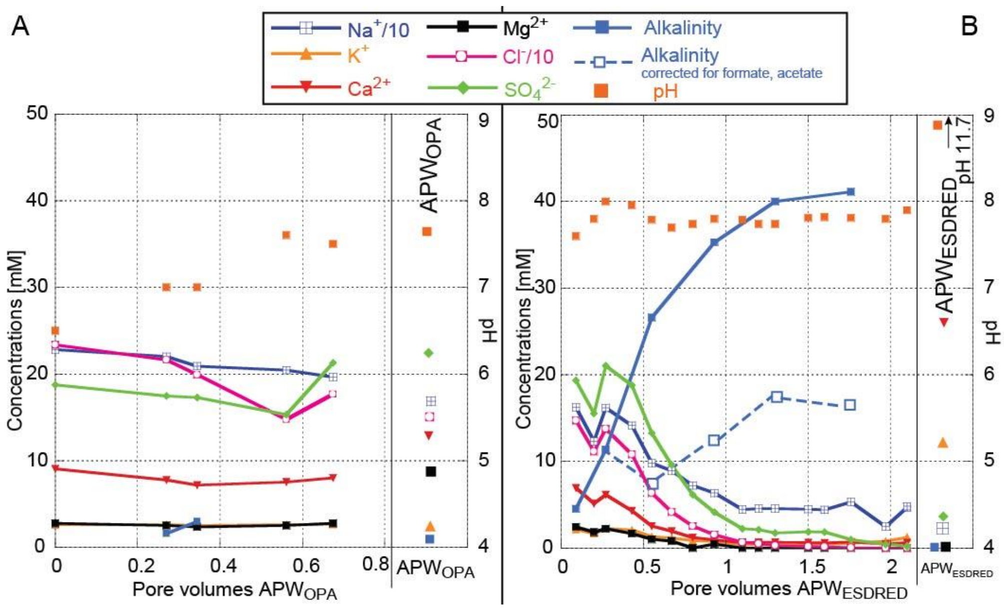

Figure 8-5: Detailed plot of the outflow chemistry: (A) equilibration phase with APW$_{OPA}$ infiltration; (B) high-pH phase with APW$_{ESDRED}$ infiltration.

The chloride breakthrough occurred after ~1 PV$_{ESDRED}$, while δ^{2}H did not show a breakthrough at current time scale (Figure 8-6). The δ^{2}H curve showed an initial plateau of ~0.2 PV, while the half-height of the breakthrough curve was reached after 0.85 PV.

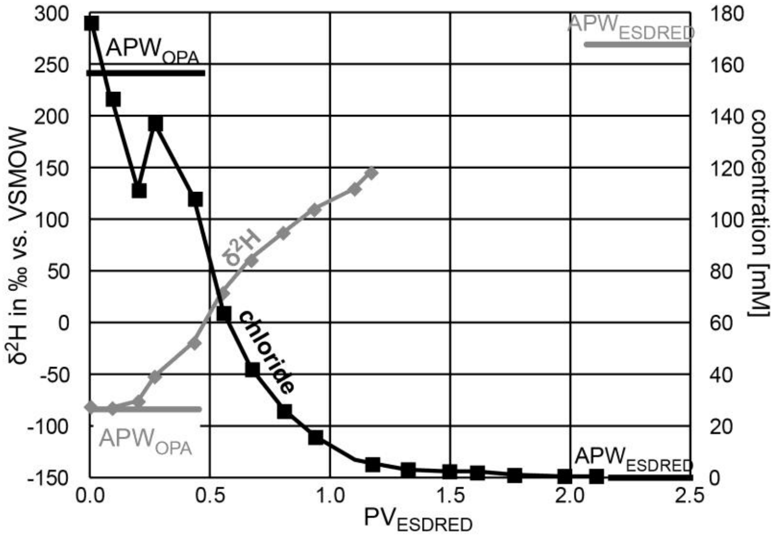

Figure 8-6: δ^{2}H and chloride breakthrough curve during the high-pH phase.

8.2.3. Computed tomography (CT)

The calculations of core volumes were based on the HU histograms of each dataset (see *chapter 3*). The experimental setup was segmented and a region of interest (ROI) was defined for s/b. The voxels were counted and multiplied by the voxel dimensions (see *section 8.1.2*). For the first CT scanner the ROI was 1000–3055 HU and 1123–3055 HU for the second. The different measurement parameters of the two CT scanners required two different ROI (*chapter 3*). The ROI used for the second CT scanner was obtained by fitting the core volume/diameter data of the second scanner to the one of the first scanner using the scans after 0 and 6 days of APW$_{ESDRED}$ infiltration. The change of CT scanners induced a significant error in all datasets, making interpretation of volume and diameter evolution difficult. The bulk core density is linearly dependent to the HU. The color code of tomographic images is the following: bright shades represent low X-ray attenuations (HU) or densities and dark shades high attenuations (*chapters 3 & 4*). The uncertainty of the calculated absolute volumes was ~1 vol%. In the comparison between the initial core volume and the first CT based volume, the uncertainty of the measurements is even higher, as two different methods were used. The absolute volumes shown in Figure 8-7 have to be considered with caution, as volume calculations in s/b are difficult to perform due to the heterogeneity of the material and measurement artifacts like core hardening.

The pre-experimental core volume was 86.4 cm^3, based on measured core length and diameter. After applying a confining fluid pressure of 1.75 MPa, the core volume decreased by ~3 vol%. The APW$_{ESDRED}$ infiltration induced small core expansion by ~0.7 vol% (Figure 8-7).

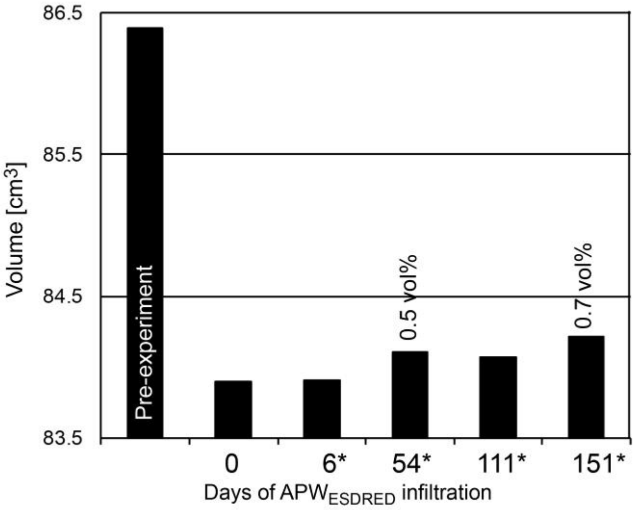

*Figure 8-7: S/b core volumes calculation based on CT scan datasets. * second CT scanner (Siemens Somatom AS).*

The core diameter calculations were performed the same way as the volume calculations (*chapter 3*). In doing this for all CT-slices of a dataset, the evolution of the core sectional area and the core diameter over time could be evaluated along the core axis (Figure 8-8B). The APW$_{ESDRED}$ infiltration induced a diameter increase near the inlet and in the middle parts of the s/b core, while no change was observed at the outlet (Figure 8-8B). The curve after 151 days of APW$_{ESDRED}$ infiltration showed a slightly different trend, which is assumed to be an artefact of the internal data processing (different CT scanner).

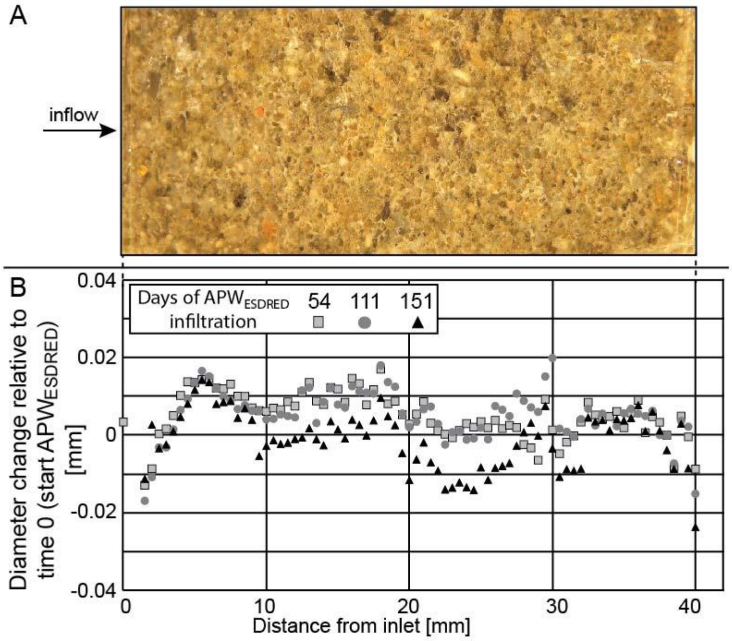

Figure 8-8: Core diameter based on CT image calculation: (A) optical image of the s/b core; (B) diameter evolution of the core relative to day 0.

Tomographic cross-sections of the s/b core at time 0 (equilibration phase) showed a material with bright grains of quartz, in a bentonite matrix, exhibiting lower attenuation and hence darker shades. A zone of increased X-ray attenuation was observed after 54 days of APW$_{ESDRED}$ infiltration in the inlet filter and got more pronounced over time (Figure 8-9). After 151 days this zone had a diameter of 6 mm, penetrating into the first 1 mm of the s/b core.

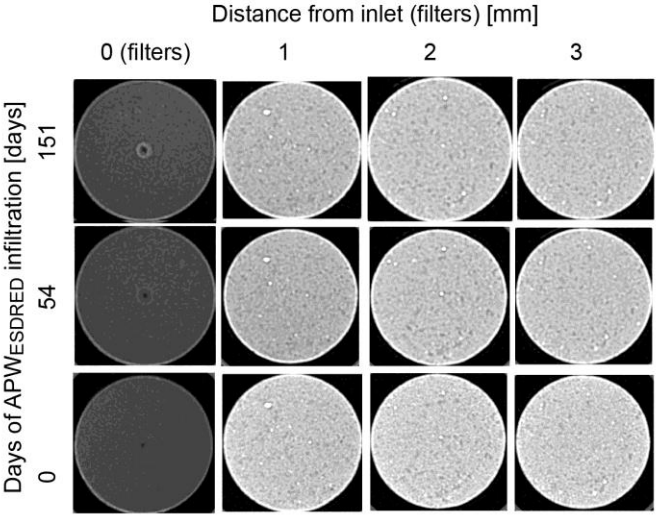

Figure 8-9: CT images of the interface inlet filter–s/b core after 0, 54 and 151 days of APW$_{ESDRED}$ infiltration.

8.2.4. Post-mortem analysis: physical parameters

The two dried inlet filters gained 35 mg of weight whereas the outlet filters lost 11 mg. As the outlet filter was still intact, it has to be assumed that the loss of weight was rather a measurement artefact. The s/b core weighed 178.63 g at the end in wet condition, which is a loss of 1.13 g. The core length was 41.84 mm, shrunk by 2.67 mm. The core diameter was 51.4 mm near the inlet, 52.4 mm in the middle part and 51.5 mm near the outlet. The water content showed in both profiles lower values in the middle part of the core, with higher values at the rim. The saturated density was in both profiles near constant values with reduced values at the core rim. The measured porosities were between 32.5% and 33.8%. The degree of saturation varied between 0.82 and 0.94. The dry bentonite density varied between 1.09 g/cm^3 and 1.11 g/cm^3, based on the formula of Agus and Schanz, 2008 (*chapter 7*).

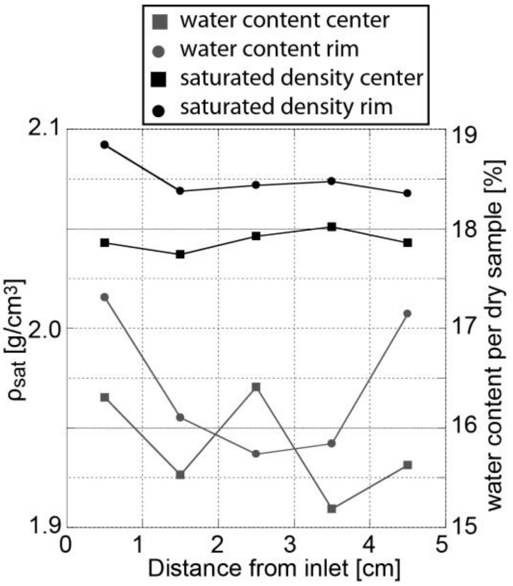

Figure 8-10: Saturated density and water content profiles in the s/b core.

8.2.5. XRD analysis

The XRD spectrum of s/b showed the following major minerals: quartz (2.12, 2.45, 3.34, 4.25 Å), montmorillonite (11–12 Å (001), 8.48 Å (002), 5.63 Å (003)), cristobalite (4.0 Å), alkali and plagioclase feldspar (3.1–3.2 Å), muscovite and/or illite (9.98 Å), gypsum (7.58 Å), and calcite (3.0 Å) (Figures 7-11 & 8-12). Variations in the (001) montmorillonite reflection resulted from different hydration states and cation occupancy. The differentiation of di- and trioctahedral sub-groups of smectite was done on the (060) reflection (Brindley and Brown, 1980). Peaks at ~1.49 Å are related to dioctahedral and peaks at ~1.52 Å to trioctahedral smectites. The °Δ2Θ((003) - (002)) of EG saturated samples may be used to identify illite/smectite (I/S) interlayers (Moore and Reynolds, 1989). Quartz exhibited in s/b much stronger intensities compared to other minerals, masking reflections and made a proper identification of the (001) smectite peaks difficult.

The (001)-spacing of the raw s/b was 11.39 Å, which is a characteristic value for a smectite saturated with monovalent cations (Ferrage et al., 2005) (Figure 7-11). The s/b sample had a (060) reflection at 1.499 Å, which is characterized for a dioctahedral smectite (e.g. montmorillonite). The EG saturated sample had a (001) peak at 16.9 Å, (002) peak at 8.48 Å, and a (003) peak at 5.63 Å, corresponding to a °Δ2Θ((003) - (002)) of 5.34°, which is after (Moore and Reynolds, 1989) a pure montmorillonite with no I/S. $\text{APW}_{\text{Äspö}}$ and APW_{OPA} saturation s/b showed a similar pattern to raw s/b with stronger gypsum peaks, which are interpreted as an artefact of sample drying.

All filters showed a broad hump of amorphous material 4.0 Å from the PVC-filter material (Figure 8-11). Quartz, smectite and feldspar were detected on the clay side of both filter pairs. The (001)-spacing of smectite was at 12.3 Å in both filter pairs. The inlet filter had further peaks at 1.519 Å and 1.522 Å, which are related to trioctahedral smectite like saponite. The 1.52 Å calcite peak was just observed in the inlet filter.

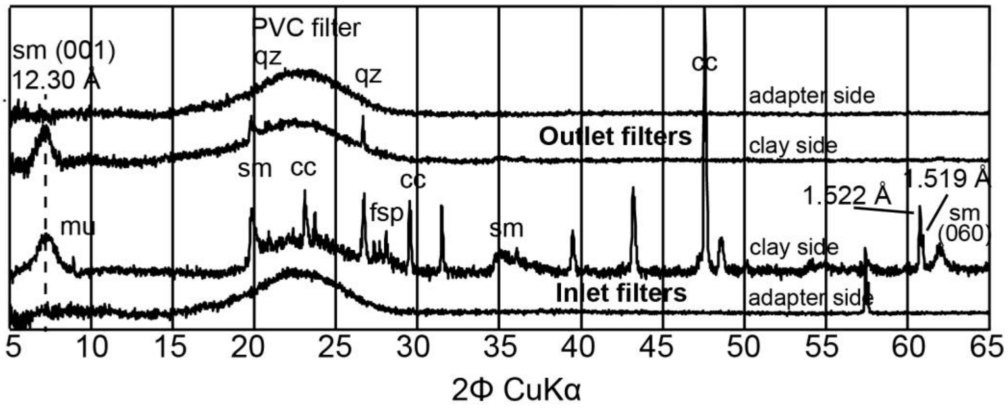

Figure 8-11: XRD spectra of the inlet filters and the outlet filters. Sm: smectite; qz: quartz, fsp: feldspar; mu: muscovite; cc: calcite.

XRD measurements of the core showed strong quartz reflections, with strong intensity variations, which originated most likely from sample preparation (Figure 8-12). The (001) reflection of smectite showed a value of 13.6 Å at the interface. The rest of the core had this peak at 12.4 Å. The larger d-spacing at the interface indicated that the predominant interlayer cation of smectite was calcium, while the lower value in the rest of the core can be interpreted as sodium and potassium adsorption (Ferrage et al., 2005). The (060) peak of smectite was in all measurements at 1.498 Å and hence it could be identified as dioctahedral clay like montmorillonite. EG saturated spectra showed for all samples (001) smectite peaks at 16.8 Å, (002) peaks at 8.43 Å and (003) peaks at 5.62 Å, which corresponds to a °Δ2Θ((003) - (002)) of 5.23°, and thus no significant illite interstratification. All samples showed clear peaks of mica like muscovite or illite and feldspar. Cristobalite peak intensities were increased in the first 0.3 mm by ~75% (error 17%). Calcite peak intensities were increased in the first 11 mm, by 9 times at the interface, 3.8 times in 0.05 mm distance from the inlet and 2 times in 0.65 mm distance.

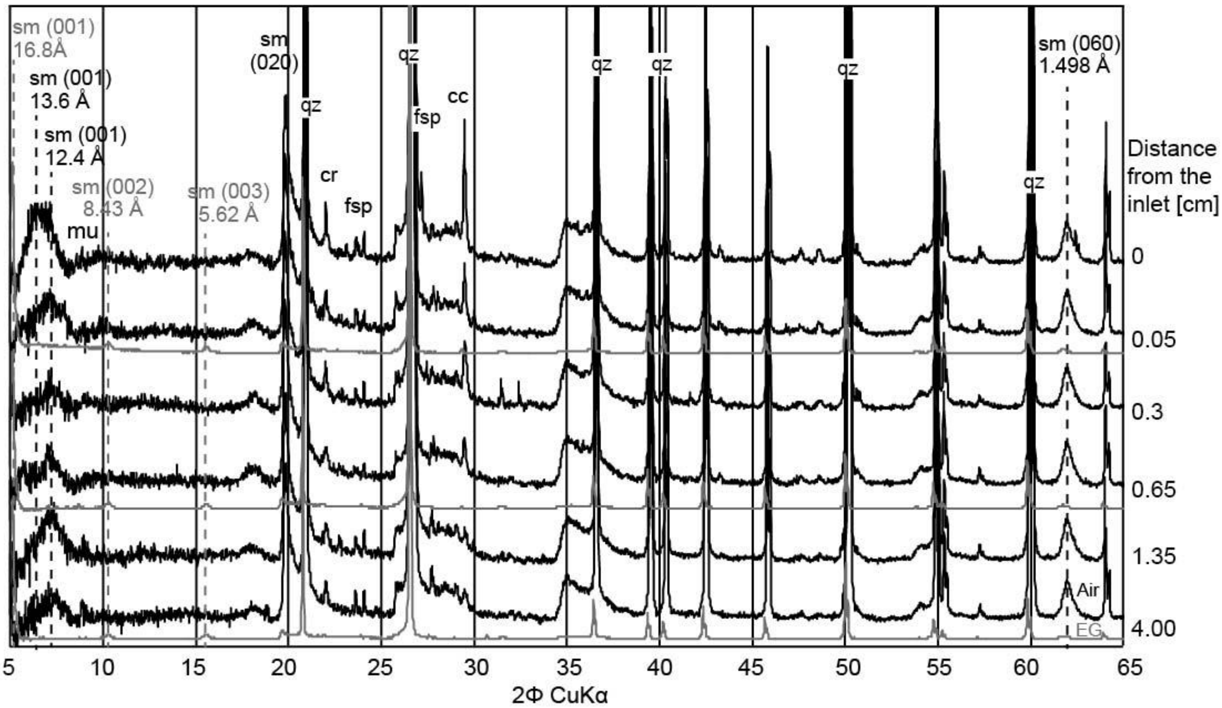

Figure 8-12: XRD spectra of the s/b core. Black curves were measured at 33 %rh (relative humidity), gray curves were EG saturated. Qz: quartz; sm: smectite; cr: cristobalite; fsp: feldspar; cc: calcite; mu: muscovite.

8.2.6. Microscopy and SEM/EDX analysis

Capillary tubes. The inlet capillary tube showed in back-scattered electron (BSE) images attached broken-off filter material and precipitates, consisting mainly of Ca and S, indicating the occurrence of gypsum and calcite (Figure 8-13A). The outlet capillary tube showed in BSE images mineral precipitates, consisting mainly of Ca (Figure 8-13B).

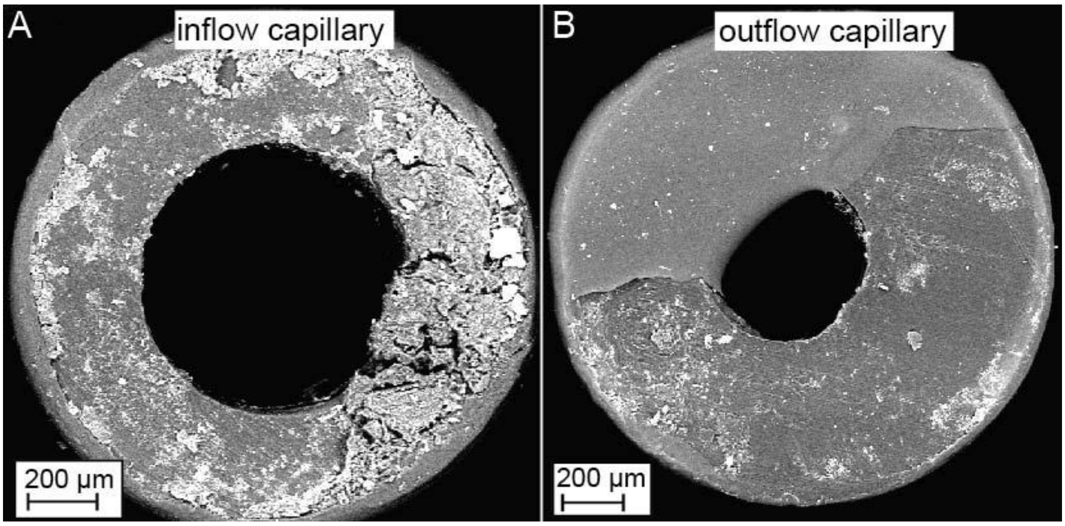

Figure 8-13: BSE images of the inlet capillary (A) and outlet capillary (B).

Filters. The inlet filter showed whitish-yellowish discoloration and fragments of s/b material on the surface facing the core, consisting mainly of SiO_2, Al_2O_3 and CaO (Al_2O_3/SiO_2 0.25) (Figures 8-14A and D), indicating the presence of pristine smectite and calcite, which is in agreement to XRD measurements. The outlet filter showed on the core facing surface attached s/b material (Figure 8-14B).

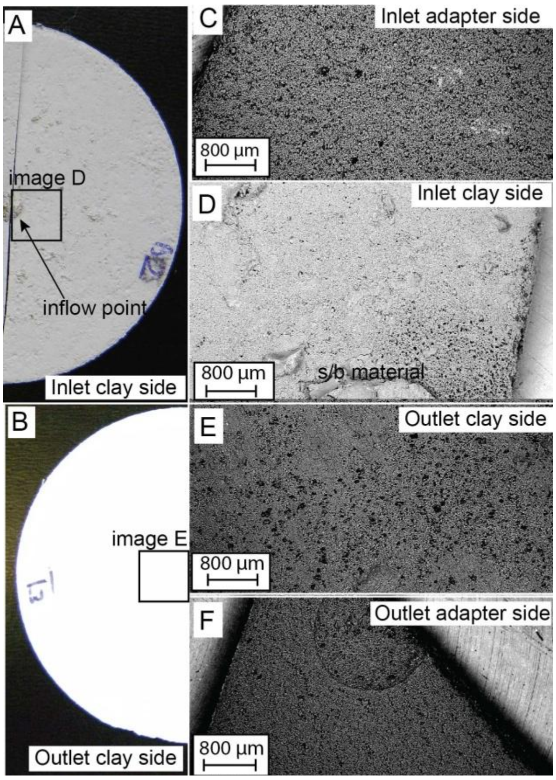

Figure 8-14: In- and outlet filters: (A & B) optical image of the in- and outlet filters; (C & D) BSE images of the inlet filters; (E&F) BSE images of the outlet filters. Filter diameter 50 mm.

S/b core. The s/b core smelled of rotten-eggs after dismantling, indicating the formation of H_2S, most likely related to microbial activity. The inlet surface of the s/b core exhibited few, newly grown black spots of 1–2 mm size after dismantling that are possibly related to microbial activity (Figures 8-1A and C). The outflow surface showed no alterations after the experiment (Figures 8-15B and D).

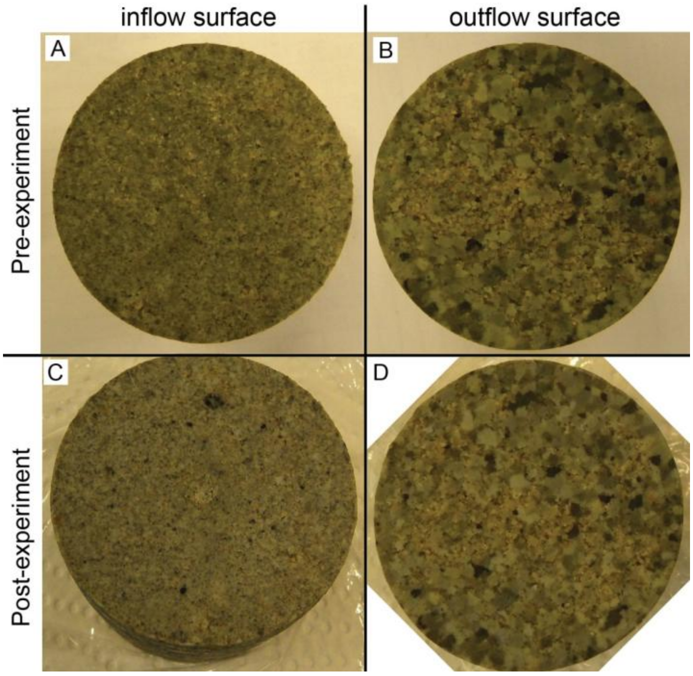

Figure 8-15: S/b core before (A&B) and after (C&D) the experiment: (A&C) inflow surface; (B&D) outflow surface. S/b core diameter 50 mm.

The surface of the SEM sample exhibited holes from fallen out quartz grains, which were artifacts of sample polishing and which may have an effect on the BSE images. In the first 9 mm from the inlet, the core showed in the clay matrix white spots in optical images, which are related to newly formed calcite crystals (Figure 8-16). BSE images of the inflow region showed a core sample dominated by quartz grains of <1 mm size (Figures 8-16 & 8-17B). The quartz grains were rounded and built up an interconnected framework, within a bentonite matrix (Figure 8-17D). The pristine s/b material showed in EDX bulk area measurements a chemistry dominated by SiO_2, Al_2O_3 and Fe_2O_3, which indicates a quartz dominated composition (Table 8-3). EDX point measurements of the bentonite matrix showed a clay-characteristic composition (Table 8-3), similar to pure MX-80 bentonite (*chapter 5*).

Table 8-3: SEM-EDX measurements of s/b and newly formed Ca-minerals.

	s/b (pristine)	**s/b matrix (pristine)**	**Ca-minerals**
Type of measurement	**bulk**	**spot (point)**	**spot**
		[wt%]	
SiO_2	86±3	69±1.2	14±4
Al_2O_3	8±1.7	21±1	5±1
Fe_2O_3	2.1±0.4	3.9±0.4	1.5±0.2
MgO	1.2±0.3	2.8±0.2	2.1±0.9
CaO	1.0±0.3	1.7±0.8	75±3
Na_2O	0.6±0.2	1.2±0.2	1.0±0.8
K_2O	0.5±0.1	0.6±0.1	0.4±0.2
Al_2O_3/SiO_2	0.1	0.3	0.3

In the inflow region precipitation of a new mineral phase was observed, which showed in EDX analysis CaO concentrations of 70–80 wt%, identified as calcite by XRD and Raman spectroscopy measurements (Table 8-3). The calcium enrichment was limited to the first 9 mm of the core in the clay matrix (Figures 8-17 & 8-19). The newly grown calcite occurred mainly in grain clusters of <50 µm size directly in the clay matrix and often next to large quartz grains (Figures 8-16 and 8-17). The calcite concentrations were higher in the first 4 mm, decreasing in direction of the outflow. Grains of an iron dominated mineral phase were observed in the clay matrix near the inlet (Figures 8-16A & 8-18E). Their chemistry was dominated by Fe_2O_3 (30–75 wt%) and minor amounts of CaO and SO_3.The only iron containing phase detected by XRD and Raman spectroscopy was montmorillonite (Fe_2O_3 <5 wt%). EDX analyses indicated the presence of pyrite and possibly iron-hydroxides (e.g. rust), while the existence of siderite could not be excluded.

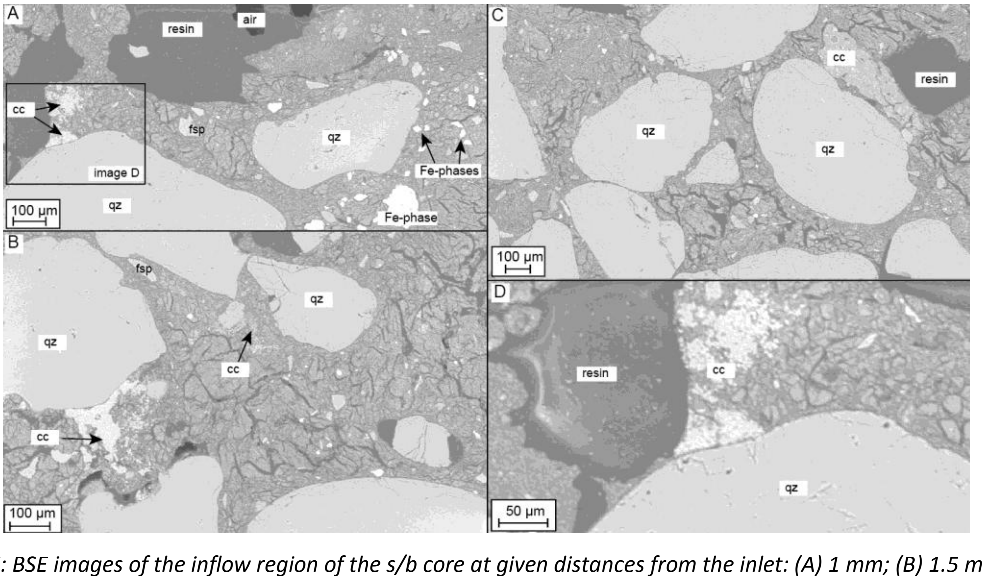

Figure 8-16: BSE images of the inflow region of the s/b core at given distances from the inlet: (A) 1 mm; (B) 1.5 mm; (C) 2.5 mm; (D) detailed view of the calcite (cc) precipitation in the bentonite matrix. Cc: calcite; qz: quartz.

Element maps of the inflow region are shown in Figures 8-17 and 8-18. The carbon map showed a sample surface laced with cracks and holes, filled up with carbon-based resin (Figure 8-17C).

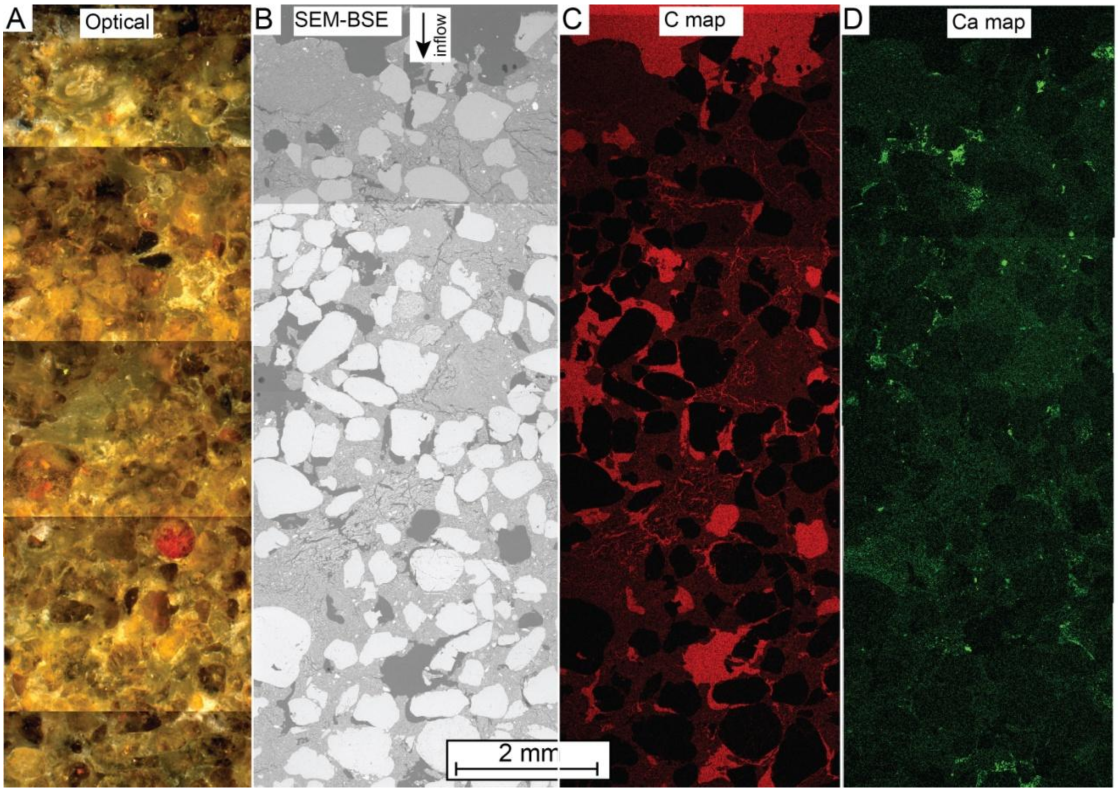

Figure 8-17: (A) Optical image of the inflow region; (B) BSE image; (C) carbon map; (D) calcium map.

Potassium enrichment, shown in the K map, is related to mineral grains of feldspar, muscovite or illite (Figure 8-18B). Feldspar grains were <50 µm in size and exhibited a roundish shape, while illite/muscovite grains were ~100 µm in size and had a roundish shape.

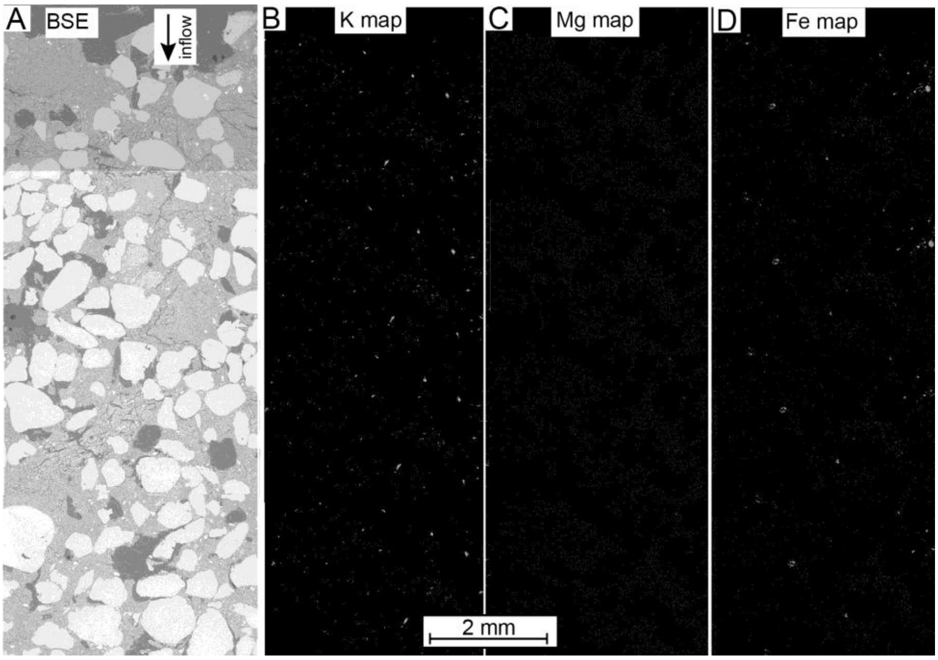

Figure 8-18: BSE images (A) of the inflow region as well as element maps of potassium (B), magnesium (C), and iron (D).

Two EDX profiles are shown in Figure 8-19, with major oxide composition of bulk area (Figure 8-19A) and single point analysis in the clay matrix (Figure 8-19B). The error was calculated based on the standard deviation of 3 replicas. The bulk area measurements were used to detect reactions in the bulk s/b and single point analyses to identify changes in the clay matrix.

The bulk area measurements showed the dominance of SiO_2 in s/b with an average of 86±1 wt% and minor variations induced by heterogeneities in the quartz grain distribution. Averaged CaO amounts of 0.96±0.25 wt% were measured but no increase near the inlet could be observed. As the enrichment was limited to the clay matrix, the calcium signal could only be seen in the single point analyses of the matrix. The SiO_2:Al_2O_3 ratio was ~0.1, which is much lower compared to the ratio in pure smectite (~0.3), indicating dominance of quartz.

The profile in the clay matrix (single point analysis) showed lower SiO_2 contents compared to the bulk area measurements while all the other oxides were increased. The Fe_2O_3 content increased from inlet to outlet from 3.6 wt% to 4.3 wt%. CaO was enriched in the first 8 mm from the inlet due to calcite precipitation.

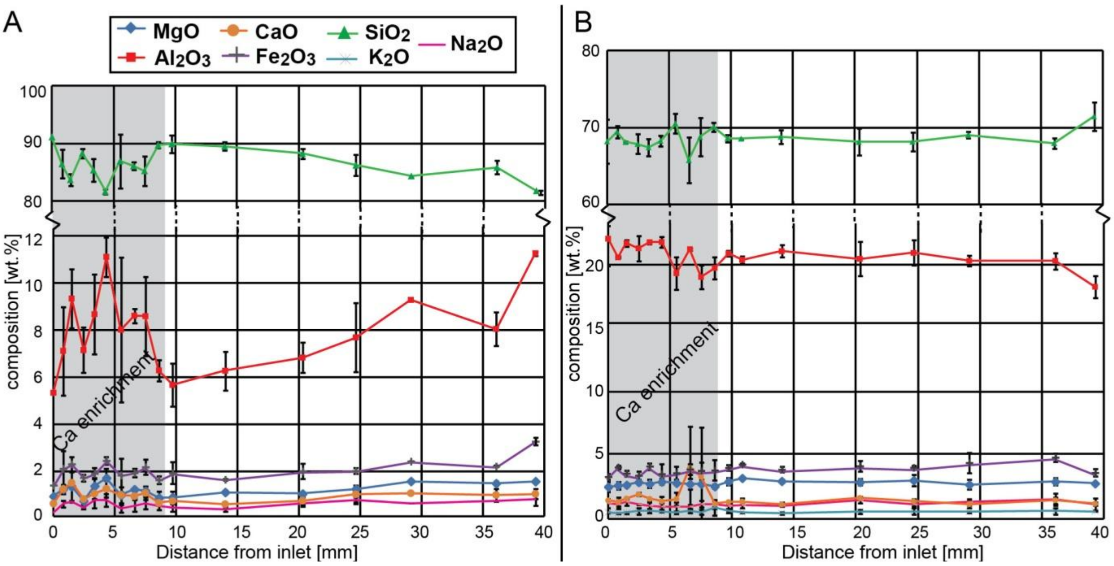

Figure 8-19: SEM-EDX oxide compositions along a central transection: (A) bulk areas measurements of 1.7 x 1.3 mm; (B) single point analysis in the clay matrix. Error bars are the standard deviation of 3 independent measurements.

Main oxide ratios were based on single point analyses of the clay matrix (Figure 8-20). The Al_2O_3:SiO_2 ratio of ~0.3 is characteristic for montmorillonite, while variations near the inlet and outlet were effects of inhomogeneous distribution of quartz grains. The MgO:SiO_2 ratio was 0.04 and the CaO:SiO_2 ratio 0.025 over the entire sample length.

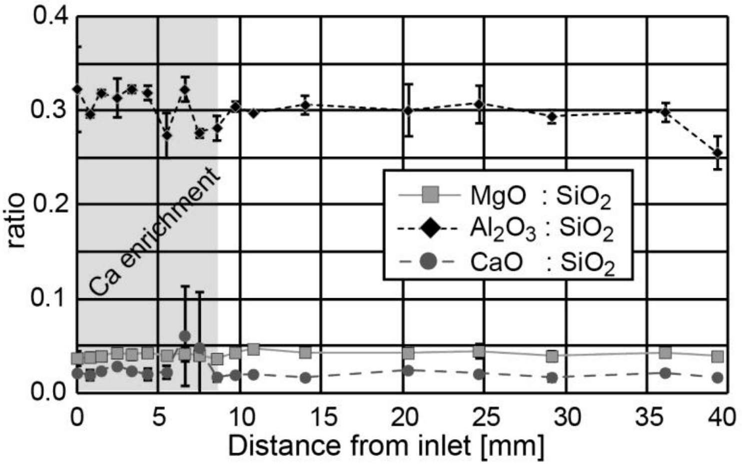

Figure 8-20: SEM-EDX elemental ratios of single point measurements in the clay matrix along a core transection.

8.2.7. Raman spectroscopy

Raman spectroscopy was used to identify mineral phases on the SEM transection sample. The Raman shift patterns of the precipitated Ca-phase showed peaks at 280, 710 and 1084 cm^{-1} and could be identified as calcite (*Figure 8-21*). The occurrence of some siderite, showing main peaks at 290 cm^{-1} and 1087 cm^{-1}, cannot be entirely excluded as the peak pattern is similar to the one of calcite.

Quartz was identified with a peak at 463 cm^{-1} (Figure 8-21). The small peaks below 400 cm^{-1} originate from the torsional vibrations and O–Si–O bending modes, whereas the peak near 463 cm^{-1} involves motion of O in Si–O symmetric stretching-bending mode (Kingma and Hemley (1994).

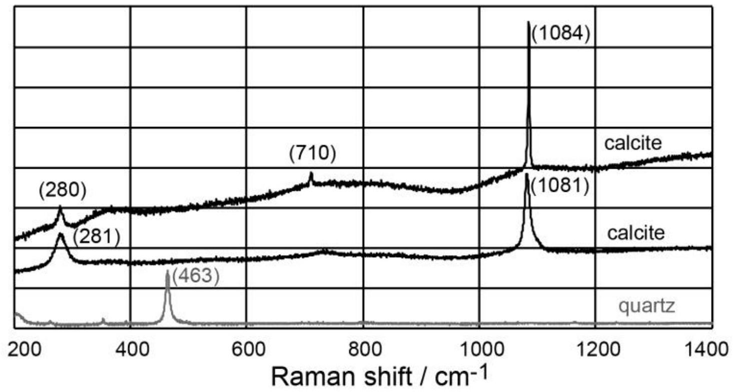

Figure 8-21: Raman spectroscopy measurements of quartz and newly formed calcite.

8.3. Discussion

The evolution of the ion concentrations and the pH in the outflow as well as the hydraulic conductivity is complex and reflects a coupling between physical and chemical processes. The main controlling processes are: ionic strength effects, internal pore-water control by minor soluble phases (sulfate and carbonate minerals), cation exchange processes, carbonate precipitation, and silicate mineral dissolution/precipitation of reactive 'cement phases' after injection of APW$_{ESDRED}$.

8.3.1. Equilibration phase

Evolution of the physical parameters. Initially, the s/b core volume decreased after applying a confining pressure, indicating a further compaction of the core under hydrostatic pressure conditions. Confining pressure conditions consolidate the quartz grain packing further and lead to a dense, most likely grain-supported framework. In a grain/clast-supported framework, the grains contact and support one another, which is in agreement to SEM data (Figure 8-17). Characteristic for such rocks is the high porosity, which is in the case of s/b expected to be completely infilled with bentonite material. The X-ray attenuation histogram of the current core showed a s/b peak at ~1310 HU, which was 65 HU lower compared to the previous s/b experiment (*chapter 7*; Figure 8-22). This indicates that the current core had a lower bulk core density (X-ray attenuation), which is in agreement with the post-mortem analysis.

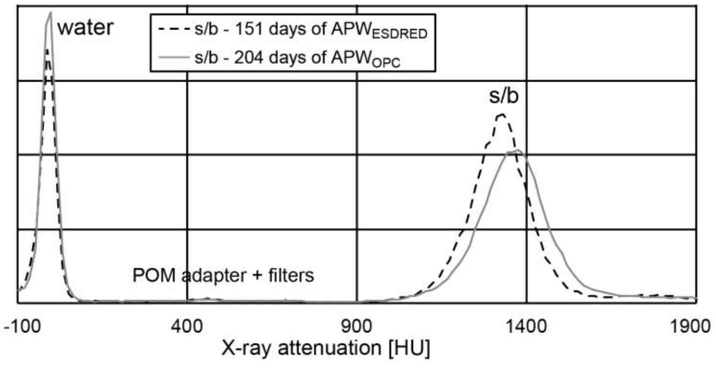

Figure 8-22: Comparison of X-ray attenuation histograms of the current experiment with the one described in chapter 7.

The hydraulic conductivity was initially strongly increased, which is related to the further compaction of the s/b core in the core infiltration device, squeezing out excess pore-water. At the end of the equilibration phase, the hydraulic conductivity was 3× lower compared to the previous s/b, applying similar pressures (*chapter 7)*. The reason for this difference is unclear and may be related to the different pressure histories of the two cores, whereby the previous s/b core experienced initially a much higher confining pressure. The current hydraulic conductivity is in agreement to Cho et al. (2000), who measured in a 70/30% s/b at a similar density a value of $\sim 2\times10^{-12}$ m/s. Gaus et al. (2014) measured in a field experiment for a 65/35% sand/MX-80 bentonite with a similar dry density a permeability of $\sim 1\times10^{-19}$ m^2, which is in agreement with the current measurements. The hydraulic conductivity of the s/b is ~1 order of magnitude higher compared to pure bentonite (see *chapters 5 & 6*).

Evolution of the outflow chemistry. The ionic strength of the outflow was initially 0.28 mol/kg and decreased to 0.24 mol/kg during the equilibration phase (Table 8-4). The initial ionic strength of the outflow showed increased values compared to both, $APW_{Äspö}$ (0.26 mol/kg) and APW_{OPA} (0.23 mol/kg). This indicates that initially a more saline fluid was expelled (Table 8-1). The same phenomenon was observed for bentonite cores (*chapters 6 & 7*) and is related to the initial compaction of the core, flushing excess anions out of the core in an osmotic medium by reducing the intergranular porosity, accessible to anions. In contrast, reduction of interlayer porosity would have resulted in a lower salinity outflow. At the end of the equilibration phase, the outflow showed a similar ionic strength to the infiltration fluid.

The pH of ~7.5 at the end of the equilibration phase was identical to the previous s/b experiment (*chapter 7*). The ion concentrations in the outflow did not reach steady conditions at the end of the equilibration phase. The reduced sulfate concentration at the beginning of the experiment were most likely induced by the $APW_{Äspö}$ (Table 8-1), containing only little sulfate. The sulfate increased after 0.6 PV, which indicates the break-through of the APW_{OPA}. The mass-balance showed a loss of sulfate in the s/b core, mainly occurring during the core compaction and saturation procedure, indicating gypsum dissolution. The SI_{gypsum} showed under-saturation, which was either induced by gypsum dissolution or by the high flow rate, while the dissolution kinetics was slower (Table 8-4). The sodium concentration in the outflow decreased, indicating replacement from the exchanger by magnesium and calcium, which are both increasing.

8.3.2. High-pH (APW_{ESDRED}) infiltration

Evolution of the outflow chemistry. The ionic strength of the outflow got strongly reduced from 0.2 to 0.06 mol/kg in 0.8 PV_{ESDRED} during the high-pH phase. This indicates that the infiltration fluid (~0.11 mol/kg) was buffered by the s/b by mineral dissolution-precipitation and ion exchange reactions.

The pH increased during the high-pH infiltration to ~7.9, which is identical to the APW_{OPC} infiltration experiment (*chapter 7*) and represents the buffering capacity of s/b with respect to high-pH conditions. The hydroxide, which is directly related to pH and was mainly infiltrated during APW_{ESDRED} (total 0.33 mmol) infiltration, reached the outflow only sparsely (3.9×10^{-5} mmol). This indicates that hydroxide was consumed by the s/b core most likely by mineral precipitation. Saponite was the only newly formed mineral phase detected on the filter surface, containing hydroxide, while the existence of brucite could not be excluded. Chloride as major anionic charge carrier dropped continuously and got replaced by organic compounds (mainly acetate) and possibly bicarbonate (carbonate alkalinity) after 0.9 PV_{ESDRED} (Figure 8-4). The mass-balance shows a difference of 1.04 mmol between cumulative inflow and outflow, indicating that some chloride is still present in the s/b core at the end of the experiment (Table 8-5). An aqueous extract of raw s/b material showed a total of 7.34 mmol Cl^-/kg of total pore-water (see *chapter 7;* based on S:L = 0.1:1). The initial inventory of the current core was therefore 0.2 mmol Cl^-, based on the initial pore-water content. This additional chloride shifts the difference to 1.24 mmol and corresponds to the initial chloride inventory of this s/b. If chloride is considered as non-reactive tracer mostly present in intergranular porosity due to anion exclusion, the chloride decrease represents a breakout curve, whereby the time required to flush out chloride to half of that of its initial concentration represents approximately one volume of flow-active porosity. This is ~0.5 PV relative to the initial full water content, indicating that 50% of the water-loss porosity is accessible for anions (anion accessible porosity, flow-active porosity). Deuterium traced APW_{ESDRED} (δ^2H) water reached the outflow after 0.2 PV, while half of that of the concentration of APW_{ESDRED} was measured after ~0.85 PV. This indicates that the apparent transport porosity was around 85% of the total water-loss porosity. It indicates that water flow took place in almost the entire pore volume, while advection was occurring. In case of a pure diffusion experiment, the half-height of the δ^2H should be at 1 PV. The ratio of the effective transport porosity for Cl^-/

δ^2H was about 3/5, indicating clearly anion exclusion. Sulfate concentrations were increased in the outflow for the first 0.3 PV_{ESDRED}, followed by a continuous drop, reaching concentrations <1 mM after 1.8 PV_{ESDRED}. The mass-balance of sulfate shows a net loss of 0.6 mmol, which corresponds to 110 mg of dissolved gypsum or 25–50% of the initial gypsum amount (Table 8-5). This is in agreement to SI, which showed under-saturation with respect to gypsum in the outflow (Table 8-4).

The mass-balance showed a loss of sodium from the core, released from the clay exchanger (Table 8-5). Potassium, magnesium and calcium were retained in the s/b core by ion exchange for K^+ and Mg^{2+}, and for Ca^{2+} possibly also by calcite precipitation. Si^{4+} got enriched in the outflow during the high-pH phase, while Al^{3+} was not detected; described later in this section. Formate, the main charge carrier of APW_{ESDRED} was observed in the outflow only for a short time period, followed by the occurrence of acetate. The alkalinity showed a drastic increase after switching to APW_{ESDRED}, related to the measured acetate and formate; both discussed later in this section. Charge imbalance was observed in the outflow after 2.4 PV, related to the low ionic strength of the outflow solution and most likely the occurrence of unknown carbonate species (Table 8-4).

Table 8-4: Saturation indices (SI) of outflow and APWs. Cc: calcite; gy: gypsum; mont; montmorillonite; qz: quartz; cristo: cristobalite; $pCO_{2(g)}$: partial pressure CO_2.

APW/Time [days]	**PV**	**Ionic Strength [mol/kg]**	**Charge error [%]**	**SI**					
				cc	gy	mont	qz	cristo	$pCO_{2(g)}$
$APW_{Äspö}$		0.26		-0.3	-0.83				-3.24
APW_{OPA}		0.24		-0.1	-0.34				-3.21
APW_{ESDRED}		0.11	3.50	1.67	-0.5	-13	-2.2	-4	-10
1	0	0.28	-3.4	-1.13	-0.55	8.51	1.24	0.44	-1.81
12	0.3	0.25	-1.0	-0.61	-0.64	8.39	1.23	0.44	-2.20
55	0.7	0.24	-0.3	0.23	-0.51	5.05	1.23	0.43	-2.40
63	0.8	0.2	-1.8	0.47	-0.57	6.39	1.17	0.38	-2.30
96	1.2	0.1	-1.5	0.67	-1.00	-	1.24	0.45	-2.44
156	1.8	0.05	0.0	0.35	-2.00	-	1.26	0.47	-2.00
241	2.4	0.05	8.4	0.52	-2.37	-	1.27	0.48	-1.91
295	2.8	0.05	8.9	0.58	-3.15	-	1.27	0.48	-1.98

Table 8-5: Ion mass-balance of in- and outflow.

Elements	**Inflow**			**Outflow**		**Δ tot**
	$APW_{Äspö}$	**APW_{OPA}**	**APW_{ESDRED}**	**Equilibration phase**	**tot**	
			[mmol]			
Na^+	4.53	2.85	1.38	10.30	14.42	-5.66
K^+	0.02	0.05	0.71	0.13	0.18	0.59
Ca^{2+}	2.79	0.20	1.51	0.40	0.51	4.00
Si^{4+}	0.0	0.00	0.00	0.07	0.18	-0.18
Al^{3+}	0.0	0.00	0.00	0.00	0.0	0.00
Mg^{2+}	0.09	0.16	0.00	0.13	0.16	0.08
Sr^{2+}	0.02	0.00	0.00	0.00	0.01	0.02
Cl^-	10.46	2.71	0.00	10.10	12.13	1.04
SO_4^{2-}	0.09	0.38	0.12	0.85	1.23	-0.64
HCO_3^-	0.01	0.01	0.00	0.08	1.23	-0.6
Formate	0.0	0.00	4.22	0.00	0.07	4.15
Acetate	0.0	0.00	0.00	0.00	0.91	-0.91

Evolution of hydraulic conductivity and core volume. The hydraulic conductivity was initially increased either by a higher infiltration fluid pressure or by emanating gas. Thereafter, the hydraulic conductivity got reduced to the level measured during the equilibration phase. Unclear is, why the drop in ionic strength of the infiltration solution, induced by the switch from APW_{OPA} to APW_{ESDRED}, had no effect on the hydraulic conductivity of the s/b core. Karnland et al. (2006) showed for MX-80 bentonite at a given density the following relation using a constant-volume cell: the lower the ionic strength of a pore-water, the lower the hydraulic conductivity.

APW_{ESDRED} infiltration induced a small core volume expansion. This is in agreement to Karnland et al. (2006), who observed for MX-80 bentonite high swelling pressures in low ionic strength NaCl solutions. This can be explained by osmotic effects, transporting pore-water into the interlayer porosity and the diffuse layer (DL), which causes swelling. At constant hydrostatic conditions, this corresponds to a volume increase. This indicates that the s/b framework is no more grain but rather matrix-supported. Unclear is why APW_{ESDRED} infiltration affected the core volume but not the hydraulic conductivity. Compared to the s/b core described in *chapter 7*, the current core had already a much lower hydraulic conductivity during the equilibration phase. The reason for this difference is not clear but may be related to the different pressure histories of the two cores. But this does not explain why the high-pH infiltration had no effect on the fluid flow, although both experiments showed similar outflow compositions as well as calcite precipitation in the inflow region. Comparing all experiments (*chapters 5, 6, 7*), it indicates that most likely extensive mineral precipitations induced the hydraulic conductivity reduction. Why the observed calcite precipitation had no effect on the fluid flow is not understood.

Gas accumulation. Gas phase A was related to gas trapped in the dead-volume of the outflow system, with volumes slightly higher compared to the previous s/b core (*chapter 7*; Figure 8-3). Two hypotheses for the origin of gas phase B (0.2–0.85 PV_{ESDRED}) were postulated: atmospheric gas trapped in the dead-volume of the inflow system and CO_2 gas produced by microbes. The first hypothesis is supported by the fact that the gas outflow only occurred up to 0.85 PV_{ESDRED}, which could have been theoretically a reasonable time for atmospheric gas to flow through the core. As a similar behavior was not observed in the previous s/b experiment and the gas quantities are rather high, this hypothesis it is assumed to be less likely. This indicates that the observed gas is most likely biological origin, as a product of fermentation (see next section).

Microbial activity and organic compounds. Formate, the main negative charge of APW_{ESDRED}, was only detected in the outflow during a short period. Increasing acetate concentrations were measured in the outflow from 0.6 PV_{ESDRED} onwards and are directly related to the measured alkalinity increase (Figure 8-4). The alkalinity increase was detected 0.2 PV prior to the formate increase and 0.4 PV prior to the acetate (Figure 8-5). The alkalinity corrected for C_{org} (acetate, formate) showed as well an increasing trend in the outflow, either related to bicarbonate (carbonate alkalinity) or another organic acid, not detected by IC. Assuming that carbon compounds induced the observed imbalance in charges of the outflow solution, an additional 9 mM of an univalent negatively charged C-species must have been present like acetate or formate (Table 8-4).

The mass-balance showed a net input of 4.15 mmol formate ($HCOO^-$) and 0.02 mmol bicarbonate into the core while 0.9 mmol acetate (CH_3COO^-), 0.07 mmol formate and 0.8 mmol bicarbonate/organic compounds (formate and acetate corrected alkalinity) were collected in the outflow (Table 8-5). 4.2 mmol of organic carbon were infiltrated while 1.9 mmol reached the outflow, which is a difference of 2.3 mmol. If the total carbon is considered (including corrected alkalinity), 4.25 mmol were infiltrated, 2.7 mmol reached the outflow. Two main processes could be identified, explaining this imbalance: calcite precipitation and CO_2 production. Assuming that the difference corresponds only to calcite precipitation, 0.16–0.2 g of calcite could have been formed, while in case only the CO_2 production is accounted, 40–50 ml of gas could have been produced, based on the ideal gas equation and a temperature of 20°C and atmospheric pressure conditions. Both assumptions are in agreement with made observations, indicating that most likely both processes played an important role and are possibly interconnected. Kerby and Zeikus (1987) showed the anaerobic microbial catabolism of formate to acetate and CO_2. They showed that the Butyribaterium methylotrophicum bacterium fermented formate to acetate in presence of H_2, forming CO_2, while pH increased. A small initial pH raise was observed during the gas phase B (Figure 8-3), but if this is related to the above described microbial activity is not clear. Further not clear is why the reaction only occurred for a certain period of time, mainly characterized by the replacement of APW_{OPA} by APW_{ESDRED}. The presence of microbes in the core is in agreement to the rotten-egg smell (H_2S) of the post-mortem core and the observed black spots on the inflow surface as well as in the inflow filters.

Dissolution of silica and silicate minerals. The silica concentration in the outflow got weakly increased by the APW_{ESDRED} infiltration. The mass-balance showed a net loss of 0.18 mmol silica, while during the APW_{ESDRED} (0.07 mM) infiltration 0.004 mmol of Si^{4+} were infiltrated. The SI with respect to SiO_2-mineral phases showed over-saturation already during the equilibration phase, which got more pronounced during the high-pH infiltration phase (Table 8-4). SEM analysis did not show any dissolved silica-phase in the inflow region, while in XRD strong intensity variations in the quartz may cover a certain trend.

Calcite enrichment. The precipitation of calcite was observed by SEM-EDX and verified by XRD and Raman spectroscopy measurements. Calcite occurred in the inlet filters and extended up to one 1 cm into the s/b core, predominantly in the clay matrix. The amount of calcite was higher near the inlet and faded out in direction of the outlet. The current s/b showed more extensive calcite precipitation relative to the previous s/b experiment. This is related most likely to the higher hydraulic conductivity during the high-pH infiltration phase as well as to the higher calcium and carbonate content of the APW_{ESDRED}, exhibiting a ~10× higher calcium concentration as well as formate. In the current experiment double the volume of high-pH fluid was infiltrated during the entire experimental time, inducing most likely the more extensive calcite precipitation.

The measured alkalinity in the outflow during the equilibration phase as well as the first measurement during the high-pH phase may represent the bicarbonate concentration. From 0.4 PV_{ESDRED} onwards, the speciation of the alkalinity, even after subtracting formate (corrected alkalinity), was not clear and may consists of bicarbonate and unknown organic compounds. The $SI_{calcite}$ based on the corrected alkalinity showed initially (0–0.3 PV) under-saturation with respect to calcite and over-saturation thereafter (Table 8-4). If the $SI_{calcite}$ really showed a saturation state in respect to the mineralogy or rather a transient state, mainly influenced by the high hydraulic conductivity of the s/b, is not clear. The over-saturation is in agreement to the observed calcite precipitation in the s/b. PhreeqC modeling showed strong calcite over-saturation in an APW_{OPA} saturated s/b at increased pH conditions (pH ~11.6). If calcite was precipitated mainly by abiotic processes or if microbial activity was involved, is not clear.

8.4. Conclusion

Applying a hydrostatic confining pressure to the compacted s/b core sample reduced the core volume by 3 vol%. Switching to an artificial 'low-pH' shotcrete solution (pH 11.6, APW_{ESDRED}) induced core expansion but had no effect on the hydraulic conductivity, showing values between $3.7–4.0\times10^{-12}$ m/s. Core expansion was triggered by the low ionic strength solution, indicating that the s/b core framework changed from mostly grain supported to matrix supported.

The outflow showed during the equilibration phase near constant to slightly decreasing ion concentrations with the exception of pH (hydroxide), which increased from 6.5 to 7.5. Switching to APW_{ESDRED} increased the alkalinity, acetate and hydroxide (pH) concentrations in the outflow, while formate was consumed and all other ions got drastically reduced. The final outflow showed an ionic strength of 0.06 mol/kg, which is half of that of the infiltrated fluid (0.11 mol/kg). During the high-pH infiltration, chloride as main negative charge carrier got replaced by acetate, formate and bicarbonate (carbonate alkalinity) after 0.9 PV.

The anion (Cl^--based) accessible porosity and therefore also the flow-active porosity was 50% of the initial water content, while the apparent transport porosity (^2H traced) was 85%. Infiltrated formate only reached the outflow during a short period, followed by high acetate concentrations. A possible microbial process could be the fermentation of formate to acetate and CO_2, which could as well explain the gas release. Rotten-egg smell after core dismantling and black spots in filter and on the sample surface indicated the presence of microbes.

Post-mortem analysis showed in the inlet filter precipitation of calcite and trioctahedral smectite, most likely saponite. In the first 9 mm of the s/b core precipitation of calcite was observed, verified by XRD and Raman spectroscopy measurements. Calcite precipitation occurred in the clay matrix (intergranular porosity) and was induced by the high-pH plume, saturating the pore-fluid with respect to calcite. The effect of the biological activity on the calcite precipitation is not clear.

The experiment attests an effective pH buffering capacity for s/b, while the pore-water chemistry got strongly altered. No sealing was observed, although extensive mineral precipitation occurred.

References

Agus, S.S., Schanz, T., 2008. A method for predicting swelling pressure of compacted bentonites. Acta Geotechnica 3, 125-137.

Bäckblom, G., 2007. ESDRED: Deliverable D4 of Module 5, WP2. Supporting documents of second training workshop, final technical report. Proc. of the Third Low pH Workshop, Paris June 13–14, 2007. European Commission, Brussels, Belgium.

Berner, U., Kulik, D.A., Kosakowski, G., 2013. Geochemical impact of a low-pH cement liner on the near field of a repository for spent fuel and high-level radioactive waste. Physics and Chemistry of the Earth, Parts A/B/C 64, 46-56.

Brindley, G.W., Brown, G., 1980. Crystal Structures of Clay Minerals and Their X-ray Identification. Mineralogical Society.

Cho, W.-J., Lee, J.-O., Kang, C.-H., 2000. Hydraulic Conductivity of Sand-Bentonite Mixture for a Pentitial Backfill Material for a High-level Radioactive Waste Repository. Journal of the Korean Nuclear Society 32, 495-503.

Dolder, F., Mäder, U., Jenni, A., Schwendener, N., 2014. Experimental characterization of cement–bentonite interaction using core infiltration techniques and 4D computed tomography. Physics and Chemistry of the Earth, Parts A/B/C 70–71, 104-113.

Fernández, R., Rodríguez, M., de la Villa, R.V., Cuevas, J., 2010. Geochemical constraints on the stability of zeolites and C-S-H in the high pH reaction of bentonite. Geochimica et Cosmochimica Acta 74, 890-906.

Fernández, R., Vigil de la Villa, R., Ruiz, A.I., García, R., Cuevas, J., 2013. Precipitation of chlorite-like structures during OPC porewater diffusion through compacted bentonite at 90°C. Applied Clay Science 83–84, 357-367.

Ferrage, E., Lanson, B., Sakharov, B.A., Drits, V.A., 2005. Investigation of smectite hydration properties by modeling experimental X-ray diffraction patterns. Part I. Montmorillonite hydration properties. Mineralogical Society of America, Washington, DC, USA.

García Calvo, J.L., Hidalgo, A., Alonso, C., Fernández Luco, L., 2010. Development of low-pH cementitious materials for HLRW repositories: Resistance against ground waters aggression. Cement and Concrete Research 40, 1290-1297.

Gaus, I., Garitte, B., Senger, R., Gens, A., Vasconcelos, R., Garcia-Sineriz, J.-L., Trick, T., Wieczorek, K., Czaikowski, O., Schuster, K., Mayor, J.C., Velasco, M., Kuhlmann, U., Villar, M.V., 2014. The HE-E Experiment: Lay-out, Interpretation and THM Modelling. Nagra Working Report, Nagra, Wettingen, Switzerland.

Karnland, O., Olsson, S., Nielsson, U., 2006. Mineralogy and sealing properties of various bentonites and smectite-rich clay materials. SKB Technical Report 06-30, Stockholm, Sweden.

Karnland, O., Olsson, S., Nilsson, U., Sellin, P., 2007. Experimentally determined swelling pressures and geochemical interactions of compacted Wyoming bentonite with highly alkaline solutions. Physics and Chemistry of the Earth, Parts A/B/C 32, 275-286.

Karnland, O., Olsson, S., Dueck, A., Birgersson, M., Nilsson, U., Hernan-Håkansson, T., Pedersen, K., Nilsson, S., Eriksen, T., Rosborg, B., 2009. Long term test of buffer material at the Äspö Hard Rock Laboratory, LOT project. Final report on the A2 test parcel. SKB Technical Report 09-29, Stockholm, Sweden.

Karnland, O., 2010. Chemical and mineralogical characterization of the bentonite buffer for the acceptance control procedure in a KBS-3 repository. SKB Technical Report 10-60, Stockholm, Sweden.

Kerby, R., Zeikus, J., 1987. Anaerobic catabolism of formate to acetate and CO2 by Butyribacterium methylotrophicum. Journal of Bacteriology 169(5):2063-8.

Kingma, K.J., Hemley, R.J., 1994. Raman spectroscopic study of microcrystalline silica. American Mineralogist 79, 269-273.

Lancaster, J.L., Martinez, M.J., 2007. Mango - Multi-image analysis GUI. Research Imaging Institute, UT Health Science Center at San Antonio, TX, USA, URL: http://ric.uthscsa.edu/mango/index.html.

Lothenbach, B., Scrivener, K., Hooton, R.D., 2011. Supplementary cementitious materials. Cement and Concrete Research 41, 1244-1256.

Lothenbach, B., Rentsch, D., Wieland, E., 2013. Hydration of a silica fume blended low-alkali shotcrete cement. Physics and Chemistry of the Earth, Parts A/B/C.

Mäder, U., 2009. Reference pore water for the Opalinus Clay and "Brown Dogger" for the provisional safety-analysis in the framework of sectoral plan - interim results (SGT-ZE). Nagra Working Report, Nagra, Wettingen, Switzerland.

Moore, D.M., Reynolds, R.C., 1989. X-ray diffraction and the identification and analysis of clay minerals. Oxford University Press, New York.

Mosser-Ruck, R., Cathelineau, M., 2004. Experimental transformation of Na,Ca-smectite under basic conditions at 150 °C. Applied Clay Science 26, 259-273.

Nagra, 2002. Demonstration of disposal feasibility for spent fuel, vitrified high-level waste and long-lived intermediate-level waste (Entsorgungsnachweis). Nagra Technical Report NTB 02-05, Nagra, Wettingen, Switzerland.

Ramirez, S., Cuevas, J., de la Villa, R.V., Leguey, S., 2002. Hydrothermal alteration of La Serrata bentonite (Almeria, Spain) by alkaline solutions. Applied Clay Science 21, 257– 269.

Rothfuchs, T., Czaikowski, O., Hartwig, L., Hellwald, K., Komischke, M., Miehe, R., Zhang, C.-L., 2012. Self-bealing barriers of sand/bentonite-mixtures in a clay repository. GRS Technical report 302, Braunschweig, Germany.

Savage, D., Benbow, S., 2007. Low pH Cements. SKI Report 2007:32, Swedish Nuclear Power Inspectorate, Stockholm, Sweden.

Schindelin, J., Arganda-Carreras, I., Frise, E., Kaynig, V., Longair, M., Pietzsch, T., Preibisch, S., Rueden, C., Saalfeld, S., Schmid, B., Tinevez, J.-Y., White, D.J., Hartenstein, V., Eliceiri, K., Tomancak, P., Cardona, A., 2012. Fiji: an open-source platform for biological-image analysis. Nat Meth 9, 676--682.

9 Scoping calculation: reproducing experimental data of the ordinary Portland cement fluid/bentonite experiment using the reactive transport code CrunchFlow

9.1. Introduction

Numerical modeling is widely used to predict the long-term behavior of bentonite buffer in contact to cement. The performance of the codes can be checked by reproducing experimental results. Further, modeling helps for the understanding of ongoing processes in the bentonite-cement system: experimental analyzes show the combined results of all processes, which can be difficult to interpret.

Various reactive transport codes are in use to model the interaction between cement and bentonite buffer: CrunchFlow (Fernández et al., 2009b, 2010b; Fernández et al., 2011a), MC-Bent (Yamaguchi et al., 2007), OpenGeoSys-GEMS (Berner et al., 2013; Kosakowski and Berner, 2013; Kosakowski et al., 2014), PRECIP (Savage et al., 2002), PhreeqC (Gaucher and Blanc, 2006; Gaucher et al., 2004), Raiden-3 (Watson et al., 2009), TOUGHREACT (Lehikoinen, 2009). An overview is given in Savage et al. (2011). Savage et al. (2002) used PRECIP (Noy, 1998), with thermodynamic and kinetic data from the EQ3/6 database (Wolery, 1992) and from Walther (1996), respectively. A single effective diffusion coefficient of initially 10^{-10} m^2 s^{-1} was used, which had to be modified manually over time, depending on porosity alteration and hydraulic conductivity. Bentonite, saturated with low salinity groundwater, reacted with cementitious pore-water from ordinary Portland cement (OPC) at different ages (pH 11.3, 12.5, 13.2) at 25°C and 70°C. Most alterations were observed at high-pH conditions with calcium silicate hydrate (C–S–H) and zeolite formed in the bentonite close to the fluid reservoir and primary minerals dissolved. The extension of the reaction zone was up to 60 cm in $\sim$1000 years. Total porosity decreased due to mineral precipitation, reducing the fluid-flow. Gaucher et al. (2004) used PhreeqC in a one dimensional, diffusive transport domain (thermodynamic equilibrium chemistry without kinetics). The PhreeqC llnl.dat database (Wolery, 1992) was used, extended by cementitious and zeolite phases. The system consisted of an OPC pore-fluid in contact with a MX-80 bentonite buffer, saturated with a Callovian-Oxfordian pore-water. A single diffusion coefficient of 10^{-11} m^2/s was used. Three main stages were distinguished over a period of 100’000 years: (1) cation population on the montmorillonite exchanged from sodium to potassium and calcium dominated, (2) illitisation of montmorillonite and precipitation of zeolites, (3) replacement of zeolites by cement minerals (like C–S–H). The bentonite minerals buffered the high-pH plume that controlled the CO_2 partial pressure. Watson et al. (2009) used the code Raiden-3 (Ueda et al., 2007), a fully coupled, 1D reactive transport code. Thermodynamic data are from the EQ3/6 database (Wolery, 1992; Wolery and Daveler, 1992) and extended by zeolites from Chipera and Apps (2001). K-Na-OH dominated cementitious pore-fluids altered the mineralogy by 2 mm in 1 year, clogging the porosity by precipitation of hydrotalcite, gibbsite, and brucite. Ca dominated (pH 11.3) pore-fluids only caused minor alterations. They reported further that the montmorillonite stability was very sensitive to different thermodynamic data available. Fernández et al. (2010b) used the multi-component reactive transport code CrunchFlow (Steefel, 2006). The standard CrunchFlow database (datacom) was used, which is based on EQ3/6, extended by data from the default databases of SUPCRT92 (SLOP98) and PhreeqC. The model approach was based on diffusion experiments in bentonite performed at 60°C and 90°C using a Na–K-OH (pH 13.5) and a $Ca(OH)_2$ based cementitious solution (pH 11.5). Dissolution of montmorillonite was observed only with the Na-K solution. Further, the precipitation of Mg-silicates (talc-like), hydrotalcite, and brucite, along with cation exchange was observed at 60°C, while at 90°C the alteration affected a larger area. The $Ca(OH)_2$ based fluid caused mainly precipitation of brucite and calcite. Porosity decrease was observed near the interface for both infiltration solutions. Kosakowski and Berner (2013) used the OpenGeoSys-GEM coupling, while OpenGeoSys was used for mass-transport with GEM (Gibbs Energy Minimization) code GEMS3K for geochemical modeling. They modeled the evolution of the cement/clay rock interface in a cementitious repository for low- and intermediate level nuclear waste. Diffusive and partially also advective flow calculations showed strong porosity reduction near the interface in the clay, with mineral dissolution (kaolinite, siderite, montmorillonite) and precipitation (zeolite, hydro-magnetite, hydrotalcite, illite).

The current modeling approach used the reactive transport code CrunchFlow to reproduce the experimental data of the bentonite–APW_{OPC} (ordinary Portland cement pore-water) interaction experiment described in *chapters 4 & 5.* The idea is to reproduce the experimental results and verify the basic concepts and processes, described in chapter 5. The innovation of this approach was the discrimination of two porosity domains with different transport properties: the conventional intergranular porosity and the porosity influenced by the negatively charged clay sheet surfaces and therefore depleted in anions *(CrunchFlow script in Appendix 11.3)*.

9.2. Code properties

The modeling was performed using the reactive transport code CrunchFlow (Steefel, 2001, 2006; Steefel and Yabusaki, 1996) in global implicit multi-component reactive transport mode (GIMRT). The code takes into account diffusion and advection, aqueous speciation, surface complexation, ion exchange, and mineral dissolution/precipitation, whereby the latter are kinetically controlled. To consider various pH and $p(CO_2)$ conditions, the rate constant can be given for high and low pH as well as for changing $p(CO_2)$.

In the current study, the CrunchFlowMC version was used, in which a twofold porosity model for clay materials is considered (Steefel, 2010). The porosity consists of intergranular porosity with a charge-balanced pore-fluid (macroporosity or free-water porosity) and microporosity (interlayer and diffuse layers), whose net charge balance is a fraction of the negative surface charge of the clay sheets. The Donnan equilibrium defines the chemistry in the microporosity. The ionic strength in the macroporosity influences diffusive and interlayer thickness based on osmotic considerations (Steefel, 2010). This means that an infiltrating high ionic strength fluid reduces the microporosity and hence increases the macroporosity if total volume is kept constant. The microporosity was calculated based on the specific surface area of montmorillonite multiplied with a Debye length factor and the ratio of a temperature depended factor divided by the root of the ionic strength of the pore-solution (Tournassat and Appelo, 2011). Diffusive transport occurs in both porosities based on different diffusion coefficients, whereas only the macroporosity is affected by advection. Another fraction of the negative charge clay sheets is compensated by immobile cations in the Stern layer (Ehrenstein, 2001). It is represented as surface complexation in this model approach. The sum of the cations on the surface sites and the cations in the microporosity represents the cation exchange capacity (CEC). The code is able to run several input files in series, updating each time the inflow and porosity parameters.

9.3. Thermodynamic and kinetic data

The current study used 16 aqueous primary species (Table 9-1), 42 aqueous secondary species (Table 9-2) and 40 minerals (Table 9-3). The primary species and secondary species were taken from the EQ3/6 database (Wolery, 1992).

Table 9-1: Primary species.

Primary species
H^+
H_2O
Al^{3+}
Ca^{2+}
Cl^-
Fe^{3+}
HCO_3^-
H_4SiO_4
K^+
Mg^{2+}
Na^+
SO_4^{2-}
$Zr(OH)_2^{2+}$
Tracer

Table 9-2: Secondary species.

Secondary species	**log k (25°C)**
AlSO4+	-3.9
Al(SO4)2-	-5.9
Al(OH)2+	10.6
AlO2-	10.6
Al(OH)4-	22.88
AlOH++	4.96
CaCO3(aq)	7.1
CaHCO3+	-1.11
CaSO4(aq)	-2.3
CaOH+	12.78
FeCl++	8.57
FeSO4+	-4.04
Fe(SO4)2-	-5.38
Fe(OH)3(aq)	12.56
Fe2(OH)2++++	2.95
FeCl2+	-2.13
FeOH++	2.19
Fe(OH)2+	5.67
Fe(OH)4-	21.6
KSO4-	-0.85
KCl(aq)	1.49
KOH(aq)	14.46
MgCO3(aq)	7.35
MgHCO3+	-1.07
MgOH+	11.44
MgSO4(aq)	-2.37
SiO(OH)3-	9.81
SiO2(OH)2--	23.14
NaCl(aq)	0.77
NaCO3-	9.06
NaHCO3(aq)	0.25
NaSO4-	-0.7
NaOH(aq)	14.18
CO2(aq)	-6.35
CO3--	10.33
HSO4-	-1.99
OH-	14
Zr++++	-0.24
SiO2(aq)	0
CaHSiO3+	8.57
NaHSiO3(aq)	7.76
SiO2(OH)2--	23.14

*Table 9-3: Equilibrium and kinetic constants. (1) CEMDATA07 (Lothenbach et al., 2008); (2) EQ3/6 (Wolery, 1992); (3) Thermoddem (Blanc et al., 2007); (4) Savage et al. (2002); (5) Palandri and Kharaka (2004).*kinetics of zircon was slowed down as it was used as inert filter material.*

Minerals	Chemical Formula	Log $K_{25°C}$	Ref.	Neutral mechanism		Base mechanism			Ref.
				Log $k_{25°C}$	E [kcal/mole]	Log $k_{25°C}$	E [kcal/mole]	n	
Anorthite	$CaAl_3Si_2O_8$	26.58	2	-9.1	4.3				5
Anhydrite	$Ca(SO_4)$	-4.36	1	-7.0	5.0				1
Brucite	$Mg(OH)_2$	16.30	2	-8.2	10.0				1
Calcite	$CaCO_3$	1.85	2	-5.8	5.6	-3.5	35.4	1 (pCO2)	5
Chalcedony	SiO_2	-3.46	3	-12.5	21.0				5
Clinochlore-14A	$Mg_5Al(Si_3Al)O_{10}(OH)_8$	67.24	2	-9.4	15.0	-14.5		-0.52 (OH-)	5
Cristobalite	SiO_2	-3.45	2	-12.3	15.5				5
Dolomite	$CaMg(CO_3)_2$	2.51	2	-7.5	12.5	-5.1		0.5 (OH-)	5
Gibbsite	$Al(OH)_3$	7.76	2	-11.5	14.6	-16.7	80.1	-0.784 (OH-)	5
Gypsum	$Ca[SO_4] \times 2H_2O$	-4.48	3	-2.8	0.0				5
Illite	$K_{0.6}Mg_{0.25}Al_{2.3}Si_{3.5}O_{10}(OH)_2$	9.03	2	-11.0	15.0				5
Montmor-MX80	$(Ca_{0.02}Mg_{0.03}Na_{0.11}K_{0.02})$ $(Al_{1.62}, Mg_{0.19}, Fe_{0.17})$ $(Si_{3.98}, Al_{0.02})O_{10}(OH)_2$	5.99	2	-14.4	11.5	-14.4	48.0	-0.13 (OH-)	5
Muscovite	$KAl_2[(OH)_2AlSi_3O_{10}]$	13.59	2	-13.6	5.3	-14.6	22.0	-0.22 (OH-)	5
Quartz	SiO_2	-4.00	2	-13.4	21.5	-16.3	108366.0	-0.5 (OH-)	5
Saponite(Mg)	$Mg_{3.17}(Si_{3.66}Al_{0.34}O_{10})(OH)_2\cdot 5(H_2O)$	26.25	2	-10.0	15.0				4
Talc	$Mg_3Si_4O_{10}(OH)_2$	21.14	2	-12.0	10.0				5
Zircon			2	-99.0	35.0				5
Al(OH)3am	$Al(OH)_3$	0.24	1	-7.0	5.0				1
Brucite	$Mg(OH)_2$	16.30	2	-7.0	5.0				1
CAH10	$CaAl_2(OH)_8\cdot 6H_2O$	-7.49	1	-7.0	5.0				1
C2AH8	$Ca_2Al_2(OH)_{10}\cdot 3H2O$	-13.56	1	-7.0	5.0				1
C2FH8	Ca2Fe2(OH)10·3H2O	-17.60	1	-7.0	5.0				1
C4FH13	Ca4Fe2(OH)14·6H2O	-29.40	1	-7.0	5.0				1

CSH_jen	$(CaO)_{1.67}(SiO_2)(H_2O)_{2.1}$	-13.16	1	-7.0	5.0	1
CSH_tob2	$(CaO)_{0.83}(SiO_2)(H_2O)_{1.3}$	-8.00	1	-7.0	5.0	1
Ettringite	$Ca_6Al_2[(OH)_{12}\vert(SO_4)_3]\cdot 26\ H_2O$	-44.84	1	-7.0	5.0	1
Fe(OH)3mic	$Fe(OH)_{3,am}$	-4.60	1	-7.0	5.0	1
Fe-Hemicarbonate	Ca4Fe2(CO3)0.5(OH)13·5.5H2O	-33.10	1	-7.0	5.0	1
Fe-Ettringite	Ca6Fe2(SO4)3(OH)12·26H2O	-43.94	1	-7.0	5.0	1
Fe-Hemicarboaluminate	Ca4Fe2(CO3)0.5(OH)13·5.5H2O	-33.10	1	-7.0	5.0	1
Fe-Monocarbonate	$Ca_4Fe_2(CO_3)(OH)_{12}\cdot 5H_2O$	-35.49	1	-7.0	5.0	1
Fe-Monosulfate	Ca4Fe2(SO4)(OH)12·6H2O	-33.18	1	-7.0	5.0	1
Fe-Stratlingite	$Ca_2Fe_2SiO_2(OH)_{10}\cdot 3H_2O$	-23.69	1	-7.0	5.0	1
Hemicarboaluminate	Ca4Al2(CO3)0.5(OH)13·5.5H2O	-29.12	1	-7.0	5.0	1
HydrogarnetOH	$Ca_3Al_2(OH)_{12}$	-20.84	1	-7.0	5.0	1
HydrogarnetFe	$Ca_3Fe_2(OH)_{12}$	-25.16	1	-7.0	5.0	1
HydrogarnetSi	$Ca_3Al_2(SiO_4)_{0.8}(OH)_{8.8}$	-29.87	1	-7.0	5.0	1
HydrotalciteC	Mg4Al2(OH)12 CO3·3H2O	-51.14	1	-7.0	5.0	1
HydrotalciteOH	Mg4Al2(OH)14·3H2O	-56.02	1	-7.0	5.0	1
HydrotalciteFe	Mg4Fe2(OH)14·3H2O	-59.99	1	-7.0	5.0	1
Monocarboaluminate	Ca4Al2(CO3)(OH)12·5H2O	-31.46	1	-7.0	5.0	1
Monosulfoaluminate	Ca4Al2(SO4)(OH)12·6H2O	-29.24	1	-7.0	5.0	1
Portlandite	$Ca(OH)_2$	22.81	1	-7.0	5.0	1
Stratlingite	$Ca_2Al_2SiO_2(OH)_{10}\cdot 3H_2O$	-19.70	1	-7.0	5.0	1
SiO2,am	SiO_2	1.48	1	-7.0	5.0	1
Sygenite	$K_2Ca(SO_4)_2\cdot H_2O$	-7.20	1	-7.0	5.0	1
Tricalcium aluminate	$Ca_4Al_2(OH)_{14}\cdot 6H_2O$	-25.40	1	-7.0	5.0	1

9.4. Initial conditions

The 1D model represented a simplified core infiltration experiment. It consisted of an inflow reservoir, a filter, and a bentonite core. A more detailed description of the experimental setup is given in *chapters 4 & 5*. The temperature was set to 25°C. The system was discretized in 27 cells; 2 inlet filter cells of 0.1 cm length and 25 cells of 0.2 cm for the bentonite core (Figure 9-1).

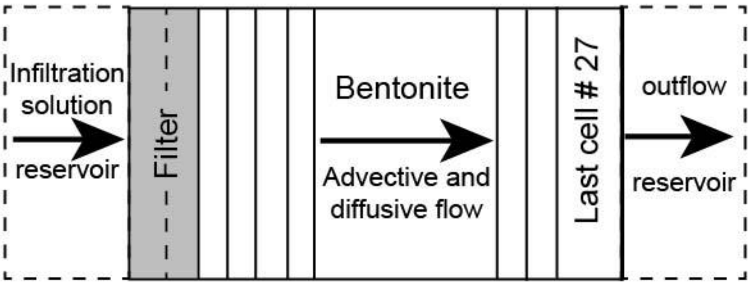

Figure 9-1: Sketch of the 1D CrunchFlow model of the experiment.

The boundary on the inlet filter side was defined as flux, consisting of a hidden ghost cell with constant fluid composition (infiltration solution). At the end of the bentonite (last cell #27), the flow entered into a second ghost cell (Figure 9-1). Both boundary conditions were set to flux, allowing advection, but no back-diffusion. The outflow was monitored using cell #27, the last cell of the bentonite. Two different infiltration solutions were used: APW_{OPA}, a clay pore-water to equilibrate the core, and APW_{OPC}, an artificial ordinary Portland cement pore-water with a pH of 13.4. For the filter material an inert zircon (log rate -50) was used, with a macroporosity of 80%, including a negligible amount of montmorillonite with microporosity to prevent the code from crashing (Table 9-3).

The bentonite core consisted of a mineralogy using MX-80 data of Karnland (2010): montmorillonite 81.4 wt%, quartz 4.9 wt%, plagioclase 3.5 wt%, muscovite 3.4 wt%, gypsum 3.4 wt%, cristobalite 2.8 wt%, illite 0.8 wt%, and calcite 0.2 wt%. For the initial bentonite pore-water the chemistry of the first syringe of the experiment was used (Table 9-5). The initial porosity was taken from Fernández et al. (2011b), who calculated for a bentonite of similar density, based on anion exclusion estimations, the distribution between micro- (interlayer) and macroporosity (intergranular) of 85% and 15%, respectively. In our case using a wet core weight and a water content of 186.69 g and 32.6 wt%, respectively, the macroporosity was 7 vol% and the microporosity 40 vol%. The microporosity occurred only in the montmorillonite. Mineral precipitation or dissolution changed the macroporosity of the core. For this reason the porosity was updated in the calculation with the restriction of complete pore clogging, as this would stop flow and hence the calculation. This was implemented in the code by setting the threshold porosity to 1%. The SumMicroMacro was set to false, while the microporosity and the Debye length were updated. This means that the microporosity varied with the ionic strength of the pore-fluid. Initially, the code sets solids plus macroporosity to 100 vol%, while the microporosity was considered as additional porosity. Therefore, total core volume is not constant, representing experimental observations. The Debye length factor defines the multiples of the original Debye length and was set to 0.8, based on Holmboe et al. (2012). 10% of the surface charge was balanced by cations in the Stern layer while the diffuse layer charge balanced 90%. Using the cation exchange capacity (CEC) of montmorillonite of 0.756 eq/g measured by Karnland (2010), this gives for the Stern layer an amount of 0.0756 meq/g_{mont} (1.25×10^{-7} mol/m^2; surface complex sites) and for the diffusive layer 0.68 meq/g_{mont} (fixed mineral charge). The specific surface area of montmorillonite was set to 788 m^2/g (Tournassat et al., 2003). The following cation exchange coefficients were used as selectivity coefficients for surface complexation (given as surface complexation reaction) (Bradbury and Baeyens, 2002; Fernández and Mäder, 2011; Tournassat et al., 2004): Na-montmorillonite 4.6, Ca-montmorillonite 8.8, K-montmorillonite 4.6 and Mg-montmorillonite 8.86. The diffusion coefficients were set for macro- and microporosity independently using coefficients from Fernández and Mäder (2011). The diffusion coefficients including tortuosity ($D_0\times\tau$) in the microporosity were in the range of 10^{-12} m^2/s for monovalent and 10^{-13} m^2/s for divalent cations, and 10^{-16} m^2/s for anions. The diffusion coefficients in the macroporosity were in the range of 10^{-10} –10^{-9} m^2/s. The advective flow was assumed to be equal to the specific flux (Darcy flux), calculated from the measured volumetric flow rates of the core infiltration outflow. Based on the measurements, the Darcy flux was considered to be constant in certain time intervals (Table 9-4).

Table 9-4: Darcy velocities used for the advective flow.

Fluid	Time [days]	Advective flow measured [m/s]	Advective flow adapted to Cl^- [m/s]
APW_{OPA}	0-135	5.48E-10	5.48E-10
APW_{OPC}	136-300	1.73E-10	6E-10
	300-420	1.50E-10	1.50E-10
	420-660	5.71E-11	5.71E-11

Table 9-5: Infiltration solution and bentonite initial pore-water composition (macroporosity).

	APW_{OPA}	APW_{OPC}	Bentonite (initial)
pH	7.65	13.4	7.50
		mmol/kg	
Ca^{2+}	11.93	1.32	18
Mg^{2+}	9.1	-	9
K^+	2.7	222.0	3
Na^+	165.9	118.654	400
Cl^-	charge	-	337
Si^{4+}	0.01	0.06	1.75
Al^{3+}	0.0006	0.03	0.0014
SO_4^{2-}	22.1	2.9	53
HCO_3^-	0.66	1.5	2.87
$Zr(OH)_2^{2+}$	-	-	-
Tracer	0.1	0.4	-

9.5. Results and Discussion

Evolution of physical parameters and outflow chemistry. Modeling the ***APW_{OPA} infiltration period*** with the measured specific flux, a perfect fit of modeled and measured ion concentrations was achieved (Figure 9-2A). The modeled pH of the first 4 aliquots was below the measured value, most likely due to a technical artefact in the experiment (*chapter 5*). As described in Fernández and Mäder (2011), the Ca^{2+} concentration was during the equilibration period slightly too high in the model, related to the gypsum dissolution/precipitation.

Doing the same for the ***APW_{OPC} infiltration period***, the modeled chloride and calcium concentrations were too high, while sulfate was too low compared to the measured concentrations (Figure 9-2A). Modeled sodium, potassium and magnesium concentrations showed a perfect fit with the measured data (Figure 9-2A). The discrepancy between modeled and measured anion concentrations and calcium occurred in the model during the transient-flow phase (136–300 days), while the measured flow seemed to be too low to reproduce these ion concentrations correctly (Figure 9-2A). Fitting the advective flow to the measured Cl^- concentration, led to a 3× higher Darcy velocity (see Table 9-4, Figure 9-2B). Using a higher Darcy velocity, modeled anion and calcium concentrations fit perfectly the measured concentrations; while the rest of the cations showed significant deviations (Figure 9-2B). It is not clear, why a higher Darcy velocity during the transient-flow phase showed a better fit to the measured chloride, sulfate and calcium concentrations, while most of the cations showed the opposite trend.

The modeled pH of the outflow was slightly too low in both models during the high-pH infiltration period, while the pH buffering happened directly at the inflow (Figure 9-3). The sulfate evolution in the outflow was mainly a function of gypsum dissolution/precipitation. A comparison of model results using gypsum data of two different databases (EQ3/6 (Wolery, 1992), Thermoddem (Blanc et al., 2007)) using identical kinetics showed that only gypsum from the Thermoddem database reproduced the sulfate increase correctly, while the gypsum from the EQ3/6 database reduced the concentration strongly. Modifying the kinetic coefficients of gypsum changed only the time-point of the increase (it increases much earlier) but not the slope (rate) of the curve. After ~420 days of infiltration, the advective flow decreased drastically, leading to a diffusion-dominated flow regime in both models (Péclet number ~1). The silica and alumina increase in the outflow could not be modeled. The problem was that in the model, released silica and aluminum was incorporated in mineral phases rather than accumulated in the pore-fluid. It indicates a lack of thermodynamic and kinetic data for such conditions.

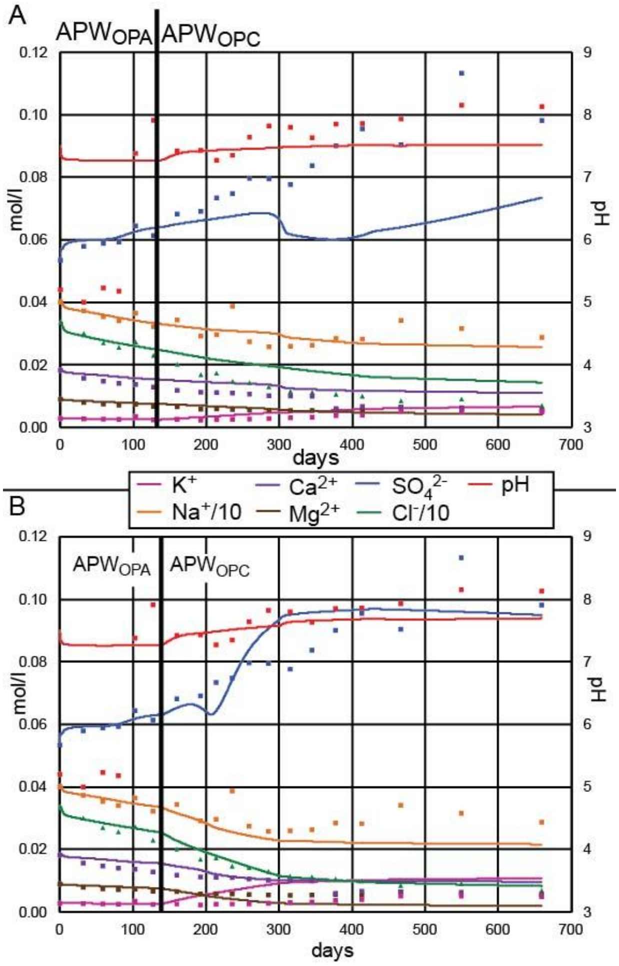

Figure 9-2: Comparison of the modeled results (lines) and the measured outflow data (symbols; see chapter 5): using the measured hydraulic conductivities; (B) using for the transient phase during the APW_{OPC} infiltration (136–300 days) an increased hydraulic conductivity.

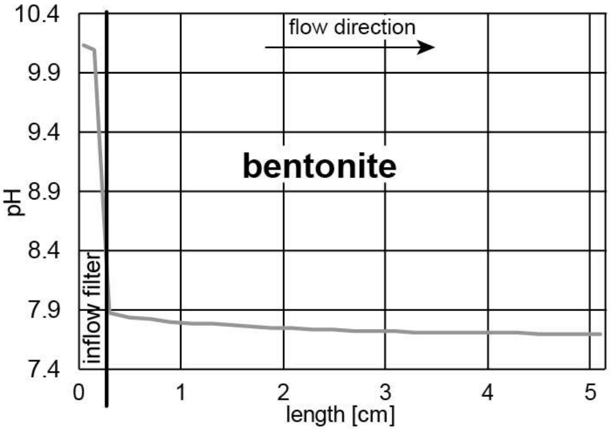

Figure 9-3: Modeled pH along a core transection after 660 days of infiltration.

Mineralogy. The post-mortem mineralogy of the bentonite core and the inlet filters is shown in *chapter 5*. The modeled mineralogy at the beginning and after 660 days of infiltration is shown in Figure 9-4. The model predicted precipitation of small amounts of talc, brucite, gypsum, saponite and calcite in the inlet filter, which is in agreement to the post-mortem analysis of the filter. Further precipitation of saponite, talc and gypsum in the inflow region of the bentonite was predicted, while montmorillonite, cristobalite and quartz dissolved. In the rest of the core, gypsum dissolved completely. The size of the reaction plume in the model was in the range of 0.6–0.7 mm, which in agreement to the observations made in the experiment. The main discrepancy of the model was the lack of calcite precipitation in the bentonite. The modeled gypsum precipitation in the inflow region was likely identical to a weak SO_4^{2-} enrichment observed by SEM-EDX (*chapter 5*). The modeled dissolution of cristobalite was in agreement to the experiment. In the model talc precipitation in filter and bentonite core buffered the pH of the system. In the experiment, it was not entirely clear which mineral phase was the main pH buffer, while a possible phase could be saponite. The interlayer porosity increased during the experiment from ~40 vol% to 46–48 vol% (Figure 9-4). The interlayer as well as the intergranular porosity got strongly reduced in the bentonite directly at the fluid inflow.

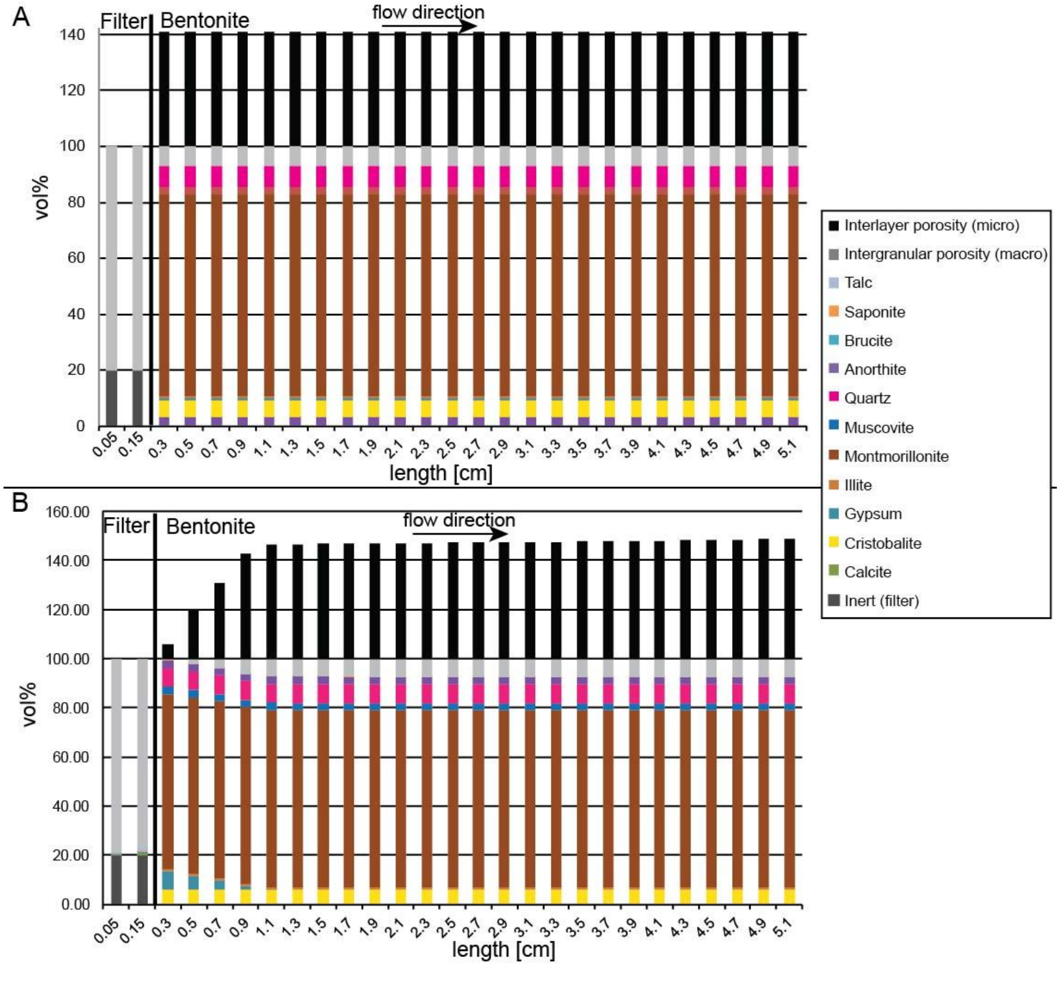

Figure 9-4: Minerals assemblage: (A) at the beginning (0 days); (B) after 660 days of infiltration.

The comparison of the measured (SEM-EDX) and modeled chemistry along a transection in the core is shown in Figure 9-5, whereas only the modeled solids chemistry was considered. The core could be reproduced by the model to some degree, with the exception of alumina, which was in the model much too low. As alumina was mainly occurring in the smectite, we can assume that the montmorillonite used for modeling had too low alumina content. The measured silica and alumina decrease in the inflow region of the bentonite could be reproduced by the model. The calcium and magnesium enrichment in the first mm of the bentonite core was not reproduced but rather occurred in the inlet filter.

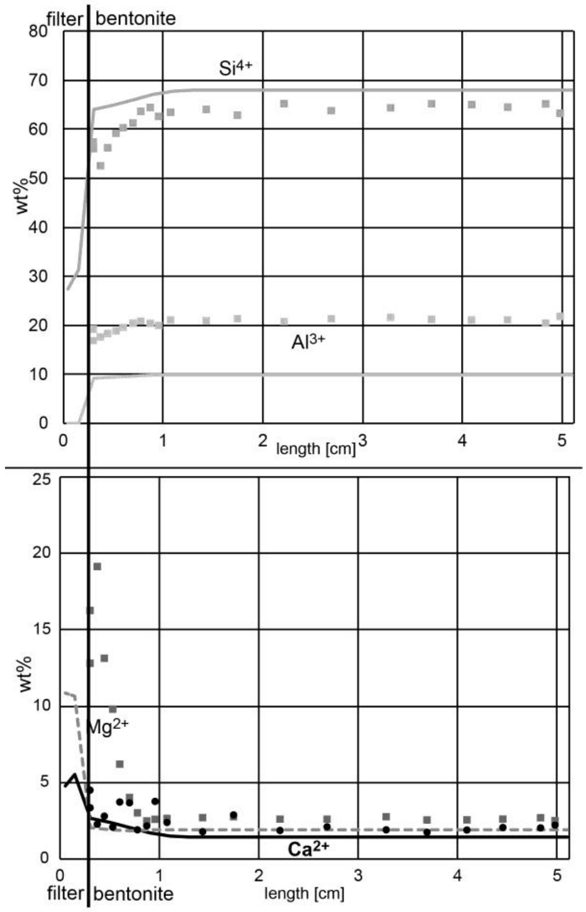

Figure 9-5: Measured chemical composition of the experiment (symbols) and of the model (line) along a transection through the core after 660 days of infiltration. 100 wt% refer to the sum of Si, Al, Ca, Mg (measured by EDX).

9.6. Conclusions

Reactive transport modeling using CrunchFlow could reproduce the measured data to some extent. The outflow chemistry of the experiment could be reproduced correctly by the model during the equilibration phase, while the high-pH phase showed some deviations. Modeling showed that the measured specific flux (Darcy flux) during the transient phase could only reproduce cation concentrations, while anions and calcium only match the measured outflow concentration using a higher specific flux. The main problem is possibly related to an imprecise calculation of the two porosity domains. After 420 days of infiltration, the model could reproduce the Cl^- concentration in the outflow, indicating a diffusive dominated flow.

The following key processes already concluded based on experimental data were also identified in the modeling results:

- Mineral reactions occurred in the model mainly in the filter, which is in contrast to the experiment. The predicted precipitation of talc, brucite, gypsum, saponite and calcite in the inlet filter was in agreement to the observations in the experiment, due to back-diffusion and pH decrease in the filter.
- The model predicts the precipitations of saponite and gypsum in the bentonite while montmorillonite and minor amounts of cristobalite and quartz are dissolved, in agreement with post-mortem data.
- Porosity reduction in the inflow region of the bentonite core resulted from the model. In the experiment, hydraulic conductivity decreased substantially due to this porosity reduction. The simplified model approach using constant flow cannot reproduce this porosity-conductivity coupling.
- The model predicts Mg phase precipitations in the filter due to upstream diffusion of Mg in the microporosity of the bentonite core. Therefore, the model can confirm this major process derived in *chapter 5*. In general, post-mortem data showed minor Mg phases in the filter, but major Mg enrichment in the core at the inlet.

Main problems are the lack of accurate thermodynamic and kinetic data, specifically for high-pH conditions and more time for fine tuning of the model.

References

Berner, U., Kulik, D.A., Kosakowski, G., 2013. Geochemical impact of a low-pH cement liner on the near field of a repository for spent fuel and high-level radioactive waste. Physics and Chemistry of the Earth, Parts A/B/C 64, 46-56.

Blanc, P., Lassin, A., Piantone, P., 2007. Thermoddem a database devoted to waste minerals. BRGM, (Orléans, France). http://thermoddem.brgm.fr.

Bradbury, M.H., Baeyens, B., 2002. Sorption of Eu on Na- and Ca-montmorillonites: experimental investigations and modelling with cation exchange and surface complexation. Geochimica et Cosmochimica Acta 66, 2325-2334.

Chipera, S.J., Apps, J.A., 2001. Geochemical Stability of Natural Zeolites. Reviews in Mineralogy and Geochemistry 45, 117-161.

Ehrenstein, G., 2001. Surface charge. Biophysics Textbook online.

Fernández, R., Cuevas, J., Mäder, U.K., 2009. Modelling concrete interaction with a bentonite barrier. European Journal of Mineralogy 21, 177-191.

Fernández, R., Cuevas, J., Mäder, U.K., 2010. Modeling experimental results of diffusion of alkaline solutions through a compacted bentonite barrier. Cement and Concrete Research 40, 1255-1264.

Fernández, R., Mäder, U., Steefel, C., 2011a. Modelling of a bentonite column experiment with CrunchFlow including new clay-specific transport features. Mineralogical Magazine 75(3), 839.

Fernández, R., Mäder, U., 2011. Modelling the bentonite column experiment with CrunchFlow and comparison of results with PhreeqC, including diffuse layer features. Internal Nagra Working Report, Wettingen, Switzerland.

Fernández, R., Mäder, U., Jenni, A., 2011b. Multi-component advective-diffusive transport experiment in MX-80 compacted bentonite: Method and results of 1st phase of experiment. Internal Nagra Working Report, Wettingen, Switzerland.

Gaucher, E.C., Blanc, P., Matray, J.-M., Michau, N., 2004. Modeling diffusion of an alkaline plume in a clay barrier. Applied Geochemistry 19, 1505-1515.

Gaucher, E.C., Blanc, P., 2006. Cement/clay interactions - A review: Experiments, natural analogues, and modeling. Waste Management 26, 776-788.

Holmboe, M., Wold, S., Jonsson, M., 2012. Porosity investigation of compacted bentonite using XRD profile modeling. Journal of Contaminant Hydrology 128, 19-32.

Karnland, O., 2010. Chemical and mineralogical characterization of the bentonite buffer for the acceptance control procedure in a KBS-3 repository. SKB Technical Report 10-60, Stockholm, Sweden.

Kosakowski, G., Berner, U., 2013. The evolution of clay rock/cement interfaces in a cementitious repository for low- and intermediate level radioactive waste. Physics and Chemistry of the Earth, Parts A/B/C.

Kosakowski, G., Berner, U., Wieland, E., Glaus, M., Degueldre, C., 2014. Geochemical evolution of the L/ILW near-field. Nagra Technical Report NTB 97-04, Nagra, Wettingen, Switzerland.

Lehikoinen, J., 2009. Bentonite-Cement Interaction – Preliminary Results from Model Calculations. POSIVA Working Report 2009-37, Eurajoki, Finland.

Lothenbach, B., Matschei, T., Möschner, G., Glasser, F.P., 2008. Thermodynamic modelling of the effect of temperature on the hydration and porosity of Portland cement. Cement and Concrete Research 38, 1-18.

Noy, D.J., 1998. User Guide to PRECIP, a Program for Coupled Flow and Reactive Solute Transport. Brit. Geol. Surv. Tech. Rep. WE/98/13. British Geological Survey, Keyworth, UK.

Palandri, J.L., Kharaka, Y.K., 2004. A compilation of rate parameters of water-mineral interaction kinetics for application to geochemical modelling, Open File Report 2004-1068. U.S. Geological Survey (USGS) and National Energy Technology Laboratory - United States Department of Energy.

Savage, D., Noy, D., Mihara, M., 2002. Modelling the interaction of bentonite with hyperalkaline fluids. Applied Geochemistry 17, 207-223.

Savage, D., Soler, J.M., Yamaguchi, K., Walker, C., Honda, A., Inagaki, M., Watson, C., Wilson, J., Benbow, S., Gaus, I., Rueedi, J., 2011. A comparative study of the modelling of cement hydration and cement–rock laboratory experiments. Applied Geochemistry 26, 1138-1152.

Steefel, C.I., Yabusaki, S.B., 1996. OS3D/GIMRT, Software for multicomponent-multidimensional reactive transport: User’s Manual and Programmer’s Guide, PNL-11166. Pacific Northwest National Laboratory, Richland, Washington.

Steefel, C.I., 2001. GIMRT, version 1.2: Software for Modeling Multicomponent, Multidimensional Reactive Transport, User's Guide, UCRL-MA-143182. Lawrence Livermore National Laboratory: Livermore, California.

Steefel, C.I., 2006. CrunchFlow. Software for Modeling Multicomponent Reactive Flow and Transport, User's manual. E. S. Division Ed. Lawrence Berkeley National Laboratory: Berkeley, CA.

Steefel, C.I., 2010. Development of an explicit diffuse layer model for CrunchFlow, Update. E. S. Division Ed. Lawrence Berkeley National Laboratory: Berkeley, CA.

Tournassat, C., Neaman, A., Villéras, F., Bosbach, D., Charlet, L., 2003. Nanomorphology of montmorillonite particles: Estimation of the clay edge sorption site density by low-pressure gas adsorption and AFM observations. American Mineralogist 88, 1989-1995.

Tournassat, C., Ferrage, E., Poinsignon, C., Charlet, L., 2004. The titration of clay minerals: II. Structure-based model and implications for clay reactivity. Journal of Colloid and Interface Science 273, 234-246.

Tournassat, C., Appelo, C.A.J., 2011. Modelling approaches for anion-exclusion in compacted Na-bentonite. Geochimica et Cosmochimica Acta 75, 3698-3710.

Ueda, H., Takase, H., Savage, D., Benbow, S., Noda, M., 2007. Evaluation of the kinetics of cement–bentonite interaction in a HLW repository using the reactive solute transport simulator, 15th International Conference on Nuclear Engineering, Nagoya, Japan.

Walther, J.V., 1996. Relation between rates of aluminosilicate mineral dissolution, pH, temperature, and surface charge. American Journal of Science 296, 693-728.

Watson, C., Hane, K., Savage, D., Benbow, S., Cuevas, J., Fernández, R., 2009. Reaction and diffusion of cementitious water in bentonite: Results of "blind" modelling. Applied Clay Science 45, 54-69.

Wolery, T.J., 1992. EQ3/6, a software package for geochemical modeling of aqueous systems: Package overview and installation guide (Version 7.0), Other Information: PBD: 14 Sep 1992, p. Medium: ED; Size: 70 p.

Wolery, T.J., Daveler, S.A., 1992. EQ6, a computer program for reaction path modelling of aqueous geochemical systems: Theoretical manual, user's guide, and related documentation (version 7.0). Lawrence Livermore National Laboratory,Livermore, California, USA, UCRL-MA-110662 PT IV.

Yamaguchi, T., Sakamoto, Y., Akai, M., Takazawa, M., Iida, Y., Tanaka, T., Nakayama, S., 2007. Experimental and modeling study on long-term alteration of compacted bentonite with alkaline groundwater. Physics and Chemistry of the Earth, Parts A/B/C 32, 298-310.

10 Conclusions

Method

The feasibility of the combination of X-ray computed tomography (CT) and core infiltration technique was demonstrated. It is a useful tool to record indirectly mineral alterations and directly variations in bulk density, volume and diameter of compacted bentonite and s/b cores during long-term experiments using high-pH solutions. The physical integrity of all interface regions (core–filter) was preserved in this setup with a total pressure boundary condition on the core sample. This is in contrast to some past experiments carried out at constant-volume condition, where shrinkage in bentonite led to the formation of preferential pathways and breakthrough of a high-pH plume. Constant confining pressure constraints may be more realistic for a repository environment due to the ability of the surrounding and unaltered bentonite to compensate volumetric changes at the interface.

Experiments

In the current study, compacted and saturated MX-80 bentonite and 65/35% sand/MX-80 bentonite (s/b) core samples were exposed to different high-pH cementitious pore-fluids: artificial ordinary Portland cement pore-water (APW_{OPC}, pH 13.4, ionic strength 0.28 mol/kg) and artificial 'low-pH' shotcrete pore-water (APW_{ESDRED}, pH 11.8, ionic strength 0.11 mol/kg). Prior to high-pH infiltration, the core samples were equilibrated in the core infiltration setup using an artificial clay pore-water (APW_{OPA}, pH 7.6, ionic strength 0.23 mol/kg). The behavior of bentonite and s/b cores was controlled by several physical and chemical processes: ionic-strength effects and coupled transient compaction/de-compaction, cation exchange processes, dissolution/precipitation of carbonate (e.g. calcite), sulfate (e.g. gypsum) and silicate minerals (e.g. cristobalite, saponite).

A simple two-porosity concept is used as basis for interpretation and discussion: microporosity (interlayer porosity) comprises interlayer volumes of smectite and outer diffuse layers (DL), e.g. all water that is affected by permanent clay surface charges. Macroporosity ("free pore water") is the remaining intergranular porosity containing water not affected by surface charges. It is also approximately the flow-active porosity when advection takes place, or approximately also corresponds to the anion-accessible porosity. Diffusive transport is slower compared to advection and occurs in the entire porosity (interlayer and intergranular porosity). In case of clogging of the macroporosity (intergranular porosity), the diffusive transport in the microporosity (interlayer porosity) will be the main transport mechanism.

Bentonite experiments. Initially, the apparent hydraulic conductivity did increase in bentonite due to core compaction and a resultant additional outflow. The true hydraulic conductivity was 6×10^{-14}–1×10^{-13} m/s during APW_{OPA} infiltration. APW_{OPC} and APW_{ESDRED} infiltration reduced the hydraulic conductivity to 3.1–4.2×10^{-15} m/s, while the flow regime changed from advective to diffusive-dominated, with Péclet numbers ≤1. This drop was in both cases induced mainly by mineral precipitations (calcite, saponite) in bentonite (and possibly filter) and possibly also partly by a high ionic strength pore-fluid. In case of high ionic strength solutions (APW_{OPC}), the hydraulic conductivity of bentonite was reduced at constant hydrostatic conditions due to osmotic effects, whereby the interlayer porosity and the DL got reduced. This induced core compaction at constant pressure conditions, which also reduced the flow-active (intergranular) porosity. This is in agreement to observed bentonite core shrinkage in both experiments, while in case of APW_{ESDRED} infiltration, it has to be assumed that the fluid evolved in the core from a low to a high ionic strength pore-fluid in the inflow region.

The outflow exhibited first an increased ionic strength after starting the experiment, explained by core compaction and expelling excess ions from the intergranular pore-space. The outflow was characterized by increasing sulfate concentrations due to gypsum dissolution, replacing chloride as initial main anionic charge carrier and keeping the ionic strength of the outflow high. Sodium was enriched in the outflow, indicating replacement from the clay exchanger by magnesium and calcium, which were both reduced in the outflow. The pH was in both cores buffered at ~8, while all hydroxide was efficiently removed by saponite and possibly brucite and talc precipitation. Formate as main anionic charge carrier of APW_{ESDRED}, did not reach the outflow at current time-scale and no information on its (bio)chemical stability within the core could be gained.

Precipitation of calcite was observed in the inflow filters and in the macroporosity of the adjacent inflow region of both cores, induced by the high-pH plume of the infiltration solutions. In the ESDRED experiment, calcite growth was limited to small-scale preferential flow path in the first µm of the clay matrix. In the OPC experiment, calcite occurred in the first mm of the inflow region, spread across the entire bentonite matrix.

Precipitation of an Mg-rich mineral phase was observed in the inflow regions of both cores, while in the OPC experiment this Mg-enriched zone was more pronounced and extensive. The newly formed magnesium phase could be identified as saponite (trioctahedral smectite), while the occurrence of brucite and talc were only confirmed in the inflow filter of the OPC experiment. Silica got enriched in the outflow, indicating dissolution of silicate-minerals, most likely cristobalite.

Sand/bentonite experiments. The hydraulic conductivity of s/b was 4×10^{-12}–1×10^{-11} m/s during the equilibration phase. APW_{OPC} infiltration reduced the hydraulic conductivity by ~1 order of magnitude to 9.7×10^{-13} m/s, while APW_{ESDRED} infiltration had no effect during the time frame of the experiment (8 months). The hydraulic conductivity of s/b was reduced at constant hydrostatic conditions by mineral precipitations (calcite, saponite) in s/b (and possibly filter) and probably partly also by a high ionic strength (APW_{OPC}) solution. In case of high ionic strength solutions (APW_{OPC}), the reduction in hydraulic conductivity could have been induced by osmotic effects, whereby the interlayer porosity and the corresponding DL got reduced. This compacted further the s/b sample near the fluid inlet by reducing the intergranular porosity at constant hydrostatic conditions. In both cores, the infiltration solution got strongly altered in the inflow region, showing at the outflow a pore-fluid of low ionic strength, inducing the overall observed core expansion. This expansion indicates that the s/b framework changed from mostly grain-supported to matrix-supported.

Chloride as main anionic charge carrier of the clay pore-water used for core equilibration was replaced by the alkalinity (bicarbonate) and in case of the ESDRED experiment as well by acetate and formate. Hydroxide, the main anionic charge carrier of APW_{OPC} was consumed by saponite and possibly brucite and talc precipitation. Formate, the main negative charge carrier of APW_{ESDRED} was strongly consumed and transformed by inferred microbial activity. The outflow had in both experiments an ionic strength of ~0.05 mol/kg. Core expansion was observed in both s/b samples, induced by low ionic strength pore-fluids, which increased the interlayer porosity (swelling) and hence the core volume. The pH of s/b was buffered in both cores at ~8.6. Formate reached the outflow only for a short period, followed by a strong increase of acetate, indicating microbial activity. Black spots on the core surface, a rotten-egg smell of the post-mortem core material (sulfate reduction) and gas accumulation in the outflow supported this hypothesis (possibly CO_2 from formate degradation). Not clear is, if the microbes only occurred at the interface or also in the s/b core. The occurrence of gas in the outflow may indicate a two-phase flow that was active during the experiment. The anion accessible porosity (based on Cl^-) and therefore also the flow-active porosity of s/b was 30–50% of the initial water content, while the apparent transport porosity for water (^2H traced) was 67–85% of the water content.

Extensive calcite precipitation in inflow filters and macroporosity of the s/b cores was observed, induced by the high-pH plume of the infiltration solutions. Precipitation of an Mg-mineral phase was observed in the inflow region of the OPC experiment, while in the ESDRED experiment, the new mineral phase was limited to the inlet filter. Mg-rich minerals were identified as saponite, while in the inlet filters of the OPC experiment also talc and possibly brucite were detected. Silica enrichment in the outflow was observed in both experiments, indicating dissolution of a SiO_2-phase. Only in the OPC experiment the SiO_2-phase could be identified as cristobalite.

OPC experiments. APW_{OPC} infiltration reduced the hydraulic conductivity in bentonite and s/b, while the values in bentonite were ~3 orders of magnitude lower using confining fluid pressures of ~4 and 1.7 MPa, respectively. The strong reduction is explained mainly by extensive mineral precipitations (calcite, saponite) and possibly also partly by the high ionic strength APW_{OPC}, reducing the flow-active porosity. It is inferred that at constant hydrostatic conditions, high ionic strength pore-fluids reduce the interlayer porosity and the DL, which induce core compaction and hence a reduction of the intergranular porosity, which may results in a lower hydraulic conductivity.

In both cores, hydroxide, the main anionic charge carrier of APW_{OPC} was strongly consumed by mineral reactions in the inflow region. In bentonite, the OH^- got replaced by sulfate from gypsum dissolution, while in s/b the OH^- was only marginally replaced by bicarbonate (alkalinity), inducing a strong drop in the ionic strength of the pore-fluid. It further explains the different behavior of the core volumes, while bentonite shrunk (high ionic strength pore-fluid) and s/b expanded (low ionic strength pore-fluid). The high pH of APW_{OPC} got buffered in bentonite at ~8 and in s/b at ~8.6, with bentonite showing a higher ionic strength outflow and s/b a lower one.

Precipitation of calcite, saponite and possibly brucite was observed in both cores/filters, while in s/b the precipitates were more extensive due to the higher hydraulic conductivity and larger fluid throughput. Silica enrichment in the outflow indicated dissolution of cristobalite.

ESDRED experiments. APW_{ESDRED} infiltration reduced the hydraulic conductivity in bentonite but not in s/b. As it is assumed that the hydraulic conductivity got mainly reduced by mineral precipitation, the contradictory behavior of the two materials is not clear. It could be theoretically explained by the different ionic strength of the pore-fluids, while in case of high ionic strength fluids, the flow-active porosity got reduced. In case of bentonite, the pore-fluid got strongly enriched in sulfate due to gypsum dissolution, increasing the ionic strength of the APW_{ESDRED}. In s/b, the high hydraulic conductivity, inhibiting kinetically the buffering by gypsum, along with the low gypsum content did not induce sulfate enrichment in the pore-water. Not clear is why in case of s/b the mineral precipitations (calcite) did not clog the macroporosity and hence reduced the fluid flow. Formate and hydroxide were both consumed, reducing the ionic strength of the pore-fluid relative to APW_{ESDRED}. The same process explains the bentonite core shrinkage (high ionic strength pore-fluid) and the s/b core expansion (low ionic strength pore-fluid).

The high ionic strength outflow of bentonite was dominated by sulfate, while the low ionic strength outflow of s/b by organic acids (formate, acetate) and carbonate alkalinity. Formate, the main anionic charge carrier of APW_{ESDRED}, was not detected in the outflow of bentonite, while in s/b it was only observed for a short period, followed by increased acetate concentrations. In s/b, the occurrence of acetate, gas and black spots in inlet filters and on the core surface indicated the presence of microbes, not observed in bentonite. The high pH of APW_{ESDRED} got buffered in bentonite at ~8 and in s/b at ~8.6.

Calcite precipitation was observed in the inflow region of both cores. Mg-enrichment (saponite) only occurred in bentonite and was restricted in the s/b experiment to the inlet filters. Enrichment of silica in the outflow indicated dissolution of a SiO_2-mineral that could not be identified by XRD or SEM.

Hypothetical long-term evolution of the experiments. The hydraulic conductivity reduction changed the transport regime from advective to diffusive-dominated, slowing down the alteration of the buffer material. This change is induced by a clogging of the macroporosity (intergranular porosity), while diffusion occurs as well in the microporosity (interlayer porosity). In this case, anion transport will be strongly reduced, as they are excluded from the microporosity and hence cation diffusion will be the main transport process.

As the pore-water was strongly influenced by gypsum dissolution and resultant sulfate enrichment, the main question is for how long this process will determine the system. And followed by this arises the next question: what would happen to the ionic strength of the pore-fluid and thereby to the physical properties of the bentonite after complete dissolution of gypsum?

Only ~20 wt% of the gypsum got dissolved during the course of the experiments. The diffusive transport of sulfate out the system will be the limiting factor for gypsum dissolution. A rather high initial gypsum content along with high sulfate concentrations in the equilibration fluid (APW_{OPA}) will further delay the process and complete gypsum dissolution may not occur over hundreds or thousands of years. In the hypothetical case that gypsum gets completely dissolved from the material, the ionic strength of the pore-fluid is assumed to decrease drastically, like observed in s/b. Even the high ionic strength APW_{OPC} fluid will be strongly buffered, losing its ion load by mineral precipitation. A low ionic strength pore-water would increase the interlayer porosity by means of osmotic effects, which leads to swelling, in case additional space is available, or an increase in swelling pressure. In the current constant pressure device, the effect of low ionic strength pore-water on the fluid flow is not clear but may induce a higher hydraulic conductivity, as observed in the s/b–APW_{ESDRED} experiment. As the fluid flow reduction was mainly induced by mineral precipitations in the macroporosity, it is not clear, if a change in the ionic strength of the pore-water could lead to a higher hydraulic conductivity.

The long-term evolution of s/b will be mainly controlled by the amount of bentonite (35%), which is assumed to buffer the high-pH fluid. In the APW_{OPC} experiment, the alteration is strongly slowed down due to the low hydraulic conductivity of bentonite. In the APW_{ESDRED} experiment, showing no reduction in hydraulic conductivity after switching fluids, the alteration of the material will happen much faster, while the microbial processes in this case could not be addressed.

Advection-dominated vs. diffusion-dominated transport. In the current core infiltration approach, a small advective flux was induced to accelerate and extend the bentonite and s/b alteration, but not changing the chemical evolution of the system fundamentally. In a nuclear waste repository advective transport is not expected to occur, while diffusive transport will be the only transport process (Bradbury et al., 2012; Nagra, 2002). The main implication between diffusive and advective transport are the amount of solution and ions transported through the core. In case of diffusion it is assumed that the pore-water has enough time to equilibrate with the mineralogy near the inflow, limiting reactions to a small zone, while in an advective dominated flow regime (e.g., during initial bentonite saturation) the buffering happens over a larger distance, while small flow rates guarantee equilibration with the mineralogy. The chemical buffering capacity of bentonite will be the limiting factor, controlling the extension of the reaction plume.

Initially, all experiments showed an advective flow regime during the equilibration phase. APW_{OPC} infiltration reduced the hydraulic conductivity in bentonite and s/b drastically, while APW_{ESDRED} infiltration reduced only the fluid flow in bentonite but not in s/b. The Péclet number based on chloride was ≤1 in bentonite during the high-pH infiltration, indicating a change from advection to diffusion. In case of clogging of the intergranular (macro) porosity by mineral precipitation, diffusion in the interlayer porosity will be the dominate transport process. This indicates that the observed reactions were most likely induced partly by a diffusive-like flow, while the advection was of minor importance, in particular after the transient phase was finished. CT scans confirmed that mineral reactions are progressing even during a diffusive dominated flow regime.

Implications

Implication for a nuclear waste repository. In the current experiments, the reaction plume extended 0.2–8 mm into the bentonite cores after 1–2 years of high-pH infiltration. This is a larger extent if extrapolated linearly compared to pure diffusion-based models for bentonite, where reaction zones were predicted to extend only 5–10 cm into the buffer after 10’000 years (Bradbury et al., 2012; Gaucher et al., 2004; Savage et al., 2002). It implies that the current experimental approach enhanced mineral reactions by using an increased fluid flow, compared to pure diffusion-dominated flow regimes.

Bentonite buffer and s/b backfill material exhibited both a strong pH-buffering capacity, as predicted by models (Bradbury et al., 2012; Gaucher et al., 2004; Kosakowski and Berner, 2013; Kosakowski et al., 2014). High-pH fluids influenced the mineralogy and the chemistry of the pore-fluid, which further affected the hydraulic conductivity and the volume/swelling pressure. The high-pH mineral reactions were limited to the inflow zone, while gypsum partially dissolved in the entire sample. No complete pore clogging was observed but the hydraulic conductivity was rather strongly reduced in most of the experiments, explained by clogging of the intergranular porosity (macroporosity) by mineral precipitation (calcite, saponite). This may delay the saturation of the bentonite buffer adjacent to cement liners. It may well be that interlayer (micro) porosity may stay open and that primarily intergranular (macro) porosity may be clogged by mineral precipitation.

Open issues. Not all questions could be answered in this thesis and some issues remained open:

- Did the newly grown calcium and magnesium-rich minerals consist only of calcite and saponite, or were there also other minerals like C–(A)–S–H, brucite, and zeolites present?
- How was saponite formed in the experiment and could it have been formed by mineral transformation from montmorillonite?
- Would the experiments have run differently in case the system had been CO_2 and O_2 free and what is the relationship between carbon dioxide and calcite precipitation in the reaction zone?
- How would have higher temperatures influenced the experiments?
- What happened to the formate (from APW_{ESDRED}) in the bentonite core and how was it transformed in detail into acetate in the s/b core (microbial pathways)?
- Why was no microbial activity observed in bentonite or could it be that there was not enough space for microbes?
- What is the origin of the high alkalinity measured in the outflow of s/b?
- How does the reaction zone look like if examined at higher resolution (e.g. FIB-SEM)? Are the pore throats still open or are they partially clogged by the mineral precipitations?
- How were minerals formed at constant-pressure conditions? Did they replace the primary mineralogy or were they formed in voids?

Ideas for future experiments. After we could show in this work that the combination of computed tomography and core infiltration device is an effective tool to track mineral alterations and volume changes in bentonite and s/b cores, there are various other problems where this approach could be used:

(1) An idea would be to perform core infiltration experiments using on one side a mortar and on the other side a bentonite sample, providing information on the interface and the mortar alteration.

(2) Another process, which could be monitored by CT, is two-phase flow in s/b, while a mixture of solution and gas is infiltrated.

(3) Another idea would be to study the effect of periodic changes from high to low ionic strength infiltration fluids and vice versa on the core volume, bentonite erosion and fluid flow, as associated to ingress of glacial water during an ice age.

(4) Interesting would also be to study the mineral growth in fractures, infiltrating different saline hydrothermal waters, while crystal growth could be monitored by CT.

(5) An interesting experiment would be to trace an infiltration fluid with heavy elements (ions), which may allow gaining information on the ion transport in the cores by CT, as heavy elements have a stronger X-ray attenuation.

Reference

Bradbury, M.H., Berner, U., Curti, E., Hummel, W., Kosakowski, G., Thoenen, T., 2012. The long term geochemical evolution of the nearfield of the HLW repository. Nagra Technical Report NTB 12-01, Nagra, Wettingen, Switzerland.

Gaucher, E.C., Blanc, P., Matray, J.-M., Michau, N., 2004. Modeling diffusion of an alkaline plume in a clay barrier. Applied Geochemistry 19, 1505-1515.

Kosakowski, G., Berner, U., 2013. The evolution of clay rock/cement interfaces in a cementitious repository for low- and intermediate level radioactive waste. Physics and Chemistry of the Earth, Parts A/B/C.

Kosakowski, G., Berner, U., Wieland, E., Glaus, M., Degueldre, C., 2014. Geochemical evolution of the L/ILW near-field. Nagra Technical Report NTB 97-04, Nagra, Wettingen, Switzerland.

Nagra, 2002. Demonstration of disposal feasibility for spent fuel, vitrified high-level waste and long-lived intermediate-level waste (Entsorgungsnachweis). Nagra Technical Report NTB 02-05, Nagra, Wettingen, Switzerland.

Savage, D., Noy, D., Mihara, M., 2002. Modelling the interaction of bentonite with hyperalkaline fluids. Applied Geochemistry 17, 207-223.

11 Appendices

11.1. X-ray Computed Tomography (CT) – density calculations

The initial idea was to determine material densities by means of CT data, allowing precise mineral determination. Two approaches were used, while both showed not a satisfying result. The first approach (1) used the reference material sample to determine absolute densities while the second approach (2) was based on calculating the X-ray attenuations of expected mineral phases and compare them to the measured data.

(1) Reference material sample. The reference material sample consisted of well-defined materials of known density, showing a linear trend between X-ray attenuations (HU values) and densities (y=0.0012x+1.037; Figure 11-1). Plotting the measured HU values of bentonite in an X-ray attenuation–density plot (Figure 11-1), a bentonite density of 2.4 g/cm^3 at the inlet and 2.5 g/cm^3 at the outlet is derived using HU values of 1140 and 1204 HU, respectively. The s/b showed HU values of 1418 HU at the inlet and 1438 HU at the outlet, resulting in densities of 2.7 g/cm^3 and 2.8 g/cm^3, respectively. These densities were clearly higher compared to the post-mortem determined saturated densities of 1.92 g/cm^3 for bentonite and 2.1 g/cm^3 for s/b but slightly lower compared to the measured grain densities of 2.7–2.8 g/cm^3 for bentonite and s/b.

The newly formed mineral phases (calcite and saponite) in the inlet filter as well as in the bentonite showed averaged HU values of 1300–1400 HU. This value corresponds to a 'theoretical', CT-based density of 2.5–2.6 g/cm^3 using Figure 11-2 for the X-ray attenuation-density transformation (calcite density 2.71 g/cm^3). This indicates that these newly formed mineral phases were denser compared to bentonite. This favored the hypothesis of having a mineral phase rather than a gel-like phase. A more precise determination could not be done with this HU value range, as most of the expected silicate and carbonate minerals have similar densities. One of the problems of this calculation was that in our calculation it is assumed that the X-ray attenuation is only a function of the material density but not of the chemical composition of the materials. In reality, larger atoms attenuate X-rays stronger compared to light one. As all reference materials were carbon-based, consisting of rather light elements, while the measured minerals rather consisted of heavy elements like silica, aluminum, calcium, or iron, and thus misinterpreting the absolute densities of high density minerals.

It can be concluded that for s/b the interpolated, CT-based densities were different from the saturated rock density. In bentonite, the attenuation signal was rather influenced by the high water content, reducing values strongly. But no direct link between saturated densities and X-ray attenuation was observed.

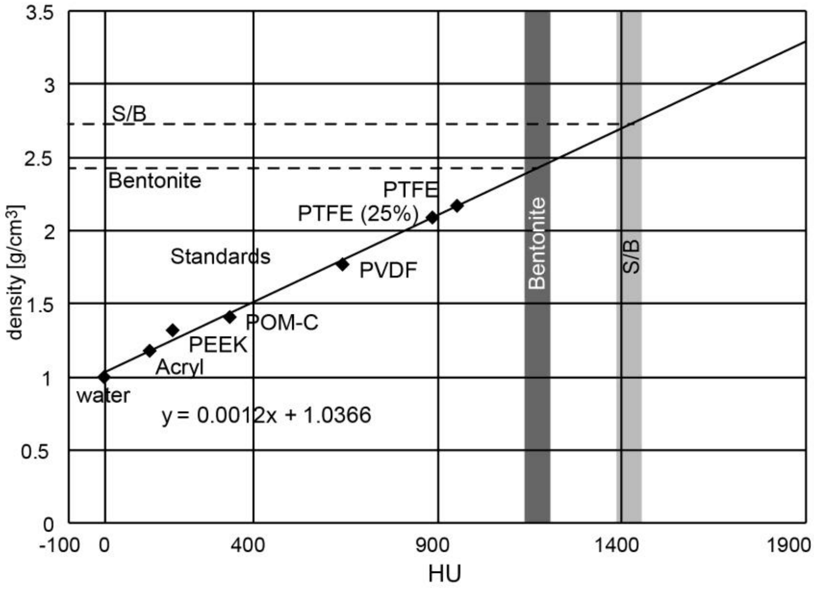

Figure 11-1: HU values–density plot with the reference materials as well as bentonite and s/b.

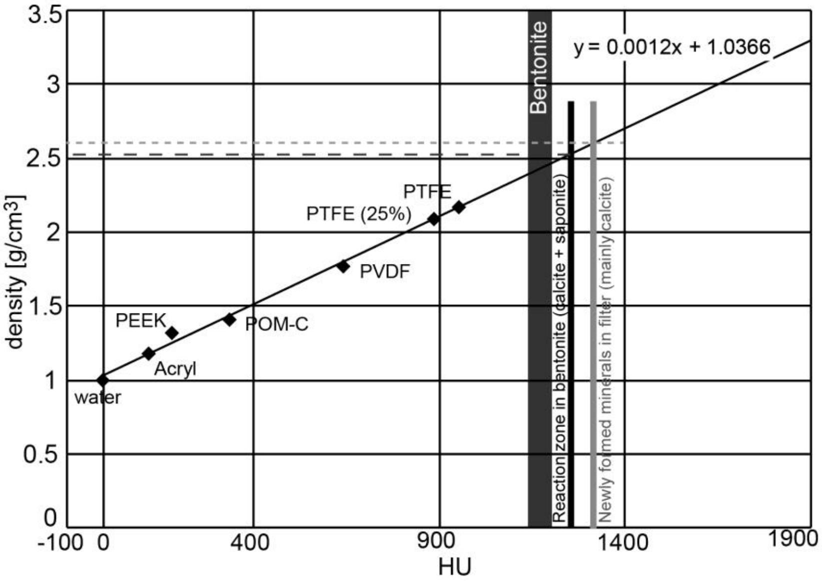

Figure 11-2: HU values plotted against densities including bentonite, s/b and the newly precipitated minerals in the filter as well as in the bentonite.

(2) Calculation of X-ray attenuations. The HU values of minerals may be mathematically defined by density and chemical composition. The idea of this approach was to calculate the X-ray attenuation (HU values) of expected and known mineral phases by calculating the corresponding mass-attenuation coefficients. The mass-attenuation coefficient was calculated by using published mass-attenuation data for each element (Table 11-1), published in Hubbell and Seltzer (1996) at an X-ray energy of 130 keV. The mass-attenuation of each element was summed up using the stoichiometric formula and finally divided by the number of atoms. Multiplying this value with the known mineral density gave the linear-attenuation coefficient of the mineral. The linear attenuation coefficient can be transformed to HU values by the given formula in *chapter 3*. Hubbell and Seltzer (1996) provided further mass-attenuation values for certain materials, which were used for a comparison with the calculated values.

For Acrylic, the difference between calculated and published (Hubbell and Seltzer, 1996) X-ray attenuation values was in the range of ±20 HU whereas for other materials like PVC the result was less convincing. A comparison of calculated and measured HU values is shown in Table 11-2. For well characterized materials, like in the reference material sample, the measured and calculated X-ray attenuations showed a good agreement. In our experiment using rock cores, the identification of minerals was much more difficult. Post-mortem analysis showed mainly the precipitation of calcite and most likely saponite in the cores, while in the inlet filters calcite was observed. Newly grown calcite in the filter showed attenuation values between 1300 and 1400 HU, which are lower compared to the calculated ~1948 HU. The same was observed for saponite, with lower measured attenuation values compared to the calculated data.

The calculation of X-ray attenuations of known and expected mineral phases showed values of 1550–1950 HU, all plotting in the same range. This indicates that a precise identification of a single mineral phase by means of calculated CT data is rather difficult and will only be possible if prior to the measurement the mineral phases are known. The second problem was in our case that the resolution of the medical CT scanners was not high enough to resolve single mineral phases, which makes an identification of the newly formed mineral phases difficult. And finally the effect of data processing on the measured X-ray attenuation is not clear and may influence the values.

Table 11-1: Mass attenuation coefficients of certain elements from Hubbell and Seltzer (1996) at 130 keV.

Element	z	μ/ρ [cm^2/g]
H^+	1	0.2778
C^{4+}	6	0.1421
O^{2-}	8	0.1446
Na^+	11	0.145
Mg^{2+}	12	0.153
Al^{3+}	13	0.1532
Si^{4+}	14	0.1631
S^{4-}	16	0.1753
Cl^{2-}	17	0.1494
Ca^{2+}	20	0.2113
Ti^{4+}	22	0.2176
$Fe^{3+/2+}$	26	0.2832

Table 11-2: Calculated and measured HUs.

Name	Formula	Density [g/cm^3]	HU calculated from elements [HU]	HU measured [HU]	Error [HU]
Water	H_2O	1	0	-4	±23
Acryl	$[C_5H_8O_2]_n$	1.18	138	120	±18
PEEK	$C_{19}H_{14}O_3$	1.32	234	182	±19
POM-C	$-[(CH_2-O)_n-(CH_2-CH_2-O-)_m]$	1.41	363	337	±21
PVDF	$-(C_2H_2F_2)_n-$	1.76	593	643	±25
PTFE (25%)	$(C_2F_4)_n$	2.09	816	886	±28
PTFE	$(C_2F_4)_n$	2.17	886	953	±28
Bentonite			1232	1205	±91
S/B			1425	1407	±99
Calcite	$CaCO_3$	2.71	1948		
Montmorillonite	$(Na,Ca)_{0.3}(Al,Mg)_2Si_4O_{10}(OH)_2\,(2xH_2O)$	2.7	1171		
Montmorillonite without H_2O	$(Na,Ca)_{0.3}(Al,Mg)_2Si_4O_{10}(OH)_2$	2.7	1561		
Quartz	SiO_2	2.65	1546		

References

Hubbell, J.H., Seltzer, S.M., 1996. Tables of X-ray mass attenuation coefficients and mass energy-absorption coefficients 1 keV to 20 MeV for elements Z=1 to 92 and 48 additional substances of dosimetric interest [electronic resource]. U.S. Department of Commerce, Technology Administration, National Institute of Standards and Technology, Gaithersburg, MD.

11.2. Tables

Table 11-3: Experiment Bent-CT 1 (Bentonite – APW_{OPC})

Days	PV	PV_{OPC}	Mobile	Fluid	P_{conf}	P_{inf}	P_{exf}	T	Syr.	Fluid	Eh	Q (avg)	k (avg)
					[bar]	[bar]	[bar]	[°C]	#	[ml]	[mS/cm]	[ml/day]	[m/s]
0.0					0.0	0.0							
2.0					0.0	0.0							
2.0					5.3	0.0							
2.1					12.5	0.0							
2.8					12.3	0.0							
2.9					20.9	0.0							
3.0					20.8	0.0							
3.1					20.5	0.0							
3.2					20.4	0.0							
3.7					20.1	0.0							
3.8					29.9	0.0							
4.0					29.6	0.0							
4.0				OPA	32.1	11.9							
4.1				OPA	32.0	11.8							
4.3				OPA	32.0	11.8							
4.7				OPA	31.9	11.5							
4.7				OPA	42.3	21.0							
5.8				OPA	41.6	19.1							
6.0				OPA	41.6	20.5							
11.0				OPA	41.1	13.5							
11.0				OPA	41.1	21.6							
11.8				OPA	40.8	20.5							
12.0					0.0	0.0							
Restart													
13.1				OPA	5.6	0.0	0.2	21.1	1				
13.2				OPA	11.1	0.0	0.2	21.1	1				
13.9				OPA	30.6	8.1	0.2	21.2	1				
14.0				OPA	41.9	21.0	0.2	21.3	1				
17.2				OPA	41.7	20.7	0.2	21.7	1				
17.9	0.00			OPA	41.7	20.7	0.2	21.7	1				
18.8	0.00			OPA	41.7	20.7	0.2	21.5	1	0.05		0.054	
19.9	0.00			OPA	41.6	20.2	0.2	21.6	1	0.05			
20.2	0.00		CT1-1	OPA									
20.3	0.00			OPA	41.2	20.1	0.2	21.7	1	0.07		0.128	2.6E-13
20.9	0.01			OPA	41.2	20.1	0.2	21.7	1	0.30		0.425	
22.2	0.01			OPA	41.3	20.1	0.2	21.7	1	0.60		0.230	
23.2	0.01			OPA	41.3	20.1	0.2	21.6	1	0.60			1.6E-13
24.2	0.01			OPA	41.2	20.1	0.2	21.6	1	0.60			
24.9	0.01			OPA	41.2	20.0	0.2	21.6	1	0.62		0.027	
26.0	0.02			OPA	41.2	20.0	0.2	21.4	1	0.70		0.077	
26.8	0.02			OPA	41.1	19.9	0.2	21.4	1	0.80		0.118	2.8E-13
27.2	0.02			OPA	41.2	20.3	0.2	21.4	1	0.85		0.146	
27.2	0.02		CT1-2	OPA									
27.3	0.02			OPA	40.8	20.2	0.2	21.4	1	0.90		0.272	1.6E-13
30.9	0.02			OPA	40.9	20.1	0.2	21.5	1	1.10		0.067	
31.9	0.03			OPA	40.9	20.0	0.2	21.7	1	1.15		0.048	
32.8	0.03			OPA	40.9	20.0	0.2	21.2	1	1.20		0.054	
34.9	0.03			OPA	41.0	19.9	0.2	22.2	1	1.50		0.142	1.6E-13
37.8	0.04			OPA	41.0	19.9	0.2	22.3	1	1.70		0.068	
39.8	0.04			OPA	41.0	19.7	0.2	22.4	1	1.84		0.070	
39.9	0.04		CT1-3	OPA									
40.9	0.04			OPA	40.7	19.8	0.2	22.3	1	2.00		0.146	1.3E-13
45.8	0.05			OPA	42.9	20.6	0.2	22.9	1	2.20		0.041	
48.1	0.05			OPA	42.7	20.4	0.2	23	1	2.40		0.088	1.2E-13
48.1	0.05			OPA	42.7	20.4	0.6	23	2	2.40		0.088	
52.8	0.06			OPA	42.7	20.0	0.6	22.9	2	2.70		0.064	
55.8	0.07			OPA	42.8	19.8	0.6	22.9	2	3.00		0.101	

58.8	0.07			OPA	42.7	19.7	0.6	22.7	2	3.20		0.066	
61.9	0.07			OPA	42.7	19.3	0.6	22.6	2	3.40		0.065	1.1E-13
63.1	0.08			OPA	42.7	21.2	0.6	22.7	2	3.50		0.084	
65.9	0.08			OPA	42.7	21.8	0.6	22.6	2	3.70		0.072	
68.9	0.09			OPA	42.9	21.6	0.6	22.7	2	4.00		0.099	
74.1	0.10			OPA	43.0	21.0	0.6	23.1	2	4.40		0.077	1.1E-13
75.8	0.10			OPA	43.0	20.8	0.6	23.2	2	4.50		0.057	
76.8	0.10			OPA	43.0	20.7	0.6	23.2	2	4.60		0.103	
76.8	0.10			OPA	43.0	20.7	0.6	23.2	3	4.60		0.103	
79.8	0.10			OPA	42.6	20.3	0.6	23.5	3	4.80		0.066	1.1E-13
84.1	0.11			OPA	42.7	19.6	0.6	23.3	3	5.10		0.071	
87.2	0.12			OPA	42.7	21.1	0.6	23.4	3	5.30		0.064	
91.1	0.12			OPA	42.7	21.1	0.6	23.7	3	5.60		0.077	
93.8	0.13			OPA	42.7	21.1	0.6	24	3	5.80		0.072	1.2E-13
96.8	0.13			OPA	42.8	21.0	0.6	24	3	6.10		0.100	
101.8	0.14			OPA	42.8	22.2	0.6	23.9	3	6.50		0.081	
101.8	0.14		CT1-4	OPA						6.50			
102.0	0.14			OPA	42.3	18.9	0.6	23.9	4	6.50			1.2E-13
103.8	0.14			OPA	42.6	21.8	0.6	23.8	4	6.60		0.056	
105.1	0.15			OPA	42.6	21.7	0.6	23.8	4	6.75		0.119	
107.8	0.15			OPA	42.5	21.2	0.6	23.2	4	6.90			
110.8	0.16			OPA	42.4	21.7	0.6	23.1	4	7.30		0.133	1.3E-13
114.8	0.17			OPA	42.4	21.7	0.6	22.8	4	7.60		0.075	
119.1	0.17			OPA	42.4	21.6	0.6	22.9	4	7.95		0.081	
119.2	0.17			OPA	42.4	21.6	0.6	22.9	5	7.95	0.8		
126.9	0.17			OPA	42.3	21.6	0.6	22.13	5	7.95	26.5		1.3E-13
128.5	0.17			OPA	42.0	21.6	0.6	22.34	5	7.95	26.6		
135.1	0.18			OPA	41.8	21.7	0.6	21.87	5	8.35	26.7	0.061	
135.9	0.18			OPA	41.7	21.5	0.6	21.86	5	8.45	26.6	0.133	
135.9	0.18	0.0		OPC	41.7	21.2	0.6	21.86	5	8.45	26.6		
136.0	0.18	0.01		OPC	41.8	21.3	0.6	21.86	5	8.45	26.7		
137.8	0.19	0.01		OPC	41.7	21.5	0.6	21.68	5	8.56	26.7	0.062	6.6E-14
137.8	0.19	0.01	CT1-5+6	OPC						8.56			
138.1	0.19	0.01		OPC	41.5	21.2	0.6	22.09	5	8.57		0.041	
138.8	0.19	0.01		OPC	41.6	21.2	0.6	21.88	5	8.60	27.3	0.041	8E-14
138.8	0.19	0.01	CT1-7	OPC						8.60			
138.9	0.19	0.01		OPC	41.4	21.1	0.6	21.93	5	8.60			
139.9	0.19	0.01		OPC	41.5	21.2	0.6	21.92	5	8.70	28.8	0.100	
143.1	0.19	0.01		OPC	41.5	21.2	0.6	21.95	5	8.75	27.0	0.016	
143.8	0.19	0.01		OPC	41.6	21.2	0.6	21.98	5	8.75	29.4		
143.8	0.19	0.01	CT1-8	OPC						8.75			
143.9	0.19	0.01		OPC	41.3	21.2	0.6	21.79	5	8.75			
145.8	0.19	0.02		OPC	41.3	21.2	0.6	22.09	5	8.75	27.8		
147.8	0.19	0.02		OPC	41.2	21.2	0.6	21.77	5	8.75			
147.8	0.19	0.03		OPC	41.2	21.2	0.6	21.77	6	8.75			
151.1	0.19	0.03		OPC	41.2	21.1	0.6	21.7	6	8.80		0.015	
151.8	0.19	0.03		OPC	41.2	21.1	0.6	21.7	6	8.80			5.9E-14
151.9	0.19	0.03	CT1-9	OPC						8.80			
154.0	0.19	0.03		OPC	41.0	21.1	0.6	21.76	6	8.85		0.017	
160.9	0.20	0.03		OPC	41.0	21.0	0.6	22.09	6	9.35	26.9	0.073	
164.9	0.21	0.03		OPC	40.9	21.0	0.6	21.38	6	9.50	28.1	0.037	
168.2	0.21	0.03		OPC	40.9	21.0	0.6	21.15	6	9.75	27.9	0.078	8.8E-14
168.2	0.21	0.03		OPC	40.9	21.0	0.6	21.15	7	9.75			
171.1	0.21	0.03		OPC	40.9	21.0	0.6	21.01	7	9.75	27.1		
171.9	0.21	0.04		OPC	40.8	20.9	0.6	21.15	7	9.75			
171.9	0.21	0.04	CT1-10	OPC						9.75			
172.0	0.21	0.04		OPC	40.6	20.9	0.6	20.9	7	9.75			
174.0	0.21	0.04		OPC	40.6	20.9	0.6	21.02	7	9.75	28.5		
175.1	0.21	0.04		OPC	40.7	21.0	0.6	21.02	7	9.75			
178.8	0.21	0.04		OPC	40.6	21.0	0.6	21	7	9.75	26.5		4.9E-14
184.1	0.22	0.04		OPC	40.5	20.8	0.6	20.7	7	10.05		0.057	
188.3	0.22	0.04		OPC	40.6	20.9	0.6	20.8	7	10.10	26.3	0.012	
190.0	0.22	0.05		OPC	40.7	20.9	0.6	21	7	10.10	28.6		
197.5	0.22	0.05		OPC	40.5	20.9	0.6	20.64	7	10.20	25.6	0.013	3.3E-14

204.0	0.23	0.05		OPC	40.5	20.8	0.6	20.3	7	10.35	25.6	0.023	
206.9	0.23	0.05		OPC	40.4	20.7	0.6	20.05	7	10.45	26.3	0.034	
207.8	0.23	0.06		OPC	40.4	20.1	0.6	20.06	7	10.47	25.8	0.021	5.2E-14
207.9	0.23	0.07	CT1-11	OPC						10.47		0.000	
208.0	0.23	0.07		OPC	40.2	19.7	0.6	20.18	7	10.48	25.6		
212.8	0.23	0.07		OPC	40.3	19.8	0.6	19.84	7	10.65	25.2	0.035	
212.8	0.23	0.07		OPC	40.3	19.8	0.6	19.84	8	10.65	25.2		
216.1	0.23	0.07		OPC	40.2	19.8	0.6	20.63	8	10.75	24.9	0.030	6E-14
219.0	0.24	0.08		OPC	40.2	19.7	0.6	20.03	8	10.90	24.9	0.052	
224.1	0.24	0.08		OPC	40.2	19.8	0.6	19.89	8	11.10	24.9	0.040	
233.0	0.25	0.08		OPC	40.2	19.7	0.6	19.64	8	11.45	24.8	0.039	
233.8	0.25	0.08		OPC	40.1	19.7	0.6	19.44	8	11.50	24.9	0.061	6.2E-14
233.8	0.25	0.08		OPC	40.1	19.7	0.6	19.44	9	11.50	24.9		
236.1	0.25	0.09		OPC	40.1	19.8	0.6	19.82	9	11.58	24.6	0.036	
240.9	0.26	0.09		OPC	40.1	19.8	0.6	19.4	9	11.71	24.7	0.027	
248.3	0.26	0.09		OPC	40.1	21.0	0.6	19.46	9	11.97	24.5	0.035	4.9E-14
251.1	0.26	0.09		OPC	40.0	21.2	0.6	19.42	9	12.07	24.3	0.035	
254.8	0.27	0.09		OPC	39.9	21.0	0.6	18.99	9	12.20	24.5	0.035	
254.8	0.27	0.09		OPC	39.9	21.0	0.6		10	12.20			
257.9	0.27	0.09		OPC	40.1	21.0	0.6	19.25	10	12.32	24.3	0.040	4.4E-14
261.8	0.27	0.10		OPC	40.1	20.9	0.6	19.14	10	12.39	24.4	0.018	
266.0	0.27	0.10		OPC	40.0	20.9	0.6	19.08	10	12.54	24.3	0.036	
269.9	0.28	0.10		OPC	40.0	20.9	0.6	18.86	10	12.66	24.3	0.031	
272.8	0.28	0.10		OPC	39.8	21.0	0.6	18.73	10	12.75	24.2	0.031	
272.8	0.28	0.10	CT1-12	OPC						12.75			3.5E-14
272.9	0.28	0.11		OPC	39.7	21.0	0.6	18.93	10	12.75			
275.0	0.28	0.11		OPC	39.9	21.2	0.6	18.76	10	12.79	23.8	0.019	
277.8	0.28	0.11		OPC	39.7	21.0	0.6	18.71	10	12.87	23.8	0.028	4.1E-14
277.8	0.28	0.12		OPC	39.7	21.0	0.6	18.71	11	12.87			
282.9	0.28	0.12		OPC	39.7	20.9	0.6	18.47	11	13.02	23.8	0.029	
284.9	0.28	0.12		OPC	39.8	20.9	0.6	18.67	11	13.08	23.7	0.030	
290.0	0.29	0.12		OPC	39.7	20.8	0.6	18.59	11	13.23	23.6	0.029	4.4E-14
297.1	0.29	0.13		OPC	39.8	20.5	0.6	19	11	13.45	23.5	0.032	
301.1	0.30	0.13		OPC	39.8	20.6	0.6	19.09	11	13.58	23.4	0.032	
301.1	0.30	0.13		OPC	39.8	20.6	0.6	19.09	12	13.58	23.4		
307.8	0.30	0.13		OPC	39.9	20.5	0.6	19.05	12	13.77	23.3	0.028	3.9E-14
310.8	0.30	0.14		OPC	39.7	20.8	0.6	18.66	12	13.87	23.2	0.033	
311.9	0.30	0.14		OPC	39.8	20.8	0.6	18.99	12	13.89	23.2	0.019	
319.8	0.31	0.14		OPC	39.7	20.6	0.6	18.91	12	14.12	23.1	0.029	
324.8	0.31	0.14		OPC	39.7	20.8	0.6	18.77	12	14.26	22.9	0.028	4.1E-14
328.8	0.31	0.14		OPC	39.8	20.7	0.6	19.18	12	14.38	22.9	0.030	
331.0	0.31	0.14		OPC	39.8	20.6	0.6	19.14	12	14.44	22.8	0.028	
331.0	0.31	0.14		OPC	39.8	20.6	0.6	19.14	13	14.44	22.8		
339.0	0.32	0.14		OPC	39.8	20.9	0.6	19.32	13	14.68	22.7	0.030	3.9E-14
341.8	0.32	0.14		OPC	39.7	20.9	0.6	19.41	13	14.75	22.5	0.026	
343.1	0.32	0.15	CT1-13	OPC						14.75			
343.1	0.32	0.15		OPC	39.7	20.8	0.6	19.65	13	14.76	23.1	0.007	2.3E-14
343.9	0.32	0.15		OPC	39.6	20.7	0.6	19.6	13	14.77	22.3	0.013	
347.9	0.32	0.15		OPC	39.6	20.8	0.6	19.61	13	14.88	22.4	0.028	
349.9	0.33	0.15		OPC	39.7	20.9	0.6	19.79	13	14.93	22.4	0.025	3.7E-14
360.3	0.33	0.16		OPC	39.8	20.9	0.6	19.93	13	15.24	22.2	0.030	
360.3	0.33	0.16		OPC	39.8	20.9	0.6	19.93	14	15.24	22.2		
363.8	0.33	0.16		OPC	39.8	20.8	0.6	20.11	14	15.32	22.2	0.023	
363.8	0.33	0.16	CT1-15	OPC						15.32			3.3E-14
364.0	0.33	0.16		OPC	39.5	20.8	0.6	20.08	14	15.32			
370.7	0.34	0.16		OPC	39.8	20.8	0.6	20.15	14	15.48	22.0	0.024	
373.8	0.34	0.17		OPC	39.6	20.8	0.6	19.9	14	15.55	22.3	0.023	
376.8	0.34	0.17		OPC	39.6	20.7	0.6	19.94	14	15.63	22.2	0.027	3.9E-14
382.8	0.34	0.18		OPC	39.6	20.7	0.6	20.08	14	15.79	22.1	0.027	
388.9	0.35	0.18		OPC	39.7	20.8	0.6	20.47	14	15.95	22.0	0.026	
390.8	0.35	0.18		OPC	39.7	20.7	0.6	20.53	14	16.01	22.0	0.031	
390.8	0.35	0.18	CT1-16	OPC						16.01	22.0		3.6E-14
390.9	0.35	0.18		OPC	39.6	20.8	0.6	20.53	15	16.01	22.0		
398.9	0.35	0.18		OPC	39.8	20.9	0.6	21.64	15	16.21	21.9	0.025	

402.8	0.36	0.18		OPC	39.8	20.8	0.6	21.71	15	16.31	21.8	0.026	
409.8	0.36	0.19		OPC	39.7	20.7	0.6	21.24	15	16.50	21.8	0.027	3.9E-14
412.8	0.36	0.19		OPC	39.7	20.9	0.6	21.33	15	16.58	21.8	0.027	
416.8	0.36	0.20		OPC	39.8	20.8	0.6	21.64	15	16.68	21.8	0.025	
419.8	0.37	0.20		OPC	39.9	20.8	0.6	21.92	15	16.77	21.7	0.030	
423.8	0.37	0.20		OPC	39.8	20.9	0.6	22.28	15	16.88	21.6	0.028	4.7E-14
425.8	0.37	0.20		OPC	39.9	20.8	0.6	22.44	15	16.94	21.7	0.030	
425.8	0.37	0.20		OPC	39.9	20.8	0.6	22.44	16	16.94	21.7		
430.8	0.37	0.20		OPC	39.9	20.8	0.6	22.69	16	17.05	21.6	0.022	
436.9	0.37	0.20		OPC	40.1	20.9	0.6	23.47	16	17.19	21.5	0.023	3.2E-14
450.0	0.38	0.20		OPC	40.1	20.9	0.6	23.43	16	17.53	21.4	0.026	
451.0	0.38	0.20		OPC	40.0	20.9	0.6	23.42	16	17.55	21.4	0.020	
451.0	0.38	0.20	CT1-17	OPC						17.55			
451.1	0.38	0.20		OPC	39.9	20.9	0.6	23.51	16	17.55			2.2E-14
451.8	0.38	0.21		OPC	40.0	20.8	0.6	23.4	16	17.56	21.7	0.014	
454.9	0.38	0.21		OPC	39.9	20.9	0.6	23.26	16	17.59	21.4	0.010	
457.9	0.38	0.21		OPC	39.8	20.9	0.6	23.35	16	17.66	21.4	0.023	
460.8	0.39	0.21		OPC	39.9	20.6	0.6	23.31	16	17.71	21.4	0.017	2.3E-14
462.9	0.39	0.21		OPC	40.0	20.9	0.6	23.35	16	17.75	21.4	0.019	
462.9	0.39	0.21		OPC	40.0	20.9	0.6	23.35	17	17.75	21.4		
471.1	0.39	0.21		OPC	39.6	20.8	0.6	22.73	17	17.85	21.5	0.012	1.8E-14
472.9	0.39	0.21		OPC	39.8	20.8	0.6	22.53	17	17.87	21.6	0.011	
474.8	0.39	0.21		OPC	39.6	20.9	0.6	22.61	17	17.89	21.5	0.010	
478.8	0.39	0.21		OPC	39.8	20.8	0.6	22.74	17	17.95	21.6	0.015	
482.9	0.39	0.21		OPC	39.8	20.8	0.6	22.42	17	18.01	21.6	0.015	
485.8	0.39	0.21		OPC	39.5	20.7	0.6	22.08	17	18.04	21.8	0.010	1.8E-14
487.8	0.39	0.21		OPC	39.6	20.8	0.6	21.94	17	18.07	21.7	0.015	
492.8	0.39	0.22		OPC	39.5	20.7	0.6	21.72	17	18.13	21.7	0.012	
499.8	0.40	0.22		OPC	39.5	20.7	0.6	21.84	17	18.22	22.0	0.013	
499.8	0.40	0.22	CT1-18	OPC						18.22	22.0		2.7E-14
499.9	0.40	0.22		OPC	39.3	20.6	0.6	21.82	17	18.22			
500.9	0.40	0.22		OPC	39.5	20.7	0.6	21.86	17	18.25	22.4	0.031	
503.9	0.40	0.22		OPC	39.5	20.7	0.6	21.86	17	18.27	22.0	0.007	
506.8	0.40	0.22		OPC	39.4	20.6	0.6	21.64	17	18.30	22.0	0.010	1.4E-14
513.1	0.40	0.22		OPC	39.4	20.7	0.6	21.36	17	18.37	22.0	0.011	
518.1	0.40	0.22		OPC	39.3	20.7	0.6	21.31	17	18.41	22.2	0.008	
521.8	0.40	0.22		OPC	39.3	20.8	0.6	21.21	17	18.45	22.3	0.011	
528.9	0.40	0.22		OPC	39.4	20.6	0.6	21.3	17	18.53	22.2	0.011	1.5E-14
532.2	0.40	0.22		OPC	39.4	20.6	0.6	21.21	17	18.57	22.3	0.012	
532.2	0.40	0.22		OPC	39.4	20.6	0.6	21.21	18	18.57	22.3		
536.9	0.41	0.22		OPC	39.3	20.6	0.6	20.93	18	18.61	22.3	0.008	
541.9	0.41	0.22		OPC	39.3	20.7	0.6	20.84	18	18.64	22.4	0.006	9.7E-15
545.9	0.41	0.23		OPC	39.1	20.6	0.6	20.58	18	18.67	22.5	0.006	
548.9	0.41	0.23		OPC	39.2	20.6	0.6	20.4	18	18.68	22.6	0.005	
551.9	0.41	0.23		OPC	39.2	20.6	0.6	20.53	18	18.71	22.6	0.010	
555.9	0.41	0.23		OPC	39.1	20.5	0.6	20.34	18	18.74	22.7	0.006	1E-14
557.9	0.41	0.23		OPC	39.2	20.6	0.6	20.31	18	18.75	22.7	0.008	
557.9	0.41	0.23	CT1-19	OPC						18.75	22.7		
558.0	0.41	0.23		OPC	39.0	20.5	0.6	20.32	18	18.75	22.7		
562.9	0.41	0.23		OPC	39.0	20.5	0.6	19.42	18	18.78	22.8	0.006	9.7E-15
566.9	0.41	0.23		OPC	38.9	20.5	0.6	19.29	18	18.80	23.0	0.005	
570.9	0.41	0.23		OPC	38.8	20.5	0.6	19.66	18	18.83	23.0	0.007	
573.9	0.41	0.23		OPC	38.9	20.5	0.6	19.71	18	18.86	23.2	0.008	
577.5	0.41	0.23		OPC	38.9	20.5	0.6	19.61	18	18.88	23.2	0.007	8.9E-15
580.9	0.41	0.23		OPC	38.9	20.4	0.6	19.75	18	18.90	23.1	0.006	
588.6	0.41	0.23		OPC	38.9	20.4	0.6	19.28	18	18.95	23.1	0.007	
597.9	0.41	0.23		OPC	38.8	20.4	0.6	19.15	18	19.00	23.2	0.005	
604.9	0.42	0.23		OPC	38.9	20.4	0.6	19.45	18	19.05	23.2	0.007	1.2E-14
607.5	0.42	0.23		OPC	39.0	20.5	0.6	19.9	18	19.08	23.0	0.011	
611.9	0.42	0.23		OPC	39.0	20.5	0.6	19.73	18	19.11	23.0	0.006	
614.5	0.42	0.23		OPC	39.0	20.5	0.6	19.87	18	19.13	22.9	0.010	
618.9	0.42	0.23		OPC	38.8	20.4	0.6	19.66	18	19.15	22.9	0.005	6.6E-15
619.0	0.42	0.23		OPC	38.9	20.6	0.6	19.68	18	19.15	23.0		
619.0	0.42	0.23	CT1-20	OPC						19.15			

619.1	0.42	0.23		OPC	38.7	20.2	0.6	19.52	18	19.15			
620.9	0.42	0.23		OPC	38.8	20.5	0.6	19.62	18	19.16	24.4	0.003	8.3E-15
622.9	0.42	0.24		OPC	38.9	20.3	0.6	19.72	18	19.17	23.3	0.007	
626.0	0.42	0.24		OPC	38.8	20.4	0.6	19.65	18	19.19	23.0	0.005	
627.9	0.42	0.24		OPC	38.7	20.3	0.6	19.66	18	19.20	22.9	0.008	4.5E-15
627.9	0.42	0.24		OPC	38.7	20.3	0.6	19.66	19	19.20	22.9		
630.0	0.42	0.24		OPC	38.8	20.3	0.6	19.83	19	19.20	22.7		
633.0	0.42	0.24		OPC	38.9	20.5	0.6	19.74	19	19.21	22.8	0.003	
639.9	0.42	0.24		OPC	38.7	20.3	0.6	19.69	19	19.23	22.9	0.003	
646.9	0.42	0.24		OPC	38.9	20.3	0.6	19.6	19	19.25	23.0	0.003	3.8E-15
653.9	0.42	0.24		OPC	38.9	20.5	0.6	19.46	19	19.27	23.2	0.003	
655.9	0.42	0.24		OPC	38.9	20.5	0.6	19.48	19	19.28	23.3	0.005	
655.9	0.42	0.24		OPC	38.9	25.5	0.6	19.48	19	19.28	23.3		
656.9	0.42	0.24		OPC	38.7	25.4	0.6	19.53	19	19.28	23.3	0.002	3.9E-15
660.9	0.42	0.24		OPC	38.8	25.2	0.6	19.47	19	19.30	23.3	0.005	
660.9	0.42	0.24		OPC	38.8	28.7	0.6	19.5	19	19.30	23.3		
662.8	0.42	0.24		OPC	38.8	28.7	0.6	19.63	19	19.32	23.3	0.008	
664.9	0.42	0.24		OPC	38.8	28.8	0.6	19.82	19	19.33	23.3	0.005	7E-15
667.9	0.42	0.25		OPC	38.8	28.6	0.6	19.83	19	19.35	23.3	0.008	
671.9	0.42	0.25		OPC	38.9	28.7	0.6	20.17	19	19.38	23.4	0.007	
674.9	0.42	0.25		OPC	38.8	28.6	0.6	20.04	19	19.40	23.4	0.007	
681.9	0.42	0.25		OPC	38.9	28.6	0.6	20.17	19	19.46	22.9	0.008	8.7E-15
688.9	0.43	0.25		OPC	39.0	28.8	0.6	20.72	19	19.52	22.8	0.009	
697.2	0.43	0.25		OPC	39.2	28.8	0.6	20.9	19	19.60	22.4	0.010	
703.8	0.43	0.25		OPC	39.0	28.7	0.6	20.4	19	19.65	22.3	0.008	
709.9	0.43	0.25		OPC	38.9	28.7	0.6	20.58	19	19.70	22.3	0.008	1E-14
716.8	0.43	0.25		OPC	39.0	28.7	0.6	20.85	19	19.78	22.1	0.011	
723.8	0.43	0.25		OPC	39.0	28.7	0.6	20.92	19	19.85	21.9	0.010	
724.0	0.43	0.26	CT1-26	OPC						19.85			9.6E-15
731.9	0.43	0.26		OPC	38.9	28.6	0.6	20.88	19	19.89	21.7	0.005	
737.9	0.43	0.26		OPC	39.0	28.6	0.6	21.21	19	19.96	21.6	0.012	
744.9	0.44	0.26		OPC	38.9	28.6	0.6	21.05	19	20.04	21.6	0.011	
752.3	0.44	0.26		OPC	39.0	28.6	0.6	21.53	19	20.13	21.5	0.012	7.2E-15
752.3	0.44	0.26		OPC	39.0	28.6	0.6	21.53	20	20.13	21.5		
758.9	0.44	0.26		OPC	39.4	28.8	0.6	22.56	20	20.19	21.2		
759.3	0.44	0.26		OPC	39.3	28.9	0.6	22.63	20	20.19	21.2		
759.3	0.44	0.26		OPC	39.2	21.9	0.6	22.63	20	20.19	21.2		
759.8	0.44	0.26		OPC	39.2	21.9	0.6	22.56	20	20.19	21.1		
759.8	0.44	0.26		OPC	39.2	12.5	0.6	22.56	20	20.19	21.1		
760.1	0.44	0.26		OPC	19.3	12.6	0.6	22.63	20	20.19	22.6		
760.1	0.44	0.26		OPC	39.2	5.3	0.6	22.63	20	20.19	22.6		
760.8	0.44	0.26		OPC	39.3	5.5	0.6	22.57	20	20.19	21.1		
760.8	0.44	0.26		OPC	30.5	0.0	0.6	22.57	20	20.19	21.1		
760.8	0.44	0.26		OPC	30.8	0.0	0.6	22.57	20	20.19	21.2		
760.8	0.44	0.26		OPC	20.2	0.0	0.6	22.57					
760.9	0.44	0.26		OPC	20.4	0.0	0.6	22.57					
760.9	0.44	0.26		OPC	10.1	0.0	0.6	22.57					
760.9	0.44	0.26		OPC	10.3	0.0	0.6	22.57					
760.9	0.44	0.26		OPC	7.0	0.0	0.6	22.57					
760.9	0.44	0.26		OPC	4.6	0.0	0.6	22.57					
760.9	0.44	0.26		OPC	3.0	0.0	0.6	22.57					

Table 11-4: Experiment Bent-CT 2 (Bentonite – APW$_{ESDRED}$)

Days	PV	PV$_{ESDRED}$	Mobile	Fluid	P$_{conf}$	P$_{inf}$	P$_{exf}$	T	Syr.	Fluid	Eh	Q (AVG)	k (AVG)
						[bar]		[°C]	#	[ml]	[mS/cm]	[ml/day]	[m/s]
0.0				OPA	6.2	0.0	0.2	22.7	1	0.00			
0.1				OPA	6.2	0.0	0.2	22.7	1	0.00			
0.2				OPA	6.1	0.0	0.2	22.7	1	0.00			
1.0				OPA	6.0	0.0	0.2	22.8	1	0.00			
1.0				OPA	16.7	0.0	0.2	22.8	1	0.00			
2.2				OPA	15.0	0.0	0.2	22.8	1	0.00			
2.2				OPA	32.0	11.0	0.2	22.8	1	0.00			
2.2				OPA	31.8	11.0	0.2	22.8	1	0.00			
2.9				OPA	29.9	11.0	0.2	22.6	1	0.00			
2.9				OPA	41.9	22.1	0.2	22.6	1	0.00			
3.0				OPA	40.5	22.5	0.2	22.7	1	0.00			
3.1				OPA	41.0	22.0	0.2	22.7	1	0.00			
3.9				OPA	39.9	22.2	0.2	22.7	1	0.00			
4.9				OPA	39.7	22.1	0.2	22.6	1	0.00			
5.9	0.0			OPA	41.1	22.1	0.2	22.7	1	0.00			
6.0	0.0			OPA	41.1	22.1	0.2	22.7	1	0.00			
11.1	0.0			OPA	41.9	21.8	0.2	23.1	1	0.45			
12.9	0.0			OPA	41.9	21.3	0.2	23.2	1	0.60			
13.9	0.0			OPA	43.0	22.0	0.2	23.2	1	0.70		0.088	
16.9	0.0			OPA	42.4	21.7	0.2	23.5	1	1.10		0.101	1.4E-13
21.2	0.0			OPA	42.6	21.6	0.2	23.3	1	1.30		0.086	
28.1	0.0			OPA	42.7	21.7	0.2	23.7	1	1.90		0.086	
30.9	0.0			OPA	42.6	21.6	0.2	24	1	2.20		0.088	
33.9	0.1			OPA	42.6	21.6	0.2	24	1	2.50		0.090	1.2E-13
38.9	0.1			OPA	42.7	21.6	0.2	23.9	2	3.00		0.091	
42.1	0.1			OPA	42.6	21.6	0.2	23.8	2	3.00		0.083	
44.9	0.1			OPA	42.4	21.6	0.2	23.2	2	3.15		0.081	1.1E-13
47.9	0.1			OPA	42.2	21.5	0.2	23.1	2	3.40		0.081	
51.9	0.1			OPA	42.1	21.4	0.2	22.8	2	3.70		0.081	
63.9	0.1			OPA	42.0	21.3	0.2	22.38	2	4.50		0.078	
65.9	0.1			OPA	41.8	21.3	0.2	22.34	2	4.65		0.078	
65.9	0.1			OPA	41.8	21.3	0.2	22.34	3	4.65		0.078	1E-13
75.9	0.1			OPA	41.7	21.3	0.2	21.95	3	5.25		0.075	
80.1	0.1			OPA	41.8	21.3	0.2	21.95	3	5.55		0.075	
84.9	0.1			OPA	41.7	21.2	0.2	21.87	3	5.95		0.075	1E-13
84.9	0.1			OPA	41.7	21.2	0.2	21.87	4	5.95		0.075	
91.1	0.1			OPA	41.6	21.2	0.2	21.76	4	6.05		0.071	
97.9	0.1			OPA	41.6	21.2	0.2	22.05	4	6.35		0.069	
102.0	0.1			OPA	41.4	21.3	0.2	21.31	4	6.55		0.068	6E-14
105.2	0.1			OPA	41.3	21.3	0.2	21.06	4	6.75		0.068	
108.2	0.1			OPA	41.3	21.0	0.2	21.01	4	6.75	30.0	0.066	
108.2	0.1			OPA	41.3	21.0	0.2	21.01	5	6.75		0.066	
108.9	0.1			OPA	41.2	20.9	0.2	21.45	5	6.75		0.066	8.7E-14
108.9	0.1		CT2-10	OPA			0.2	21.45	5	6.75		0.066	
109.1	0.1			OPA	38.5	21.0	0.2	20.9	5	6.75		0.066	
109.2	0.1			OPA	34.6	20.9	0.2	21.1	5	6.75		0.066	
112.2	0.1			OPA	35.8	20.9	0.2	21.1	5	6.80		0.066	4.4E-14
114.2	0.1			OPA	36.0	20.9	0.2	21.11	5	6.85		0.066	
115.9	0.1			OPA	36.1	20.9	0.2	21	5	6.94		0.066	
121.2	0.2			OPA	36.0	20.9	0.2	20.72	5	7.15		0.066	
125.3	0.2			OPA	36.1	20.8	0.2	20.8	5	7.35		0.037	5.9E-14
127.0	0.2			OPA	36.0	20.9	0.2	21	5	7.45		0.039	
134.6	0.2			OPA	36.0	20.8	0.2	20.64	5	7.85		0.043	

Days	PV	PV_{ESDRED}	Mobile	Fluid	P_{conf}	P_{inf}	P_{exf}	T	Syr.	Fluid	Eh	Q (AVG)	k (AVG)
141.0	0.2			OPA	35.4	20.8	0.2	20.3	5	8.15		0.044	
144.0	0.2			OPA	35.9	20.8	0.2	20.08	5	8.25		0.043	6.9E-14
144.0	0.2			OPA	35.9	20.8	0.2	20.08	6	8.25		0.043	
145.1	0.2			OPA	35.8	20.7	0.2	20.08	6	8.25	39.5	0.042	
149.9	0.2			OPA	35.7	20.6	0.2	19.84	6	8.35	33.1	0.039	
153.2	0.2			OPA	35.8	20.7	0.2	20.04	6	8.35	32.7	0.036	3.7E-14
155.6	0.2			OPA	35.7	20.6	0.2	20.03	6	8.40	30.8	0.036	
161.2	0.2			OPA	35.8	20.7	0.2	19.83	6	8.45	28.9	0.036	
170.1	0.2			OPA	35.8	20.6	0.2	19.64	6	8.65	28.8	0.036	
177.9	0.2			OPA	35.7	20.6	0.2	19.4	6	8.85	28.7	0.036	3.3E-14
185.4	0.2			OPA	35.7	20.7	0.2	19.48	6	9.13	28.8	0.038	
188.2	0.2			OPA	35.7	21.6	0.2	19.27	6	9.25	28.8	0.039	
191.9	0.2			OPA	35.6	21.3	0.6	18.99	6	9.35	28.9	0.036	5E-14
198.9	0.2			OPA	35.5	21.2	0.6	18.99	7	9.56	28.8	0.034	
203.1	0.2			OPA	35.5	21.1	0.6	19.08	7	9.74	28.7	0.035	
207.0	0.2			OPA	35.5	21.1	0.6	18.86	7	9.90	29.0	0.036	
209.9	0.2			OPA	35.4	21.2	0.6	18.73	7	10.02	28.9	0.037	5.6E-14
212.1	0.2			OPA	35.3	21.1	0.6	18.76	7	10.11	29.0	0.037	
214.9	0.2			OPA	35.5	21.2	0.6	18.8	7	10.23	28.9	0.037	
220.0	0.2			OPA	35.4	21.2	0.6	18.47	8	10.44	29.0	0.038	6E-14
222.0	0.2			OPA	35.4	20.9	0.6	18.67	8	10.53	29.0	0.038	
227.0	0.2			OPA	35.4	21.1	0.6	18.58	8	10.73	28.9	0.038	
234.1	0.2			OPA	35.5	21.1	0.6	19	8	11.04	28.8	0.039	
238.2	0.2			OPA	35.5	21.0	0.6	19	8	11.08	28.8	0.037	5E-14
238.2	0.2			OPA	35.5	21.0	0.6	19	9	11.08	28.8	0.037	
244.9	0.2			OPA	35.5	21.1	0.6	18.91	9	11.12		0.034	
247.9	0.2			OPA	35.3	20.9	0.6	18.91	9	11.25	29.1	0.034	
248.9	0.2			OPA	35.5	21.0	0.6	18.99	9	11.27	28.9	0.034	4.9E-14
256.9	0.2			OPA	35.4	20.9	0.6	18.94	9	11.58	27.8	0.035	
261.9	0.3			OPA	35.3	21.0	0.6	18.73	9	11.81	28.8	0.035	
265.9	0.3			OPA	35.4	21.0	0.6	19.24	9	11.99	28.7	0.036	
268.0	0.3			OPA	35.4	21.0	0.6	19.14	9	12.08	28.8	0.036	6.2E-14
268.0	0.3			OPA	35.4	21.0	0.6	19.14	10	12.08	28.8	0.036	
270.9	0.3			OPA	35.5	21.0	0.6	19.17	10	12.21	28.7	0.036	
270.9	0.3	0.00		ESDRED	35.5	20.9	0.6	19.17	10	12.21	28.7	0.036	
271.8	0.3	0.00		ESDRED	35.5	21.0	0.6	19.2	10	12.25	28.6	0.036	
276.1	0.3	0.00		ESDRED	35.5	20.9	0.6	19.32	10	12.44	28.5	0.037	
278.8	0.3	0.01		ESDRED	35.6	20.8	0.6	19.41	10	12.56	28.5	0.037	6.3E-14
280.2	0.3	0.01	CT2-13	ESDRED			0.6		11	12.58			
280.2	0.3	0.01		ESDRED	35.4	20.9	0.6	19.65	11	12.58			
281.0	0.3	0.01		ESDRED	35.3	20.8	0.6	19.6	11	12.61	28.5	0.039	
284.9	0.3	0.01		ESDRED	35.3	20.8	0.6	19.61	11	12.62	28.6	0.039	
285.8	0.3	0.01		ESDRED	35.4	20.8	0.6	19.68	11	12.66	28.8	0.039	6.2E-14
285.8	0.3	0.01	CT2-14	ESDRED			0.6	19.68	11	12.66	28.8		
285.9	0.3	0.01		ESDRED	35.1	20.7	0.6	19.68	11	12.66	28.8		
286.9	0.3	0.01		ESDRED	35.2	20.9	0.6	19.8	11	12.66	28.8		
288.9	0.3	0.01		ESDRED	35.2	20.9	0.6	19.85	11	12.72	28.4	0.023	
297.3	0.3	0.02		ESDRED	35.3	21.9	0.6	19.93	11	12.98	28.4	0.023	4.3E-14
297.9	0.0	0.00	CT2-15	ESDRED	35.4	21.9	0.6	19.93	11		28.4		
298.8	0.3	0.02		ESDRED	35.4	21.8	0.6	19.92	11	13.04	28.4	0.023	
300.9	0.3	0.02		ESDRED	35.3	21.8	0.6	20.11	11	13.10	28.4	0.023	4.2E-14
304.9	0.3	0.02		ESDRED	34.9	21.9	0.6	20.03	11	13.19	28.8	0.023	
304.9	0.3	0.02		ESDRED	34.9	21.9	0.6	20.03	12	13.19	28.8	0.023	
307.8	0.3	0.02		ESDRED	35.1	21.9	0.6	20.15	12	13.28	28.8	0.026	3.7E-14
310.8	0.3	0.02		ESDRED	35.1	22.0	0.6	19.9	12	13.35	28.8	0.025	
313.9	0.3	0.03		ESDRED	35.0	21.9	0.6	19.94	12	13.41	28.9	0.024	

Days	PV	PV_{ESDRED}	Mobile	Fluid	P_{conf}	P_{inf}	P_{exf}	T	Syr.	Fluid	Eh	Q (AVG)	k (AVG)
319.8	0.3	0.03		ESDRED	35.0	21.8	0.6	20.08	12	13.56	29.0	0.024	
325.9	0.3	0.03		ESDRED	35.1	22.1	0.6	20.47	12	13.73	28.9	0.025	3.3E-14
327.9	0.3	0.03		ESDRED	35.1	21.1	0.6	20.53	12	13.78	28.9	0.025	
327.9	0.3	0.03	CT2-16	ESDRED			0.6	20.53	12	13.78	28.9	0.025	
328.0	0.3	0.03		ESDRED	34.8	21.3	0.6	20.53	12	13.78	28.9	0.025	
331.9	0.3	0.03		ESDRED	34.9	20.7	0.6	20.87	12	13.84	28.8	0.024	3.0E-14
331.9	0.3	0.03		ESDRED	34.9	20.7	0.6	20.87	13	13.84	28.8	0.024	
336.0	0.3	0.04		ESDRED	35.2	20.8	0.6	21.64	13	13.89	28.8	0.022	
339.8	0.3	0.04		ESDRED	35.2	20.8	0.6	21.71	13	13.99	28.7	0.023	
346.9	0.3	0.04		ESDRED	35.0	20.7	0.6	21.24	13	14.12	28.8	0.022	2.8E-14
349.9	0.3	0.04		ESDRED	34.9	20.7	0.6	21.33	13	14.18	28.9	0.022	
356.9	0.3	0.04		ESDRED	35.2	20.7	0.6	21.92	13	14.30	28.8	0.021	
362.9	0.3	0.05		ESDRED	35.3	20.7	0.6	22.44	13	14.41	28.8	0.021	
367.9	0.3	0.05		ESDRED	35.3	20.7	0.6	22.69	13	14.50	29.0	0.021	2.7E-14
374.0	0.3	0.05		ESDRED	35.7	20.8	0.6	23.47	13	14.59	29.0	0.018	
375.3	0.3	0.05		ESDRED	35.6	20.8	0.6	23.4	13	14.61	29.0	0.015	
387.0	0.3	0.05		ESDRED	35.6	20.4	0.6	23.43	14	14.71	29.2	0.020	1.9E-14
388.1	0.3	0.05		ESDRED	35.6	20.7	0.6	23.42	14	14.72	29.2	0.020	
388.1	0.3	0.05	CT2-17	ESDRED			0.6		14	14.72			
388.2	0.3	0.05		ESDRED	35.3	20.7	0.6	23.51	14	14.72			1.2E-14
391.9	0.3	0.05		ESDRED	35.4	20.8	0.6	23.28	14	14.73	29.9	0.006	
395.0	0.3	0.05		ESDRED	35.3	20.8	0.6	23.35	14	14.74	29.5	0.006	
397.9	0.3	0.05		ESDRED	35.4	20.7	0.6	23.31	14	14.76	29.3	0.006	
408.2	0.3	0.05		ESDRED	35.1	20.7	0.6	22.73	14	14.78	29.6	0.005	5E-15
409.9	0.3	0.05		ESDRED	35.6	20.6	0.6	22.53	14	14.79	29.6	0.005	
415.9	0.3	0.06		ESDRED	35.2	20.7	0.6	22.71	14	14.81	30.1	0.005	
419.9	0.3	0.06		ESDRED	35.2	20.6	0.6	22.42	14	14.82	31.4	0.004	
424.9	0.3	0.06		ESDRED	34.8	20.5	0.6	21.94	14	14.82	30.7	0.004	3.4E-15
427.3	0.3	0.06		ESDRED	34.8	20.6	0.6	21.91	14	14.82	30.8	0.004	
429.9	0.3	0.06		ESDRED	34.7	24.9	0.6	21.82	14	14.82	31.0	0.003	
433.3	0.3	0.06		ESDRED	34.8	24.9	0.6	21.8	14	14.83	31.3	0.003	
436.9	0.3	0.06		ESDRED	34.7	24.8	0.6	21.84	14	14.83	31.7	0.003	1.7E-15
436.9	0.3	0.06	CT2-18	ESDRED			0.6		14	14.83		0.003	
437.0	0.3	0.06		ESDRED	34.4	24.8	0.6	21.85	14	14.83		0.002	
438.0	0.3	0.06		ESDRED	34.6	24.9	0.6	21.85	14	14.83		0.002	
440.9	0.3	0.06		ESDRED	34.6	24.9	0.6	21.86	14	14.84		0.002	
443.9	0.3	0.06		ESDRED	34.5	24.9	0.6	21.66	14	14.84		0.002	4.1E-15
450.1	0.3	0.06		ESDRED	34.4	24.8	0.6	21.36	14	14.84		0.002	
455.1	0.3	0.06		ESDRED	34.4	24.9	0.6	21.32	14	14.84		0.002	
465.9	0.3	0.06		ESDRED	34.2	24.7	0.6	21.3	14	14.85	9.1	0.002	
469.2	0.3	0.06		ESDRED	34.4	24.7	0.6	21.21	14	14.86	11.2	0.002	2.4E-15
474.0	0.3	0.06		ESDRED	34.1	24.7	0.6	20.93	14	14.86	11.4	0.002	
476.0	0.3	0.06		ESDRED	34.2	24.7	0.6	20.91	14	14.87	18.2	0.002	
478.9	0.3	0.06		ESDRED	34.2	24.8	0.6	20.84	14	14.87	24.0	0.002	
483.0	0.3	0.06		ESDRED	34.1	24.7	0.6	20.58	14	14.88	28.7	0.002	4.6E-15
486.0	0.3	0.06		ESDRED	34.1	25.5	0.6	20.37	14	14.88	28.0	0.002	
489.0	0.3	0.06		ESDRED	34.1	25.2	0.6	20.53	14	14.88	34.3	0.002	
493.0	0.3	0.06		ESDRED	34.0	25.1	0.6	20.39	14	14.89	35.5	0.002	
494.9	0.3	0.06		ESDRED	34.1	25.2	0.6	20.31	14	14.89	36.9	0.002	1.6E-15
494.9	0.3	0.06	CT2-19	ESDRED			0.6	20.31	14	14.89	36.9	0.002	
495.1	0.3	0.06		ESDRED	34.3	25.0	0.6	20.32	14	14.89	36.9	0.002	
500.0	0.3	0.06		ESDRED	34.3	25.0	0.6	19.44	14	14.90	39.9	0.002	
504.0	0.3	0.06		ESDRED	34.2	24.8	0.6	19.29	14	14.90	40.5	0.002	2.5E-15
508.0	0.3	0.06		ESDRED	34.1	24.8	0.6	19.66	14	14.90	40.2	0.002	
511.0	0.3	0.06		ESDRED	34.2	25.3	0.6	19.7	14	14.94		0.002	
514.6	0.3	0.06		ESDRED	34.3	24.9	0.6	19.61	14	14.95		0.002	2.9E-15

Days	PV	PV_{ESDRED}	Mobile	Fluid	P_{conf}	P_{inf}	P_{exf}	T	Syr.	Fluid	Eh	Q (AVG)	k (AVG)
518.0	0.3	0.06		ESDRED	34.2	25.0	0.6	19.75	14	14.96		0.002	
525.6	0.3	0.06		ESDRED	34.1	24.6	0.6	19.28	14	14.97		0.002	
535.0	0.3	0.06		ESDRED	34.1	24.7	0.6	19.15	14	14.97		0.002	
542.0	0.3	0.06		ESDRED	34.2	24.6	0.6	19.47	14	15.00		0.002	2.8E-15
543.0	0.3	0.06		ESDRED	34.2	24.6	0.6	19.72	14	15.00		0.002	

Table 11-5: Experiment S/B-CT 3 (Sand/Bentonite – APW$_{OPC}$)

Days	PV	PV$_{OPC}$	Mobile	Fluid	P_{conf}	P_{inf}	P_{exf}	T	Syr.	Fluid	pH	EC	Q (AVG)	k (AVG)
						[bar]		[°C]	#	[ml]		[mS/cm]	[ml/day]	[m/s]
0				OPA	0.0		0.2	19.1	1					
0.0				OPA	3.0		0.2	19.1	1	0.0				
0.0				OPA	6.2		0.2	19.1	1	0.0				
0.0				OPA	6.1		0.2	19.1	1	0.0				
0.1				OPA	6.0		0.2	19.1	1	0.0				
0.3				OPA	6.1		0.2	19.1	1	0.0				
0.3				OPA	6.1		0.2	19.1	1	0.0				
1.1				OPA	6.1		0.2	19.1	1	0.0				
1.1				OPA	16.8		0.2	19.1	1	0.0				
1.1				OPA	16.7		0.2	19.1	1	0.0				
2.1				OPA	16.2		0.2	18.9	1	0.0				
3.0				OPA	15.9		0.2	18.9	1	0.0				
3.0				OPA	31.4		0.2	18.9	1	0.0				
3.0	0.0			OPA	31.3	11.1	0.2	18.9	1	0.8			288.0	
3.0	0.1			OPA	31.2	11.1	0.2	18.9	1	19.1			1008.0	
3.1	0.1			OPA	31.9	0.0	0.2	18.9	1	19.5			37.1	5.70E-10
3.1	0.1			OPA	41.2	1.0	0.2	18.9	2	19.9		8.9	24.0	
3.1	0.1			OPA	41.0	1.0	0.2	18.9	2	20.1		12.4	14.4	
3.1	0.1			OPA	41.0	1.0	0.2	18.9	2	20.3		10.9	6.40	
3.2	0.1			OPA	40.6	0.9	0.2	19.0	2	20.5		10.9	6.37	
3.4	0.1			OPA	31.8	1.0	0.2	19.1	2	20.7		14.4	2.81	8.90E-11
3.9	0.1			OPA	32.1	1.0	0.2	18.9	2	21.1		11.9	1.15	
4.9	0.1			OPA	32.0	1.2	0.2	18.9	2	21.3		12.1	0.87	
6.2	0.1			OPA	32.0	1.1	0.2	18.9	2	21.5		14.8	0.77	6.20E-12
6.9	0.1			OPA	31.9	1.1	0.2	18.7	2	21.7		15.7	1.67	
6.9	0.1		CT3-12	OPA			0.2		2	21.9				
9.1	0.1			OPA	31.8	1.2	0.2	18.8	2	22.3		16.3		6.20E-12
11.9	0.1			OPA	31.8	1.1	0.2	18.3	2	22.5		17.9	0.59	
12.9	0.2			OPA	31.8	1.1	0.2	18.8	3	22.9		18.7	0.20	3.20E-12
12.9	0.2			OPA	21.3	1.1	0.2	18.8	3	23.1		18.7		
13.0	0.2			OPA	21.6	1.2	0.2	18.8	3	23.3		18.8		
13.9	0.2			OPA	21.6	1.1	0.2	18.9	3	23.5		19.1	0.41	
18.2	0.2			OPA	16.7	1.1	0.2	18.6	3	24.1		18.9	1.87	1.10E-11
19.0	0.2			OPA	16.6	1.0	0.2	18.7	3	24.3		19.7	3.43	
20.9	0.3			OPA	16.7	1.1	0.2	18.6	4	24.7		19.9	0.34	2.00E-11
21.1	0.3			OPA	15.4	1.0	0.2	18.6	4	24.9		19.9	0.38	
24.0	0.4			OPA	15.3	1.0	0.2	18.0	4	25.1		19.4	0.44	3.00E-11
26.9	0.5			OPA	14.3	0.7	0.2	18.8	5	25.9		19.5	0.37	
30.2	0.5			OPA	14.3	0.7	0.2	18.2	5	26.1		19.9	0.36	
30.9	0.5			OPA	14.4	0.8	0.2	18.9	5	26.3		20.0	0.38	1.90E-11
31.1	0.5			OPA	16.1	0.8	0.2	18.9	5	26.7		19.9	0.38	
31.9	0.5			OPA	16.1	0.9	0.2	19.0	5	26.9		20.1	0.38	
32.1	0.5			OPA	16.1	0.9	0.2	19.0	5	27.1		20.1	0.39	1.60E-11
32.9	0.5			OPA	16.0	0.8	0.2	19.0	5	27.3		18.7	0.39	
33.9	0.6			OPA	16.2	0.9	0.2	19.1	5	27.5		20.1	0.40	
35.2	0.6			OPA	16.1	0.9	0.2	19.1	5	27.7		21.4	0.40	2.00E-11
38.0	0.7			OPA	16.0	0.8	0.2	18.9	6	28.1		19.9	0.41	
41.9	0.7			OPA	16.1	0.8	0.2	19.1	6	28.3		19.7	0.41	
42.3	0.7			OPA	16.0	0.8	0.2	19.1	6	28.4		19.6	0.42	
42.3	0.7			OPA	16.0	0.8	0.2	19.1	7	28.6		19.6	0.42	2.10E-11
44.9	0.8			OPA	16.2	0.8	0.2	18.7	7	28.7		19.5	0.43	
45.9	0.8			OPA	16.1	0.8	0.2	19.0	7	28.9		19.8	0.43	
53.9	1.0			OPA	16.1	0.9	0.2	18.9	7	29.0		19.9	0.43	2.20E-11
53.9	1.0			OPA	16.1	0.9	0.2	18.9	8	29.2		19.9	0.43	
58.9	1.1			OPA	16.1	0.8	0.2	18.8	8	29.3		19.9	0.44	
62.9	1.1			OPA	16.2	0.9	0.2	19.2	8	29.5		19.4	0.44	
65.0	1.2			OPA	16.0	0.8	0.2	19.1	8	29.6		19.5	0.43	
65.0	1.2			OPA	16.0	0.8	0.2	19.1	9	29.8		19.5	0.43	

Days	PV	PV_{OPC}	Mobile	Fluid	P_{conf}	P_{inf}	P_{exf}	T	Syr.	Fluid	pH	EC	Q (AVG)	k (AVG)
73.1	1.3			OPA	16.1	0.8	0.2	19.3	9	29.9		18.9	0.43	1.70E-11
75.8	1.3			OPA	16.1	0.8	0.2	19.4	9	30.1		19.0	0.43	
83.9	1.4			OPA	16.1	0.8	0.2	19.8	9	30.2		17.9	0.43	
83.9	1.4			OPA	16.1	0.8	0.2	19.8	10	30.4		17.9	0.43	1.40E-11
94.3	1.5			OPA	16.2	0.7	0.2	19.9	10	30.5		18.5	0.42	
100.9	1.5			OPA	16.3	0.9	0.2	20.0	10	30.7		18.4	0.42	
101.2	1.5			OPA	16.2	0.9	0.2	20.0	10	30.8		19.1	0.42	
104.8	1.6			OPA	16.2	0.9	0.2	20.1	10	31.0		19.9	0.41	9.90E-12
107.8	1.6			OPA	16.2	0.9	0.2	19.9	10	31.1		19.7	0.41	
116.8	1.7			OPA	16.2	0.9	0.2	20.1	10	31.3		19.8	0.41	
117.9	1.7			OPA	16.1	0.9	0.2	20.0	10	31.4		19.8	0.40	
117.9	1.7			OPA	16.1	0.9	0.2	20.0	11	31.6		19.8	0.40	9.80E-12
122.9	1.8			OPA	16.3	0.9	0.2	20.5	11	31.7		19.7	0.40	
128.9	1.8			OPA	16.1	0.9	0.2	20.9	11	31.9		20.3	0.40	
133.0	1.9			OPA	16.2	0.8	0.2	21.6	11	32.0		20.2	0.40	
133.0	1.9			OPA	16.2	1.0	0.2	21.6	11	32.2		20.2	0.40	1.10E-11
136.8	2.0			OPA	16.2	1.0	0.2	21.7	11	32.3		20.3	0.40	
143.9	2.1			OPA	16.4	1.0	0.2	21.2	11	32.5		20.4	0.40	
143.9	2.1			OPA	16.4	1.0	0.2	21.2	12	32.6		20.4	0.40	
146.9	2.1			OPA	16.4	1.0	0.2	21.3	12	32.8		20.4	0.40	1.40E-11
153.9	2.3			OPA	16.3	1.0	0.2	21.9	12	32.9		20.4	0.40	
157.2	2.3			OPA	16.4	1.1	0.2	22.3	12	33.1		20.4	0.41	
157.2	2.3			OPA	16.4	1.0	0.2	22.3	12	33.2		20.4	0.41	1.70E-11
157.9	2.4			OPA	16.3	1.0	0.2	22.3	12	33.4		20.2	0.41	
159.9	2.4			OPA	16.4	1.0	0.2	22.4	12	33.5		20.3	0.42	
159.9	2.4			OPA	16.4	1.0	0.2	22.4	13	33.7		20.3	0.42	
164.9	2.6			OPA	16.4	1.1	0.2	22.7	13	33.8		20.8	0.42	
171.0	2.7			OPA	16.4	1.0	0.2	23.5	13	34.0		21.0	0.43	2.00E-11
172.3	2.7			OPA	16.5	1.0	0.2	23.4	13	34.1		20.8	0.43	
172.3	2.7			OPA	16.5	1.0	0.2	23.4	14	34.3		20.8	0.43	
184.0	3.0			OPA	16.4	1.0	0.2	23.4	14	34.4		20.9	0.43	
188.9	3.1			OPA	16.4	1.0	0.2	23.3	14	34.6		20.7	0.43	1.70E-11
191.9	3.1			OPA	16.4	1.0	0.2	23.4	14	34.7		20.7	0.44	
191.9	3.1			OPA	16.4	1.0	0.2	23.4	15	34.9		20.7	0.44	
205.2	3.3			OPA	16.4	1.0	0.2	22.7	15	35.0		20.3	0.44	
212.9	3.5			OPA	16.3	1.0	0.2	22.7	15	35.2		20.0	0.44	
212.9	3.5			OPA	16.3	1.0	0.2	22.7	16	35.3		20.0	0.44	1.40E-11
219.9	3.6			OPA	16.3	0.9	0.2	22.1	16	35.5		20.1	0.44	
226.9	3.7			OPA	16.3	0.9	0.2	22.8	16	35.6		20.2	0.44	
230.3	3.7			OPA	16.3	0.9	0.2	21.9	16	35.8		20.3	0.43	
230.3	3.7			OPA	16.2	0.9	0.2	21.9	16	35.9		20.3	0.43	1.40E-11
233.9	3.8			OPA	16.3	0.9	0.2	21.8	16	36.1		19.6	0.43	
233.9	3.8		CT3-18	OPA			0.2	21.8	16	36.2		19.6	0.43	2.20E-11
235.0	3.8			OPA	16.3	0.9	0.2	21.9	16	36.5		21.3	0.45	
235.0	3.8			OPA	16.3	0.9	0.2	21.9	17	36.7		21.3	0.45	
240.9	4.0			OPA	16.3	0.9	0.2	21.7	17	36.8		21.8	0.45	
247.1	4.1			OPA	16.2	0.9	0.2	21.4	17	37.0		21.8	0.45	2.80E-11
252.1	4.2			OPA	16.2	1.0	0.2	21.4	17	37.1		22.0	0.45	
252.1	4.2			OPA	16.2	1.0	0.2	21.4	18	37.3		22.0	0.45	
255.9	4.2			OPA	16.1	1.0	0.2	21.1	18	37.4		22.2	0.45	
262.9	4.4			OPA	16.2	1.0	0.2	21.3	18	37.6		22.3	0.45	1.50E-11
271.0	4.5			OPA	16.1	1.0	0.2	20.9	18	37.7		21.1	0.45	
275.9	4.5			OPA	16.1	0.9	0.2	20.8	18	37.9		21.2	0.45	
275.9	4.5			OPA	16.1	0.9	0.2	20.8	19	38.0		21.2	0.45	
280.0	4.6			OPA	16.2	0.9	0.2	20.6	19	38.2		22.0	0.45	1.10E-11
283.0	4.6			OPA	16.1	0.9	0.2	20.4	19	38.3		21.2	0.45	
286.0	4.6			OPA	16.2	0.9	0.2	20.5	19	38.5		22.3	0.44	
287.0	4.6			OPA	16.2	0.9	0.2	20.7	19	38.6		22.9	0.44	
290.0	4.7			OPA	16.2	0.9	0.2	20.4	19	38.8		22.4	0.44	7.40E-12
297.0	4.7			OPA	16.0	0.9	0.2	19.4	19	38.9		22.4	0.43	
300.0	4.7			OPA	16.0	0.9	0.2	19.4	19	39.1		22.3	0.43	

Days	PV	PV_{OPC}	Mobile	Fluid	P_{conf}	P_{inf}	P_{exf}	T	Syr.	Fluid	pH	EC	Q (AVG)	k (AVG)
300.2	4.7			OPA	16.0	1.6	0.2	19.2	19	39.2		22.3	0.43	5.10E-12
301.0	4.7			OPA	16.1	1.6	0.2	19.3	19	39.2	7.3	22.3	0.43	
301.3	4.7			OPA	16.2	1.6	0.2	19.8	19	39.4	7.2	22.2	0.43	
303.9	4.8			OPA	16.1	1.6	0.2	19.7	19	58.5		22.4	0.43	
304.1	4.8			OPA	16.1	1.6	0.2	19.7	19	58.7		22.4	0.43	
304.3	4.8			OPA	16.1	1.6	0.2	19.6	19	58.7		22.4	0.43	
305.0	4.8			OPA	16.1	1.6	0.2	19.7	19	58.8		22.4	0.45	2.20E-11
306.0	4.8			OPA	16.1	1.6	0.2	19.8	19	59.0	7.2	22.5	0.45	
308.0	4.9			OPA	16.1	1.6	0.2	19.7	19	78.1		22.5	0.45	
308.0	4.9			OPA	16.1	1.6	0.2	19.7	20	78.3		22.5	0.45	2.60E-11
311.6	4.9			OPA	16.2	1.6	0.2	19.6	20	78.4		22.6	0.45	
315.0	4.9			OPA	16.1	1.6	0.2	19.8	20	78.6		22.7	0.45	
322.6	5.2			OPA	16.1	1.6	0.2	19.3	20	78.7		22.8	0.45	
322.6	5.2			OPA	16.1	1.6	0.2	19.3	21	78.9		22.8	0.45	7.80E-12
332.0	5.4			OPA	16.0	1.5	0.2	19.2	21	79.0		23.0	0.46	
334.3	5.5			OPA	16.1	1.5	0.2	19.3	21	79.2		23.1	0.46	
334.3	5.5			OPA	16.1	1.5	0.2	19.5	22	79.3		23.1	0.46	
338.9	5.6			OPA	16.1	1.5	0.2	19.5	22	79.5		23.1	0.46	1.40E-11
341.6	5.7			OPA	16.1	1.5	0.2	19.9	22	79.6		23.1	0.47	
346.0	5.7			OPA	16.2	1.5	0.2	19.7	22	79.8		23.0	0.46	
348.6	5.8			OPA	16.2	1.5	0.2	19.9	22	79.9		22.9	0.47	
350.0	5.8			OPA	16.1	1.5	0.2	19.9	22	80.1		22.9	0.46	8.60E-12
350.3	5.8			OPA	16.2	1.6	0.2	19.9	22	80.2		22.9	0.47	
351.1	5.8			OPA	16.1	1.6	0.2	19.9	22	80.4		22.9	0.47	
351.1	5.8			OPA	16.2	1.6	0.2	19.9	22	80.6		22.9		
351.1	5.8			OPA	16.2	1.6	0.2	19.9	23	80.8		22.9		4.00E-11
351.6	5.8			OPA	16.1	1.6	0.2	19.8	23	104.0	7.1	23.0		
351.6	5.8	0.0		OPC	16.1	1.7	0.2	19.8	23	104.2		22.9		
353.0	5.9	0.0		OPC	16.1	1.6	0.2	19.7	23	104.4		23.0		
353.1	5.9	0.0		OPC	16.1	1.6	0.2	19.7	23	104.6		22.9		1.00E-11
353.1	5.9	0.0	CT3-20	OPC		1.6	0.2		23	104.8				
353.2	5.9	0.0		OPC	15.9	1.6	0.2	19.6	23	105.0				
355.0	5.9	0.0		OPC	16.0	1.6	0.2	19.8	23	105.2		22.7		
355.0	5.9	0.0		OPC	16.1	1.6	0.2	19.7	23	105.4		22.8		
355.2	5.9	0.0	CT3-21	OPC		1.6	0.2		23	105.6				
355.2	5.9	0.0		OPC	16.2	1.6	0.2	19.7	23	105.8				
356.0	5.9	0.1		OPC	16.1	1.6	0.2	19.7	23	106.0		22.2		
356.2	5.9	0.1		OPC	16.1	1.6	0.2	19.7	23	129.2	7.3	22.2		1.10E-11
357.0	5.9	0.1		OPC	16.1	1.6	0.2	19.7	23	129.4		21.6	0.57	
357.2	5.9	0.1	CT3-22	OPC	16.0	1.6	0.2	19.7	23	129.6		21.6	0.57	
360.1	6.0	0.1		OPC	16.1	1.6	0.2	19.7	24	130.1		20.0	0.53	8.20E-12
360.4	6.0	0.1		OPC	16.1	1.6	0.2	19.7	24	155.3	8.3	19.7	0.51	
361.3	6.0	0.1		OPC	15.9	1.6	0.2	19.7	24	155.5		19.4	0.46	
362.0	6.0	0.1		OPC	16.1	1.6	0.2	19.7	25	155.9		18.9	0.26	5.80E-12
364.1	6.0	0.2		OPC	16.1	1.6	0.2	19.8	25	156.1		18.1	0.29	
364.1	6.0	0.2		OPC	16.1	1.7	0.2	19.8	25	156.3		18.1	0.29	
364.3	6.0	0.2		OPC	16.0	1.6	0.2	19.8	25	181.5	7.5	17.9	0.29	
367.1	6.0	0.2		OPC	16.1	1.6	0.2	19.8	25	181.7		16.9	0.27	4.9E-12
367.1	6.0	0.2	CT3-23	OPC		1.6	0.2	19.8	25	181.9		16.9	0.27	
367.2	6.0	0.2		OPC	15.9	1.6	0.2	19.8	25	182.2		17.4	0.27	
369.3	6.0	0.2		OPC	16.1	1.6	0.2	19.7	25	182.4		15.9	0.26	3.0E-12
369.3	6.0	0.2		OPC	16.1	1.6	0.2	19.7	26	182.6		15.9	0.26	
373.2	6.1	0.2		OPC	16.1	1.6	0.2	19.7	26	182.8		14.3	0.26	
374.0	6.1	0.2		OPC	16.1	1.6	0.2	19.7	26	209.0	7.5	13.9	0.26	
374.2	6.1	0.3		OPC	16.2	1.6	0.2	19.7	26	235.2	7.4	13.8	0.25	
375.0	6.1	0.3		OPC	16.1	1.6	0.2	19.7	26	235.4		13.6	0.24	4.1E-12
377.2	6.1	0.3		OPC	16.0	1.6	0.2	19.8	26	235.6		12.9	0.23	
380.5	6.1	0.3		OPC	16.1	1.6	0.2	19.6	26	235.8		12.1	0.23	
381.0	6.1	0.3		OPC	16.0	1.6	0.2	19.6	26	236.0		11.9	0.22	
381.9	6.1	0.3		OPC	16.0	1.6	0.2	19.5	26	262.3	7.5	11.5	0.22	3.4E-12
382.0	6.1	0.3	CT3-24	OPC		1.7	0.2	19.6	26	262.5		11.8	0.22	

Days	PV	PV_{OPC}	Mobile	Fluid	P_{conf}	P_{inf}	P_{exf}	T	Syr.	Fluid	pH	EC	Q (AVG)	k (AVG)
382.1	6.1	0.3		OPC	16.1	1.5	0.2	19.6	26	262.7			0.22	
383.0	6.1	0.3		OPC	16.1	1.5	0.2	19.7	26	262.9		11.3	0.22	4.30E-12
383.0	6.1	0.3		OPC	16.1	1.5	0.2	19.7	27	263.1		11.3	0.22	
385.0	6.2	0.3		OPC	16.0	1.5	0.2	19.7	27	263.3		10.9	0.22	
388.0	6.2	0.3		OPC	15.9	1.5	0.2	19.5	27	263.5		10.3	0.22	
388.2	6.2	0.3		OPC	15.9	1.5	0.2	19.5	27	263.7		10.3	0.22	
389.0	6.2	0.3		OPC	16.0	1.5	0.2	19.4	27	290.9	7.6	10.0	0.21	3.50E-12
390.0	6.2	0.3		OPC	16.0	1.5	0.2	19.5	27	318.1		9.8	0.21	
390.0	6.2	0.3		OPC	16.0	2.1	0.2	19.5	27	345.4		9.8	0.21	
391.0	6.2	0.4		OPC	16.1	2.1	0.2	19.5	27	373.6		9.6	0.22	
394.9	6.2	0.4		OPC	16.1	2.1	0.2	19.5	27	401.8		8.9	0.22	3.30E-12
395.0	6.2	0.4		OPC	16.0	2.3	0.2	19.5	28	430.0		8.9	0.22	
395.4	6.2	0.4		OPC	16.0	2.3	0.2	19.1	28	458.2	7.6	8.7	0.22	
396.9	6.2	0.4		OPC	16.2	2.3	0.2	19.6	28	486.4		8.4	0.22	
399.0	6.3	0.4		OPC	16.1	2.3	0.2	19.8	28	514.6		8.1	0.22	3.50E-12
401.9	6.3	0.5		OPC	16.0	2.3	0.2	19.8	28	542.8		7.4	0.23	
402.5	6.3	0.5		OPC	16.0	2.3	0.2	20.0	28	571.0		7.4	0.23	
402.9	6.3	0.5		OPC	16.1	2.3	0.2	19.9	28	599.2	7.6	7.3	0.23	
405.9	6.3	0.5		OPC	16.1	2.3	0.2	20.2	28	627.5		6.8	0.23	3.40E-12
408.1	6.3	0.5		OPC	16.1	2.3	0.2	20.2	28	655.7		6.5	0.23	
408.9	6.4	0.5		OPC	16.0	2.3	0.2	20.0	28	684.9	7.6	6.4	0.23	
410.0	6.4	0.5		OPC	16.1	2.3	0.2	20.2	28	714.1		6.2	0.22	
410.0	6.4	0.5		OPC	16.1	2.3	0.2	20.2	29	743.3		6.2	0.22	2.10E-12
411.0	6.4	0.5		OPC	16.2	2.3	0.2	20.1	29	772.5		6.1	0.22	
411.0	6.4	0.5	CT3-25	OPC		2.4	0.2	20.1	29	801.7		6.1	0.22	
411.9	6.4	0.5		OPC	16.0	2.3	0.2	20.2	29	860.1		5.9	0.23	3.1E-12
415.1	6.4	0.6		OPC	16.0	2.3	0.2	20.3	29	889.3		5.6	0.22	
415.9	6.4	0.6		OPC	16.1	2.3	0.2	20.2	29	889.6	7.6	5.4	0.22	
418.9	6.4	0.6		OPC	16.0	2.3	0.2	20.4	29	918.8		5.1	0.22	
422.1	6.4	0.6		OPC	16.1	2.3	0.2	20.7	29	948.0		4.9	0.22	2.1E-12
422.9	6.4	0.6		OPC	16.0	2.3	0.2	20.7	29	948.2	7.7	4.9	0.22	
424.0	6.5	0.6		OPC	16.1	2.3	0.2	20.8	29	978.4		4.7	0.22	
424.0	6.5	0.6		OPC	16.1	2.3	0.2	20.8	30	1008.6		4.7	0.22	
431.3	6.5	0.7		OPC	16.2	2.3	0.2	21.0	30	1038.8		4.3	0.22	2.1E-12
433.3	6.5	0.7		OPC	16.1	2.3	0.2	20.8	30	1069.0		4.1	0.21	
437.0	6.5	0.7		OPC	16.1	2.3	0.2	20.6	30	1100.2		3.9	0.21	
437.9	6.5	0.7		OPC	16.0	2.3	0.2	20.5	30	1131.4		3.9	0.21	
437.9	6.5	0.7		OPC	16.0	2.3	0.2	20.5	31	1162.7		3.9	0.21	2.0E-12
438.9	6.5	0.7		OPC	16.0	2.3	0.2	20.4	31	1162.9	7.8	3.8	0.21	
441.0	6.5	0.7		OPC	16.2	2.3	0.2	20.7	31	1163.1		3.7	0.21	
443.9	6.6	0.7		OPC	16.3	2.3	0.2	20.7	31	1163.3		3.6	0.21	
445.9	6.6	0.7		OPC	16.1	2.3	0.2	20.9	31	1163.5		3.5	0.20	1.6E-12
446.9	6.6	0.7		OPC	16.2	2.3	0.2	20.9	31	1163.7	7.9	3.4	0.20	
453.0	6.6	0.7		OPC	16.2	2.3	0.2	20.9	31	1164.3		3.3	0.08	1.3E-12
453.0	6.6	0.7		OPC	16.2	2.3	0.2	20.9	32	1164.5		3.3	0.08	
457.9	6.6	0.8		OPC	16.1	2.3	0.2	20.9	32	1164.8		3.1	0.06	
458.1	6.6	0.8	CT3-26	OPC		2.2	0.2	20.9	32	1165.0			0.06	3.8E-13
459.2	6.6	0.8		OPC	16.2	2.3	0.2	20.9	32	1165.4	7.9	3.0	0.06	
461.9	6.6	0.8		OPC	16.2	2.3	0.2	21.0	32	1165.6		3.0	0.05	
465.9	6.6	0.8		OPC	16.1	2.3	0.2	20.9	32	1165.8		2.8	0.06	
471.9	6.6	0.8		OPC	16.1	2.3	0.2	21.2	32	1166.0		2.8	0.06	7.5E-13
472.9	6.6	0.8		OPC	16.1	2.3	0.2	21.2	32	1166.2	7.9	2.8	0.06	
478.9	6.6	0.8		OPC	16.1	2.3	0.2	21.1	32	1166.4		2.6	0.06	
480.9	6.6	0.8		OPC	16.1	2.3	0.2	21.3	32	1166.6		2.6	0.07	
483.3	6.7	0.8		OPC	16.2	2.3	0.2	21.3	32	1166.9		2.6	0.06	8.5E-13
483.3	6.7	0.8		OPC	16.2	2.3	0.2	21.3	33	1167.1		2.6	0.06	
486.9	6.7	0.8		OPC	16.2	2.3	0.2	21.7	33	1167.3		2.5	0.07	
487.9	6.7	0.8		OPC	16.2	2.3	0.2	21.9	33	1167.5	8.2	2.4	0.07	
493.0	6.7	0.9		OPC	16.2	2.3	0.2	22.6	33	1167.7		2.5	0.07	1.2E-12
499.9	6.7	0.9		OPC	16.2	2.3	0.2	22.6	33	1167.9		2.4	0.07	
501.1	6.7	0.9		OPC	16.3	2.3	0.2	22.9	33	1168.1	7.9	2.3	0.07	

Days	PV	PV_{OPC}	Mobile	Fluid	P_{conf}	P_{inf}	P_{exf}	T	Syr.	Fluid	pH	EC	Q (AVG)	k (AVG)
504.2	6.7	0.9		OPC	16.2	2.3	0.2	22.9	33	1168.3		2.2	0.07	
507.9	6.7	0.9		OPC	16.2	2.3	0.2	22.8	33	1168.5		2.4	0.07	9.3E-13
513.9	6.7	0.9		OPC	16.3	2.3	0.2	22.6	33	1168.7		2.2	0.07	
513.9	6.7	0.9		OPC	16.3	2.3	0.2	22.6	34	1169.0		2.2	0.07	
515.9	6.8	0.9		OPC	16.2	2.2	0.2	22.5	34	1169.2	7.8	2.2	0.07	
515.9	6.8	0.9	CT3-27	OPC	17.0	1.4	0.2	22.5	34	1169.4			0.07	1.0E-12
516.1	6.8	0.9		OPC	17.3	2.2	0.2	22.6	34	1169.6		2.2	0.07	
518.1	6.8	0.9		OPC	16.2	2.2	0.2	22.4	34	1169.8		2.2	0.07	
520.9	6.8	0.9		OPC	16.2	2.2	0.2	22.1	34	1170.0		2.2	0.07	
523.9	6.8	0.9		OPC	16.2	2.2	0.2	22.2	34	1170.2		2.1	0.07	9.3E-13
534.1	6.8	1.0		OPC	16.1	2.2	0.2	22.5	34	1170.4		2.1	0.07	
536.0	6.8	1.0		OPC	16.2	2.2	0.2	22.5	34	1170.6	7.8	2.1	0.07	
537.9	6.8	1.0		OPC	16.1	2.2	0.2	22.4	34	1170.8		2.1	0.07	
541.9	6.8	1.0		OPC	16.2	2.2	0.2	22.4	34	1171.1		2.1	0.07	7.4E-13
549.9	6.8	1.0		OPC	16.4	2.2	0.2	22.6	34	1171.3		2.1	0.07	
549.9	6.8	1.0		OPC	16.4	2.2	0.2	22.6	35	1171.5		2.1	0.07	
551.9	6.8	1.0		OPC	16.2	2.2	0.2	22.6	35	1171.7	7.9	2.1	0.07	
555.9	6.8	1.0		OPC	16.2	2.2	0.2	22.3	35	1171.9		2.1	0.07	8.4E-13
556.0	6.8	1.0	CT3-28	OPC	17.0	1.4	0.2	22.3	35	1172.1		2.1	0.07	
557.9	6.9	1.0		OPC	16.2	2.2	0.2	22.1	35	1172.5		2.0	0.07	
557.9	6.9	1.0		OPC	16.3	2.4	0.2	22.1	35	1172.7		2.0	0.07	
559.3	6.9	1.0		OPC	16.1	2.6	0.2	22.1	35	1172.9		2.0	0.07	
559.9	6.9	1.0		OPC	16.2	2.6	0.2	22.1	35	1173.2		2.0	0.07	
563.0	6.9	1.0		OPC	16.2	2.6	0.2	22.0	35	1173.4		2.0	0.07	
564.3	6.9	1.0		OPC	16.1	2.6	0.2	22.1	35	1173.6		2.0	0.07	4.3E-13
565.9	6.9	1.0		OPC	16.2	2.6	0.2	22.0	35	1173.8		2.0	0.07	
569.9	6.9	1.0		OPC	16.1	2.5	0.2	21.9	35	1174.0		2.0	0.06	
569.9	6.9	1.0		OPC	16.2	2.7	0.2	21.9	35	1174.2		2.0	0.06	
571.9	6.9	1.0		OPC	16.1	2.7	0.2	21.9	35	1174.4	7.9	2.1	0.06	5.3E-13
573.9	6.9	1.0		OPC	16.1	2.7	0.2	21.9	35	1174.6		2.0	0.06	
577.2	6.9	1.0		OPC	16.1	2.7	0.2	21.9	35	1174.8		2.0	0.06	
577.2	6.9	1.0		OPC	16.2	0.2	0.2	21.9	35	1175.0		2.0	0.06	
578.0	6.9	1.0		OPC	16.2	0.2	0.2	22.0	35	1175.3		2.1	0.06	
578.0	6.9	1.0		OPC	16.2	0.0	0.2	22.0	35	1175.5		2.1	0.06	
578.0	6.9	1.0		OPC	13.8	0.0	0.2	22.0	35	1175.7		2.1	0.06	
578.3	6.9	1.0		OPC	13.8	0.0	0.2	22.0	35	1175.9		2.1	0.05	
578.3	6.9	1.0		OPC	12.4	0.0	0.2	22.0	35	1176.1		2.1	0.05	
578.9	6.9	1.0		OPC	12.5	0.0	0.2	22.0	35	1176.3				
578.9	6.9	1.0		OPC	8.7	0.0	0.2	22.0	35	1176.3				
578.9	6.9	1.0		OPC	0.3	0.0	0.2	22.0	35	1176.3				

Table 11-6: Experiment S/B-CT 4 (Sand/Bentonite – APW_{ESDRED})

Days	**PV**	**PV_{ESDRED}**	**Mobile**	**Fluid**	**P_{conf}**	**P_{inf}**	**P_{exf}**	**T**	**Syr.**	**Fluid**	**EC**	**Q (av.)**	**k (av.)**
						[bar]		[°C]	#	[ml]	[mS/cm]	[ml/day]	[m/s]
0.0				OPA	1.0	0.0	0.2	20.0	1				
0.0				OPA	3.5	0.0	0.2	20.0	1				
0.1				OPA	6.1	0.0	0.2	20.0	1				
0.1				OPA	6.1	0.0	0.2	20.0	1				
0.1				OPA	6.0	0.0	0.2	20.0	1				
0.2				OPA	6.0	0.0	0.2	20.0	1				
0.2				OPA	7.2	0.0	0.2	20.0	1				
0.2				OPA	7.1	0.0	0.2	20.0	1				
0.2				OPA	10.6	0.0	0.2	20.0	1				
0.4				OPA	10.2	0.0	0.2	20.0	1				
1.0				OPA	9.9	0.0	0.2	19.8	1				
1.0				OPA	16.1	0.0	0.2	19.8	1				
1.0				OPA	15.9	0.0	0.2	19.8	1				
1.0				OPA	16.1	0.9	0.2	19.9	1				
1.0				OPA	15.9	0.9	0.2	19.9	1				
1.1				OPA	15.8	0.9	0.2	19.9	1				
1.2				OPA	15.6	1.1	0.2	19.9	1				
1.3	0.0			OPA	15.6	1.1	0.2	19.9	1	0.3		1.02	
1.3	0.0			OPA	15.5	1.1	0.2	19.9	1	0.5		1.69	
2.1	0.1			OPA	15.0	1.1	0.2	19.9	1	3.5		3.20	
2.1	0.1			OPA	15.0	1.1	0.2	19.9	2	3.5			1.0E-10
2.2	0.1			OPA	15.0	1.1	0.2	19.9	2	3.5	25.2		
3.1	0.2			OPA	14.8	1.1	0.2	19.8	2	5.5	23.8	2.67	
3.1	0.2			OPA	14.7	0.9	0.2	19.8	2	5.5	23.8		1.2E-10
3.1	0.2			OPA	18.5	0.9	0.2	19.8	2	5.6	23.8	2.68	
4.0	0.2			OPA	17.8	0.9	0.2	19.7	2	6.4	23.7	2.19	
6.0	0.3			OPA	17.6	0.9	0.2	19.7	2	7.5	23.4	1.52	
7.0	0.3			OPA	17.7	0.9	0.2	19.7	2	7.8	23.1	1.30	
7.0	0.3			OPA	17.7	0.9	0.2	19.7	3	7.8	23.1		7.5E-11
8.0	0.3			OPA	17.7	0.9	0.2	19.7	3	8.6	22.8	1.23	
11.1	0.3			OPA	17.6	0.9	0.2	19.7	3	9.2	22.5	0.91	
12.3	0.3			OPA	17.6	0.9	0.2	19.6	3	9.6	22.3	0.85	
12.9	0.3			OPA	17.5	0.9	0.2	19.7	3	9.6	21.7		2.6E-11
13.0	0.3			OPA	17.5	0.9	0.2	19.7	3	9.7	21.3	0.81	
13.0	0.3			OPA	17.5	0.9	0.2	19.7	4	9.7	21.3		
15.1	0.4			OPA	17.5	0.9	0.2	19.8	4	10.3	22.1	0.73	
18.1	0.4			OPA	17.5	0.9	0.2	19.8	4	11.1	22.0	0.65	2.5E-11
20.3	0.4			OPA	17.5	0.9	0.2	19.7	4	11.5	22.3	0.59	
24.3	0.4			OPA	17.5	0.9	0.2	19.8	4	12.2	22.1	0.52	
28.2	0.4			OPA	17.6	0.9	0.2	19.8	4	12.3		0.45	
32.0	0.5			OPA	17.4	0.9	0.2	19.6	4	12.7	22.5	0.41	4.6E-12
32.0	0.5			OPA	17.4	1.4	0.2	19.6	4	12.7	22.5		
32.2	0.5			OPA	17.5	1.4	0.2	19.6	4	12.8		0.41	
32.2	0.5			OPA	17.3	1.5	0.2	19.6	4	12.8			5.6E-12
32.2	0.5			OPA	17.6	1.7	0.2	19.7	4	12.8	22.5		
33.0	0.5			OPA	17.5	1.7	0.2	19.7	4	12.7			
33.0	0.5		CT4-24	OPA						13.3			
33.2	0.5			OPA	17.2	1.7	0.2	19.6	4	13.4			
33.2	0.5			OPA	17.2	1.7	0.2	19.6	4	13.4			
34.1	0.5			OPA	17.2	1.7	0.2	19.7	4	14.4	22.5	0.43	
36.1	0.5			OPA	17.3	1.7	0.2	19.7	4	14.5			

Days	PV	PV$_{ESDRED}$	Mobile	Fluid	P$_{conf}$	P$_{inf}$	P$_{exf}$	T	Syr.	Fluid	EC	Q (av.)	k (av.)
39.0	0.5			OPA	17.3	1.6	0.2	19.5	4	15.2	22.3	0.40	
41.0	0.6			OPA	17.3	1.6	0.2	19.4	4	15.6	22.3	0.39	9.2E-12
41.0	0.6			OPA	17.2	2.0	0.2	19.5	4	15.6	22.3		
42.0	0.6			OPA	17.1	2.0	0.2	19.5	4	15.9	22.4	0.39	
42.2	0.6			OPA	17.3	2.0	0.2	19.5	4	16.0	22.4	0.39	4.8E-12
42.2	0.6			OPA	17.3	2.0	0.2	19.5	5	16.0	22.4		
45.9	0.6			OPA	17.3	2.0	0.2	19.5	5	17.2	22.6	0.38	
47.9	0.6			OPA	17.3	1.9	0.2	19.6	5	17.6	22.5	0.37	
50.0	0.7			OPA	17.3	1.9	0.2	19.8	5	18.2		0.37	
52.9	0.7			OPA	17.3	1.9	0.2	19.8	5	18.6	21.3	0.36	3.3E-12
55.0	0.7			OPA	17.4	1.9	0.2	20.0	5	18.8	22.2	0.35	
56.0	0.7			OPA	17.3	1.9	0.2	20.1	5	18.9	23.1	0.34	
56.0	0.7	0.0		ESDRED	17.3	1.9	0.2	20.1	6	18.9	23.1		
57.0	0.7	0.0		ESDRED	17.4	1.9	0.2	20.2	6	19.0	22.4	0.34	1.6E-12
59.1	0.7	0.0		ESDRED	17.4	1.9	0.2	20.2	6	19.5	22.8	0.34	
60.0	0.7	0.0		ESDRED	17.4	1.9	0.2	20.0	6	19.9	22.8	0.34	
61.2	0.7	0.1		ESDRED	17.4	1.9	0.2	20.2	6	20.5	22.8	0.34	5.5E-12
62.0	0.8	0.1		ESDRED	17.3	1.9	0.2	20.2	6	21.4	22.6	0.35	
62.0	0.8	0.1	CT4-25	ESDRED									
62.2	0.8	0.1		ESDRED	17.2	1.9	0.2	20.2	6	21.5			
62.9	0.8	0.1		ESDRED	17.3	1.9	0.2	20.2	6	21.9	22.5	0.35	
62.9	0.8	0.1		ESDRED	17.3	1.9	0.2	20.2	7	21.9	22.5		1.1E-11
66.1	0.8	0.2		ESDRED	17.5	1.9	0.2	20.3	7	23.4	21.8	0.36	
66.9	0.8	0.2		ESDRED	17.3	1.9	0.2	20.3	7	23.6	21.4	0.36	
67.4	0.9	0.2		ESDRED	17.4	1.9	0.2	20.3	7	23.8	21.1	0.36	5.4E-12
68.9	0.9	0.2		ESDRED	17.4	1.9	0.2	20.3	7	24.4	20.7	0.36	
69.9	0.9	0.2		ESDRED	17.4	1.9	0.2	20.4	7	24.7	20.3	0.36	
69.9	0.9	0.2		ESDRED	17.4	1.9	0.2	20.4	8	24.7	20.3		
73.1	0.9	0.2		ESDRED	17.4	1.9	0.2	20.7	8	25.7	19.0	0.36	4.9E-12
74.0	0.9	0.3		ESDRED	17.5	1.9	0.2	20.7	8	26.1	18.8	0.36	
75.0	0.9	0.3		ESDRED	17.4	1.9	0.2	20.8	8	26.3	18.4	0.36	
75.0	0.9	0.3		ESDRED	17.4	1.9	0.2	20.8	9	26.3	18.4		
82.3	1.0	0.4		ESDRED	17.5	1.9	0.2	21.0	9	28.7			4.9E-12
84.3	1.1	0.4		ESDRED	17.4	1.9	0.2	20.8	9	29.4		0.35	
88.0	1.1	0.4		ESDRED	17.4	1.9	0.2	20.7	9	30.5	9.7	0.35	
88.9	1.1	0.4		ESDRED	17.4	1.9	0.2	20.5	9	30.9	3.4	0.35	5.3E-12
88.9	1.1	0.4		ESDRED	17.4	1.9	0.2	20.5	10	30.9			
92.0	1.1	0.5		ESDRED	17.3	1.9	0.2	20.8	10	31.8	12.8	0.35	
94.9	1.2	0.5		ESDRED	17.4	1.9	0.2	20.7	10	32.5	12.1	0.35	
96.9	1.2	0.5		ESDRED	17.4	1.9	0.2	20.9	10	33.1	12.1	0.35	
99.2	1.2	0.5		ESDRED	17.5	1.9	0.2	21.0	10	33.4	11.6	0.34	3.6E-12
101.9	1.2	0.5		ESDRED	17.3	1.9	0.2	20.9	10	34.1	11.2	0.34	
103.3	1.2	0.6		ESDRED	17.3	1.9	0.2	20.9	10	34.2	10.7	0.33	
103.3	1.2	0.6		ESDRED	17.3	1.9	0.2	20.9	11	34.2	10.7		
108.9	1.3	0.6		ESDRED	17.5	1.9	0.2	20.9	11	35.5	9.8	0.33	2.8E-12
109.1	1.3	0.6	CT4-26	ESDRED						35.5			
109.2	1.3	0.6		ESDRED	17.4	1.9	0.2	21.0	11	35.5			
110.2	1.3	0.6		ESDRED	17.4	1.8	0.2	20.9	11	36.0	9.5	0.33	
112.9	1.3	0.6		ESDRED	17.4	1.8	0.2	21.0	11	36.4	9.1	0.33	4.9E-12
113.2	1.3	0.6		ESDRED	17.4	1.9	0.2	20.9	11	36.4	9.0		
117.0	1.3	0.7		ESDRED	17.5	1.9	0.2	20.9	11	37.5	8.3	0.32	
117.0	1.3	0.7		ESDRED	17.5	1.9	0.2	20.9	12	37.5	8.3		
122.9	1.4	0.7		ESDRED	17.4	1.9	0.2	21.2	12	39.2	7.5	0.32	4.1E-12
130.0	1.5	0.8		ESDRED	17.4	1.9	0.2	21.1	12	40.6	6.9	0.31	

Days	PV	PV$_{ESDRED}$	Mobile	Fluid	P$_{conf}$	P$_{inf}$	P$_{exf}$	T	Syr.	Fluid	EC	Q (av.)	k (av.)
132.0	1.5	0.8		ESDRED	17.4	1.9	0.2	21.2	12	41.2		0.31	
132.0	1.5	0.8		ESDRED	17.4	1.9	0.2	21.2	13	41.2			
137.9	1.5	0.9		ESDRED	17.5	1.9	0.2	21.6	13	42.6	6.3	0.31	3.5E-12
144.0	1.6	0.9		ESDRED	17.6	1.9	0.2	22.6	13	43.9	5.9	0.31	
146.9	1.6	0.9		ESDRED	17.6	1.9	0.2	22.6	13	44.8	5.8	0.31	
147.0	1.6	0.9		ESDRED	17.6	1.9	0.2	22.6	14	44.8	5.8		
151.0	1.6	1.0		ESDRED	17.6	1.9	0.2	22.6	14	45.8	5.7	0.31	3.7E-12
155.2	1.7	1.0		ESDRED	17.6	1.9	0.2	22.9	14	46.8	5.5	0.30	
158.9	1.7	1.0		ESDRED	17.5	1.9	0.2	22.8	14	47.6	5.3	0.30	
165.0	1.8	1.1		ESDRED	17.6	1.9	0.2	22.6	14	49.0	5.2	0.30	3.3E-12
165.0	1.8	1.1		ESDRED	17.6	1.9	0.2	22.6	15	49.0	5.2		
167.0	1.8	1.1		ESDRED	17.6	1.9	0.2	22.5	15	49.2	5.2	0.30	
167.0	1.8	1.1	CT4-27	ESDRED						49.2	5.2		
167.1	1.8	1.1		ESDRED	17.5	1.9	0.2	22.6	15	49.2	5.2		
169.2	1.8	1.1		ESDRED	17.1	1.9	0.2	22.4	15	50.0	5.1	0.30	3.5E-12
171.9	1.8	1.1		ESDRED	17.0	1.9	0.2	22.1	15	50.6	5.0	0.30	
174.9	1.8	1.2		ESDRED	17.1	1.9	0.2	22.2	15	51.2	5.0	0.29	
175.9	1.8	1.2		ESDRED	17.1	1.9	0.2	22.2	15	51.4	4.9	0.29	
175.9	1.8	1.2		ESDRED	17.1	1.9	0.2	22.2	16	51.4	4.9		3.2E-12
185.1	1.9	1.2		ESDRED	17.1	1.9	0.2	22.5	16	53.4	4.8	0.29	
192.9	2.0	1.3		ESDRED	17.1	1.9	0.2	22.4	16	55.2	4.7	0.29	
194.3	2.0	1.3		ESDRED	17.0	1.9	0.2	22.5	16	55.5	4.6	0.29	3.3E-12
194.3	2.0	1.3		ESDRED	17.0	1.9	0.2	22.5	17	55.5	4.6		
200.9	2.0	1.4		ESDRED	17.1	1.9	0.2	22.6	17	56.9	4.6	0.28	
206.9	2.1	1.4		ESDRED	17.1	1.8	0.2	22.3	17	58.1	4.6	0.28	
207.0	2.1	1.4	CT4-28	ESDRED						58.1	4.6		
207.2	2.1	1.4		ESDRED	17.1	1.8	0.2	22.3	17	58.2		0.28	5.3E-12
208.9	2.1	1.4		ESDRED	17.0	1.8	0.2	22.1	17	58.7	4.6	0.28	
214.0	2.1	1.5		ESDRED	17.0	1.8	0.2	22.0	17	59.7	4.6	0.28	
216.3	2.2	1.5		ESDRED	16.9	1.8	0.2	22.0	17	60.3	4.5	0.28	
216.3	2.2	1.5		ESDRED	16.9	1.8	0.2	22.0	18	60.3	4.5	0.28	3.7E-12
220.9	2.2	1.5		ESDRED	17.0	1.8	0.2	21.9	18	61.3	4.5	0.28	
222.9	2.2	1.5		ESDRED	17.0	1.8	0.2	21.9	18	61.7	4.5	0.28	
228.2	2.3	1.6		ESDRED	17.0	1.8	0.2	21.9	18	62.8	4.4	0.28	
231.1	2.3	1.6		ESDRED	17.0	1.8	0.2	22.1	18	63.5	4.4	0.28	3.3E-12
231.1	2.3	1.6		ESDRED	17.0	1.8	0.2	22.1	19	63.5	4.4		
234.9	2.3	1.6		ESDRED	16.9	1.8	0.2	21.9	19	64.3	4.3	0.27	
241.9	2.4	1.7		ESDRED	17.0	1.8	0.2	22.0	19	65.7	4.3	0.27	
245.0	2.4	1.7		ESDRED	16.9	1.8	0.2	21.8	19	66.3	4.3	0.27	3.1E-12
248.9	2.4	1.7		ESDRED	17.0	1.8	0.2	21.5	19	67.3	4.4	0.27	
251.9	2.4	1.8		ESDRED	16.6	1.8	0.2	21.6	19	67.8	4.4	0.27	
251.9	2.4	1.8		ESDRED	16.9	1.8	0.2	21.6	20	67.8	4.4		
258.3	2.5	1.8		ESDRED	16.8	1.8	0.2	21.7	20	69.2	4.3	0.27	3.3E-12
265.1	2.5	1.9		ESDRED	16.9	1.8	0.2	21.5	20	70.6	4.3	0.27	
270.4	2.6	1.9		ESDRED	16.8	1.8	0.2	21.5	20	71.6	4.3	0.27	
277.5	2.6	2.0		ESDRED	16.7	1.8	0.2	21.1	20	73.6	4.3	0.27	
277.5	2.6	2.0		ESDRED	16.7	1.8	0.2	21.1	21	73.6	4.3		3.6E-12
282.2	2.7	2.0		ESDRED	17.0	1.8	0.2	21.3	21	74.1	4.3	0.26	
286.4	2.7	2.0		ESDRED	16.9	1.8	0.2	21.4	21	75.4	4.3	0.26	
291.0	2.7	2.1		ESDRED	17.0	1.7	0.2	21.1	21	76.4	4.3	0.26	3.4E-12
291.0	2.7	2.1		ESDRED	17.0	1.7	0.2	21.1	22	76.4	4.3		
295.1	2.8	2.1		ESDRED	16.9	1.7	0.2	21.4	22	77.2	4.3	0.26	
295.1	2.8	2.1		ESDRED	16.9	0.9	0.2	21.4	22	77.2	4.3		
295.3	2.8	2.1		ESDRED	16.8	0.9	0.2	21.4	22	77.3	4.3	0.26	

Days	PV	PV$_{ESDRED}$	Mobile	Fluid	P$_{conf}$	P$_{inf}$	P$_{exf}$	T	Syr.	Fluid	EC	Q (av.)	k (av.)
296.3	2.8	2.1		ESDRED	16.8	0.9	0.2	21.3	22	77.3	4.3		8.1E-12
298.0	2.8	2.1		ESDRED	16.8	0.9	0.2	20.9	22	77.5	4.3	0.26	
298.0	2.8	0.0		ESDRED	12.1	0.0	0.2	20.9		77.5			
298.0	2.8	0.0		ESDRED	10.0	0.0	0.2	20.9		77.5			
298.1	2.8	0.0		ESDRED	10.1	0.0	0.2	20.9		77.5			
298.1	2.8	0.0		ESDRED	6.8	0.0	0.2	20.9		77.5			
298.1	2.8	0.0		ESDRED	7.1	0.0	0.2	20.9		77.5			
298.1	2.8	0.0		ESDRED	4.1	0.0	0.2	20.9		77.5			
298.2	2.8	0.0		ESDRED	4.5	0.0	0.2	20.9		77.5			
298.2	2.8	0.0		ESDRED	0.5	0.0	0.2	20.9		77.5			

Table 11-7: Chemistry of experiment Bent-CT1 (Bentonite – APW_{OPC})

Name	**APW**	**Time**	**PV**	**Syr. vol.**	**pH**	**Alkalinity**	**Na^+**		**K^+**		**Ca^{2+}**		**Mg^{2+}**		**Cl^-**		**SO_4^{2-}**		**Sr^{2+}**		**Al^{3+}**		**Si^{4+}**	
		[days]		[ml]		[mM]	[mM]	Error	[mM]	Error	[mM]	Error	[mM]	Error	[mM]	Error	[mM]	Error	[mM]	Error	[mM]	Error	[mM]	Error
CT1_1	OPA	30.6	0.03	2.4	5.2	2.9	400.1	20.0	2.8	0.1	18.3	0.9	9.0	0.5	337.3	16.9	53.4	2.7						
CT1_2	OPA	62.5	0.08	2.2	5.0		373.2	18.7	2.7	0.1	15.7	0.8	8.0	0.4	300.4	15.0	57.9	2.9	0.17	0.01	0.001	0.000	1.75	0.09
CT1_3	OPA	89.3	0.12	1.9	5.2	3.5	353.6	17.7	2.6	0.1	14.8	0.7	7.4	0.4	270.2	13.5	58.9	2.9						
CT1_4	OPA	110.6	0.16	1.3	5.2		340.9	17.0	2.5	0.1	14.1	0.7	7.2	0.4	256.3	12.8	59.3	3.0						
CT1_5	OPA	133.5	0.18	0.8	7.4		364.9	18.2	3.5	0.2	13.7	0.7	7.4	0.4	272.6	13.6	64.4	3.2						
CT1_6	OPC	158.0	0.20	1	7.9		322.3	16.1	2.4	0.1	12.9	0.6	6.7	0.3	229.8	11.5	61.4	3.1						
CT1_7	OPC	190.5	0.22	0.9	7.4	13.5	343.9	17.2	2.6	0.1	11.8	0.6	6.6	0.3	201.5	10.1	68.2	3.4	0.13	0.01	0.003	0.001	2.89	0.14
CT1_8	OPC	222.9	0.24	0.85	7.4	13.5	292.0	14.6	2.3	0.1	11.2	0.6	5.8	0.3	168.6	8.4	69.1	3.5						
CT1_9	OPC	244.3	0.26	0.7	7.3		296.6	14.8	2.5	0.1	11.2	0.6	5.9	0.3	173.3	8.7	73.4	3.7						
CT1_10	OPC	266.3	0.27	0.67	7.4		387.1	19.4	2.6	0.1	11.0	0.6	5.8	0.3	146.9	7.3	74.7	3.7						
CT1_11	OPC	289.5	0.29	0.71	7.6	9.1	274.2	13.7	2.6	0.1	10.6	0.5	5.6	0.3	142.2	7.1	79.6	4.0	0.12	0.01	0.003	0.001	3.66	0.18
CT1_12	OPC	316.0	0.31	0.86	7.8	9.1	258.1	12.9	2.8	0.1	10.2	0.5	5.5	0.3	129.8	6.5	79.5	4.0						
CT1_13	OPC	345.6	0.32	0.8	7.8		259.8	13.0	3.1	0.2	10.0	0.5	5.4	0.3	114.9	5.7	77.7	3.9						
CT1_14	OPC	375.5	0.34	0.77	7.6	9.6	263.2	13.2	3.2	0.2	10.0	0.5	5.4	0.3	112.0	5.6	83.7	4.2	0.10	0.01	0.003	0.001	4.30	0.21
CT1_15	OPC	408.0	0.36	0.93	7.9	9.6	284.7	14.2	3.8	0.2	6.0	0.3	5.7	0.3	105.9	5.3	90.1	4.5						
CT1_16	OPC	444.0	0.38	0.81	7.9	10.7	282.7	14.1	4.0	0.2	6.7	0.3	5.5	0.3	100.0	5.0	95.5	4.8						
CT1_17	OPC	497.0	0.40	0.82	7.9	10.7	341.6	17.1	5.1	0.3	6.5	0.3	6.5	0.3	85.1	4.3	90.4	4.5	0.10	0.00	0.003	0.001	5.22	0.26
CT1_18	OPC	580.0	0.41	0.63	8.2		315.8	15.8	5.1	0.3	5.9	0.3	6.3	0.3	90.8	4.5	113.2	5.7						
CT1_19	OPC	690.1	0.43	0.93	8.1		287.5	14.4	4.9	0.2	5.3	0.3	5.6	0.3	69.5	3.5	98.1	4.9						
CT1_20	OPC	756.6	0.43	0.06	7.9																			
Infiltration solutions																								
$APW_{Äspö}$				29.8	7.2	0.2	88.2	4.4	0.3	0.0	56.1	2.8	1.6	0.1	205.1	10.3	1.8	0.1	0.43	0.02	0.000	0.000	0.01	0.00
APW_{OPA}	start			8.5	7.6	0.7	165.9	8.3	2.7	0.1	11.9	0.6	9.1	0.5	157.5	7.9	22.1	1.1	0.00	0.00	0.001	0.000	0.01	0.00
APW_{OPA}	end				7.6		165.9	8.3	2.7	0.1	10.6	0.5	8.1	0.4	146.6	7.3	21.0	1.0						
APW_{OPC}	start			11.7	13.4		115.4	5.8	180.7	9.0	1.3	0.1	<0.4		<0.05		2.9	0.1	0.00	0.00	0.034	0.002	0.17	0.01
APW_{OPC}	end				13.3		114.0	5.7	173.3	8.7	<0.25		<0.4		<0.05		2.9	0.1						

Table 11-8: Chemistry of experiment Bent-CT2 (Bentonite – APW$_{ESDRED}$)

Name	APW	Time	PV	Vol.	pH	Alk.	Na^+		K^+		Ca^{2+}		Mg^{2+}		Cl^-		SO_4^{2-}		Formate	Propionate	Sr^{2+}	Al^{3+}	Si^{4+}
		days		ml		mM	mM	Error	mM	Error	mM	Error	mM	Error	mM	Error	mM	Error	mM	mM	mM	mM	mM
CT2_1	OPA	16.97	0.05	2.5	7.71	3.7	394	20	3	0.1	18	0.9	9	0.4	333	16.7	53	2.7					
CT2_2	OPA	49.92	0.10	2.2	7.9	4.5	368	18	3	0.1	16	0.8	8	0.4	307	15.4	59	2.9			0.2	0.001	1.79
CT2_3	OPA	75.39	0.13	1.3	8.0	4.5	364	18	3	0.1	16	0.8	8	0.4	269	13.5	57	2.9	<0.43	0.7			
CT2_4	OPA	96.52	0.14	0.8	7.57		347	17	3	0.1	14	0.7	7	0.4	273	13.7	60	3.0					
CT2_5	OPA	126.07	0.18	1.5	8.0	5.7	386	19	3	0.1	15	0.8	8	0.4	269	13.5	63	3.1					
CT2_6	OPA	167.95	0.20	1.1	7.9	5.7	387	19	3	0.2	14	0.7	9	0.4	291	14.6	68	3.4			0.2	0.003	2.22
CT2_7	OPA	203.41	0.22	0.9	8.0		347	17	3	0.1	14	0.7	7	0.4	250	12.5	63	3.1					
CT2_8	OPA	229.91	0.24	0.9	7.8		346	17	3	0.1	14	0.7	7	0.4	281	14.0	65	3.2					
CT2_9	OPA	256.47	0.26	1.0	7.9	5.7	367	18	4	0.2	12	0.6	8	0.4	260	13.0	68	3.4	<0.43	0.4			
CT2_10	OPA	273.43	0.27	0.5	8.0	5.7	327	16	3	0.1	13	0.6	8	0.4	228	11.4	62	3.1	<0.43				
CT2_11	ESDRED	291.85	0.28	0.6	7.9	5.7	349	17	3	0.1	13	0.7	8	0.4	247	12.3	68	6.8	<0.43		0.1	0.003	2.68
CT2_12	ESDRED	318.37	0.29	0.7	8.0	6.1	335	17	3	0.1	14	0.7	8	0.4	225	11.3	65	6.5	<0.43				
CT2_13	ESDRED	353.23	0.31	0.8	7.9	6.1	360	18	3	0.1	11	0.5	8	0.4	233	11.6	74	3.7	<0.43	0.4	0.1	<0.0019	4.28
CT2_14	ESDRED	458.77	0.32	0.4	8.0		624	62	5	0.3	13	0.7	14	0.7	203	10.2	67	3.4	<0.43	0.3			
Infiltration fluids																							
APW$_{Äspö}$				29.0	7.2		92	5	0	0.0	13	0.7	14	0.7	203	10.2	67	3.4	0	0	0.4	0.0004	<0.007
APW$_{OPA}$	start			12.2	7.6		166	8	3	0.1	13	0.7	14	0.7	203	10.2	67	3.4	0	0	0.0	0.0006	<0.007
APW$_{OPA}$	end				7.3		239	12	4	0.2	13	0.7	14	0.7	203	10.2	67	3.4					
APW$_{ESDRED}$	start			2.8	11.8		25	1	13	0.6	13	0.7	14	0.7	203	10.2	67	3.4	76.02	<0.05	0.0	0.0019	0.07
APW$_{ESDRED}$	end				11.4		24	1	12	0.6	13	0.7	14	0.7	203	10.2	67	3.4	66.13	<0.3			

Table 11-9: Chemistry of experiment S/B-CT3 (Sand/Bentonite – APW$_{OPC}$)

Name	**APW**	**Time**	**PV**	**Vol.**	**pH**	**Alk.**	**Na$^+$**		**K$^+$**		**Ca^{2+}**		**Mg^{2+}**		**Cl-**		**SO$_4^{2-}$**		**Acetate**	**C$_{org}$**	**C$_{inorg}$**	**Sr^{2+}**	**Al^{3+}**	**Si^{4+}**
		[days]		[ml]		[mM]	[mM]	Error	[mM]	Error	[mM]	Error	[mM]	Error	[mM]	Error	[mM]	Error	[mM]	[mM]	[mM]	[mM]	[mM]	[mM]
CT3_1	OPA	1.5	0.08	2.2	6.4		178	9	2.4	0.1	14.4	0.7	3.2	0.2	160.0	8.0	24.2	1.2				0.2	0.0	1.3
CT3_2	OPA	5.3	0.13	1.7	7.0	1.5	167	8	2.4	0.1	15.4	0.8	2.4	0.1	164.6	8.2	21.0	1.1						
CT3_3	OPA	11.5	0.25	2.8	6.8		187	9	2.4	0.1	14.4	0.7	2.6	0.1	176.2	8.8	26.7	1.3						
CT3_4	OPA	19.0	0.44	5.2	6.5		192	10	2.5	0.1	13.6	0.7	2.7	0.1	176.2	8.8	31.5	1.6						
CT3_5	OPA	25.3	0.58	3.8	6.7		197	10	2.4	0.1	12.7	0.6	2.8	0.1	170.7	8.5	31.0	1.6						
CT3_6	OPA	33.4	0.73	3.8	5.6	1.2	196	10	2.4	0.1	11.8	0.6	2.7	0.1	160.2	8.0	28.4	1.4				0.1	0.0	1.8
CT3_7	OPA	41.4	0.81	6.3	6.1		186	9	2.3	0.1	10.4	0.5	2.5	0.1	161.8	8.1	27.4	1.4	3.6					
CT3_8	OPA	51.8	1.15	5.1	6.5	1.3	190	9	2.4	0.1	9.9	0.5	2.5	0.1	156.4	7.8	25.3	1.3						
CT3_9	OPA	67.0	1.39	6.5	6.7		191	10	2.3	0.1	9.2	0.5	2.5	0.1	155.8	7.8	21.8	1.1		55.8	<0.21			
CT3_10	OPA	87.7	1.73	9.0	7.0	26.2	192	10	2.2	0.1	8.4	0.4	2.7	0.1	153.6	7.7	10.3	0.5				0.1	0.0	2.1
CT3_11	OPA	115.9	2.08	9.3	7.5		191	10	2.3	0.1	7.9	0.4	2.8	0.1	156.6	7.8	6.6	0.3						
CT3_12	OPA	141.4	2.42	9.2	7.4		198	10	2.3	0.1	8.0	0.4	3.2	0.2	162.9	8.1	7.9	0.4						
CT3_13	OPA	159.0	2.73	8.3	7.5	29.4	196	10	2.4	0.1	7.9	0.4	3.3	0.2	159.9	8.0	9.5	0.5						
CT3_14	OPA	174.1	3.11	10.2	7.4		197	10	2.4	0.1	8.1	0.4	3.5	0.2	151.4	7.6	11.5	0.6						
CT3_15	OPA	187.4	3.35	9.5	7.5		162	8	1.9	0.1	6.6	0.3	3.0	0.2	135.5	6.8	11.0	0.6						
CT3_16	OPA	208.3	3.82	9.5	7.4		203	10	2.5	0.1	7.9	0.4	3.9	0.2	137.9	6.9	11.4	0.6						
CT3_17	OPA	233.7	4.16	9.1	7.5		202	10	2.3	0.1	8.4	0.4	4.2	0.2	143.9	7.2	11.9	0.6						
CT3_18	OPA	253.8	4.52	9.7	7.5	15.2	165	8	2.0	0.1	7.0	0.3	3.7	0.2	146.9	7.3	11.2	0.6				0.1	0.0	1.7
CT3_19	OPA	284.5	4.87	9.0	7.7		179	9	2.2	0.1	7.7	0.4	4.2	0.2	155.2	7.8	11.3	0.6						
CT3_20	OPA	299.3	5.15	7.5	7.8		207	10	2.4	0.1	9.1	0.5	5.1	0.3	185.0	9.3	13.5	0.7						
CT3_21	OPA	321.2	5.50	9.3	7.6		186	9	2.1	0.1	8.5	0.4	4.8	0.2	162.1	8.1	12.7	0.6						
CT3_22	OPA	336.9	5.83	8.9	7.5		206	10	2.3	0.1	9.5	0.5	5.4	0.3	164.6	8.2	12.6	0.6						
CT3_23	OPC	354.2	5.91	1.8	7.5		182	9	2.1	0.1	8.2	0.4	4.7	0.2	152.4	7.6	11.4	0.6						
CT3_24	OPC	359.24	5.97	1.4	7.6	18.4	196	10	2.2	0.1	8.1	0.4	4.7	0.2	133.1	6.7	9.7	0.5				0.1	0.0	1.8
CT3_25	OPC	365.3	6.04	1.8	7.4		136	7	1.6	0.1	4.9	0.2	2.9	0.1	111.6	5.6	8.4	0.4						
CT3_26	OPC	376.2	6.14	2.3	8.0		98	5	1.2	0.1	2.4	0.1	1.6	0.1	74.4	3.7	5.3	0.3	0.5			0.0	<0.002	1.6
CT3_27	OPC	389.0	6.22	1.9	8.1		84	4	1.1	0.1	1.7	0.1	1.0	0.1	59.1	3.0	2.9	0.1	0.2					
CT3_28	OPC	402.74	6.36	3.1	8.0	22.8	66	3	1.0	0.1	1.1	0.1	0.6	0.1	41.6	2.1	1.2	0.1	0.0					
CT3_29	OPC	417.02	6.47	2.2	8.0		39	2	0.8	0.0	0.6	0.0	0.0		21.0	1.0	0.3	0.0	0.3			0.0	<0.002	1.8
CT3_30	OPC	430.96	6.54	2.0	8.2		29	1	0.7	0.0	0.4	0.0	0.0		13.5	0.7	0.1	0.0	1.5					
CT3_31	OPC	445.45	6.59	1.2	8.3		18	1	0.7	0.0	0.3	0.0	0.0		4.7	0.2	0.0	0.0	0.7					
CT3_32	OPC	468.1	6.70	1.7	8.3		31	2	1.2	0.1	0.3	0.0	0.0		7.4	0.4	0.0	0.0	0.7			0.0	<0.002	2.1
CT3_33	OPC	498.60	6.75	2.3	8.6	23.9	23	1	0.9	0.0	<0.2		0.0		5.7	0.3	<0.04		0.0					
CT3_34	OPC	531.91	6.83	1.5	8.6	23.9	23	1	1.2	0.1	<0.2		0.0		2.5	0.1	0.1	0.0	0.0					
CT3_35	OPC	563.54	6.87	0.7	8.6		23	1	1.4	0.1	<0.2		0.0		1.9	0.1	0.1	0.0	0.0					
Infiltration fluids																								
APW$_{Äspö}$					7.2	0.2	88	4	0.3	0.0	56.1	2.8	1.6	0.1	205.1	10.3	1.8	0.1				0.4	0.0	0.0
APW$_{OPA}$	start				7.6	0.7	166	8	2.7	0.1	11.9	0.6	9.1	0.5	157.5	7.9	22.1	1.1				0.0	0.0	0.0
APW$_{OPA}$	end				7.6		167	8	3.7	0.2	12.9	0.6	10.1	0.5	158.5	7.9	23.1	1.2						

Name	**APW**	**Time**	**PV**	**Vol.**	**pH**	**Alk.**	**Na^+**		**K^+**		**Ca^{2+}**		**Mg^{2+}**		**Cl-**		**SO_4^{2-}**		**Acetate**	**C_{org}**	**C_{inorg}**	**Sr^{2+}**	**Al^{3+}**	**Si^{4+}**
APW_{OPC}	start				13.5	309.0	123	6	186.7	37.3	0.6	0.0	<0.41		2.5	0.1	3.5	0.2				0.0	0.0	0.2
APW_{OPC}	end				13.4		120	6	182.6	9.1	0.5	0.1	<0.41		<0.05		3.1	0.2						

Table 11-10: Chemistry of experiment s/b – CT4 (Sand/Bentonite – APW$_{ESDRED}$)

Name	**APW**	**Time**	**PV**	**Vol.**	**pH**	**Alk.**	**Na$^+$**		**K$^+$**		**Ca^{2+}**		**Mg^{2+}**		**Cl$^-$**		**SO$_4^{2-}$**		**Acetate**	**Formate**	**Sr^{2+}**	**Al^{3+}**	**Si^{4+}**
		[days]		[ml]		[mM]	[mM]	Error	[mM]	Error	[mM]	Error	[mM]	Error	[mM]	Error	[mM]	Error	[mM]	[mM]	[mM]	[mM]	[mM]
CT4_1	OPA	1.1	0.00	3.5	6.5		228	5	102.4	2.6	363.7	9.1	67.8	2.8	233.7	11.7	18.7	0.9					
CT4_2	OPA	6.0	0.27	4.3	7.0		220	4	103.0	2.6	312.1	7.8	61.5	2.5	216.3	10.8	17.4	0.9					
CT4_3	OPA	12.0	0.34	1.9	7.0	1.6	209	4	100.1	2.6	288.2	7.2	57.5	2.4	199.3	10.0	17.3	0.9			0.10	0.001	1.76
CT4_4	OPA	41.2	0.56	4.6	7.6	3.0	205	4	103.5	2.6	303.0	7.6	61.4	2.5	147.7	7.4	15.3	0.8	<0.3	<0.4			
CT4_5	OPA	55.0	0.67	3.0	7.5		197	4	104.4	2.7	321.0	8.0	67.3	2.8	176.8	8.8	21.3	1.1	<0.3	<0.4			
CT4_6	ESDRED	62.9	0.80	3.0	7.6		163	3	84.5	2.2	278.0	6.9	59.0	2.4	147.2	7.4	19.4	1.0	<0.3	<0.4	0.11	<0.0019	1.57
CT4_7	ESDRED	66.4	0.88	2.8	7.6	4.5	123	2	64.8	1.7	207.0	5.2	44.8	1.8	111.5	5.6	15.5	0.8	<0.3	<0.4			
CT4_8	ESDRED	72.5	0.95	1.6	7.8		162	3	87.9	2.2	247.0	6.2	54.0	2.2	137.5	6.9	21.0	1.1	<0.3	<0.4			
CT4_9	ESDRED	82.0	1.11	4.6	8.0	11.4	142	3	82.2	2.1	173.0	4.3	40.6	1.7	108.2	5.4	18.8	0.9	<0.3	0.3	0.06	<0.0019	1.88
CT4_10	ESDRED	96.1	1.23	3.3	8.0		98	2	52.1	1.3	102.0	2.5	25.0	1.0	63.7	3.2	13.3	0.7	0.6	11.6			
CT4_11	ESDRED	110.1	1.35	3.3	7.8	26.6	89	2	44.9	1.1	78.0	1.9	20.0	0.8	41.7	2.1	9.6	0.5	9.7	9.9			
CT4_12	ESDRED	124.5	1.48	3.7	7.7		72	1	33.6	0.9	48.0	1.2	0.0	0.0	25.5	1.3	6.1	0.3	22.2	<0.4	0.02	<0.0019	2.01
CT4_13	ESDRED	132.0	1.60	3.6	7.7		63	1	30.5	0.8	38.0	0.9	10.7	0.4	15.4	0.8	4.1	0.2	20.1	<0.4			
CT4_14	ESDRED	156.0	1.80	4.2	7.8	35.3	44	1	15.0	0.4	25.8	0.6	<10	<0.4	6.6	0.3	2.2	0.1	23.1	<0.4			
CT4_15	ESDRED	170.5	1.85	2.4	7.8		46	1	15.5	0.4	27.3	0.7	<10	<0.4	4.8	0.2	2.1	0.1	27.1	<0.4			
CT4_16	ESDRED	185.1	2.00	4.1	7.7		46	1	15.4	0.4	26.4	0.7	<10	<0.4	2.8	0.1	1.7	0.1	21.1	<0.4			
CT4_17	ESDRED	205.3	2.17	4.8	7.7	40.0	45	1	16.2	0.4	25.3	0.6	<10	<0.4	2.0	0.1	1.9	0.1	22.6	<0.4			
CT4_18	ESDRED	223.7	2.28	3.2	7.8		44	1	16.0	0.4	23.9	0.6	<10	<0.4	1.5	0.1	1.9	0.1	24.9	<0.4			
CT4_19	ESDRED	241.5	2.44	3.2	7.8		53	1	22.0	0.6	28.6	0.7	<10	<0.4	0.5	0.0	1.0	0.0	28.5	<0.4	0.01	<0.0019	2.07
CT4_20	ESDRED	264.7	2.65	3.8	7.8	41.1	25	0	31.2	0.8	18.8	0.5	<10	<0.4	0.2	0.0	0.4	0.0	25.2	<1.1			
CT4_21	ESDRED	284.2	2.70	2.8	7.8		47	1	46.9	1.2	25.4	0.6	<10	<0.4	0.2	0.0	0.2	0.0	25.5	<1.1			
CT4_22	ESDRED	294.5	2.80	1.1	7.9		48	1	49.1	1.3	25.5	0.6	<10	<0.4	0.2	0.0	0.2	0.0	26.2	<1.1			
Infiltration fluids																							
APW$_{Äspö}$					7.2	0.2	88	9	0.3	0.1	56.1	2.8	1.6	0.3	205.1	10.3	1.8	0.1			0.43	0.000	<0.007
APW$_{OPA}$	start				7.4	0.7	170	17	2.7	0.1	12.4	0.6	9.4	1.9	157.4	7.9	22.7	1.1			0.00	0.001	<0.007
APW$_{OPA}$	end				7.3		158	16	2.8	0.1	11.4	0.6	8.5	1.7	151.9	7.6	21.7	1.1	<0.85	<1.1			
APW$_{ESDRED}$	start				11.7	17.0	24	2	12.6	0.6	26.0	1.3	<0.4		9.8	0.5	4.2	0.2	<0.3	66.1	0.00	0.001	0.07
APW$_{ESDRED}$	end				11.6		17	2	8.7	0.4	17.6	0.9	<0.4		<0.05		1.5	0.1	<0.85	79.6			

Table 11-11: Chemistry of experiment s/b – CT3 (Sand/Bentonite – APW$_{OPC}$)

Time [days]	**APW**	**C$_{Org}$** [mM]	Error	**C$_{Inorg}$** [mM]	Error	**D$_2$O** [‰ vs. VSMOW]
1.5	OPA					
5.3	OPA					
11.5	OPA					
19.0	OPA					
25.3	OPA					
33.4	OPA					
41.4	OPA					
51.8	OPA					
67.0	OPA	55.8	2.8	<0.21		
87.7	OPA					
115.9	OPA					
141.4	OPA					
159.0	OPA					
174.1	OPA					
187.4	OPA					
208.3	OPA					
233.7	OPA					
253.8	OPA					
284.5	OPA					
299.3	OPA					
321.2	OPA					
336.9	OPA					-81.9
354.2	OPC					-78.8
359.2	OPC					-68.8
365.3	OPC					-45.5
376.2	OPC					-4.4
389.0	OPC					36.8
402.7	OPC					61.2
417.0	OPC					89.5
431.0	OPC					108.5
445.4	OPC					122.9
468.1	OPC					139.1
498.6	OPC					150.5
531.9	OPC					
563.5	OPC					
			Infiltration fluids			
APW$_{Äspö}$						-81.5
APW$_{OPA}$						-81.6
APW$_{OPC}$		0.0		1.50	0.07	273.7

Table 11-12: Chemistry of experiment s/b – CT4 (Sand/Bentonite – APW_{ESDRED})

APW	**Time** [days]	C_{Org} [mM]	Error	C_{Inorg} [mM]	Error	D_2O [‰ vs. VSMOW]
OPA	1.1					
OPA	6.0	4.1	0.2	1.9	0.1	
OPA	12.0					
OPA	41.2					
OPA	55.0					-81.3
ESDRED	62.9					-82.7
ESDRED	66.4					-76.1
ESDRED	72.5					-52.1
ESDRED	82.0					-19.3
ESDRED	96.1					28.8
ESDRED	110.1					60.6
ESDRED	124.5					87.2
ESDRED	132.0					109.7
ESDRED	156.0					129.8
ESDRED	170.5					145.5
ESDRED	185.1					
ESDRED	205.3					
ESDRED	223.7					
ESDRED	241.5					
ESDRED	264.7					
ESDRED	284.2					
ESDRED	294.5					
Infiltration fluids						
$APW_{Äspö}$						-81.5
APW_{OPA}						-81.6
APW_{ESDRED}		86.2	4.3	0.3	0.1	267.0

Table 11-13: Durations of experiments.

Experiment	**CT1**	**CT2**	**CT3**	**CT4**
Infiltration APW	**OPC**	**ESDRED**	**OPC**	**ESDRED**
Name	Bent-CT1	Bent-CT2	S-B-CT3	S-B-CT4
Duration [days]	748	543	579	298
APW$_{\text{Äspö}}$	80	62	22	33
APW$_{\text{OPA}}$	136	271	352	56
APW$_{\text{OPC}}$	625	-	227	-
APW$_{\text{ESDRED}}$	-	272	-	242

Table 11-14: Overview of all CT scans.

Experiment	**CT1**		**CT2**		**CT3**		**CT4**	
Infiltration APW	**OPC**		**ESDRED**		**OPC**		**ESDRED**	
No. of scans	20		8		11		5	
Siemens Somatom Emotion 6 (old)	19		8		7		1	
Siemens Somatom Definition AS 40 (new)	1		0		4		4	
Name and time [days]	CT1-1	0	CT2-10	0	CT3-12	0	CT4-24	0
	CT1-2	0	CT3-13	9	CT3-18	0	CT4-25	6
	CT1-3	0	CT2-14	15	CT3-20	1	CT4-26	54
	CT1-4	0	CT3-15	27	CT3-21	3	CT4-27	111
	CT1-5	2	CT2-16	57	CT3-22	5	CT4-28	151
	CT1-6	2	CT3-17	117	CT3-23	15		
	CT1-7	3	CT2-18	166	CT3-24	30		
	CT1-8	8	CT3-19	224	CT3-25	59		
	CT1-9	16			CT3-26	106		
	CT1-10	36			CT3-27	164		
	CT1-11	72			CT3-28	204		
	CT1-12	137						
	CT1-13	207						
	CT1-15	228						
	CT1-16	255						
	CT1-17	354						
	CT1-18	364						
	CT1-19	423						
	CT1-20	483						
	CT1-26	588						

Table 11-15: Overview of all XRD powder samples.

Experiment	**CT1**		**CT2**		**CT3**		**CT4**	
Infiltration APW	**OPC**		**ESDRED**		**OPC**		**ESDRED**	
Name	CT1_X		Bent-CT2_X		CT3-X		CT4-X	
XRD scan at 0 %rh			x					
XRD scan at 100 %rh			x					
XRD scan at 33 %rh	x		x		x		x	
XRD scan EG sat.	x				x		x	
Name and distance [cm]	CT1-1	4.6	Bent-CT2-1	4.5	CT3-1	4.1	CT3-1	4
	CT1-2	4.25	Bent-CT2-2	4.1	CT3-2	3.8	CT3-2	3.6
	CT1-3	3.8	Bent-CT2-3	3.5	CT3-3	3.25	CT3-3	3.05
	CT1-4	3.35	Bent-CT2-4	2.9	CT3-4	2.75	CT3-4	2.45
	CT1-5	2.65	Bent-CT2-5	2.3	CT3-5	2.25	CT3-5	1.8
	CT1-6	2.12	Bent-CT2-6	1.7	CT3-6	1.7	CT3-6	1.35
	CT1-7	1.7	Bent-CT2-7	1.1	CT3-7	1.25	CT3-7	1.1
	CT1-8	1.3	Bent-CT2-8	0.7	CT3-8	0.75	CT3-8	0.9
	CT1-9	1	Bent-CT2-9	0.45	CT3-9	0.25 (off-cen)	CT3-9	0.65
	CT1-10	0.7	Bent-CT2-10	0.2	CT3-10	0.25	CT3-10	0.3
	CT1-11	0.4	Bent-CT2-11	0.5			CT3-11	0.05
	CT1-12	0.2 (off-center)	Bent-CT2-12	0.5 (off-center)			CT3-12	0
	CT1-13							
	CT1-14	0.2						
	CT1-15	0.05						
	CT1-16	0						

11.3. CrunchFlow script

```
TITLE
Experiment Bentonite_APW_OPC
END

DATABASE
CEMDATA07_EQ3_6_Thermoddem_Florian.dbs
END

RUNTIME
time_units      days
timestep_max    0.1
timestep_init   1.e-17
debye-huckel    true
lag_activity    true
database_sweep  false
hindmarsh       true
time_tolerance  0.001
correction_max  2.0
gimrt           true
master_variable H+
speciate_only   false
screen_output   100
save_restart    crunch.rst
later_inputfiles    opc1.in opc1a.in opc2.in
END

OUTPUT
time_units    days
spatial_profile  XXXX (duration of the phase)
time_series_at_node      Exclusion.out 27 1 1
time_series_print        XXX
time_series_interval     1
END

PRIMARY_SPECIES
H+
Na+
K+
Ca++
Mg++
Al+++
HCO3-
Cl-
SO4--
Zr(OH)2++
H4SiO4
Tracer
Fe+++
END

SECONDARY_SPECIES
AlSO4+
Al(SO4)2-
Al(OH)2+
AlO2-
Al(OH)4-
AlOH++
CaCO3(aq)
CaHCO3+
CaSO4(aq)
CaOH+
FeCl++
FeSO4+
Fe(SO4)2-
Fe(OH)3(aq)
Fe2(OH)2++++
FeCl2+
FeOH++
Fe(OH)2+
Fe(OH)4-
KSO4-
KCl(aq)
KOH(aq)
MgCO3(aq)
MgHCO3+
MgOH+
MgSO4(aq)
SiO(OH)3-
SiO2(OH)2--
NaCl(aq)
NaCO3-
NaHCO3(aq)
NaSO4-
NaOH(aq)
CO2(aq)
CO3--
HSO4-
OH-
Zr++++
SiO2(aq)
CaHSiO3+
NaHSiO3(aq)
END

SURFACE_COMPLEXATION
>montmor     on Montmor-MX80 -no_edl
END

ION_EXCHANGE
UseDoubleLayer   Montmor-MX80
END

MINERALS
Anorthite
Calcite
Cristobalite(alpha)
Gypsum_Th
Illite
Montmor-MX80
Muscovite
Quartz
Zircon
Al(OH)3am_CD
Anhydrite_CD
Brucite_CD
CAH10_CD
C2AH8_CD
C2FH8_CD
C4AH13_CD
CSH_jen_CD
CSH_tob2_CD
Chalcedony
Ettringite_CD
Fe(OH)3mic_CD
Fe-Hemicarbonate_CD
Fe-Ettringite_CD
Fe-Monocarbonate_CD
Fe-Monosulfate_CD
Fe-Stratlingite_CD
Hemicarboaluminate_CD
HydrogarnetOH_CD
HydrogarnetFe_CD
HydrogarnetSi_CD
HydrotalciteC_CD
HydrotalciteOH_CD
HydrotalciteFe_CD
Monocarboaluminate_CD
Monosulfoaluminate_CD
Portlandite_CD
Tricarboaluminate_CD
Saponite(Mg)
Talc
Clinochlore-7A
Clinochlore-14A
END

GASES
CO2(g)
END

POROSITY
fix_microporosity  0.3944
UpdateDDL              true
CalculateMicroporosity  on Montmor-MX80
SumMicroMacroporosity   false
DebyeLengths            0.8
porosity_update         true
END

TEMPERATURE
set_temperature      25.0
END

DISCRETIZATION
distance_units  centimeters
xzones          2  0.1  25  0.2
END

Condition botfilter
(Identical to infiltration solution)
units            mmol/kg
temperature      25.0
Tracer            0.0
Zircon           0.20
Montmor-MX80       1e-10
END

Condition infiltration_solution
(Infiltration solutions; varies with phases)
units            mmol/kg
temperature      25.0
Tracer       1
END

Condition Bentonite
!! Spritze Nr. 1 CT1
units            mmol/kg
temperature      25.0
pH               7.5
Ca++               18
Mg++               9.0
K+               3.0
Na+               400.0
Cl-             337
H4SiO4          1.75
Al+++            0.0014
SO4--            53.0
Zr(OH)2++         0.0
Fe++      0.0
Fe+++      0.0
HCO3-            2.87
Tracer           0.0
CO2(aq)      CO2(g)     3.e-04
>montmor          12.567e-8
FixedMineralCharge    0.00068
Montmor-MX80     0.7199  specific_surface_area   788.0
Calcite          0.002
Gypsum_Th         0.0086
Cristobalite(alpha)  0.058
Quartz        0.076
Anorthite       0.031
Muscovite       0.03
Illite     0.007
END

INITIAL_CONDITIONS
botfilter   1-2 1-1 1-1
Bentonite   3-27 1-1 1-1
END

BOUNDARY_CONDITIONS
X_begin   infiltration_solution   Flux
X_end     Bentonite               Flux
END

TRANSPORT
distance_units          meters
time_units              second
fix_diffusionMP 1.3E-12
fix_diffusion   1.3E-9

D_MP  H+       8.57e-12
D_MP  Na+       1.33e-12
D_MP  K+       1.96e-12
D_MP  Al+++     0.514e-12
D_MP  Cl-      1.0e-16
D_MP  Mg++      0.70e-12
D_MP  Ca++      0.79e-12
D_MP  H4SiO4    1.0e-12
D_MP  SO4--     1.0e-12
D_MP  HCO3-     1.0e-16
D_MP  Tracer    1.87e-12
D_25  H+       8.57e-9
D_25  Na+       1.33e-9
D_25  K+       1.96e-9
D_25  Al+++    0.514e-9
D_25  Cl-      2.03e-9
D_25  Mg++      0.70e-9
D_25  Ca++      0.79e-9
D_25  H4SiO4    1.0e-9
D_25  SO4--     1.06e-9
D_25  HCO3-     1.18e-9
D_25  Tracer    1.87e-9
END

FLOW
distance_units  meters
time_units  seconds
constant_flow XXXXXX
threshold_porosity      0.01
tuortuosity_below 1e-10
turtuosity_above 1.0
END
```

Declaration of consent

on the basis of Article 28 para. 2 of the RSL05 phil.-nat.

Name/First Name:	Dolder Florian
Matriculation Number:	04-921-946
Study program:	Earth Sciences
	Bachelor ☐ Master ☐ Dissertation ☑
Title of the thesis:	Experimental characterization and quantification of cement - bentonite interaction using core infiltration techniques coupled with X-ray tomography
Supervisor:	PD Dr. Urs Mäder

I declare herewith that this thesis is my own work and that I have not used any sources other than those stated. I have indicated the adoption of quotations as well as thoughts taken from other authors as such in the thesis. I am aware that the Senate pursuant to Article 36 para. 1 lit. r of the University Act of 5 September, 1996 is authorised to revoke the title awarded on the basis of this thesis. I allow herewith inspection in this thesis.

Bern, 19.June 2015

Place/Date

Signature

12 Curriculum Vitae

Personal Information

Name	Dolder
First name	Florian
Date of birth	June 11, 1983
Nationality	Swiss
E-mail	fdolder@gmail.com

Academic Background

Feb 2011 – Sept 2015	**PhD in Phil.-Nat at University of Bern** Topic: Experimental characterization and quantification of cement-bentonite interaction using core infiltration techniques coupled with X-ray tomography.
2007 – 2009	**MSc. ETH in Earth Sciences**
2004 – 2007	**BSc. ETH in Earth Sciences**